

HIGH VELOCITY JET NOISE SOURCE LOCATION AND REDUCTION

TASK 3 - EXPERIMENTAL INVESTIGATION OF SUPPRESSION PRINCIPLES

Volume I - Suppressor Concepts Optimization

AD A094293

TECHNICAL CONTRIBUTORS:

R.H. Brown	E.J. Stringas
W.S. Clapper	P.G. Vogt
W. Joy	R.W. Whittaker
M.A. Smith	J.P. Wolf

**GENERAL ELECTRIC COMPANY
AIRCRAFT ENGINE GROUP
CINCINNATI, OHIO 45215**



DECEMBER 1978

FINAL REPORT

Document is available to the U.S. public through
the National Technical Information Service,
Springfield, Virginia 22161.

Prepared for

**U.S. DEPARTMENT OF TRANSPORTATION
FEDERAL AVIATION ADMINISTRATION
Systems Research & Development Service
Washington, D.C. 20590**

NOTICE

The contents of this report reflect the views of the General Electric Company which is responsible for the facts and the accuracy of the data presented herein. The contents do not necessarily reflect the official views or policy of the Department of Transportation. This report does not constitute a standard, specification or regulation.

1. Report No. FAA-RD-76-79, III-I		2. Government Accession No.		3. Recipient's Catalog No.	
4. Title and Subtitle HIGH VELOCITY JET NOISE SOURCE LOCATION AND REDUCTION, Task 3 - Experimental Investigation of Suppression Principles, Volume I - Verification of Suppression Principles and Development of Suppression Prediction Methods				5. Report Date December 1978	
				6. Performing Organization Code	
7. Author(s) P.R. Gliebe, R. Motsinger, A. Sieckman W.S. Clapper (Task 3 Technical Director and Editor) E.J. Stringas (Technical Project Manager)				8. Performing Organization Report No. R78AEG627	
9. Performing Organization Name and Address General Electric Company Advanced Engine Engineering Division Aircraft Engine Group Cincinnati, Ohio 45215				10. Work Unit No.	
				11. Contract or Grant No. DOT-OS-30034	
12. Sponsoring Agency Name and Address U.S. Department of Transportation Federal Aviation Administration Systems Research and Development Service Washington, D.C. 20590				13. Type of Report and Period Covered Task 3, Volume I October 1974 - October 1977	
				14. Sponsoring Agency Code	
15. Supplementary Notes Related documents to be issued include the following final reports: Task 1 - Activation of Facilities and Validation of Source Location Techniques, Task 1 Supplement - Certification of the General Electric Jet Noise Anechoic Test Facility, Task 2 - Theoretical Developments and Basic Experiments, Task 4 - Development/Evaluation of Techniques for "Inflight" Investigation, Task 5 - Investigation of "Inflight" Aero-Acoustic Effects, Task 6 - Noise Abatement Nozzle Design Guide, FAA Program Monitor: R.S. Zuckerman.					
16. Abstract <p>Experimental investigations of suppression principles were conducted including developing an experimental data base, developing a better understanding of jet noise suppression principles, and formulating empirical methods for the acoustic design of jet noise suppressors. Acoustic scaling has been experimentally demonstrated, and five "optimum" nozzles have been selected for subsequent anechoic free-jet testing.</p> <p>This report is organized into four volumes under separate cover: Volume I - Verification of Suppression Principles and Development of Suppression Prediction Methods, Volume II - Parametric Testing and Source Measurements, Volume III - Suppressor Concepts Optimization, and Volume IV - Laser Velocimeter Time-Dependent Cross Correlation Measurements.</p> <p>The experimental studies reported in Volume II involved acquisition of detailed far-field, acoustic data and of aerodynamic jet-flow-field data on several baseline and noise-abatement nozzles. These data were used to validate the theoretical jet noise prediction method of Task 2 and to develop and validate the empirical noise-prediction method presented herein.</p> <p>A series of seven suppressor configurations (ranging from geometrically simple to complex) were tested to establish the relative importance of four jet noise mechanisms (fluid shielding, convective amplification, turbulent mixing, and shock noise). In general, mechanical suppressors exhibit a significant reduction in shock noise relative to a baseline conical nozzle, reduce the effectiveness of fluid shielding (increase rather than suppress noise), reduce the effectiveness of convective amplification (reduce noise), and produce a modest reduction in turbulent mixing noise.</p> <p>Aerodynamic flow-field measurement (mean-velocity profiles) were demonstrated to be useful in verifying flow-field predictions. Noise source location devices such as the Ellipsoidal Mirror (EM) were demonstrated to be less useful than the Laser Velocimeter (LV), because the LV provides discrete volume element information not available from EM measurements.</p> <p>The empirical jet-noise prediction method has been developed to predict the static, acoustic characteristics of multielement suppressors applicable to both advanced turbojets and variable-cycle engines (which are representative of power plants for future, supersonic-cruise aircraft).</p>					
17. Key Words (Suggested by Author(s)) Jet Noise, suppression mechanisms, semi-empirical prediction methods, theory/data comparisons, accuracy, computerized method				18. Distribution Statement Document is available to the U.S. public through the National Technical Information Service, Springfield, Virginia 22161.	
19. Security Classif. (of this report) UNCLASSIFIED		20. Security Classif. (of this page) UNCLASSIFIED		21. No. of Pages 350	
				22. Price*	

* For sale by the National Technical Information Service, Springfield, Virginia 22151

METRIC CONVERSION FACTORS

Approximate Conversions to Metric Measures			
Symbol	When You Know	Multiply by	To Find
LENGTH			
in	inches	2.5	centimeters
ft	feet	30	centimeters
yd	yards	0.9	meters
mi	miles	1.6	kilometers
AREA			
sq ft	square feet	0.09	square centimeters
sq yd	square yards	0.8	square meters
sq mi	square miles	2.6	square kilometers
acre	acres	0.4	hectares
MASS (weight)			
ounce	ounces	28	grams
lb	pounds	0.45	kilograms
short ton	short tons	0.9	metric tons
VOLUME			
liters	liters	1	liters
qt	quarts	0.95	liters
pt	pints	0.47	liters
gal	gallons	3.8	liters
cu ft	cubic feet	0.03	cubic meters
yd ³	cubic yards	0.76	cubic meters
TEMPERATURE (exact)			
°F	Fahrenheit temperature	5/9 (after subtracting 32)	Celsius temperature
°C	Celsius temperature	9/5 (then add 32)	Fahrenheit temperature

* 1 in = 2.54 centimeters. For other exact conversions and more detailed tables, see NIST Special Publication 800-43, NIST Special Publication 800-43-1, and NIST Special Publication 800-43-2.

Approximate Conversions from Metric Measures			
Symbol	When You Know	Multiply by	To Find
LENGTH			
mm	millimeters	0.04	inches
cm	centimeters	0.4	inches
m	meters	3.3	feet
dm	decimeters	1.1	yards
km	kilometers	0.6	miles
AREA			
sq cm	square centimeters	0.16	square inches
sq m	square meters	1.2	square yards
sq km	square kilometers	0.4	square miles
ha	hectares (10,000 m ²)	2.5	acres
MASS (weight)			
g	grams	0.035	ounces
kg	kilograms	2.2	pounds
t	metric tons (1,000 kg)	1.1	short tons
VOLUME			
ml	milliliters	0.03	fluid ounces
l	liters	2.1	pints
l	liters	1.06	quarts
l	liters	0.26	gallons
m ³	cubic meters	35	cubic feet
m ³	cubic meters	1.3	cubic yards
TEMPERATURE (exact)			
°C	Celsius temperature	9/5 (then add 32)	Fahrenheit temperature
°F	Fahrenheit temperature	5/9 (then subtract 32)	Celsius temperature



PREFACE

This report describes the work performed under Task 3 of the DOT/FAA High Velocity Jet Noise Source Location and Reduction Program (Contract DOT-OS-30034). The objectives of the contract were:

- Investigation, including scaling effects, of the aerodynamic and acoustic mechanisms of various jet noise suppressors.
- Analytical and experimental studies of the acoustic source distribution in such suppressors, including identification of source location, nature, and strength and noise reduction potential.
- Investigation of in-flight effects on the aerodynamic and acoustic performance of these suppressors.

The results of these investigations are expected to lead to the preparation of a design guide report for predicting the overall characteristics of suppressor concepts, from models to full scale, static to in-flight conditions, as well as a quantitative and qualitative prediction of the phenomena involved.

The work effort in this program was organized under the following major Tasks, each of which is reported in a separate Final Report:

Task 1 - Activation of Facilities and Validation of Source Location Techniques.

Task 2 - Theoretical Developments and Basic Experiments.

Task 3 - Experimental Investigation of Suppression Principles.

Task 4 - Development and Evaluation of Techniques for "In Flight" Investigation.

Task 5 - Investigation of "In Flight" Aero-Acoustic Effects on Suppressed Exhausts.

Task 6 - Preparation of Noise Abatement Nozzle Design Guide Report.

Task 1 was an investigative and survey effort designed to identify acoustic facilities and test methods best suited to jet noise studies. Task 2 was a theoretical effort complemented by theory verification experiments which extended across the entire contract period of performance.

The subject of the present, Task 3, report series (FAA-RD-76-79 III - I, II, III, and IV) was formulated as a substantial part of the contract effort to gather various test data on a wide range of high velocity jet nozzle suppressors. These data, together with supporting theoretical advances from Task 2, have led to a better understanding of jet noise and jet noise

suppression mechanisms, as well as to a validation of scaling methods. Task 3 helped to identify several "optimum" nozzles for simulated in-flight testing under Task 5, and to provide an extensive, high quality data bank leading to formulation of methods and techniques useful for designing jet noise suppressors for application in the Task 6 design guide as well as in future studies.

Task 4 was similar to Task 1, except that it dealt with the specific test facility requirements, measurement techniques, and analytical methods necessary to evaluate the "in-flight" noise characteristics of simple and complex suppressor nozzles. This effort provided the capability to conduct the "flight" effects test program of Task 5.

TABLE OF CONTENTS

<u>Section</u>		<u>Page</u>
1.0	SUMMARY	1
2.0	INTRODUCTION	11
3.0	ENGINEERING CORRELATION (M*S) JET NOISE PREDICTION METHOD	13
3.1	General Description of the Engineering Correlation Method	13
3.2	Organization and Procedure	14
3.2.1	Types of Nozzle	15
3.2.2	Development of the Prediction Method for Multi-element Jet Noise Suppressors	18
3.2.2.1	Basic Jet Noise	19
3.2.2.2	Premerged Noise Prediction	19
3.2.2.3	Merged Jet Prediction	35
3.2.2.4	Summary of Prediction Elements	38
3.2.3	Literature Sources Considered in Developing the Correlation	39
3.3	Engineering Correlation Predictions and Data Comparisons for the Task 3 Jet Suppressor Nozzles	39
3.3.1	Overall Summary of the Adequacy of the Correlation Procedure	39
3.3.2	Conical Nozzles	44
3.3.2.1	Definition of Method and Data Base Used	44
3.3.2.2	Summary of Prediction Elements	44
3.3.2.3	Data Comparisons and Accuracy	45
3.3.3	Multitube Nozzles	45
3.3.3.1	Definition of Method and Data Base Used	45
3.3.3.2	Summary of Prediction Elements	54
3.3.3.3	Data Comparisons and Accuracy	54
3.3.4	Multichute or Spoke Nozzles	64
3.3.4.1	Definition of the Method and Data Base Used	64
3.3.4.2	Summary of Prediction Elements	65
3.3.4.3	Data Comparisons and Accuracy	65
3.3.5	Dual-Flow Nozzles	73
3.3.5.1	Definition of Method and Data Base Used	73
3.3.5.2	Summary of Prediction Elements	79
3.3.5.3	Data Comparison and Accuracy	81

TABLE OF CONTENTS (Continued)

<u>Section</u>	<u>Page</u>
3.3.6 Ejector Nozzles	81
3.3.6.1 Definition of Method and Data Base Used	81
3.3.6.2 Summary of Prediction Elements for Ejectors	103
3.3.6.3 Data Comparisons	105
4.0 THEORETICAL PREDICTION METHOD AND VERIFICATION OF PRINCIPLES	114
4.1 Jet Noise Mechanisms	114
4.2 Analytical Model Description	123
4.2.1 Aerodynamic Flow-Field Model	123
4.2.2 Sound/Flow Interaction (Shielding) Model	124
4.2.3 Source Spectrum Model	127
4.2.4 Shock-Cell Noise Model	128
4.2.5 Aeroacoustic Model Integration	131
4.3 Theory/Data Comparisons and Discussion of Suppression Mechanisms	135
4.3.1 Summary Comparisons of PNL Characteristics for Baseline and Various Suppressor Nozzles	136
4.3.2 Conical Nozzle Data/Theory Comparison	154
4.3.3 Annular Plug Nozzle Data/Theory Comparison	157
4.3.4 Coplanar, Coannular Nozzle Data/Theory Comparison	157
4.3.5 36-Chute, AR = 2.0, Turbojet Suppressor Nozzle Data/Theory Comparisons	162
4.3.6 8-Lobe Nozzle Data/Theory Comparison	167
4.3.7 104-Tube Nozzle Data/Theory Comparison	167
4.3.8 36-Chute, Dual-Flow Nozzle Data/Theory Comparison	172
4.3.9 Discussion of Suppression Mechanisms	176
4.3.10 Mean-Velocity Decay Characteristics Data/Theory Comparisons	190
5.0 CONCLUSIONS	201
6.0 RECOMMENDATIONS	202
Appendix A M*S -- Engineering Correlation Model -- CDC Version Computer Program Input and Output Manual	203
Introduction	203
Program Nomenclature	203
Description of Program and Subroutines	203
Input Description	236
Output Description	236
Sample Cases	252
Program Source Code Listing	269

TABLE OF CONTENTS (Concluded)

<u>Section</u>		<u>Page</u>
Appendix B	Data Base for the Engineering Correlation from Published Literature	293
Appendix C	Proposed ARP 876 Gas Turbine Jet Exhaust Noise Prediction	321
Appendix D	Prediction of Single Stream Shock-Cell Noise - Revised Procedure	339
LIST OF SYMBOLS		342
REFERENCES		345

LIST OF ILLUSTRATIONS

<u>Figure</u>		<u>Page</u>
1-1.	Evaluation of Noise Mechanisms for a Conical Nozzle.	2
1-2.	Correlation Between Measured and Predicted Effective Perceived Noise Level, EPNL, for all Types of Suppressor Nozzles.	4
1-3.	Typical Peak Static Noise Suppression Characteristics.	6
1-4.	Summary of Range and Noise Characteristics for Several Baseline and Suppressor Nozzles.	9
3-1.	Nozzle Types Included in the Correlation.	16
3-2.	Axial Location of Peak Strouhal Number for Supersonic, Circular Jets.	21
3-3.	Generalized Axial Location of Peak Strouhal Number for Supersonic, Circular Jets.	22
3-4.	Beginning of Peak Noise Generation (X_p/D) for Convergent and Convergent/Divergent Round Nozzles.	23
3-5.	Axial Distribution of Jet Noise for a 4-in., Round, Convergent Nozzle.	25
3-6.	Axial Distribution of Jet Noise for Multitube Suppressors.	26
3-7.	Total Noise Level in Any One-Third-Octave Band, Radiated from the Nozzle Exit, as a Function of $(X/D)/(X/D)_{peak}$.	27
3-8.	Analytical Model for the Merging Location of Adjacent Jets.	28
3-9.	Analytical Model for the Expansion Rate of the Jet Stream.	28
3-10.	Length of Potential Core, X_c/D , as a Function of Jet Mach Number.	29
3-11.	Comparison of Beam Patterns for Conical and Multitube Nozzles.	32
3-12.	Multitube Nozzle Far-Field Spectra in Forward Quadrant (40° to 90° Angle to Inlet).	33
3-13.	Multitube Nozzle Far-Field Spectra in Rear Quadrant (100° to 150° Angle to Inlet).	34

LIST OF ILLUSTRATIONS (Continued)

<u>Figure</u>		<u>Page</u>
3-14.	Correlation Between Measured and Predicted Maximum Perceived Noise Level (PNL) for all Types of Suppressor Nozzles.	40
3-15.	Correlation Between Measured and Predicted Effective Perceived Noise Level (EPNL) for all Types of Suppressor Nozzles.	41
3-16.	Correlation Between Measured and Predicted Maximum Perceived Noise Level (PNL) for a Conical Nozzle.	46
3-17.	Correlation Between Measured and Predicted Effective Perceived Noise Level (EPNL) for a Conical Nozzle.	47
3-18.	Typical Check of Predicted and Measured Maximum Perceived Noise Level versus Jet Velocity for a Conical Nozzle.	48
3-19.	Representative Check of Predicted versus Measured PNL Directivity for a Conical Nozzle.	49
3-20.	Representative Check of Predicted versus Measured Spectra of a Conical Nozzle (50° Inlet Angle).	50
3-21.	Representative Check of Predicted versus Measured Spectra for a Conical Nozzle (90° Inlet Angle).	51
3-22.	Representative Check of Predicted versus Measured Spectra for Conical Nozzle (130° Inlet Angle).	52
3-23.	Correlation Between Measured and Predicted Maximum Perceived Noise Level (PNL) for Single-Flow, Multitube Nozzles.	55
3-24.	Correlation Between Measured and Predicted Effective Perceived Noise Level (EPNL) for Single-Flow, Multitube Nozzles.	56
3-25.	Correlation Between Measured and Predicted Maximum Perceived Noise Level (PNL) for Special Nozzles.	57
3-26.	Correlation Between Measured and Predicted Effective Perceived Noise Level (EPNL) for Special Nozzles.	58

LIST OF ILLUSTRATIONS (Continued)

<u>Figure</u>		<u>Page</u>
3-27.	Typical PNL Directivity and One-Third-Octave Band Spectra for a 104-Tube Nozzle at 1400-ft/sec Jet Velocity.	60
3-28.	Typical PNL Directivity and One-Third-Octave Band Spectra for a 104-Tube Nozzle at 2195-ft/sec Jet Velocity.	61
3-29.	Typical PNL Directivity and One-Third-Octave Band Spectra for a 66-Tube Nozzle at 1252-ft/sec Jet Velocity.	62
3-30.	Typical PNL Directivity and One-Third-Octave Band Spectra for a 66-Tube Nozzle at 2478-ft/sec Jet Velocity.	63
3-31.	Correlation Between Measured and Predicted Maximum Perceived Noise Level (PNL) for Single-Flow, Multichute/Spoke Nozzles.	67
3-32.	Correlation Between Measured and Predicted Effective Perceived Noise Level (EPNL) for Single-Flow, Multichute/Spoke Nozzles.	68
3-33.	Typical PNL Directivity and One-Third-Octave Band Spectra for a 36-Chute Nozzle at 1197-ft/sec Jet Velocity.	69
3-34.	Typical PNL Directivity and One-Third-Octave Band Spectra for a 36-Chute Nozzle at 2396-ft/sec Jet Velocity.	70
3-35.	Typical PNL Directivity and One-Third-Octave Band Spectra for a 32-Element, Deep-Chute Nozzle at 1400-ft/sec Jet Velocity.	71
3-36.	Typical PNL Directivity and One-Third-Octave Band Spectra for a 32-Element, Deep-Chute Nozzle at 2490-ft/sec Jet Velocity.	72
3-37.	Empirical Correlation of the Velocity Ratio Effect for Coannular Nozzles.	75
3-38.	Empirical Correlation of the Area Ratio Effect on the Maximum Noise Reduction of Coannular Nozzles.	76
3-39.	Normalized Sound Power versus Specific Thrust (from Reference 38).	77
3-40.	Normalized Sound Power versus Specific Thrust (from Reference 39).	78

LIST OF ILLUSTRATIONS (Continued)

<u>Figure</u>		<u>Page</u>
3-41.	Correlation Between Measured and Predicted Maximum Perceived Noise Level (PNL) for Dual-Flow Nozzles with a Multitube Suppressor on the Outer Stream.	82
3-42.	Correlation Between Measured and Predicted Effective Perceived Noise Level (EPNL) for Dual-Flow Nozzles with a Multitube Suppressor on the Outer Stream.	83
3-43.	PNL Directivity of a Dual-Flow Nozzle with a 69-Tube Suppressor on the Outer Stream.	84
3-44.	One-Third-Octave Band Spectra for a Dual-Flow Nozzle with a 69-Tube Suppressor on the Outer Stream.	85
3-45.	Correlation Between Measured and Predicted Maximum Perceived Noise Level (PNL) for Dual-Flow Nozzles with a Multichute/Spoke Suppressor on the Outer Stream.	86
3-46.	Correlation Between Measured and Predicted Effective Perceived Noise Level (EPNL) for Dual-Flow Nozzles with a Multichute/Spoke Suppressor on the Outer Stream.	87
3-47.	PNL Directivity for Dual-Flow Nozzles with a Multichute Suppressor on the Outer Stream.	88
3-48.	One-Third-Octave Band Spectra for a Dual-Flow Nozzle with a 36-Chute Suppressor on the Outer Stream.	89
3-49.	One-Third-Octave Band Spectra for a Dual-Flow Nozzle with a 40-Chute Suppressor on the Outer Stream.	90
3-50.	Example of Far-field Directivity with Ejector.	92
3-51.	Effect of Ejector on Normalized Reference Sound Pressure Level as a Function of Nozzle Pressure Ratio.	93
3-52.	Reduction of Reference Sound Pressure Level as a Function of Ejector Inlet Area Relative to Nozzle Area.	95
3-53.	Effect of Centerbody Plug on the Effective Ratio of Ejector Area to Nozzle Area.	96
3-54.	Effect on Nozzle Exit Temperature on Reference Sound Pressure Level.	97

LIST OF ILLUSTRATIONS (Continued)

<u>Figure</u>		<u>Page</u>
3-55.	Effect of Ejector-Length to Nozzle-Equivalent-Diameter Ratio on Reference Sound Pressure Level.	98
3-56.	Effect of Ejector on Far-Field Directivity of Peak, Premerged, One-Third-Octave Band Noise Level.	99
3-57.	Effect of Ejector on the One-Third-Octave Band Spectrum of the Far-Field Noise.	100
3-58.	Acoustic Ray Analysis for Treated Ejectors.	102
3-59.	Directivity Correlation for Ejector Treatment Effects.	104
3-60.	Typical PNL Directivity for Dual-Flow Nozzles with Hard-wall Ejectors.	106
3-61.	One-Third-Octave Band Spectra for a Dual-Flow Nozzle with a 36-Chute Suppressor and Hard-wall Ejector.	107
3-62.	One-Third-Octave Band Spectra for a Dual-Flow Nozzle with a 69-Tube Suppressor and Hard-wall Ejector.	108
3-63.	PNL Directivity and One-Third-Octave Band Spectra for a 66-Tube Nozzle with a Hard-wall Ejector, 1224-ft/sec Jet Velocity.	109
3-64.	PNL Directivity and One-Third-Octave Band Spectra for a 66-Tube Nozzle with a Hard-wall Ejector, 2465-ft/sec Jet Velocity.	110
3-65.	Treated Ejector Insertion Loss at 1.4 Pressure Ratio.	111
3-66.	Treated Ejector Insertion Loss at 2.2 Pressure Ratio.	112
3-67.	Treated Ejector Insertion Loss at 4.0 Pressure Ratio.	113
4-1.	Comparison of Experimental and Predicted Jet Noise Directivity Patterns for Cold Jets.	117
4-2.	Comparison of Experimental and Predicted Density Exponent for Heated Jets at 90° to the Inlet.	120
4-3.	Comparison of Predicted Shock-Noise with Measured Conical Nozzle Spectra.	122

LIST OF ILLUSTRATIONS (Continued)

<u>Figure</u>		<u>Page</u>
4-4.	Parallel Shear-Flow Model of the Jet.	126
4-5.	Primary Components of a Conical-Nozzle, Shock-Cell Noise Spectrum, $D_h = D_{eq}$.	129
4-6.	Primary Components of a Noncircular-Nozzle, Shock-Cell Noise Spectrum $D_h < D_{eq}$.	130
4-7.	Shock-Associated Noise Spectrum, 1.5-in. Diameter Conical Nozzle.	132
4-8.	Shock-Associated Noise Spectrum, 6:1 Aspect Ratio Rectangular Jet.	133
4-9.	Generalized Volume Element Model.	134
4-10.	Comparison of Predicted and Measured Sideline Normalized PNL for a Conical Nozzle.	140
4-11.	Comparison of Predicted and Measured Normalized PNL for an Annular Plug Nozzle.	143
4-12.	Comparison of Predicted and Measured Normalized PNL for a Coplanar, Coannular Nozzle.	144
4-13.	Comparison of Predicted and Measured Normalized PNL for a 36-Chute Turbojet Suppressor Nozzle.	147
4-14.	Comparison of Predicted and Measured Normalized PNL for a 36-Chute, Dual-Flow, Suppressor Nozzle.	151
4-15.	Predicted Vs. Measured PNL Directivity for a Convergent, Conical Nozzle.	155
4-16.	Predicted Vs. Measured SPL Spectra for a Convergent, Conical Nozzle.	156
4-17.	Predicted Vs. Measured PNL Directivity for a Convergent, Plug Nozzle.	158
4-18.	Predicted Vs. Measured SPL Spectra for a Convergent, Plug Nozzle.	159
4-19.	Predicted Vs. Measured PNL Directivity for a Coplanar, Coannular Jet.	160

LIST OF ILLUSTRATIONS (Continued)

<u>Figure</u>		<u>Page</u>
4-20.	Predicted Vs. Measured SPL Spectra for a Coplanar, Coannular Jet.	161
4-21.	Predicted Vs. Measured PNL Directivity for a 36-Chute, Turbojet Suppressor Nozzle.	163
4-22.	Example of Suspected Numerical Error in Spectrum Prediction at $\theta_1 = 150^\circ$ with Adjacent Spectra (140° and 160°) Unaffected; 36-Chute, Turbojet Suppressor.	164
4-23.	Predicted Vs. Measured SPL Spectra for a 36-Chute, Turbojet Suppressor.	165
4-24.	Comparison of Predicted and Measured Effect of Area Ratio on Peak PNL Suppression for a 36-Chute, Turbojet Suppressor.	166
4-25.	Predicted Vs. Measured PNL Directivity for an 8-Lobe Daisy Suppressor (Aerotraine); $V_a = 0$.	168
4-26.	Predicted Vs. Measured PNL Directivity for an 8-Lobe Daisy Suppressor; $V_a = 275$ ft/sec.	169
4-27.	Predicted Vs. Measured PNL Spectra for an 8-Lobe Daisy Suppressor; $V_a = 0$.	170
4-28.	Predicted Vs. Measured SPL Spectra for an 8-Lobe Daisy Suppressor; $V_p = 275$ ft/sec.	171
4-29.	Predicted Vs. Measured PNL Directivity for a 104-Tube Suppressor Nozzle (Aerotraine).	173
4-30.	Predicted Vs. Measured SPL Spectra for a 104-Tube Suppressor Nozzle; $V_j = 2200$ ft/sec.	174
4-31.	Equivalent-Area Modeling of Coannular Plug/Cowl Geometry for a 36-Chute, AR = 2.0, Dual-Flow, Suppressor Nozzle; $A_o/A_j = 1.92$.	175
4-32.	Predicted Vs. Measured PNL Directivity for a 36-Chute, Dual-Flow Suppressor.	177
4-33.	Predicted Vs. Measured SPL Spectra for a 36-Chute, Dual-Flow Suppressor.	178

LIST OF ILLUSTRATIONS (Continued)

<u>Figure</u>		<u>Page</u>
4-34.	Relative Contributions of Noise Mechanisms to PNL Directivity.	180
4-35.	Relative Contributions of Noise Mechanisms to SPL Spectra at $\theta_1 = 50^\circ$.	181
4-36.	Relative Contributions of Noise Mechanisms to SPL Spectra at $\theta_1 = 90^\circ$.	182
4-37.	Relative Contributions of Noise Mechanisms to SPL Spectra at $\theta_1 = 130^\circ$.	183
4-38.	PNL Suppression Composition for a 36-Chute, AR = 2.0, Suppressor Nozzle.	186
4-39.	Comparison of Predicted, Basic, Turbulent-Mixing Noise Spectra at $\theta_1 = 90^\circ$ for a Conical and a 36-Chute Nozzle.	188
4-40.	Modification of Basic Mixing-Noise PNL by Convective Amplification and Fluid Shielding.	189
4-41.	Comparison of Mean-Velocity Decay Rates for a 36-Chute Nozzle.	191
4-42.	Predicted Vs. Measured Mean-Velocity Axial Decay; Conical Nozzle.	192
4-43.	Predicted Vs. Measured Mean-Velocity Axial Decay; Convergent, Plug Nozzle.	193
4-44.	Predicted Vs. Measured Mean-Velocity Axial Decay; Coannular Nozzle.	194
4-45.	Predicted Vs. Measured Mean-Velocity Axial Decay; 36-Chute Nozzle.	195
4-46.	Predicted Vs. Measured Mean Velocity Axial Decay; 8-Lobe Nozzle.	196
4-47.	Predicted Vs. Measured Mean Velocity Axial Decay; 104-Tube Nozzle.	197
4-48.	Predicted Vs. Measured Mean Velocity Axial Decay; 36-Chute, Dual-Flow Nozzle.	198

LIST OF ILLUSTRATIONS (Concluded)

<u>Figure</u>		<u>Page</u>
A-1.	Computer Program Flow Chart.	211
A-2.	Nozzle Types Included in the Correlation.	248
A-3.	Fortran Symbol Convention for Acoustic Arena Variables.	249
A-4.	Definition of Cant Angles for Multielement Nozzles.	250
C-1.	Variable Density Index ω .	326
C-2.	Pure Jet Mixing Noise Nondimensional Polar Prediction Carpet.	327
C-3.	Jet Noise Characteristics, 90° to 20° Angle to Intake Axis, 90° to 160° Angle to Jet Axis.	328
C-4.	Jet Noise Characteristics, 100° Angle to Intake Axis, 80° Angle to Jet Axis.	329
C-5.	Jet Noise Characteristics, 110° Angle to Intake Axis, 70° Angle to Jet Axis.	330
C-6.	Jet Noise Characteristics, 120° Angle to Intake Axis, 60° Angle to Jet Axis.	331
C-7.	Jet Noise Characteristics, 130° Angle to Intake Axis, 50° Angle to Jet Axis.	332
C-8.	Jet Noise Characteristics, 140° Angle to Intake Axis, 40° Angle to Jet Axis.	333
C-9.	Jet Noise Characteristics, 150° Angle to Intake Axis, 30° Angle to Jet Axis.	334
C-10.	Jet Noise Characteristics, 160° Angle to Intake Axis, 20° Angle to Jet Axis.	335
D-1.	Group Source Spectrum, G (sn), and Average Correlation Coefficient, C_1 (sn).	341

LIST OF TABLES

<u>Table</u>		<u>Page</u>
1-1.	Typical Summary of Nozzle Static and Projected Flight Peak PNL Suppression Characteristics.	7
3-1.	Linear Regression Analysis Results for Suppressor Nozzles.	43
3-2.	Data Base for Single-Flow, Multitube Nozzles.	53
3-3.	Data Base for Single-Flow, Multichute/Spoke Nozzles.	66
3-4.	Data Base for Dual-Flow Nozzles.	80
3-5.	Data Base for Ejector Nozzles.	91
4-1.	Summary of Configurations for Verification of Suppression Principles.	137
4-2.	PNL Data/Theory Comparison for Bertin Aerotrain Test Series; 400-ft Sideline.	150
A-1.	Definition of Fortran Symbols.	204
A-2.	Overall Flow of Program.	210
A-3.	Input Format.	237
A-4.	Input Variable Descriptions.	243
A-5.	Output Symbol Descriptions.	251
A-6.	Input Data Card Listing Sample Case.	252
B-1.	Unsuppressed Conical Nozzle.	294
B-2.	Conical Nozzle with Daisy Suppressor.	299
B-3.	Conical Nozzle with Multitube Suppressor.	300
B-4.	Conical Nozzle with Chute or Spoke Suppressor.	302
B-5.	Unconventional Nozzles.	303
B-6.	Unsuppressed Annular Nozzle.	304
B-7.	Daisy Suppressor with Plug.	306
B-8.	Simple Plug with Multitube Suppressor.	307

LIST OF TABLES (Concluded)

<u>Table</u>		<u>Page</u>
B-9.	Simple Plug with Chute or Spoke Suppressor.	308
B-10.	Unsuppressed Coannular Nozzle.	309
B-11.	Coannular Nozzle with Daisy Suppressor.	311
B-12.	Coannular Nozzle with Multitube Suppressor.	312
B-13.	Coannular Nozzle with Chute or Spoke Suppressor.	313

1.0 SUMMARY

The High Velocity Jet Noise Source Location and Reduction Program (Contract DOT-OS-30034) was conceived to bring analytical and experimental knowledge to bear on understanding the fundamentals of jet noise for simple and complex suppressors.

Task 3, the subject of this report, involved the experimental investigation of suppression principles, including developing an experimental data base, developing a better understanding of jet noise suppression principles, and formulating empirical methods for the acoustic design of jet noise suppressors. Acoustic scaling has been experimentally demonstrated, and five "optimum" nozzles were selected for anechoic, free-jet testing in Task 5.

Volume I - Verification of Suppression Principles and Development of Suppression Prediction Methods - Some of the experimental studies (reported in Volume II) involved acquisition of detailed, far-field, acoustic data and of aerodynamic jet-flow-field data on several baseline and noise-abatement nozzles. These data were analyzed and used to validate the theoretical jet noise prediction method of Task 2 (referred to as M*G*B, designating the authors' initials) and to develop and validate the empirical noise-prediction method presented herein (referred to as M*S, designating the last name initials of the authors).*

The Task 2 theoretical studies conclude that four primary mechanisms influence jet noise suppression: fluid shielding, convective amplification, turbulent mixing, and shock noise. A series of seven suppressor configurations (ranging from geometrically simple to complex) were evaluated in Task 3 to establish the relative importance of each of the four mechanisms. Typical results of this evaluation of noise mechanisms are summarized in Figure 1-1 in terms of perceived noise level (PNL) directivity for a conical nozzle. In general, mechanical suppressors exhibit a significant reduction in shock noise relative to a baseline conical nozzle, reduce the effectiveness of fluid shielding (increase rather than suppress noise), reduce the effectiveness of convective amplification (reduce noise), and produce a modest reduction in turbulent mixing noise. The largest amount of shock noise reduction correlates with the suppressor which has the smallest characteristic dimension. Fluid shielding decreases because suppressors cause the mean velocity and temperature of the jet plume to decay faster than the conical baseline. A reduction in convection Mach number (and hence in convective amplification) occurs because a suppressor plume decays very rapidly. Turbulent mixing noise is reduced through alteration of the mixing process that results from segmenting the exhaust jet.

*The Task 3 empirical (M*S) method was initially intended for nozzle geometries which could not be modeled in the purely analytical Task 2 (M*G*B) method (a multielement nozzle with a treated ejector, for example).

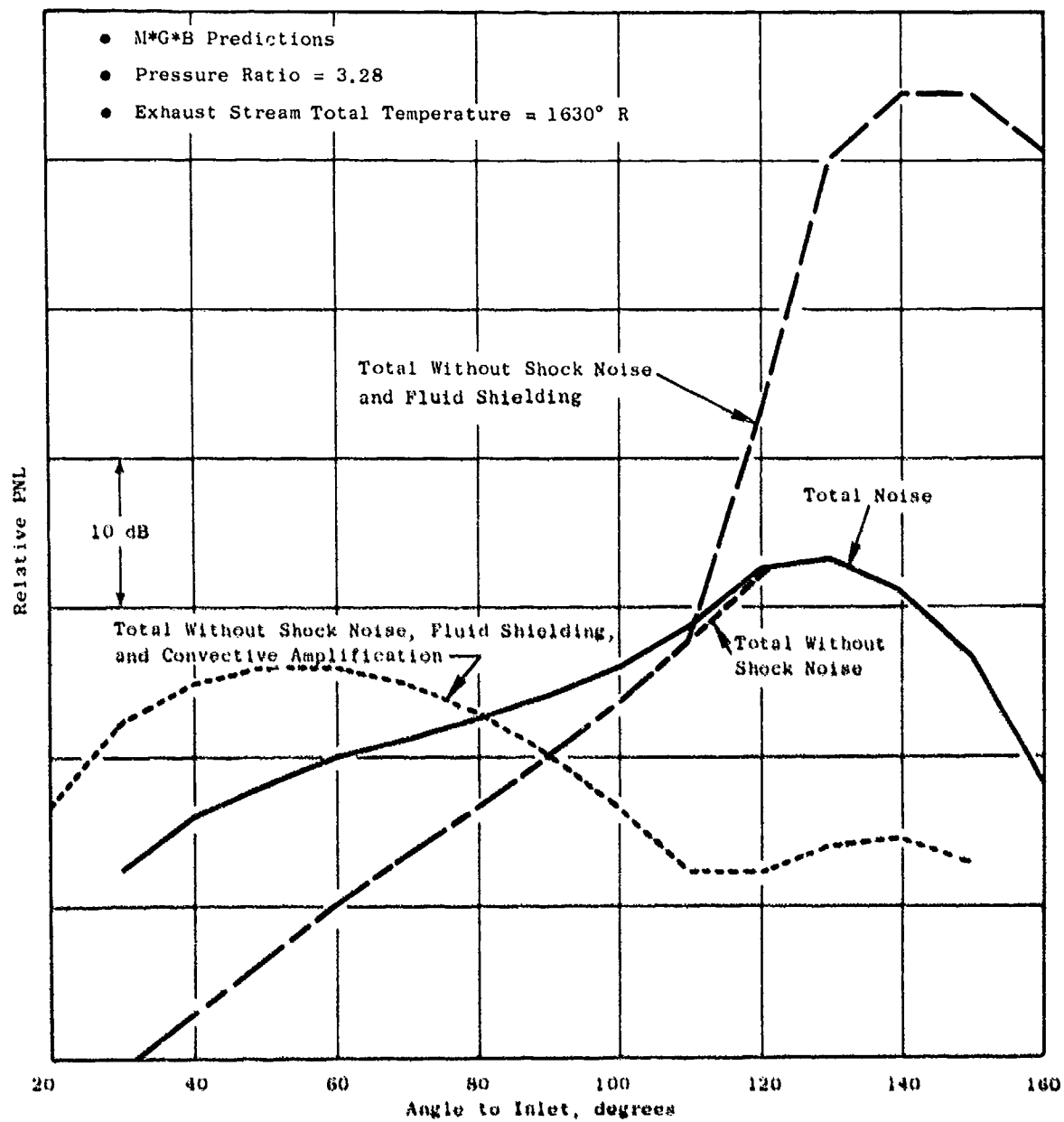


Figure 1-1. Evaluation of Noise Mechanisms for a Conical Nozzle.

Aerodynamic flow-field measurements (mean-velocity profiles) were demonstrated to be useful in verifying the flow-field predictions which were calculated by the M*G*B (theoretical) noise-prediction program. Noise source location devices such as the Ellipsoidal Mirror (EM) were demonstrated to be less useful than the Laser Velocimeter (LV) for the M*G*B theory verification studies because the LV provides data which may be directly compared with predictions made using the M*G*B program. Axial and radial mean-velocity profiles are typical examples of such comparisons.

The empirical M*S jet noise prediction method has been developed to predict the static acoustic characteristics of multielement suppressors applicable to both advanced turbojets and variable-cycle engines (which are representative of power plants for future supersonic cruise aircraft). The effect of external flow on the M*S jet noise prediction is discussed in the Task 6 Design Guide Report. Inputs required to use the M*S computational procedure include: element type, element number, suppressor area ratio and radius ratio, chute-spoke planform and cant angle, and plug diameter. The prediction accuracy is estimated to be +3.3 Effective Perceived Noise Decibels (EPNdB) at a 95% confidence level. Figure 1-2 illustrates the correlation between measured and predicted EPNLs for all types of suppressors.

The merits of both the M*S and M*G*B computational techniques can be stated as follows. The empirical (M*S) jet noise prediction method, based on correlations of scale-model jet data, serves as a useful preliminary design and prediction tool for selecting the basic nozzle type (chute, spoke, multi-tube, etc.) and primary geometric parameters (element number, area ratio, etc.) for a given application. It is also useful in evaluating the acoustic performance of a given suppressor nozzle, provided the nozzle is one of the types from which the correlation was derived. Further, the method is useful for doing parametric studies since the computation procedure is relatively simple and economical of both computer time and cost. The theoretical (M*G*B) prediction method, on the other hand, is more suited to detailed design and analysis of a suppressor nozzle. It can supply detailed information on the jet plume flow development as well as the far-field acoustic characteristics. It is also capable of evaluating changes in nozzle planform shape, element placement and spacing, etc. In addition, the theoretical prediction model is a useful diagnostic tool, capable of assessing the relative roles the various mechanisms play in the noise suppression process, and can also serve as a source location analysis tool.

Volume II - Parametric Testing and Source Measurements - A parametric experimental series was conducted to provide far-field acoustic data on 47 baseline and suppressor nozzle configurations and to provide aerodynamic nozzle performance on 18 of the configurations. The data presented in this volume were taken for use in the current program as well as to provide an extensive, high-quality, data base for future studies. The impact of varying the area ratio and velocity ratio of dual-flow, baseline nozzle configurations was investigated, and the importance of shock noise was assessed. The impact of varying area ratio and element number was parametrically studied for both single and dual-flow suppressors; core plug geometry, velocity ratio, and

- Flyover calculation using static data corrected to free-field conditions.
- The "Reference" level is the predicted value of noise for each nozzle, at a specified set of thermodynamic conditions, plus an arbitrary value of 100 dB.

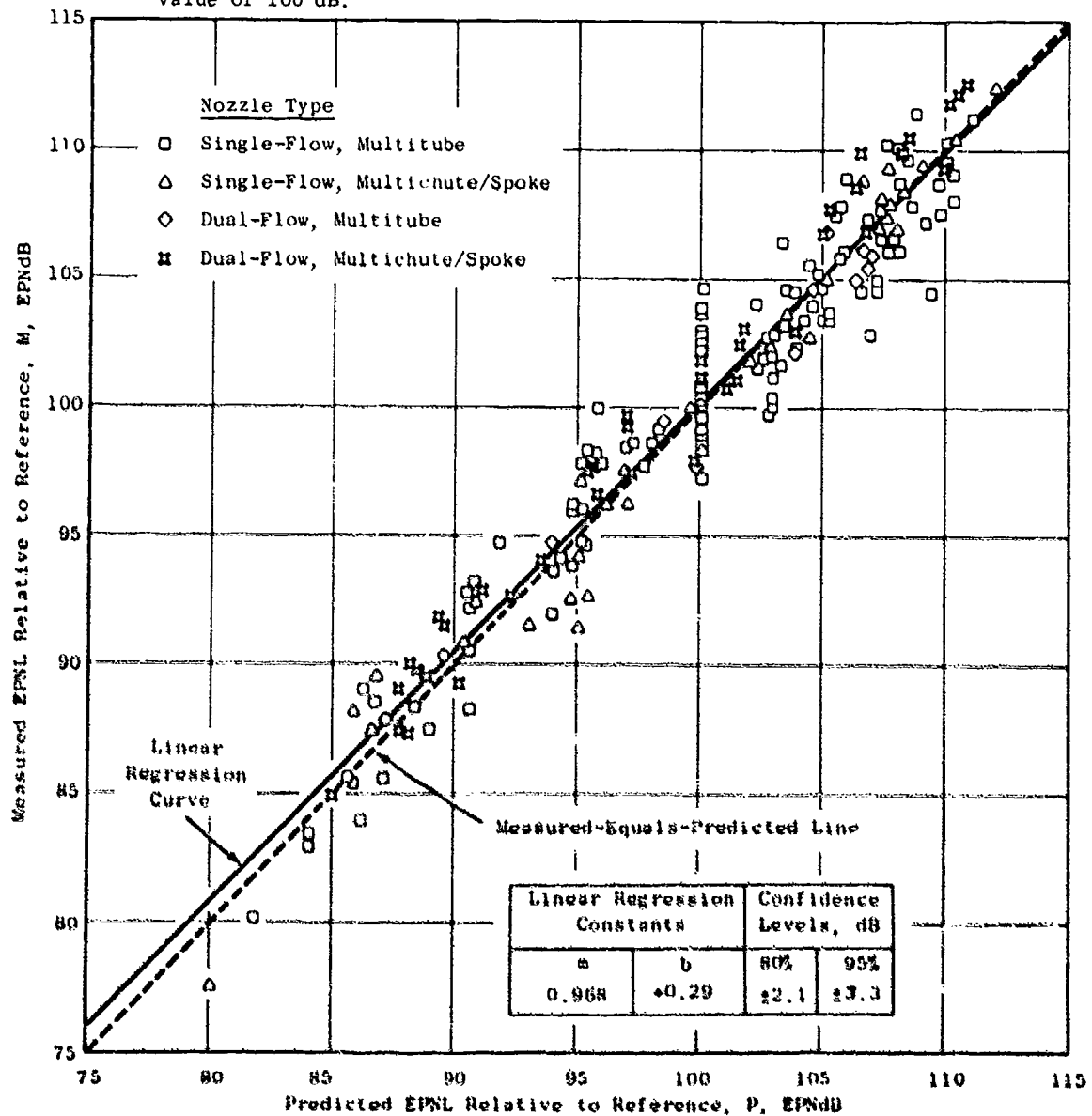


Figure 1-2. Correlation Between Measured and Predicted Effective Perceived Noise Level, EPNL, for all Types of Suppressor Nozzles.

weight flow ratio were evaluated for dual-flow suppressors. These studies establish absolute static suppression levels on the basis of normalized maximum PNL, for several families of suppressor nozzles, as illustrated in Figure 1-3.

Parametric testing identified the following primary trends for single-flow and for dual-flow suppressors during static operation:

Single Flow

- Suppression increases with increasing area ratio at high jet velocity.
- Suppression decreases with increasing area ratio at low jet velocity.
- Suppression level is affected by element type (spoke systems suppress slightly better than chutes).

Dual Flow

- Suppression increases with increasing area ratio.
- Suppression increases with increasing element number at high jet velocity.
- Suppression level is affected by core plug geometry (by 2 to 3 decibels (dB)).
- Suppression increases 3 to 4 dB when a treated ejector is added to a suppressor configuration.

Selective, free-jet tests conducted on eight configurations indicate that suppression generally decreases in flight. Typical static versus free-jet results are shown in Table 1-1.

The aerodynamic performance test data recorded on 18 of the configurations at both static and wind-on conditions are also included in this volume. Base pressure measurements were taken on several of the models in order to determine base drag (which is thought to be responsible for the poor aerodynamic performance of most mechanical suppressors in flight). These wind tunnel tests identified the following primary trends in aerodynamic performance:

- Performance decreases with increasing element number.
- Performance increases with increasing chute depth.
- Performance increases with increasing ratio of inner flow area to outer flow area.

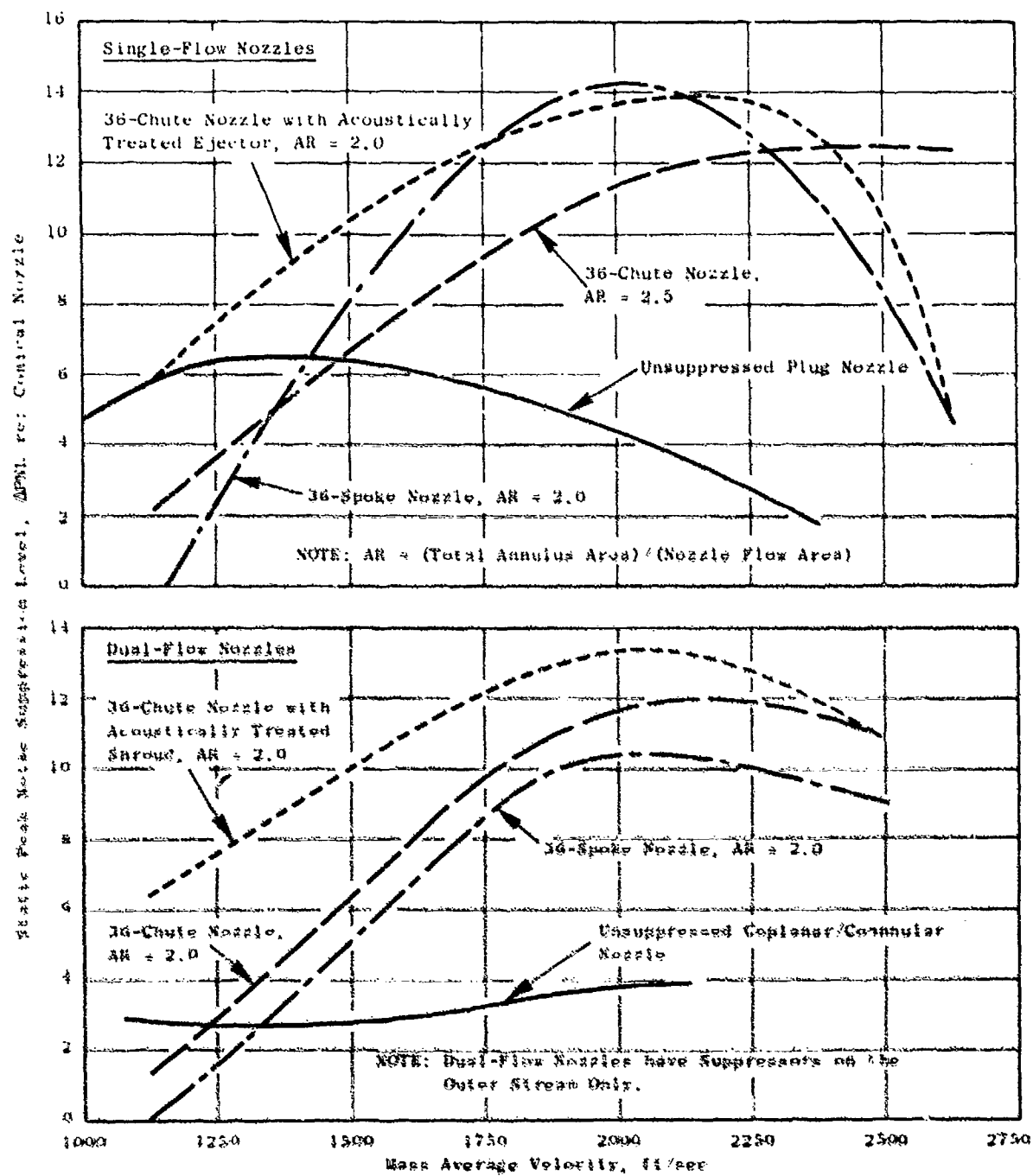


Figure 1-3. Typical Peak Static Noise Suppression Characteristics.

Table 1-1. Typical Summary of Nozzle Static and Projected Flight Peak PNL Suppression Characteristics.

- Suppression Levels are Relative to a Conical Nozzle at Equivalent Flight Conditions
- $V_j = 2500$ ft/sec

<u>Configuration</u>	<u>Suppression Level, db</u>	
	<u>Static</u>	<u>Flight</u>
Plug Nozzle - 0.789 Radius Ratio	1.3	3.0
Plug Nozzle - 0.85 Radius Ratio	2.3	3.7
8-Lobe Nozzle	5.6	5.6
AR = 2.5 36-Chute Nozzle	13.5	10.9
AR = 2.5 36-Chute Nozzle with Auxiliary Flow	12.5	9.4
104 Tube Nozzle	12.0	12.0

- Performance is affected by element type (chutes perform better than spokes because spokes have higher base drag).

The base pressure correlations provide a procedure for predicting suppressor nozzle aerodynamic performance.

Volume III - Suppressor Concepts Optimization - Several studies were conducted to attempt an optimization of suppressor concepts. The end product of this overall effort was to design five nozzles for static and free-jet testing in Task 5. Trade studies of performance versus suppression, aircraft integration studies, and development of a figure of merit method of analysis all make up the activities in this "optimization" process.

Trade studies of suppression versus aerodynamic performance indicate that a properly selected and designed mechanical suppressor can attain a delta suppression to delta thrust coefficient ratio ($\Delta PNL/\Delta C_{f_g}$) of almost 3.0 (based on static suppression and wind-on aerodynamic performance).

The aircraft integration study consisted of ranking nine baseline and suppressor nozzles with respect to performance level, suppression level, weight, impact on aircraft mission range, and noise footprint. In general, suppression level was found to be the most important design variable, with performance and weight ranking second and third, respectively.

The appropriate figure of merit, considering all the design variables, was found to be aircraft range. However, use of range as the figure of merit requires that the aircraft mission be specified, and several techniques for cursorily ranking the suppressors based solely on suppression level, performance, and weight may also be identified. A summary of the range versus noise characteristics of typical nozzle configurations is presented in Figure 1-4. Once a noise goal is specified, adding a suppressor provides a significant range improvement over an unsuppressed system because adding a suppressor is less costly than reducing noise by enlarging the engine to reduce jet velocity.

The design of the five optimum nozzles was based on data from previous studies, performed by government and industry, on the M*G*B and M*S models discussed above and on the parametric data obtained in the acoustic and aerodynamic performance test series reported in Volume II. The configurations were designed and fabricated for open-throat, anechoic, free-jet testing in Task 5. The configurations chosen for evaluation were: (1) a 32-chute, single-flow nozzle; (2) a 40-shallow-chute, dual-flow nozzle; (3 and 4) a 36-chute, dual-flow nozzle, with and without a treated ejector; and (5) a 54-element, coplanar-mixer, plug nozzle.

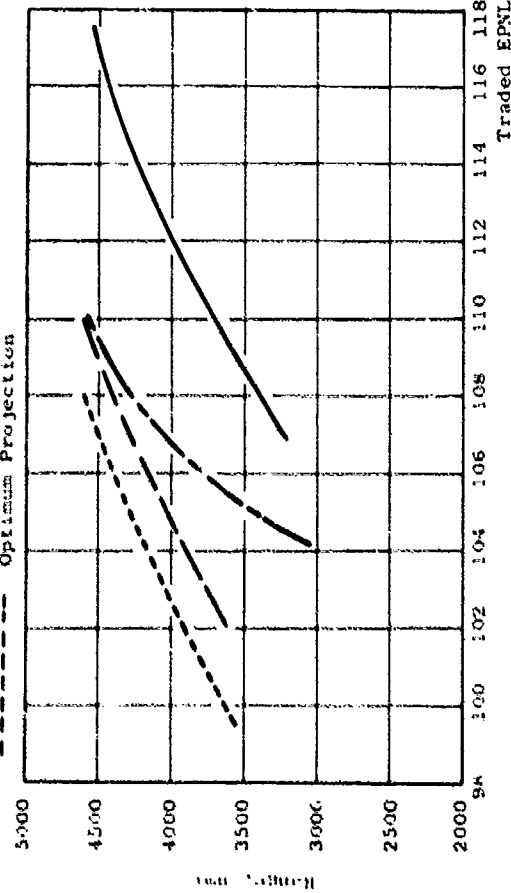
Demonstration of acoustic scaling for several suppressor configurations was conducted to assure the adequacy of using scale-model results to project full-scale suppression levels. Full-scale data were obtained on several suppressor configurations using J79 and J85 engines. The suppressors evaluated were: (1) a baseline conical nozzle, (2) a 32-chute nozzle with and without

- Four Engines
- 12,500-ft Balance Field Length; 53,500-lbf Thrust Engine
- NASA Aircraft

VARIABLE-CYCLE ENGINE

Nozzle Type

- Fully Mixed, Conical
- - - 36-Chute, AR = 2.5
- - - 40-Shallow-Chute
- - - Optimum Projection



TURBOJET ENGINE

Nozzle Type

- Baseline, Conical
- - - 32-Chute
- - - 57-Tube + Ejector

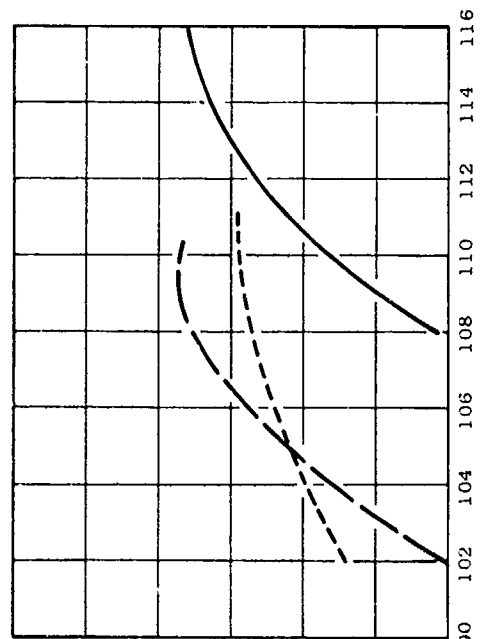


Figure 1-4. Summary of Range and Noise Characteristics for Several Baseline and Suppressor Nozzles.

a treated ejector, (3) an 8-lobe nozzle, and (4) a 104-tube nozzle. Scale-model data were obtained for these same configurations to allow comparison of scale-model and full-scale results. In general, peak full-scale suppression levels projected from scale-model data were verified by the full-scale engine results. Directivity patterns were duplicated within +2 PNdB (the largest differences occurring with the conical nozzle configuration). Some spectral anomalies were observed for select cases; however, they were not of sufficient magnitude to invalidate the scale-model results. The conclusion resulting from this study is that full-scale noise levels can be predicted from scale-model test results using Strouhal scaling laws.

Volume IV - Laser Velocimeter Time Dependent Cross Correlation Measurements - In-jet/in-jet and in-jet/far-field exhaust noise diagnostic measurements conducted using a Laser Velocimeter (LV) are reported in this volume. Measurements were performed on a conical nozzle and a coannular plug nozzle. Two-point, space/time measurements using a two-LV system were completed for the conical nozzle. Measurements of mean velocity, turbulent velocity, eddy convection speed, and turbulent length scale were made for a subsonic ambient jet and for a sonic heated jet. For the coannular plug nozzle, a similar series of two-point, laser-correlation measurements were performed. In addition, cross correlations between the laser axial component of turbulence and a far-field acoustic microphone were performed.

Volumes I, II, III, and IV contain the results of a comprehensive effort to identify and integrate the theoretical studies, parametric test data, acoustic and performance diagnostic measurements, and system studies. A logical procedure has evolved for conducting suppressor design trade-offs.

2.0 INTRODUCTION

The first 20 years of commercial aircraft operation with jet propulsion have clearly demonstrated the need for effective high velocity jet noise suppression technology in order to meet community acceptance. Aircraft system studies show that an efficient jet noise suppression device is required if a commercial supersonic aircraft is to be economically viable as well as environmentally acceptable. The current state of the art of high velocity jet noise suppression would make a supersonic transport (SST), with advanced technology engines, meet 1969 noise rules (at best). This state of the art is represented by the material in References 1 through 6.

Reference 1 describes analytical and experimental investigations which were conducted in the early 1960's. This study established a basis for development of mathematical and empirical methods for the predictions of jet-flow-field, aerodynamic characteristics and for determining the directional characteristics of jet noise suppressors. This work was limited in the sense that the suppressors evaluated had only modest suppression potential, and the measurement techniques available did not allow the acquisition of high-frequency, spectral data necessary to establish full-scale, PNL suppression levels.

The development of commercial SST vehicles by the U.S. and by the British-French multinational corporation in the 1960's placed extreme emphasis on the need for effective and efficient noise suppression devices. Phase I of work, conducted by the Boeing and General Electric companies, is summarized in References 2 and 3. Primary emphasis was on jet noise suppressor development through model and engine testing applicable to an afterburning turbojet engine. Suppressor designs were based primarily on empirical methods. Phase II of this effort, References 4 and 5, continued the suppressor development with a stronger emphasis placed on the integration of analytical studies and experimental test data. Specifically, the Boeing Company concentrated on optimization of tube-type-suppressor systems and related semiempirical prediction methods. General Electric focused on the development both of chute and of tube-type-suppressor systems with primary emphasis placed on optimization of chute-type-suppressor nozzles.

Similar studies were conducted by the British and French in development of the Concorde, and typical results are summarized in Reference 6.

The design technology represented in References 1 through 6 is primarily semiempirical. The absence of general design rules based on engineering principles led to the Government's formulation of the High Velocity Jet Noise Program, Contract DOT-OS-30034, in 1973. The purpose has been to achieve fundamental understanding, on a quantitative basis, of the mechanisms of jet noise generation and suppression and to develop design methods.

This report presents the results of Task 3 of the contract. It provides the experimental data base which was used in conjunction with the supporting

theories from Task 2 to develop a better understanding of jet noise and jet noise suppression.

The report is organized into four volumes (FAA-RD-76-79, III - I, II, III, IV) and is presented in a format consistent with the Task 3 work plan division of subtasks. Volume I, under this cover, is entitled "Verification of Suppression Principles and Development of Suppression Prediction Methods." Volume II is a data report entitled "Parametric Testing and Source Measurements," and Volume III is an analysis report entitled "Suppressor Concepts Optimization." Volume IV is an analysis report entitled "Laser Velocimeter Time Dependent Cross Correlation Measurement."

Volume I uses the data base (Volume II) and the Task 2 theoretical model (Reference 7) to postulate the suppression mechanisms. Volume I also presents an independent, empirical, static jet-noise-prediction method which was developed from engineering correlations of the test data. Volume II presents the data and results of the parametric acoustic tests, the aerodynamic performance tests, and the Laser Velocimeter tests. Volume III presents the results of a trade study of performance versus suppression, an aircraft integration study, a "figure of merit" methodology, and a summary of the five "optimum" nozzles selected for testing in Task 5. An acoustic-scaling investigation was conducted to support the suppressor concepts optimization activities and is presented as an appendix to Volume III. Volume IV presents the results of the in-jet/in-jet and in-jet/far-field cross correlation investigations.

The work reported in the present volume represents two approaches to verifying suppression principles. One approach (Section 3.0) is to correlate the data from this and other programs in order to develop a comprehensive, empirical, jet-noise-prediction method (subsequently referred to as the M*S method, designating the last name initials of the two authors). The second approach (Section 4.0) is to use actual data to verify the theoretical suppression principles developed in Task 2 and included in the theoretical jet noise prediction method developed in Task 2 (subsequently referred to as the M*G*B method, designating the last name initial of each of the three authors). Appendix A is a user's guide describing the mechanics of using the M*S prediction computer program.

3.0 ENGINEERING CORRELATION (M*S) JET NOISE PREDICTION METHOD

A comprehensive, empirical, jet-noise-prediction method has been developed by correlating extensive data from this program and available data from other published sources. This engineering correlation prediction model has been designated as the M*S model (after the authors: Moisinger and Sieckman) for ease of reference, as well as to distinguish it from the more theoretical prediction model (M*G*B) developed in Task 2 (Reference 7).

The data were correlated by means of basic engineering principles and physical parameters. The resulting M*S prediction method includes unsuppressed conical nozzles; multitube and multichute, single- and dual-flow, suppressed nozzles; and multitube/chute nozzles with hard-wall and treated ejectors. In each case the predicted noise based upon the engineering correlation is compared with the measured noise.

The correlation for conical and multielement-suppressor nozzles has been programmed (in Fortran Y language) and a description of content and procedure for use is included in Appendix A of this report volume.

3.1 GENERAL DESCRIPTION OF THE ENGINEERING CORRELATION METHOD

The basic reasoning and concepts involved in the correlation method are as follows:

- The characteristics of jet noise (overall level, spectral distribution, and directivity) are established by the empirical correlation for conical nozzles.
- Multielement nozzles are assemblies of conical nozzle sources from which the air flows in discrete elements. These elements coalesce, or merge together, as each jet plume expands.
- The premerged and postmerged regions are separate sources of noise generation, each of which can be treated as a simple or "equivalent" conical noise source.
- The shape of the nozzle element (whether a tube, spoke, chute, or other such device for dividing the flow at the nozzle exit into many discrete elements) affects the character of the noise only at frequencies with wave lengths comparable to or smaller than the principal dimension of the element.
- The premerged noise detected in the far field is affected by the path each acoustic ray must take in radiating from the source to the observer, particularly with regard to whether it must pass through other elements of jets issuing from the nozzle. Specifically, multielement nozzles radiate only part of the noise actually

generated in the premerged region to the observer. The balance is shielded or absorbed by the turbulent mixing zones of adjacent jets. The data show that this effect is dependent upon (and the engineering correlation includes) the effects of far-field angle (relative to the refraction critical angle), area ratio of the multielement nozzle, and size of the interfering jet relative to the wavelength of the radiated noise.

- The postmerged noise is determined by the use of a mean velocity, a temperature, and a density (each estimated from fundamental fluid dynamics) as if the merged jet were from a conical nozzle having such flow conditions at the nozzle discharge plane.
- The effect upon noise of a shroud surrounding the premerged mixing zone of a multielement suppressor can be correlated empirically, assuming the same thermodynamic conditions for the fully expanded jet as if the shroud were not in place. The effect of adding point-reacting, acoustic treatment in the shroud can be predicted from basic engineering principles using "ray" acoustics.

This method is in contrast to the purely empirical method which consists of the curve-fitting of normalized data.

In order to establish the applicability and validity of this reasoning process and these concepts, the prediction model was first postulated, and the resulting, calculated, far-field noise levels were compared with measured data in one-third-octave band detail over a range of far-field angles. This was done iteratively, with initial emphasis on the multitube nozzle, until the detailed formulation was evolved which provided satisfactory correlation for all the observed spectral and directional characteristics of the noise. The fullest possible range of variables as provided by the data was used. The basic formulations as established from the multitube correlation were then modified, as found appropriate from other basic supporting data, in order to extend the correlation to other nozzle types. This is described in the following sections: the final results of the engineering correlation for each nozzle, a summary of the data base supporting the correlation, and a comparison of predicted and measured peak PNL and EPNL for a calculated, level flyover assuming no effects of flight (e.g., relative velocity) on the noise generation or radiation. The effect of flight and the subsequent modification of the M*S jet noise prediction technique are treated in detail in the Task 6 Design Guide report.

3.2 ORGANIZATION AND PROCEDURE

The following paragraphs summarize and discuss the types of nozzles included in the correlation, the range of variables for which the correlation is applicable, principal factors or concepts included for each suppressor type, and the data base used to develop the correlation.

3.2.1 Types of Nozzles

The types of nozzles for which the M*S computer program in Appendix A can be applied, and for which the correlation has been checked against measured data in this report, are summarized in Figure 3-1. Coannular plug nozzles with inverted velocity profiles are not handled by the M*S program since this is currently being done under NASA Contract NAS3-20619. In each suppressor case, an ejector shroud option can be included. It should be noted that the ranges for nozzle pressure ratio and total temperature are interdependent in that they generally both increase or decrease together as on the operating line of a turbojet engine; the data base for the correlation is generally consistent with operating conditions expected for typical engines.

Summary descriptions are given in the following paragraphs of the nozzle design parameters for which the correlation applies; a listing is included of the range of variables for which the predicted noise has been checked against data to establish the statistical confidence limits. The ranges on velocity and temperature are set by the SAE correlation (see Section 3.3.2). Extrapolations of the temperature effects are possible, but extrapolations of velocity should be avoided because polynomial curve fits are used which are subject to error outside of the indicated range. Pressure ratio is limited only by the data base used to check the shock-cell noise correlation. The limit on diameter is set only to keep the maximum noise frequencies within the 50 Hz to 10 kHz range for meaningful PNL determination. The M*S model may also be utilized to predict scale model jet noise spectra by simply exercising it at its lower diameter limit (i.e., $D \geq 0.8$ ft). The output thus obtained can be put into any scaling routine (separate from the M*S model) to scale down the data to model size. If PNL is not required, and the computer program in Appendix A is modified to calculate higher frequencies, the diameter limits can be extended. Guides for good design practice when departures from other limitations in the M*S method are made (such as non-coplanar tube ends) are given in the Task 6 Design Guide.

Conical Nozzle - The correlation includes both converging and converging-diverging (design point only) nozzles in the sense that a prediction of mixing noise, alone, plus a separate prediction of shock noise are included.

The range of applicability of both the jet-mixing and the shock-cell noise correlations are:

Jet Velocity, V_j (ft/sec)	$400 < V_j < 2860$
Jet Total Temperature, T_j ($^{\circ}$ R)	$519 < T_j < 2100$
Nozzle Pressure Ratio	$1.0 < P_T/P_0 < 4.0$
Nozzle Diameter, D (ft)	$0.8 < D$

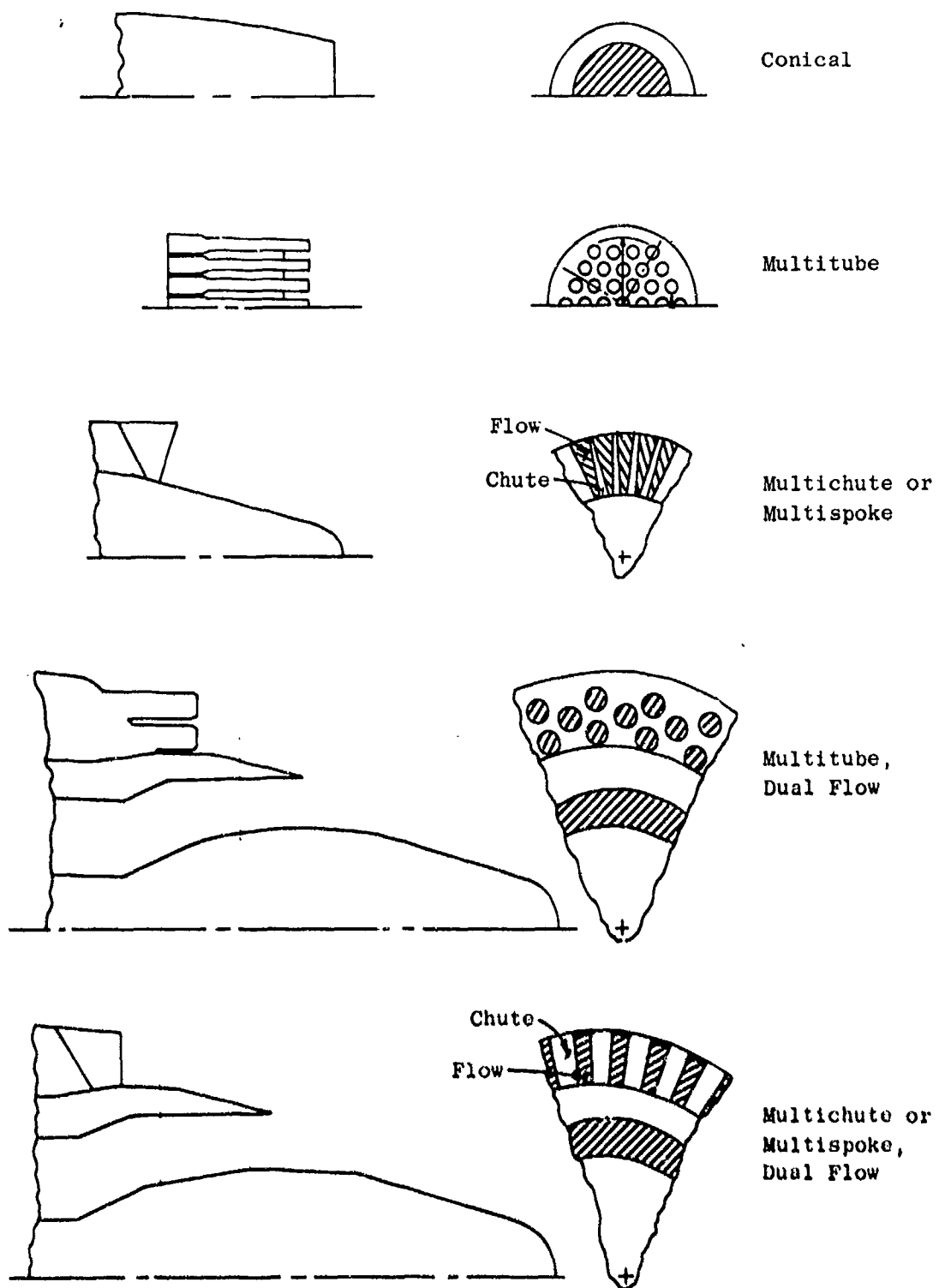


Figure 3-1. Nozzle Types Included in the Correlation.

Multitube, Single-Flow Nozzle - The multitube, single-flow nozzle correlation includes nozzles with an arbitrary number of tubes having simple converging ends, coplanar termination, all tubes parallel (except the outer row can be canted relative to the axis), uniform center-to-center spacing of tubes in a hexagonal array, and the option of a centerbody plug.

The ranges of the variables specifically associated with the multitube nozzles which were correlated (in addition to the variables listed under the conical nozzle) are:

Suppressor Area Ratio, AR	$2.0 \leq AR \leq 8.0$
Number of Elements, N	$7 \leq N \leq 253$
Suppressor Radius Ratio, R_r	$0 \leq R_r \leq 0.75$
Cant Angle of Outer Row Tubes, β (degrees)	$0 \leq \beta \leq 5$

Multichute or Spoke, Single-Flow Nozzle - This correlation includes both chutes and spokes without discrimination. It was evolved based on the more complex planform variations of chute configurations and was found to apply equally well to spokes. The planform of nozzle elements may be trapezoidal (not limited to radial lines); the termination can be canted, and a centerbody plug is included.

The ranges of variables specifically correlated with the data (in addition to the variables listed under the conical nozzle) are:

Suppressor Area Ratio	$1.5 < AR < 2.5$
Number of Elements	$24 \leq N \leq 64$
Suppressor Radius Ratio	$0 \leq R_r \leq 0.783$
Exit Cant Angle (degrees)	$-10 \leq \beta \leq 15$

Coannular-Flow, Multielement Suppressor on Outer Stream - In this case, the multielement nozzle is applied to the outer stream of a coannular exhaust. The velocity of the outer stream may be selected to be higher or lower than the inner stream (although the case of primary practical interest is for the highest velocity stream to have the suppressor). The same conditions apply in this case as for the single-flow, multielement nozzles (tubes with converging ends, coplanar termination, etc.).

The ranges of variables specifically correlated with the data for dual-flow nozzles with multichute/spoke suppressors on the outer stream (in addition to the variables listed under the conical nozzle) are:

Suppressor Area Ratio	$1.5 \leq AR \leq 3.0$
Number of Elements	$20 \leq N \leq 40$
Suppressor Radius Ratio	$0.653 \leq R_r \leq 0.783$
Exit Cant Angle (degrees)	$\beta = 0$

A comparison of predicted and measured data was made for a multitube suppressor on the outer stream of a dual-flow nozzle. This nozzle, the velocity ratios, and the outer-to-inner flow-area ratios are defined and discussed in Section 3.3.5.1.

Multielement Nozzle with Ejector - Hard-wall or treated ejectors with single- or dual-flow, multielement suppressors are also included. The hard-wall ejector correlation is derived on a purely empirical basis, but the effect of adding treatment is predicted by means of the engineering correlation of the basic data. Thus the treatment for which the check against measured data was made (the single-layer liner with honeycomb separating the solid backplate and perforated faceplate, single degree of freedom, SDOF) may be extrapolated to other types of point-reacting treatment provided the resistance and reactance are specified for the desired frequencies.

The range of variables for which the correlation was established (in addition to those for the conical nozzle and multielement suppressors) are:

Area Ratio of Ejector Relative to Area Ratio of Nozzle	$1.0 < \frac{AR_{ej}}{AR_n} < 1.97$
Ratio of Hard-Wall Ejector Length to Equivalent Conical Nozzle Diameter	$0 < L_H/D_{eq} < 4.0$
Ratio of Treated Ejector Length to Equivalent Conical Nozzle Diameter	$0 < L_T/D_{eq} < 2.0$
Ratio of Ejector Inside Diameter to Nozzle Element Envelope Diameter	$1.0 < D_{ej}/D_n < 1.28$

3.2.2 Development of the Prediction Method for Multielement Jet Noise Suppressor

In order to establish a prediction of jet noise radiated from multiple element nozzles by the engineering correlation method, the following quantitative information is required:

- Basic jet noise radiated by a simple, conical nozzle in terms of the sound pressure level in each frequency band of interest
- Premerged Noise Prediction:
 - Amount of noise radiated locally along the length of the jet for each frequency band of interest
 - Distance downstream from the nozzle discharge plane at which the flows from adjacent elements merge sufficiently to preclude any further high-frequency noise generation
 - Effective number of elements which radiate sound to the far field
- Merged Jet Prediction:
 - Flow area, velocity, and density of the merged jet when the flow from each of the individual elements coalesces

This information is then used in the basic procedure described for the appropriate nozzle type in Section 3.3. Discussion of the sources and the development of this information as it is used in the prediction program is summarized in the following paragraphs.

3.2.2.1 Basic Jet Noise

Basic jet noise radiated from a simple, conical nozzle is determined by empirical correlation of measured data. Details of the method and discussion are included in Section 3.3.2.

3.2.2.2 Premerged Noise Prediction

(a) Noise Radiation Locally Along the Length of the Jet

The radiated noise is established from measured data for: (1) the axial location of the peak noise level in each one-third-octave band and then (2) the axial distribution of the noise level for each one-third-octave band. The following development is given for multitube suppressors; it is also used for multichute/spoke suppressors by establishing the equivalent diameter of the flow passage (discussed in Section 3.3).

Axial Location of Peak Noise - For subsonic jets from conical nozzles, Lee, et al., (Reference 1) showed the axial location of the peak noise radiation is well correlated by a Strouhal number and the distance from the nozzle exit according to:

$$fD/V = (1.25 X/D)^{-1.22}$$

(3-1)

This relation was previously developed empirically by Howes, et al. (Reference 8).

Potter and Jones (Reference 9) clearly show that this relationship does not hold for supersonic jets, (as does Reference 10). Examples of data for various supersonic Mach numbers are compared in Figure 3-2, with the relationship defined in Equation 3-1, above. The noise from supersonic jets is radiated further downstream than for subsonic jets. The higher the Mach number, the further downstream the peak noise radiation occurs. Also, the peaks of the highest frequencies are radiated only after a certain distance downstream; this contrasts with subsonic nozzles for which the highest frequency occurs in the immediate vicinity of the nozzle exit.

The Strouhal number (for peak noise) rises asymptotically versus X/D such that there is a minimum X/D at which the peak Strouhal number occurs. The asymptote is a function of Mach number. If this asymptote is used as the start of the peak noise radiation (rather than the nozzle discharge plane as used for subsonic jets) the data as given in Figure 3-2 collapse, as shown in Figure 3-3, on a line defined by:

$$fD/V = [1.25 (X - X_p)/D]^{-1.22} \quad (3-2)$$

where X_p = location of beginning of peak noise radiation.

This equation is the same as developed for subsonic jets (Equation 3-1) except for the change in the location at which peak noise radiation begins. The data of Reference 9 follow a slightly shallower slope, as indicated by the second line in Figure 3-3. In the present analysis for multielement suppressors, the low-frequency end of the spectrum is dominated by the merged flow so that the axial location of the low-frequency source is not a factor. Hence, it is not necessary to make a judgment whether the data in Reference 9 or 10 are more appropriate. Nevertheless, it is probably significant that the data from Reference 10 follow the same curve as the subsonic jet when the proper starting point for noise reduction is used. For this reason the correlation given by Equation 3-2 is adopted.

It is necessary to determine the location of the beginning of peak noise radiation (X_p); once this is determined, the peak noise location for all other one-third-octave bands is determined by Equation 3-2. Data for measured locations of the beginning of peak noise radiation are used to establish a relationship for X_p as a function of jet exit Mach number in Figure 3-4. The line giving the best fit is:

$$X_p/D = 6.0778151 \quad (3-3)$$

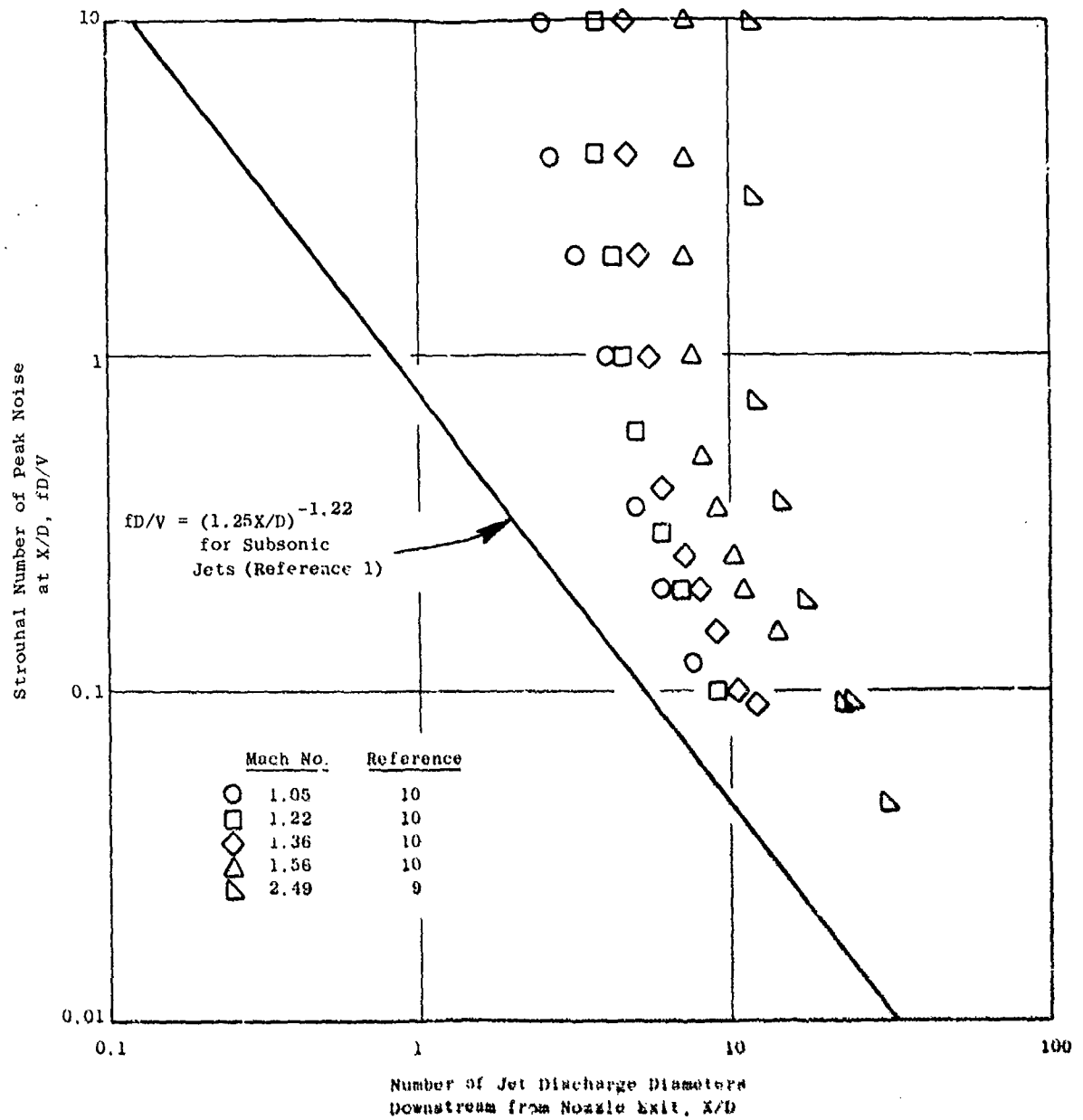


Figure 3-2. Axial Location of Peak Strouhal Number for Supersonic, Circular Jets.

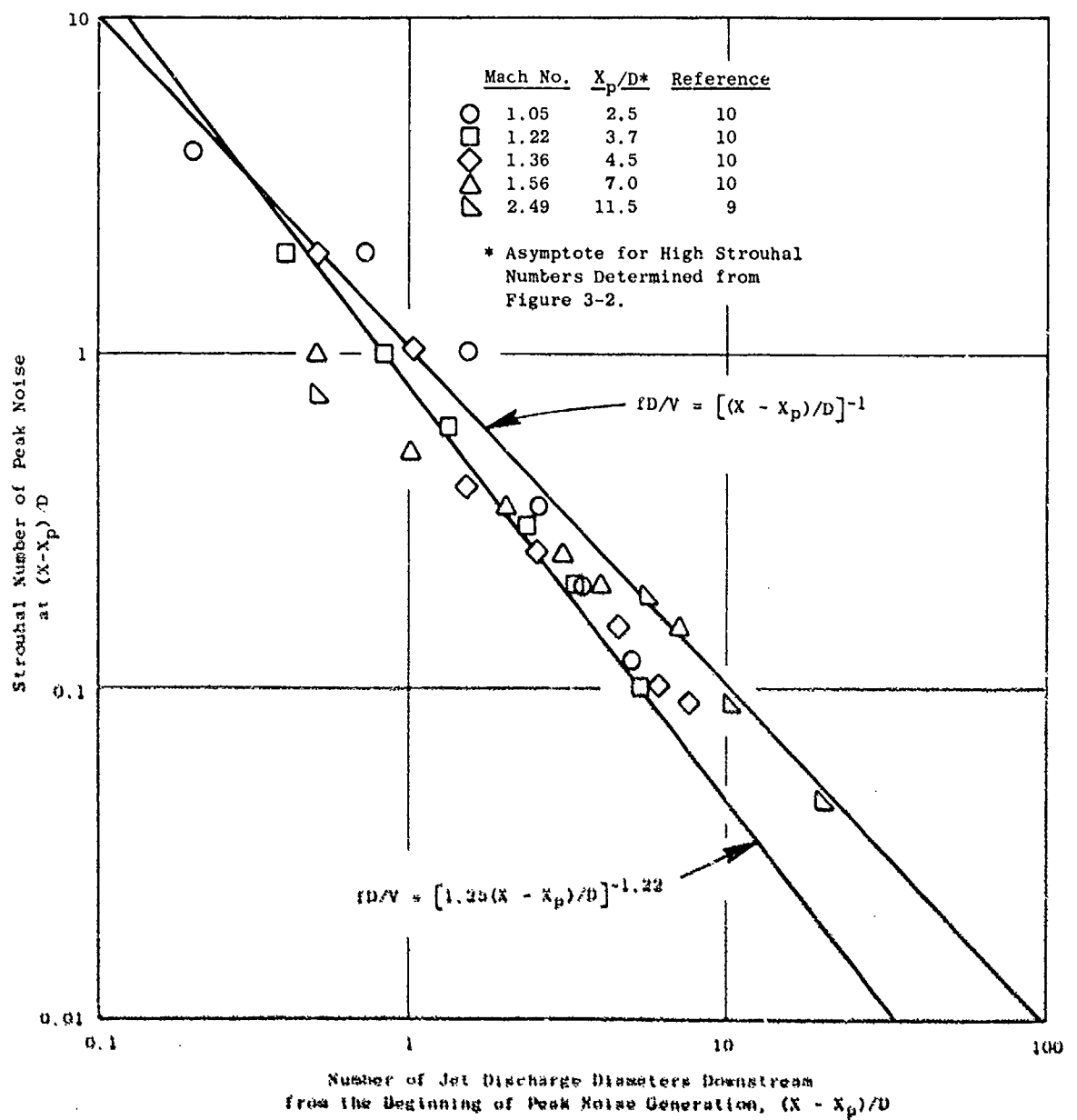


Figure 3-3. Generalized Axial Location of Peak Strouhal Number for Supersonic, Circular Jets.

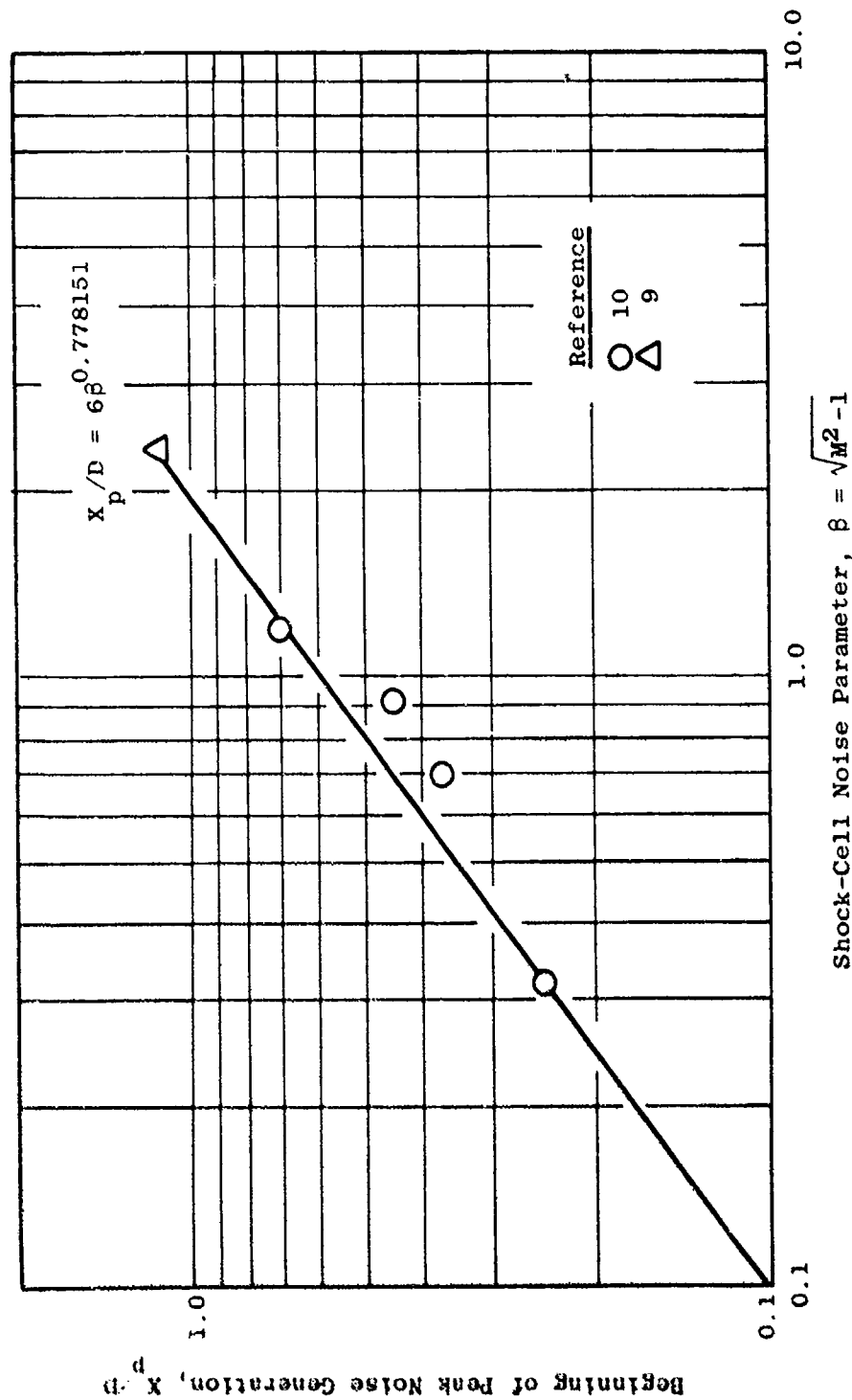


Figure 3-4. Beginning of Peak Noise Generation (X_p/D) for Convergent and Convergent/Divergent, Round Nozzles.

where

$$\beta = \sqrt{M^2 - 1}$$

Axial Distribution of Noise - The axial distribution of noise radiated to the far field is given in Reference 10 not only for a round, converging nozzle but also for a 37-tube, suppressor nozzle as shown in Figures 3-5 and 3-6, respectively. In both figures, the data are presented in terms of one-third-octave band SPL per unit X/D versus the axial distance downstream. It is possible to normalize the data with remarkably good data collapse as shown on the figures. The normalization is accomplished for each one-third-octave band by picking the X/D at which the peak noise occurs, determining the value of the SPL at that location, and then determining the SPL relative to the peak SPL for other values of X/D relative to the X/D at which the peak noise occurs. The results of this procedure show that this normalization causes the data to collapse for all one-third-octave band frequencies reported. Also, the normalized data for the multitube suppressor collapses on the same curve as the round, converging nozzle, showing that the two configurations have identical characteristics.

These data are in terms of SPL per unit X/X_{peak} which is an awkward form for engineering use. Therefore, the acoustic energy has been summed along the length of the jet with the result given Figure 3-7. The summation has been normalized to the one-third-octave band SPL, based on the requirement that all the acoustic energy along the length of the jet must equal the one-third-octave band level as seen in the far field. As an example of the use of this curve, note that, at the axial distance from the nozzle of 0.5 times the distance to the peak (i.e., $(X/D)/(X/D)_{\text{peak}} = 0.5$), the noise level is 9 dB below the one-third-octave band level of the entire jet length.

(b) Axial Location of Merging of Adjacent Flow Streams

High-frequency noise is no longer generated by individual tubes downstream of the location where the flow has merged; this is called the "cutoff" effect. The location of merging is defined as illustrated in Figure 3-8. The analytical model (adapted from Chen, Reference 11) of the expansion of the jetstream versus distance for a single-jet nozzle is illustrated in Figure 3-9. The radius from the centerline of the jet to the boundary of the mixing zone, δ , is:

$$\delta = (D_t/2)(1 + X/X_c) \quad (3-4)$$

Data correlating measured values of the length of the potential core are given in Figure 3-10 for convergent and convergent/divergent nozzles; the potential core lengths are the same for the two types of nozzles. (This correlation should not be interpreted to mean that the shock structures of the two nozzles are the same.)

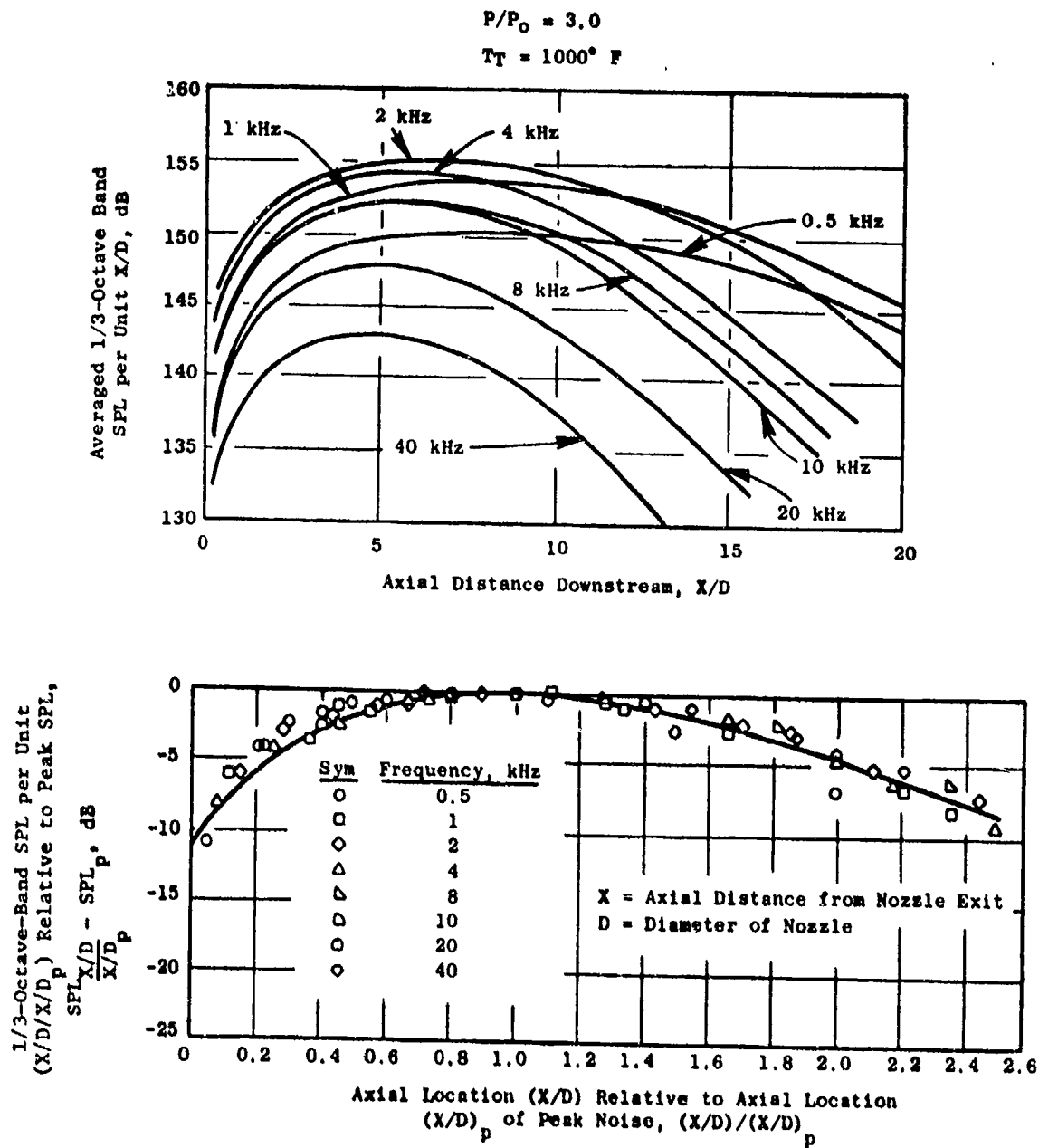


Figure 3-5. Axial Distribution of Jet Noise for a 4.0-in., Round, Convergent Nozzle.

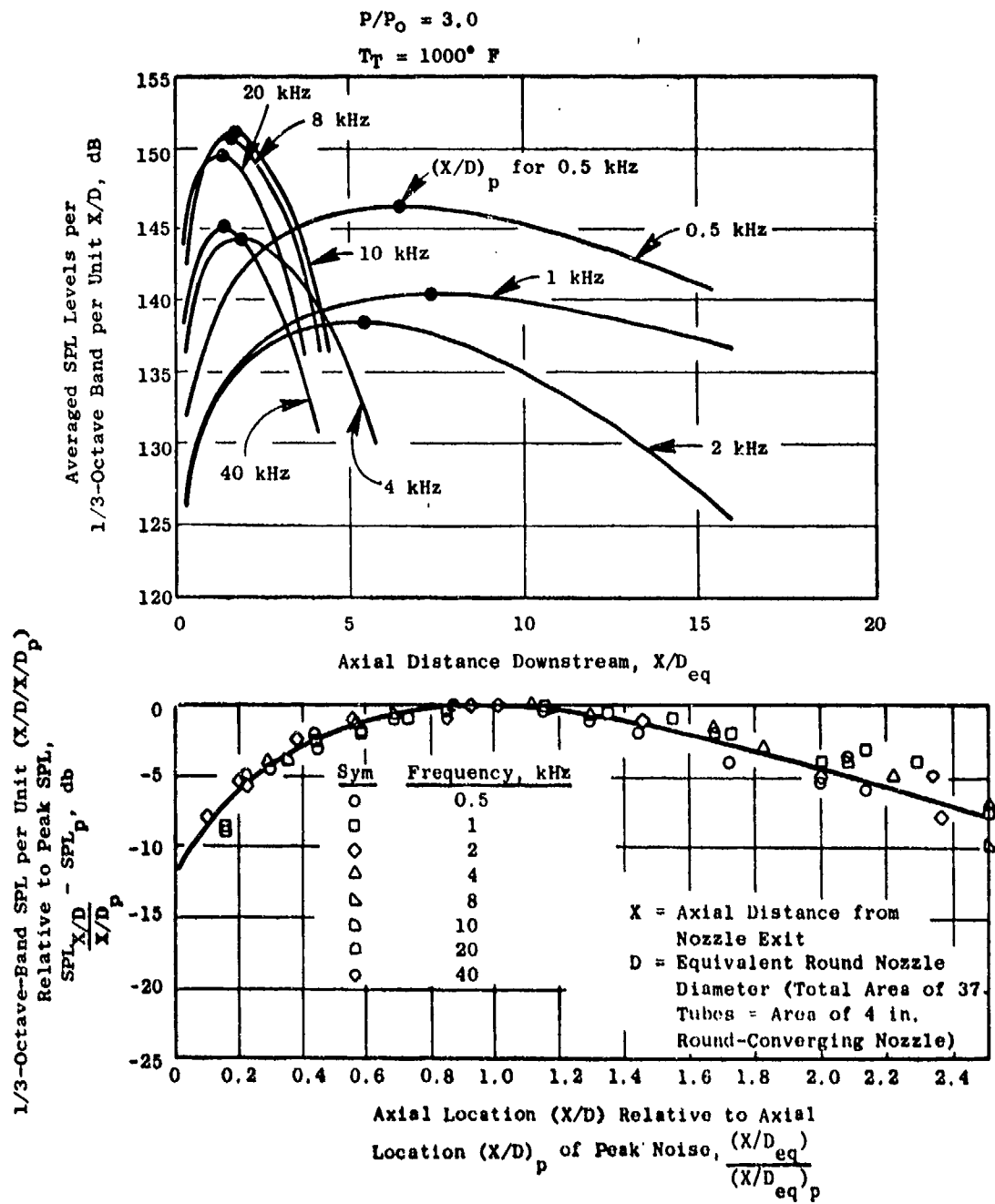


Figure 3-6. Axial Distribution of Jet Noise for Multitube Suppressors.

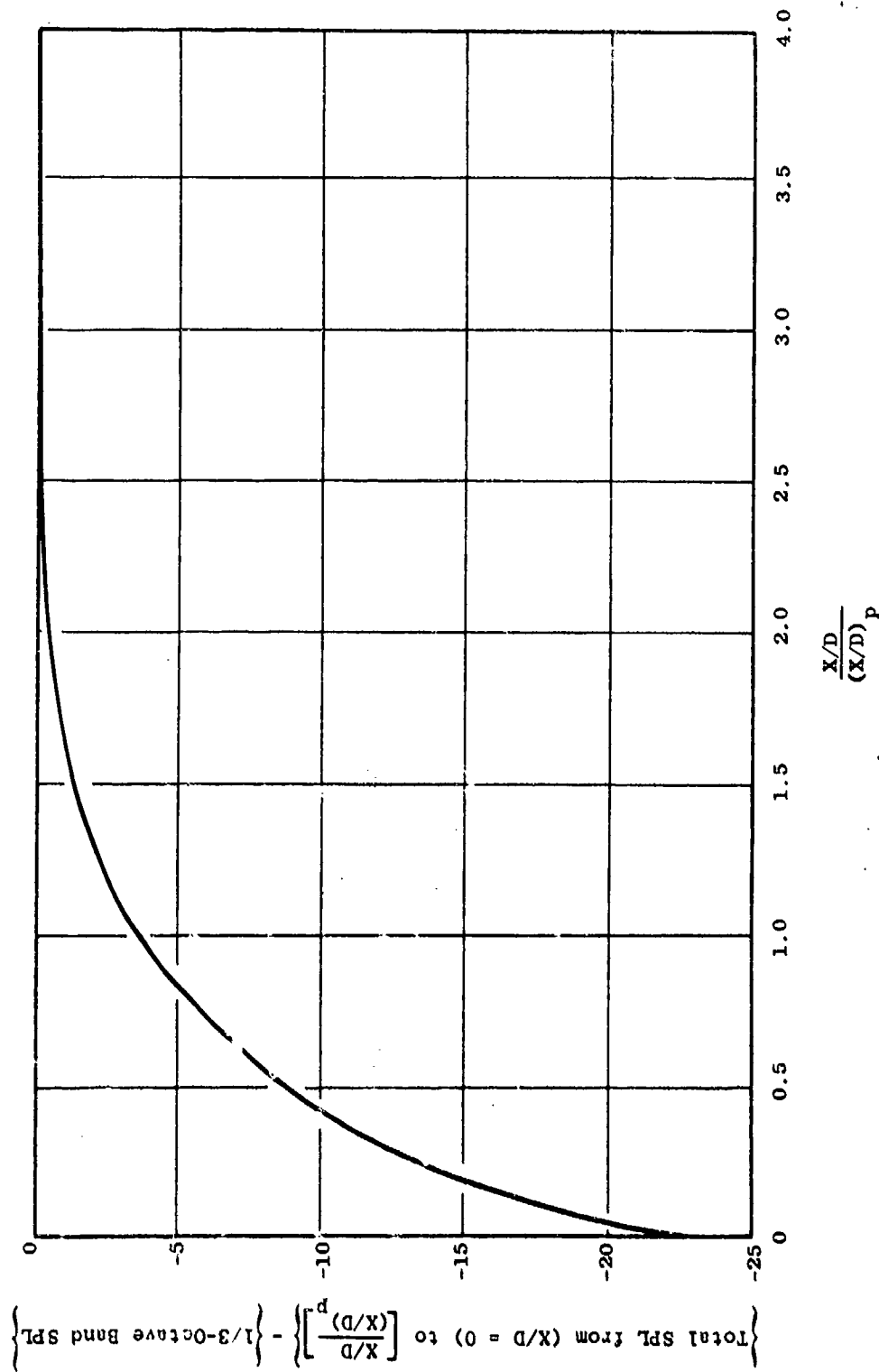


Figure 3-7. Total Noise Level in Any One-Third-Octave Band, Radiated from the Nozzle Exit, as a Function of $(X/D) / (X/D)_{\text{peak}}$.

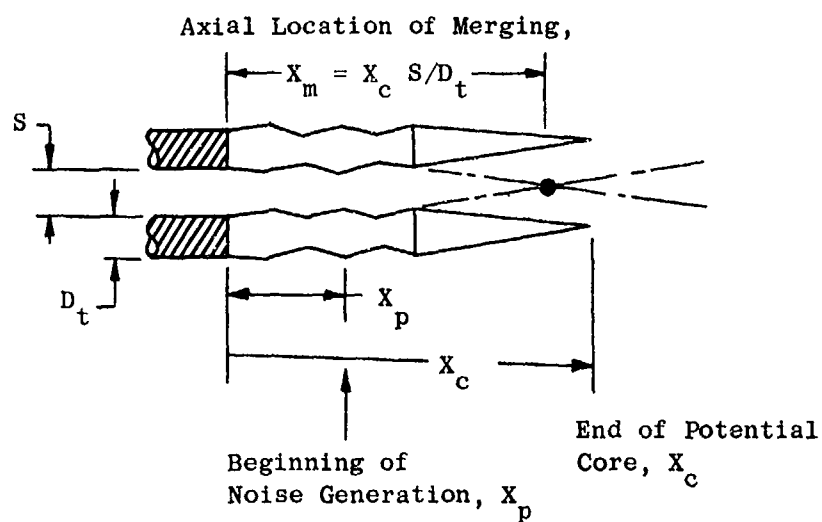


Figure 3-8. Analytical Model for the Merging Location of Adjacent Jets.

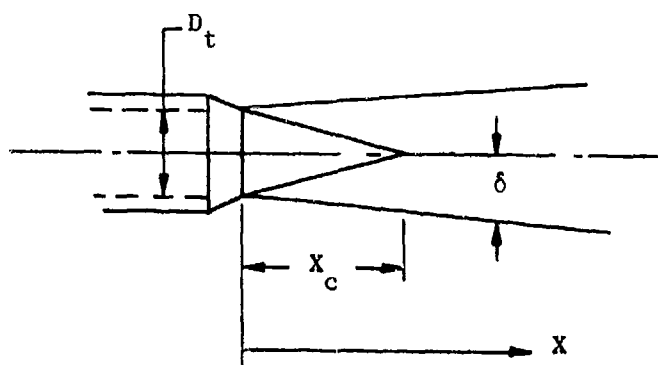
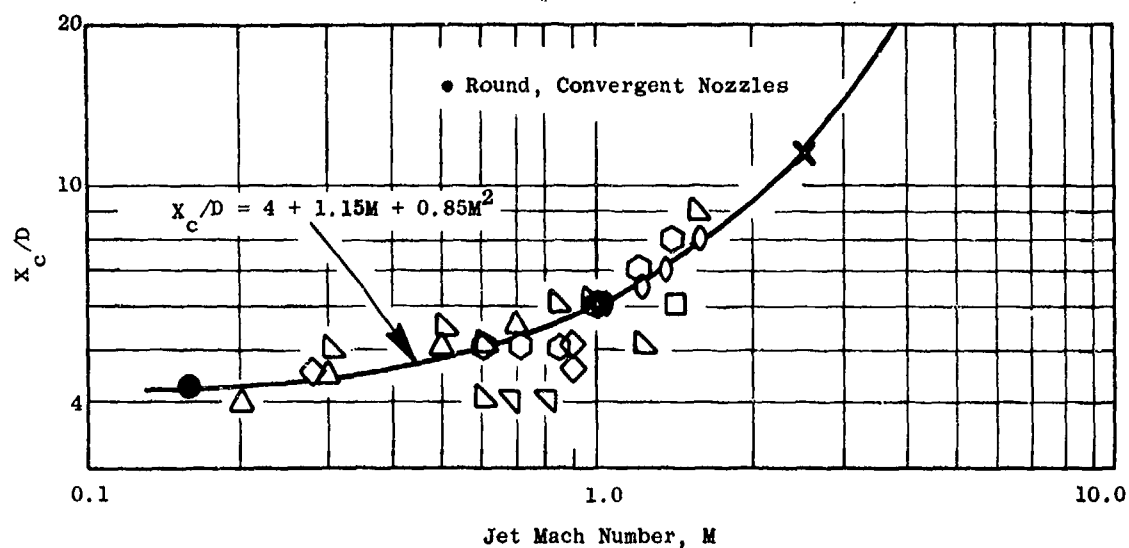


Figure 3-9. Analytical Model for the Expansion Rate of the Jet Stream.



Sym	Reference
○	12
□	13
◇	14
△	15
▽	{ 16, 17

Sym	Reference
◇	7
○	18
◇	19
□	20
▽	9

Sym	Reference
○	21
◇	22
×	23
●	24
▽	25

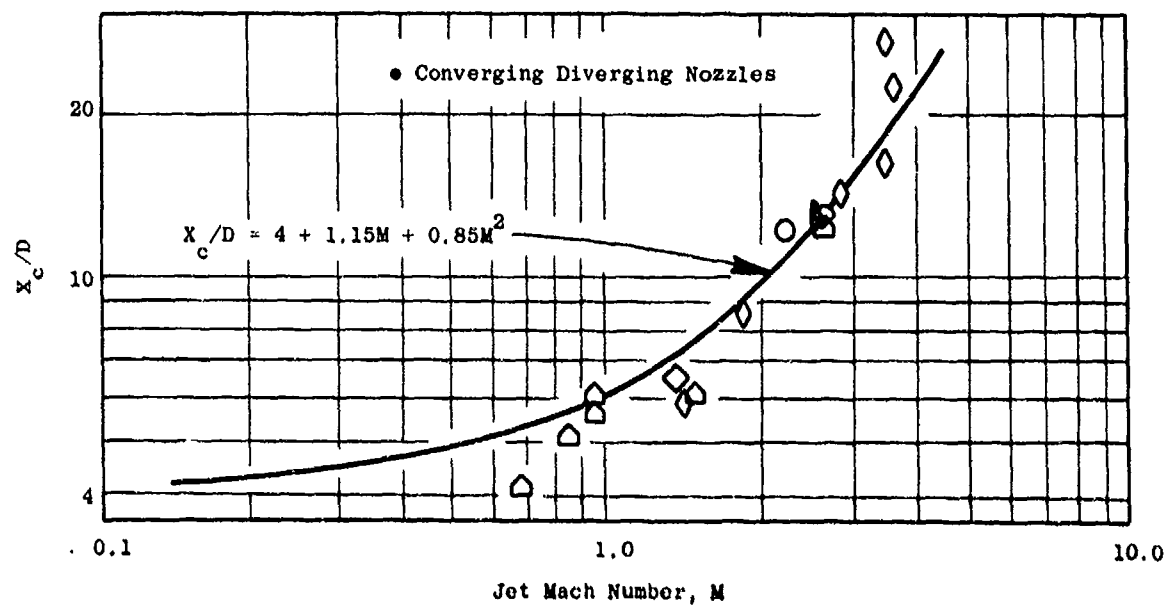


Figure 3-10. Length of Potential Core, X_c/D , as a Function of Jet Mach Number.

For adjacent jets with parallel centerlines, the merging length, X_m , is then determined by the location at which $\delta = (D_t + S)/2$ where S = Spacing between adjacent tubes.

This yields the result that:

$$X_m = X_c S / D_t \quad (3-5)$$

If the outer row is canted relative to the next inner row by an angle, β , then:

$$\left[\frac{X}{D_t} \right]_m = \frac{S}{D_t} \sin(90 - \alpha + \beta) \cos(\alpha) / \sin(2\alpha - \beta) \quad (3-6)$$

where

$$\alpha = \tan^{-1}(D_t / 2X_c)$$

X_m is now used in conjunction with X_{peak} in determining the amount of cutoff applied to a given one-third-octave band from Figure 3-7.

The cutoff effect disappears for suppressor nozzles having a plug when the radius ratio (plug radius divided by nozzle outer radius) exceeds 0.65, for any area ratio; this occurs for either single- or dual-flow cases. To account for this in the correlation, the calculated cutoff effect is applied fully only to cases with radius ratios of less than 0.6. No cutoff effect is applied where the area ratio is greater than 0.65. The cutoff effect in decibels is varied linearly between full effect and no effect in the radius ratio range of 0.6 to 0.65. This relationship was evolved empirically and was adopted on the basis of the overall check obtained by this procedure.

(c) Effective Number of Elements which Radiate Premerged to the Far Field

All tubes do not radiate noise to the far field. This is shown by the work of Eldred (26); Middleton and Clark (27); Gray, Gutierrez, and Walker (28); the Boeing Company (2, 5) and the General Electric Company (3, 4). To account for this in the correlation, when the sound has wavelengths smaller than one-half the tube diameter, only those tubes with an unobstructed line of sight to the observer are counted, and the effective number of tubes, N_{eff} , is:

$$N_{\text{eff}} = \left\{ \sum_{j=0}^K \underbrace{[2(K-j) + 1]}_{\text{Term A}} \underbrace{[1 - 1/S/D_t]}_{\text{Term B}}^j \right\}^{1/2} \quad (3-7)$$

where: K = the number of tube rows from the center, counting the center tube as 0

j = the number of rows inside the outer row, counting the outer row as 0

S = distance between tube centerlines

D_t = tube diameter

For a full hexagonal array, $K = N_o/6$ where N_o is the number of tubes in the outer row. This formulation is derived on the basis of the direct line of sight by the far-field observer, counting only that portion of the premerged jets which can be seen in a multitube suppressor of hexagonal-array configuration. The first term in the equation, Term A, represents the number of tubes facing the far-field observer on two sides of the six-sided hexagon for each tube row in the hexagonal assembly. Term B represents the ratio of the open space relative to the blocked space presented in the j rows of tubes outside the K row which is in the radiator in Term A. This number is raised to the one-half power to correlate empirically with the data.

If the sound has a wavelength, λ , larger than twice the tube diameter, all tubes are counted. For frequencies having wavelengths in the range $D/2 \geq \lambda \geq 2D$ the effect is varied linearly by one-third-octave bands, between $N_{\text{eff}} \leq N \leq N_{\text{total}}$.

Data also show that aft of the critical refraction angle (θ_c) (defined below), for data on an arc, the SPL's for the premerged portion of the frequency range remain approximately constant with angle. This is illustrated in Figure 3-11 for data from Reference 5. The directivity patterns for the suppressor are constant in the premerged region (above 2000 Hz for this scale-model nozzle) for angles greater than 120° , while for the conical (RC) nozzle, they vary significantly with angle. Below 2000 Hz the patterns of the suppressor resemble those of the simple conical nozzle. This phenomenon is also illustrated in Figures 3-12 and 3-13, which show representative, multitube-nozzle, far-field, directivity data from Reference 4; for this nozzle (scaled to full size), that portion of the spectra stemming from the premerged portion of the jet (frequencies greater than 400 Hz) is approximately constant with angle for angles greater than 110° for all jet velocities shown. The phenomenon was included as an empirical correction to the correlation.

- Pressure Ratio = 2.0
- Total Temperature = 1610° R

* Data from Reference 5, Figure 76 and 92

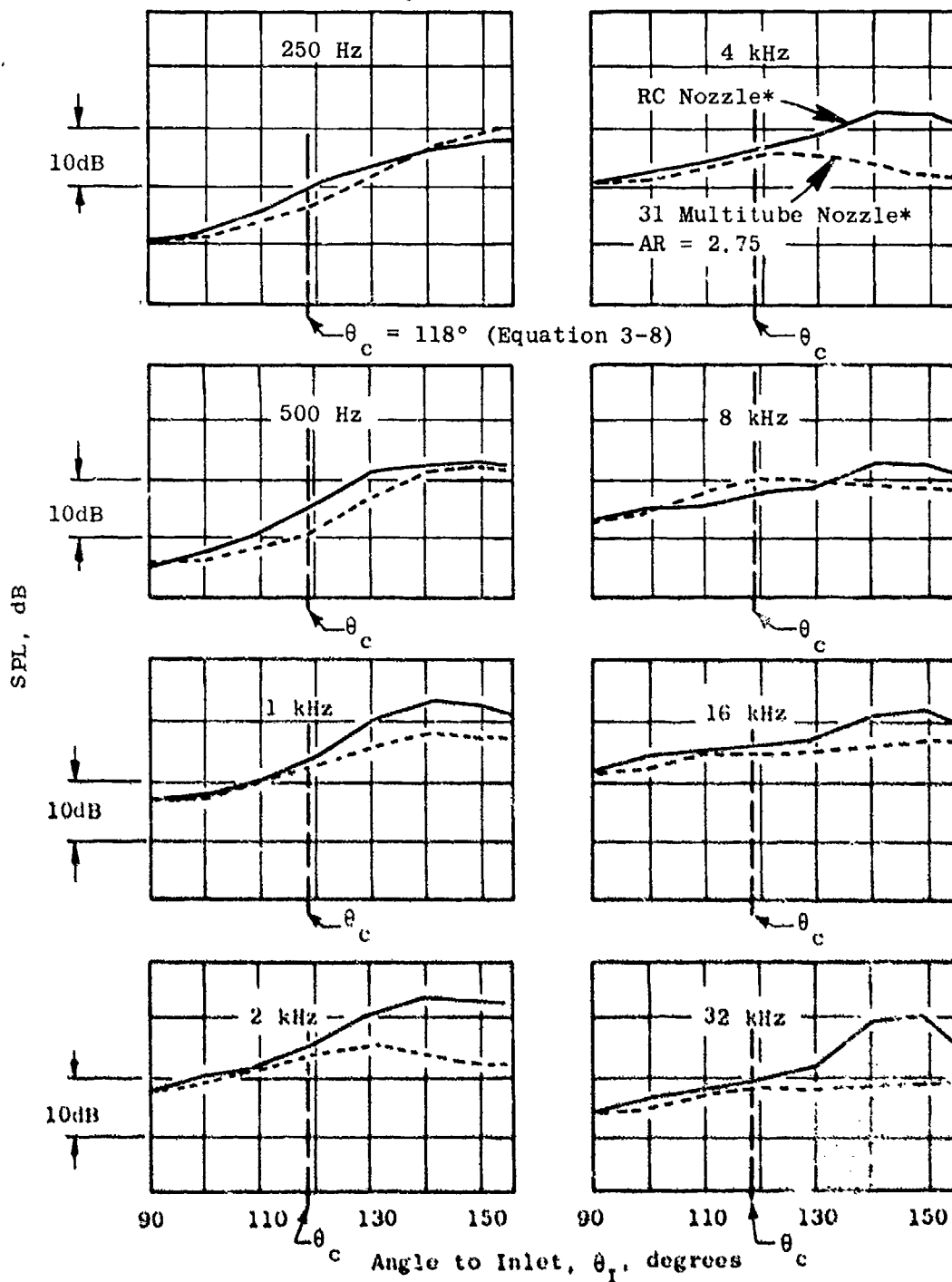


Figure 3-11. Comparison of Beam Patterns for Conical and Multitube Nozzles.

- Free Field
- No EGA
- 72 Tube/Plug
- AR = 2.95

Data (Ref)	V_j , ft/sec	T_g , ° R	P_8/P_0
○ (4)	1270	1274	1.47
△ (4)	1942	1530	2.19
□ (4)	2490	1871	2.98

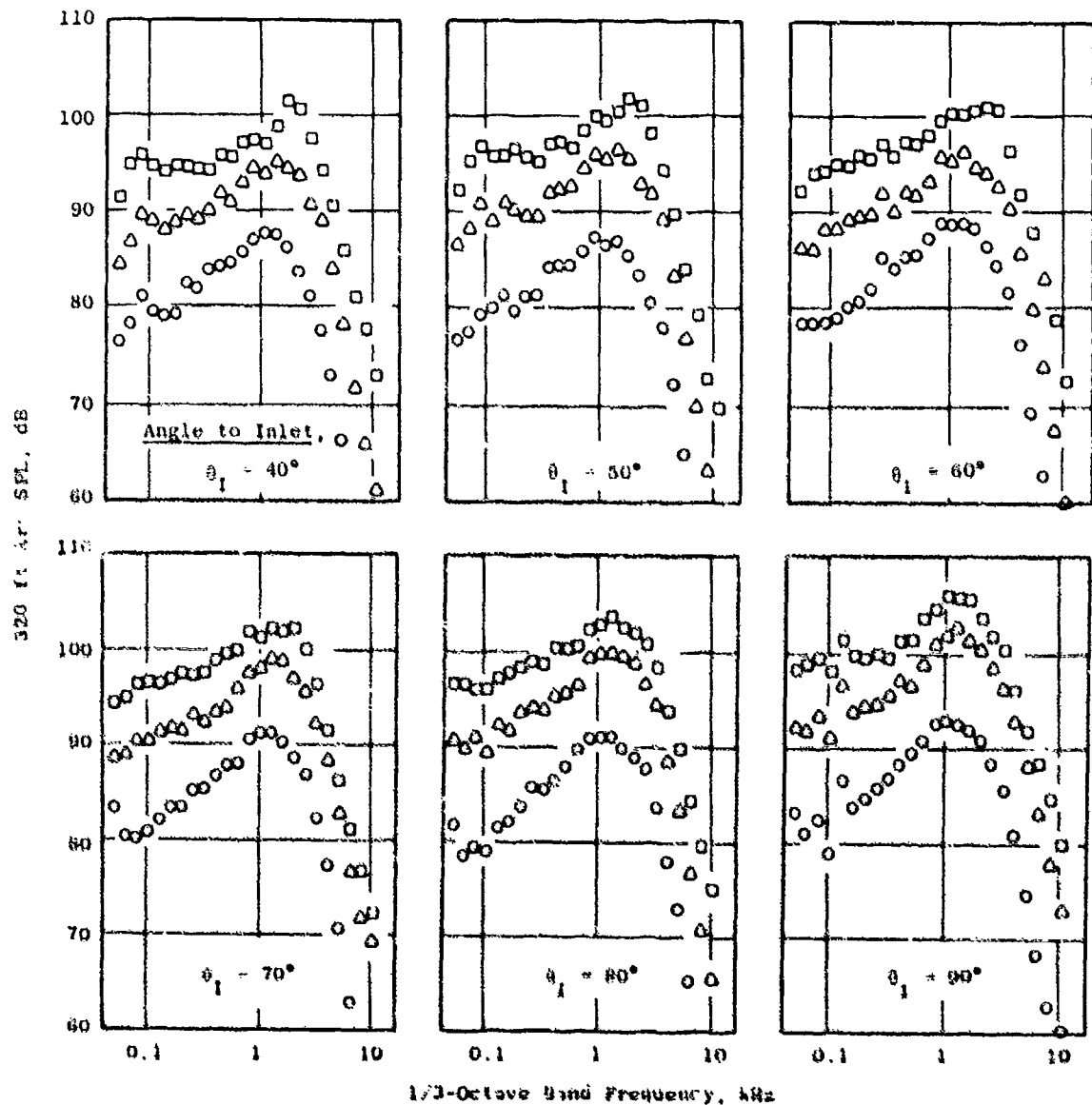


Figure 3-12. Multitube Nozzle Far-Field Spectra in Forward Quadrant (40° to 90° Angle to Inlet).

- Free Field
- No EGA
- 72 Tube/Plug
- AR = 2.95

Data (Ref)	V_j , ft/sec	T_g , °R	P_g/P_0
○ (4)	1270	1274	1.47
△ (4)	1942	1530	2.19
□ (4)	2490	1871	2.98

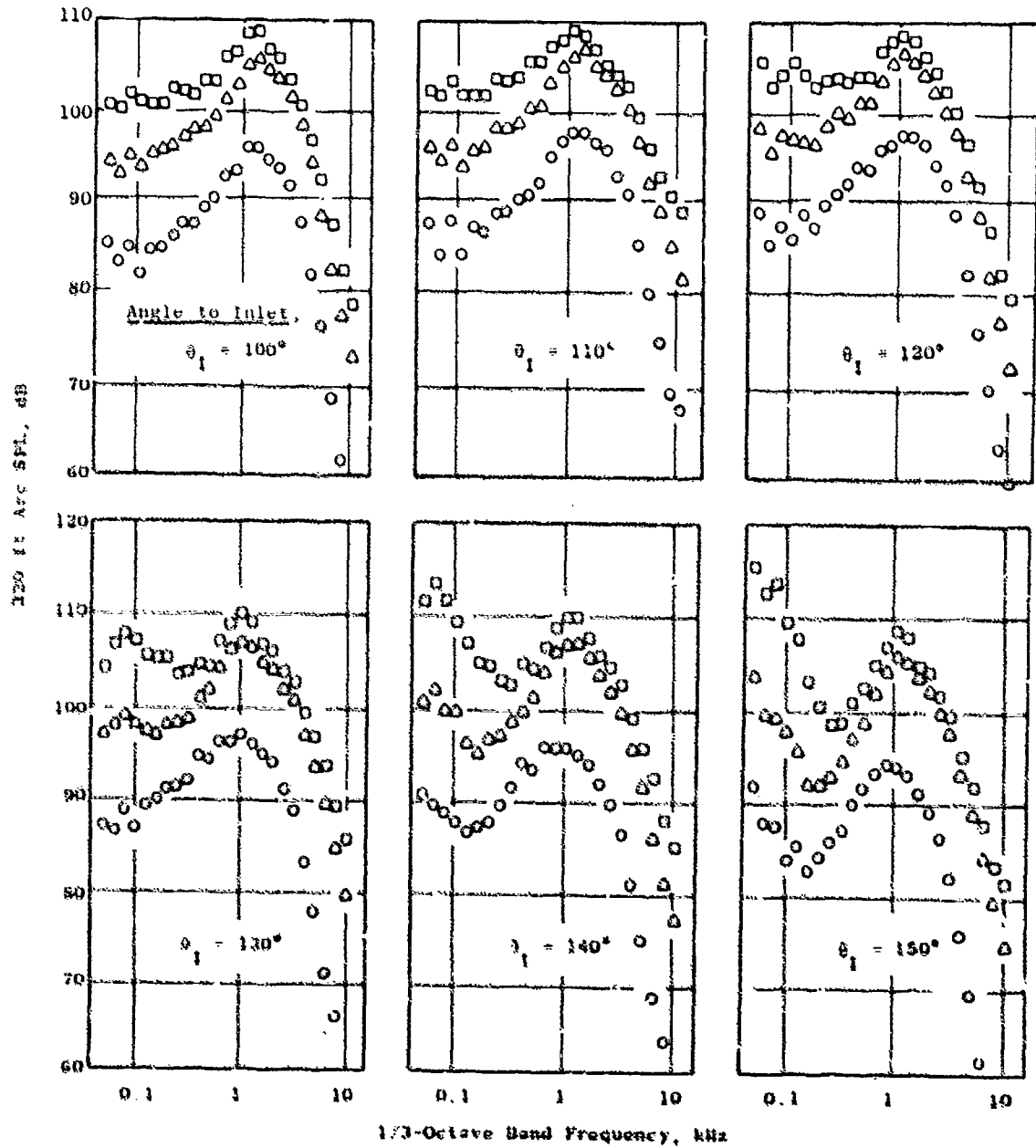


Figure 3-13. Multitube Nozzle Far-Field Spectra in Rear Quadrant (100° to 150° Angle to Inlet).

The critical angle, θ_c , relative to the inlet is given by:

$$\theta_c = 180 - \cos^{-1} \left[\frac{C_o/C_m}{1+M_m} \right], \text{ degrees} \quad (3-8)$$

where: C_o = ambient speed of sound

C_m = speed of sound based on the average of the exit flow and ambient velocities and static temperatures

M_m = mean Mach no. based on the average of the exit flow and ambient velocities and static temperatures

The predicted, high-frequency SPL's at the angle just forward of θ_c (based on the effective number of tubes) are used for all angles aft of θ_c .

3.2.2.3 Merged Jet Prediction

The method described by Potter and Crocker in Reference 29 was adapted to calculate the flow conditions of the jet when the flows from individual elements merge to form one large, mixed stream. Although the analysis was originally developed for noise prediction from clustered rocket engines, it is applicable to the multielement, jet-noise-suppressor configurations when proper adjustments for geometry are included. The complete details of the analysis are given in the original reference. In summary, it provides a solution to the mixing flow field that yields values for the area, velocity, temperature, and density of the merged jet. The solution is developed so that, at the merging location, the values can be used as if the flow were from a conical nozzle, and the low-frequency jet noise can be calculated by the conical jet noise procedure (Section 3.3.2).

Since the present problem involves air mixing with air, the Potter and Crocker formulation has been simplified. The following equations summarize the simplified forms that are used (keeping the original notation as defined after the equation):

Merged Jet Velocity

$$\theta^3 \propto K_2 (C_3 - C_4) M_A + c^2 (a K_2 P C_A M_A + U_3^2 / 2gJ) - \theta K_1 - T_A C_A = 0 \quad (3-9)$$

Merged Jet Area

$$A_5 = \frac{n\pi (R_2 - R_1)^2}{(\sqrt{n} - 1)^2} \quad (3-10)$$

Merged Jet Density

$$\rho_5 = \rho_3 P / \theta^2 \alpha \quad (3-11)$$

Merged Jet Static Temperature

$$T_5 = P_a \alpha M_a^2 / P \rho_3 R_u \quad (3-12)$$

where:

- A_3 = Total nozzle exhaust area, ft^2
- A_5 = Area of merged jet, ft^2
- C_a = Constant-pressure specific heat of ambient air, $\text{Btu/lb } ^\circ \text{R}$
- C_3 = Constant-pressure specific heat of air at the nozzle exhaust, $\text{Btu/lb } ^\circ \text{R}$
- J = 778 ft lb/Btu
- K_1 = $[C_3 T_3 + U_3^2 / 2gJ - T_a C_a] / P$, Btu/lb
- K_2 = $P_a / (R_u P_3 P^2)$, $^\circ \text{R}$
- M_a = Molecular weight of air, lb/lb mole
- n = Total number of tubes in exhaust nozzle
- P_a = Ambient pressure, lb/ft^2
- P_3 = Total pressure at nozzle exit plane*, lb/ft^2
- P = $[(P_3 - P_a)g / (U_3^2 \rho_3)] + 1$, dimensionless
- R_u = Universal gas constant = 1545 $\text{ft lb/}^\circ \text{R lb mole}$
- R_1 = Radius of individual tube, ft
- R_2 = Radius of circle circumscribing the tube bundle, ft
- T_a = Ambient temperature, $^\circ \text{R}$
- T_3 = Static temperature of the fully expanded jet at the nozzle exit, $^\circ \text{R}$
- T_5 = Static temperature of the merged jet, $^\circ \text{R}$

* Reference 29 defines this as the static pressure.

U_3 = Velocity of the fully expanded jet at the nozzle exit, ft/sec

α = A_5/A_3 = Ratio of merged jet area to total nozzle exhaust area

θ = Ratio of merged-jet velocity to nozzle-exit-jet velocity

ρ_3 = Density of the fully expanded jet for the nozzle discharge conditions, lb/ft³

ρ_5 = Density of the merged jet, lb/ft³

All definitions are as originally given (after corrections for misprints in the use of the gravitational constant, g) with the exception of the parameter P . This parameter was developed from the momentum equation in the form:

$$\frac{\rho_3 A_3 U_3^2}{g} + P_3 A_3 = \frac{\rho_5 A_5 U_5^2}{g} + P_a A_3 \quad (3-13)$$

When rearranged to solve for the conditions at Station 5 the parameter, P , appears:

$$\rho_5 A_5 U_5^2 = \rho_3 A_3 U_3^2 \left[1 + \frac{(P_3 - P_a)g}{\rho_3 U_3^2} \right] = \rho_3 A_3 U_3^2 P \quad (3-14)$$

This shows that the pressure, P_3 , should be the static pressure. When P_3 was interpreted as the total pressure, however, the (low frequency) noise prediction checked remarkably well. This was therefore adopted as an empirical modification of the original analysis.

Since the equation for velocity is a third-order equation, "Newton's Method," as defined in Reference 30, is used to determine an application root. After determining this root, the equation is simplified and the quadratic equation is used to solve for the other roots to see if they lie in the range of applicability. The root determined by "Newton's Method" for $0 < \theta < 1$ was invariably applicable and is therefore always used in the computer program to determine the merged velocity, even if another root is real. In that event, the additional root is printed out so that it can be checked for impact on noise.

In the case where a plug was involved, the nozzle outer diameter is defined as below, and the area, A_5 , is determined. All other equations remain the same.

$$R_2 = \sqrt{n(AR)R_1^2 - R_0^2} \quad \text{for } R_r \leq 0.6 \quad (3-15)$$

$$R_2 = K_0 \sqrt{n(AR)R_1^2 - R_0^2} \quad \text{for } R_r \geq 0.6$$

where: $K_0 = -1.947 \log_{10} (R_r/1.954) [1 - 0.2525 \log_{10} (T_8/1750)] \sqrt{R_r/0.716}$

R_r = suppressor radius ratio

AR = nozzle area ratio (annulus area filled by the suppressor divided by the nozzle flow area)

R_g = nozzle plug radius (ft)

All other variables are as previously defined.

3.2.2.4 Summary of Prediction Elements

The following method is used in the computer program (Appendix A) for determining noise levels for multielement suppressor nozzles; exceptions to this procedure for specific nozzle types are specified in Section 3.3.

1. The SPL versus angle for each one-third-octave band is determined from the conical nozzle correlation (Section 3.3.2) for an individual element prior to merging, based on the nozzle exit conditions, and for the merged jet based on the flow conditions and area calculated according to the "Merged Jet Thermodynamic Conditions" portion of this section, (Equations 3-9 through 3-12).
2. Noise is calculated for the flow from tubes (prior to merging) as follows:
 - (a) The axial location of the peak noise generation is determined for each one-third-octave band by means of Equations 3-2 and 3-3. Using the one-third-octave band midpoint frequency, Equation 3-2 is solved for X/D , designated as $(X/D)_{peak}$ for each one-third-octave band.
 - (b) The axial location, $(X/D)_m$ at which noise is no longer generated by flow from the individual tubes is determined by Equation 3-6 for each one-third-octave band.
 - (c) The ratio of the value determined in (b) to that in (a), above, is used as the value for each one-third-octave band of

$$(X/D)_m / (X/D)_{peak}$$

in Figure 3-7 to obtain the SPL level relative to the overall one-third-octave band SPL (determined in Step 1); this determines the SPL in the one-third-octave band for noise from an individual tube.

- (d) The noise from the nozzle is then determined based upon the effective number of tubes as determined by Equation 3-7.

- (e) Aft of the critical angle the SPL on the arc for the premerged noise is held constant and equal to the corresponding SPL just forward of the critical refraction angle, defined by Equation 3-8.

3. Noise for the merged flow (determined in Step 1) is then added to that from premerged flow (Step 2) for each one-third-octave band.

Finally, shock-cell noise is calculated for each nozzle type as discussed in Section 3.3 and, when present, is added to the mixing noise.

3.2.3 Literature Sources Considered in Developing the Correlation

The published literature which supplied the data base for the Engineering Correlation (in addition to the data from the current program) is identified in Appendix B. The contents of Appendix B are organized according to the type of nozzle and type of suppressor, with separate tables for each combination. The references included in these tables are identified in the Bibliography included as a part of the Appendix.

Specific references for each nozzle type are separately identified in Section 3.3 including a definition of the nozzle geometries, parameters, and the range of test conditions.

3.3 ENGINEERING CORRELATION PREDICTIONS AND DATA COMPARISONS FOR THE TASK 3 JET SUPPRESSOR NOZZLES

3.3.1 Overall Summary of the Adequacy of the Correlation Procedure

The correlation between measured and predicted noise levels for all types of suppressor nozzles (as described in Section 3.2.1) is shown in Figure 3-14 for perceived noise level (PNL as calculated per Reference 31) at the sideline angle at which the maximum PNL occurred and in Figure 3-15 for effective perceived noise level (EPNL). All comparisons are presented at distances of 1500 to 2400 feet, depending on the literature source. In order to estimate the EPNL, the static test data for the nozzle were used to calculate a PNL history for a level flyover, without the use of any flight effects upon noise generation or radiation.

The measured and predicted data in Figures 3-14 and 3-15 are presented relative to a "reference" level in order to assure that the full range of the noise variation was the consequence of thermodynamic variation and not size variation. Thus, when sets of data were from two nozzles of different sizes (flow areas), the noise for each was predicted at a reference set of thermodynamic conditions (a pressure ratio of about 2.5 and a temperature resulting in a jet velocity of about 2000 ft/sec); noise at other conditions was then normalized relative to the reference conditions. The data in the figures are in the form, therefore, as given by:

- The "Reference" level is the predicted value of noise for each nozzle, at a specified set of thermodynamic conditions, plus an arbitrary value of 100 dB.

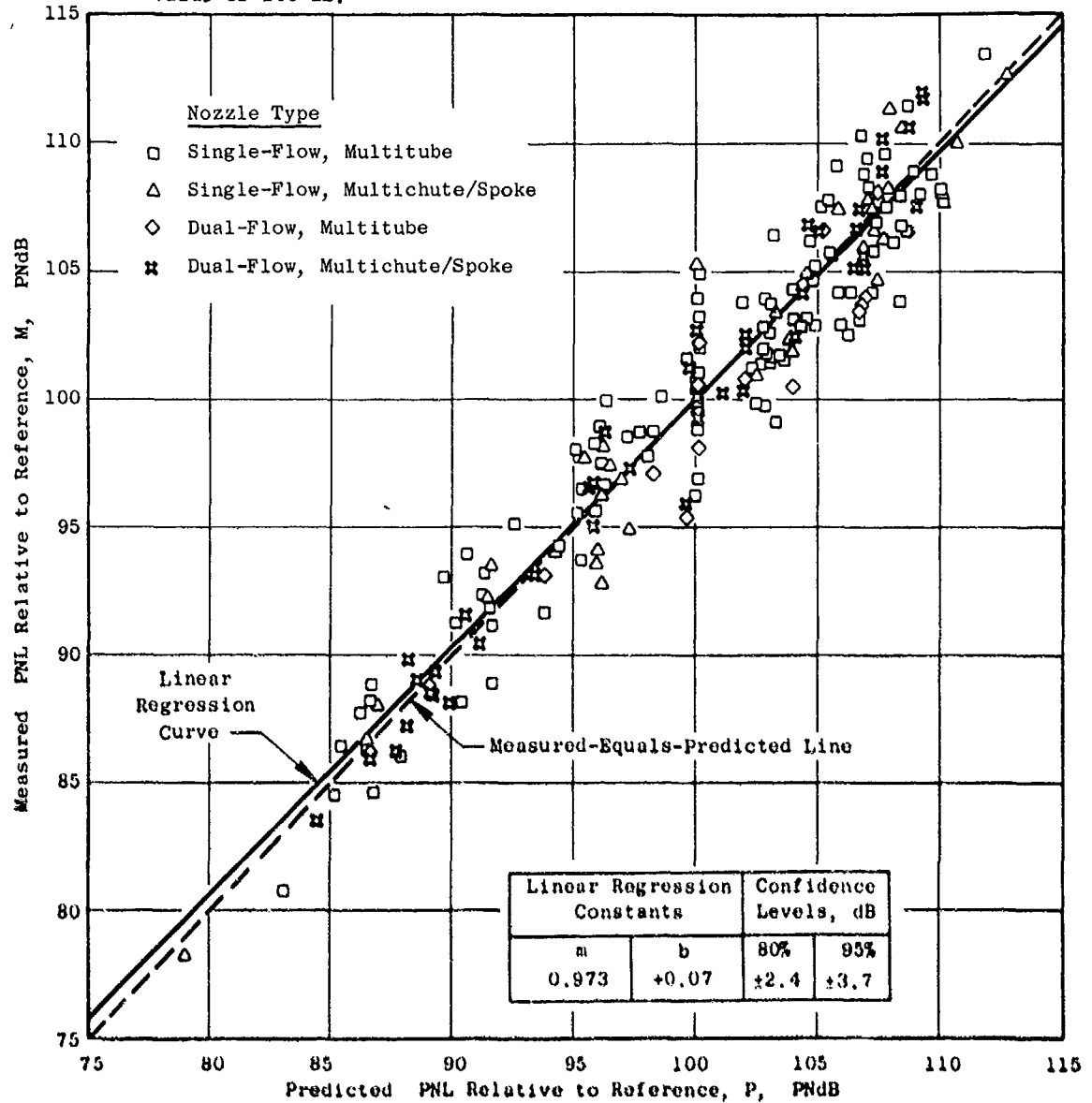


Figure 3-14. Correlation Between Measured and Predicted Maximum Perceived Noise Level (PNL) for all Types of Suppressor Nozzles.

- Flyover calculation using static data corrected to free-field conditions.
- The "Reference" level is the predicted value of noise for each nozzle, at a specified set of thermodynamic conditions, plus an arbitrary value of 100 dB.

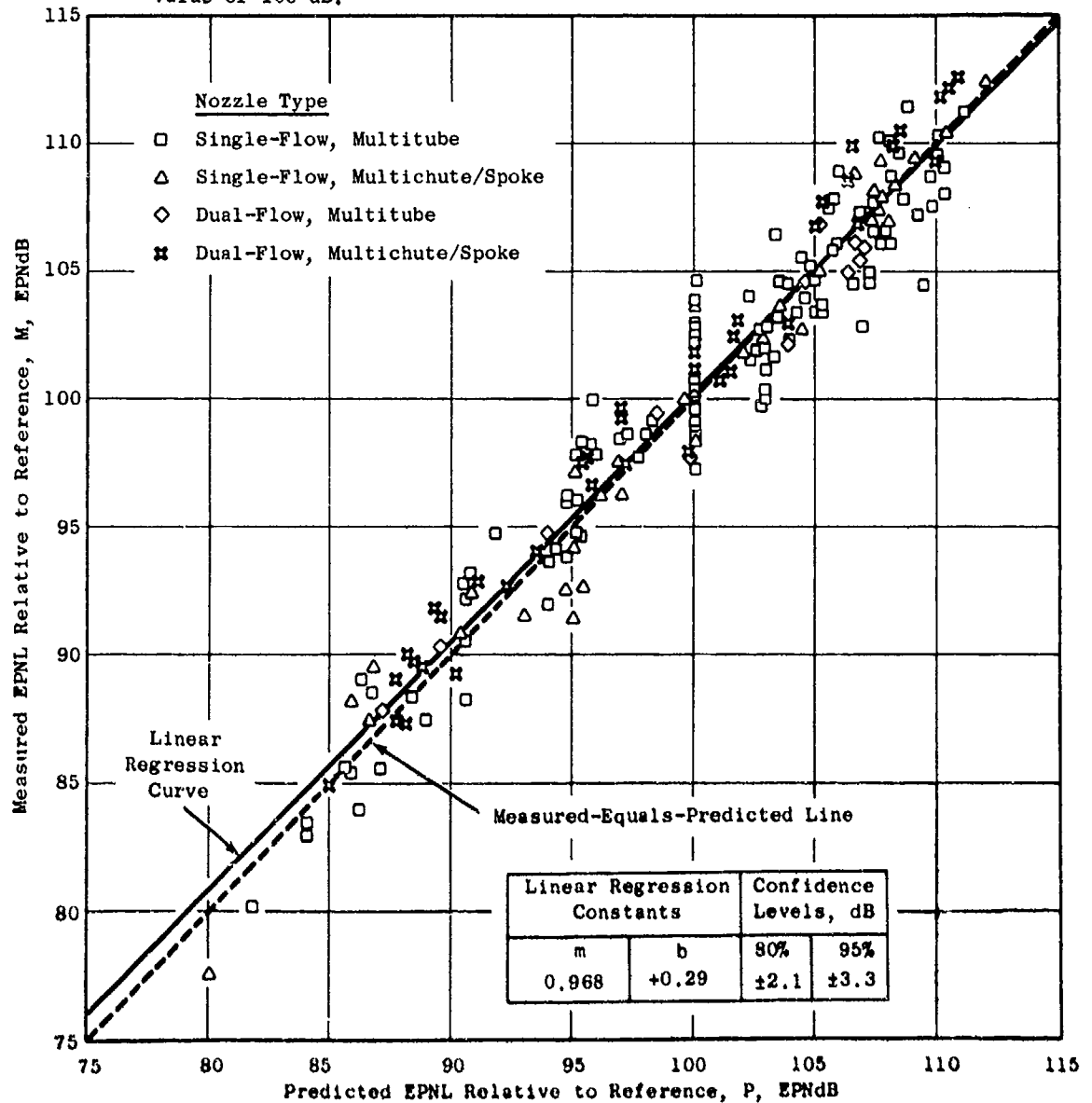


Figure 3-15. Correlation Between Measured and Predicted Effective Perceived Noise Level (EPNL) for all Types of Suppressor Nozzles.

Measured Relative to Reference:
$$M = \frac{(\text{PNL measured at test point}) - (\text{PNL predicted at reference})}{+ 100}$$

versus

Predicted Relative to Reference:
$$P = \frac{(\text{PNL predicted at test point}) - (\text{PNL predicted at reference})}{+ 100}$$

The same was done for the case of EPNL.

The data in this form were then evaluated by linear regression analysis of the form: $(M-100) = m(P-100) + b$ and the values of the resulting linear regression constants, m and b , are shown on the figures together with the spread in the data for 80% and 95% confidence. Also shown are lines through the data including: (a) a solid line representing the linear regression curve and (b) a dashed line representing the "measured equals predicted" case for reference. Further description on converting the measured value (relative to the reference value) to the "expected" value is given in Section 3.3.3.3.

The figures show that the value of b , a measure of the difference between the overall averages of the measured and predicted data, is less than 0.1 dB for the PNL and less than 0.3 dB for the EPNL correlation. Also, the value of m , which is a measure of any consistent trend for deviation of the measured from the predicted value of the noise, is within 3% of a 1:1 relationship over a range of about 35 dB.

In most cases, the slope is slightly less than 1:1; this is the result of underprediction at low jet velocities caused by the high-frequency noise (even though all the nozzle elements of a multielement suppressor are summed in those cases without cutoff) and an overprediction at high velocities (apparently caused by an underprediction of the cutoff effect). The random scatter about the mean line is within 2.4 dB for 80% confidence and within 3.7 dB for 95% confidence. Consequently, the measured data are concluded to be well correlated by the prediction method in which the expected value, M , is determined from the predicted value, P , based upon the linear regression analysis.

Such data are presented in subsequent subsections of this section for each individual nozzle type. A summary of this information is included in Table 3-1. For each nozzle type, the linear regression constants, m and b , and the 80% and 95% confidence limits are tabulated. Also, the number of nozzles which were available to establish the correlation is listed. This information is given for both the PNL and the EPNL measure of the noise. In general, the table shows that any nozzle type can be estimated within 2.6 dB or less, whether maximum PNL or EPNL, with 80% confidence.

The following subsections discuss each nozzle type individually. A definition of the prediction method and data base used, a summary of the prediction elements, and a discussion of the data comparisons and accuracy

Table 3-1. Linear Regression Analysis Results for Suppressor Nozzles.

Nozzle Type		Linear Regression Constants		Confidence Limits (dB)		Number of Nozzles
		m	b	80%	95%	
PNL	All Suppressors	0.973	0.07	2.4	3.7	43
	Conical	1.003	0.63	1.3	2.0	1
	Single-Flow, Multitube	0.951	0.19	2.6	4.1	21
	Special Nozzles	0.883	0.59	1.9	3.1	2
	Single-Flow, Multichute/Spoke	0.995	0.05	2.4	3.6	10
	Dual-Flow, Multitube	0.887	-1.81	2.3	3.8	1
	Dual-Flow, Multichute/Spoke	1.041	0.22	1.8	2.8	9
EPNL	All Suppressors	0.968	0.29	2.1	3.3	43
	Conical	0.975	-0.34	1.2	1.9	1
	Single-Flow, Multitube	0.952	0.20	2.5	3.8	21
	Special	0.937	0.06	1.9	3.1	2
	Single-Flow, Multichute/Spoke	1.003	0.11	2.0	3.0	10
	Dual-Flow, Multitube	0.911	-0.25	1.7	2.8	1
	Dual-Flow, Multichute/Spoke	1.000	0.89	1.6	2.5	9

are presented. In the presentation of data accuracy, representative comparisons are shown of frequency spectra and far-field directivity of PNL.

3.3.2 Conical Nozzles

3.3.2.1 Definition of Method and Data Base Used

The SAE ARP 876 proposed revision dated April 1, 1975 as documented in Reference 32, and included in Appendix C as the gas turbine jet exhaust noise prediction, was adapted for predicting single-stream jet mixing noise with the minor modification of increasing the predicted levels by 1.0 dB. This correlation was used, rather than later SAE draft revisions, because of timing and because the latest revision had not yet been approved by the SAE committee. The origins of the experimental data base for the prediction are listed in Reference 32.

The single-stream, shock-cell noise proposed to the SAE Jet Noise Subcommittee (A-21), Reference 33, and also included in Appendix C, was also adapted. An error in Reference 33 has been corrected in the program for the value of $H(f)$, as follows:

$$H(f) = \left[1 + \frac{2}{N} \sum_{i=1}^{N-1} C_{(sn)}^{(i)^2} \sum_{s=0}^{N-(i+1)} \frac{\cos(F) \sin(0.115F)}{(0.115F)} \right] \quad (3-16)$$

The equation for SPL then should read:

$$SPL_{(f)} = 10 \log_{10} \left[\left(\frac{\beta^2 D_j}{r} \right)^2 H(f) \right] + G_{(sn)} \quad (3-17)$$

3.3.2.2 Summary of Prediction Elements

The detailed prediction procedures for mixing and shock-cell noise are defined in Appendices C and D. In general, for pure jet mixing noise, a normalization of OASPL is given at acoustic angles from the inlet between 20 degrees and 160 degrees. This normalization is a function of the density ratio (to the "w" power), the nozzle exit area, the acoustic range, and the fully expanded jet velocity. Spectral distributions are presented as a function of modified Strouhal number. Air attenuation and extra ground attenuation (EGA), References 34 and 35 respectively, are applied as required.

Shock-cell OASPL is determined as a function of nozzle exit diameter, jet Mach number, acoustic range, and acoustic angle. Spectral distribution is determined as a function of modified Strouhal number, shock-cell spacing

and the number of shock cells. Air attenuation and EGA are applied to arrive at the far-field SPL contribution due to shock-cell noise.

3.3.2.3 Data Comparisons and Accuracy

The 1975 proposed revision to SAE ARP 876 used herein was the best correlation available at the beginning of this effort. An analysis of the accuracy of this method and other methods with respect to available data is presented in Reference 36 (Zorumski and Brown of NASA-Langley Research Center collaborating with Andre and Kapper of LTV Aerospace Corporation). This reference presents an analytical method of evaluating the accuracy of jet noise prediction methods with respect to a given data base. Although the analysis is not meant to provide a final evaluation of the "best" correlation, it does show that the 1975 proposed revision of SAE ARP 876 is as good or better than two other recently documented prediction methods and only slightly poorer than the best of the four methods reviewed. The authors also note that a one-dB upward shift in the SAE "carpet plot" would make the SAE prediction of power agree with the Lockheed experimental data base (Reference 14) within ± 1.5 dB. Reference 14 provides some checks against data which indicate that the prediction method adequately models shock noise from conical nozzles.

Another check of the accuracy of the total jet noise prediction method is provided in Figures 3-16 and 3-17 using data taken during this program. The figures show measured versus predicted maximum PNL and "static" EPNL respectively. This "static" EPNL is defined as the sum of the maximum value of tone-corrected, perceived noise and the duration correction. It is determined using the PNLT generated statically (i.e., the noise ignoring flight effects). Linear regression analysis shows that the measured value agrees with the predicted for PNL and EPNL within 1.3 and 1.2 dB, respectively, with 80% confidence.

Data showing typical checks between predicted and measured maximum PNL (normalized) versus velocity, PNL directivity, and one-third-octave band SPL spectra for the far-field angles 50° , 90° , and 130° (from the inlet) are given in Figures 3-18 through 3-22, respectively. The predicted values include both the mixing and the shock-cell noise as defined in Section 3.3.2.1.

3.3.3 Multitube Nozzles

3.3.3.1 Definition of Method and Data Base Used

The multitube-type nozzle was used as the example discussed in Section 3.2.2 for the development of the M*S engineering correlation method for multielement suppressors. The data base used for checking the predicted versus measured noise in evolving the correlation is summarized in Table 3-2. Shock noise for a single tube is calculated using the relationships for a conical nozzle; the level is then determined by the effective number of tubes, N_{eff} , per Equation 3-7, with an empirical reduction amounting, in

- The "Reference" level is the predicted value of noise for each nozzle, at a specified set of thermodynamic conditions, plus an arbitrary value of 100 dB.

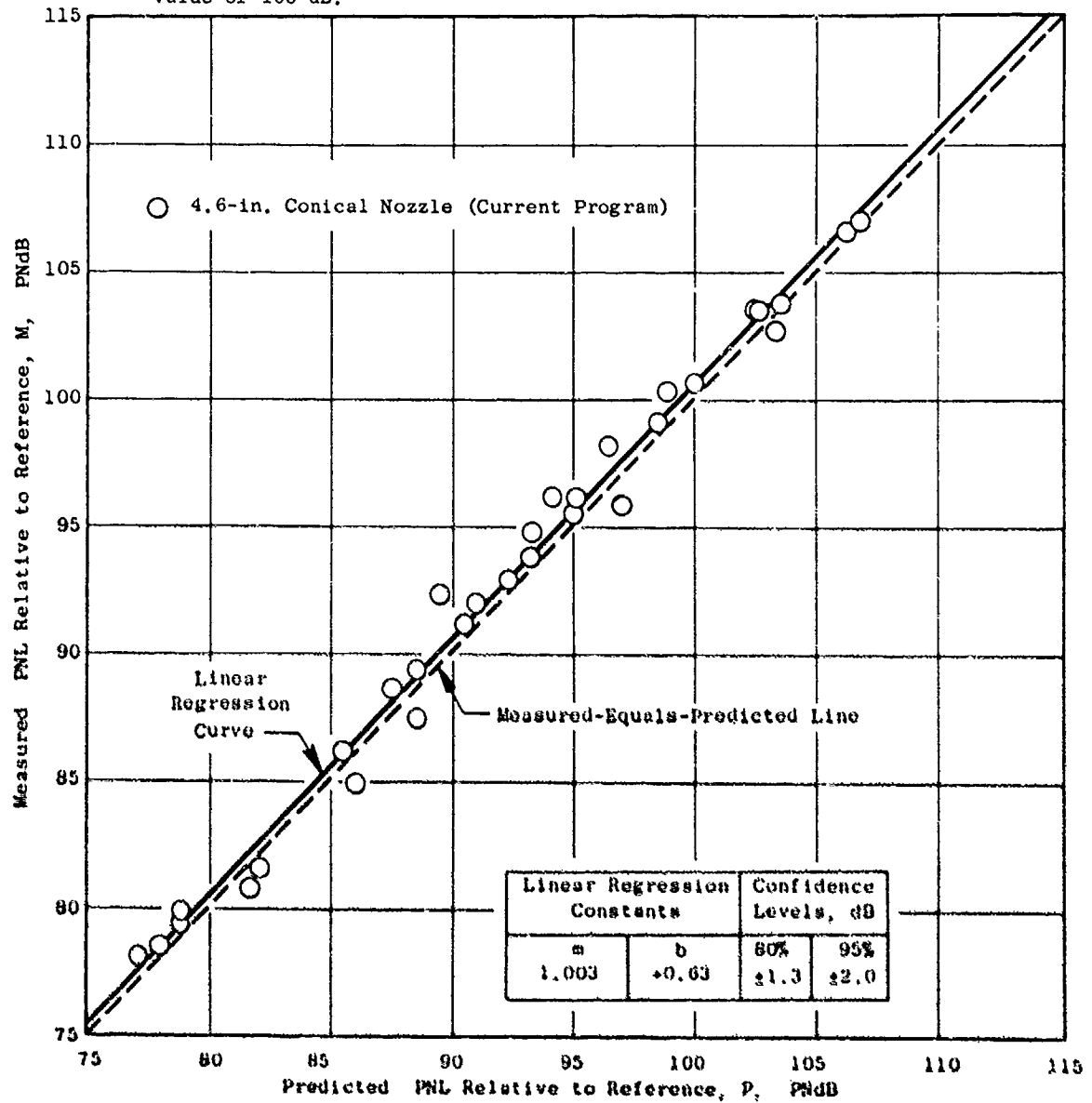


Figure 3-16. Correlation Between Measured and Predicted Maximum Perceived Noise Level (PNL) for a Conical Nozzle.

- Flyover calculation using static data corrected to free-field conditions.
- The "Reference" level is the predicted value of noise for each nozzle, at a specified set of thermodynamic conditions, plus an arbitrary value of 100 dB.

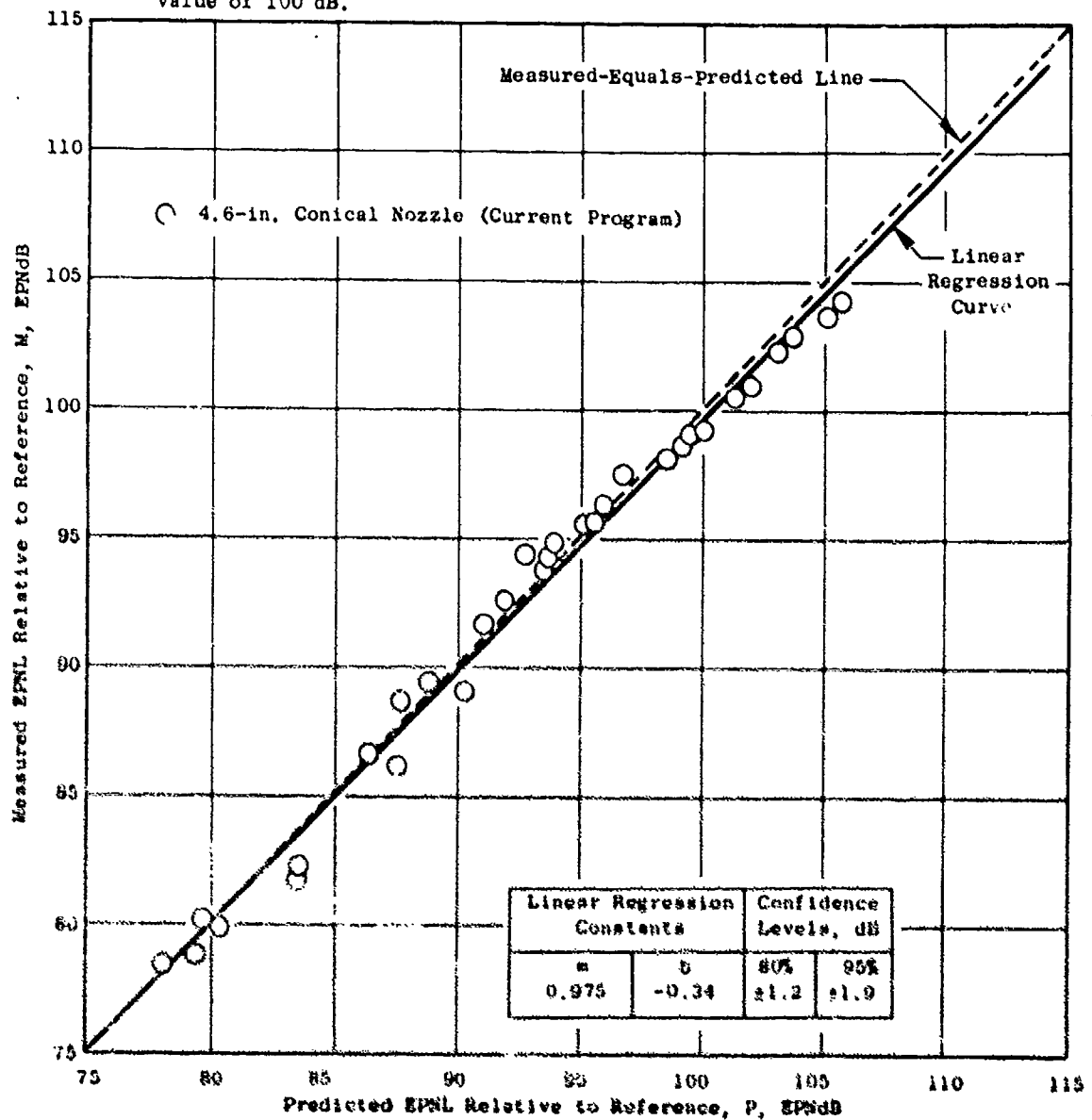


Figure 3-17. Correlation Between Measured and Predicted Effective Perceived Noise Level (EPNL) for a Conical Nozzle.

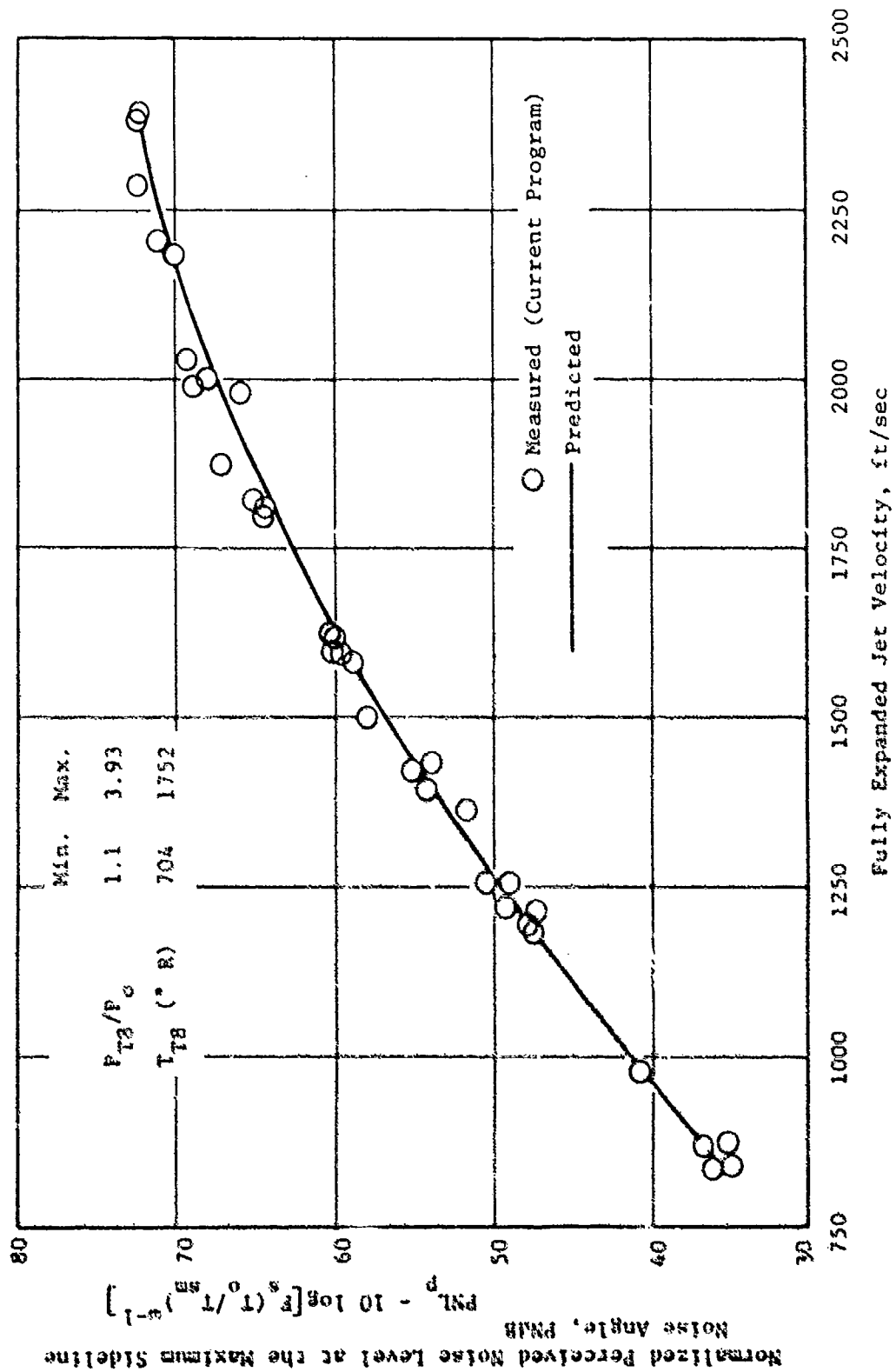


Figure 1-18. Typical Check of Predicted and Measured Maximum Perceived Noise Level Versus Jet Velocity for a Conical Nozzle.

\bigcirc $P_T/P_0 = 1.474$, $T_T = 1109^\circ R$, $V_j = 1184$ ft/sec
 \triangle $P_T/P_0 = 1.978$, $T_T = 1203^\circ R$, $V_j = 1602$ ft/sec
 $+$ $P_T/P_0 = 2.745$, $T_T = 1320^\circ R$, $V_j = 2001$ ft/sec
 \times $P_T/P_0 = 3.924$, $T_T = 1488^\circ R$, $V_j = 2397$ ft/sec
 — Predicted

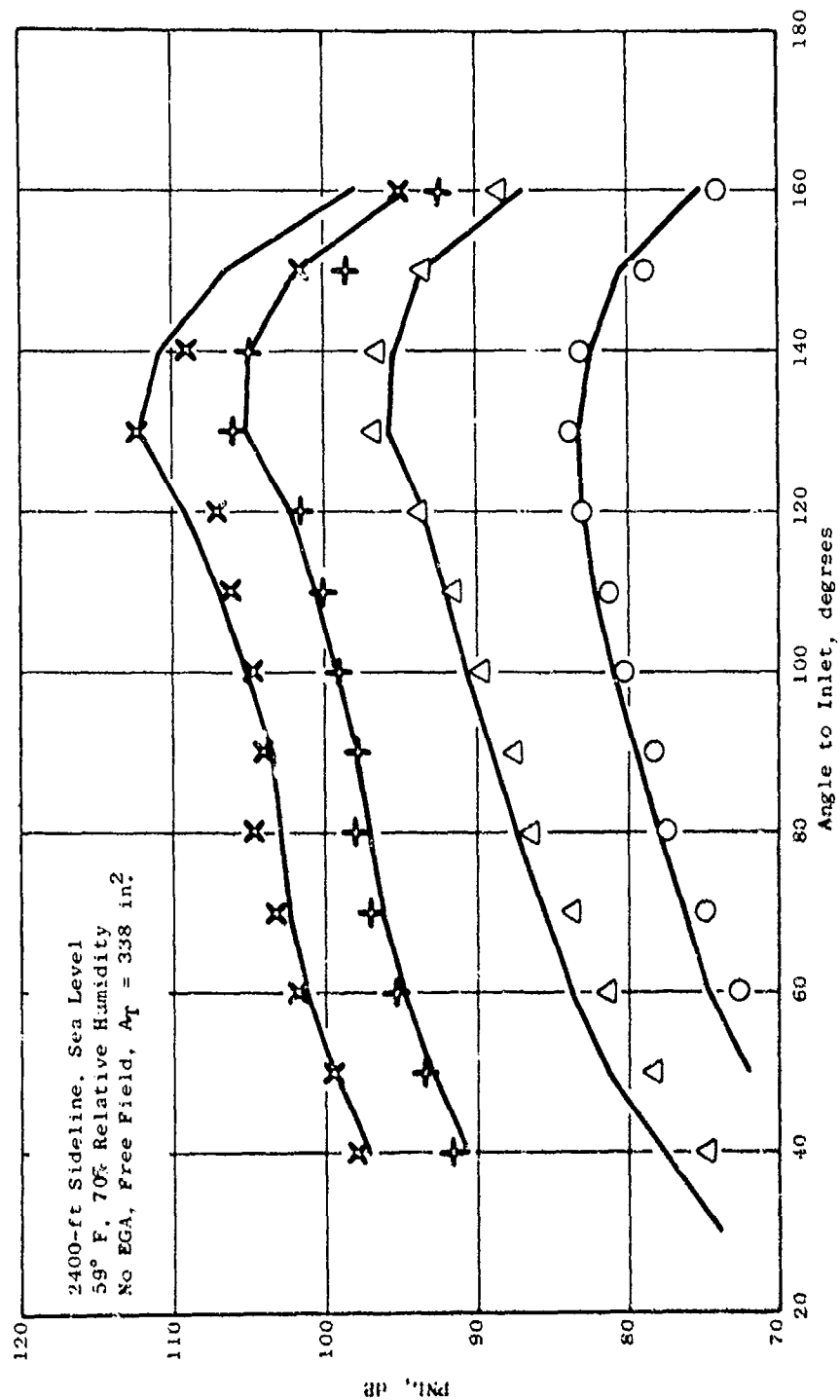


Figure 3-19. Representative Check of Predicted Versus Measured PNL Directivity for a Conical Nozzle.

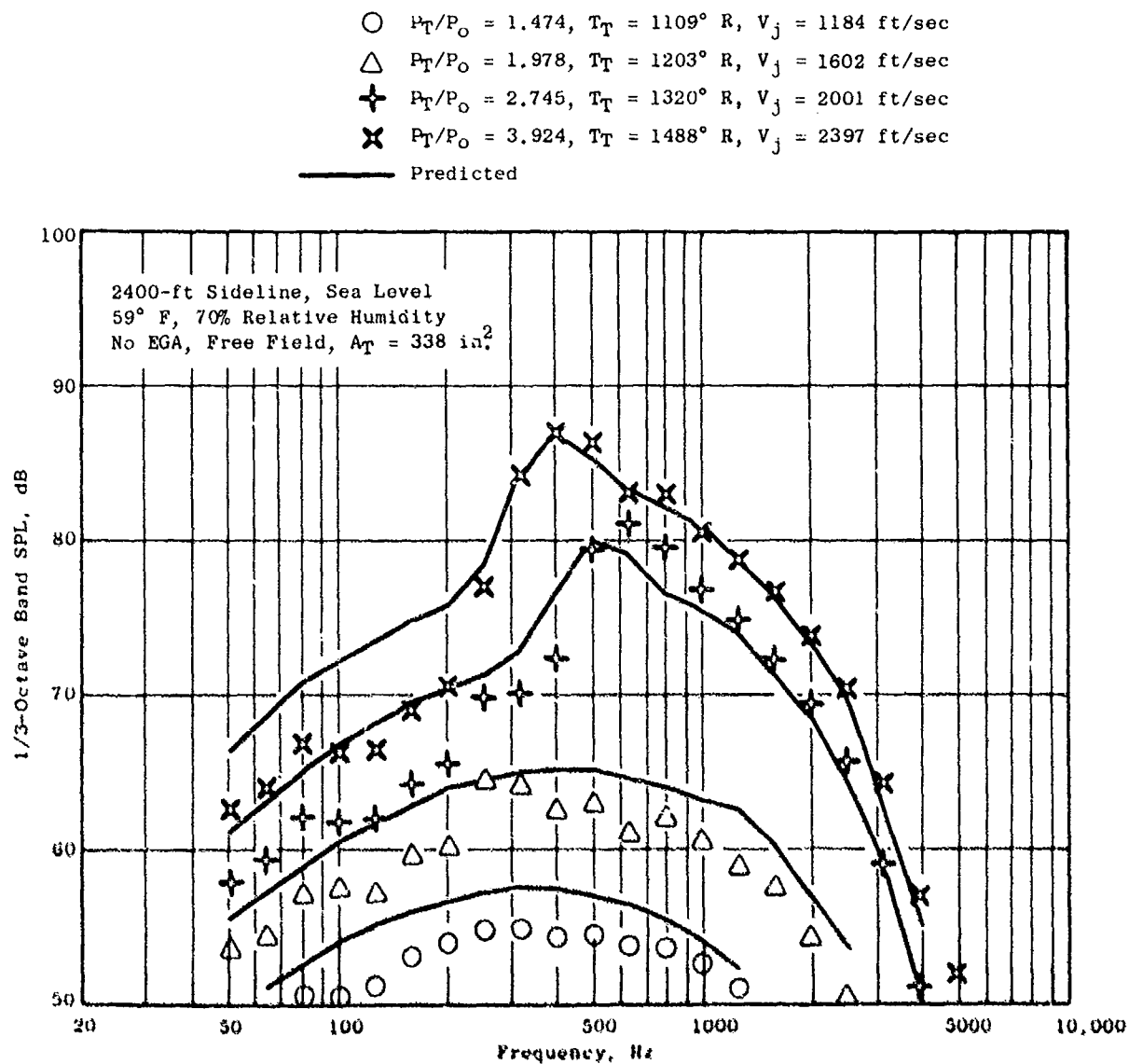


Figure 3-20. Representative Check of Predicted Versus Measured Spectra of a Conical Nozzle (50° Inlet Angle).

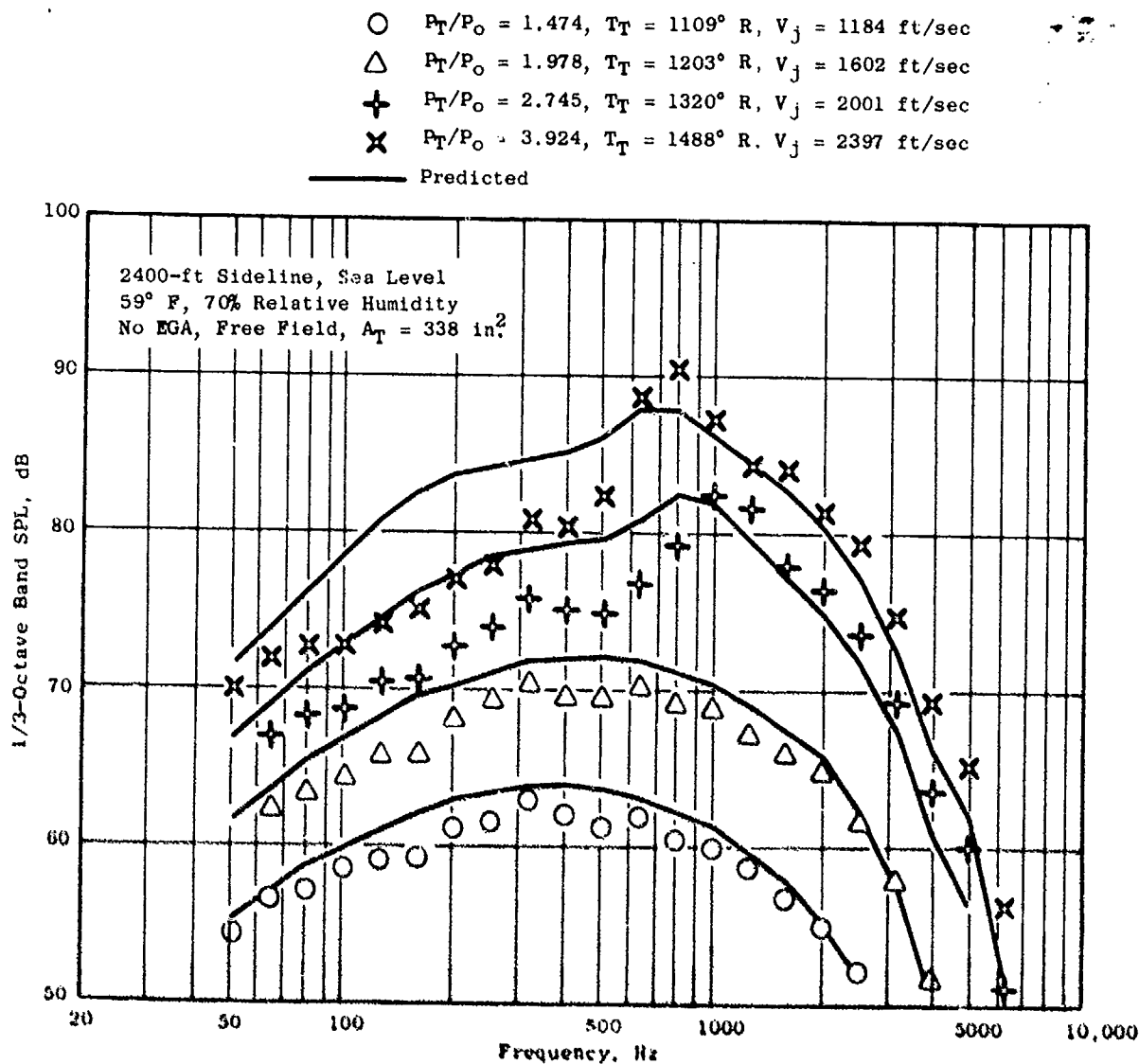


Figure 3-21. Representative Check of Predicted Versus Measured Spectra for a Conical Nozzle (90° Inlet Angle).

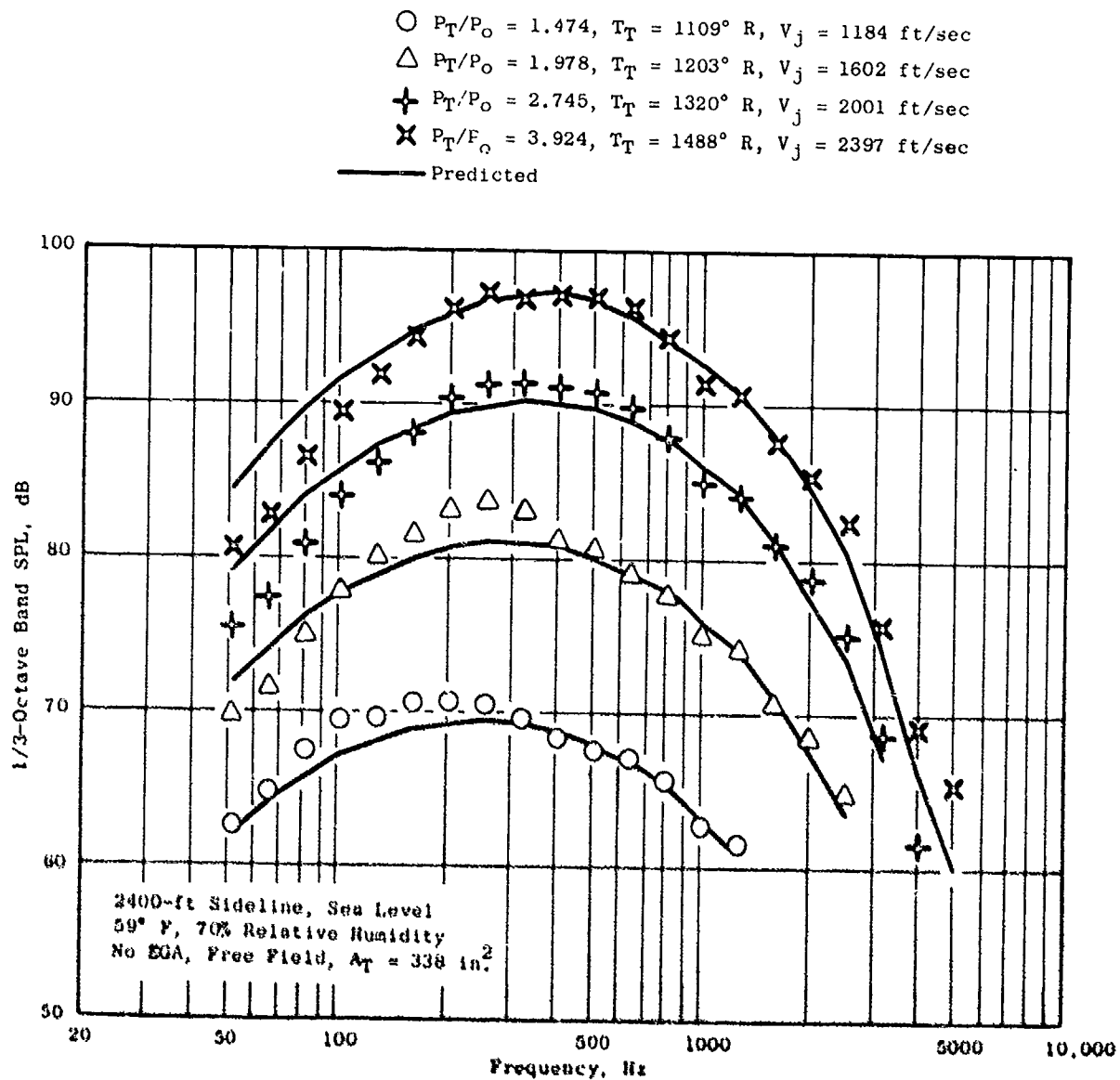


Figure 3-22. Representative Check of Predicted Versus Measured Spectra for a Conical Nozzle (130° Inlet Angle).

Table 3-2. Data Base for Single-Flow, Multitube Nozzles. (1)

Reference	Identification	Element Number/Type	Suppressor Area Ratio (2) AR	Pressure Ratio Range	Temperature Range ° R	Velocity Range fps	Comments
1	Vol I: p 656	85 Holes	2.0	1.4-3.5	1150-2700	1177-3164	Plug
		85 Holes	2.3	1.4-3.5	1150-2700	1177-3164	
		85 Holes	2.7	1.4-3.5	1150-2700	1177-3164	
		85 Holes	3.1	1.4-3.5	1150-2700	1177-3164	
		85 Holes	4.0	1.4-3.5	1150-2700	1177-3164	
		55 Holes	2.7	1.4-3.5	1150-2700	1177-3164	
		121 Holes	2.7	1.4-3.5	1150-2700	1177-3164	
		72 Tubes	2.86	1.4-3.5	1150-2700	1177-3164	
		72 Tubes	3.06	1.4-3.5	1150-2700	1177-3164	
		65 Holes	3.0	1.4-3.5	1150-2700	1177-3164	
		72 Tubes	2.73	1.4-3.5	1150-2700	1177-3164	
		37 Tubes	3.33	1.8-3.4	1460-2720	1660-3340	
		126 Tubes	3.3	1.8-3.4	960-1960	1350-2680	
2	Vol II: p 175 p 248, D179, D203	37 Tubes	4.0	1.8-3.0	1960	1920-2555	Plug
		253 Tubes	4.65	1.8-3.0	1460	1660-2310	
		37 Tubes	5.2	1.8-3.0	1960	1920-2555	
		37 Tubes	6.0	1.8-3.0	1960	1920-2555	
		72 Tubes	2.95	1.47-3.85	1270-2190	1270-2950	
		37 Tubes	3.3	2.0-4.0	1610	1875-2540	
		7 Tubes	3.3	2.0-4.0	1610	1875-2540	
		19 Tubes	3.3	2.0-4.0	1610	1875-2540	
		37 Tubes	3.3	2.0-4.0	1610	1875-2540	
		61 Tubes	2.75	2.0-4.0	1610	1875-2540	
		47 Tubes	4.5	2.0-4.0	1610	1875-2540	
		37 Tubes	6.0	2.0-4.0	1610	1875-2540	
		37 Tubes	3.3	2.0-4.0	1610	1875-2540	
3	Vol III: p 174	37 Tubes	4.5	2.0-4.0	1610	1875-2540	Plug
		37 Tubes	3.3	2.0-4.0	1610	1875-2540	
		37 Tubes	2.75	2.0-4.0	1610	1875-2540	
		31 Tubes	3.1	2.0-3.8	1960	2070-2770	
		61 Tubes	3.1	2.0-3.8	1960	2070-2770	
		65 Tubes	3.1	2.0-3.8	1960	2070-2770	
		72 Tubes	2.95	1.58-2.8	1160-1410	1200-2000	
		66 Tubes	2.7	1.47-3.85	1220-2150	1250-2925	
		104 Tubes	2.8	1.18-3.8	1000-1800	700-2630	
		Special Multitube Nozzles					
Current Program	Model No. 20	72 Tubes	2.95	1.58-2.8	1160-1410	1200-2000	Plug
4	Vol I: p 174	66 Tubes	2.7	1.47-3.85	1220-2150	1250-2925	Plug
25	Vol I: p 174	104 Tubes	2.8	1.18-3.8	1000-1800	700-2630	Plug

(1) Nozzles do not have a centerbody plug unless noted in comments.
(2) Ratio of nozzle area (annulus if plug nozzle) to flow area.

decibels, to twice the nozzle pressure ratio. This correction accounts for the fact that suppressor base pressures are considerably lower than ambient (free stream) thus increasing the effective ratio of the elemental jets (see Volume II).

In general, the multitube correlation in the computer program applies only for the conditions described in Section 3.2.1 (it is based on nozzles having hexagonal arrays of equally spaced, round tubes with parallel centerlines). Perturbations from the simple nozzle may, however, be desirable in order to improve aerodynamic performance, acoustic signature, or mechanical feasibility. A number of "advanced" nozzles have been designed and tested. This section discusses the correlation relative to the prediction of the noise from these nozzles.

Two important special nozzles are the 104-tube nozzle (Reference 25) and the 66-tube nozzle (Reference 4). The 104-tube nozzle had varying tube size, spacing, and shape. The 66-tube nozzle has nonuniform spacing, a plug, and a canted outer row of tubes. The average spacing of the outer row of tubes for both nozzles is about 10% greater than the overall average tube spacing of the nozzle.

The effect of nonuniform tube centerline spacing is calculated by assuming uniform spacing for the postmerged noise and using the actual average outer row spacing for premerged cutoff and for determining the effective number of tubes.

In addition to nonuniform spacing, the 104-tube nozzle has elliptical tubes of three different sizes. The largest variation from round is 1.79:1 and the smallest is 1.26:1. The tube size variation from the average tube size based on the actual total flow area is between -9% and +31%. These variations were predicted by assuming 104 equally spaced tubes of equal diameter where the diameter is determined by the total flow area required.

3.3.3.2 Summary of Prediction Elements

The computer program includes the procedure given in Section 3.2.2 as summarized in "Summary of Prediction Elements," with the shock-cell noise calculated as defined in Section 3.3.3.1, "Definition of Method and Data Base Used."

3.3.3.3 Data Comparisons and Accuracy

The measured versus predicted data from 21 conventional, multitube nozzles for PNL and EPNL* are shown in Figures 3-23 and 3-24, respectively. Such data for the two "special" nozzles (see Section 3.3.3.1) are given in Figures 3-25 and 3-26. The correlation accuracy for these nozzles is below

*See Section 3.3.1 for definition of method for determining EPNL.

- The "Reference" level is the predicted value of noise for each nozzle, at a specified set of thermodynamic conditions, plus an arbitrary value of 100 dB.

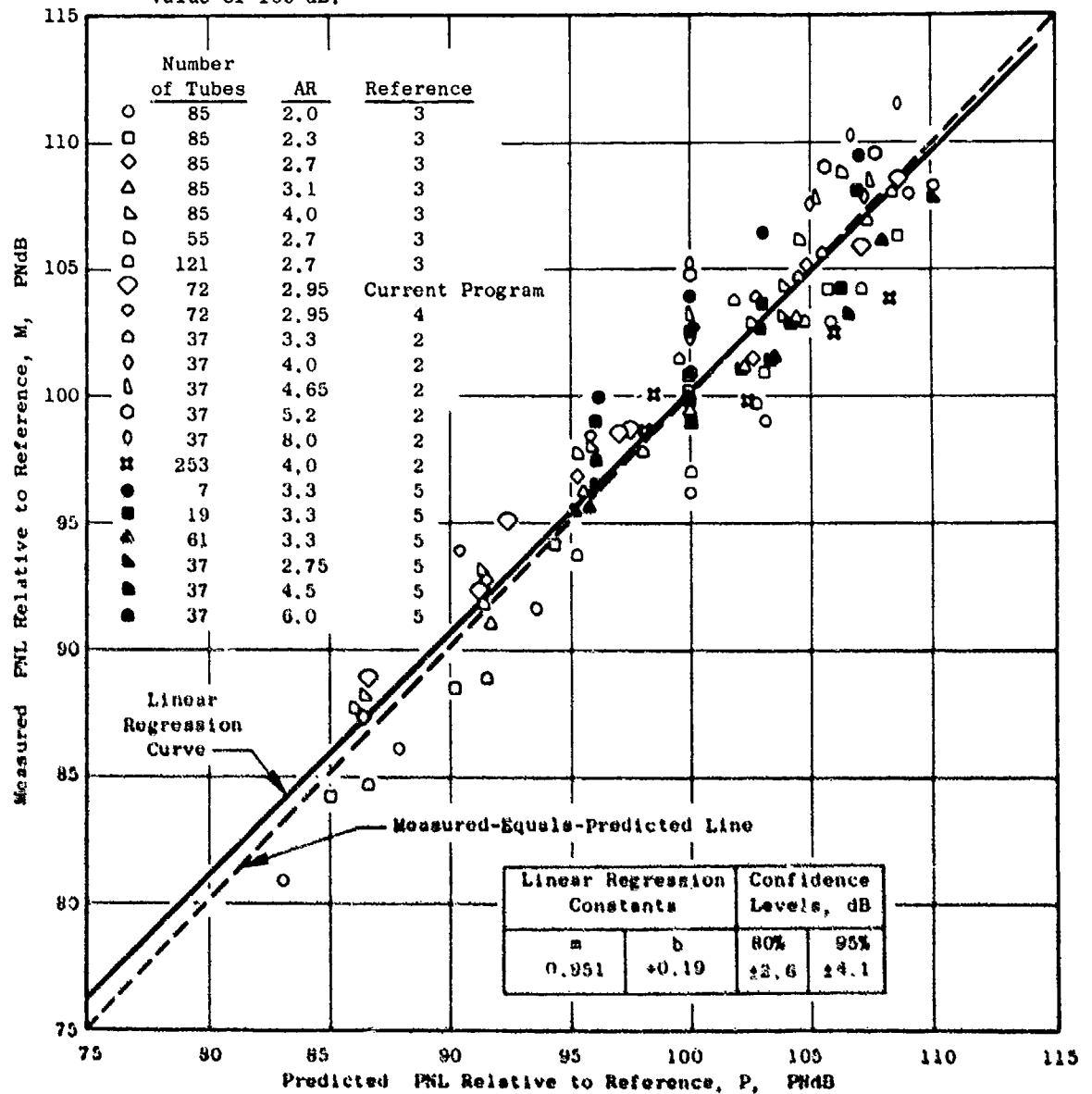


Figure 3-23. Correlation Between Measured and Predicted Maximum Perceived Noise Level (PNL) for Single-Flow, Multitube Nozzles.

- Flyover calculation using static data corrected to free-field conditions.
- The "Reference" level is the predicted value of noise for each nozzle, at a specified set of thermodynamic conditions, plus an arbitrary value of 100 dB.

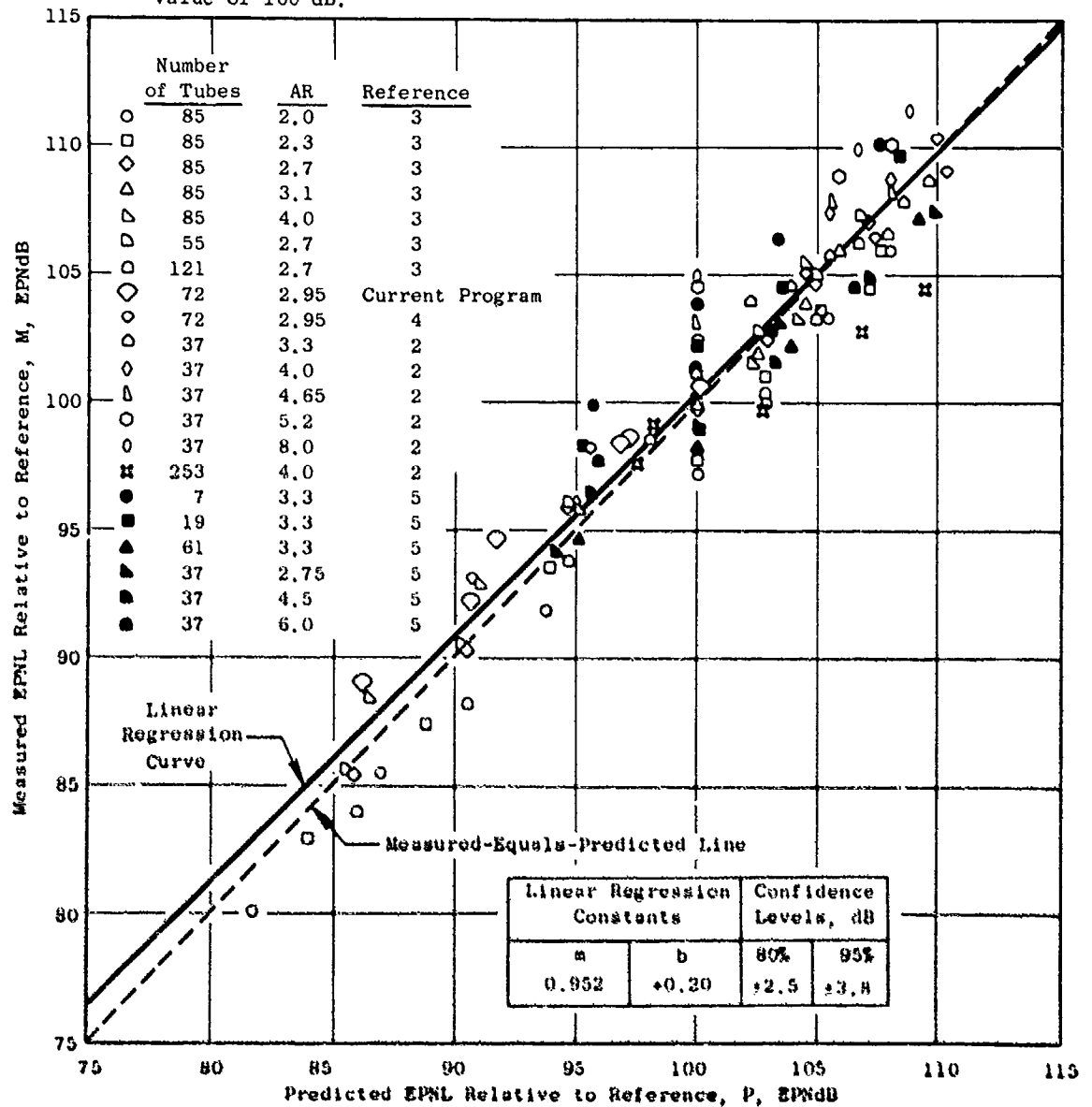


Figure 3-24. Correlation Between Measured and Predicted Effective Perceived Noise Level (EPNL) for Single-Flow, Multitube Nozzles.

- The "Reference" level is the predicted value of noise for each nozzle, at a specified set of thermodynamic conditions, plus an arbitrary value of 100 dB.

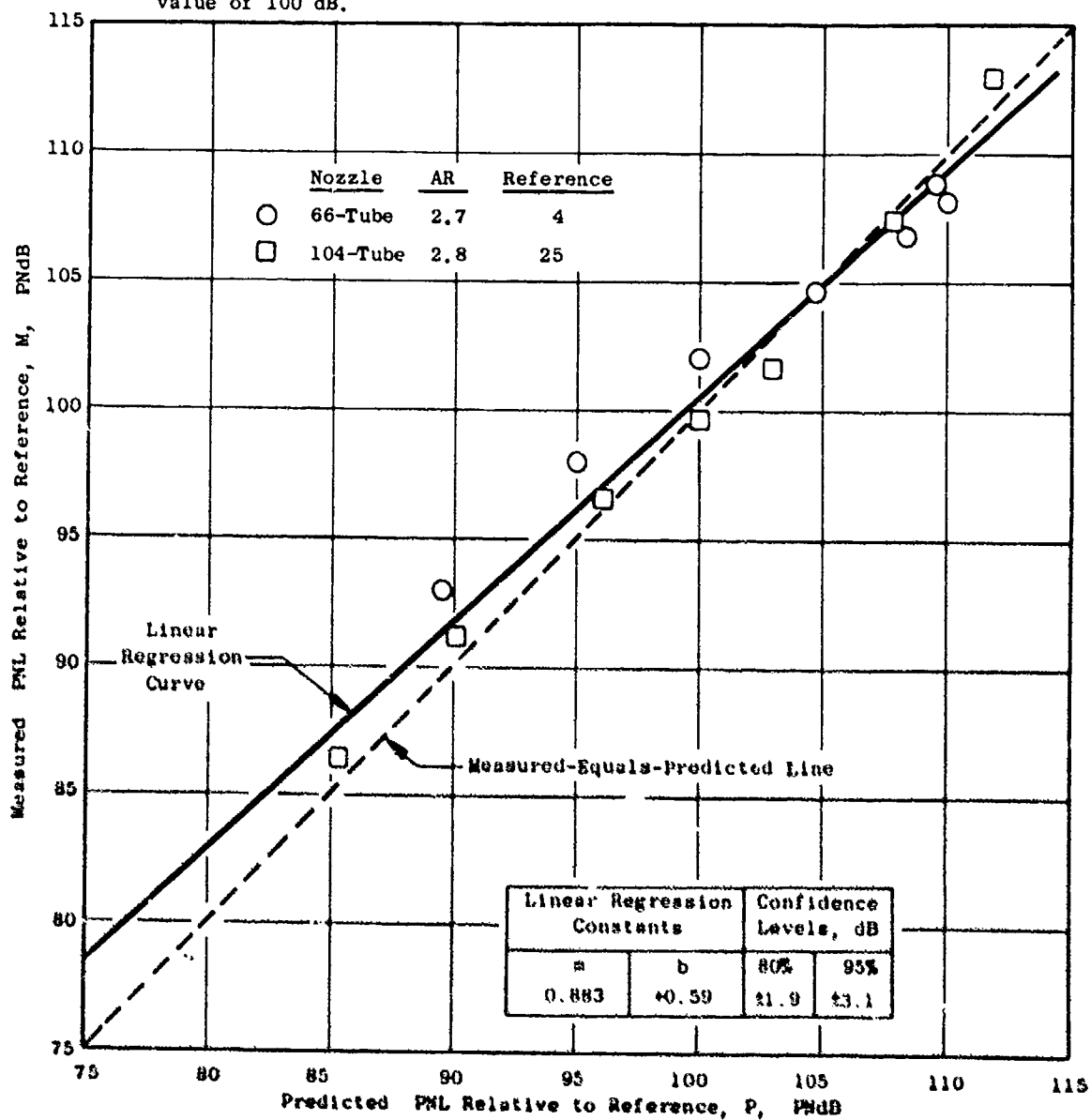


Figure 3-25. Correlation Between Measured and Predicted Maximum Perceived Noise Level (PNL) for Special Nozzles.

- Flyover calculation using static data corrected to free-field conditions.
- The "Reference" level is the predicted value of noise for each nozzle, at a specified set of thermodynamic conditions, plus an arbitrary value of 100 dB.

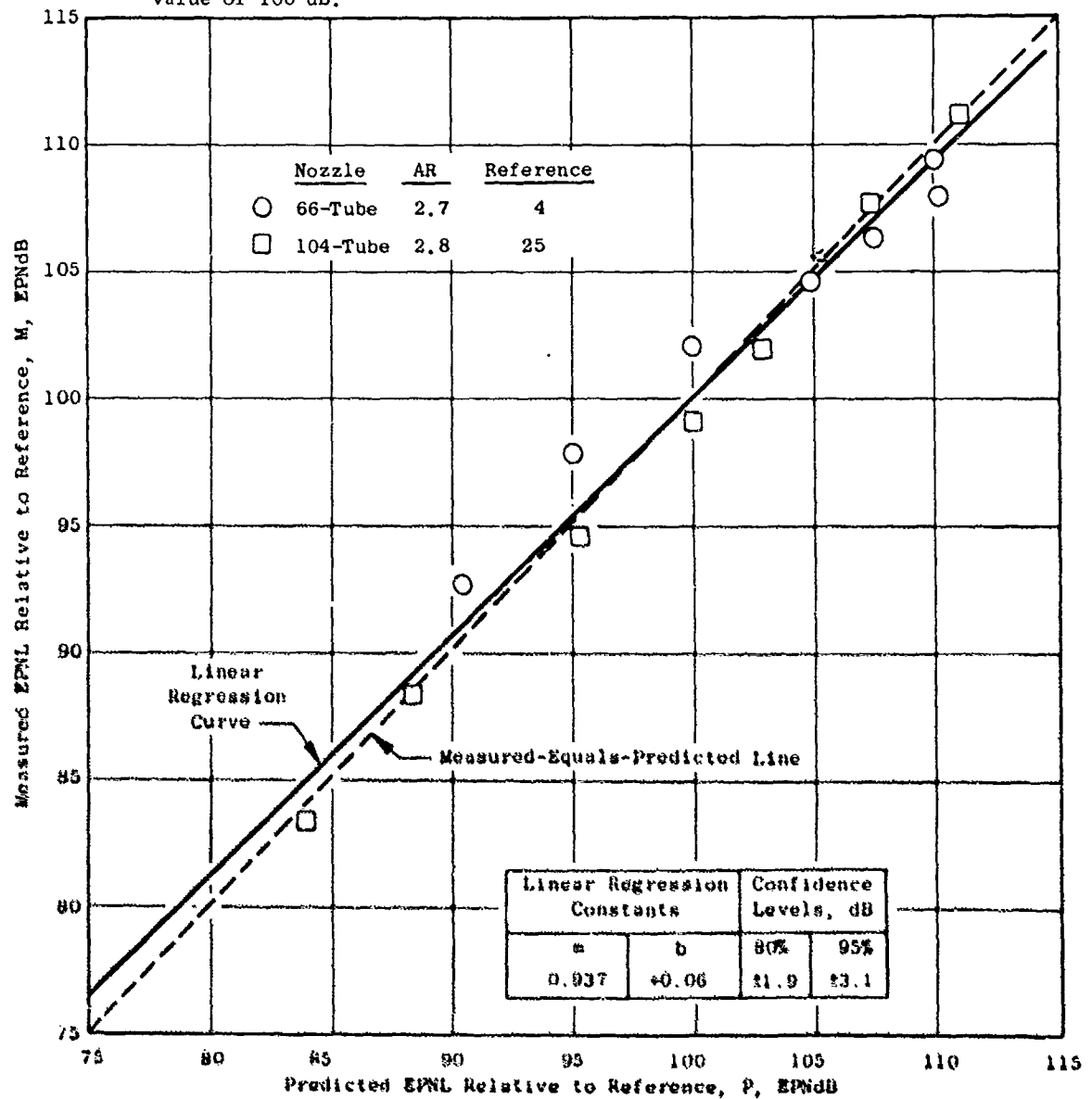


Figure 3-26. Correlation Between Measured and Predicted Effective Perceived Noise Level (EPNL) for Special Nozzles.

the average for suppressor nozzles in general (see Table 3-1). This is believed to be the result of limitations of the data base from published literature. Specifically, data from References 2 and 3 were in the form of octave-band spectra (as opposed to the current standard of one-third octave), required corrections for ground effects, and were provided only for the aft quadrant. Likewise, the data from Reference 25 were only for the aft quadrant and were not corrected to Standard Day conditions.

Even so, the 80% confidence levels for the conventional, multitube nozzles is within 2.6 dB for PNL and 2.5 dB for EPNL when the equation $M = mP + b$ is used. To emphasize the meaning of this form of the data presentation, the procedure required to estimate the expected value within the specified confidence limits, is as follows:

1. Predict the noise for the nozzle at reference conditions (pressure ratio of about 2.5, temperature yielding a fully expanded jet velocity of about 2000 ft/sec, and at the actual size and area-ratio of the nozzle).
2. Predict the noise for the nozzle at the conditions of concern (pressure ratio, temperature, and actual size and area ratio of the nozzle).
3. Determine the value of P as defined in Section 3.3.1.
4. Determine the expected value of the measured noise relative to the reference conditions from $(M-100) = m(P-100) + b$.
5. Estimate the expected value of the noise from the nozzle from:

$$\text{Expected value} = M + \left\{ \begin{array}{l} \text{PNL} \\ \text{or} \\ \text{EPNL} \end{array} \right\} \begin{array}{l} \\ \\ \text{predicted at reference conditions} \end{array} - 100$$

It is of greater importance to use this form of estimating the expected value of the noise as the value of b departs more from zero and as m deviates more from unity. This is the case for the "special" nozzles as shown in Figures 3-25 and 3-26.

Representative comparisons between measured and predicted data for 2400-ft sideline PNL versus far-field angle and for one-third-octave band spectra at 50°, 90°, and 130° from the inlet are shown in Figures 3-27 through 3-30. The first two, 3-27 and 3-28, are for the 104-tube nozzle at jet velocities of 1400 and 2195 ft/sec, respectively. The remaining two, 3-29 and 3-30, are for the 66-tube nozzle at 1252 and 2478-ft/sec velocities, respectively.

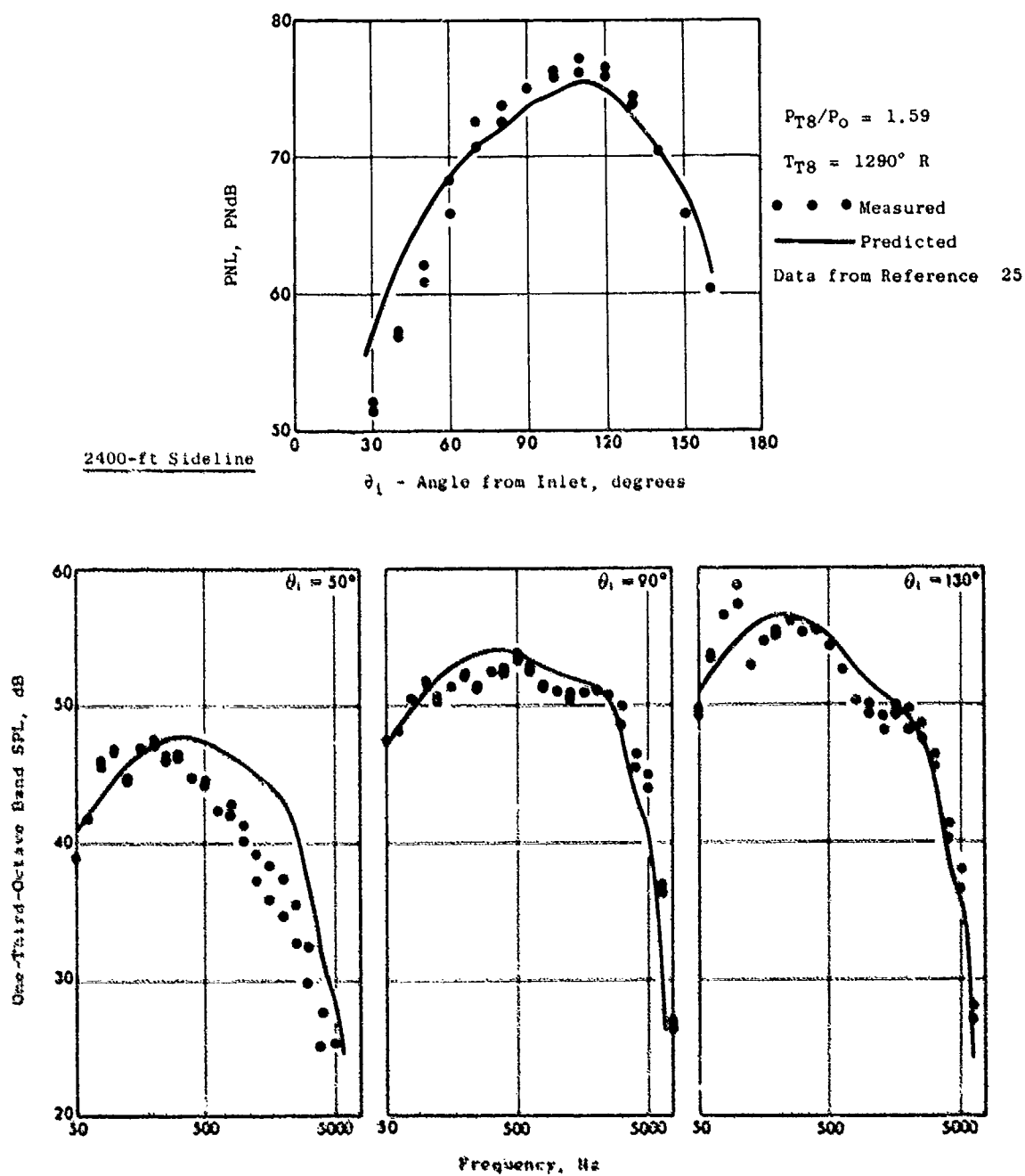


Figure 3-27. Typical PNL Directivity and One-Third-Octave Band Spectra for a 104-Tube Nozzle at 1400-ft/sec Jet Velocity.

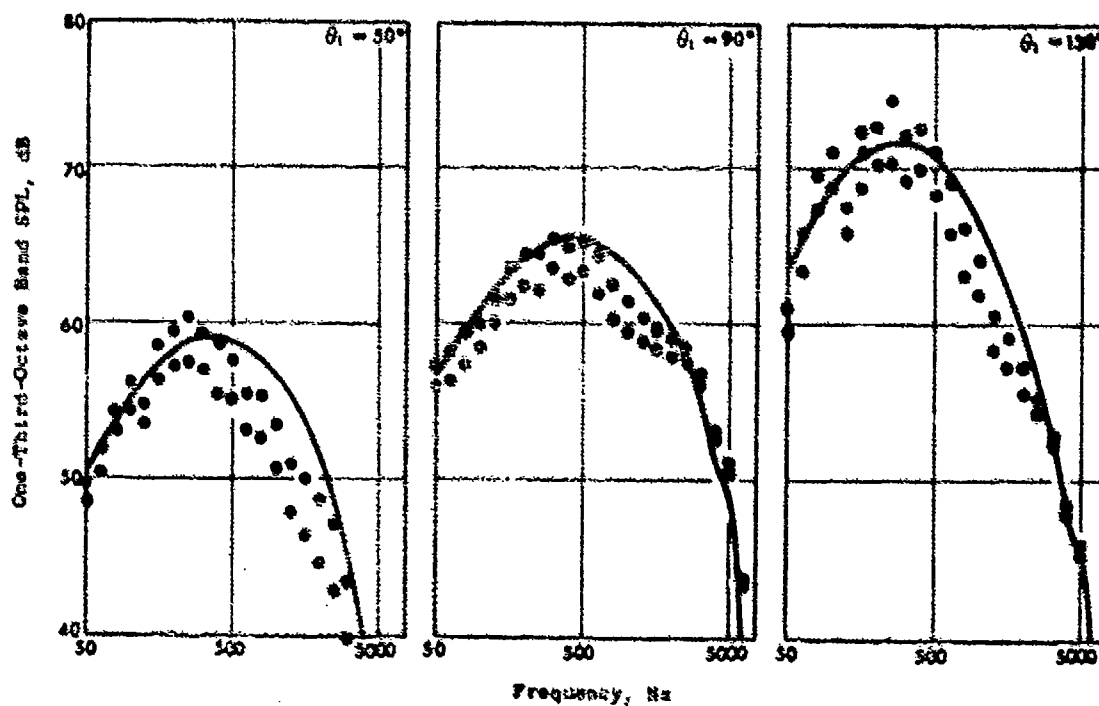
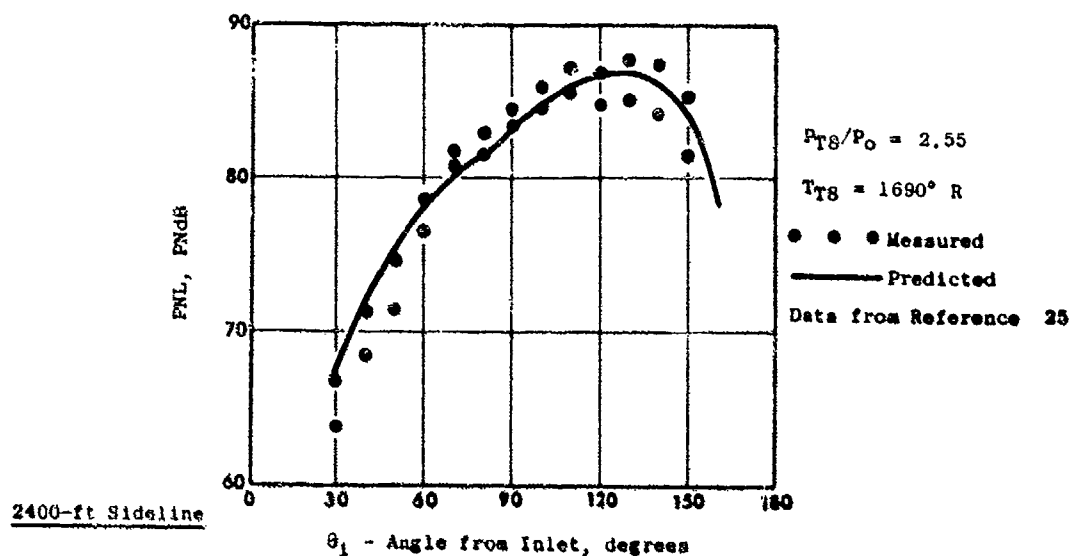
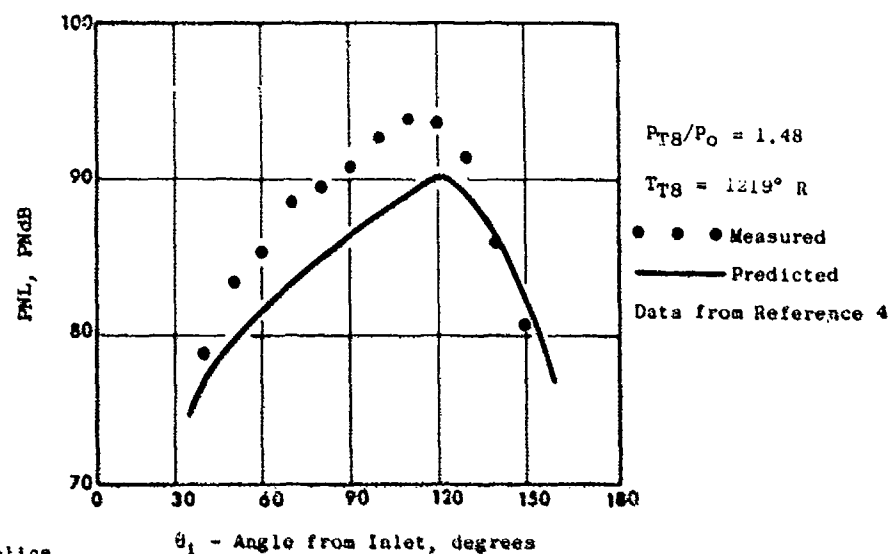


Figure 3-28. Typical PNL Directivity and One-Third-Octave Band Spectra for a 104-Tube Nozzle at 2195-ft/sec Jet Velocity.



2128-ft Sideline

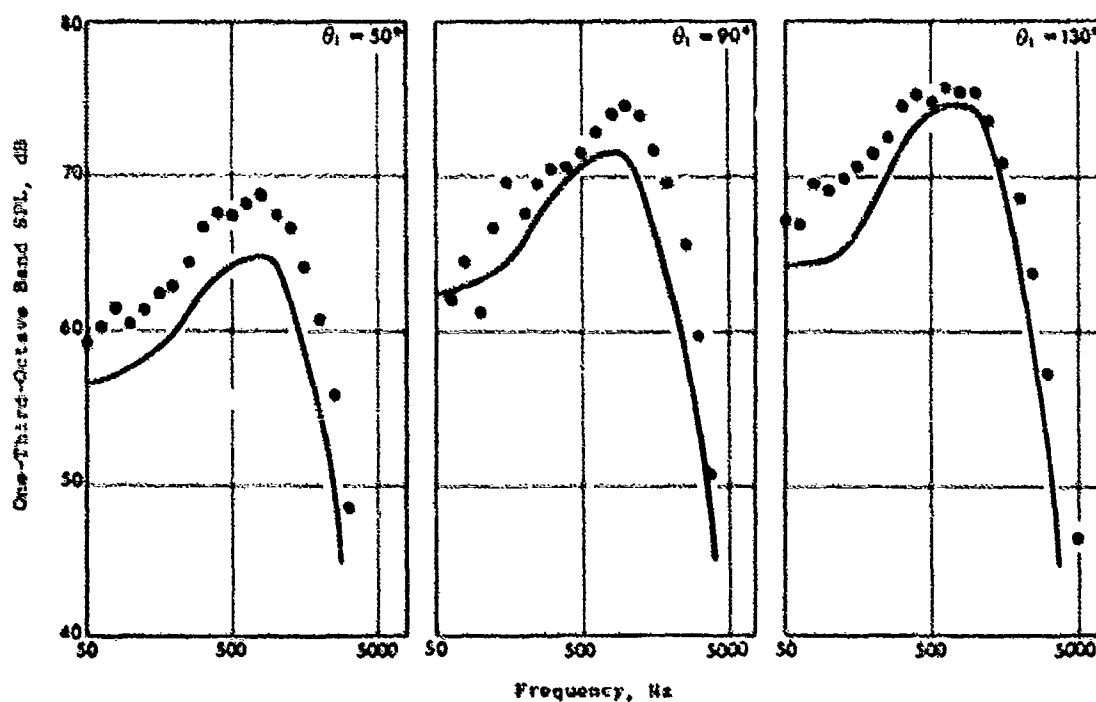


Figure 3-29. Typical PNL Directivity and One-Third-Octave Band Spectra for a 66-Tube Nozzle at 1252-ft/sec Jet Velocity.

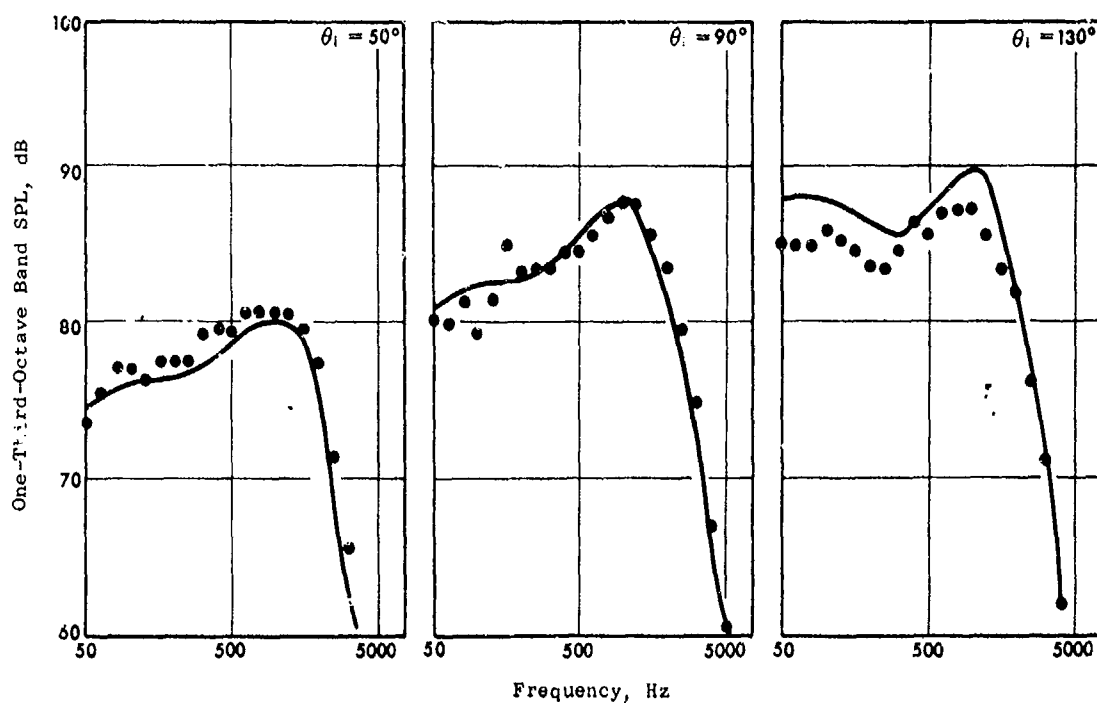
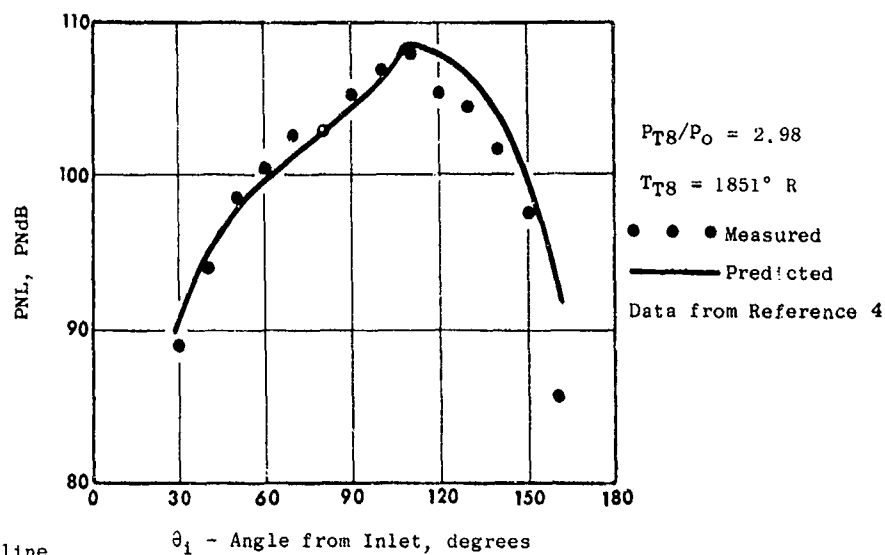


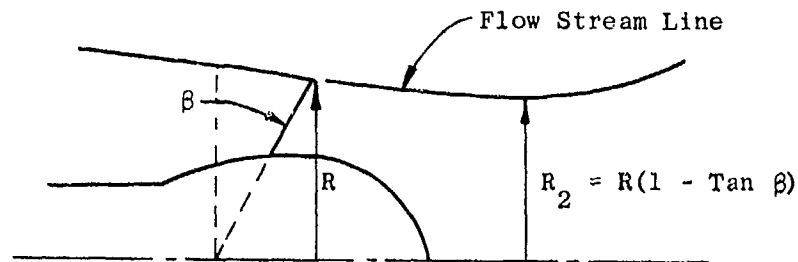
Figure 3-30. Typical PNL Directivity and One-Third-Octave Band Spectra for a 66-Tube Nozzle at 2478-ft/sec Jet Velocity.

3.3.4 Multichute or Spoke Nozzles

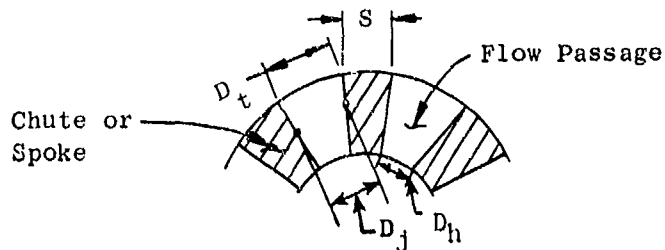
3.3.4.1 Definition of the Method and Data Base Used

The basic procedures are given in Section 3.2.2, except that a change is made from tubes to chutes or spokes. The differences are as follows:

- In determining the axial distribution and axial locations of peak noise, an equivalent diameter is used as defined by $D_{eq} = \sqrt{4A/\pi}$ where the flow area, A , is the nozzle flow-passage area between two adjacent chutes or spokes.
- In the low-frequency noise formulation, the calculation of the area of the merged jet by Equation 3-10 requires the number of elements to be the number of chutes, the circumscribing radius to be that determined by the envelope of the chutes or spokes, and the radius of the element to be $D_{eq}/2$. If the exit plane of the chutes or spokes is canted by an angle β , the radius, R_2 used in Equation 3-10 is defined by:



- The axial location of the merging of adjacent jets from the chutes or spokes is also determined by Equation 3-6 (Section 3.2.2) where S and D_t are defined by the sketch below:



- The effective number of flow-passage elements radiating noise to the far field is determined in a manner similar to tube nozzles, using Equation 3-7 in the following form:

$$N_{\text{eff}} = (2K + 1)^{1/2}$$

where: K = (Number of chutes or spokes/6)

This is equivalent to using the number of tubes in the outer row (of a multitube suppressor) that the observer sees.

The effective number of elements is applied for premerged noise for those frequencies having wavelengths smaller than $D_{\text{eq}} = \sqrt{4A/\pi}$ for supersonic flow or the outer flow width, D_t , for subsonic flow. This effect is also varied as for multitube suppressors: $D/2 \geq 2D$ and $N_{\text{eff}} \leq N_{\text{total}}$ where N_{total} = total number of chutes or spokes.

Shock noise is calculated for a single element by the relationships for conical nozzles, using the average passage width (average of the radial variation, $D_t + D_h/2$, as shown on sketch on page 62) in place of D_j (see Section 3.3.2.1). The remainder of the calculation is the same as for the multitube suppressor (see Section 3.3.3.1).

The data base used for checking the predicted versus measured noise in the correlation is summarized in Table 3-3.

3.3.4.2 Summary of Prediction Elements

The procedure for multitube suppressors (see Section 3.3.3.2) is followed with the changes noted in Section 3.3.4.1.

3.3.4.3 Data Comparisons and Accuracy

Figures 3-31 and 3-32 give predicted versus measured maximum PNL and "static" EPNL respectively for single-flow, multichute/spoke nozzles. An accuracy of ± 2.4 for PNL and ± 2.0 for EPNL with 80% confidence is indicated. The data from Reference 3 in this case was one-third-octave band data. The ground reflections were removed from the PNL by subtracting 2.7 dB which is the usual high-frequency correction for this facility. However, since the data were obtained using nozzle-centerline-height microphones, the ground reflection cancellations and reinforcements can and do extend to higher frequencies. In addition, because of the small area ratio of the suppressors involved, there is a significant amount of low-frequency noise which affects the PNL. The effect of the ground reflections on PNL therefore may vary from nozzle to nozzle and velocity to velocity and may differ from 2.7 dB. Although the actual scatter caused by this is felt to be small (less than ± 1.0 dB), it is affecting the overall scatter.

Figures 3-33 through 3-36 give typical PNL directivity and one-third-octave band spectra comparisons showing representative correlation in detail. On some multichute nozzles, at the higher end of the velocity range tested in this program, the data at the 140° angle sometimes was several PNdB higher than predicted. The cause of this discrepancy could not be explained.

Table 3-3. Data Base for Single-Flow, Multichute/Spoke Nozzles. (1)

Reference	Identification	Element Number/Type	Suppressor Area Ratio(2) AR	Pressure Ratio Range	Temperature Range ° R	Velocity Range fps	Comments
3	Vol II	p 154	2.0	1.5-4.0	1280-2200	1350-3000	
		157	2.0	1.5-4.0	1280-2200	1350-3000	
		160	2.0	1.5-4.0	1280-2200	1350-3000	
		162	2.0	1.5-4.0	1280-2200	1350-3000	
		166	1.5	1.5-4.0	1280-2200	1350-3000	
		169	2.5	1.5-4.0	1280-2200	1350-3000	
		172	2.0	1.5-4.0	1280-2200	1350-3000	
		175	2.0	1.5-4.0	1280-2200	1350-3000	
		178	2.0	1.5-4.0	1280-2200	1350-3000	
		181	3.0	1.5-4.0	1280-2200	1350-3000	
4	Vol I	184	2.0	1.5-4.0	1280-2200	1350-3000	
		p 335	2.1	1.08-3.85	1000-2120	550-2900	
		113	2.2	1.47-3.54	1125-2110	1200-2820	
		64	2.0	1.55-3.97	1330-2180	1380-2970	
		66	2.0	1.54-3.95	1250-2170	1325-2960	
		p D15	1.9	1.8-3.2	1460-1960	1659-2620	
		D105	6.0	1.8-3.4	1960	1923-2680	
		D113	4.0	1.8-3.4	1460-1960	1659-2680	
		D246	2.0	1.6-3.4	1960	1750-2680	
2	Current Program	Model No. 15	2.5				No Plug No Plug No Plug No Plug
		16	2.0				
		17	1.5				
		18	2.0				
		21	2.0				
		41	2.5				

(1) Nozzles have a centerbody plug unless noted in comments.

(2) Ratio of nozzle area (annulus if plug nozzle) to flow area.

- The "Reference" level is the predicted value of noise for each nozzle, at a specified set of thermodynamic conditions, plus an arbitrary value of 100 dB.

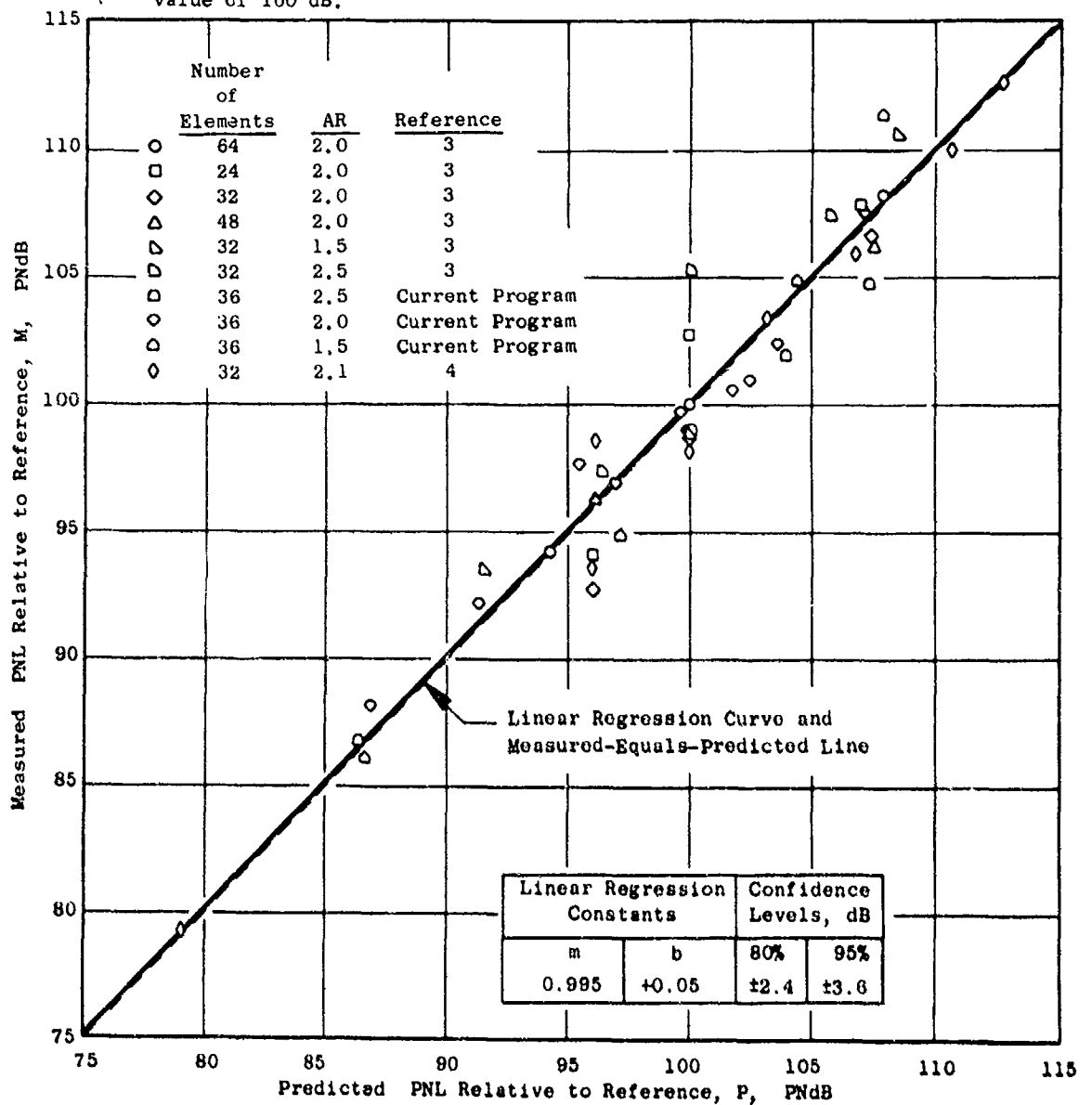


Figure 3-31. Correlation Between Measured and Predicted Maximum Perceived Noise Level (PNL) for Single-Flow, Multichute/Spoke Nozzles.

- Flyover calculation using static data corrected to free-field conditions.
- The "Reference" level is the predicted value of noise for each nozzle, at a specified set of thermodynamic conditions, plus an arbitrary value of 100 dB.

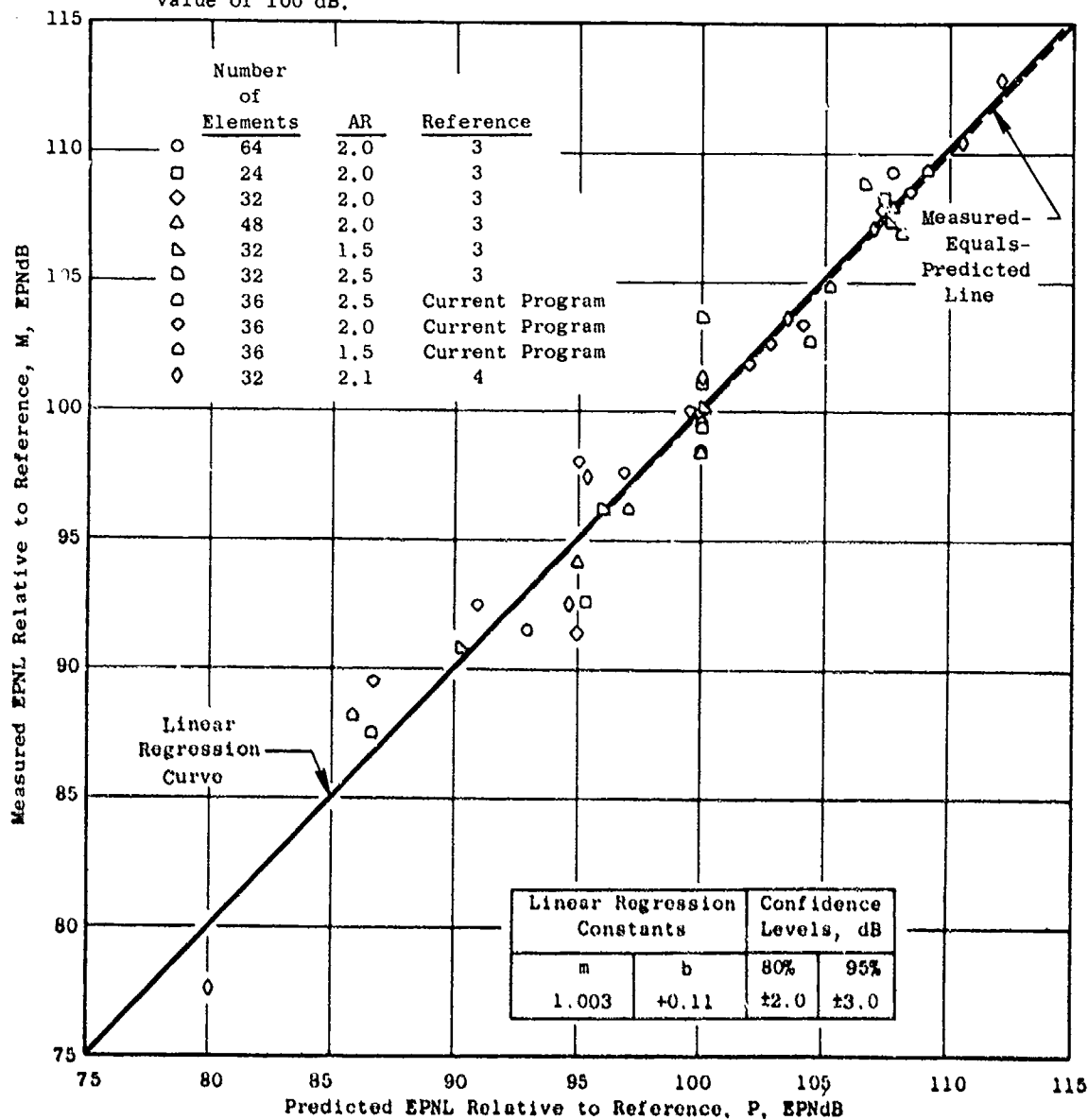


Figure 3-32. Correlation Between Measured and Predicted Effective Perceived Noise Level (EPNL) for Single-Flow, Multichute/Spoke Nozzles.

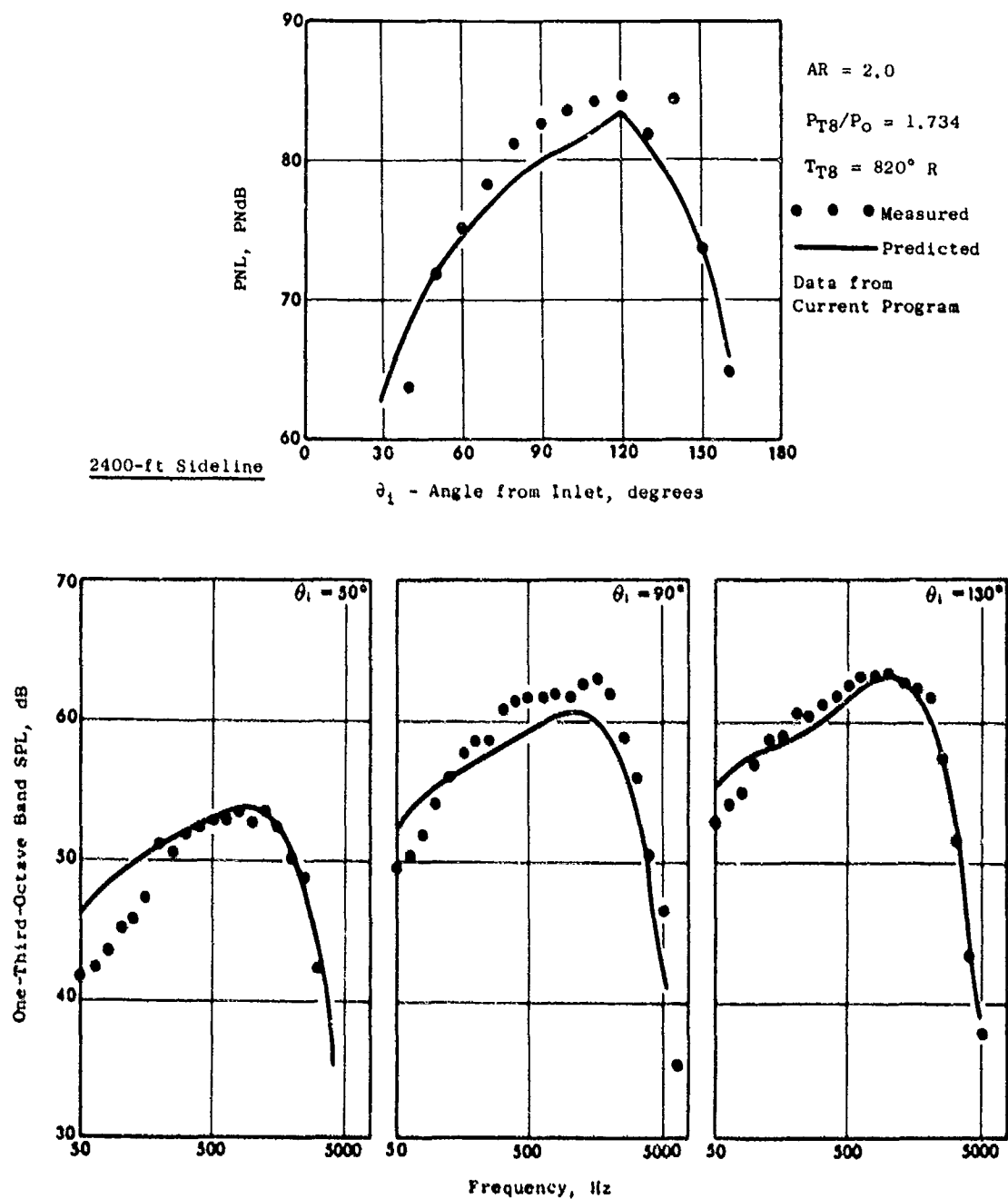


Figure 3-33. Typical PNL Directivity and One-Third-Octave Band Spectra for a 36-Chute Nozzle at 1197-ft/sec Jet Velocity.

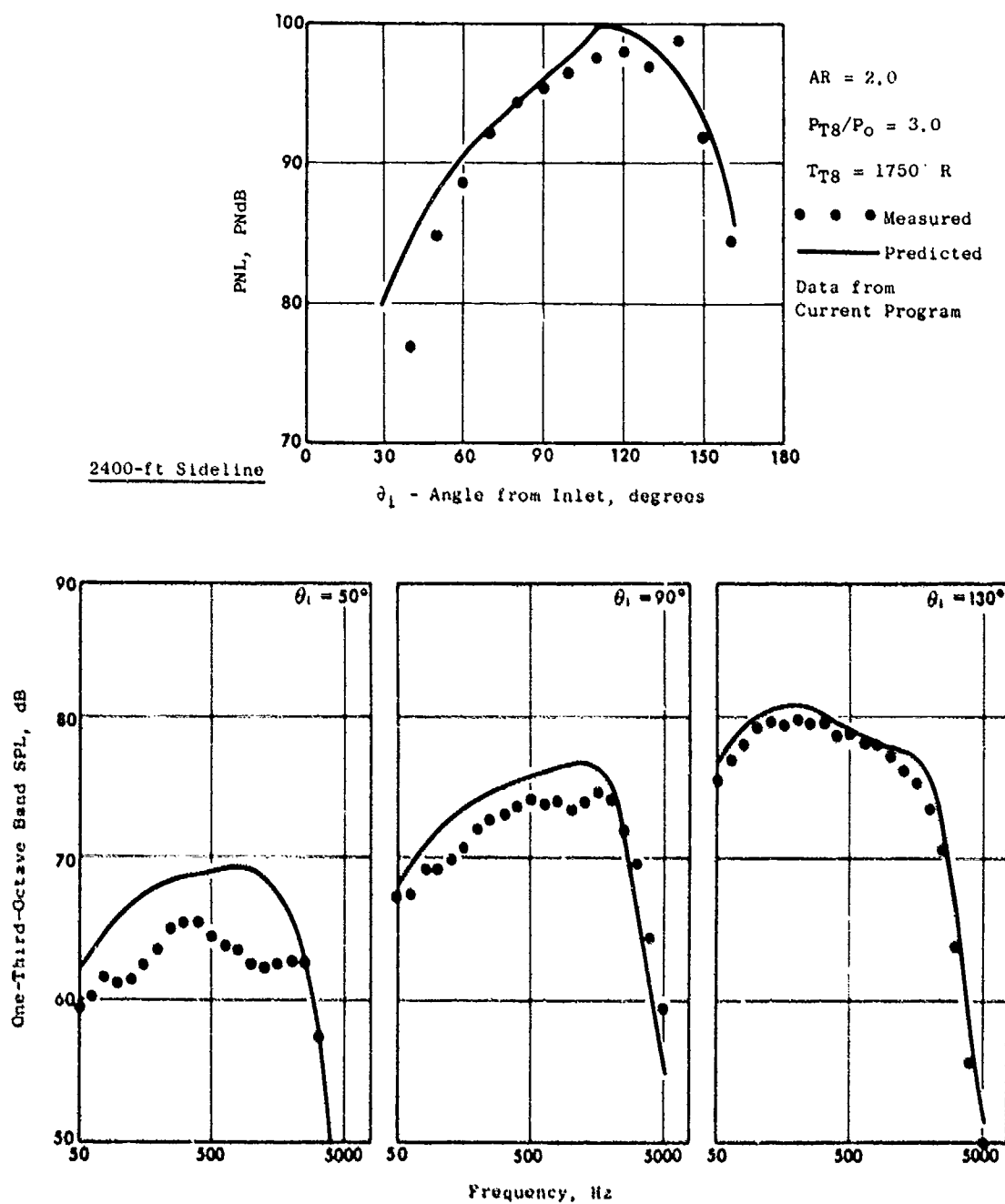


Figure 3-34. Typical PNL Directivity and One-Third-Octave Band Spectra for a 36-Chute Nozzle at 2396-ft/sec Jet Velocity.

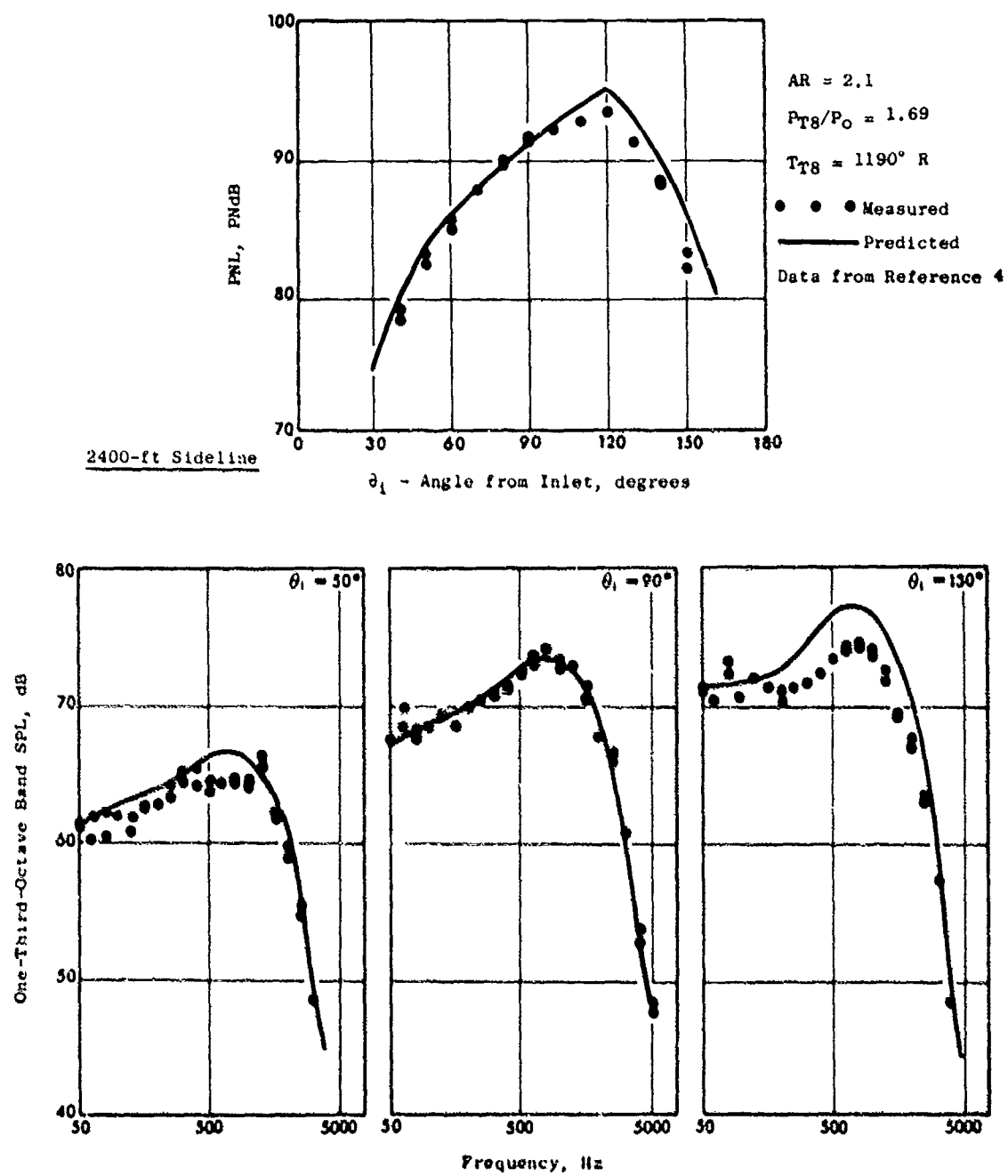


Figure 3-35. Typical PNL Directivity and One-Third-Octave Band Spectra for a 32-Element, Deep-Chute Nozzle at 1400-ft/sec Jet Velocity.

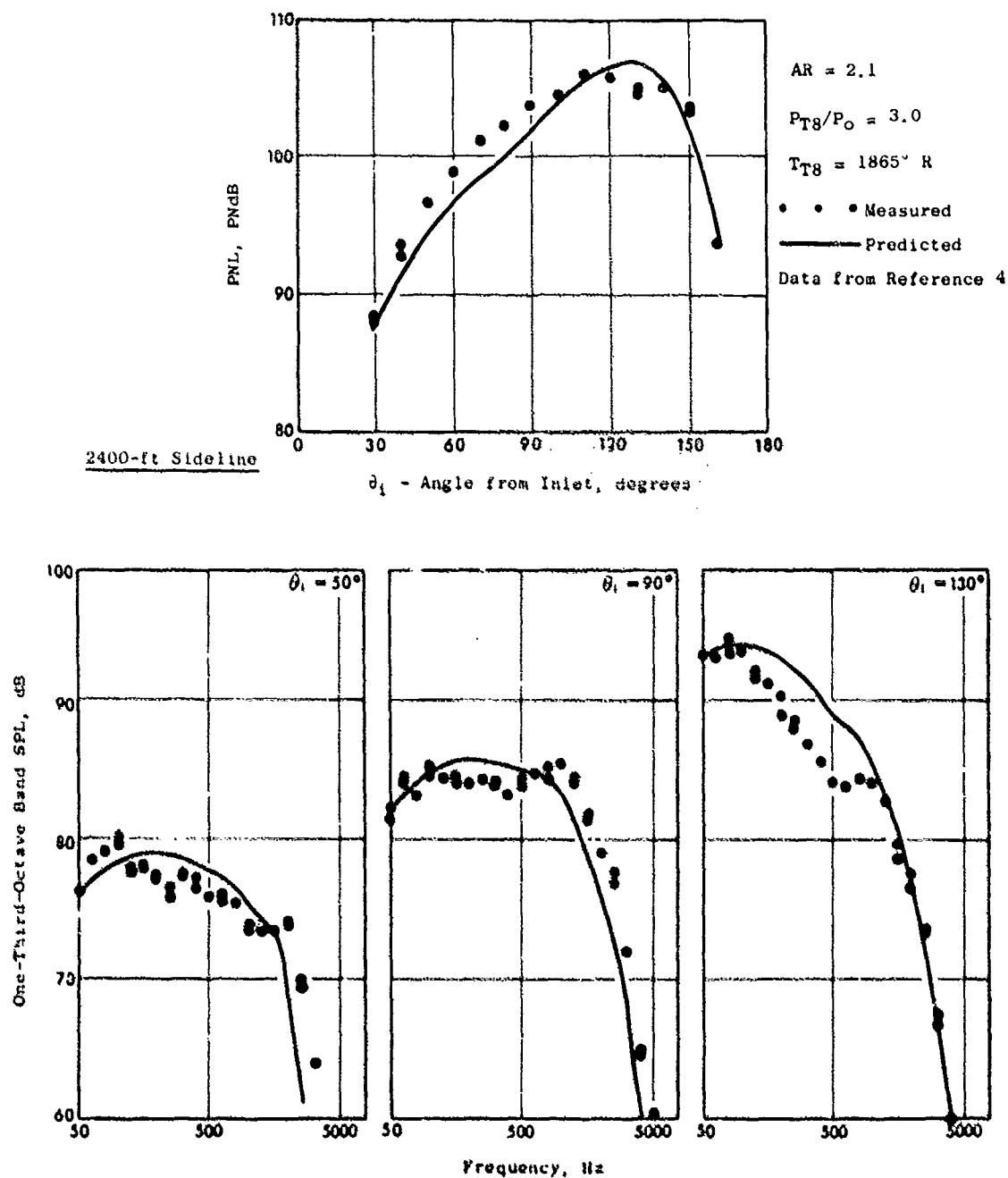


Figure 3-36. Typical PNL Directivity and One-Third-Octave Band Spectra for a 32-Element, Deep-Chute Nozzle at 2490-ft/sec Jet Velocity.

3.3.5 Dual-Flow Nozzles

3.3.5.1 Definition of Method and Data Base Used

The dual-flow correlation is for nozzles with a multielement suppressor on the outer stream. The conical jet noise correction is used in order to predict level, spectrum, and directivity, just as it was for single-flow nozzles. The concept of a premerged and a postmerged noise-generation region is used, and shock-cell noise is again added to mixing noise.

The premerged noise, including both mixing and shock noise, is determined for the multielement suppressor just as if the nozzle were a single-flow suppressor, using the procedures described in Section 3.3.3 for multi-tube, and in Section 3.3.4 for multichute or spoke suppressor nozzles. The effect which radius ratio has on the cutoff effect (Section 3.2.2) is included in the calculation. It is assumed that the nozzle is of the extended core type so that the outer stream fully merges before mixing with the inner stream; the consistency of the data with the prediction suggests that the assumption is warranted for this data base.

The postmerged mixing noise of a dual-flow nozzle with a suppressor on the outer stream is based on the outer flow (W^0 , V^0 , T^0 , P^0 , and A^0) mixed with ambient air as determined by the method described in Section 3.2.2 under "Merged Jet Thermodynamic Conditions" and then mixed with the inner stream as described below. The effect of the inner stream was found to preclude the effects of a plug; therefore, Equation 3-15 for $R_f > 0.6$ is not included for the suppressed, dual-flow-nozzle predictions.

Two approaches are used to predict postmerged mixing noise depending on whether the outer stream velocity is lower or higher than the inner stream:

- When the lower velocity is in the outer stream, the postmerged mixing noise is determined by the nozzle exit conditions of the inner stream (velocity and temperature), by the total area and corresponding equivalent diameter of the inner and outer streams, and by an empirical correction determined by the velocity ratio and area ratio of the two streams. The empirical correction is (reduction relative to the conical nozzle levels):

$$\Delta = K [1 - 4 (V^0/V^i - 0.5)^2], \text{ dB} \quad (3-18)$$

$$K = 10 \log_{10} (A^0/A^i) + 5.8, \text{ dB} \quad (3-19)$$

where: Δ = (Predicted OASPL for a conical nozzle based on the conditions defined above) - (measured OASPL for the dual-flow nozzle)

K = Area ratio effect upon Δ

V = Velocity

A = Area

superscripts:

o = Outer stream after merging (Section 3.2.2)

i = Inner stream

The data from which these relationships were derived are shown in Figures 3-37 and 3-38 for Δ and K, respectively.

This method is applicable for the following ranges of the variables: $0.65 \leq A^o/A^i \leq 8.0$ and $0.2 \leq V^o/V^i \leq 1.0$.

- When the higher velocity is in the outer stream, the postmerged mixing noise is determined by the momentum-weighted, mixed conditions for the two streams, assuming constant-area mixing of the two streams:

$$V_{\text{mixed}} = \frac{V^o W^o + V^i W^i}{W^o + W^i} \quad (3-20)$$

$$T_{\text{mixed}} = \frac{T_T^o W^o + T_T^i W^i}{W^o + W^i} \quad (3-21)$$

$$A_{\text{mixed}} = A^o + A^i \quad (3-22)$$

$$\rho_m = \frac{W^o + W^i}{A_{\text{mixed}} V_{\text{mixed}}} \quad (3-23)$$

where: V = velocity
 T_T = total temperature
 W = weight flow
 ρ = density

These conditions are used in the conical jet noise prediction. The data check providing the basis for this formulation of the mixed-stream conditions is shown in Figures 3-39 and 3-40 in terms of normalized PWL versus V_{mixed} for the following ranges of variables (from References 37, 38, and 39): $0.65 \leq A^o/A^i \leq 4.0$ and $1.0 \leq V^o/V^i \leq 2.1$. The normalization used for PWL is the same as that for a simple, conical nozzle except that thrust, $F_g = \rho A V^2/g$, is used rather than the area, A . The exponent on the density normalization then becomes $(\omega-1)$ rather than ω .

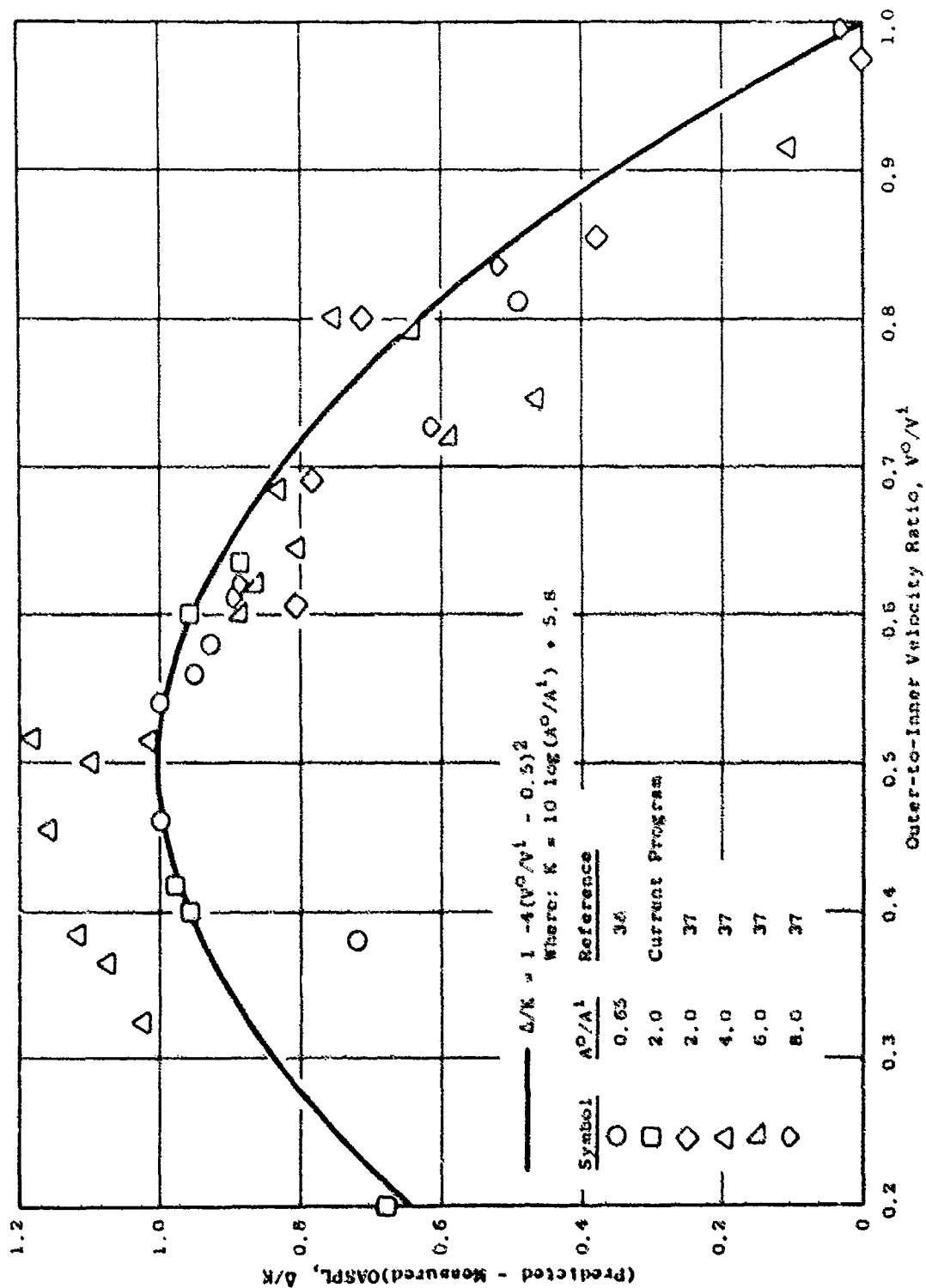


Figure 3-37. Empirical Correlation of the Velocity Ratio Effect for Coannular Nozzles.

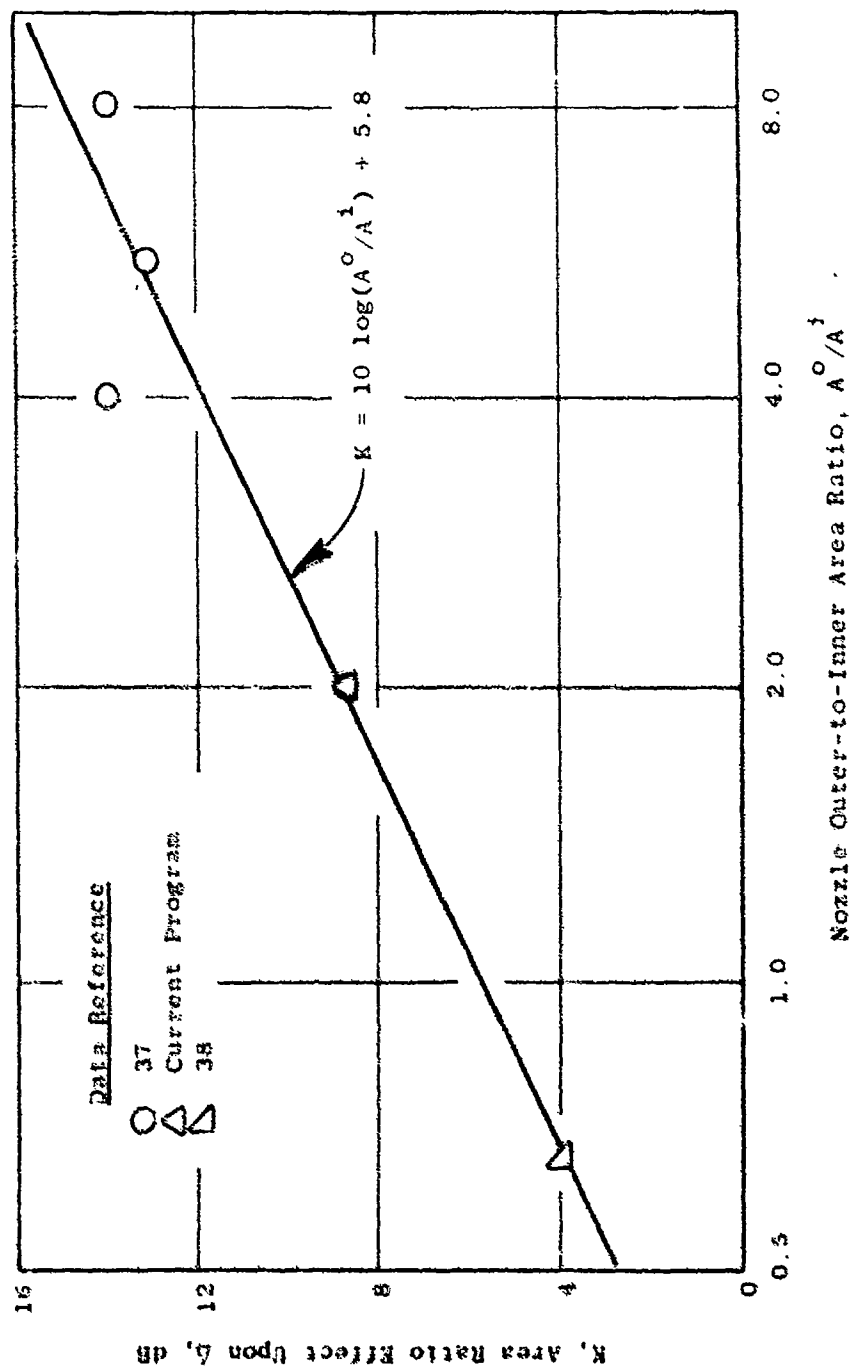


Figure 3-38. Empirical Correlation of the Area Ratio Effect on the Maximum Noise Reduction of Conical Nozzles.

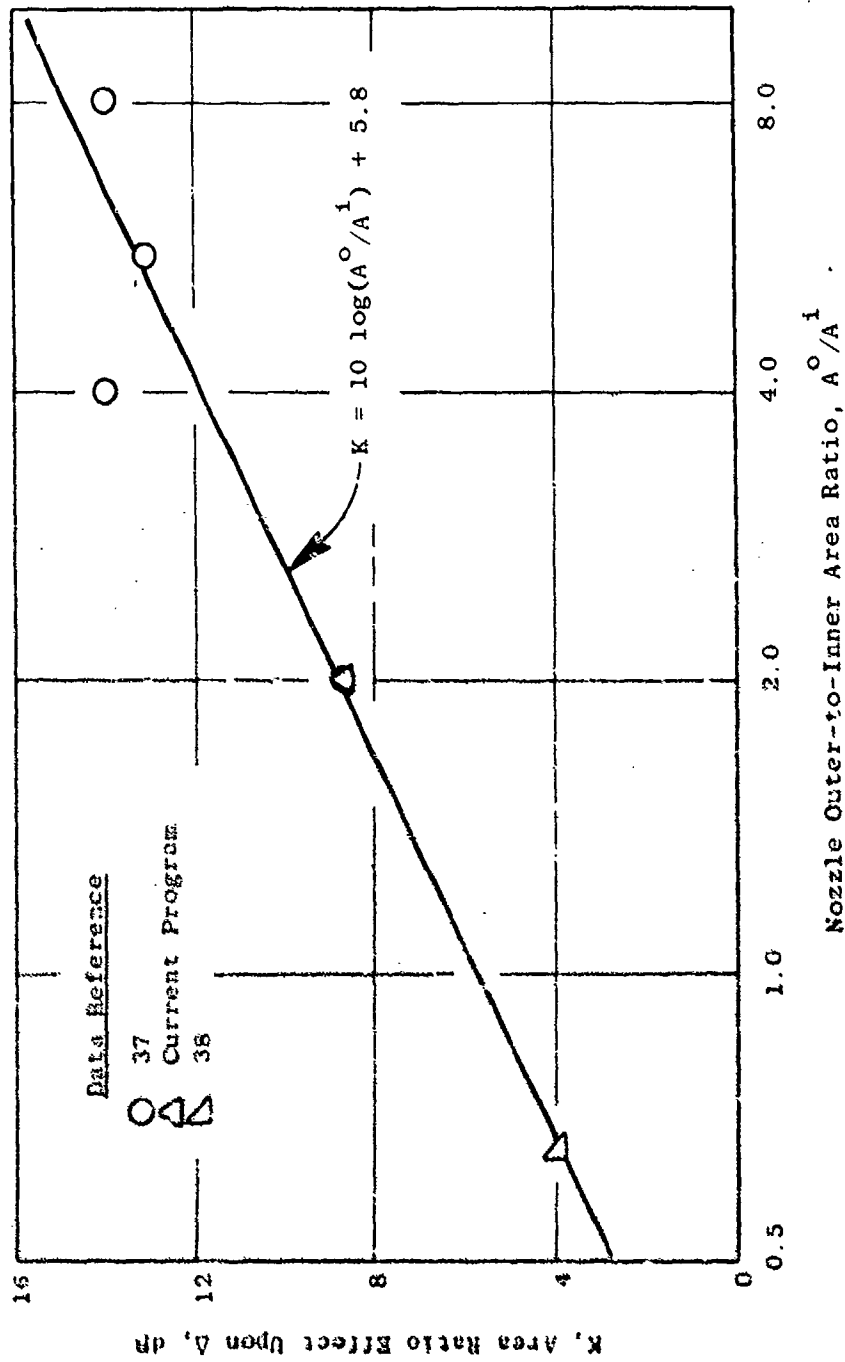


Figure 3-38. Empirical Correlation of the Area Ratio Effect on the Maximum Noise Reduction of Coannular Nozzles.

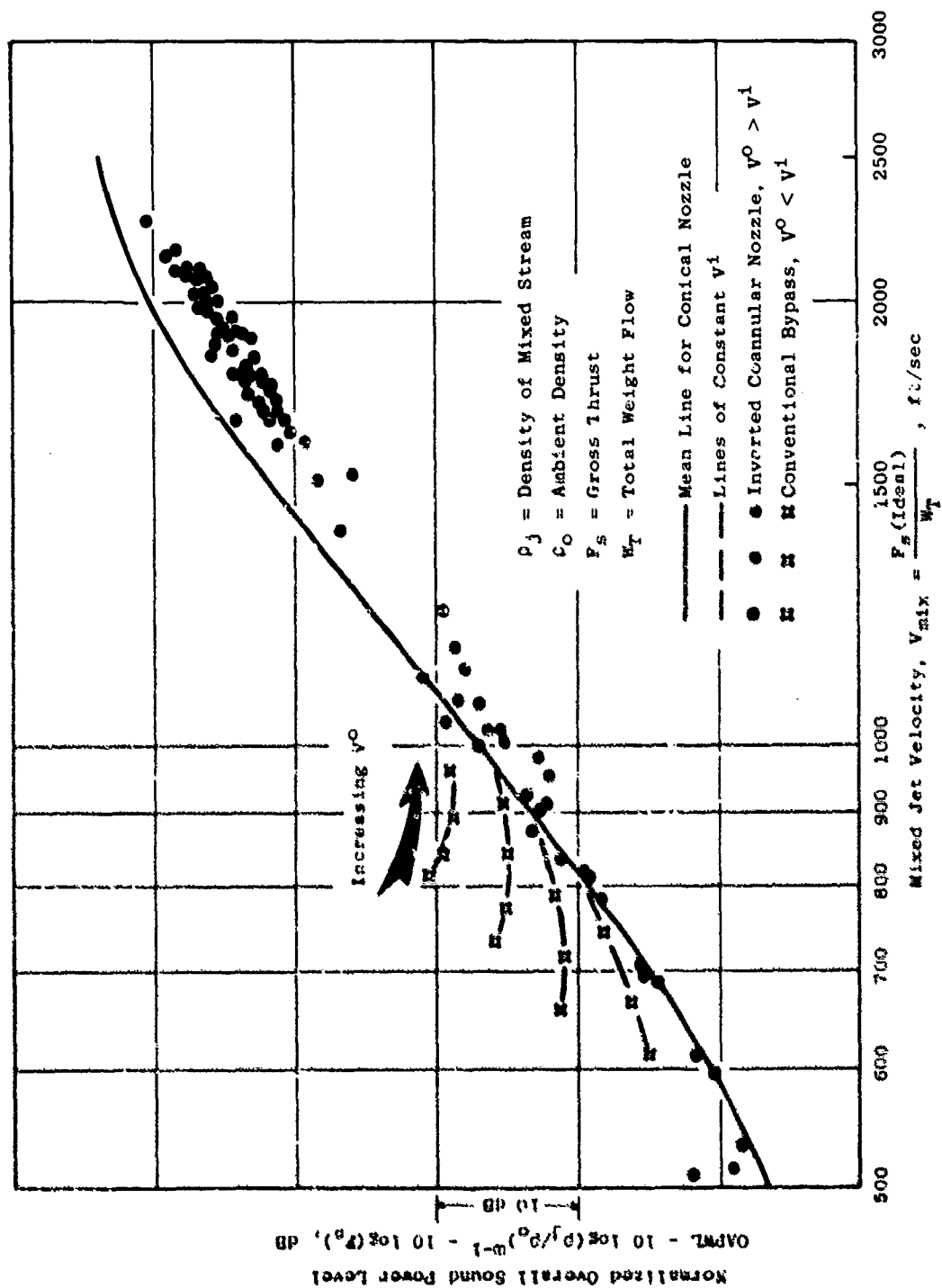


Figure 3-39. Normalized Sound Power Versus Specific Thrust (from Reference 38).

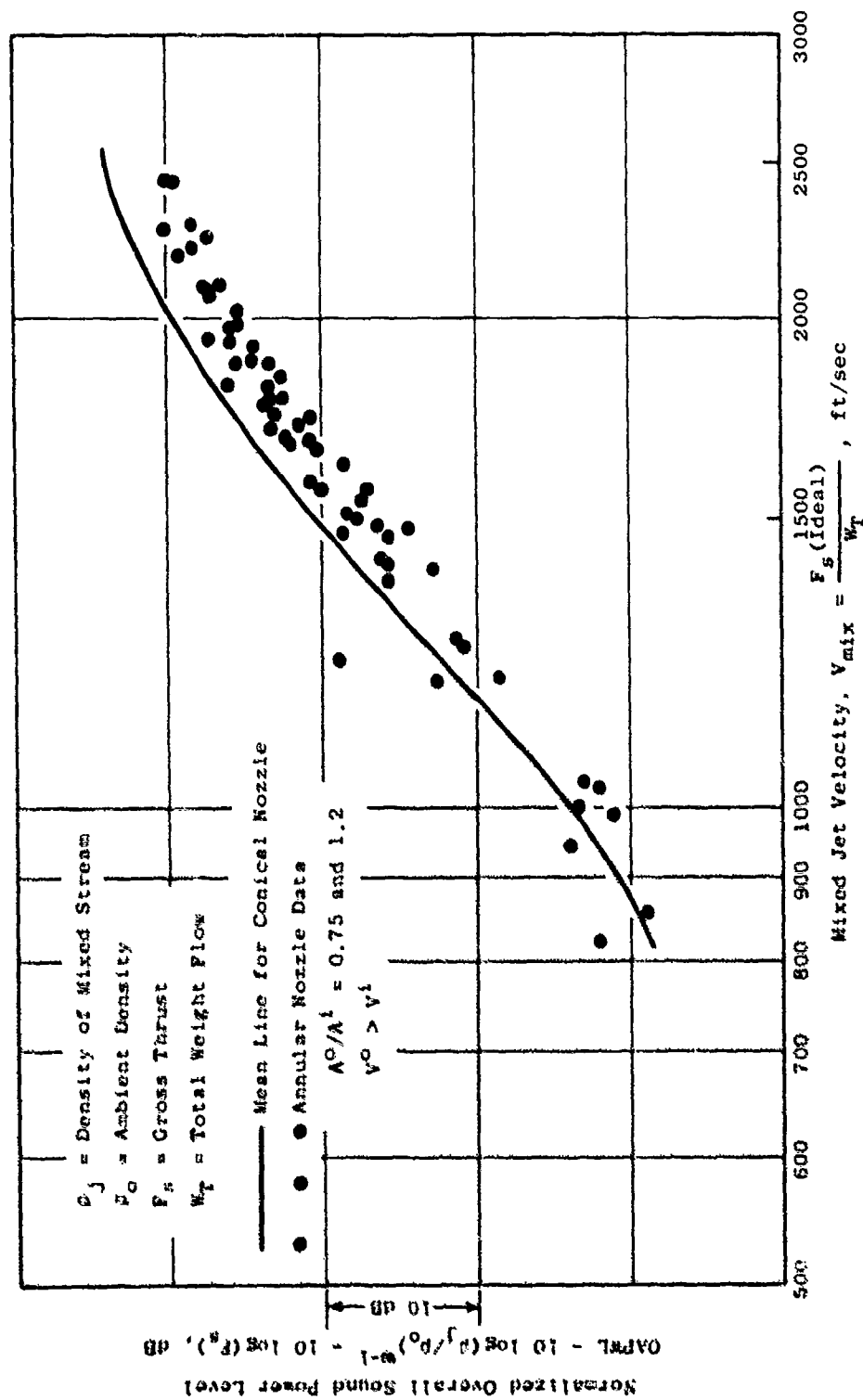


Figure 3-40. Normalized Sound Power Versus Specific Thrust (from Reference 39).

When the flow velocity of the inner stream is supersonic based on nozzle exit conditions, shock-cell noise occurs. It is determined by the conical prediction method (Section 3.3.2) based on the pressure ratio, temperature, and the equivalent diameter ($D_{eq} = \sqrt{4A/\pi}$) of the inner stream. Data (Reference 38) indicate that the outer flow does not interfere with the propagation of this noise to the far field.

The data base used for developing the correlation is shown in Table 3-4. This includes conventional, dual-flow nozzles of the type used on high-bypass-ratio, turbofan engines and inverted-flow nozzle types used on Advanced Supersonic Transport (AST) study engines. Comparisons of predicted and measured data for the suppressed, dual-flow nozzles listed in Table 3-4 are given in Section 3.3.5.3.

3.3.5.2 Summary of Prediction Elements

The following summarizes the dual-flow prediction elements included in the computer program:

1. The premerged mixing and shock noise are determined from the suppressor as if it were a single-flow nozzle, taking into account the radius ratio of the annular geometry of the suppressor in the effect upon cutoff of high frequency noise.
2. The conical nozzle correlation is used for the postmerged mixing noise according to one of the two methods below:
 - a. For the outer stream velocity (after merging with ambient air per Section 3.2.2) equal to or less than the inner stream velocity, the noise calculated using the inner stream conditions of velocity and temperature, total nozzle flow area (where the outer nozzle area is the calculated value after merging with ambient air), and an empirical adjustment as developed in Figures 3-37 and 3-38 (Equations 3-18 and 3-19).
 - b. For the outer-stream, merged velocity greater than the inner-stream velocity, the noise is calculated using the momentum-weighted mixing of the inner stream and the conditions for the outer stream (after the outer stream has merged with ambient air) and using the total area as in (a), above, assuming constant-area mixing.
3. The postmerged, shock-cell noise is determined based on the inner-stream flow conditions and equivalent diameter, assuming no effect from the outer stream.

Table 3-4. Data Base for Dual Flow Nozzles.

Reference	Identification	Element Number/Type	Suppressor Area Ratio(1) AR	Nozzle Area Ratio(2) A_0/A_1	Pressure Ratio Range	Temperature Range ° R	Velocity Range fps	Comments
37	Vol II p 2-1	---	---	2.0	1.03/1.09- 1.86/1.74	1300/1300- 519/519	370/380- 1600/970	3
		---	---	4.0	1.03/1.16- 1.83/1.84	1100/1350- 519/519	360/520- 1600/1030	3
		---	---	6.0	1.03/1.09- 1.86/1.76	1300/1300- 519/519	370/380- 1600/970	3
		---	---	8.0	1.03/1.09- 1.86/1.76	1300/1300- 519/519	370/380- 1600/970	3
38	p 51	---	---	0.65	1.48/1.17- 2.47/3.89	519/519- 1460/1990	955/520- 2000/2800	3
Current Programs	Model No. 6	---	---	2.0				3
38	Vol II p 50	69 Tubes	2.75	0.65	1.48/1.17- 2.47/3.89	519/519 1460/1990	955/520 2000/2800	4
	50	36 Chute	2.5	0.65	1.48/1.17- 2.47/3.89	519/519- 1460/1990	955/520 2000/2800	4
Current Programs	Model No. 22	36 Chute	2.5	1.92				4
	23	36 Chute	2.0					4
	24	36 Chute	2.0					4
	27	36 Chute	1.5					4
	29	36 Chute	2.0	1.92				4
	30	20 Chute	2.0	1.92				4
	31	30 Chute	2.0	1.92				4
	32	40 Chute	2.0	1.92				4
	33	16 Chute	2.5	0.65				4

- (1) Ratio of nozzle annulus area to flow area for the suppressor on the outer annulus.
(2) Ratio of the flow area of the annular nozzle to the flow area of the inner nozzle.
(3) Coannular-coplanar without centerbody plug.
(4) Coannular-nonnoplanar with centerbody plug.

3.3.5.3 Data Comparison and Accuracy

Data for a dual-flow nozzle with a multitube suppressor are given in Figures 3-41 and 3-42 for maximum PNL and EPNL, respectively. For this nozzle (one set of data) the 80% confidence limits are ± 2.3 and ± 1.7 on PNL and EPNL, respectively. Figures 3-43 and 3-44 give PNL directivity and spectra for two different operating conditions for this nozzle.

PNL and EPNL data for dual-flow nozzles with multichute suppressors are given in Figures 3-45 and 3-46, respectively. The 80% confidence limits are ± 1.8 dB for PNL and ± 1.6 dB for EPNL. This nozzle type provides the best check of predicted versus measured data of any suppressor nozzle. Figures 3-47 through 3-49 give PNL directivity and spectra for representative nozzles. As for single-flow multichute nozzles, some dual-flow multichute nozzles tested in this program had noise at 140° several PNdB higher than predicted.

3.3.6 Ejector Nozzles

3.3.6.1 Definition of Method and Data Base Used

This section includes hard-wall and treated ejectors used in conjunction with a multielement suppressor. Hard-wall and treated ejectors with an inverted-flow, coannular nozzle having a multielement suppressor on the outer stream are also included. The configurations used in evolving the correlation are defined in Table 3-5.

The correlation for hard-wall, ejector nozzles is completely empirical, and extrapolations beyond the range of the data (defined in this section) should not be relied upon. Complete empiricism was necessary because of an unexpected aspect of the far-field directivity: At the angle of maximum noise for an unshrouded suppressor nozzle, the effect of the ejector is small to negligible; the largest effect occurs aft of the refraction critical angle and in the forward quadrant, beyond 30° in front of the critical angle. This is in contrast to observations leading to the use of an effective number of elements in a multielement suppressor which is roughly given by "you only hear what you can see." The physical blockage of the line-of-sight provided by the hard-wall ejector had very little effect on the maximum far-field noise (see Figure 3-50 as an example).

Hard-wall Ejectors

Data on the effect of adding a hard-wall ejector shroud to a multielement nozzle have been correlated as summarized below:

- At the far-field angle equal to the critical angle of refraction (per Equation 3-8) plus 20° (approximately 130° from the inlet), for the one-third-octave band at which the premerged noise level for the unshrouded nozzle is the highest (f_p), the reduction in reference sound pressure level (ΔSPL_R) is established as given in Figure 3-51 as a function of the following:

- The "Reference" level is the predicted value of noise for each nozzle, at a specified set of thermodynamic conditions, plus an arbitrary value of 100 dB.

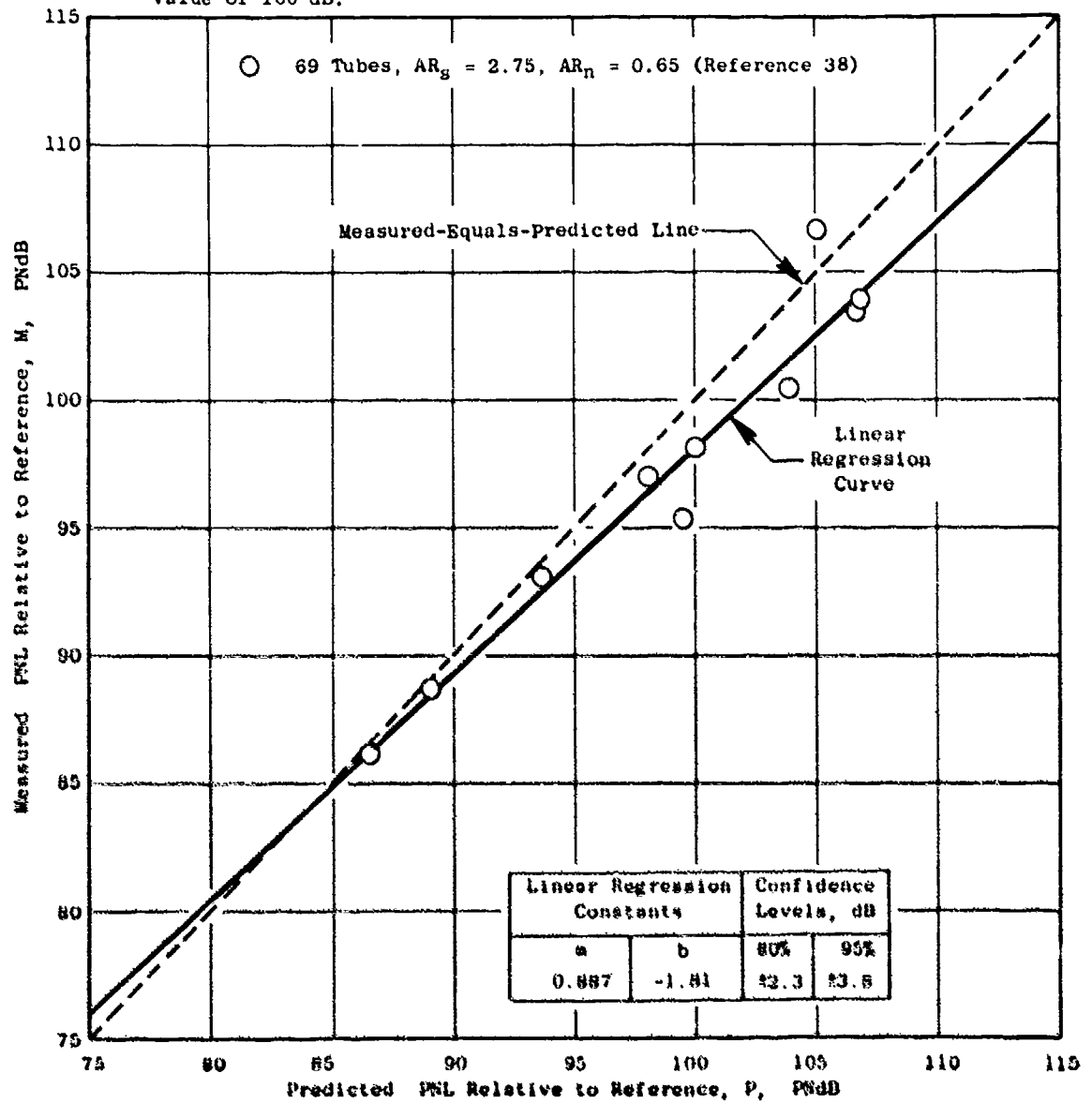


Figure 3-41. Correlation Between Measured and Predicted Maximum Perceived Noise Level (PNL) for Dual-Flow Nozzles with a Multitube Suppressor on the Outer Stream.

- Flyover calculation using static data corrected to free-field conditions.
- The "Reference" level is the predicted value of noise for each nozzle, at a specified set of thermodynamic conditions, plus an arbitrary value of 100 dB.

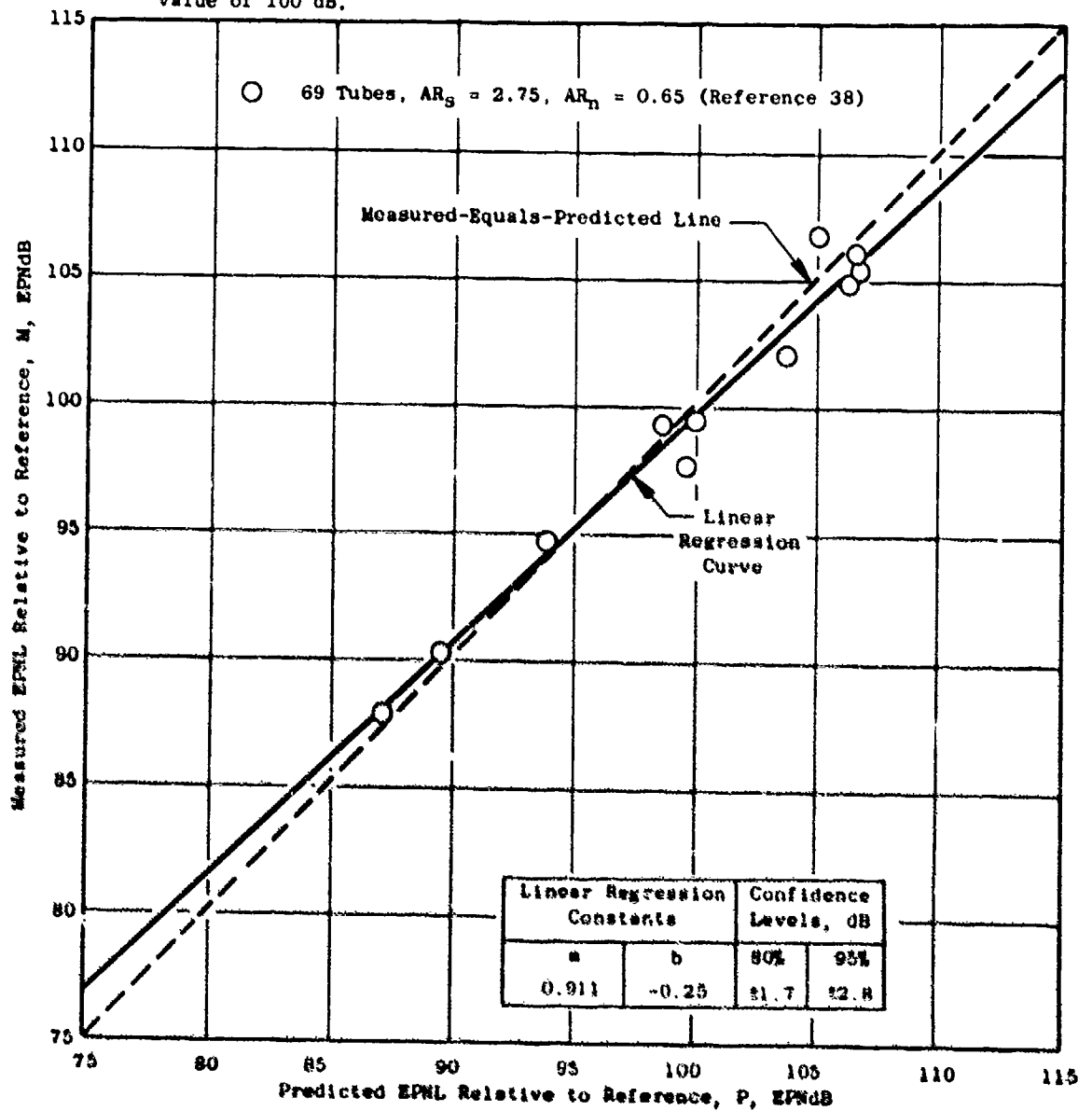


Figure 3-42. Correlation Between Measured and Predicted Effective Perceived Noise Level (EPNL) for Dual-Flow Nozzles with a Multitube Suppressor on the Outer Stream.

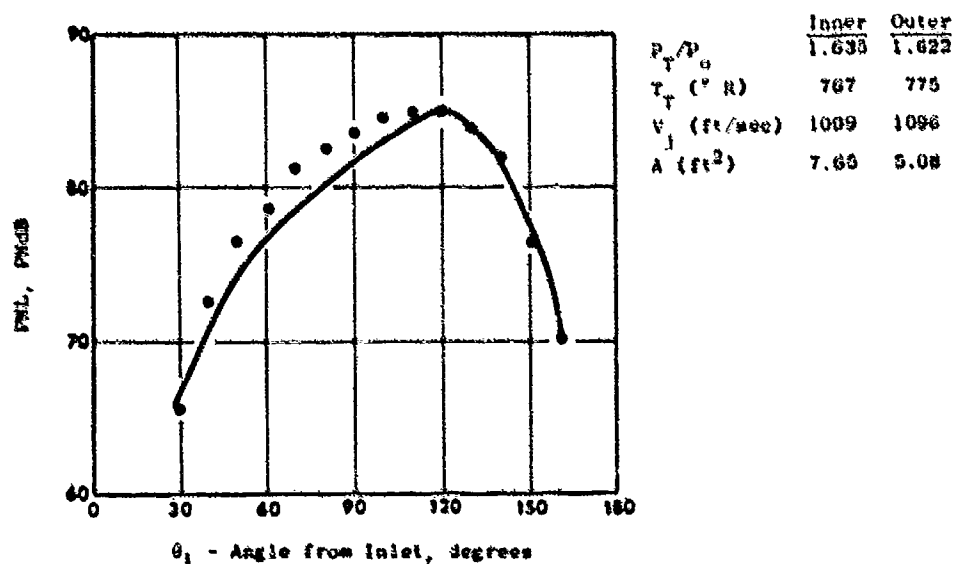
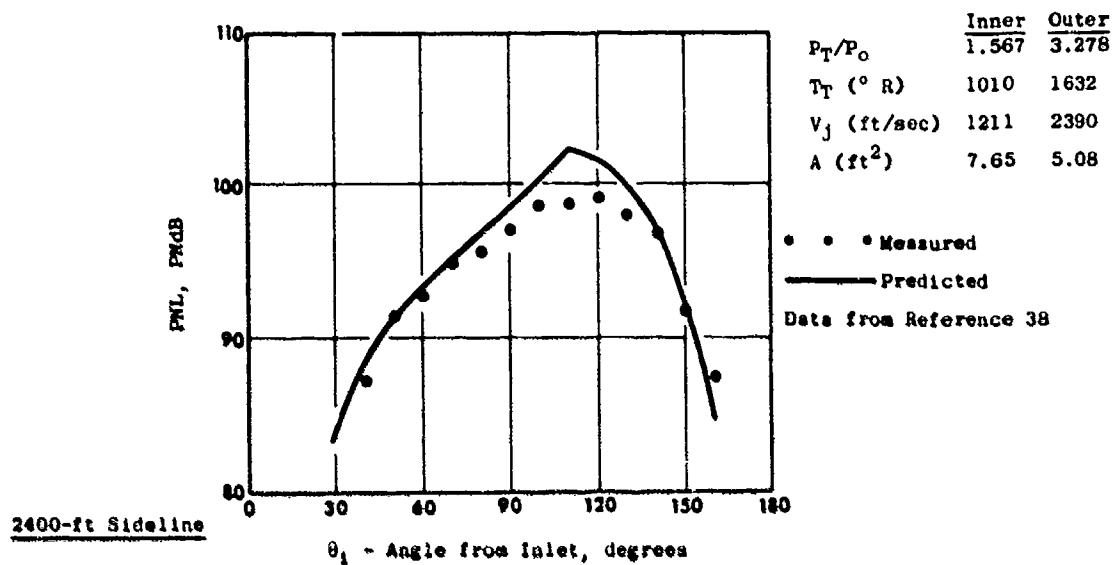


Figure 3-43. PNL Directivity of a Dual-Flow Nozzle with a 69-Tube Suppressor on the Outer Stream.

2400-ft Sideline

• • • Measured

— Predicted

Data from Reference 38

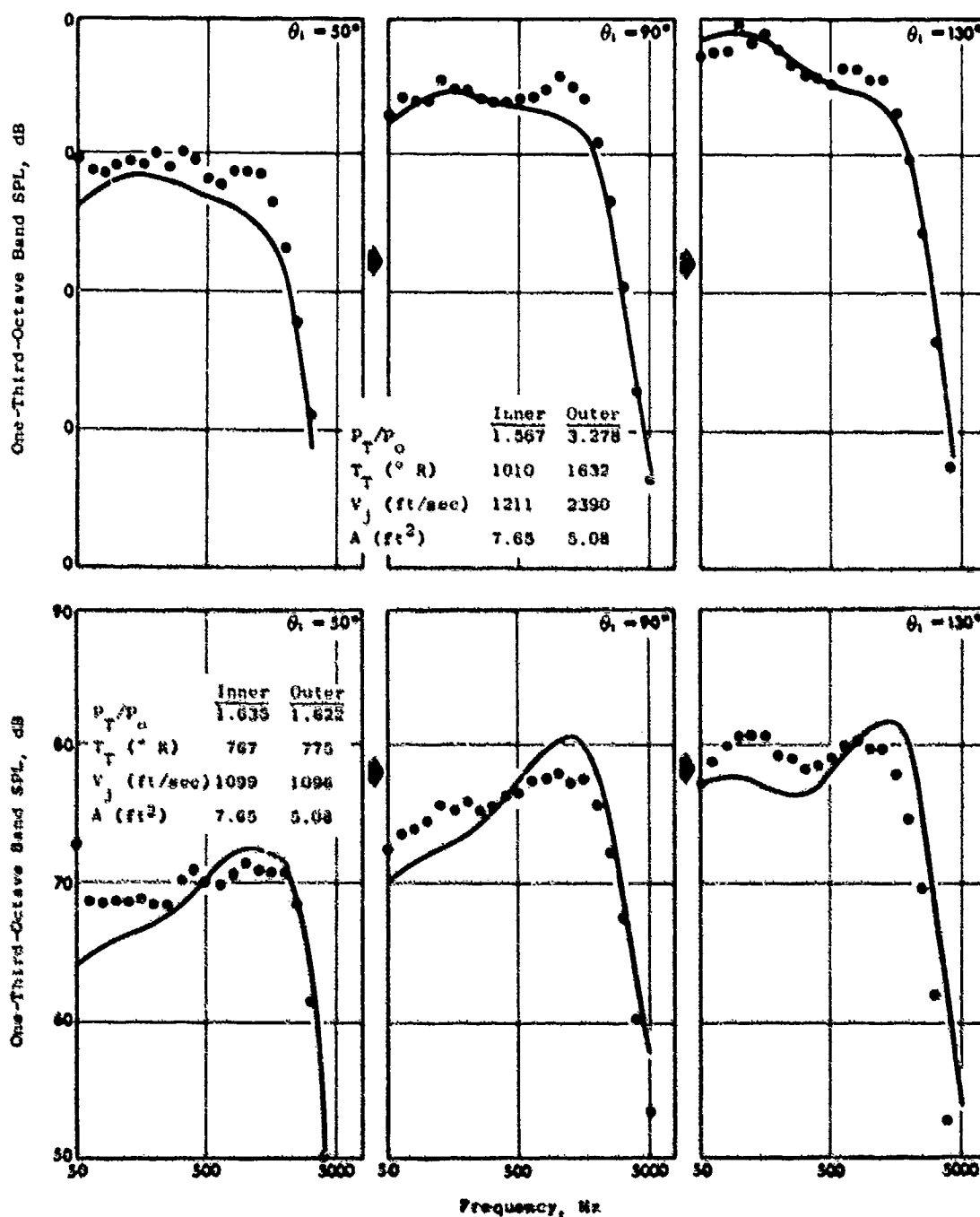


Figure 3-44. One-Third-Octave Band Spectra for a Dual-Flow Nozzle with a 69-Tube Suppressor on the Outer Stream.

- The "Reference" level is the predicted value of noise for each nozzle, at a specified set of thermodynamic conditions, plus an arbitrary value of 100 dB.

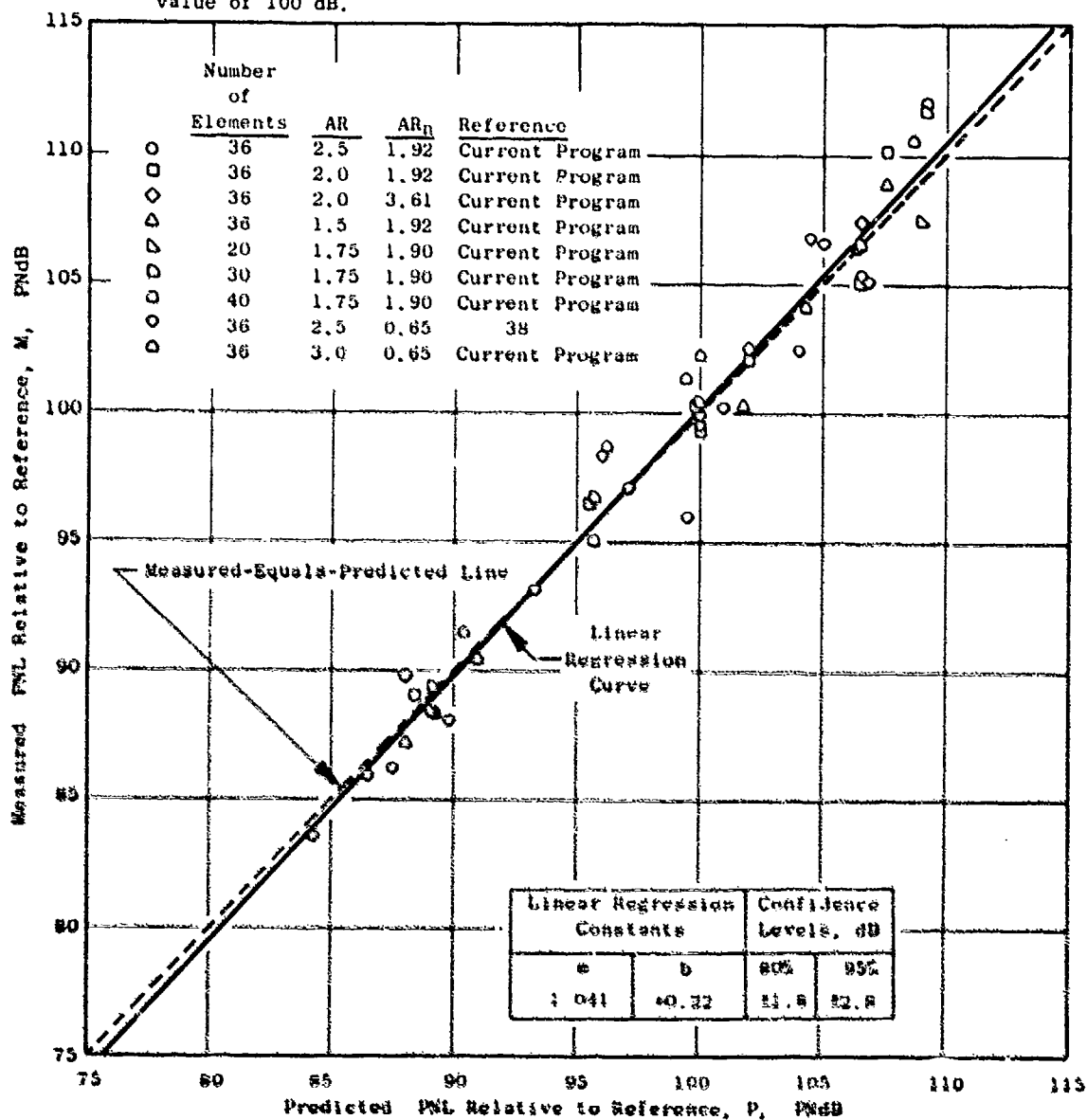


Figure 3-45. Correlation Between Measured and Predicted Maximum Perceived Noise Level (PNL) for Dual-Flow Nozzles with a Multichute/Spoke Suppressor on the Outer Stream.

- Flyover calculation using static data corrected to free-field conditions.
- The "Reference" level is the predicted value of noise for each nozzle, at a specified set of thermodynamic conditions, plus an arbitrary value of 100 dB.

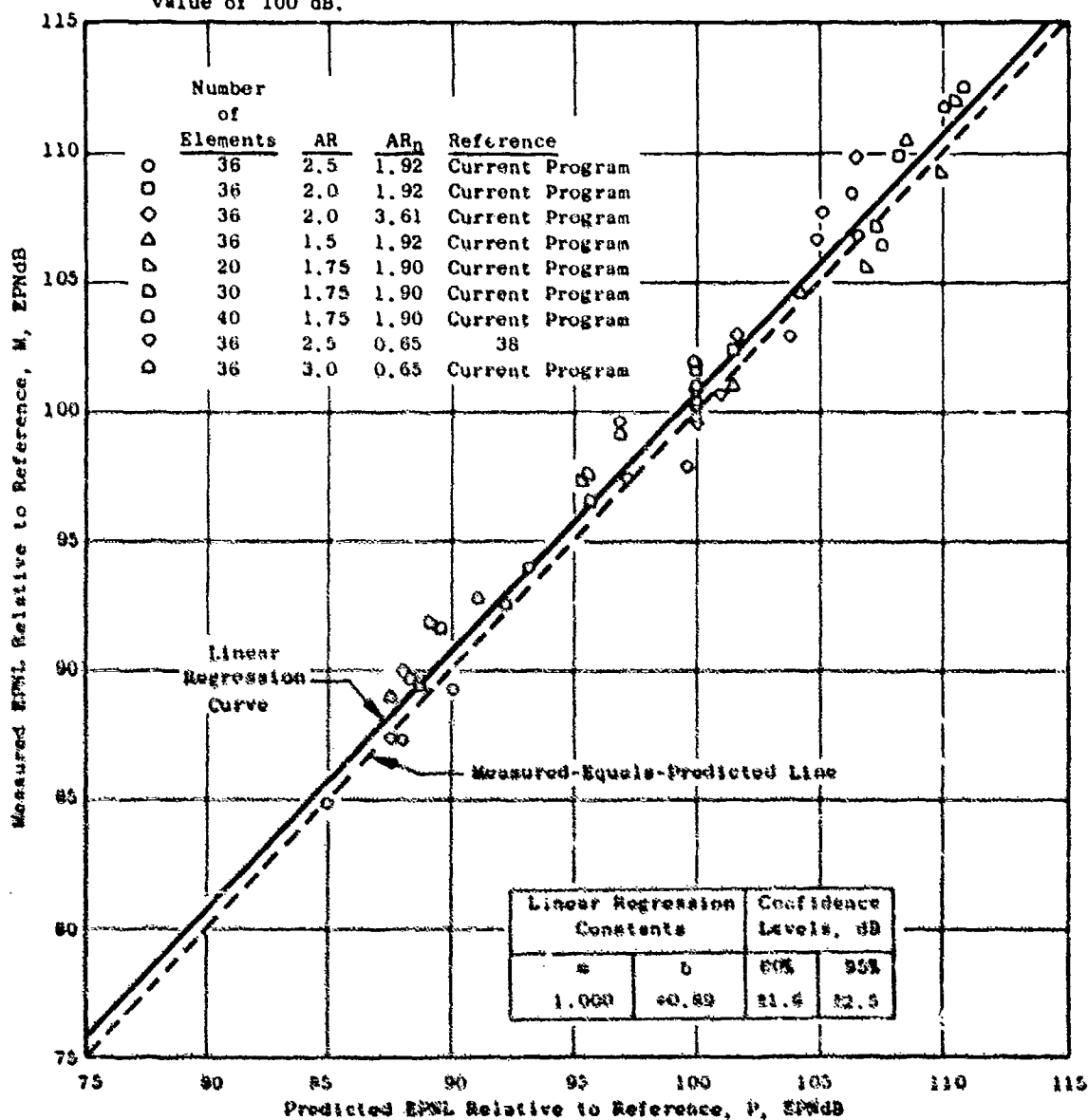


Figure 1-46. Correlation Between Measured and Predicted Effective Perceived Noise Level (EPNL) for Dual-Flow Nozzles with a Multichute/Spoke Suppressor on the Outer Stream.

2400-ft Sideline

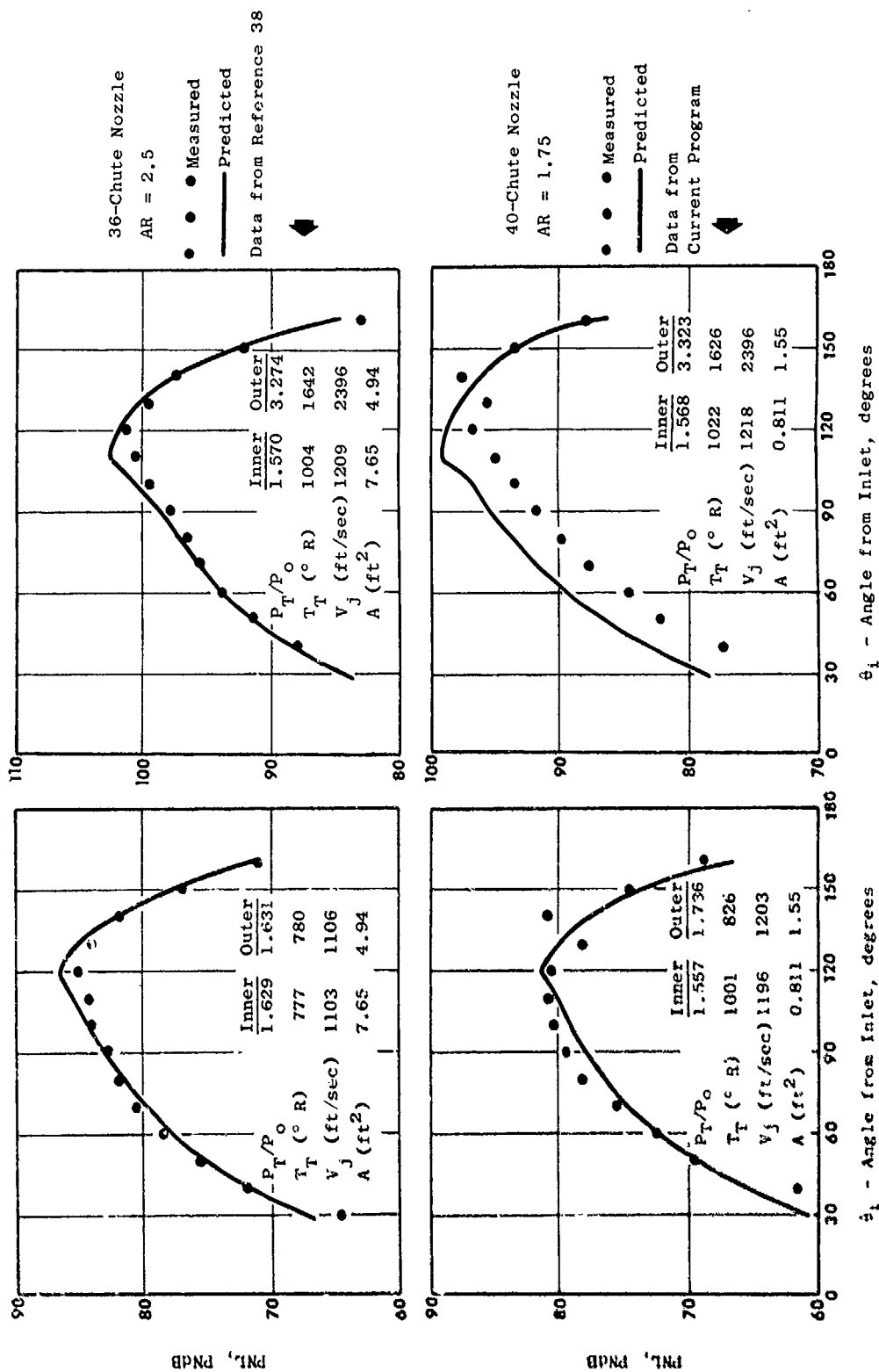


Figure 3-47. PNL Directivity for Dual-Flow Nozzles with a Multichute Suppressor on the Outer Stream.

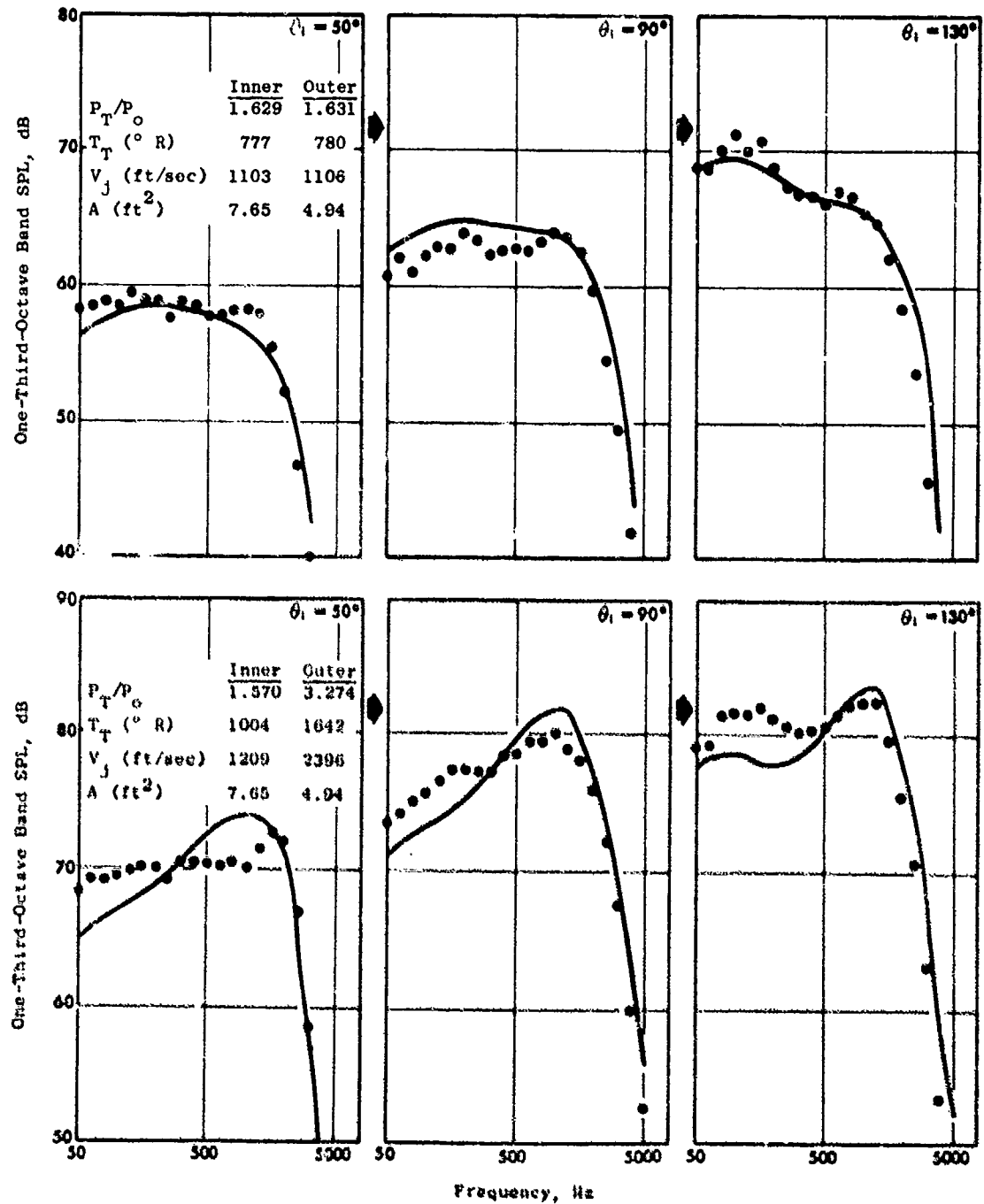


Figure 3-48. One-Third-Octave Band Spectra for a Dual-Flow Nozzle with a 36-Chute Suppressor on the Outer Stream.

2400-ft Sideline

• • • Measured
 — Predicted
 Data from
 Current Program

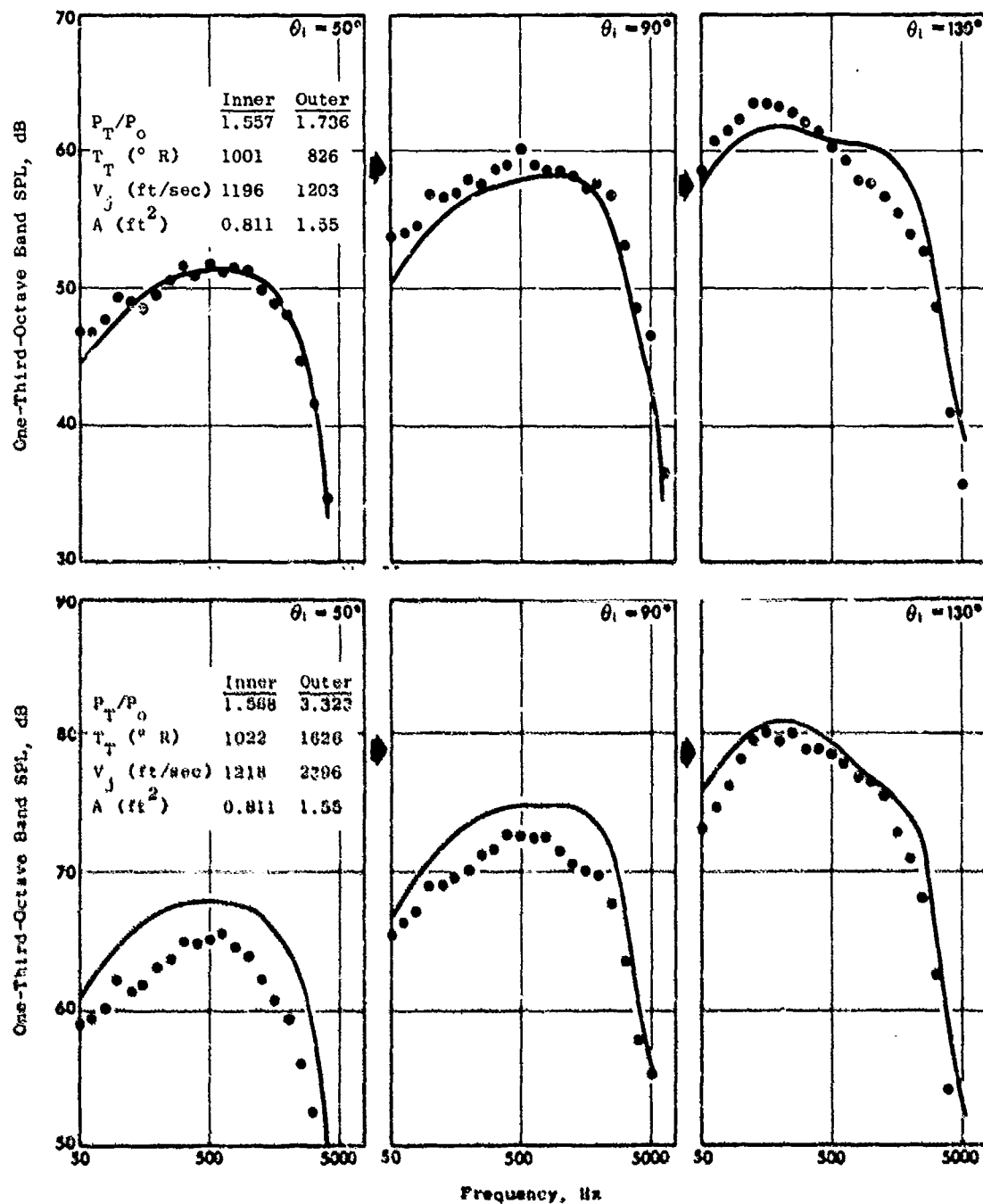


Figure 3-49. One-Third-Octave Band Spectra for a Dual-Flow Nozzle with a 40-Chute Suppressor on the Outer Stream.

Table 3-5. Data Base for Ejector Nozzles.

Reference	Identification	Element Number/Type	Suppressor Area Ratio (1): A_s/A_e	Ejector Area Ratio (2): A_e/A_n	Nozzle Area Ratio (3): A_0/A_1	L_{ej}/D_{eq} (4)	Pressure Ratio Range	Temperature Range ° R	Velocity Range fps	Comments
5	Vol II P 29	31 Tubes	2.75	2.6	Single-Flow Nozzles	2.0	2.0-4.0	1610	1870-2530	
		309 31 Tubes	2.75	3.1		2.0	2.0-4.0	1610	1870-2530	
		319 31 Tubes	2.75	3.7		2.0	2.0-4.0	1610	1870-2530	
		321 37 Tubes	2.3	3.1		2.0	2.0-4.0	1610	1870-2530	
3	Vol II P 20	77 Tubes	3.7	5.8	Single-Flow Nozzles	2.0	1.55-3.0	1140-1960	1275-2560	
		36 Chute	2.2	2.3		1.14	1.47-3.55	1160-2090	1220-2800	Plug
4	Vol I P 113	66 Tubes	2.7	2.3	Single-Flow Nozzles	1.14	1.49-3.53	1050-2070	1170-2790	Plug
		313/ 35 32 Chute	2.1	2.46		1.03	1.08-3.19	1090-1895	531-2570	Plug
40	Vol I P 12	37 Tubes	3.3	3.1	Dual-Flow Nozzles	2.0	1.4-4.0	519-2960	690-3470	
		37 Tubes	3.3	3.1		2.0	1.4-2.4	1070-1480	1020-1925	
38	Vol II P 30	68 Tubes	2.75	4.6	Dual-Flow Nozzles	2.2	1.51/1.19-1.8/3.89	519/519-1460/1980	975/550-1400/2790	Plug
		36 Chute	2.5	4.6		2.2	1.51/1.19-1.8/3.89	519/519-1460/1980	975/550-1400/2790	Plug

(1) Ratio of nozzle area (annulus if plug or dual flow nozzle) to suppressor flow area.
(2) Ratio of ejector inlet area to suppressor nozzle flow area.
(3) Ratio of the flow area of the annular nozzle to the flow area of the inner nozzle (undefined for single-flow nozzles)
(4) Ratio of the length of the ejector (from the suppressor nozzle exit plane) to the suppressor nozzle equivalent diameter, $D_{eq} = \sqrt{A_0/A_1}$.

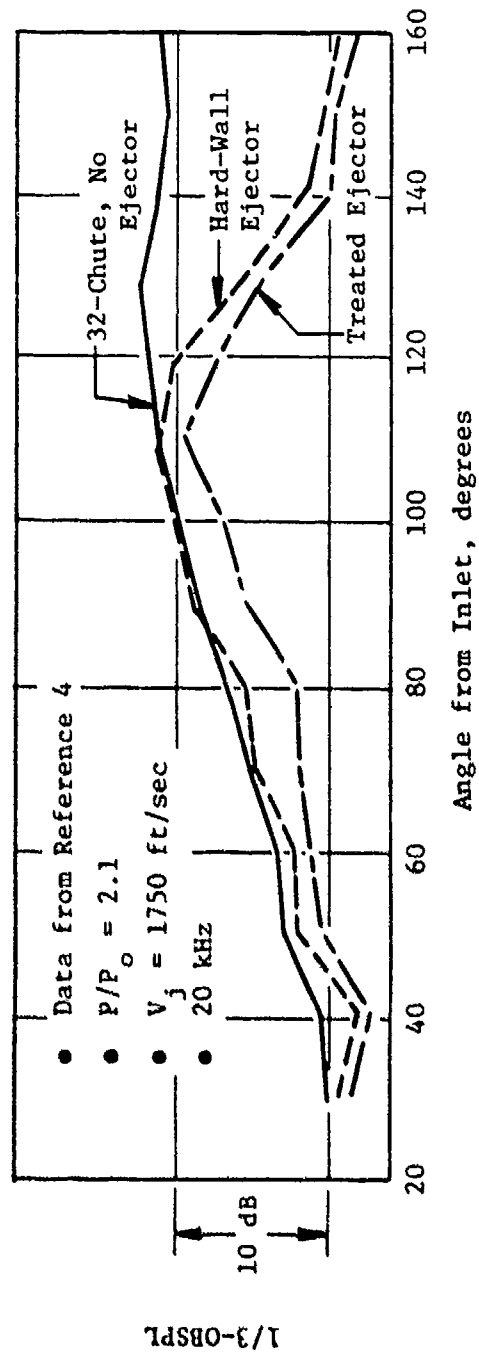


Figure 3-50. Example of Far-Field Directivity with Ejector.

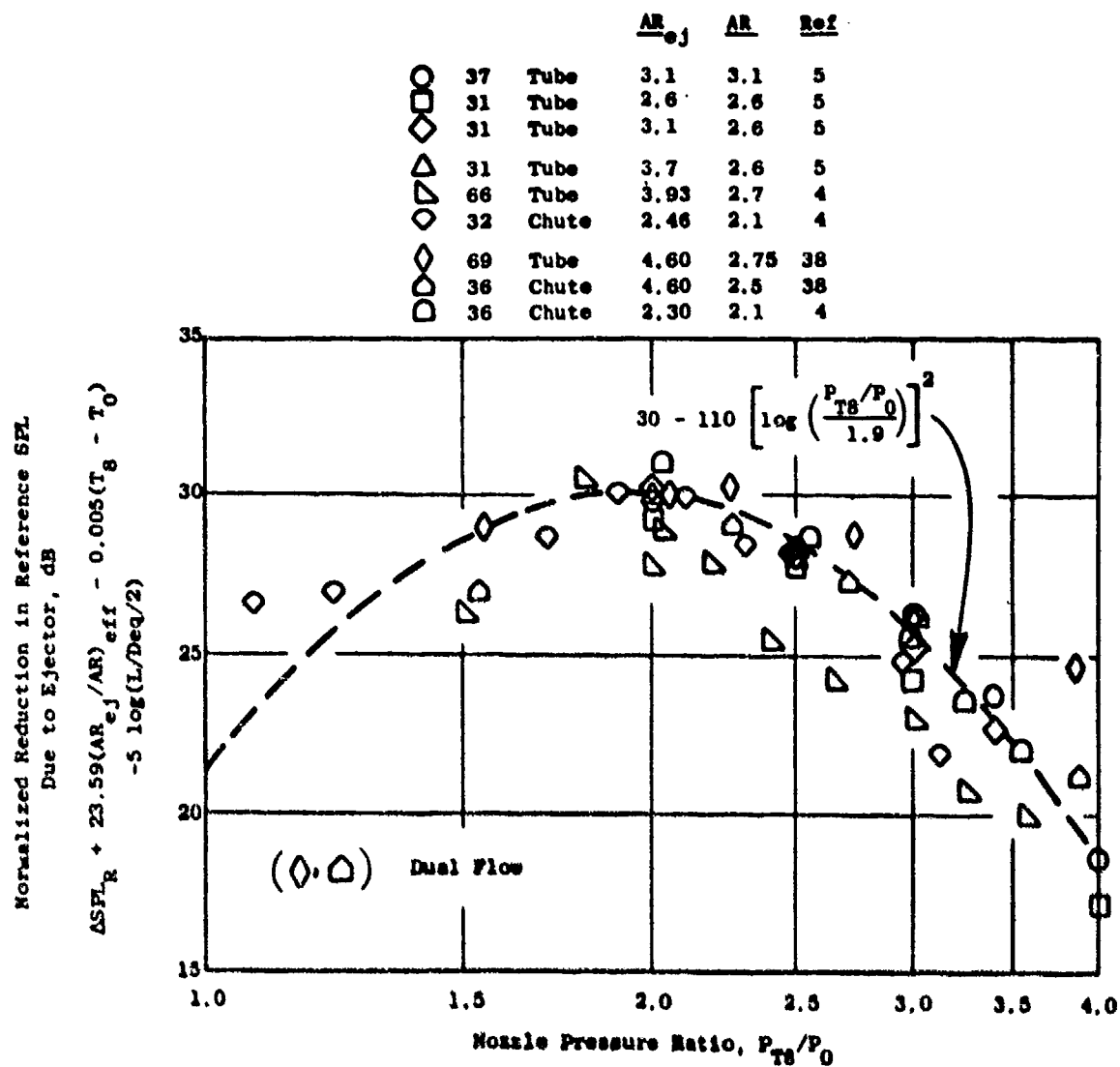


Figure 3-51. Effect of Ejector on Normalized Reference Sound Pressure Level as a Function of Nozzle Pressure Ratio.

- Nozzle Pressure Ratio (P_{T8}/P_0): This effect is shown on Figure 3-51 after the ΔSPL_R has been normalized by the other variables discussed in the following paragraphs.
- Effective Area of the Ejector Relative to the Area of the Nozzle (A_{ej}/A_n)_{eff}: This effect is shown, by itself, in Figure 3-52. The figure shows that the ΔSPL_R is linear with (A_{ej}/A_n) for each of three values of P_{T8}/P_0 . The slope so established was used in the normalization of Figure 3-52. When the nozzle includes a centerbody plug, the effective ratio of (A_{ej}/A_n) is different as established from the available data base as shown in Figure 3-53.
- Nozzle Exit Temperature (T_8): This effect is shown independently in Figure 3-54. The slope so established is used in the normalization of Figure 3-52.
- Ejector Length Relative to Nozzle Equivalent Diameter L_{ej}/D_{eq} : This effect is shown in Figure 3-55. In this figure, $D_{eq} = \sqrt{4A_8/\pi}$, where A_8 is the nozzle flow area. The overall correlation shown in Figure 3-52 uses these data normalized by $(L_{ej}/D_{eq}) = 2$.
- At the frequency of peak premerged noise, the reduction in sound pressure level, (ΔSPL_0) relative to the reduction in reference sound pressure level (ΔSPL_R) versus far-field angle is given in Figure 3-56. The far-field angle is normalized here by the refraction critical angle, θ_c .
- For other one-third-octave band frequencies, the effect of an ejector is correlated relative to the premerged peak noise frequency (f_p), defined by the one-third-octave band frequency in which the following frequency occurs:

$$f_p = 0.3 V_8/d_{eq}$$

where: V_8 = nozzle exit velocity (ft/sec)

$$d_{eq} = \frac{\text{equivalent diameter of a suppressor element (ft)}}{\sqrt{4A_{\text{element}}/\pi}}$$

The spectrum of the reduction at any one-third-octave frequency f , relative to that at the value of f_p is as shown in Figure 3-57. The figure is a plot of $(\Delta SPL_R - \Delta SPL_f)$ versus (f/f_p) using 60°, 110°, and 130° data for illustrative purposes. The effect was found to be independent of angle. Below f_p , it was assumed that $\Delta SPL_f = \Delta SPL_R$; this is relatively unimportant because of the frequency range of high noise levels generated outside the ejector.

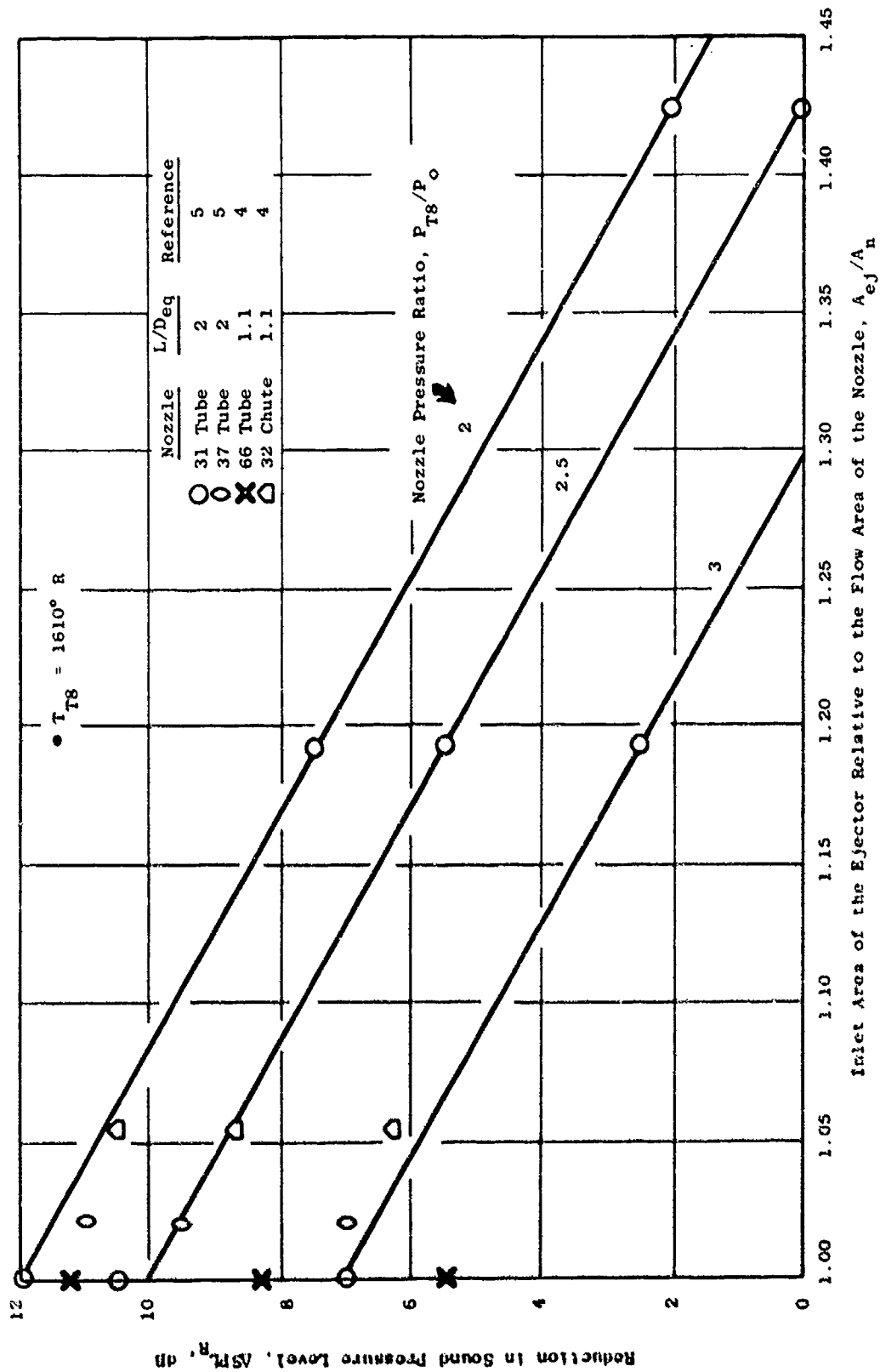


Figure 3-52. Reduction of Reference Sound Pressure Level as a Function of Ejector Inlet Area Relative to Nozzle Area.

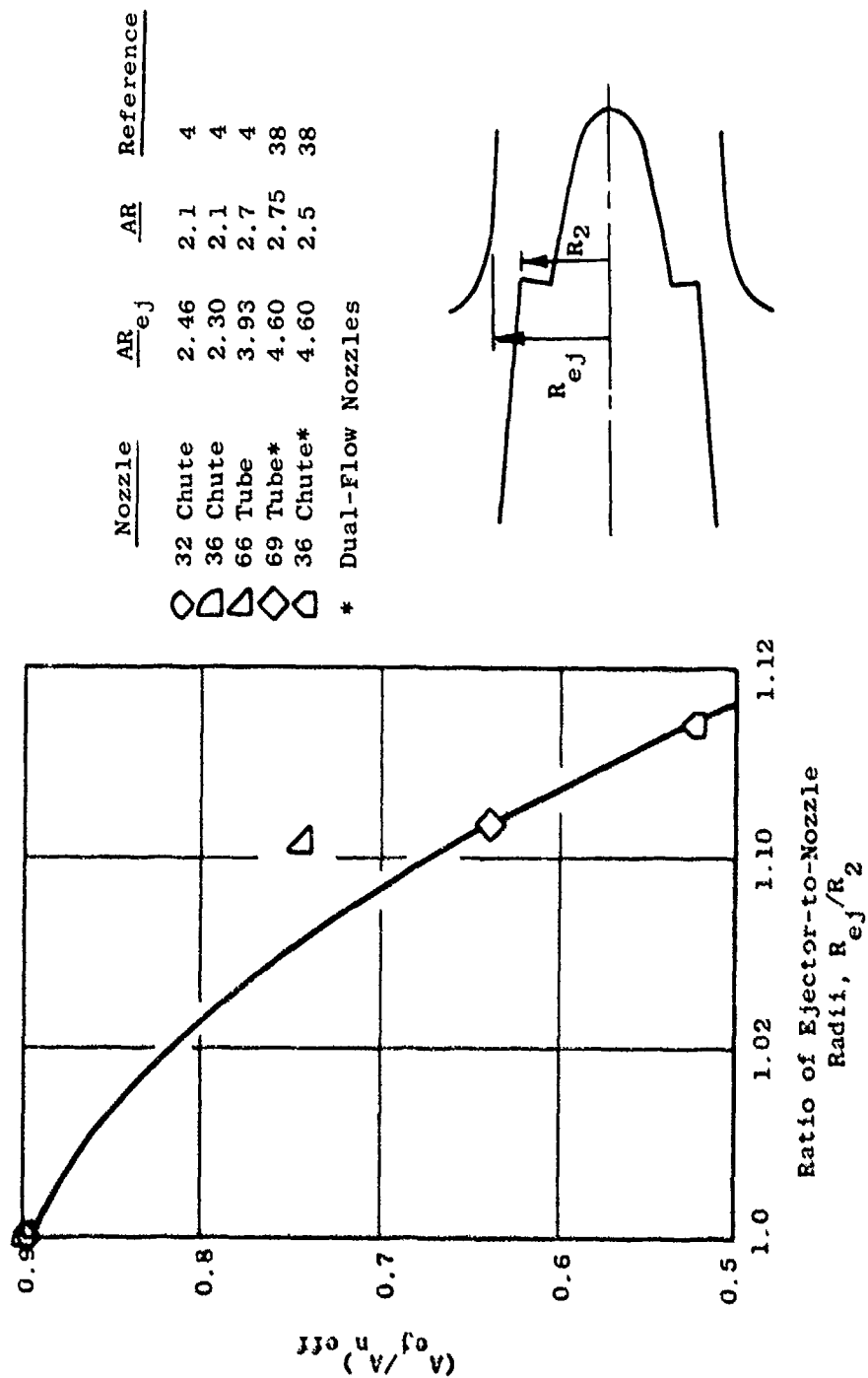


Figure 3-53. Effect of Centerbody Plug on the Effective Ratio of Ejector Area to Nozzle Area.

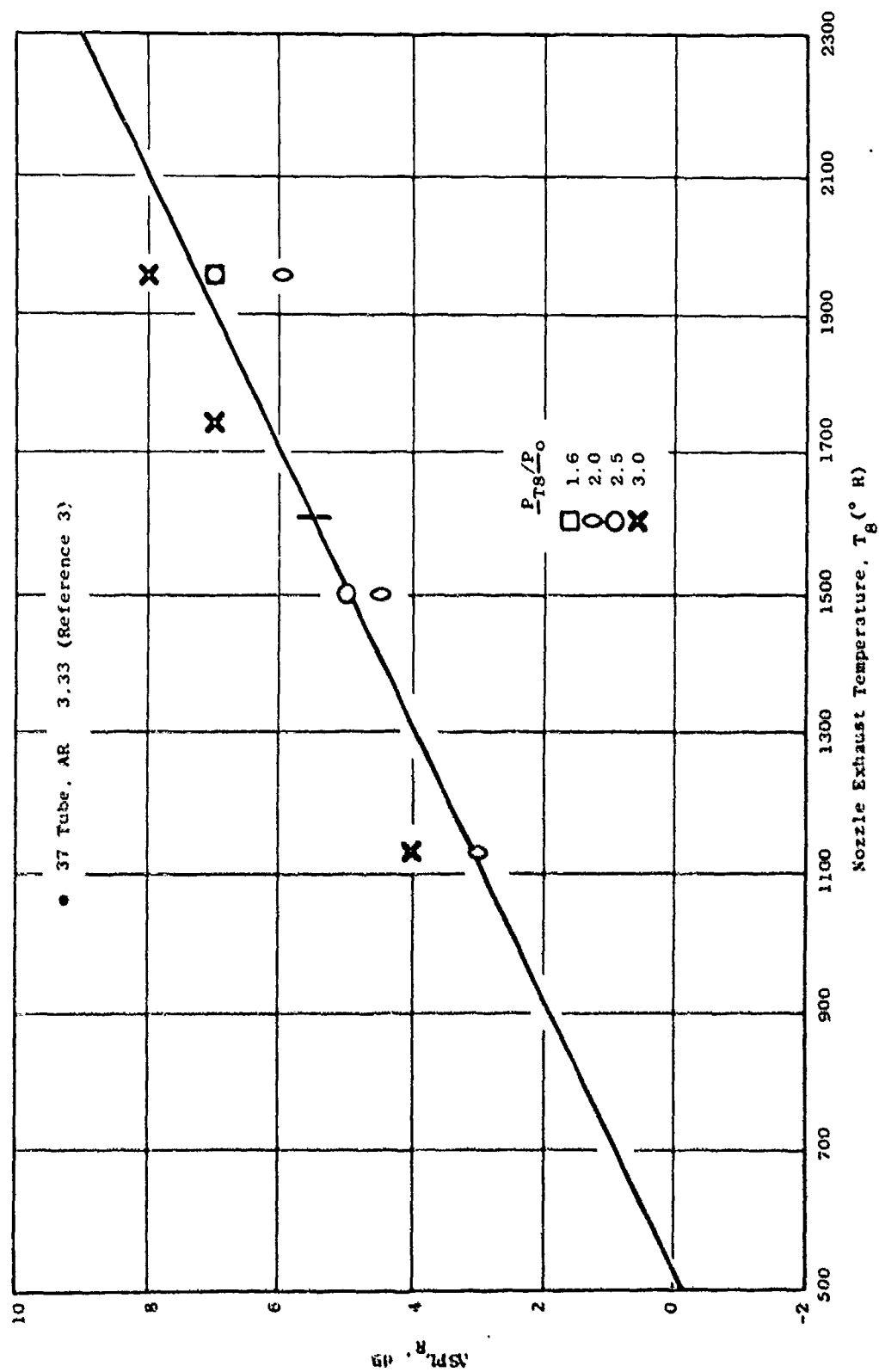


Figure 3-54. Effect of Nozzle Exit Temperature on Reference Sound Pressure Level.

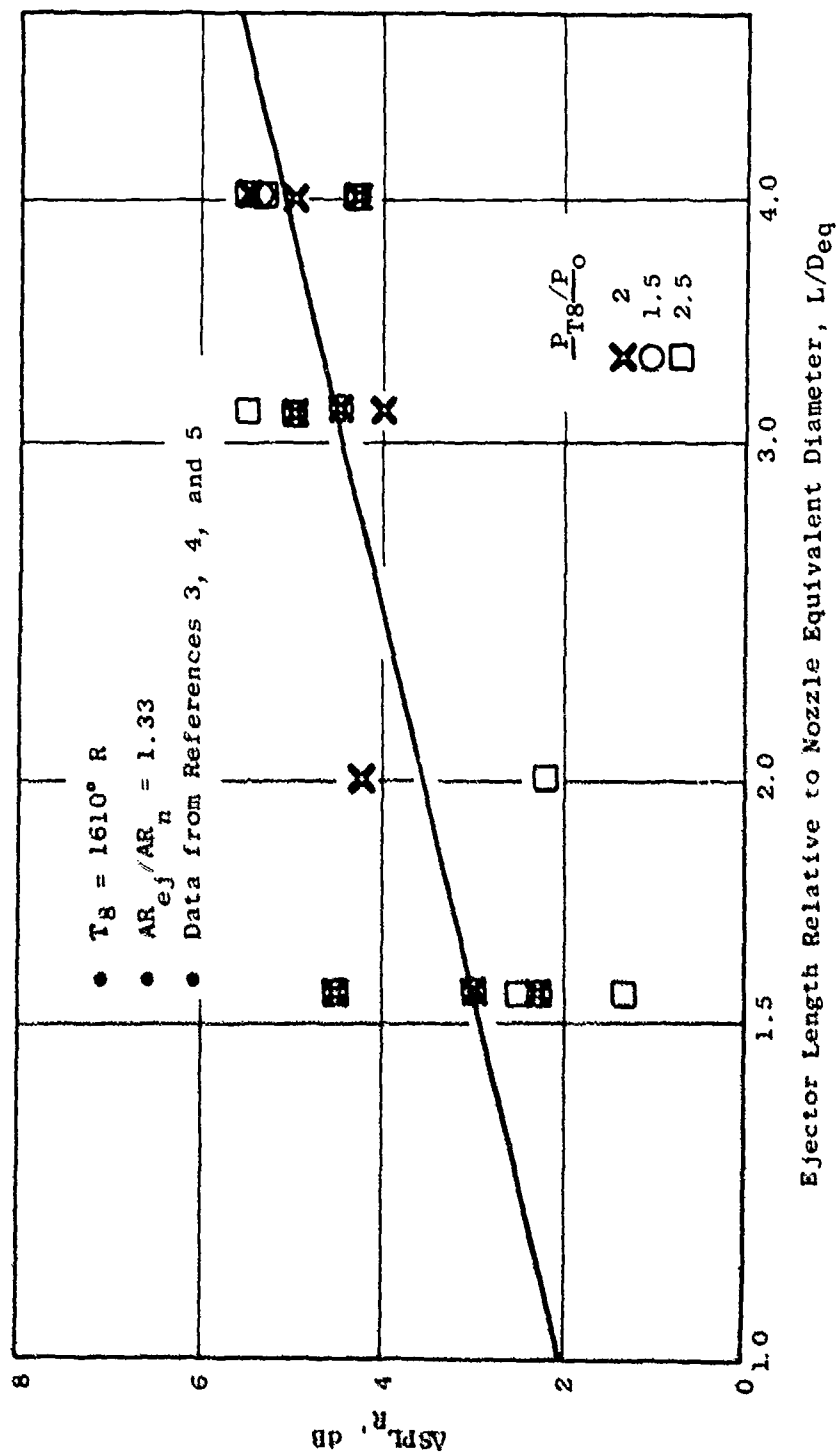


Figure 3-55. Effect of Ejector Length to Nozzle Equivalent Diameter Ratio on Reference Sound Pressure Level.

P_{T8}/P_0

Nozzle	
△ 66 Tube	1.48
○ 66 Tube	1.82
◇ 66 Tube	1.99
◊ 66 Tube	2.99
□ 32 Chute	2.46

Data from Reference 4

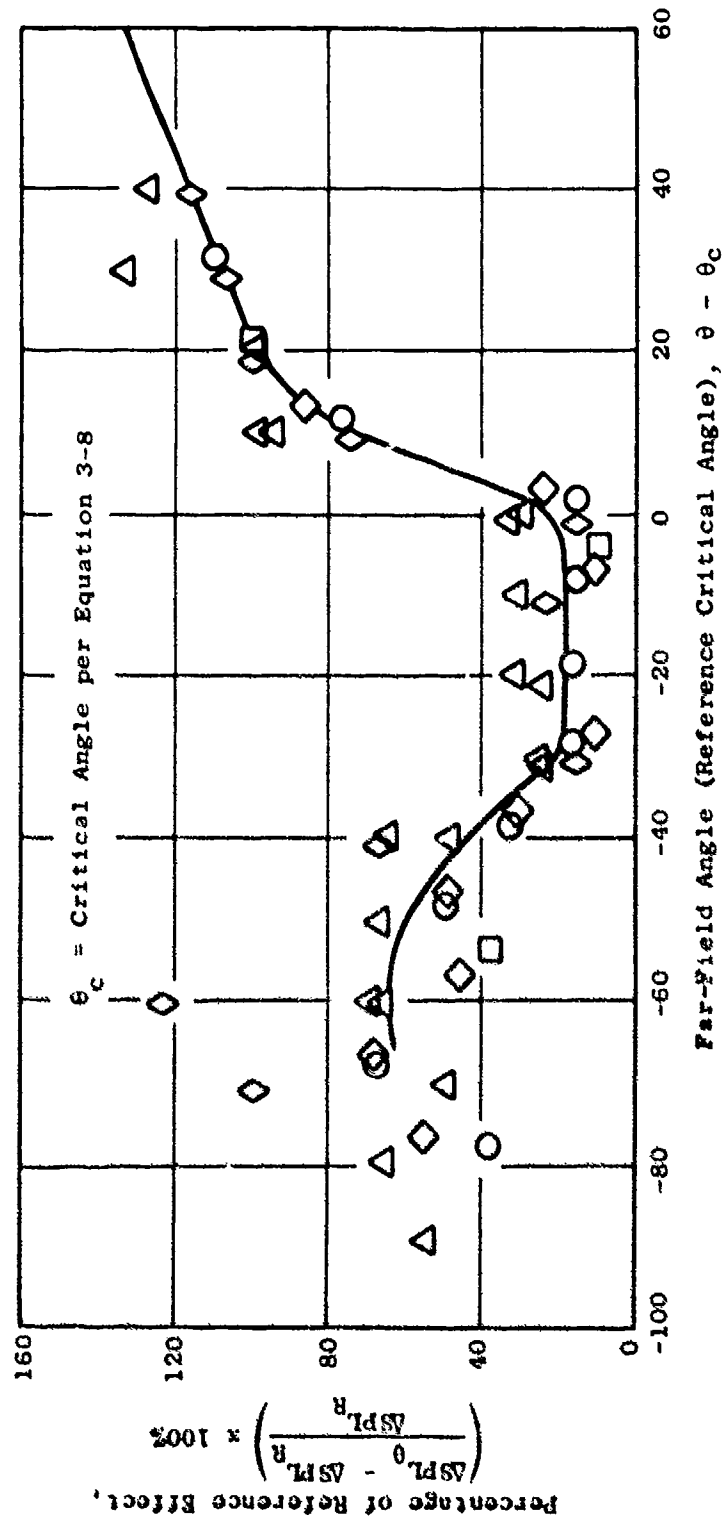
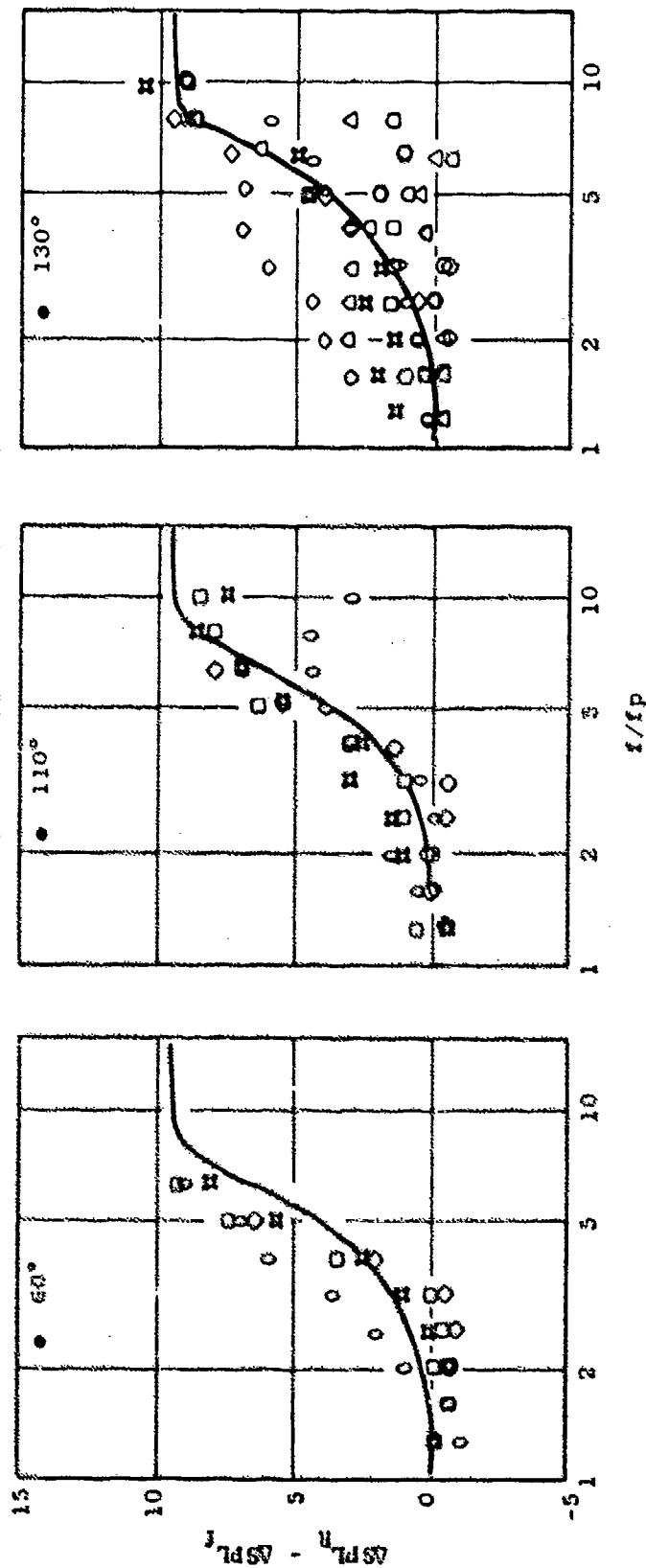


Figure 3-56. Effect of Ejector on Far-Field Directivity of Peak, Premerged, One-Third-Octave Band Noise Level.

$\frac{P_{T8}}{P_0}$	Nozzle	$\frac{AR}{e_j}$	Reference
○ 1.43	66 Tube	2.93	4
■ 1.82	66 Tube	3.93	4
○ 1.99	66 Tube	3.93	4
○ 2.99	66 Tube	3.93	4
○ 2	31 Tube	2.6	5
○ 2	31 Tube	3.1	5
○ 2	31 Tube	3.7	5
△ 2	37 Tube	3.1	5
○ 4	37 Tube	3.1	5



Ratio of 1/3-Octave Band Frequency, f ,
to the Premerged Peak Noise Frequency, f_p

Figure 3-57. Effect of Ejector on the One-Third-Octave Band Spectrum of the Far-Field Noise.

Treated Ejectors

The data on the effect of adding single-degree-of-freedom (SDOF) acoustic treatment to the ejector (Reference 40) has been correlated in terms of reduction of sound power level (Δ PWL), one-third-octave band SPL spectra, and far-field directivity. The suppression expected from the treatment is predicted analytically using the source-location information developed in Section 3.3.2 (Axial Distribution of Noise), using ray acoustics, and taking into account the absorption of energy for each interaction of the acoustic ray with the treatment. The analysis is predicated on the assumption that the ejector does not perturb the noise generation; so, the axial distribution of sources within the ejector are the same as for the bare nozzle.

The acoustic ray analysis is illustrated in Figure 3-59. A line of 25 equally spaced sources is used, located axially from the nozzle exit station to 2.5 times the peak location downstream of the nozzle exit and located radially at the periphery of the outermost element. In a one-third-octave band, the range in relative levels from the peak to 8 dB below the peak is covered (See Figure 3-6).

Angles of incidence from 10° to 80° are used in 10° increments, based on an omnidirectional source distribution, and the reductions in PWL are determined for the upper and lower band limits and the midpoint frequency of all one-third-octave bands. To determine the total PWL reduction, the number of reflections of the acoustic ray associated with an angle of incidence and source location are calculated based on the ejector length, diameter, and the flow conditions. The power reduction for each reflection is determined as discussed in the following paragraph. This reduction is then summed over all reflections. This is repeated for each source location, and, taking into account the relative level of each source (Figure 3-6), the reduction is summed over all sources. The reduction is summed over each angle of incidence to determine the total power reduction for each frequency. By anti-logarithmically averaging the reduction at the lower limiting, midpoint, and upper limiting frequencies, the reduction over a one-third-octave band is approximated.

To determine the reduction due to each reflection within the ejector, the treatment resistance and reactance must be known at the lower limiting, midpoint, and upper limiting frequencies of a given one-third-octave band. The reduction in sound power level (PWL) is determined using the following two equations:

$$a_a = \frac{4R \cos(\theta_i)}{(1+R \cos \theta_i)^2 + (X \cos \theta_i)^2} \quad (3-24)$$

where: a_a = absorption coefficient
 R = normalized specific resistance
 X = normalized specific reactance
 θ_i = incidence angle, as defined on Figure 3-58

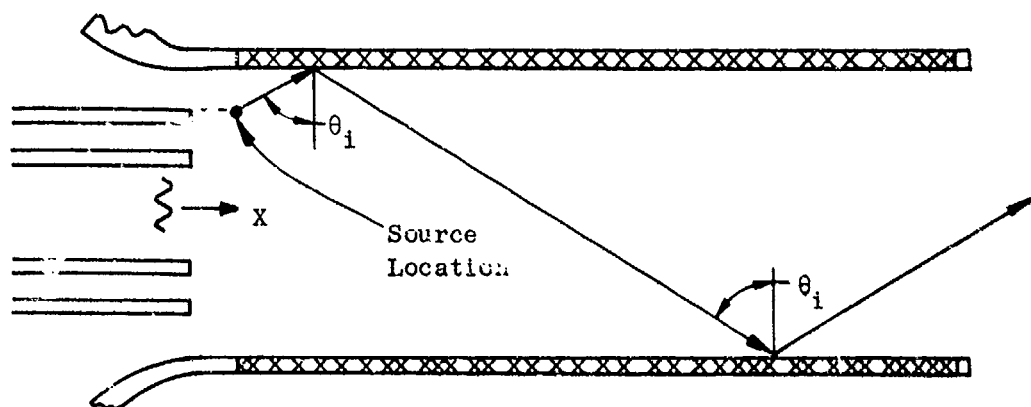


Figure 3-58. Acoustic Ray Analysis for Treated Ejector.

$$\Delta PWL = -10 \log_{10} (1 - \alpha_a), \text{ dB}$$

(3-25)

In the case of SDOF treatment, a routine to determine the resistance and reactance is included in the program. For other treatment materials, the resistance and reactance values as used in Equation 3-24 can be input independently.

To convert this reduction in PWL to a reduction in SPL, the directivity must be known. Figure 3-50 shows an example of the effect of a created ejector (data from Reference 4). Note that the change in SPL relative to the hard-wall ejector is greatest and approximately constant where the hard-wall ejector reduction in SPL is smallest (70° to 120°). At other angles the change in SPL due to treatment is smaller but constant with angle. Data from References 4, 38, and 40 and from this program have been used to develop the directivity correlation shown in Figure 3-59. The data from Reference 4 is plotted on the figure to show representative correlation.

For angles of $\theta_c - 50^\circ$ to θ_c (θ_c defined by Equation 3-8) $\Delta SPL = 1.2 \times \Delta PWL$. For all other angles, $\Delta SPL = 0.6 \times \Delta PWL$.

3.3.6.2 Summary of Prediction Elements for Ejectors

Data for a bare nozzle (without an ejector) are required in order to predict the far-field SPL at all angles and one-third-octave band frequencies. The reduction of the reference sound pressure level by a hard-wall ejector is established for one angle at the frequency of peak premerged noise by the correlation given in Figure 3-51. Parameters needed for this purpose are: nozzle pressure ratio, effective area of the ejector relative to the area of the nozzle (see Figure 3-53), nozzle exit total temperature, and ejector length relative to the equivalent nozzle diameter. The corresponding value of other angles is determined by the correlation given in Figure 3-56; the parameter needed for this purpose is the refraction critical angle as defined by Equation 3-8. The spectral distribution is then determined by applying the correlation given in Figure 3-57 (at all angles) relative to the frequency of peak, premerged noise. The frequency of peak, premerged noise, f_p , is estimated by means of $f_p = 0.3 V_8/d_{eq}$ as defined in the text of Section 3.3.6.1.

The effect of adding treatment is determined analytically using ray acoustics, assuming the axial source distribution as for an unshrouded nozzle (Section 3.2.2), calculating the sound power absorbed per interaction with the treatment (Equations 3-24 and 3-25), and determining the delta one-third-octave band power level (ΔPWL) spectrum by summing for all interactions for all angles of incidence. The ΔPWL spectrum is converted to far-field ΔSPL based upon the correlation shown in Figure 3-59.

Data from Reference 4

- 5000 Hz
- 10,000 Hz
- △ 20,000 Hz

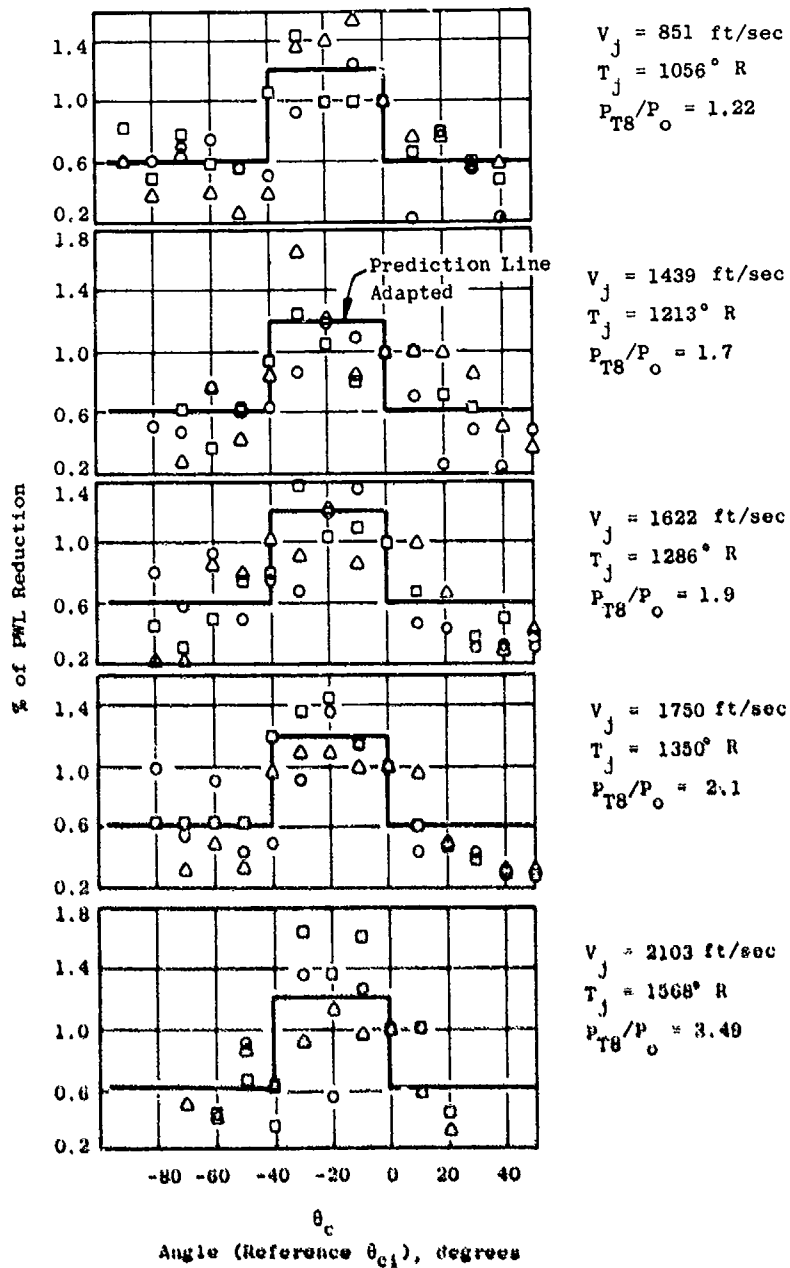


Figure 3-59. Directivity Correlation for Ejector Treatment Effects.

3.3.6.3 Data Comparisons

Because of the empirical nature of the hard-wall correlation, the check against available data is already shown on the correlation plots. Figures 3-60 through 3-64 show PNL directivity and one-third-octave band SPL comparisons for two dual-flow suppressors and one single-flow suppressor, all with hard-wall ejectors. Comparisons of predictions versus data for these nozzles without ejectors have been given in Sections 3.3.5 and 3.3.3, respectively.

For single-degree-of-freedom (SDOF) treatment, examples of predicted versus measured reduction in one-third-octave band sound power level (PWL) are given in Figures 3-65 through 3-67.

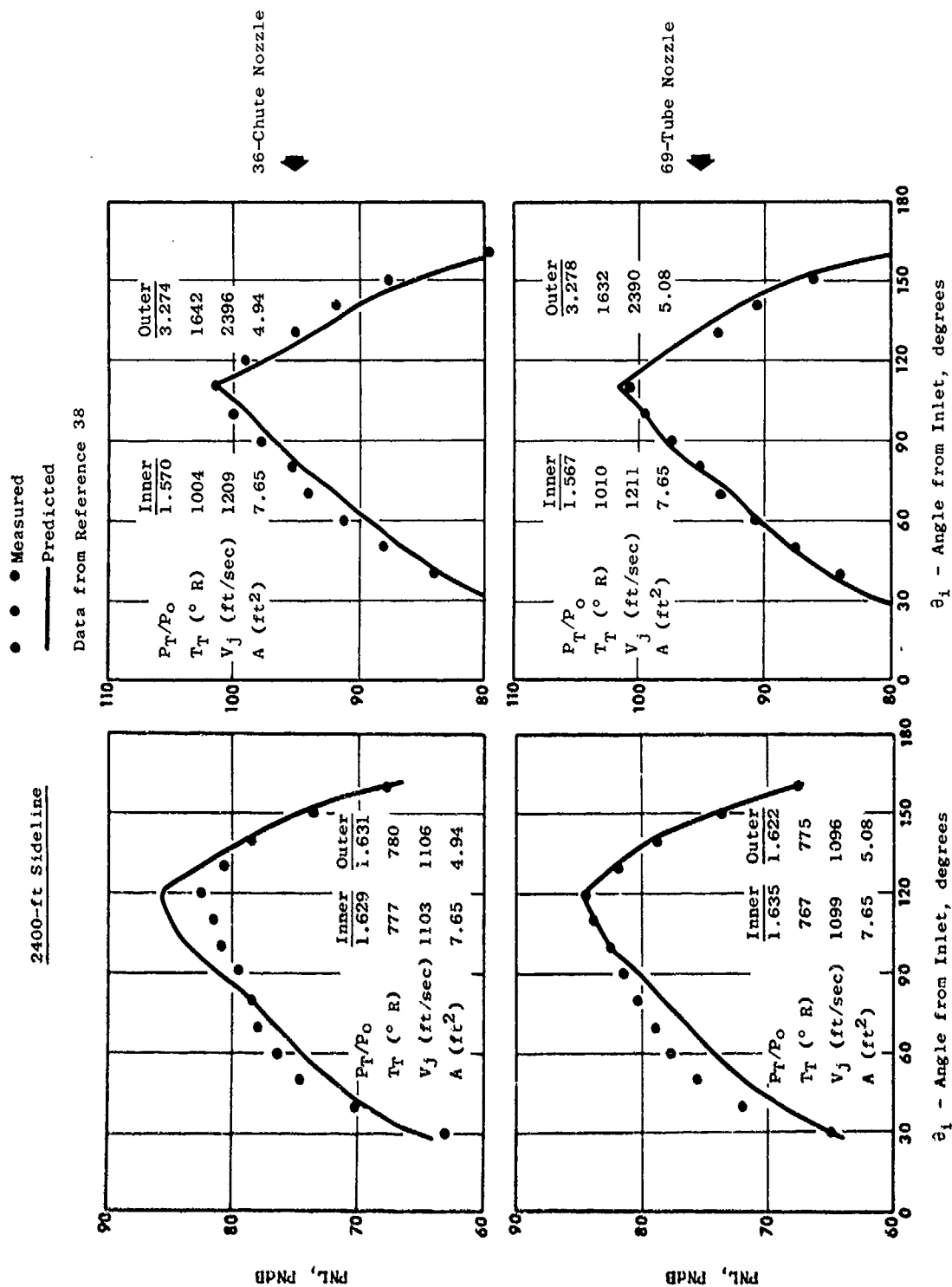


Figure 3-60. Typical PNL Directivity for Dual-Flow Nozzles with Hard-Wall Ejectors.

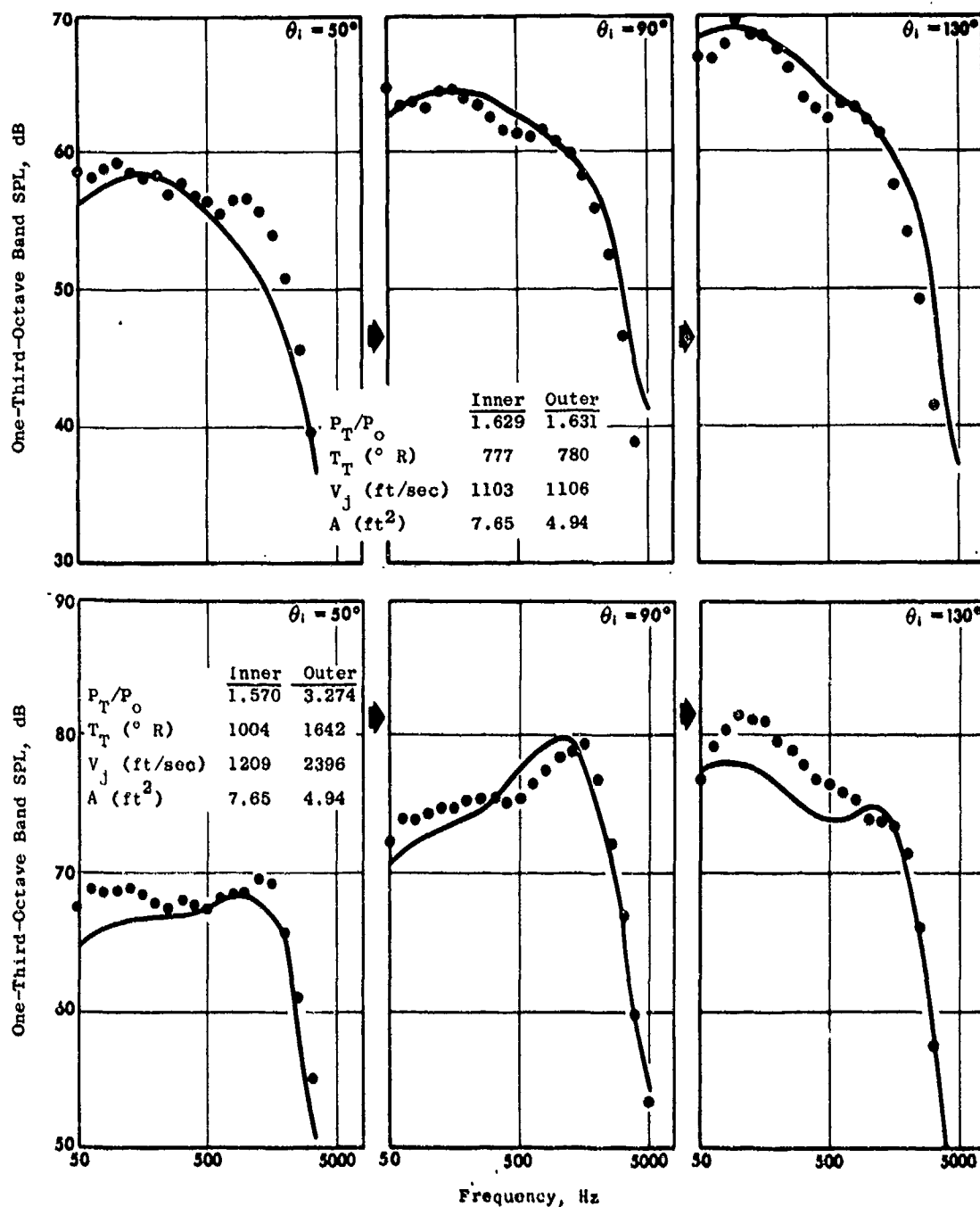


Figure 3-61. One-Third-Octave Band Spectra for a Dual-Flow Nozzle with a 36-Chute Suppressor and Hard-Wall Ejector.

2400-ft Sideline

• • • Measured

— Predicted

Data from Reference 38

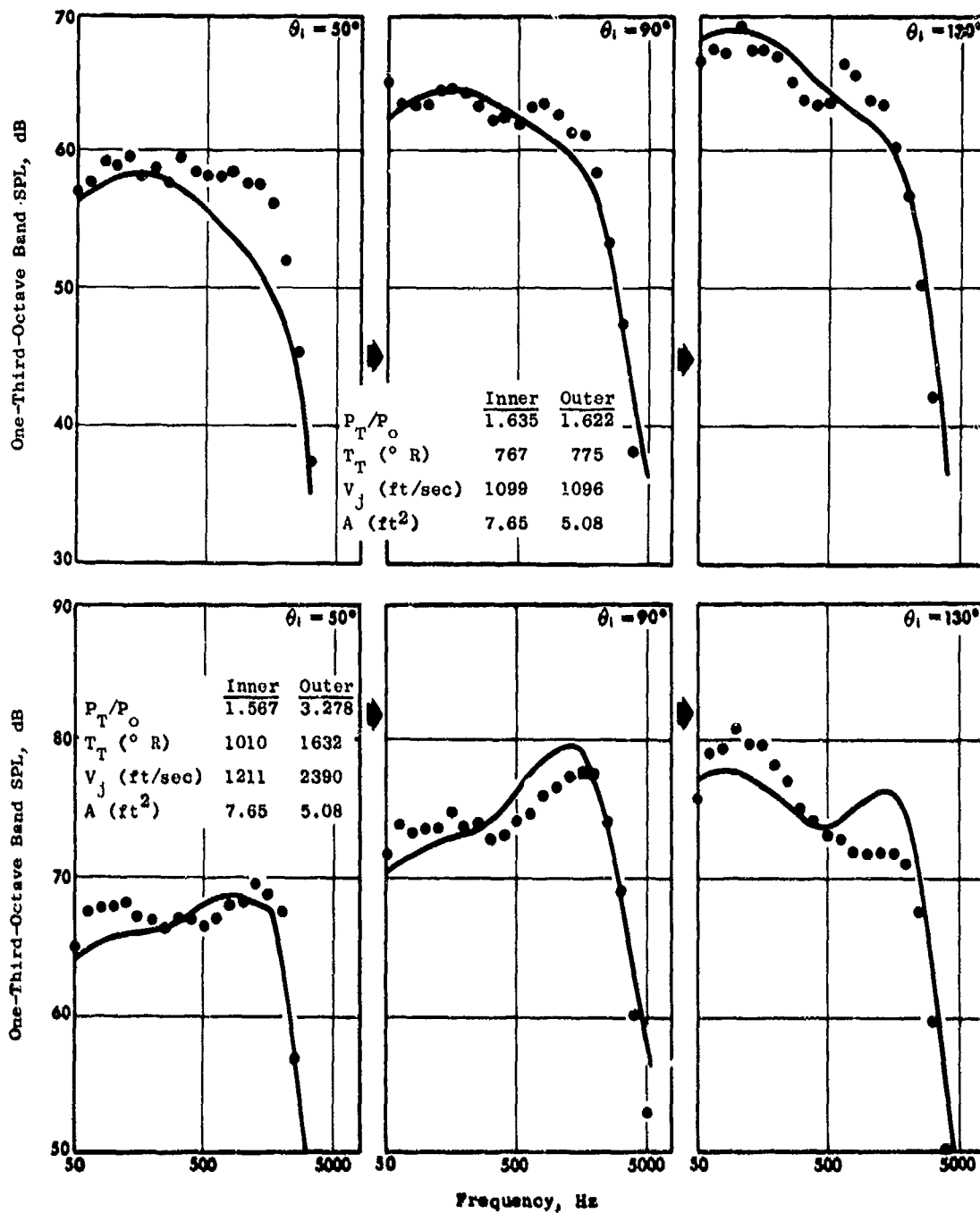


Figure 3-62. One-Third-Octave Band Spectra for a Dual-Flow Nozzle with a 69-Tube Suppressor and Hard-Wall Ejector.

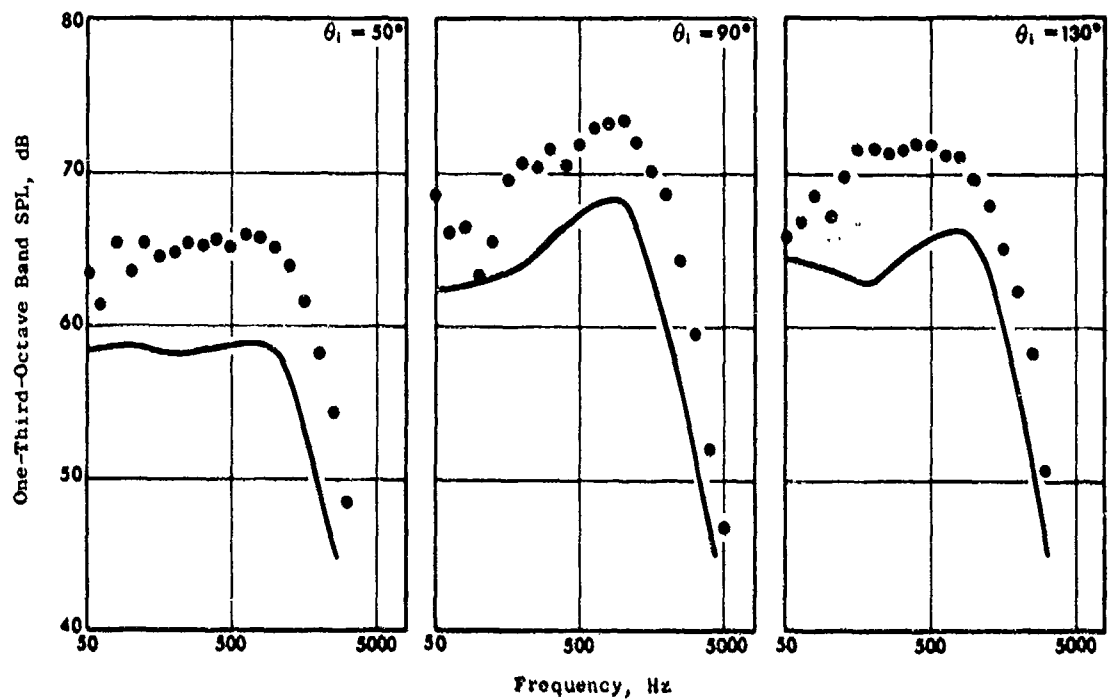
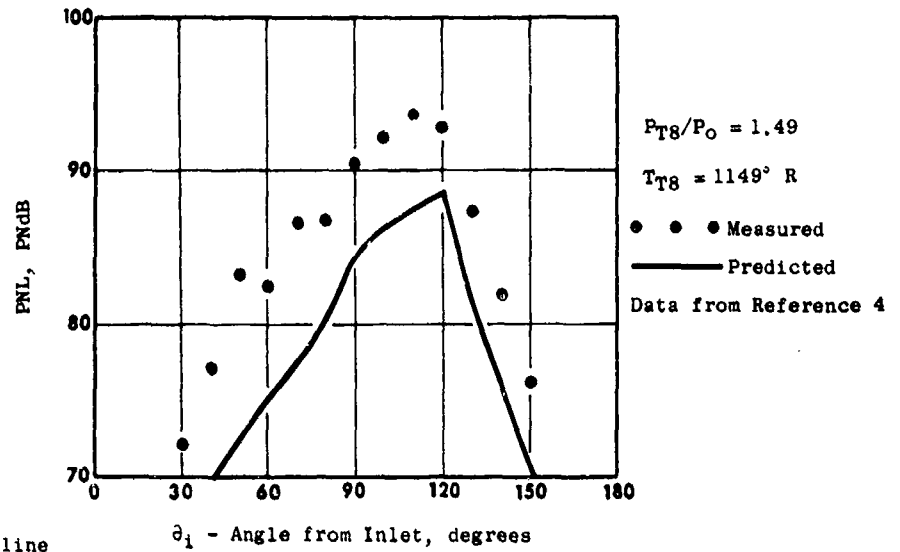


Figure 3-63. PNL Directivity and One-Third-Octave Band Spectra for a 66-Tube Nozzle with a Hard-Wall Ejector, 1224-ft/sec Jet Velocity.

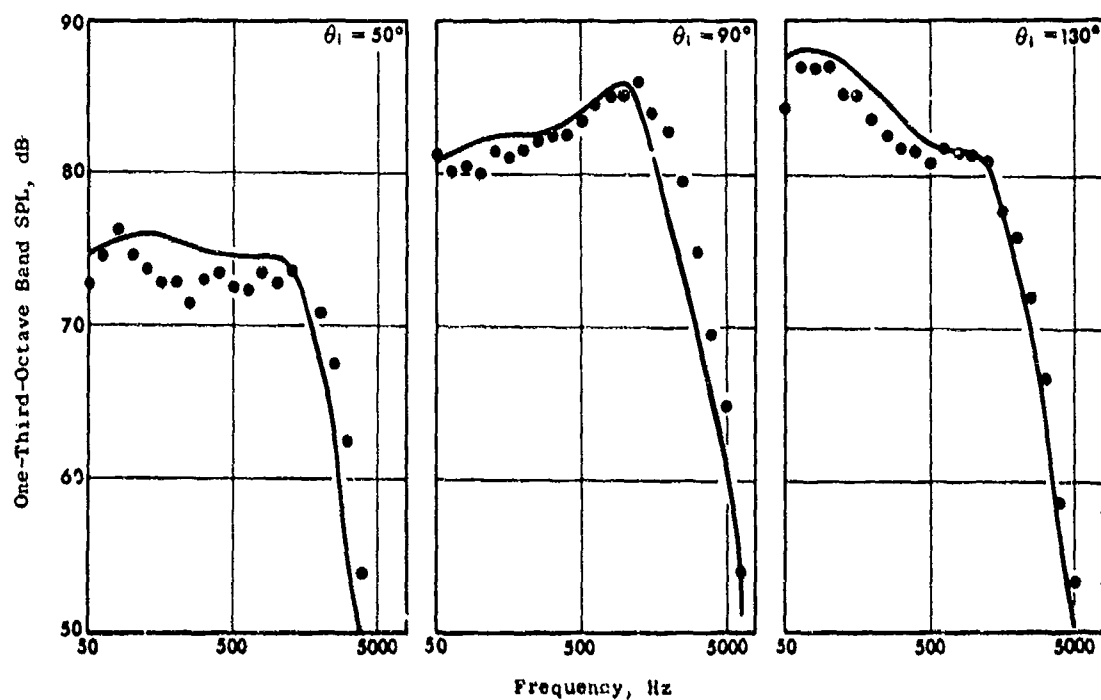
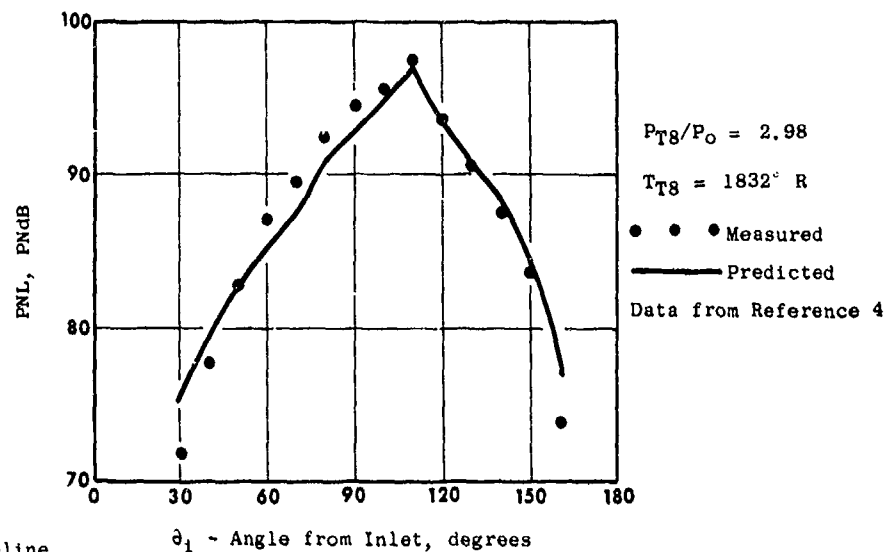


Figure 3-64. PNL Directivity and One-Third-Octave Band Spectra for a 66-Tube Nozzle with a Hard-Wall Ejector, 2465-ft/sec Jet Velocity.

- Measured
- - - Predicted
- 37-Tube Nozzle
- AR = 3.3
- $T_T = 811$ K

Reference 40

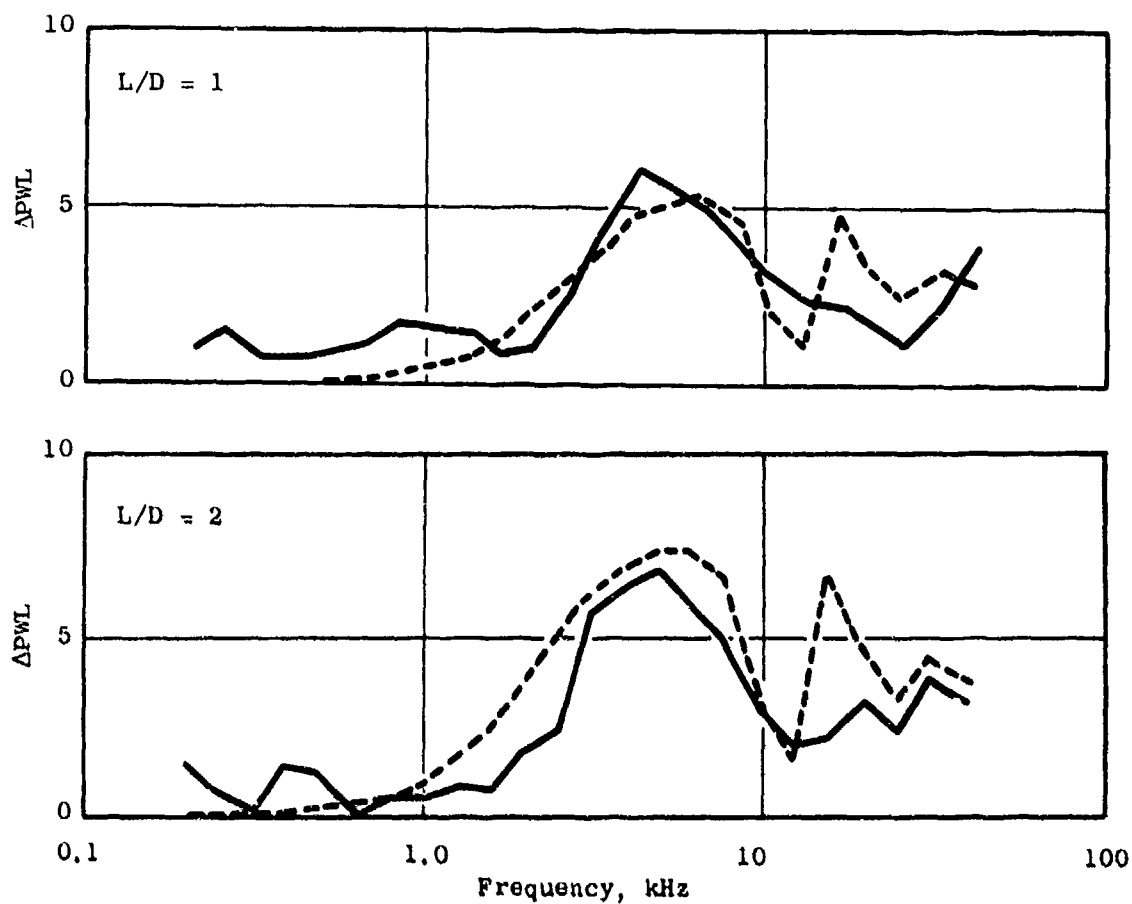


Figure 3-65. Treated Ejector Insertion Loss at 1.4 Pressure Ratio.

- Measured
- - - Predicted
- 37-Tube Nozzle
- AR = 3.3
- $T_T = 811$ K

Reference 40

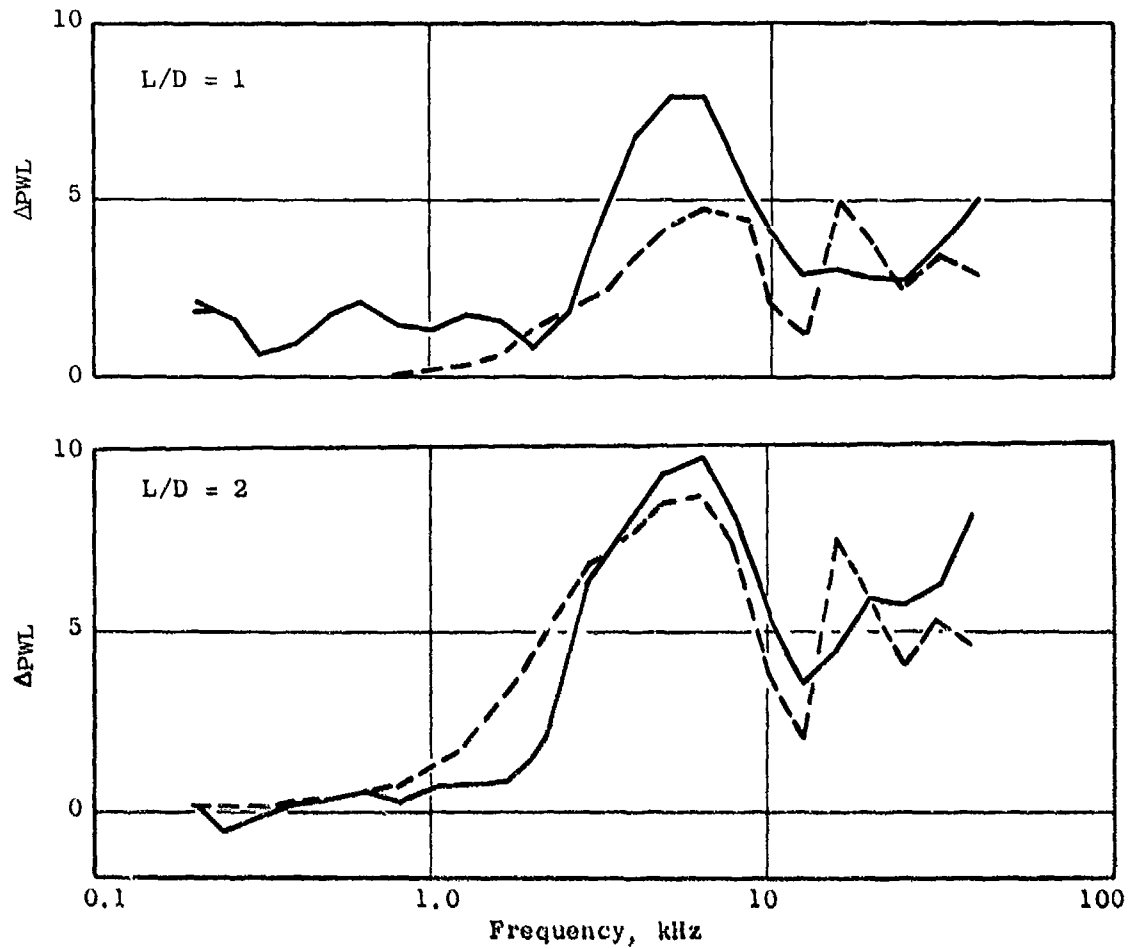


Figure 3-66. Treated Ejector Insertion Loss at 2.2 Pressure Ratio.

— Measured
- - - Predicted

• 37-Tube Nozzle
• AR = 3.3
• $T_T = 811$ K

Reference 40

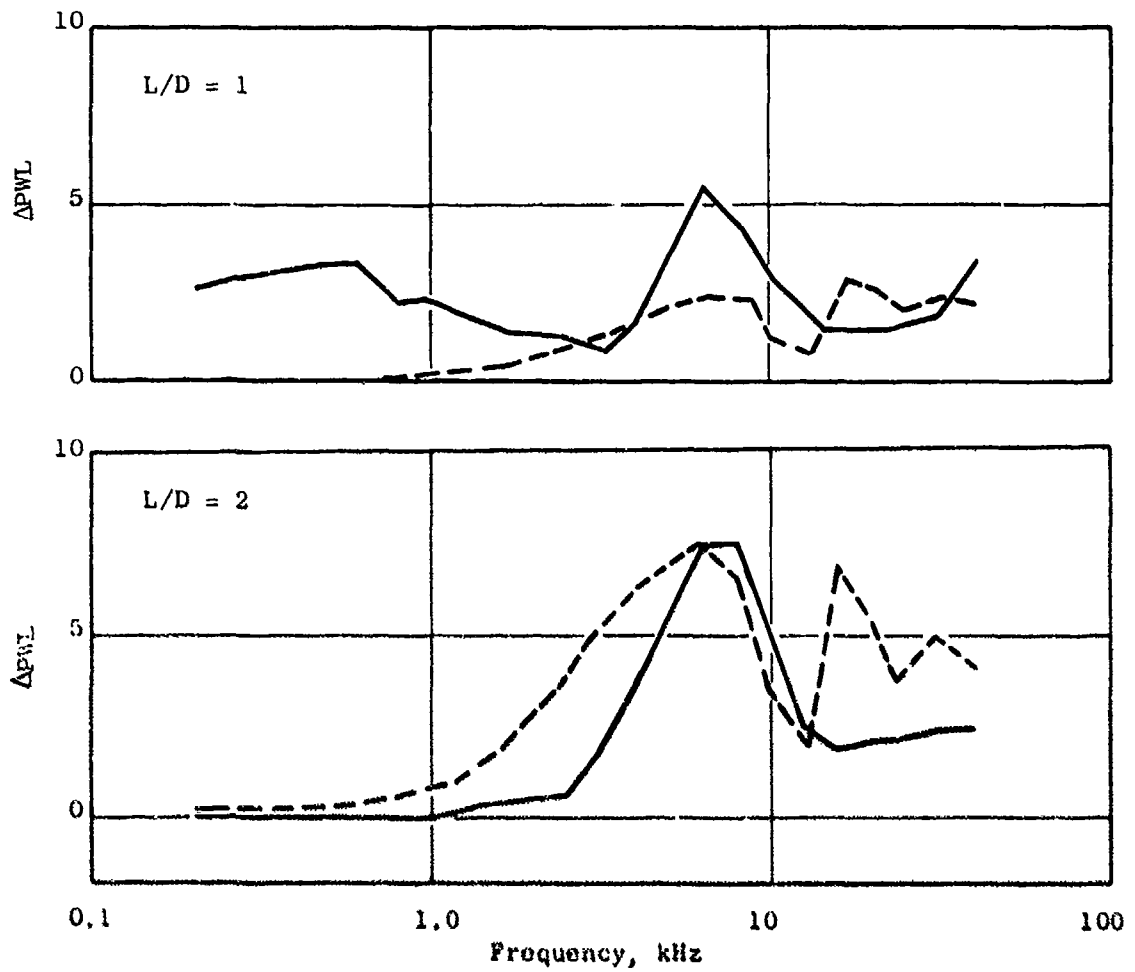


Figure 3-67. Treated Ejector Insertion Loss at 4.0 Pressure Ratio.

4.0 THEORETICAL PREDICTION METHOD AND VERIFICATION OF PRINCIPLES

Certain basic concepts of jet noise generation and suppression have evolved in the past 20 years. The theoretical developments and basic experiments performed as part of Task 2 of the High Velocity Jet Noise Source Location and Reduction Program have supported a view of the physics of jet noise and suppression/reduction. The primary purpose of these simple experiments was to verify basic suppression concepts and not to be limited by considerations which would be relevant to realistic engine system configurations.

Section 4.1 summarizes the key issues relevant to the theoretical modeling of jet noise mechanisms. This subject is treated in depth in the Task 2 report, Reference 7. Section 4.2 describes the analytical model of the theoretical M*G*B jet noise prediction method from Task 2 in sufficient depth for Section 4.3 to present a study to verify the theoretical principles by direct comparisons of the theory with the Task 3 data.

4.1 JET NOISE MECHANISMS

The jet noise theories of Lighthill (Reference 41), Ribner (Reference 42) and Ffowcs-Williams (Reference 43) have identified and quantified a number of important, physical characteristics of jet noise. These include: (1) the generation of sound by small-scale, random, turbulent-eddy fluctuations, (2) the "quadrupole" nature of the acoustic field, and (3) convective amplification of the sound due to motion of the turbulent-eddy sources relative to the observer. From these theoretical developments, a scaling principle for jet noise has been extracted (Ahuja and Bushell, Reference 44) as follows:

$$P(Q) = \text{SPL} - 10 \log_{10} (V_j/V_{\text{ref}})^8 - 10 \log_{10} (D/R)^2 - 10 \log_{10} (1 + M_c \cos \theta_1)^{-5} - 10 \log_{10} (\rho_j/\rho_{\text{ref}})^2 \quad (4-1)$$

where $Q = (fD/V_j)(1 + M_c \cos \theta_1)$

and P - normalized sound pressure level (dB)

SPL - far-field sound pressure level (dB)

V_j - nozzle exit jet velocity

V_{ref} - reference velocity

D - nozzle diameter

R - observation radius

- M_c - eddy convection Mach number
- ρ_j - nozzle exit jet density
- ρ_{ref} - reference density
- θ_i - observation angle from inlet axis ($\theta_i = 180^\circ - \theta_j$)
- Q - normalized, Doppler-shifted frequency
- f - observer frequency

According to this scaling principle, one should obtain a universal curve of P versus Q when far-field noise measurements of SPL versus f are normalized according to Equation 4-1, regardless of jet velocity, diameter, density (or temperature), frequency, or angle and radius of measurement.

Recent careful experimental studies by Lush (Reference 45), Ahuja and Bushell (Reference 49), and Hoch, et al. (Reference 46) show that this scaling principle is not able to collapse parametric data onto a single curve. For example, for cold jets at small values of Q (source Strouhal number), the factor $(1 + M_c \cos \theta_i)^{-5}$ in Equation 4-1 underestimates the variation of noise with angle. Conversely, at high values of Q , this factor overestimates the variation of noise with angle. For hot jets, the data is best correlated if the factor $(\rho_j/\rho_{ref})^2$ in Equation 4-1 is replaced by $(\rho_j/\rho_{ref})^\omega$, where the density exponent ω is itself a function of jet velocity ratio V_j/C_o (C_o is the ambient speed of sound). Only for values of V_j/C_o in excess of about 1.3 does ω approach the theoretical value of 2. Also, the observed effect of heating is to bias the SPL spectrum to lower frequencies.

Most of the above discrepancies can be resolved while retaining the Lighthill notion of ascribing jet noise to convected quadrupoles, if the fact that the turbulent eddies do not communicate directly with ambient atmosphere but are subject to a shrouding effect of the mean jet flow is accounted for. The classical theories (References 41-43) were based on a stationary-wave equation acoustic analogy which implicitly contains mean-flow propagation effects in the right-hand side or forcing function. To extract the mean-flow effects explicitly requires further manipulations to arrive at a governing equation for acoustic pressure which is clearly in the form of an inhomogenous convected-wave equation driven by convected, solenoidal, turbulent velocity fluctuations. Such an equation was first derived by Phillips (Reference 47) and has been developed more fully by Lilley (Reference 48) and Goldstein and Howes (Reference 49). General solutions to these convected-wave equations have been formulated by Pao (Reference 50), Tester and Burstin (Reference 51), and Berman (Reference 52). Earlier works by Ribner (Reference 42), Schubert (Reference 53), Powell (Reference 54), and Csanady (Reference 55) have drawn attention to the importance of mean-flow shrouding effects.

Motivated by the desire to avoid obscuring the physics by complicated numerical approaches, Mani (References 56-60) has developed closed-form

analytical solutions to the Lilley-Goldstein type equation by modelling the jet flow as a simple, round plug-flow jet. From these solutions, several novel aspects of the jet noise problem, not discernable at all from the Lighthill approach, have emerged. These include the following:

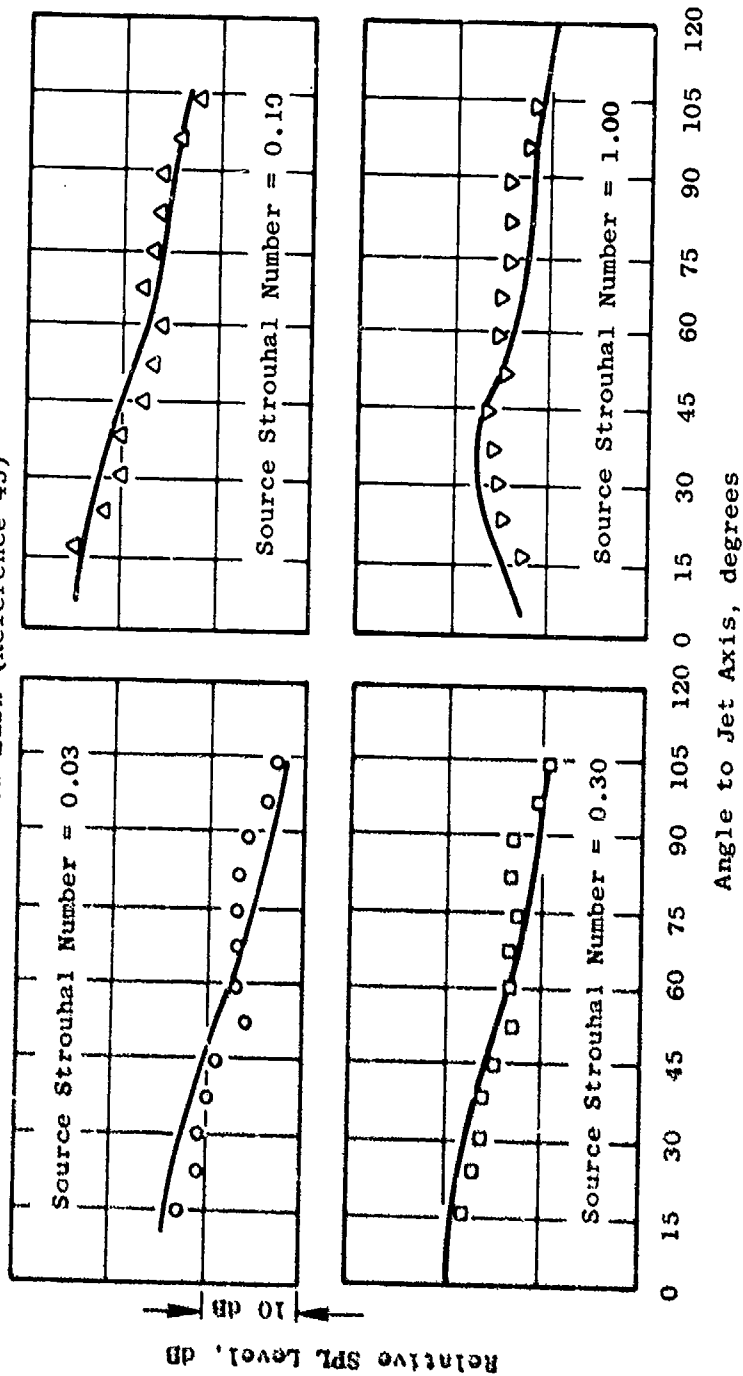
- (1) The Lighthill factor $(1 + M_c \cos \theta_i)^{-5}$ for directivity emerges only as the limit for zero flow Mach number and nonzero eddy-convection Mach number and is not even a good, low-frequency approximation. The directivity is frequency dependent.
- (2) Due to mean-flow shrouding effects, i.e., inhomogeneity of the flow in the transverse direction, transverse quadrupoles exhibit reduced convective amplification compared to longitudinal quadrupoles.
- (3) The combination of refraction and wave-trapping produce the observed fall-off in noise at angles close to the jet axis.
- (4) Mean-flow density gradients act to generate dipole and simple-source terms which scale with jet velocity as V_j^6 and V_j^4 , respectively, for constant value of jet density. These additional noise sources counteract the reduced emission of the quadrupole sources due to heating, becoming less important as jet velocity increases, since the quadrupoles scale with jet velocity as V_j^8 .

These aspects were all confirmed by Mani (References 56-60) through extensive data/theory comparisons with several sources of acoustic data. In particular, the variation in noise with observer angle θ_i was verified as to frequency dependence. Additionally, the necessity for having a variable density exponent ω was found to be adequately explained by the mean-flow shrouding effects and attendant additional noise source contributions due to heating. Figure 4-1 shows the agreement obtained between theory and experiment for a subsonic, round jet in terms of directivity characteristics. Figure 4-2 shows a comparison of the empirically derived density exponent (ω) with the values inferred from the theoretical model as a function of jet velocity ratio V_j/C_0 . These results and many other comparisons reported in References 59 and 60 have conclusively demonstrated that mean-flow shrouding is an important jet noise mechanism. These studies have also verified that Lighthill's original concept of compact turbulent eddies convecting and decaying with the flow is a reasonable physical picture of jet noise, provided that the influence of the mean flow is properly accounted for.

Another important noise mechanism for supersonic choked jets is the interaction of convecting turbulent eddies with the shock-cell formations in the jet. The shock-turbulence interaction process can produce a discrete tone or "screech" component which is related to acoustic feedback with the nozzle. For actual engine nozzles and scale nozzles operating at heated engine cycle conditions, this feedback mechanism is rarely observed and can be "tuned out" if it does appear. The component of major concern is the broadband noise usually termed shock-cell noise. Although shock-cell noise is "broadband," in that it has a wide spectrum, it can exhibit a sharp peak.

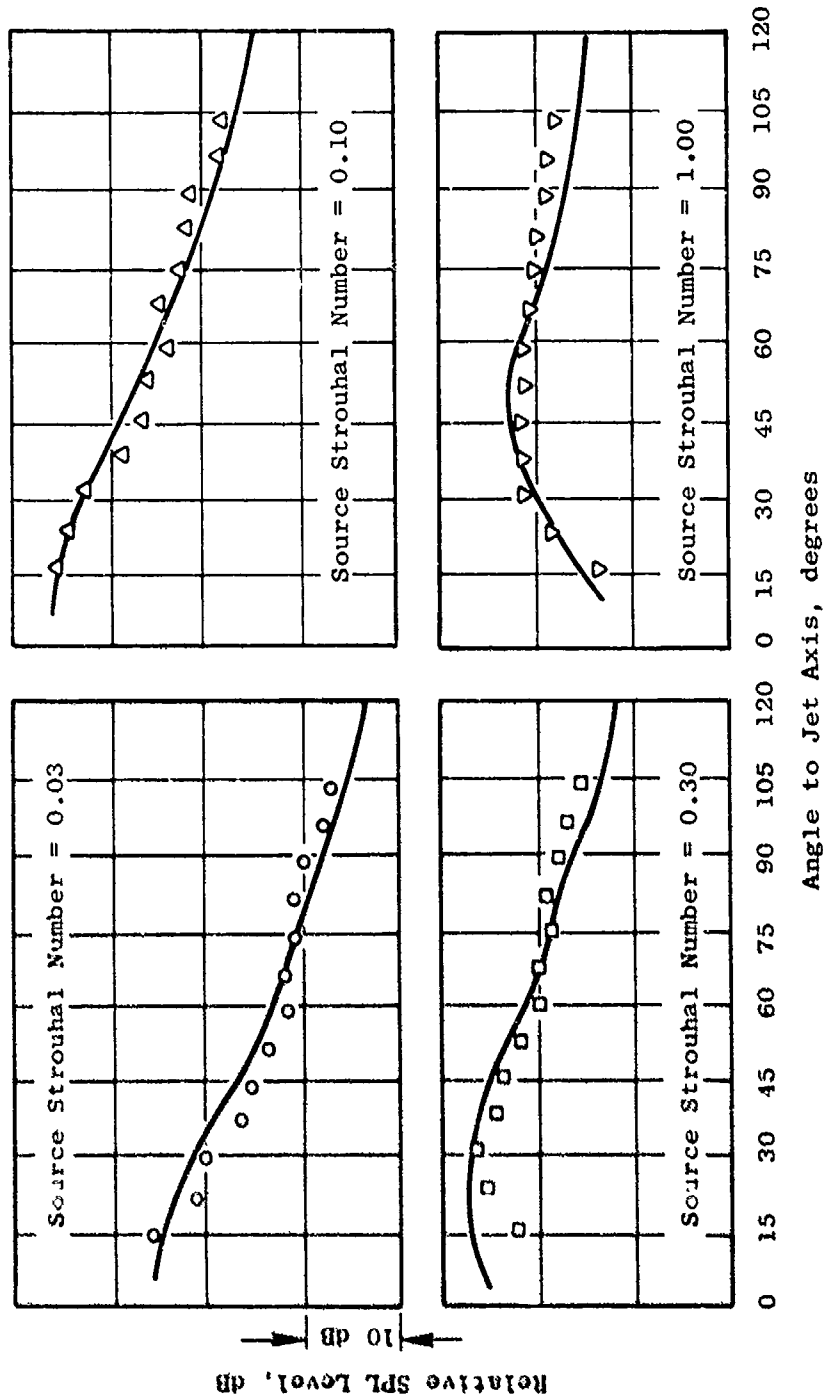
— Theory of Mani (Reference 59)

○ △ □ ▽ Data of Lush (Reference 45)



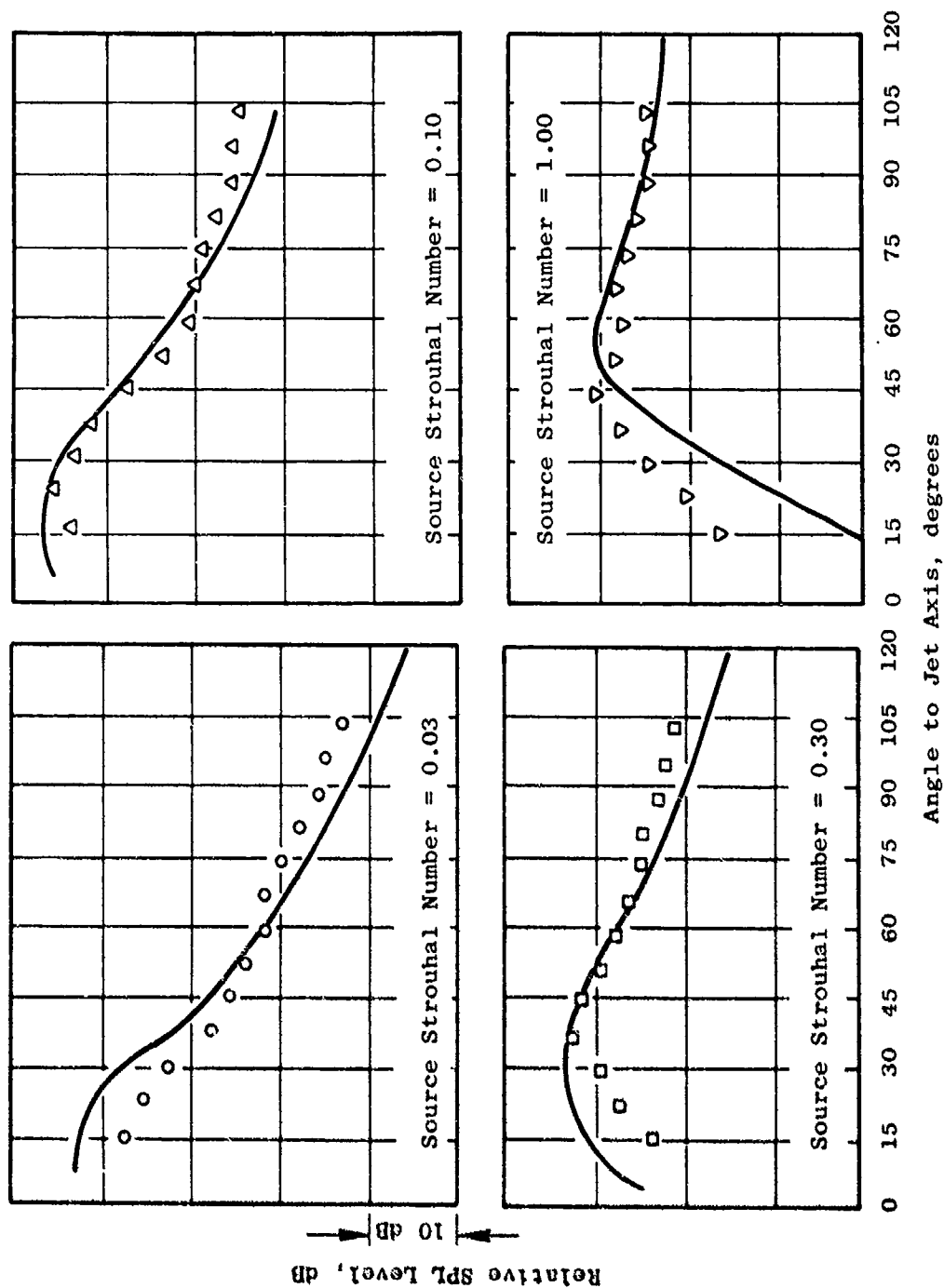
(a) $M_j = 0.366$ ($V_j = 125$ m/sec).

Figure 4-1. Comparison of Experimental and Predicted Jet Noise Directivity Patterns for Cold Jets.



(b) $M_j = 0.57$ ($V_j = 195$ m/sec).

Figure 4-1. Comparison of Experimental and Predicted Jet Noise Directivity Patterns for Cold Jets (Continued).



(c) $M_j = 0.878$ ($V_j = 300$ m/sec).

Figure 4-1. Comparison of Experimental and Predicted Jet Noise Directivity Patterns for Cold Jets (Concluded).

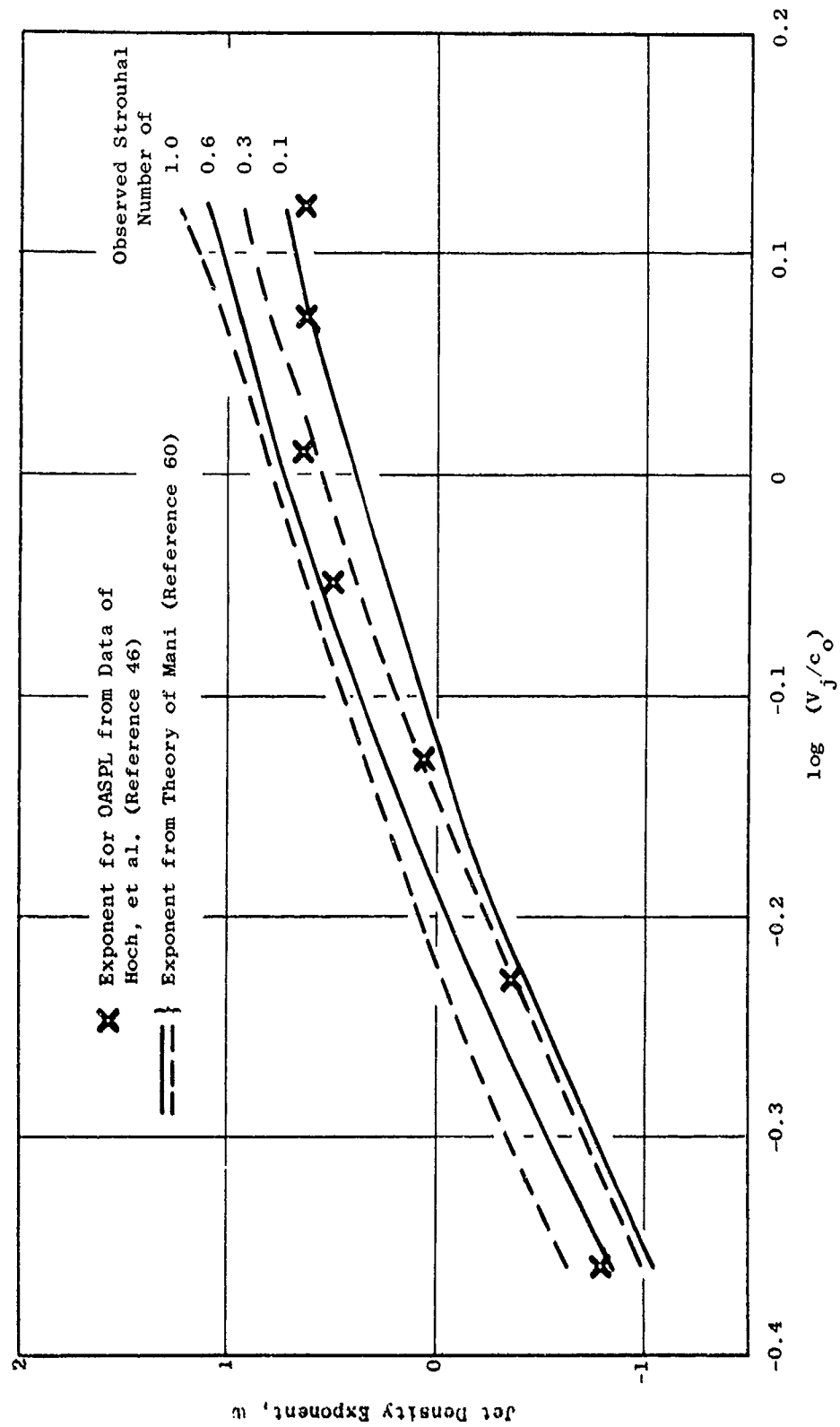


Figure 4-2. Comparison of Experimental and Predicted Density Exponent for Heated Jets at 90° to the Inlet.

A physical picture of the shock-cell noise mechanism has been proposed and modeled semiempirically by Harper-Bouene and Fisher (Reference 61). This picture is basically one of turbulent eddies passing by (or through) the shock fronts, disturbing the shocks, and causing them to emit acoustic waves. The acoustic waves constructively or destructively interfere depending on the shock spacing, eddy convection velocity, and the life time of a given eddy. From the theoretical and experimental studies in Reference 66, several important features of shock-cell noise were revealed, as follows:

- (1) The overall sound pressure level (OASPL) is independent of jet temperature.
- (2) The OASPL is nearly omnidirectional, i.e., independent of observer angle θ_i .
- (3) The OASPL varies as the fourth power of the shock-cell parameter β , where $\beta = \sqrt{M_j^2 - 1}$ and M_j is the jet exit plane Mach number based on isentropic expansion.
- (4) The spectrum peak noise frequency is proportional to jet velocity and inversely proportional to shock spacing.

Shock-cell noise tends to dominate the total jet noise spectrum in the forward quadrant ($\theta_i < 90^\circ$) at middle to high frequencies. This is illustrated qualitatively in Figure 4-3. Experimental evidence, e.g., that of Drevit et al. (Reference 62) indicates that the basic, shock-cell, noise strength is unaltered in flight and is in fact amplified by the doppler effect in the forward quadrant due to aircraft motion, by a factor $(1 - M_p \cos \theta_i)^{-4}$, where M_p is the flight Mach number. Since the turbulent mixing noise may possibly be reduced in flight in the aft quadrant ($\theta_i > 90^\circ$), it becomes increasingly important to be able to account for shock-cell noise when predicting jet noise in flight, as it may weigh heavily on the effective perceived noise level (EPNL). This calls for a thorough understanding of the shock-cell noise mechanism and effects especially for noncircular, suppressed nozzles contemplated for AST aircraft.

There are other mechanisms which may contribute to the total observed jet noise spectrum, such as lip noise and large-scale structure. These mechanisms have been studied in some detail as part of Task 2. Results of studies conducted by Siddon (Reference 63) for General Electric show lip noise to be relatively insignificant except at very low jet velocities ($V_j/C_o < 0.7$). Even at these low velocities, a well-designed, aerodynamically clean nozzle does not exhibit appreciable lip noise. These conclusions are based on extensive measurements of cross-correlations between far-field microphones and nozzle flush-mounted transducers (both internal and external) made over a wide range of nozzle velocities, nozzle types, and with and without external-flow flight simulation.

The question of orderly, large-scale structure as a possible noise mechanism is more difficult to address. Studies conducted by Laufer (Reference 64) for General Electric have not produced any concrete evidence

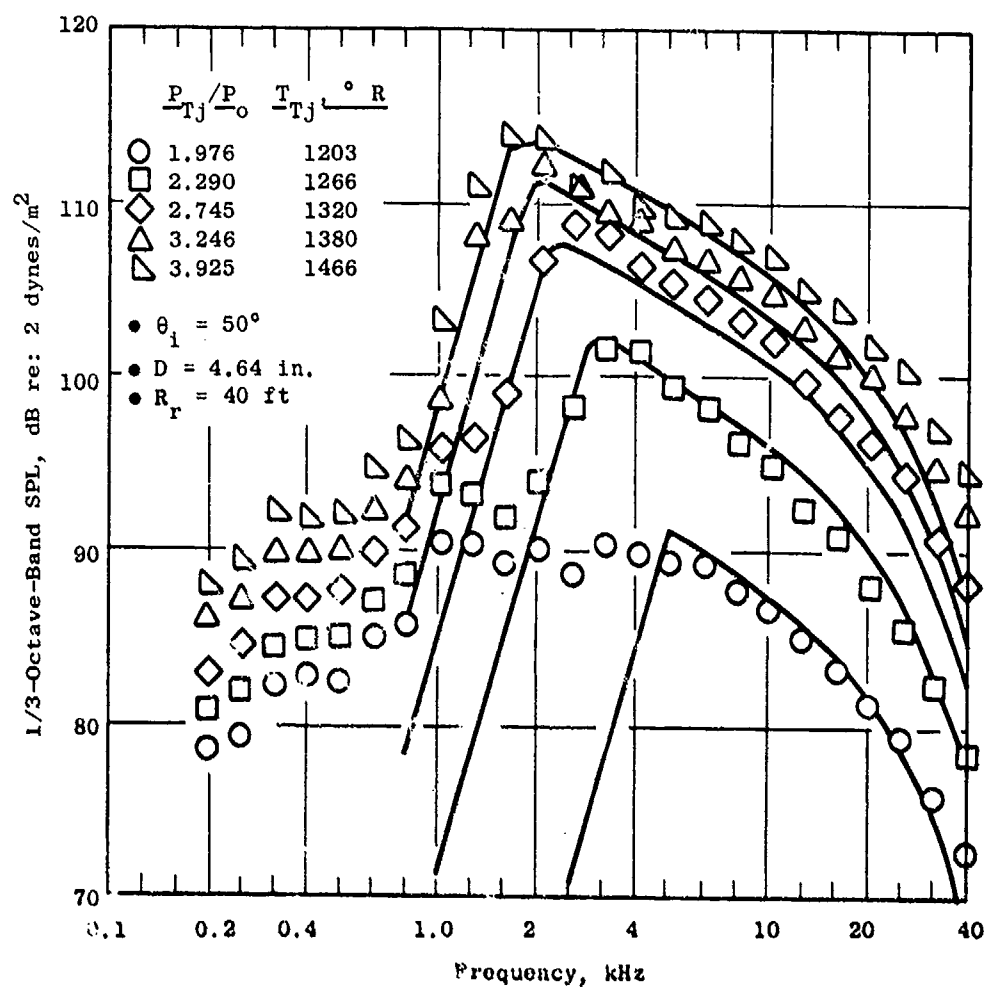
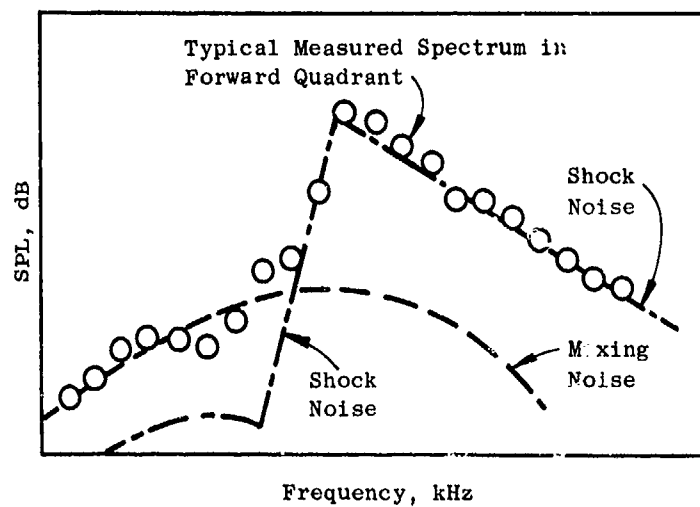


Figure 4-3. Comparison of Predicted Shock-Noise with Measured Conical Nozzle Spectra.

that large-scale structure is a direct cause of noise, although it may exist under certain flow conditions (e.g., low Reynolds number). Extensive data-theory comparisons using a prediction model which ignores large-scale structure as a noise mechanism have shown no consistent discrepancies which could be attributable to large-scale structure.

4.2 ANALYTICAL MODEL DESCRIPTION

The unified aeroacoustic prediction model was developed for predicting the noise of arbitrary jets as part of the Task 2 effort. This model is based on four primary sound generation/emission mechanisms:

- (1) Sound generation by small-scale turbulence produced in the mixing zones of the jet plume, convecting with the flow
- (2) Convective amplification due to turbulent eddy motion relative to the observer
- (3) Mean-flow shrouding (fluid shielding) of the generated sound
- (4) Shock-turbulence interaction (shock-cell broadband noise)

The model utilizes a representation of the jet plume as a "collection" of uncorrelated (nearly compact), turbulent-eddy multipole sources. These sources radiate sound with an intensity spectrum directly related to the local flow properties, i.e., mean velocity, density, turbulence intensity, and length scale. The net radiation of the generated sound from each eddy is a function of the flow environment of that eddy treated as an acoustic wave propagation through a parallel, shear-flow model of the jet plume. The shock-cell noise mechanism is modeled using extensions of the Harper-Bourne/Fisher (Reference 61) method. The turbulent mixing noise and shock-cell noise are assumed to be independent of each other. Flight effects are accounted for in both the mixing noise and the shock-cell noise calculations.

The prediction model contains four major elements: (1) an aerodynamic flow-field prediction procedure, (2) a sound-flow interaction acoustic model, (3) a mixing-noise source strength spectrum model, and (4) a shock-cell noise prediction. These four elements are described briefly in the following paragraphs.

4.2.1 Aerodynamic Flow-Field Model

The aerodynamic flow field is modeled using an extension of Reichardt's (Reference 65) theory. This extension consists of superposition of elemental solutions of Reichardt's theory to construct complex flows from nozzles of arbitrary cross section. This approach was first suggested by Alexander et al., (Reference 66) and applied to suppressor nozzle configurations by Lee, and Grose and Kendall (References 67 and 68). Reichardt's theory is

based on the experimental observation that the axial momentum profiles in the similarity region of a jet (or wake) are bell-shaped or Gaussian in shape. Utilizing this observation and hypothesizing a proportional relationship between transverse momentum and radial gradient of axial momentum, a linear parabolic governing equation for axial momentum of the diffusion type was deduced. This equation has the following form for axisymmetric flow:

$$\frac{\partial F}{\partial x} = \frac{\lambda}{r} \frac{\partial}{\partial r} \left[r \frac{\partial F}{\partial r} \right] \quad (4-2)$$

where F is the local axial momentum flux $F = (\rho u^2 - \rho_a u_a^2)$ and (x, r) are the axial and radial coordinates, respectively, ρ is the local density, and u is the local axial velocity. Subscript "a" denotes the ambient free-stream values. The proportionality factor $\lambda = \lambda(x)$ is an empirically determined mixing constant which varies linearly with axial distance along the jet. Alexander, et al. (Reference 66) have derived similar relations for stagnation enthalpy flux; i.e., $F = \rho u H$ where H is the local stagnation enthalpy relative to the free-stream value.

Because the governing equations for 4-2 ρu^2 and $\rho u H$ are linear, the summation of elemental solutions to 4-2 is also a solution. This unique feature of Reichardt's theory permits the construction of quite complex jet flow fields with relatively simple mathematics. Although more rigorous theories are available for simple jet flows, there is no other technique presently available which offers the capability of modeling jet flows typical of aircraft engine suppressor nozzles such as multiple-tube, lobe, and spoke/chute nozzles, etc.

In addition to the mean-flow quantities u and ρ , the turbulent shear stresses can be deduced from the Reichardt hypothesis that transverse momentum flux ρ_{uv} (v is the transverse component) is proportional to the transverse gradient of axial momentum flux,

$$\rho_{uv} = \lambda (\partial/\partial r) \rho u^2 \quad (4-3)$$

together with an assumption that the turbulent shear stress is approximated by $\tau = (\rho u'v') = \rho_{uv}$. The primes denote fluctuation component quantities. This flow modeling approach has been applied to coannular jet flows by Gliebe and Balsa (Reference 69).

4.2.2 Sound/Flow Interaction (Shielding) Model

Based on the successful work of Mani (References 56-60) in accounting for mean-flow shrouding effects on jet noise, Balsa (References 70 and 71) has applied the plug flow modeling approach to explaining the characteristics of noncircular jets. For example, utilizing low-frequency approximations, a solution for elliptic jets was developed (Reference 70). Also,

using a plug flow annular jet model, some aspects of the flow shrouding or shielding which takes place in multitube suppressor nozzles were explained. Finally, the solutions for mean-flow shrouding effects in coannular nozzles were developed in Reference 68.

It was found, however, that for high jet velocities ($V_j/C_0 > 1$) and high frequencies ($fD/V_j > 1$), the simple plug flow models with centerline convecting sources overestimated the mean-flow shielding effects. The result was too large a dropoff in noise near the jet axis. It was found necessary to account for mean-flow profile shape and radial source location. Closed-form solutions for the pressure fields of various high-frequency convected singularities immersed in a parallel shear flow were developed by Balsa (Reference 72), using Lilley's equation. A parallel shear flow is assumed, having continuous velocity and temperature profiles. Lilley's equation is given by:

$$\frac{1}{C^2} D^3 p - D(\Delta p) - \frac{\partial}{\partial r} (\log C^2) D \frac{\partial p}{\partial r} + 2 \frac{\partial u}{\partial r} \frac{\partial^2 p}{\partial x \partial r} = S \quad (4-4)$$

$$\text{where } D = \frac{\partial}{\partial t} + U \frac{\partial}{\partial x} \text{ and } S = \rho D [\nabla \nabla u' u'] \quad (4-5)$$

In the above, $U = U(r)$, $C = C(r)$, and $\rho = \rho(r)$ are the mean jet velocity, speed of sound, and density, respectively. The parameter Δ is the Laplacian operator, t is time, and u' is essentially the turbulent velocity fluctuation. The coordinate system and geometry are shown in Figure 4-4. Roughly speaking, the aerodynamic calculation, Section 4.2.1 provides the distributions of U , C , ρ , and S . Equation (3-5) is solved in closed form for the acoustic pressure by the WKBJ Technique. In particular, the Green's function is constructed for this equation which, when convoluted with the actual source function S , yields the solution to Lilley's equation. It turns out that the high-frequency assumption invoked in the analysis is not very restrictive and is generally fulfilled for high-velocity jets. A similar approach was used by Pao (Reference 50) for solving Phillip's equation (Reference 47).

In solution for the Green's function, several possibilities arise depending on the zeros of

$$g^2 = \frac{(1 - M \cos \theta)^2}{(C/C_0)^2} - \cos^2 \theta \quad (4-6)$$

where $M = M(r) = U(r)/C_0$. Depending on the observer angle θ , the radial velocity $U(r)$, and the density $\rho(r)$ profiles, the parameter g^2 can have one or more zeros or turning points. The precise form of the Green's function depends on the location of the source with respect to these turning points. Altogether there are six possibilities; for all of these, closed-form solutions have been obtained.

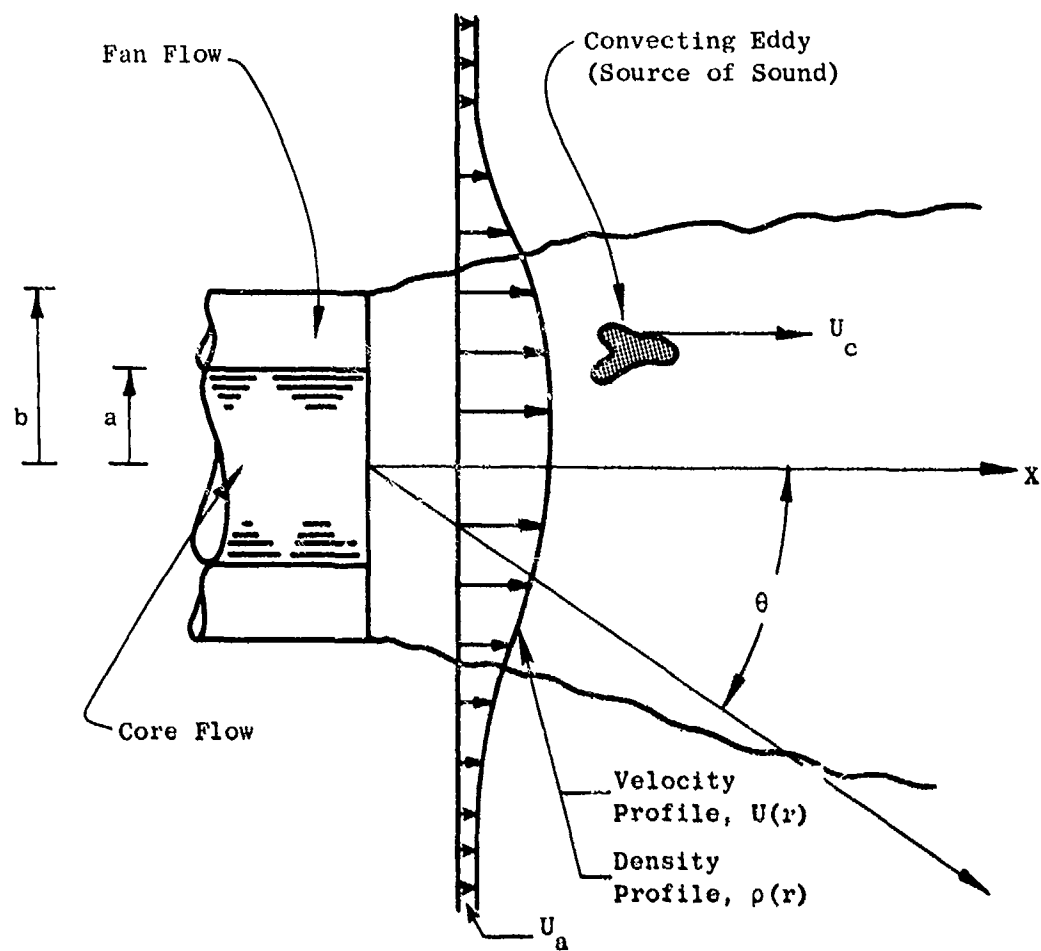


Figure 4-4. Parallel Shear-Flow Model of the Jet.

Some of these correspond to (but are not identical to) Pao's (Reference 50) S0, S1, and S2 modes. When acoustic shielding is encountered (e.g., when $r_0 < r_g$, where r_0 is the location of the source and r_g is the unique turning point), the amplitude of the Green's function is exponentially small in the far field; the argument of this exponential being $(-\omega\delta/C_0)$, where ω is the source frequency and δ is the thickness of an effective fluid layer surrounding the source. Details of the fluid shielding calculation method are given in Reference 7.

4.2.3 Source Spectrum Model

From the aerodynamic flow-field model described in Section 4.2.1, mean velocity, density, and turbulent shear-stress profiles can be computed throughout the jet. This calculation also provides the characteristic strength, frequency, and size of the acoustic convecting quadrupole sources that drive the far-field pressure fluctuations. The characteristic frequency and length scale are determined from the aerodynamic predictions of \bar{u} and u' utilizing the empirically derived similarity relations of Davies et al. (Reference 73),

$$\omega_0 \sim \frac{\partial \bar{u}}{\partial r}, \quad \ell \sim \frac{u'}{\omega_0} \quad (4-7)$$

where \bar{u} is the local mean velocity, u' is the local turbulence intensity, and ω_0 and ℓ are the characteristic frequency and length-scale, respectively.

Ribner (Reference 74) has explained how the fundamental solutions associated with the various quadrupole types can be employed to derive the axially symmetric sound field of a round jet. By employing a model of homogeneous isotropic turbulence in the moving eddy reference frame, and by examining the directional average with respect to the azimuthal coordinate of the sound field, Ribner was able to ascribe "weighting factors" to the various quadrupole contributions. This approach is employed in the present model formulation, utilizing the various quadrupole solutions developed from the high-frequency analysis of Lilley's equation. The amplitude ascribed to each of these quadrupole types is of the form

$$dI(\omega) \sim \rho_0^2 \ell^3 (u')^4 \omega^4 H(v) dv dV / R^2 C_0^5 \quad (4-8)$$

where $dI(\omega)$ is the acoustic intensity per elemental jet volume dV ; ρ_0 is the ambient density; u' is the local turbulence intensity; $H(v)$ is the Fourier transform of the moving-frame, space-time cross correlation of u' ; and v is the ratio of emission frequency ω to characteristic frequency ω_0 . Equation 4-8 is used to calculate the mixing noise amplitude and frequency content for each volume element in the jet. Details of the source spectrum calculation procedure are given in Reference 7.

4.2.4 Shock-Cell Noise Model

A shock-cell noise model was initiated to extend the work of Fisher and Harper-Bourne (FHB) to annular, dual-flow, and multielement nozzles. Considerable scale-model data was taken to extract the shock-cell noise characteristics of several nozzle types both statically and in forward flight. From detailed analysis of the data, it was concluded that the FHB concept of shock cells radiating acoustic waves as they are disturbed by turbulent eddies is a reasonable physical picture of the cause of shock-cell broadband noise. The mathematical model of this phenomenon developed by FHB for static conical nozzles has been generalized to more complex nozzle configurations.

As mentioned above, the primary physical mechanism for the production of broadband noise by the presence of shock cells in the jet plume is the emission of acoustic waves by the shock fronts as they are "disturbed" by the passage of turbulent eddies through and/or by them. The eddies, produced in the mixing layers of the plume, are themselves fluctuating "blobs" of vorticity; thus, the emitted acoustic waves from the shocks have characteristics which are related to the unsteadiness of the turbulent disturbances, i.e., the characteristic frequency and amplitude. The strength of the emitted wave must also be a function of the shock strength. The process is similar to the linear "transfer function" model of Ribner (Reference 75) where a vorticity wave of given amplitude and frequency is input to a shock, and the output is a transmitted vorticity wave, an internally generated entropy wave, and a pressure (acoustic) wave.

Each shock in the jet plume emits acoustic waves in a random or broadband fashion, related to the randomness of the disturbing turbulence. The far-field, time-average correlation of this emission, after summing the contributions from all the shocks, produces a spectrum made up of two basic components. First, the sum of the mean-square pressure signals from each shock produces a "group spectrum" which is rather broadband in character, similar to a jet mixing noise spectrum. The second component, referred to as the "interference spectrum", results from the selective reinforcement and cancellation which occurs between emitted waves from neighboring shocks. The superposition of these two components results in the rather "peaky" spectrum shape observed for shock-cell noise. This is illustrated in Figure 4-5.

Through examination of data from several nozzle types and an evaluation of the FHB formulation, a plausible extension of the present FHB model to noncircular nozzles was developed. It was found that the group spectrum component (Figure 4-5) was dependent on flow area for level scaling and on equivalent diameter for frequency scaling. The interference spectrum, however, scales with hydraulic diameter or, more correctly, shock-cell spacing. When the nozzle hydraulic diameter is significantly less than the equivalent-area diameter, the interference spectrum is displaced to higher frequencies, resulting in a total spectrum shape which is quite different from that of a conical nozzle, as shown in Figure 4-6.

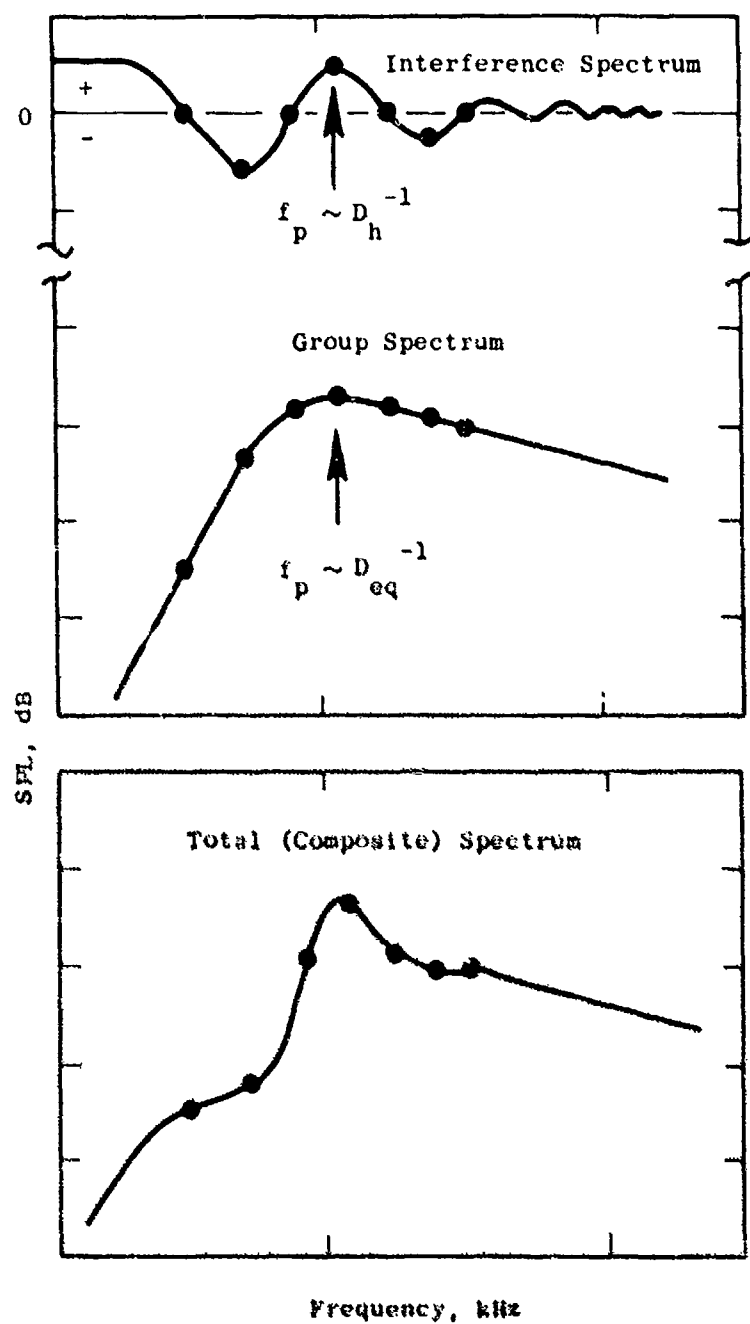


Figure 4-5. Primary Components of a Conical-
Nozzle, Shock-Cell Noise Spectrum,
 $D_h = D_{eq}$.

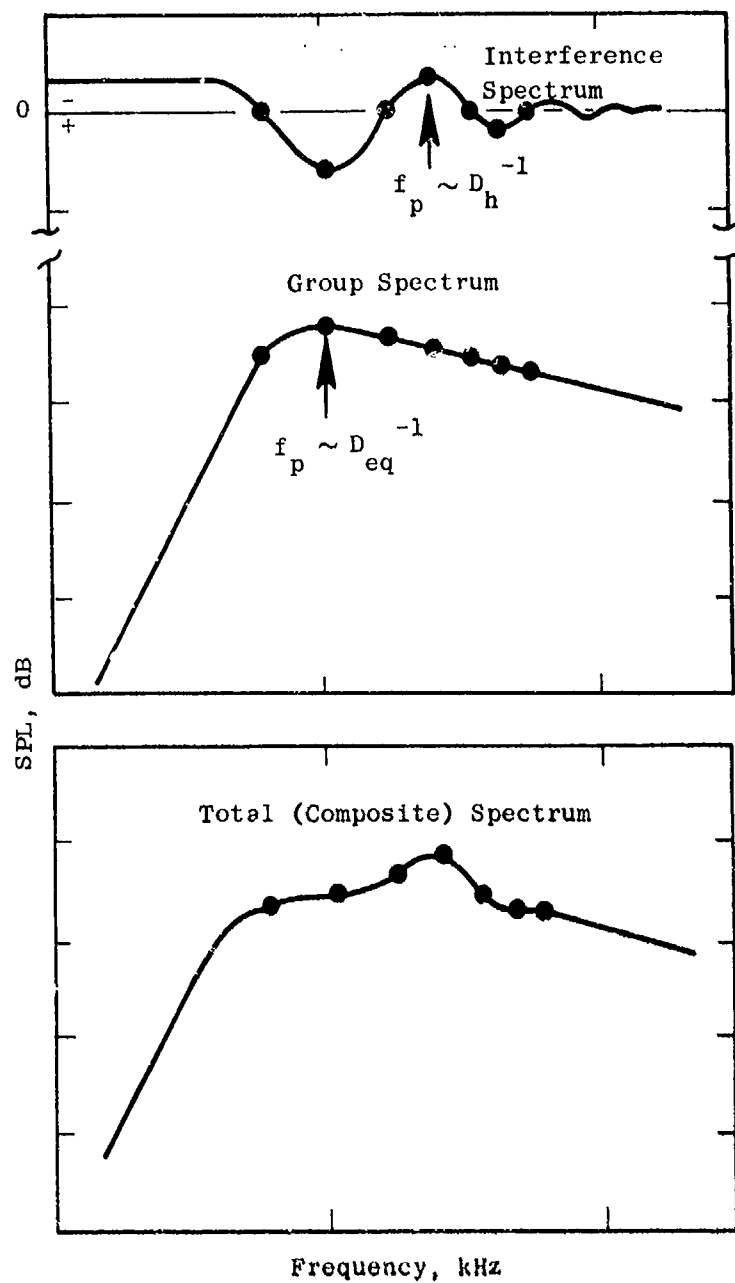


Figure 4-6. Primary Components of a Noncircular-Nozzle, Shock-Cell Noise Spectrum, $D_h < D_{eq}$.

To demonstrate the validity of the above hypothesized model extension, data from a conical nozzle and a rectangular 6:1 aspect-ratio nozzle were examined. Predictions of the shock-cell noise spectra were made for these nozzles using the modified FHB theory described qualitatively above. Results of the calculations and comparisons with measured data, for a supercritical pressure ratio condition are shown in Figures 4-7 and 4-8. Figure 4-7 shows the measured SPL spectrum at $\theta_i = 60^\circ$ forward arc location, for a 1.5-inch diameter conical nozzle operating at a pressure ratio of 2.65. Data for three temperatures are shown, giving essentially the same shock-cell noise. This verifies an important feature of the FHB theory that shock-cell noise is a function of nozzle pressure ratio and independent of jet temperature. Also shown is the FHB theory predicted spectrum, which is substantially in agreement with the measurements.

The corresponding results for a 6:1 aspect-ratio, rectangular nozzle are shown in Figure 4-8. Shown in this figure are SPL measurements; results at two azimuthal angles (ψ) are included. These results show that, even though the nozzle is nonaxisymmetric, the sound field produced by the shock cells is axisymmetric, or nearly so. Also shown is a prediction of the spectrum based on the modifications to the FHB theory previously discussed. Again substantial agreement with the measurements is observed, indicating that the proposed extensions to the shock-cell noise model for round jets to predict nonaxisymmetric jet behavior is a promising approach.

4.2.5 Aeroacoustic Model Integration

The basic analytical model elements described in Sections 4.2.1 through 4.2.4 have been integrated into a unified, aeroacoustic jet-noise-prediction computational procedure. The jet plume is divided into elemental jet volumes, each having its own source strength, spectrum and flow shrouding, as illustrated in Figure 4-9. The mean-square sound pressure emitted from such volume element is given by

$$\overline{p}^2(\omega) = \frac{\Delta f}{C_o^4 R^2} \left[\int_V \rho^2 (u')^2 dV \right] \left[\frac{\omega^4}{\omega_o^4} H(v) \right] \left[\frac{\cos^2 \theta + g_o^2}{(C/C_o) C} \right]^2 \exp[-2\omega\delta/C_o] \quad (4-9)$$

where Δf is the one-third-octave frequency bandwidth and

$$C = \sqrt{(1 - M_c \cos \theta)^2 + (au'/C_o)^2}$$

is the modified Doppler factor (Reference 43). The exponential "shielding" factor argument is given by

$$\delta = \int_{r_o}^{r_a} |g^2|^{1/2} dr \quad (4-10)$$

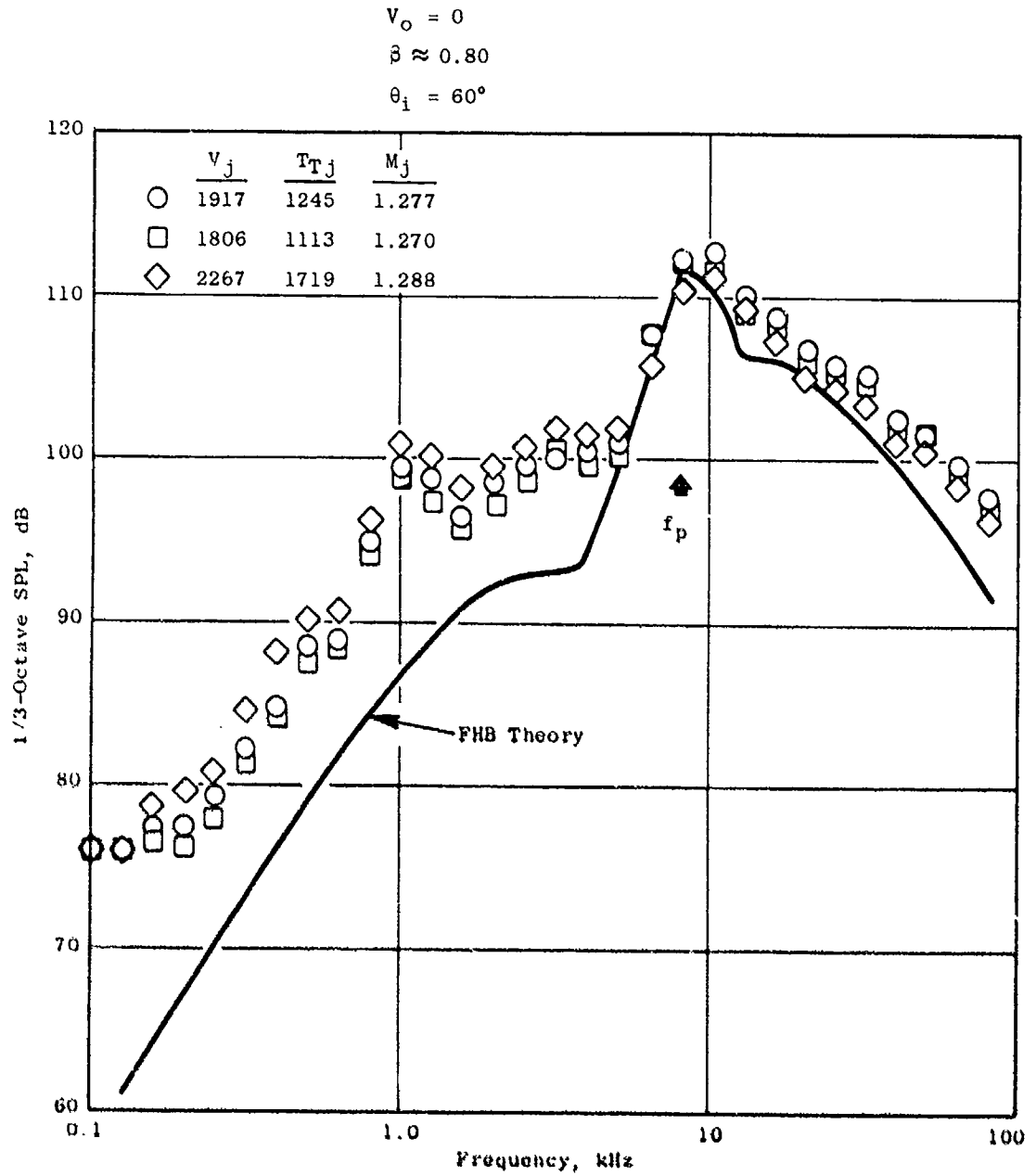


Figure 4-7. Shock-Associated Noise Spectrum, 1.5-in. Diameter Conical Nozzle.

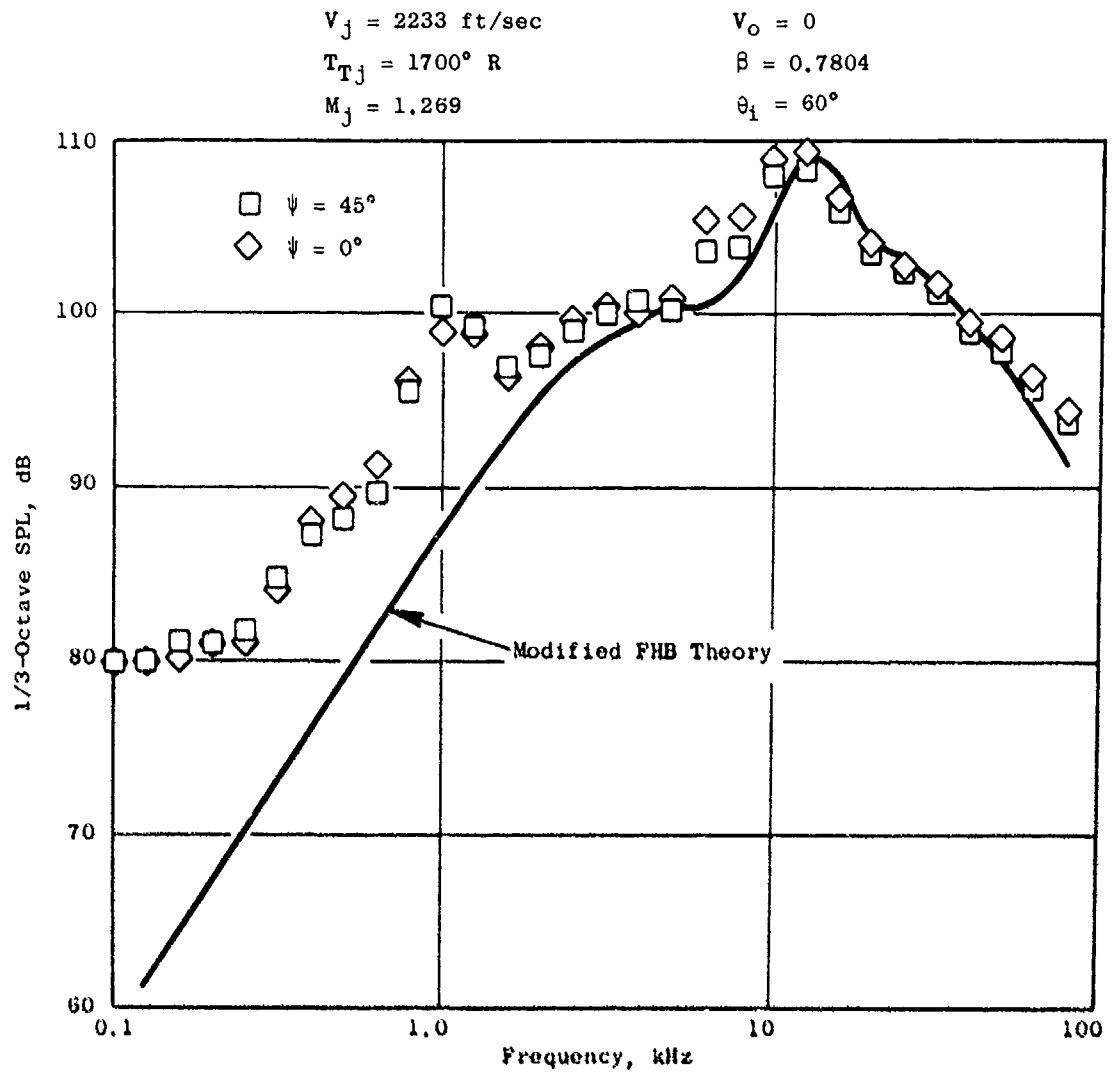
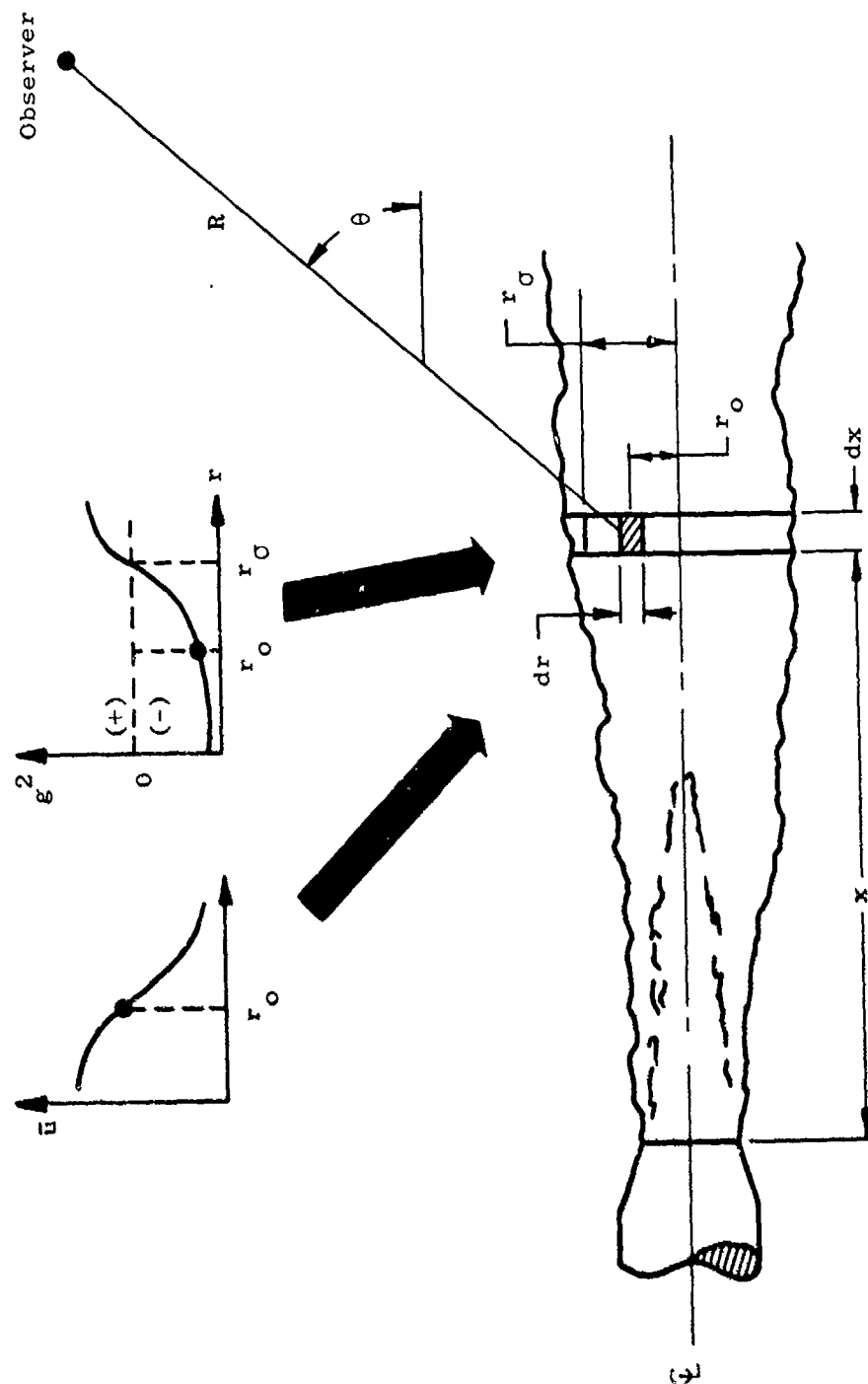


Figure 4-8. Shock-Associated Noise Spectrum, 6:1 Aspect Ratio Rectangular Jet.



This simple, closed-form solution, combined with the simple aerodynamic calculation method described in Section 4.2.1, permits a rapid, economical computation of the entire jet plume aerodynamic and acoustic characteristics, including far-field spectra at all observer angles. The contributions from each elemental jet volume are simply added on a mean-square pressure basis in each frequency band. The shock-cell noise contribution is then computed separately and added to the mixing noise contribution to yield the total far-field spectrum.

4.3 THEORY/DATA COMPARISONS AND DISCUSSIONS OF SUPPRESSION MECHANISMS

An extensive data/theory comparison study was carried out to verify the jet noise suppression mechanisms identified in Task 2. The Task 2 aero-acoustic jet noise prediction model summarized in Section 4.2 was used to predict the acoustic characteristics of seven nozzle configurations at several operating points for each configuration. These predictions were compared to the experimental data obtained from the scale-model tests conducted in Task 3 and from the Aerotrains tests conducted in Task 4 of the present program. Comparisons were made of perceived noise level (PNL) versus jet exhaust velocity, PNL directivity, and one-third octave sound-pressure-level spectra at selected observer angles for each configuration. An assessment of the relative importance of each of the noise-generation/suppression mechanisms was made for two of the configurations.

The purpose of this study was to verify the theoretical jet noise model established in Task 2 and assess the ability of this model to adequately predict the noise suppression trends of several classes of suppressor nozzles as a function of geometric variables, exhaust velocity, and temperature. Utilization of the theoretical model to explain the observed suppression characteristics in terms of the postulated mechanisms summarized in Section 4.1 was a secondary objective of this study.

The following subsections describe the important results of this study. A brief description of the nozzle configurations analyzed is first given, along with a description of the data/theory comparison format. A summary of the main results of the data/theory comparisons, in terms of peak PNL versus jet velocity, is then given for all configurations. Detailed data/theory comparisons for each configuration are presented in separate subsections beginning with a conical nozzle and progressing in order of complexity to the dual-flow, suppressed-fan nozzle. A discussion of noise generation and suppression mechanisms follows, consisting of an assessment of the relative roles of (1) turbulent mixing alteration, (2) fluid shielding, (3) eddy convection, and (4) shock-cell noise in producing the observed suppression characteristics. A separate discussion of flight effects on jet noise is included, based on data/theory comparisons of three nozzle configurations tested on the Bertin Aerotrains. The major conclusions drawn from the results of this study are then listed, followed by appropriate recommendations.

4.3.1 Summary Comparisons of PNL Characteristics for Baseline and Various Suppressor Nozzles

Theory/data comparisons were made for even nozzle configurations. These configurations, summarized in Table 4-1, are as follows:

1. Conical nozzle
2. Annular plug nozzle, $R_p/R_s = 0.85$
3. Coplanar, coannular nozzle; $A_0A_i = 2.0$
4. 36-chute, turbojet suppressor; $AR = 2.0$
5. 8-lobe daisy suppressor nozzle; $AR = 2.1$
6. 104-tube suppressor nozzle; $AR = 2.8$
7. 36-chute, suppressed-fan, dual-flow, plug nozzle

Comparisons 1, 2, and 3 are representative of baseline (unsuppressed) single and dual-flow exhaust systems. Configurations 4, 5, and 6 are representative of the three primary classes of suppressors for turbojet application (i.e., chute, lobe, and tube). Configuration 7 represents a typical, suppressed, dual-flow exhaust system. Details of the configuration geometry for these nozzles are given in Appendix A, Volume II of this report. Table 4-1 lists the appropriate figure numbers for reference.

The approach taken was to compare predicted and measured noise characteristics on the basis of full-scale engine subjective noise levels (PNL). Most of the configurations were compared using a total exhaust flow area of $A_T = 338 \text{ in.}^2$ (J79 engine size), at a sideline distance of 2400 ft. An exception was made for Configurations 5 and 6, which were analyzed using $A_T \approx 108 \text{ in.}^2$ (J85 engine size) on a 400-ft sideline. Predictions for Configurations 5 and 6 were then compared with Bertin Aerotrain measurements performed in Task 4 both for static and in-flight conditions.

Extensive data/theory comparisons of the jet noise aeroacoustic model predictions with scale-model data have been carried out in Task 2 and reported in the Task 2 final report of this program. The emphasis in those comparisons was on the ability of the model to predict detailed spectrum shapes for a wide variety of nozzle types and operating conditions. Detailed comparisons were also made of the flow-field characteristics to verify the adequacy of the aerodynamic portion of the model. Based on these comparisons, the strengths and weaknesses of the prediction model were identified, and suggestions for further refinements in the prediction procedure were made.

The present study attempts to evaluate the prediction model in the current state of development, accepting the strengths and weaknesses, as a design and analysis tool for full-scale engine exhaust system subjective noise assessments. Emphasis is therefore placed in this study on the

Table 4-1. Summary of Configurations for Verification of Suppression Principles.

Configuration	Facility	Element Type	Area Ratio	Element No.	Radius Ratio	Reference (1) Figure
1. Conical Nozzle	Cell 41	Baseline	---	---	---	A-1
2. Plug Nozzle	JENOTS	Baseline	---	---	0.85	A-34
3. Coannular-Coplanar	JENOTS	Baseline	2.0	---	---	A-6
4. Chute-Plug Nozzle	Cell 41	Chute	2.0	36	0.716	A-10
5. Lobe Nozzle	Aerotrain	Daisy Lobe	2.1	8	---	A-40
6. Multitube Nozzle	Aerotrain	Tube	2.8	104	---	A-38
7. Suppressed Annular Plug with Auxiliary Flow	Cell 41	Chute	~2.0	36	0.716	A-18

(1) Note: See Volume II, Appendix A.

prediction of sideline PNL directivity and the parametric dependence of peak PNL on jet velocity and geometry. In addition, the adequacy of the aeroacoustic model in predicting PNL suppression relative to an equivalent-thrust, conical-nozzle baseline level is also emphasized.

The data/theory comparisons presented in the Task 2 final report were generated during various stages of the aeroacoustic model development; therefore, the results for any one configuration may have been produced by a slightly different version of the prediction model than the results for the others. However, in the present study all predictions were made with the final version of the model documented in the supplement to the Task 2 final report and are therefore consistent with one another. The results of the present study, however, may not necessarily agree precisely with those presented in the Task 2 final report.

Shock-cell noise is included in the predictions for Configurations 1, 2, and 5. The more complex nozzle configurations (3, 4, 6, and 7) do not have shock-cell noise included in the predictions. The shock-cell noise portion of the model is not sufficiently developed to permit a prediction for these complex nozzles.

Full-scale, engine-size, noise predictions were made using the Task 2 jet noise aeroacoustic, prediction model for each of the seven configurations listed in Table 4-1, at several operating conditions. Results are first presented in terms of perceived noise level. PNL, normalized according to the following relationship:

$$PNL_N = PNL - 10 \log [F_s (T_o/T_{sm})^{\omega-1}]$$

where PNL = perceived noise level, PNdB

F_s = static ideal gross thrust

T_o = ambient temperature, ° R

T_{sm} = static temperature corresponding to mass-averaged velocity and total temperature, ° R

ω = jet density exponent (per SAE ARP876) based on mass-averaged velocity (V_{ma})

$$V_{ma} = \frac{w_i V_i + w_o V_o}{w_i + w_o}, \text{ mass-averaged jet velocity}$$

$$T_{T_{ma}} = \frac{w_i T_{T_i} + w_o T_{T_o}}{w_i + w_o}, \text{ mass averaged total temperature}$$

and where "w" and T_T are the mass flow and total temperature, respectively. Subscripts "i" and "o" denote inner and outer stream exit plane values,

respectively. Predictions of PNL_N versus V_{ma} were made and compared with data at observer angles of 50° , 90° , and peak-noise angle.

Figure 4-10 shows the comparison of experimental and predicted PNL_N versus V_{ma} trends for a conical nozzle, Configuration 1. The predicted levels are seen to be within the data band throughout the jet velocity range. Similar comparisons are shown in Figure 4-11 for Configuration 2, the annular plug nozzle. At $\theta_i = 50^\circ$ the agreement is good. At $\theta_i = 90^\circ$, the level is overpredicted by about 2 PNdB at low velocities ($V_{ma} < 2000$ ft/sec). The peak noise levels (Figure 4-11) are consistently overpredicted throughout the velocity range by as much as 5 PNdB. This overprediction, as will be shown in Section 4.3.4, is a result of the predicted high-frequency noise at shallow angles being too high.

The results for Configuration 3, the coplanar, coannular nozzle, are shown in Figure 4-12. The predicted levels agree with data at $\theta_i = 90^\circ$, but fall slightly below the data at $\theta_i = 50^\circ$ and at peak-noise angle. This underprediction is, on the average, about 2 PNdB; it is more pronounced at higher mass-averaged velocities.

A comparison of predicted PNL_N versus V_{ma} characteristics for Configuration 4, a 36-element, single-flow-chute suppressor nozzle, is shown in Figure 4-13. The predicted characteristics are within the data band at all three angles shown. The characteristics are seen to be much flatter than those for the conical nozzle shown in Figure 4-10. The fact that both conical-nozzle and chute-nozzle PNL_N characteristics are predicted accurately implies that PNL suppression is also predicted reasonably well.

The 8-lobe nozzle (Configuration 5) and the 104-tube suppressor nozzle (Configuration 6) require considerable computer time for predicting the jet plume; this is due to the complex, three-dimensional nature of the plume flow field. Therefore, only a limited number of cases were computed for these configurations, and the trends of PNL_N versus V_{ma} could not be evaluated. The resulting measured and predicted PNL values for the cases evaluated are listed in Table 4-2. This table lists actual PNL values rather than normalized levels (PNL_N). The measured values are those obtained from the Bertin Aerotrain tests conducted in Task 4. The Aerotrain conical-nozzle results and corresponding predictions are also listed for reference. The average standard deviation error in PNL directivity (predicted minus measured) is 1.7, 3.3, and 2.8 PNdB for the conical, 8-lobe, and 104-tube nozzles respectively, for all the cases listed in Table 4-2, over the range of θ_i from 20° to 160° .

The results for Configuration 7, the 36-chute, suppressed fan, dual-flow nozzle, are shown in Figure 4-14. Again, it is observed that the PNL_N versus V_{ma} trends are well predicted by the aeroacoustic model. Only at low velocities ($V_{ma} < 1700$ ft/sec), at $\theta_i = 50^\circ$, are the predictions outside of the data band. It is encouraging (and important) that the characteristics of a multielement, dual-stream system can be accurately predicted since it is this type of system that is currently envisioned for future SCAR (Supersonic Cruise Airplane Research) engine designs.

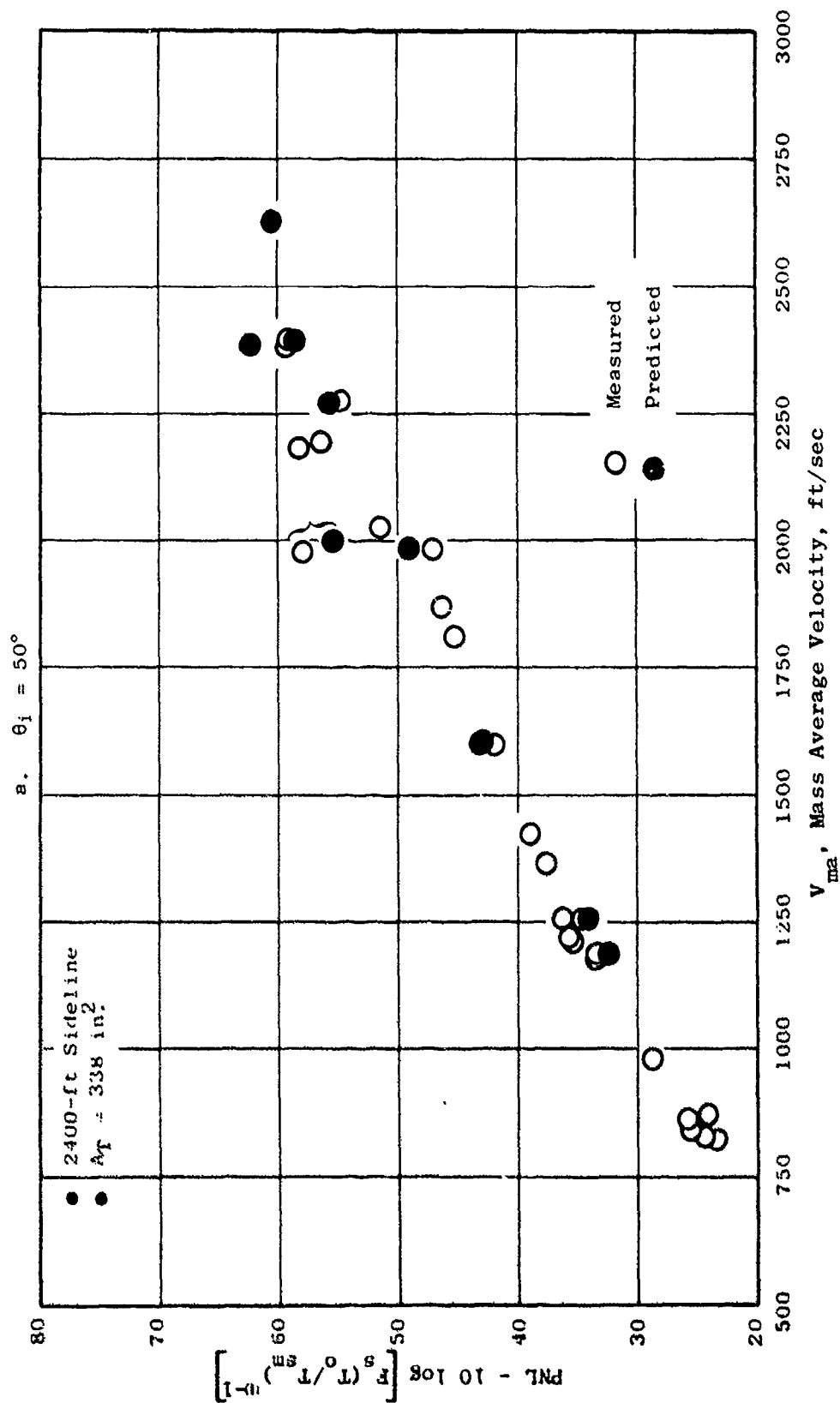


Figure 4-10. Comparison of Predicted and Measured Sideline Normalized PNL for a Conical Nozzle.

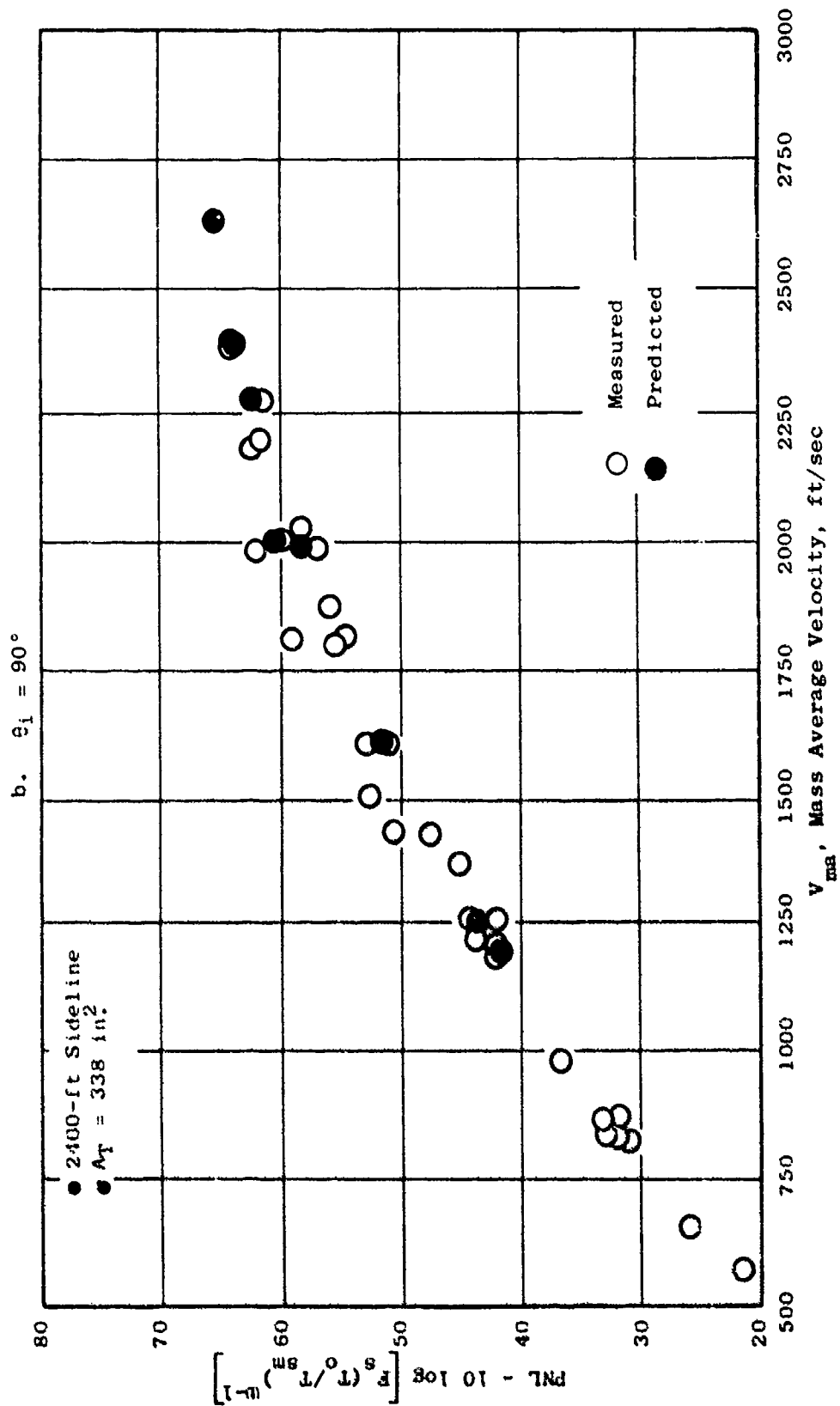


Figure 4-10. Comparison of Predicted and Measured Sideline Normalized PNL for a Conical Nozzle (Continued).

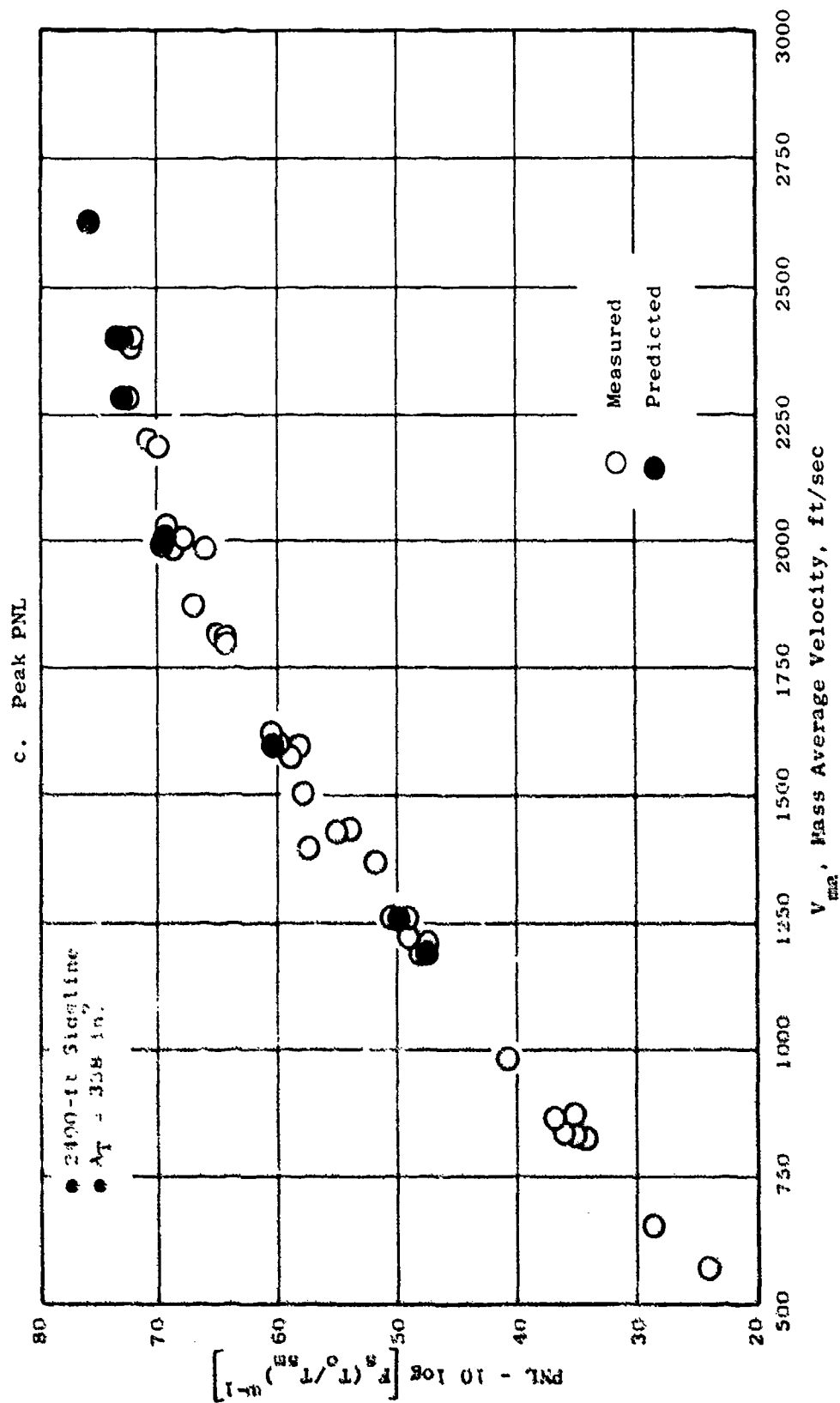


Figure 4-10. Comparison of Predicted and Measured Sideline Normalized PNL for a Conical Nozzle (Concluded).

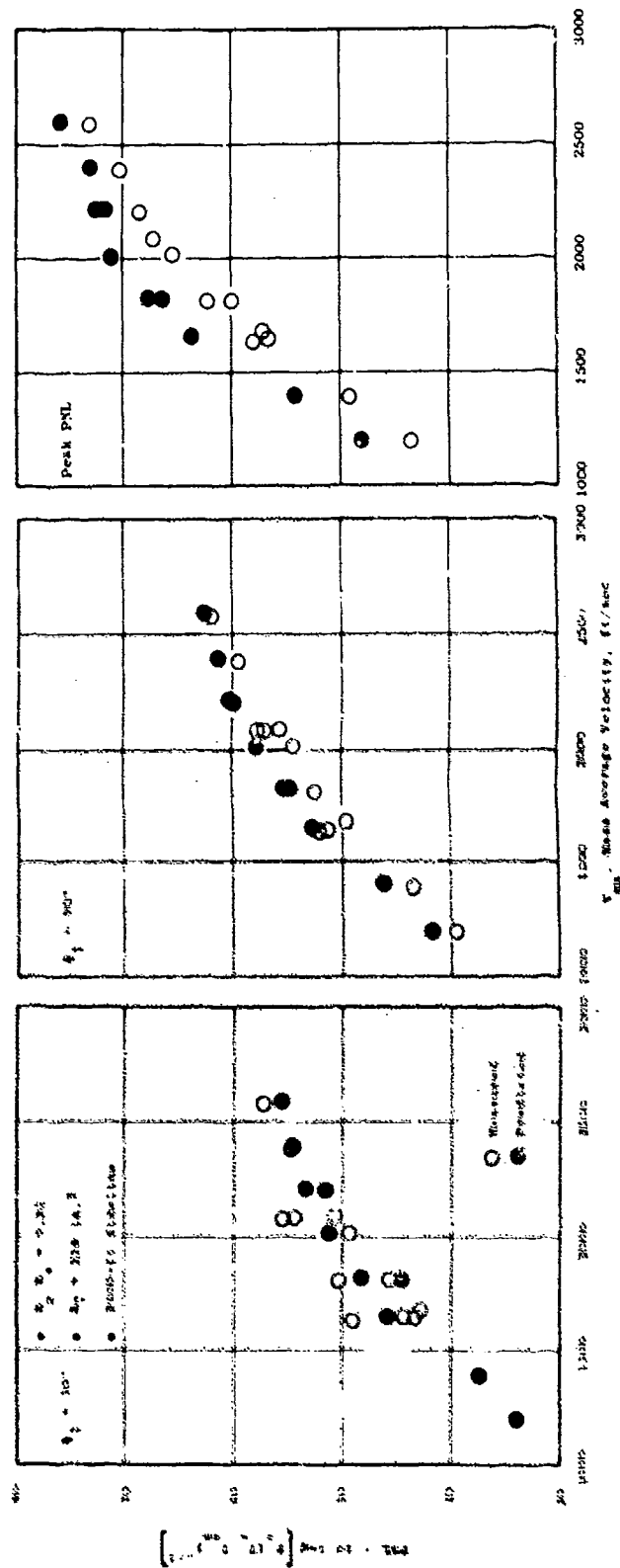


Figure 4-11. Comparison of Predicted and Measured Normalized PNL for an Annular Plug Nozzle.

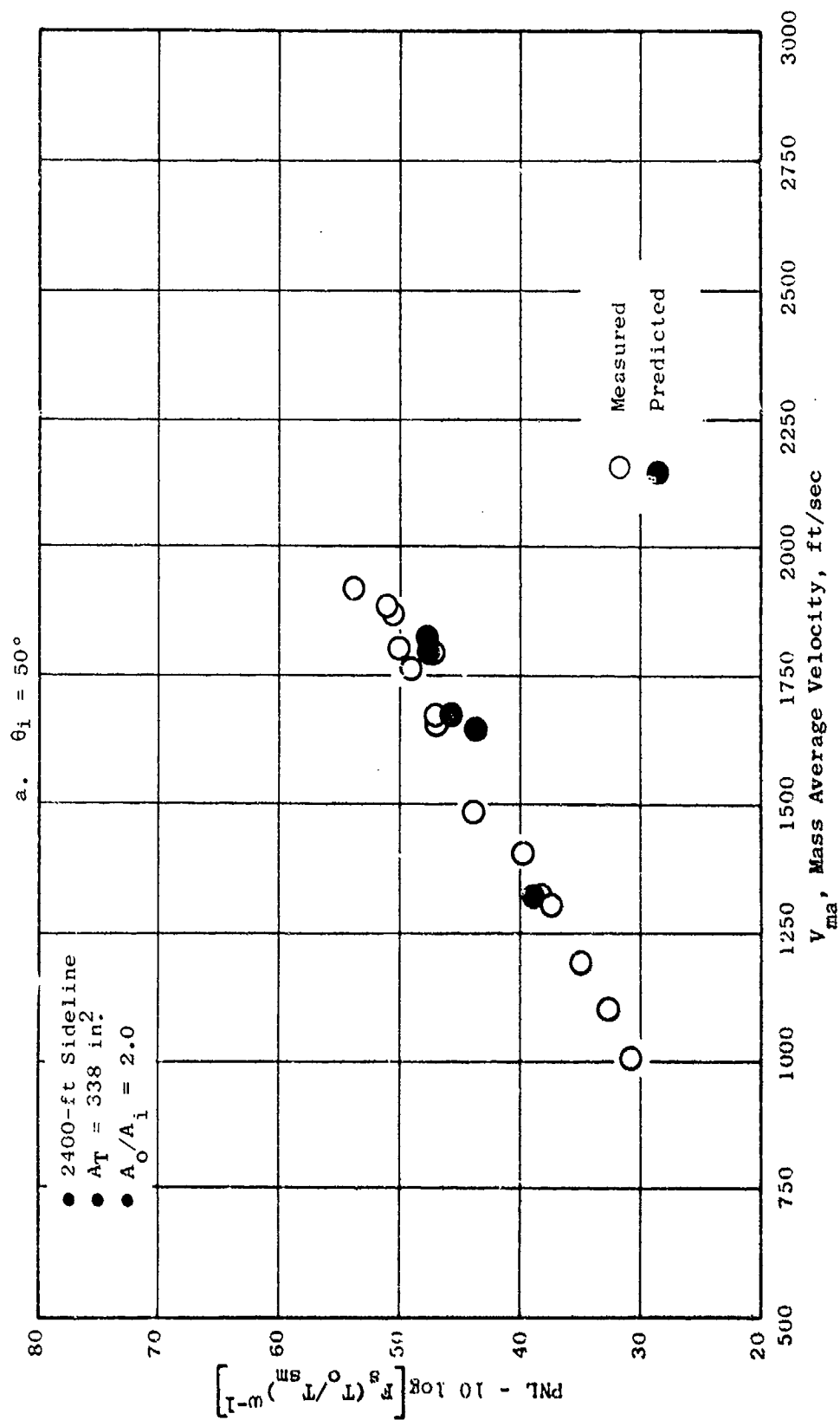


Figure 4-12. Comparison of Predicted and Measured Normalized PNL for a Coplanar, Coannular Nozzle.

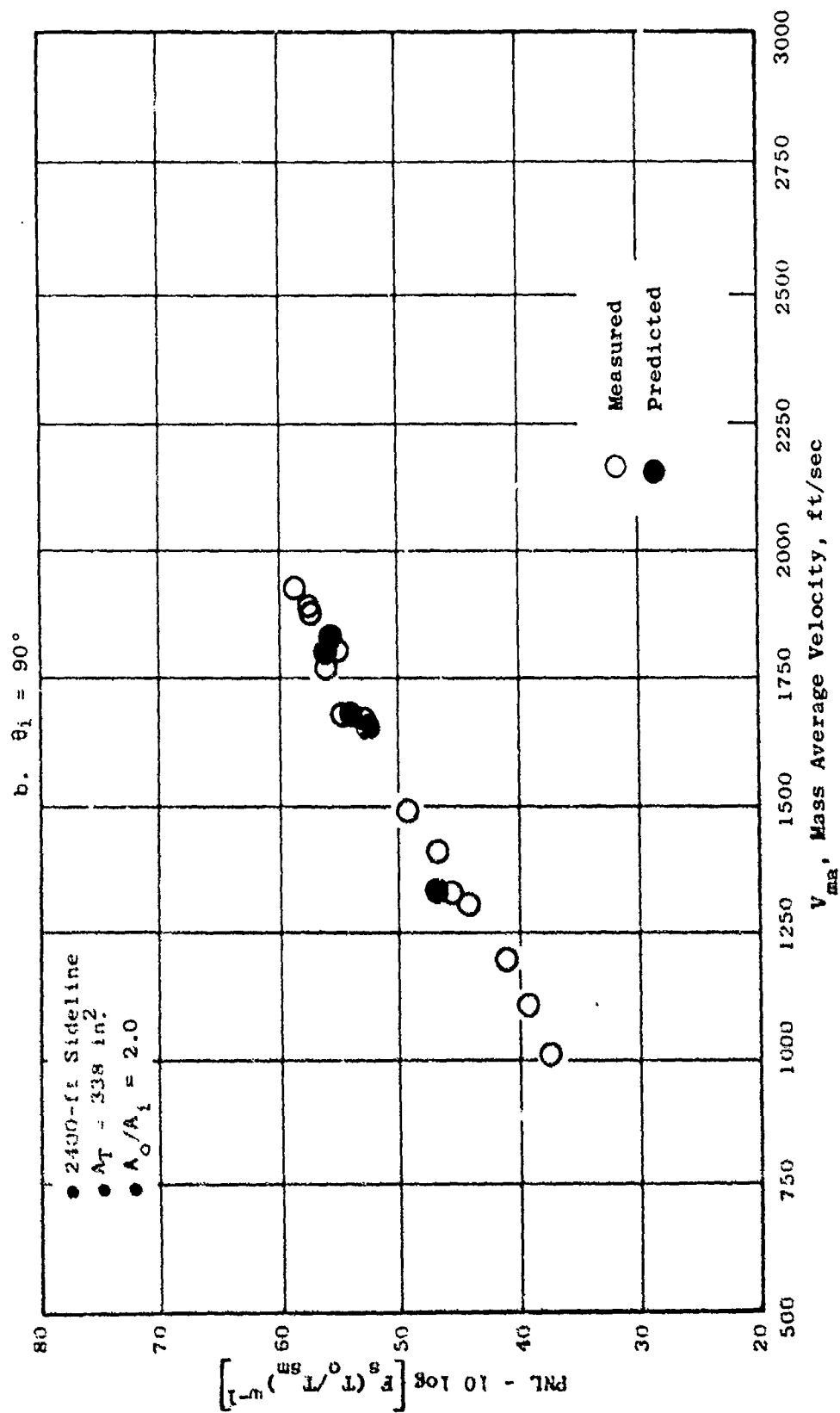


Figure 4-12. Comparison of Predicted and Measured Normalized PNL for a Coplanar, Coannular Nozzle (Continued).

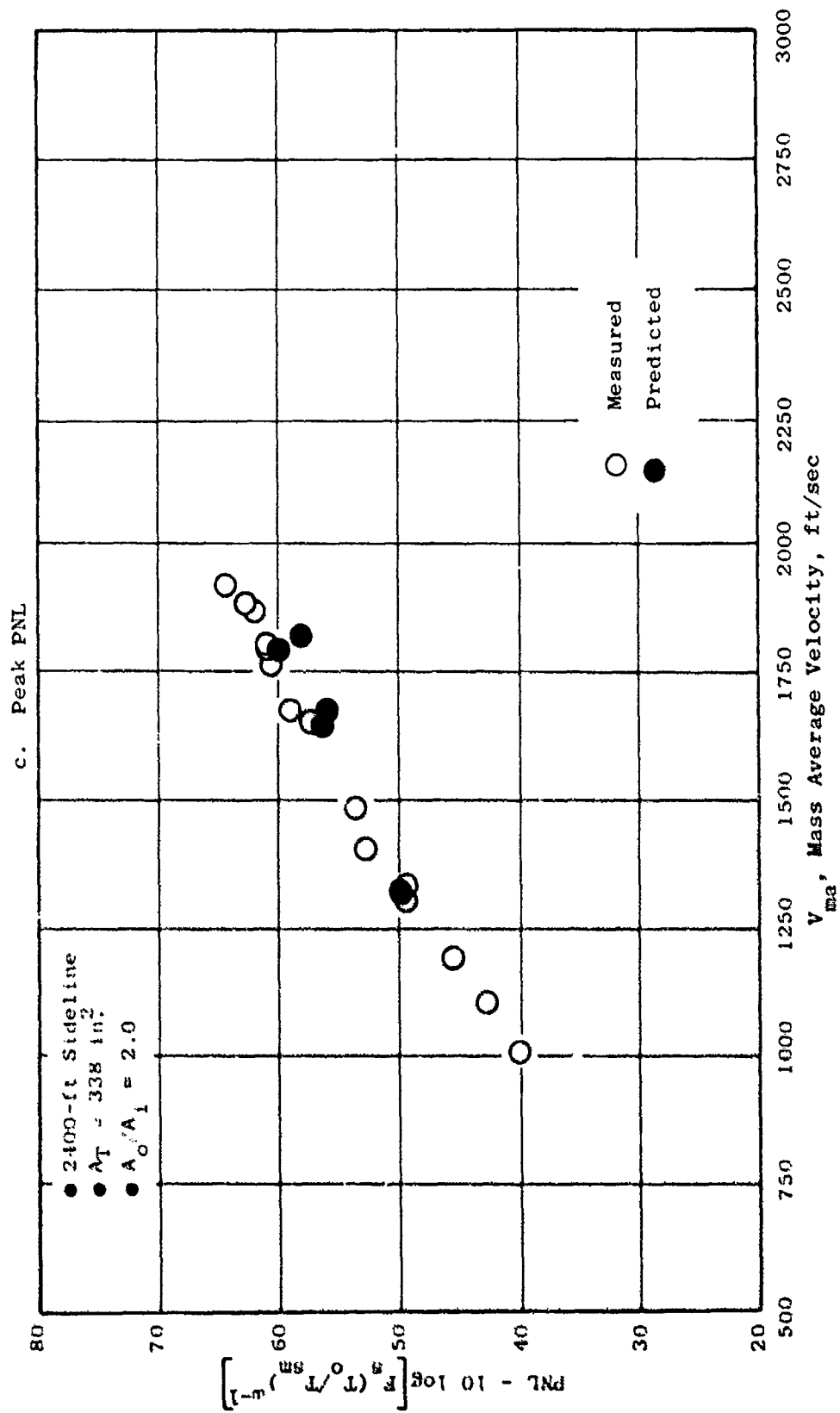


Figure 4-12. Comparison of Predicted and Measured Normalized PNL for a Coplanar, Coannular Nozzle (Concluded).

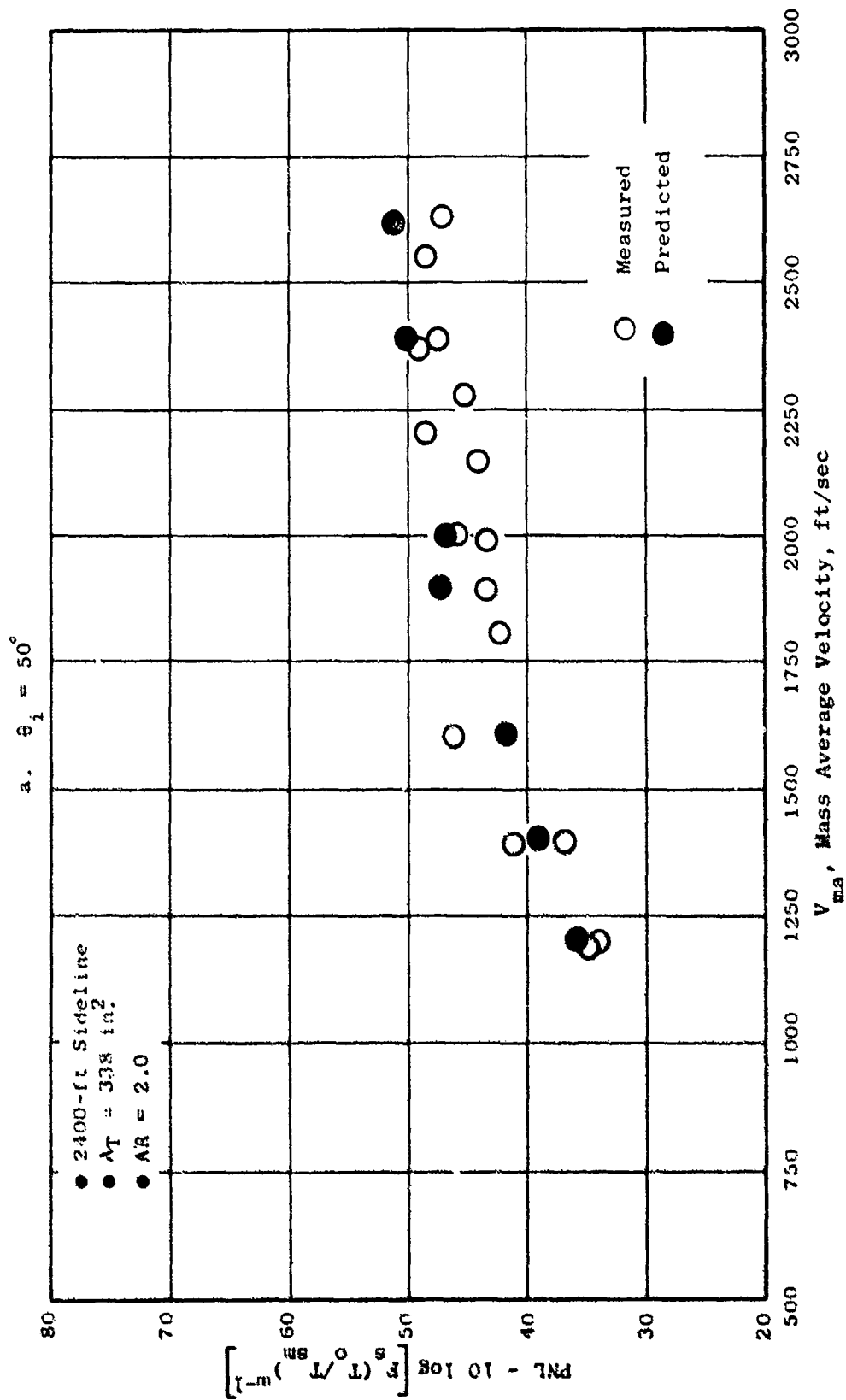


Figure 4-13. Comparison of Predicted and Measured Normalized PNL for a 36-Chute Turbojet Suppressor Nozzle.

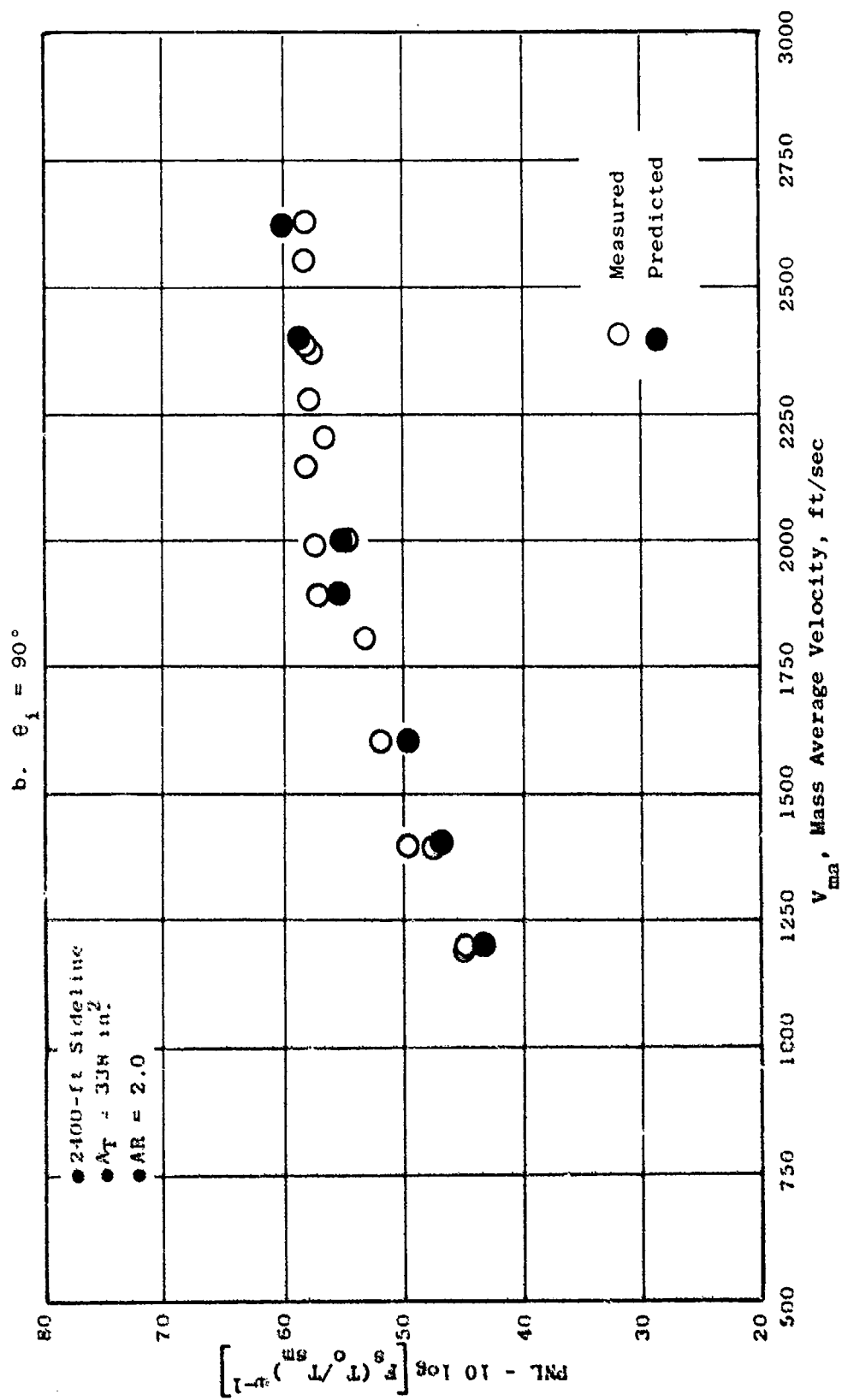


Figure 4-13. Comparison of Predicted and Measured Normalized PNL for a 36-Chute Turbojet Suppressor Nozzle (Continued).

c. Peak PNL

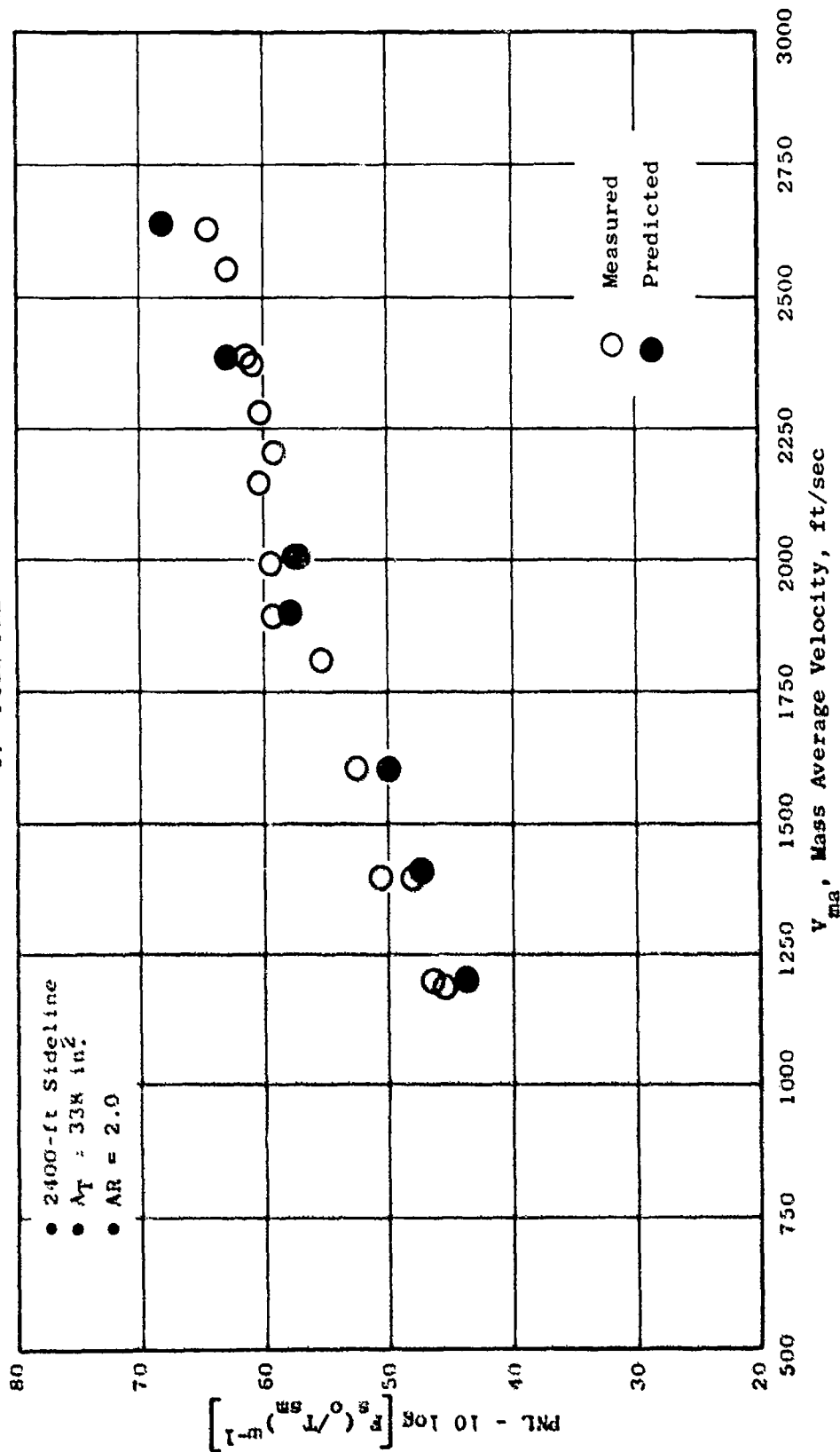


Figure 4-13. Comparison of Predicted and Measured Normalized PNL for a 36-Chute Turbojet Suppressor Nozzle (Concluded).

Table 4-2. PNL Data/Theory Comparison for Bertin Aerotraine Test Series; 400-ft Sidelane.

Case	V_{max} (ft/sec)	V_a (ft/sec)	θ_1	Config. 1 - Conical $A_T = 110 \text{ in.}^2$			Config. 5 - 8-Lobe $A_T = 104 \text{ in.}^2$			Config. 6 - 104-Tube $A_T = 120 \text{ in.}^2$		
				Pred.	Meas.	Error	Pred.	Meas.	Error	Pred.	Meas.	Error
1	1800	0	50	98.8	103.2	-4.4	98.1	101.1	-3.0	---	---	---
			90	106.8	110.1	-3.3	107.5	110.2	-2.7	---	---	---
			Peak	118.5	118.8	-0.3	115.1	115.0	+0.1	---	---	---
2	1800	275	50	100.6	103.1	-2.5	99.3	102.5	-3.2	---	---	---
			90	106.2	109.1	-2.9	107.1	108.5	-1.4	---	---	---
			Peak	114.4	111.7	+2.7	112.3	110.0	+2.3	---	---	---
3	2200	0	50	107.6	110.5	-2.9	107.1	104.7	+2.4	104.6	99.6	+5.0
			90	114.5	116.9	-2.4	113.5	113.2	+0.3	110.4	108.3	+2.1
			Peak	125.2	125.3	-0.1	122.5	118.4	+4.1	111.2	111.2	0
4	2200	275	50	110.3	111.8	-1.5	109.0	106.3	+2.7	105.6	101.9	+3.7
			90	114.1	115.5	-1.4	113.3	112.4	+0.9	110.6	108.1	+2.5
			Peak	122.7	120.7	+2.0	120.4	114.9	+5.5	111.4	109.7	+1.7

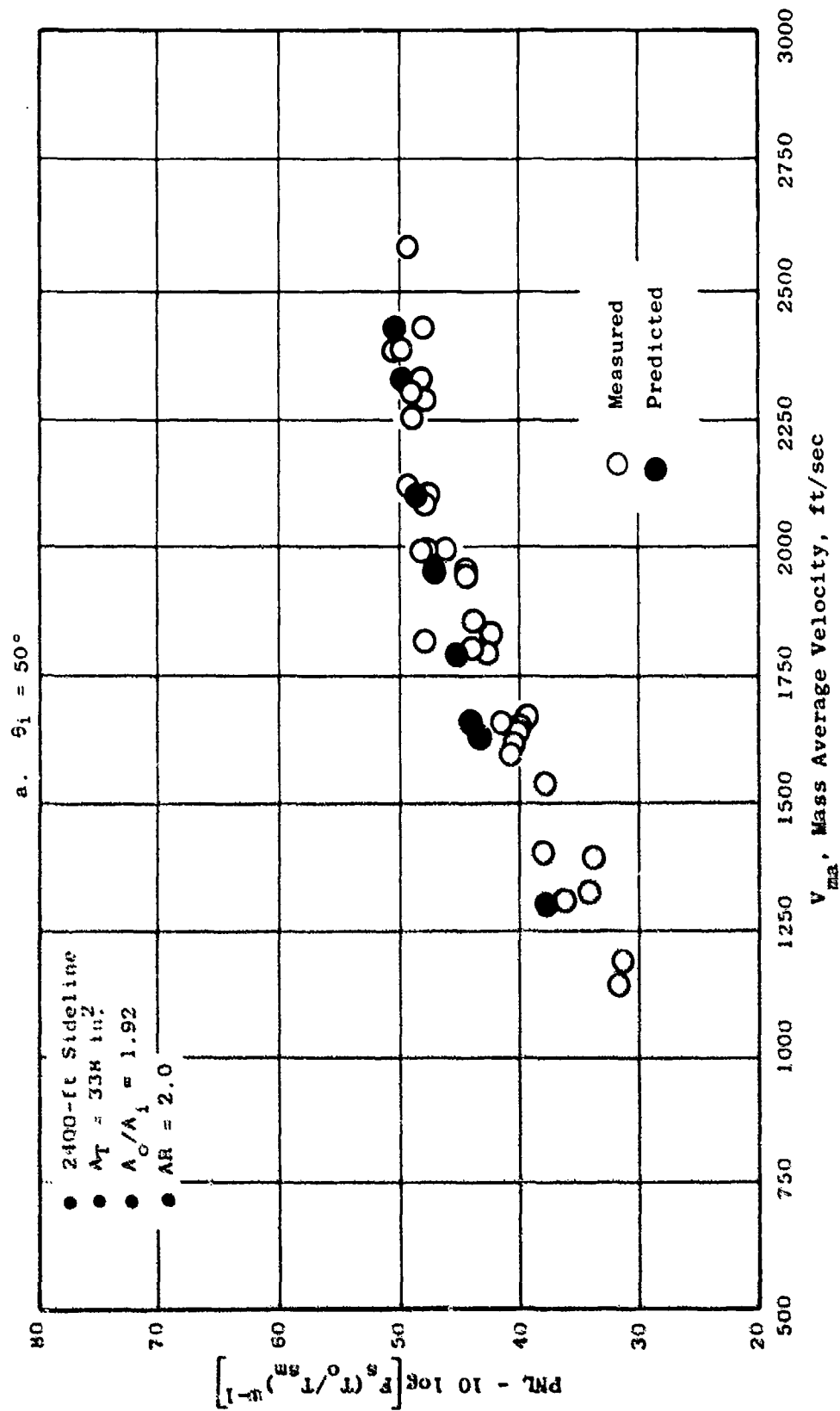


Figure 4-14. Comparison of Predicted and Measured Normalized PNL for a 36-Chute, Dual Flow, Suppressor Nozzle.

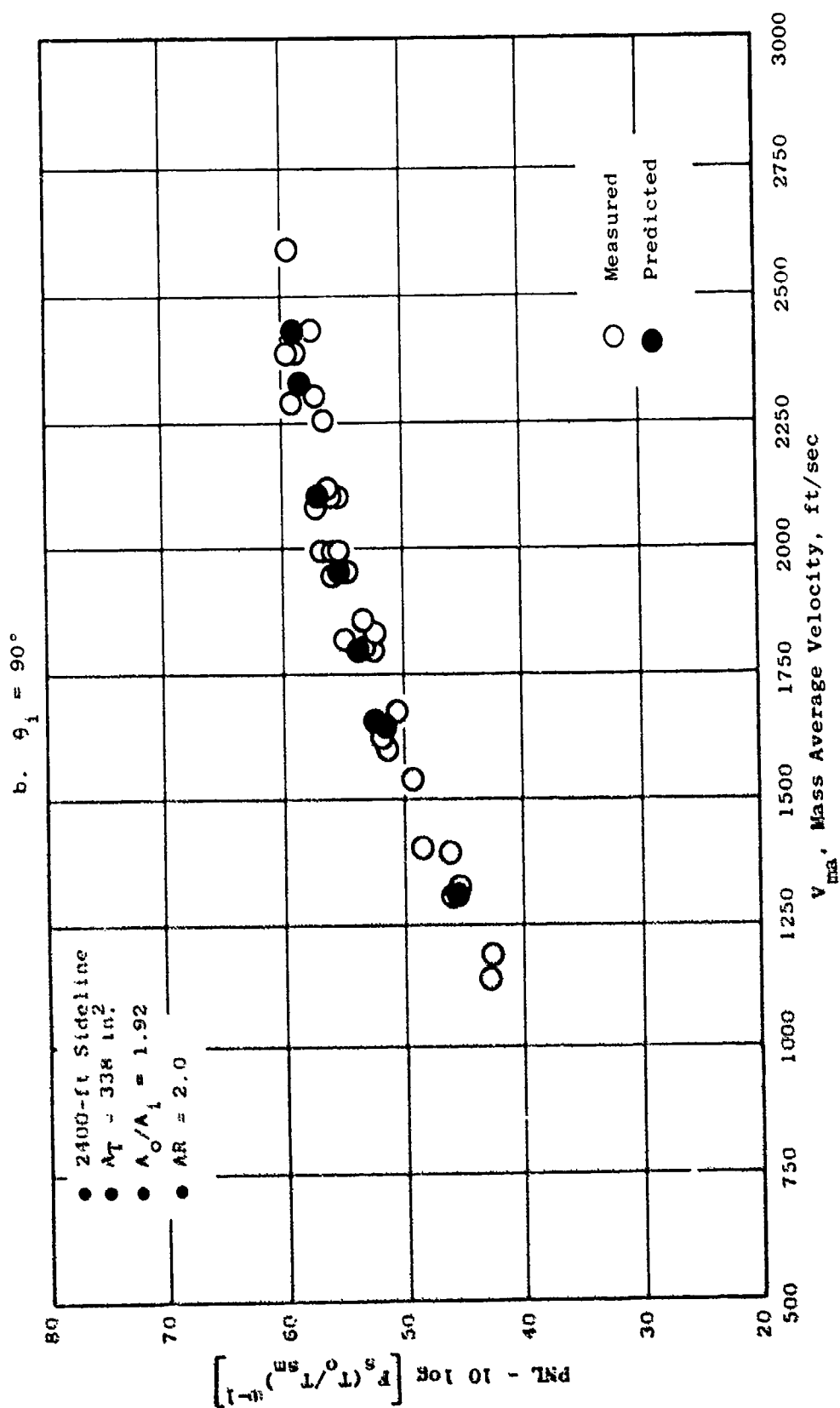


Figure 4-14. Comparison of Predicted and Measured Normalized PNL for a 36-Chute, Dual-Flow, Suppressor Nozzle (Continued).

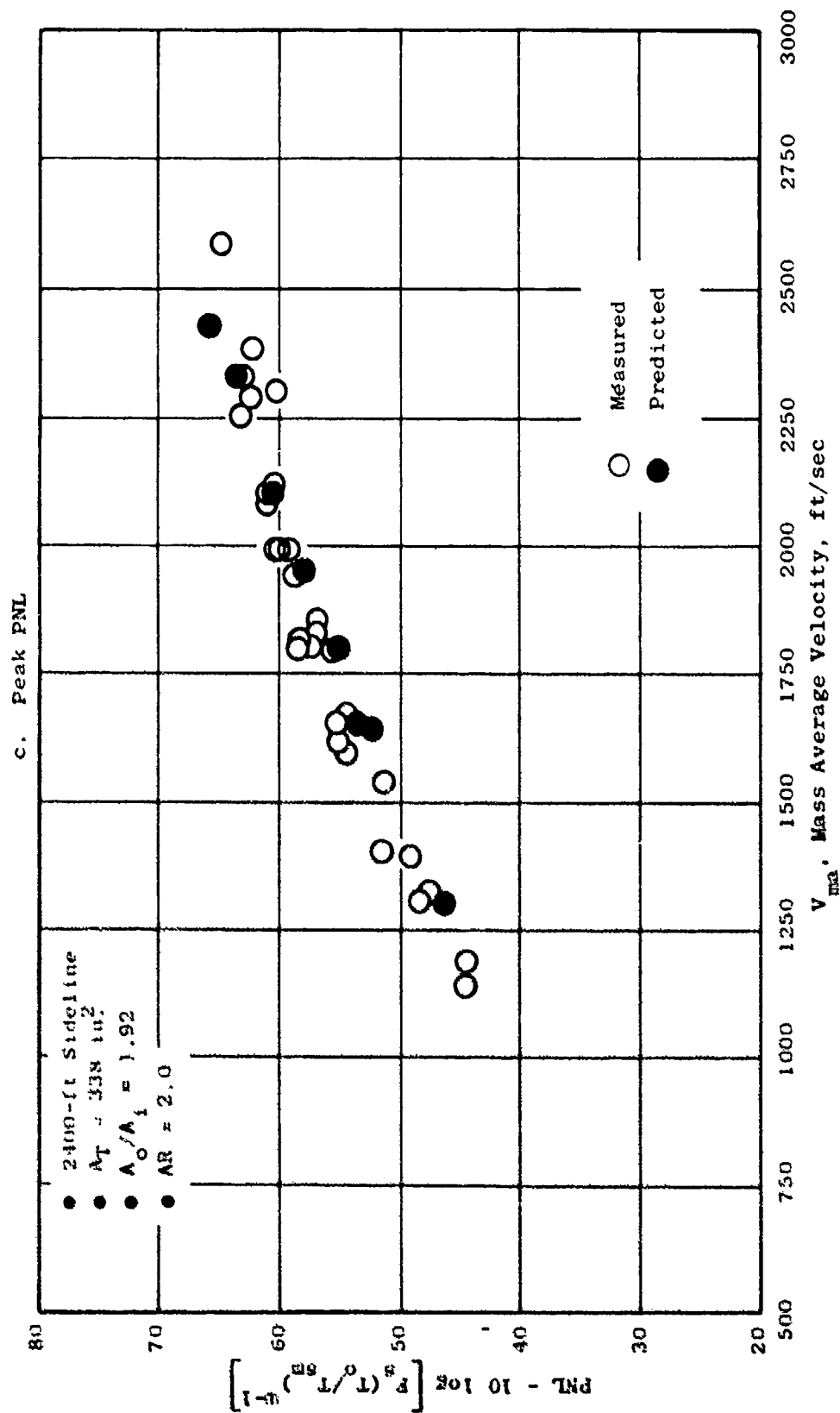


Figure 4-14. Comparison of Predicted and Measured Normalized PNL for a 36-Chute, Dual Flow, Suppressor Nozzle (Concluded).

Early in the Task 3 period, it was intended that source-location measurements from the ellipsoidal mirror (EM) device microphone would be compared with the Task 2 aeroacoustic-model-predicted source-location variables to evaluate certain assumptions and/or hypotheses in the model. During formulation of the Task 3 work elements, the model was based on a slice-of-jet concept which basically assigned an average source strength and source frequency to each axial location in the jet plume. In subsequent development of the aeroacoustic model, the slice-of-jet concept was abandoned in favor of a more rigorous volume-element or lump-of-jet formulation; wherein, each elemental volume of the jet plume is assigned a source strength, characteristic frequency, and spectral density. The ellipsoidal mirror microphone can only measure the slice-average characteristics and is therefore of little use in evaluating the prediction model source formulation and assumptions except for very special cases. The comparison of ellipsoidal mirror microphone data with model predictions was therefore not carried out. However, ellipsoidal mirror microphone data are presented in Section 3.4.5 of Volume II for several suppressor nozzles.

The laser velocimeter (LV) measurements of mean velocity and turbulence intensity were found to be of much more value than the EM in evaluating and trouble-shooting the aero-acoustic model, volume-element formulation. Extensive data/theory comparisons of predicted and measured mean velocity and turbulence intensity profiles were carried out in Task 2 and documented in the Task 2 final report. In the present study, predicted flow field and LV measurement comparisons are therefore confined to those situations which are required to illustrate a particular mechanism or physical explanation of observed acoustic behavior. Laser velocimeter data for several baseline and suppressor nozzles are presented in Section 3.4.4 of Volume II.

In summary, the results shown in Figures 4-10 through 4-14 and in Table 4-2 demonstrate that the Task 2 aeroacoustic prediction model is capable of predicting the acoustic characteristics of a wide variety of nozzle types over a wide range of operating conditions. It can serve as an accurate preliminary tool for subjective noise assessments and nozzle geometry optimization during preliminary design and analysis.

4.3.2 Conical Nozzle Data/Theory Comparisons

The comparison of predicted and measured PNL_N versus V_j (also V_{ma}) trends for a conical nozzle were discussed in Section 4.3.1 and shown in Figure 4-10. In general, the agreement between predicted and measured trends is adequate. A comparison of PNL directivity patterns at three representative jet velocities is shown in Figure 4-15. The predicted directivity patterns agree well with the measurements. A comparison of SPL spectra at several angles ($\theta_i = 50^\circ, 90^\circ, \text{ and } 130^\circ$) is shown in Figure 4-16, and the detailed spectrum shapes are well predicted by the aeroacoustic model. From the data/theory comparison results shown in Figures 4-10, 4-15, and 4-16 it can be concluded that the aeroacoustic model adequately predicts the noise characteristics of conical nozzles over the range of jet velocities evaluated.

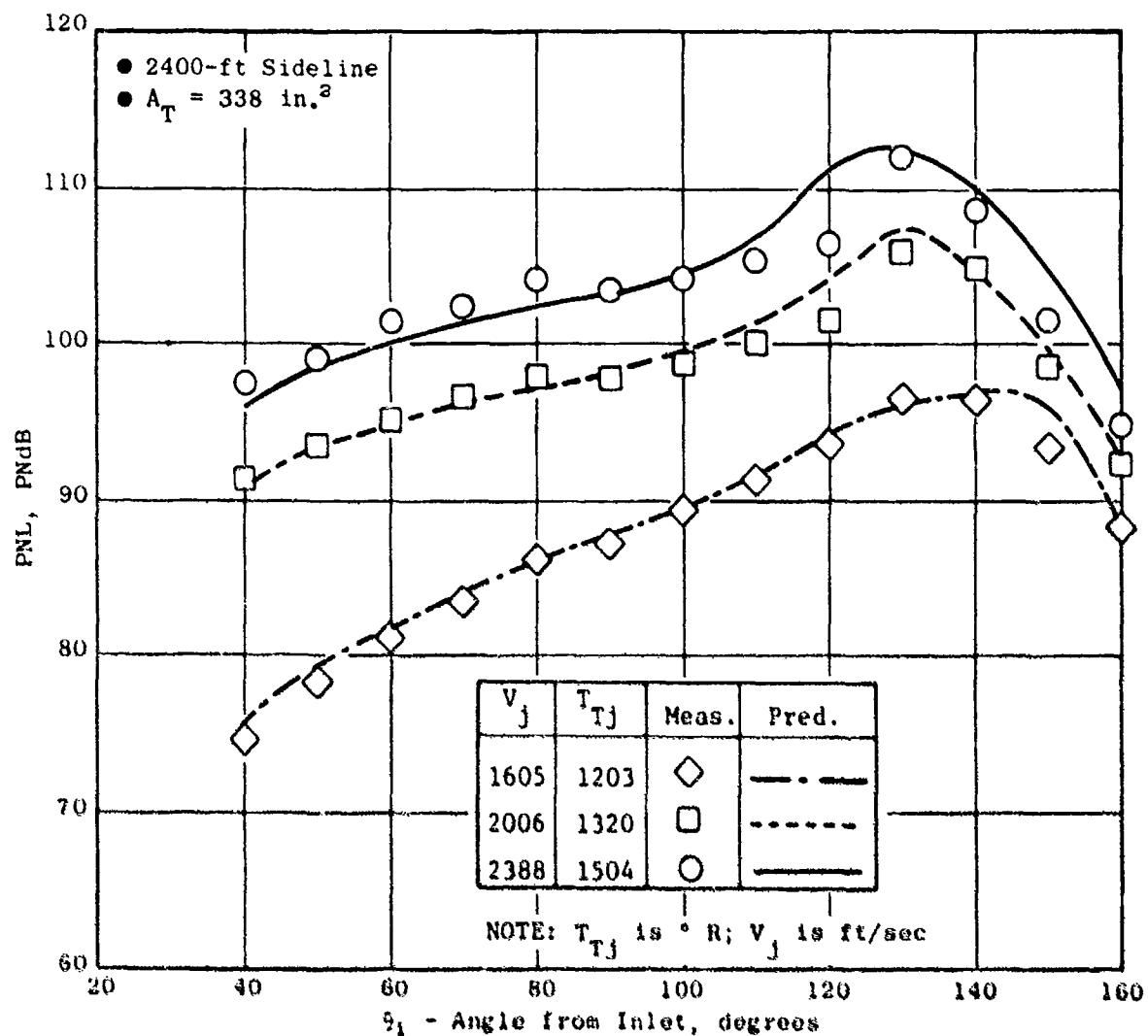
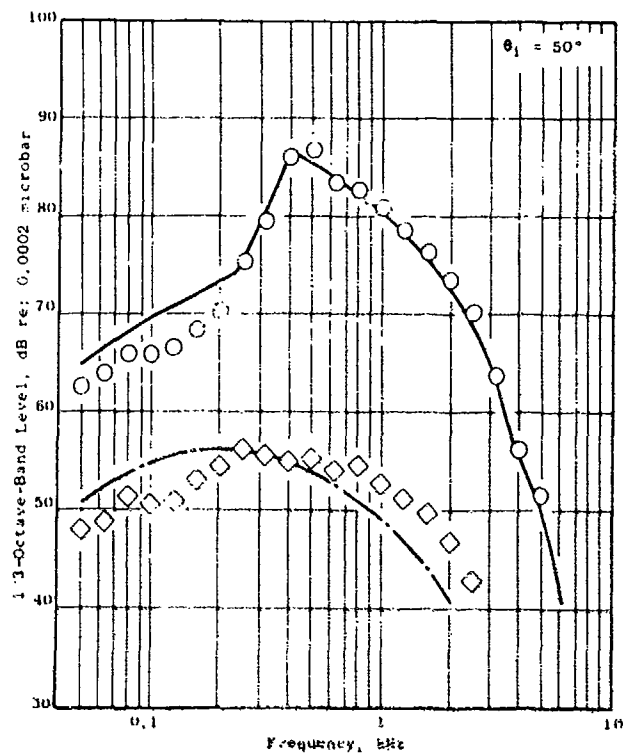


Figure 4-15. Predicted Vs. Measured PNL Directivity for a Conical Nozzle.



V_j	T_{Tj}	Meas.	Pred.
1605	1203	◇	---
2388	1504	○	---

NOTE: T_{Tj} is ° R; V_j is ft/sec

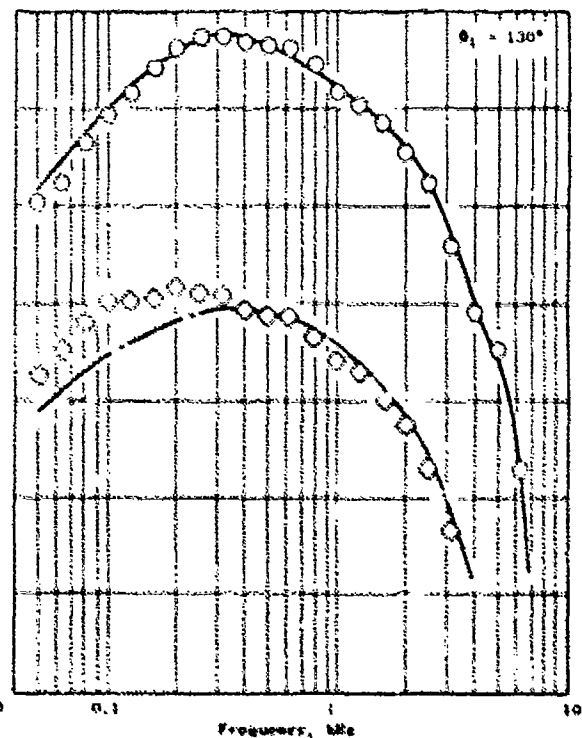
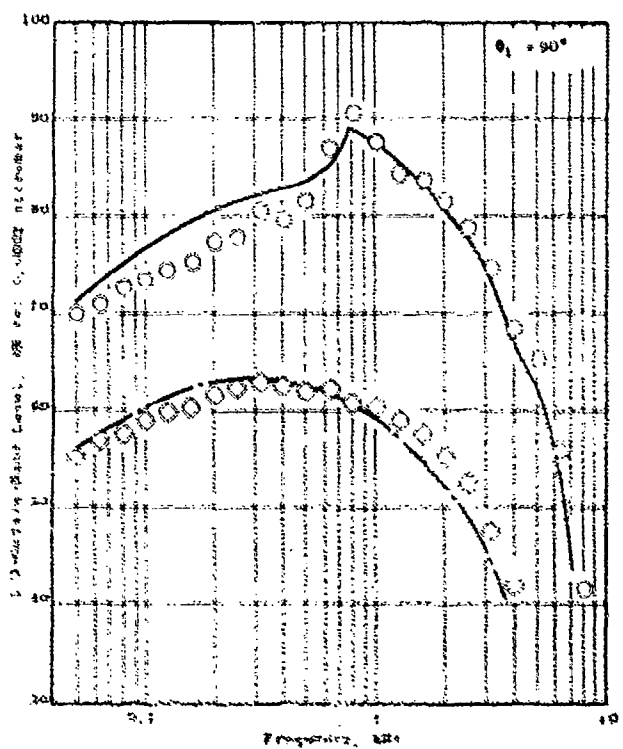


Figure 4-16. Predicted Vs. Measured SPL Spectra for a Conical Nozzle.

4.3.3 Annular Plug Nozzle Data/Theory Comparisons

The annular plug nozzle (Configuration 2) chosen for comparison has a high plug-to-shroud radius ratio, $R_p/R_s = 0.85$. This configuration is typical of a baseline nozzle for a SCAR engine propulsion system and more closely represents the baseline for high-radius-ratio, multichute nozzles. As discussed in Section 4.3.1 and shown in Figure 4-11, the predicted PNL_N versus V_j trends agree reasonably well with the measured trends at $\theta_i = 50^\circ$ and 90° , but peak PNL_N is overpredicted throughout the velocity range by 3 to 5 PNdB.

A comparison of PNL directivity for several jet velocities is shown in Figure 4-17. It can be seen from these results that the PNL is predicted quite well in the forward quadrant, i.e., $\theta_i < 110^\circ$. In the range $110^\circ \leq 140^\circ$, however, the predicted PNL levels are higher than the measurements. The corresponding SPL spectra comparisons are shown in Figure 4-18. Agreement between predicted and measured spectra is good at $\theta_i = 50^\circ$ and 90° . At $\theta_i = 130^\circ$ the low-frequency portion of the spectrum is well predicted, but the high-frequency side of the spectrum is overpredicted by about 5 dB even though the peak levels are in close agreement. Examination of the spectra at $\theta_i = 150^\circ$ shows that, at least at the higher velocities, the predicted and measured spectra agree over the entire frequency range.

4.3.4 Coplanar, Coannular Nozzle Data/Theory Comparisons

The coplanar, coannular nozzle chosen for comparison has an outer-to-inner area ratio, A_o/A_i , of 2.0. This nozzle, Configuration 3, represents a typical baseline for the suppressed-fan, dual-flow nozzle systems. In the data/theory comparisons presented herein, only inverted-flow conditions are considered since conventional-bypass, dual-flow nozzles are covered adequately in the Task 2 final report and do not fit into the high jet velocity applications being emphasized in the present study.

The predicted PNL_N versus V_{ma} trends for the coplanar, coannular nozzle agree with the measured trends, as shown in Figure 4-12. There is a tendency to underpredict the peak PNL_N at high values of V_{ma} , as shown in Figure 4-12. A comparison of PNL directivity patterns for two typical points is shown in Figure 4-19. The lower velocity case shows good agreement between data and prediction. The higher velocity case shows good agreement for $\theta_i \leq 120^\circ$, but the predicted PNL falls below the data at large values of θ_i , close to the jet axis.

Examination of the SPL spectra comparisons, Figure 4-20, shows that the underprediction of PNL near the peak noise angle is due to an underprediction of the middle-to-high-frequency noise (Figure 4-20), $200 < f < 2000$ Hz, at the high values of V_{ma} . There is also a consistent overprediction of the low-frequency portion of the spectrum at $\theta_i = 50^\circ$ and 90° , at both velocities, but this discrepancy has little or no impact on the predicted PNL.

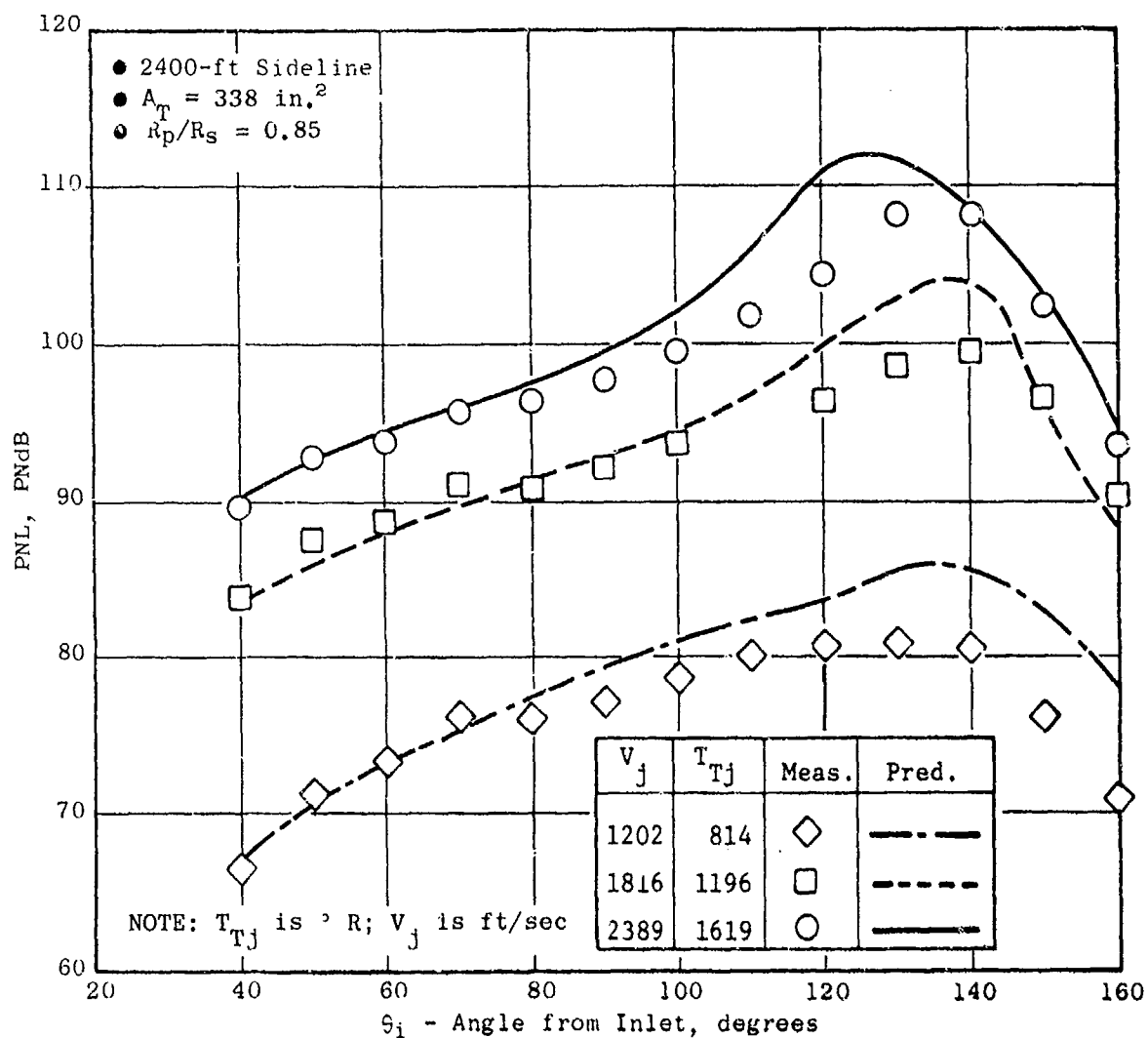


Figure 4-17. Predicted Vs. Measured PNL Directivity for a Convergent, Plug Nozzle.

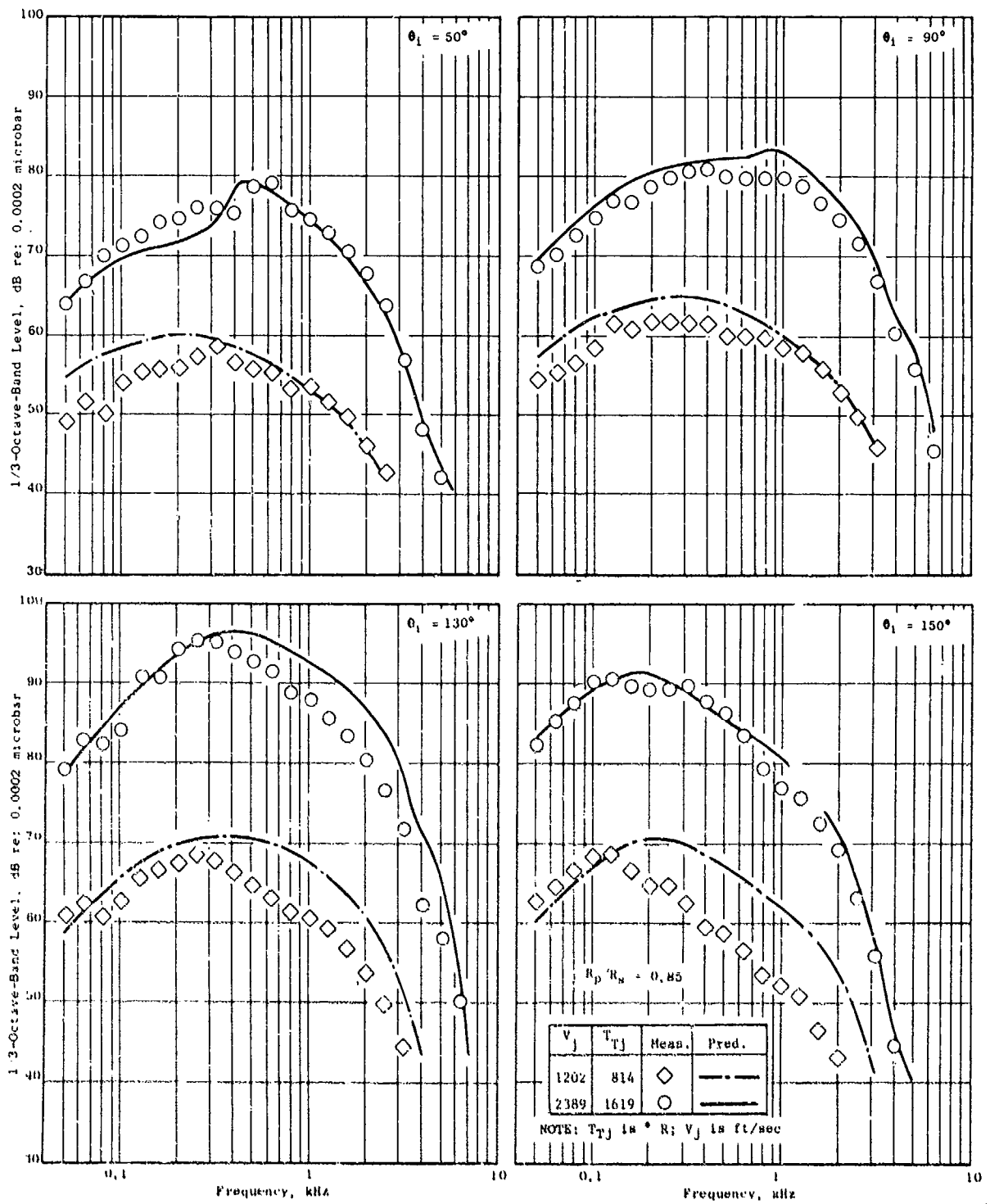


Figure 4-18. Predicted Vs. Measured SPL Spectra for a Convergent, Plug Nozzle.

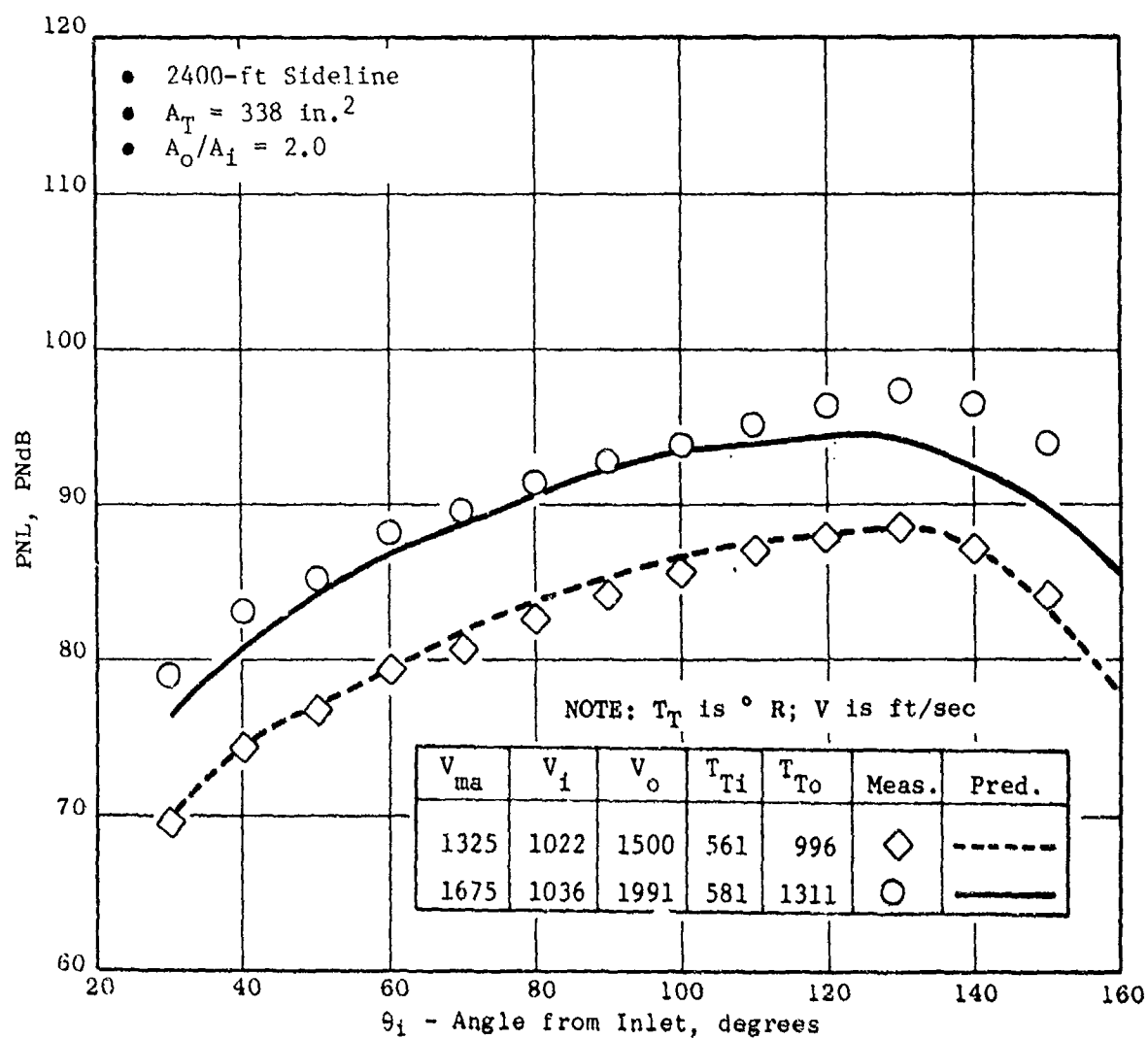
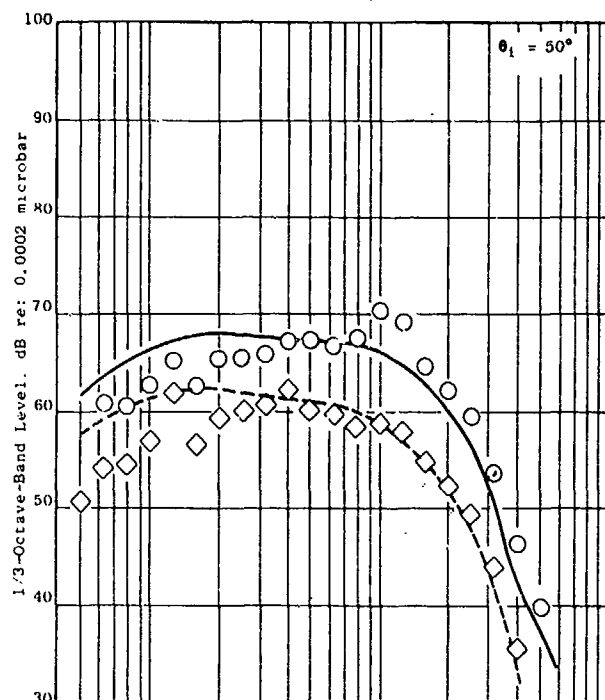


Figure 4-19. Predicted Vs. Measured PNL Directivity for a Coplanar, Coannular Jet.



NOTE: T_T is ° R; V is ft/sec

V_{ma}	V_i	V_o	T_{Ti}	T_{To}	Meas.	Pred.
1325	1022	1500	561	996	◇	-----
1675	1036	1991	581	1311	○	————

• $A_o/A_i = 2.0$

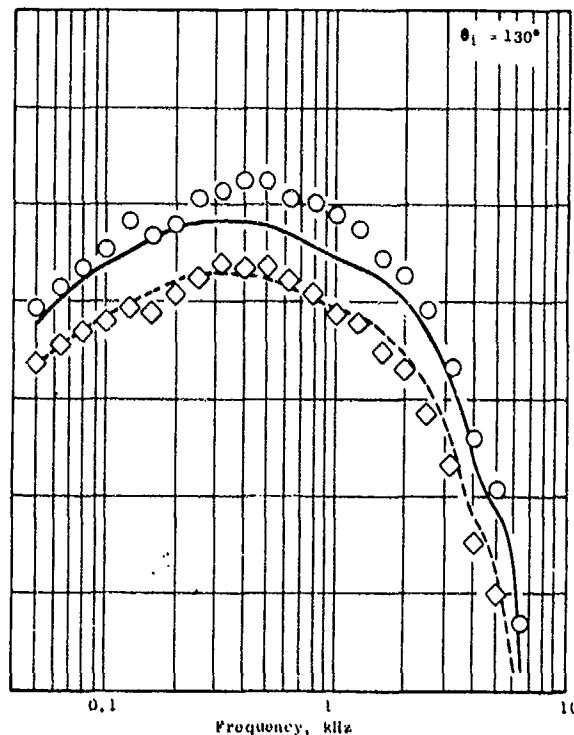
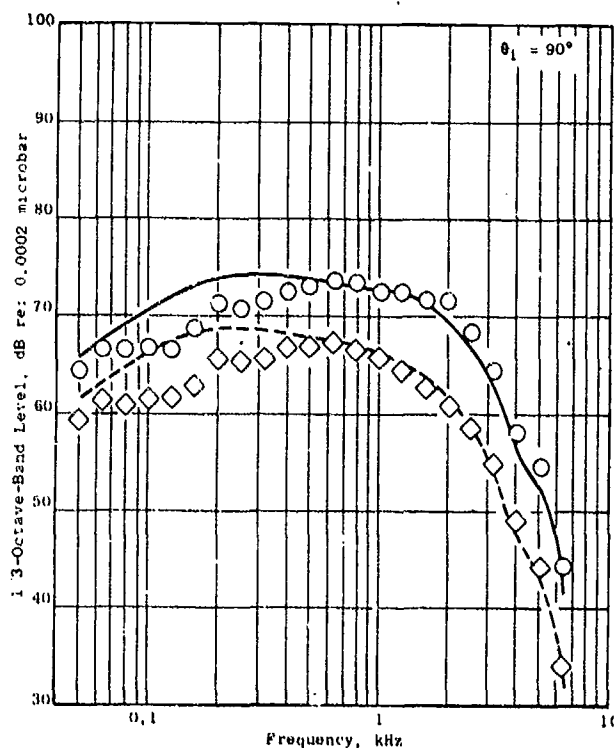


Figure 4-20. Predicted Vs. Measured SPL Spectra for a Coplanar, Coannular Jet.

4.3.5 36-Chute, AR=2.0, Turbojet, Suppressor Nozzle Data/Theory Comparisons

A comparison of predicted PNL_N versus V_j (also V_{ma}) trends with measurements for Configuration 4 are shown in Figure 4-5. In general, the predicted trends duplicate the experimental trends quite well at all three angles shown. Examples of predicted versus measured PNL directivity patterns are shown in Figure 4-21. These examples demonstrate reasonably good agreement between prediction and data. It was found that, at certain (as yet unpredictable) combinations of velocity and temperature, the aeroacoustic model will give erroneous predictions of spectra at angles close to the jet axis, usually at $\theta_i = 150^\circ$ or 160° . The cause is suspected to be in the numerical modeling of the fluid-shielding calculation, either in the turning-point evaluation, in the shielding factor integral evaluation, or the grid size and curve fitting procedures employed. The error is obvious when constant-radius arc predictions are being performed, but is less distinguishable for sideline calculations. The $\theta_i = 150^\circ$ level for $V_j = 2390$ ft/sec, shown in Figure 4-21, is a typical example; therefore, a dashed line has been drawn between 140° and 160° to indicate what the prediction would have been if the numerical error had not occurred. When the error does occur, the predictions at adjacent angles are unaffected and provide a test of whether or not a suspected angle is in error. For example, Figure 4-22 shows predicted SPL spectra at 140° , 150° , and 160° ; it is obvious from these trends that the 150° spectrum is in error.

Comparisons of predicted and measured SPL spectra are shown in Figure 4-23. The characteristic flat spectrum shape exhibited by multichute nozzles is well predicted by the theoretical model. The results shown in Figures 4-13, 4-21, and 4-23 demonstrate that the aeroacoustic prediction model can provide reasonably accurate estimates of multichute nozzle subjective noise levels, at least for this particular configuration.

To evaluate the ability of the aeroacoustic model to predict the effects of chute area ratio, predictions were made at several jet velocities for two additional suppressor nozzles having area ratio of 1.5 and 2.5. These results were then compared with the experimental results of the chute area ratio study presented in Section 3.4.2.1 of Volume II. A summary of these predicted and measured results is shown in Figure 4-24, where peak PNL suppression (relative to an equivalent-thrust, conical nozzle) is plotted versus jet velocity. The predicted points are denoted by symbols; the data has been curve-fit, and the corresponding lines are shown. These results show that a suppression peak can be predicted; i.e., suppression is not constant with varying V_j , has a definite maximum at some value of V_j , and falls off with decreasing and increasing V_j on either side of the peak. Although the predicted-suppression curve (circles) deviates from the data (solid line) at low velocities, the general trend and curve shapes are consistent.

Prediction of area-ratio effects is confined to velocities of 2000 ft/sec and above, as seen in Figure 4-24. The predicted effect of area ratio is that suppression increases as area ratio increases; this qualitatively agrees with the measured effects. The predicted drop-off in suppression at

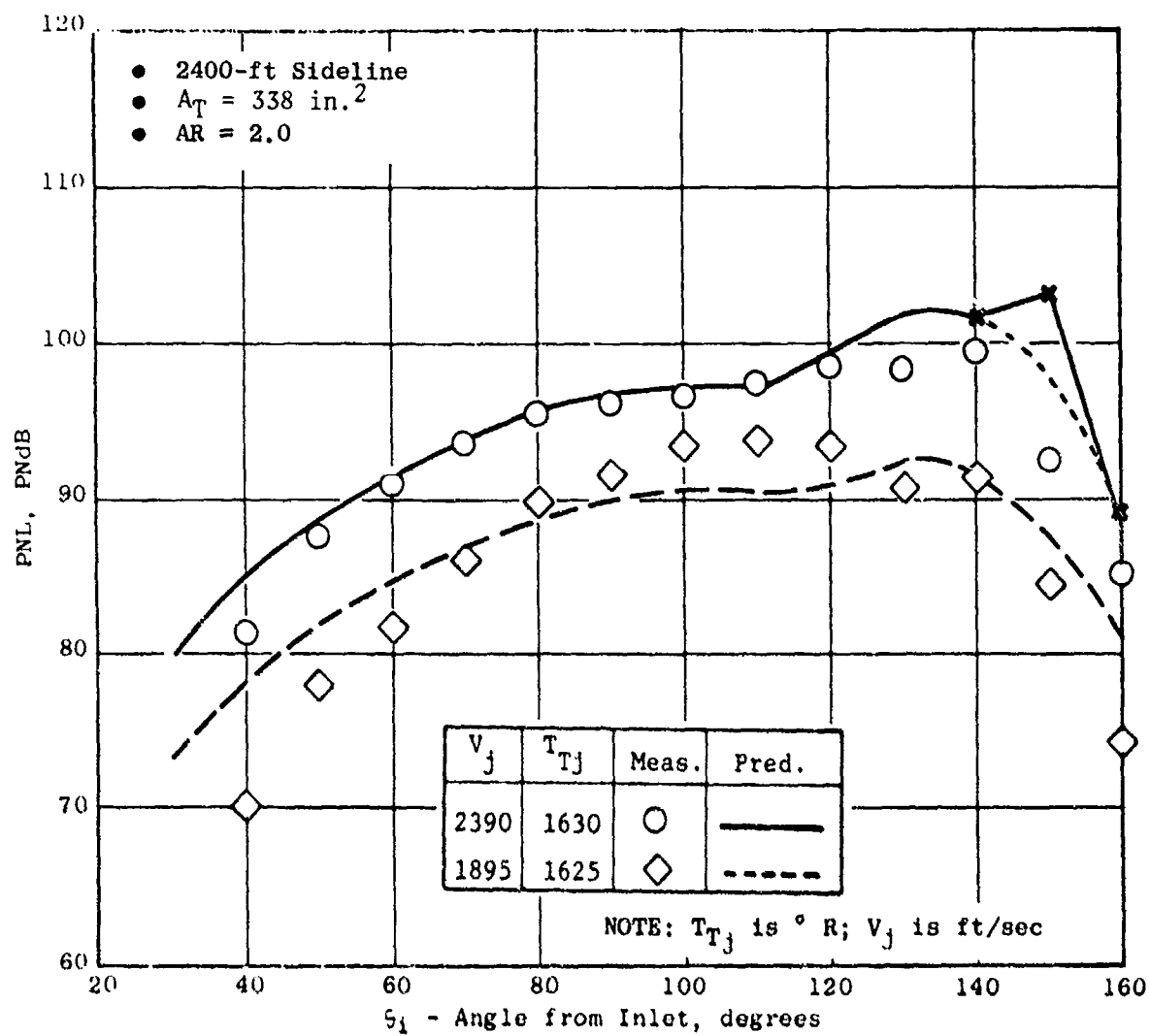


Figure 4-21. Predicted Vs. Measured PNL Directivity for a 36-Chute, Turbojet Suppressor Nozzle.

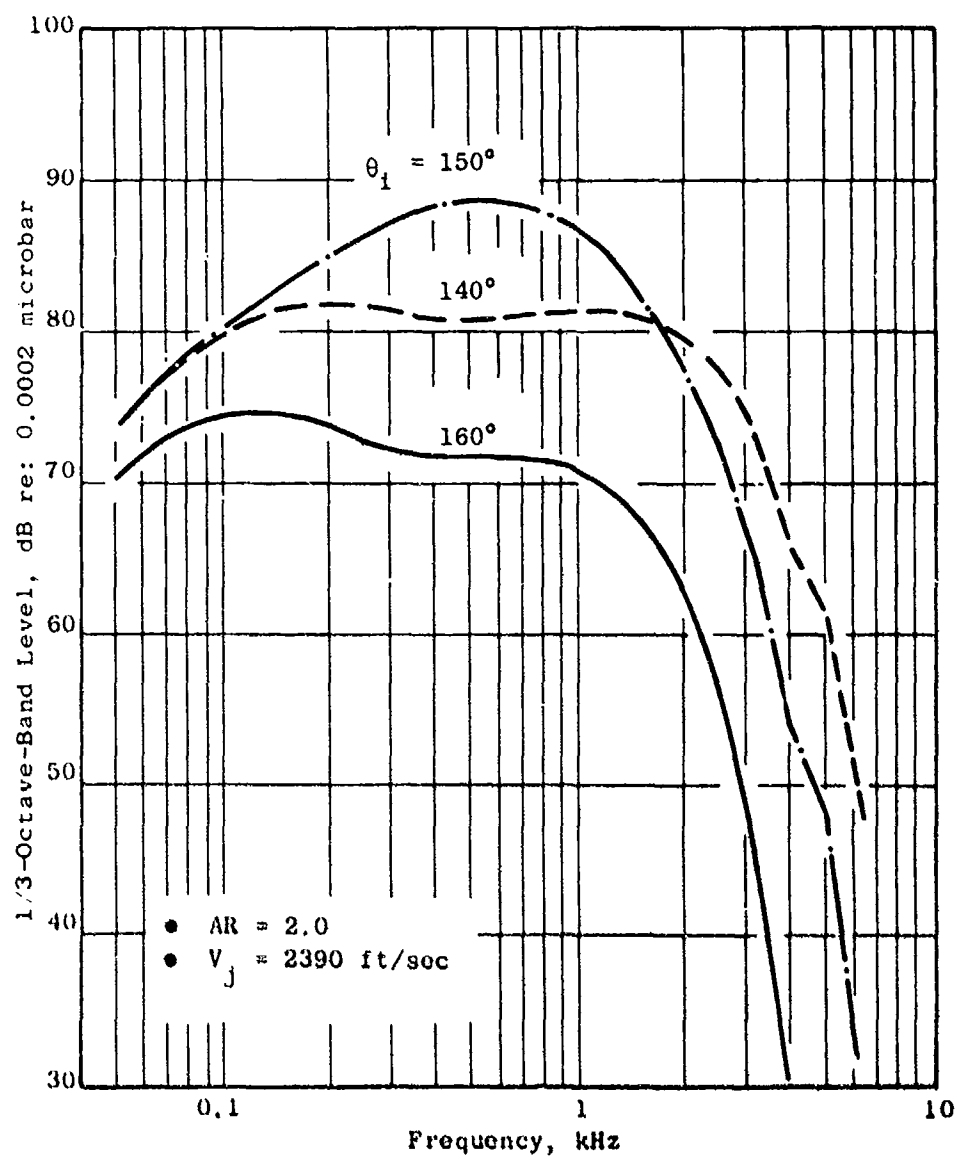
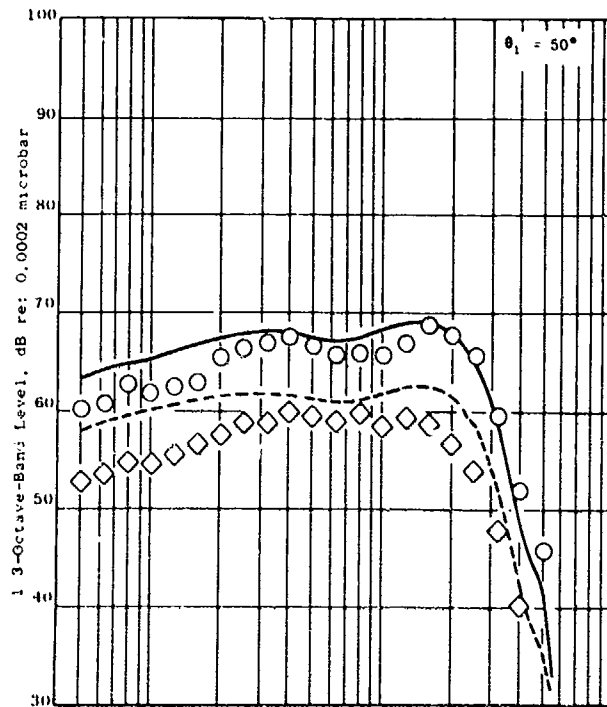


Figure 4-22. Example of Suspected Numerical Error in Spectrum Prediction at $\theta_1 = 150^\circ$, with Adjacent Spectra (140° and 160°) Unaffected; 36-Chute, Turbojet Suppressor.



NOTE: T_{Tj} is ° R; V_j is ft/sec

V_j	T_{Tj}	Meas.	Pred.
2390	1630	○	—
1895	1625	◇	- - -

• AR = 2.0

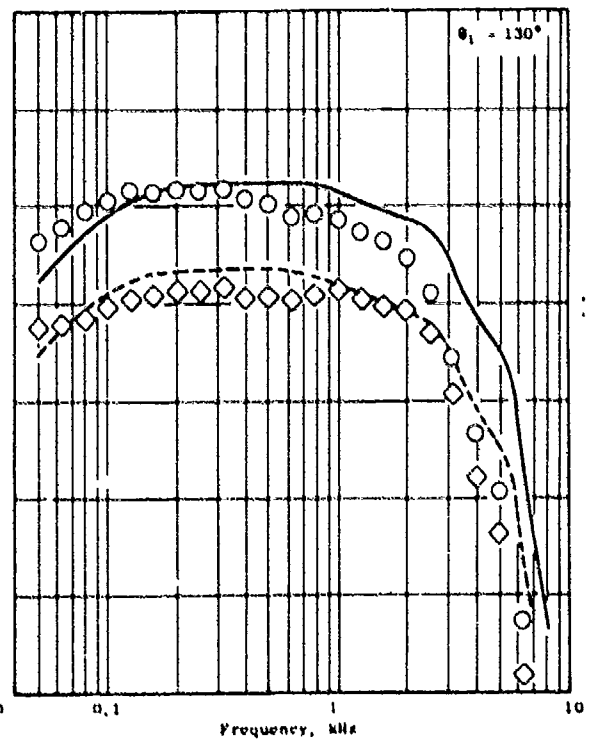
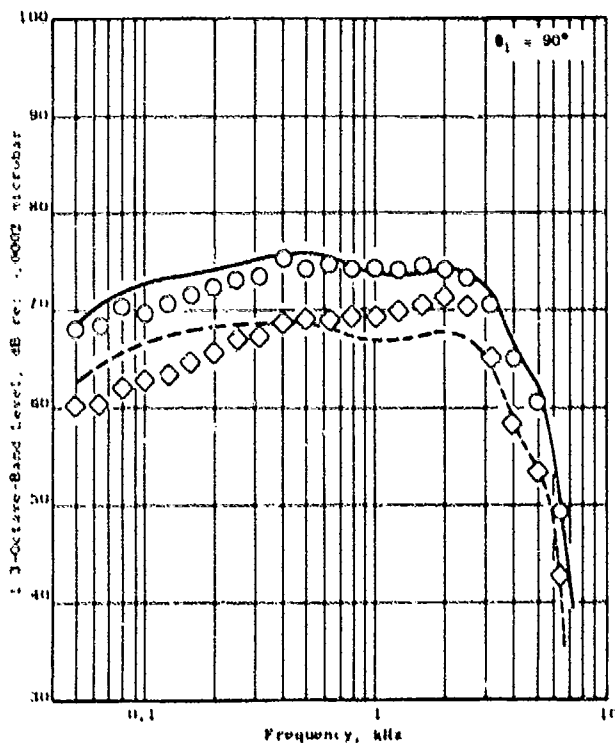


Figure 4-23. Predicted Vs. Measured SPL Spectra for a 36-Chute, Turbojet Suppressor.

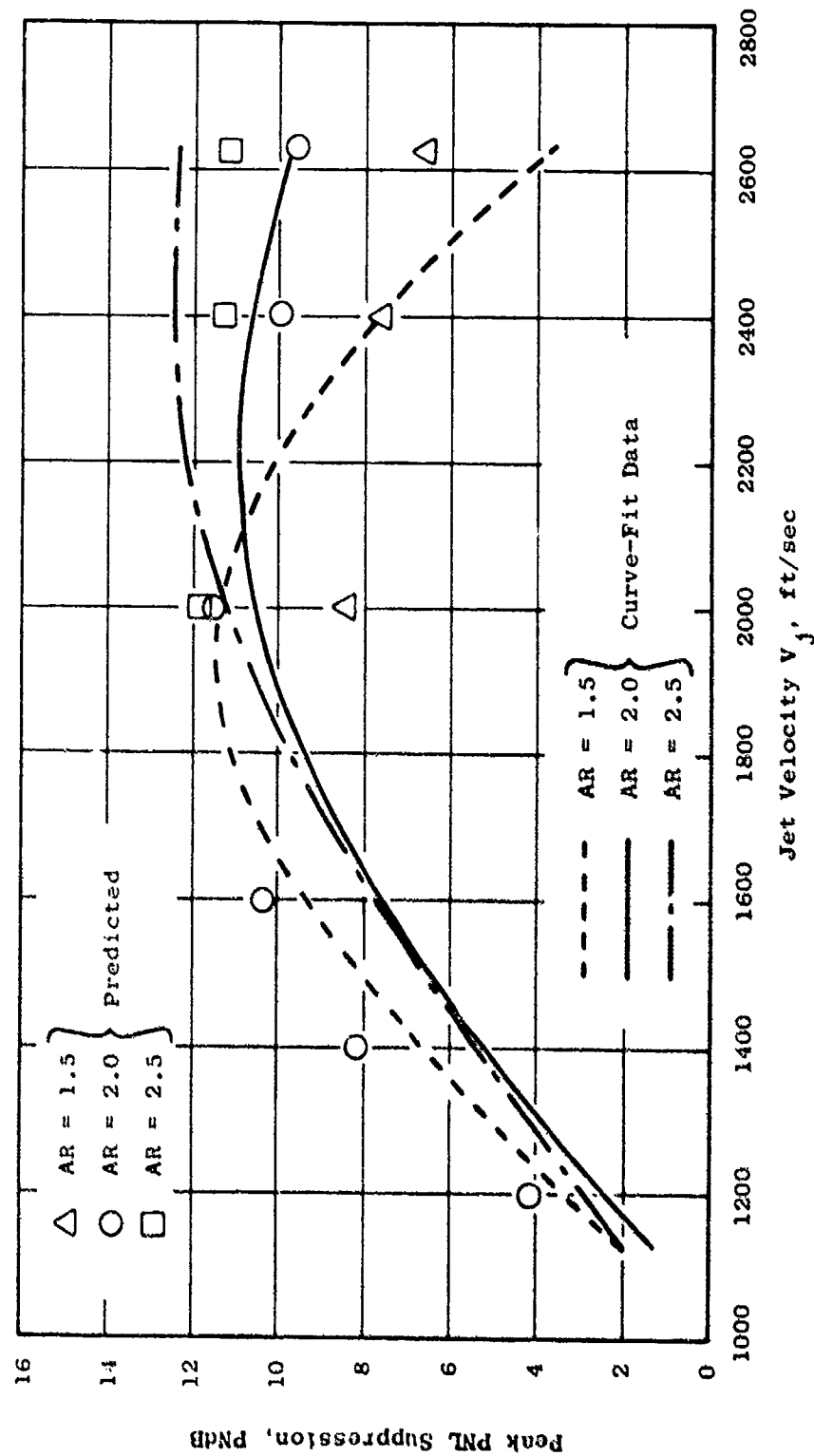


Figure 4-24. Comparison of Predicted and Measured Effect of Area Ratio on Peak PNL Suppression for a 36-Chute, Turbojet Suppressor.

high velocities for $AR = 1.5$, however, is not as steep as the measured drop-off, as Figure 4-24 shows. Also, the measured suppression curves tend to come together as $V_j = 2000$ ft/sec; whereas, the predicted suppression for $AR = 1.5$ is ≈ 3 dB below that for the other two area ratios.

4.3.6 8-Lobe Nozzle Data/Theory Comparisons

A summary of the data/theory comparison cases made for the 8-lobe nozzle, Configuration 5, is given in Table 4-2. Figure 4-25 shows the comparison of predicted and measured PNL directivity patterns for the static cases. The corresponding flight directivities at $V_a = 275$ ft/sec are shown in Figure 4-26. The predicted directivity patterns agree fairly well with the data in the forward quadrant. Close to the jet axis, however, the predicted PNL levels are considerably higher than the measured levels for $\theta_i \geq 130^\circ$. This overprediction is especially pronounced for the flight cases, Figure 4-26.

A comparison of measured and predicted SPL spectra for the static cases is shown in Figure 4-27. The spectra at 50° show good agreement in the low and middle frequencies, but poor agreement at high frequencies for the $V_j = 1800$ ft/sec case. The peculiar, high-frequency peak at 6300 Hz exhibited by the predicted spectrum at 1800 ft/sec is due to the shock-cell noise prediction. It is suspected that not enough axial stations close to the nozzle exit plane were included in the computation to yield a complete estimate of the mixing noise at high frequencies, at least for the $V_j = 1800$ ft/sec case. These observations also apply to the $\theta_i = 90^\circ$ spectra comparisons shown in Figure 4-27.

The prediction method overestimates the high-frequency portion of the spectrum at angles close to the jet axis ($\theta_i = 130^\circ$ and 150°), as Figure 4-27 illustrates. This high-frequency overprediction at angles close to the jet axis is suspected to be caused by inaccuracies, in the fluid-shielding calculation, resulting from the circumferential-averaging approximation employed. This effect is expected to be most pronounced for the 8-lobe nozzle, of all the configurations examined, because the lobe flow asymmetry persists for several diameters along the jet axis. Corresponding SPL spectra comparisons for the flight cases, $V_a = 275$ ft/sec, are shown in Figure 4-28. In general, the observations concerning the static spectra hold for the flight spectra as well. The overprediction of the high-frequency noise at angles close to the jet axis is more pronounced for the flight case, however.

4.3.7 104-Tube Nozzle Data/Theory Comparisons

A summary of the data/theory comparison results obtained for the 104-tube suppressor nozzle, Configuration 6, is given in Table 4-2. Two test point cases were computed with the aeroacoustic prediction, each computation requiring 1.8 hours on a Honeywell 6080 computer. These two cases correspond to static $V_a = 0$ and flight ($V_a = 275$ ft/sec) points at $V_j = 2200$ ft/sec.

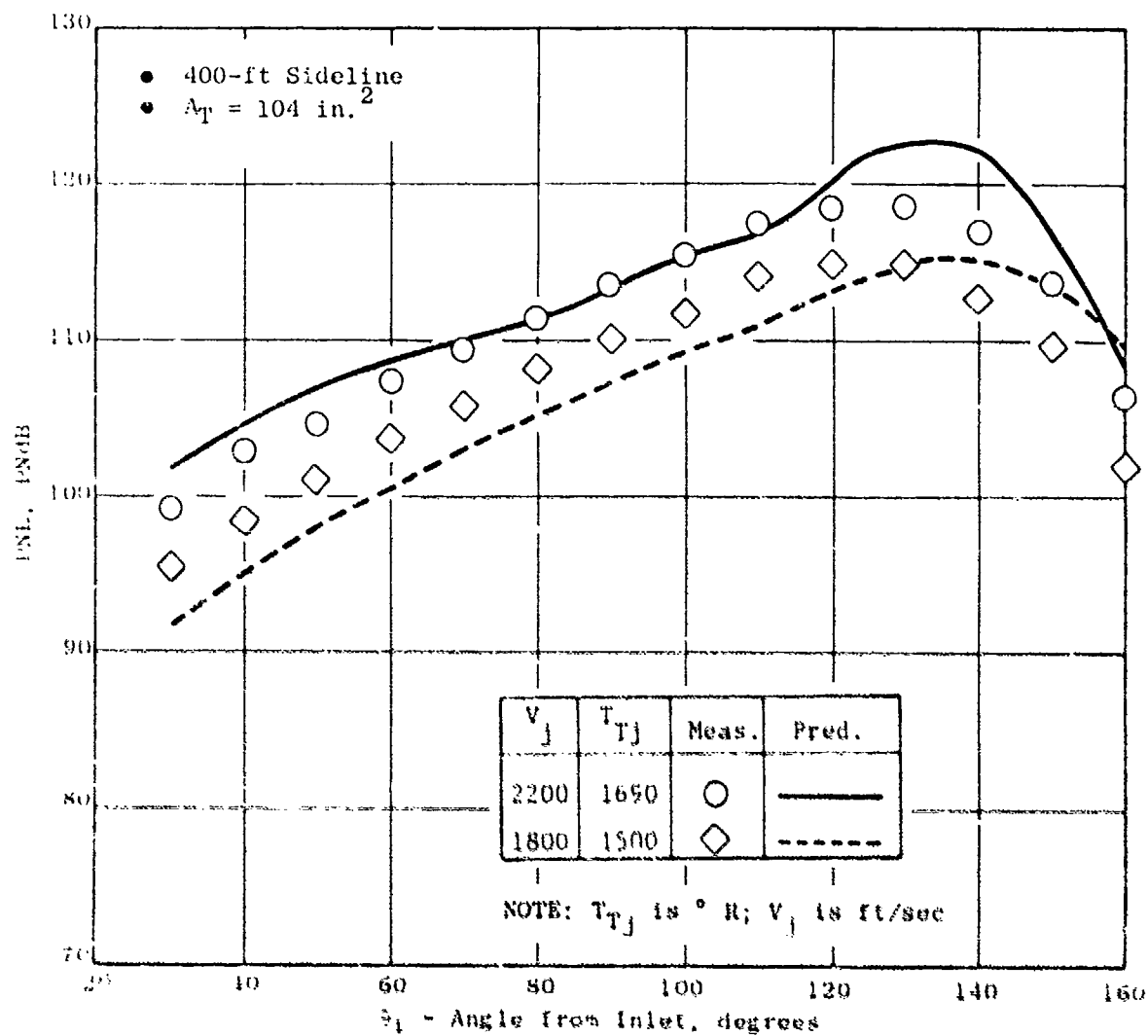


Figure 4-25. Predicted vs. Measured PNL Directivity for an 8-Lobe Daisy Suppressor (Aerotraine); $V_a = 0$.

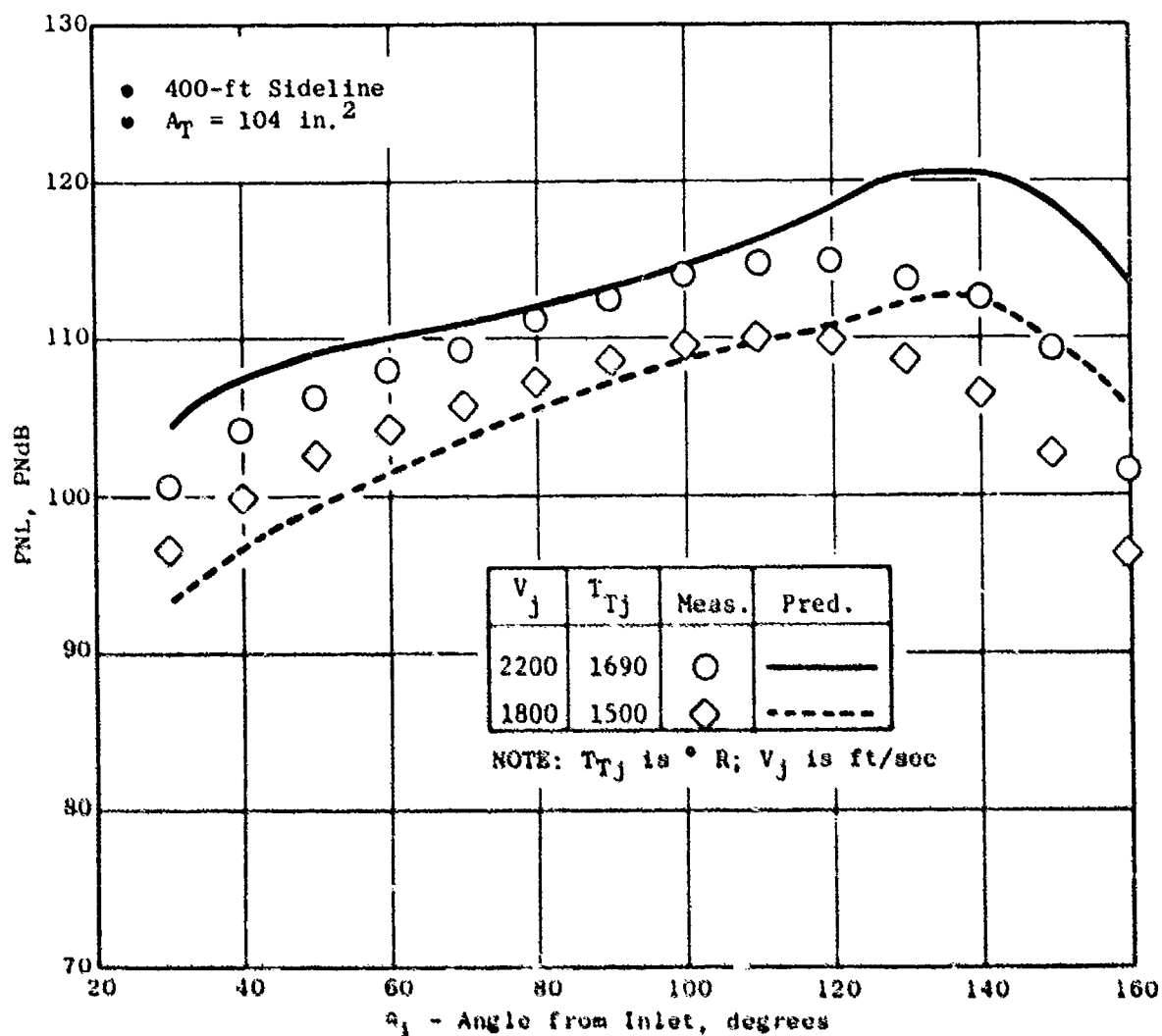


Figure 4-26. Predicted Vs. Measured PNL Directivity for an 8-Lobe Daisy Suppressor; $V_D = 275 \text{ ft/sec.}$

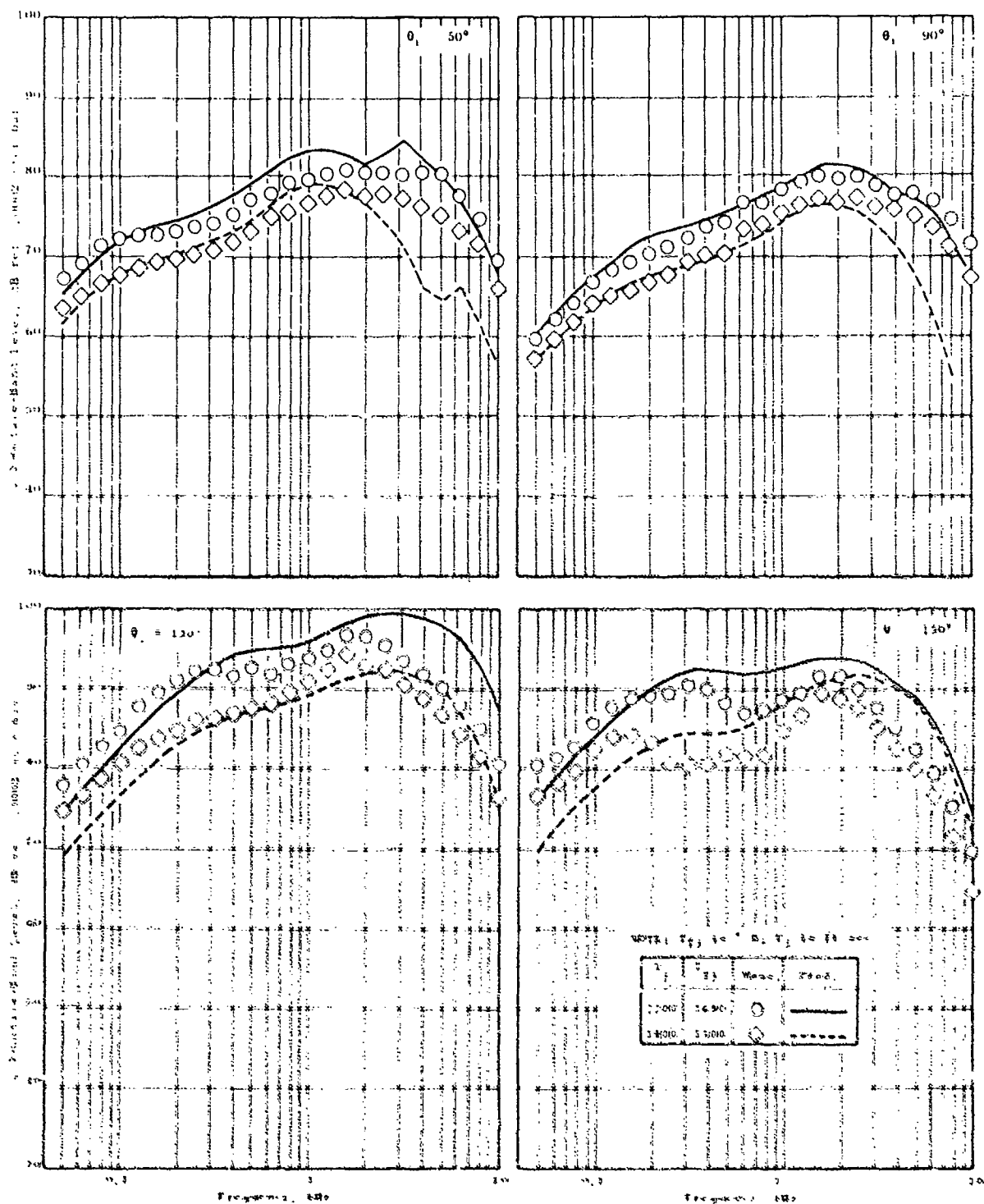


Figure 4-27. Predicted Vs. Measured SPM Spectra for an 8-Lobe Daisy Suppressor; $V_d = 0$.

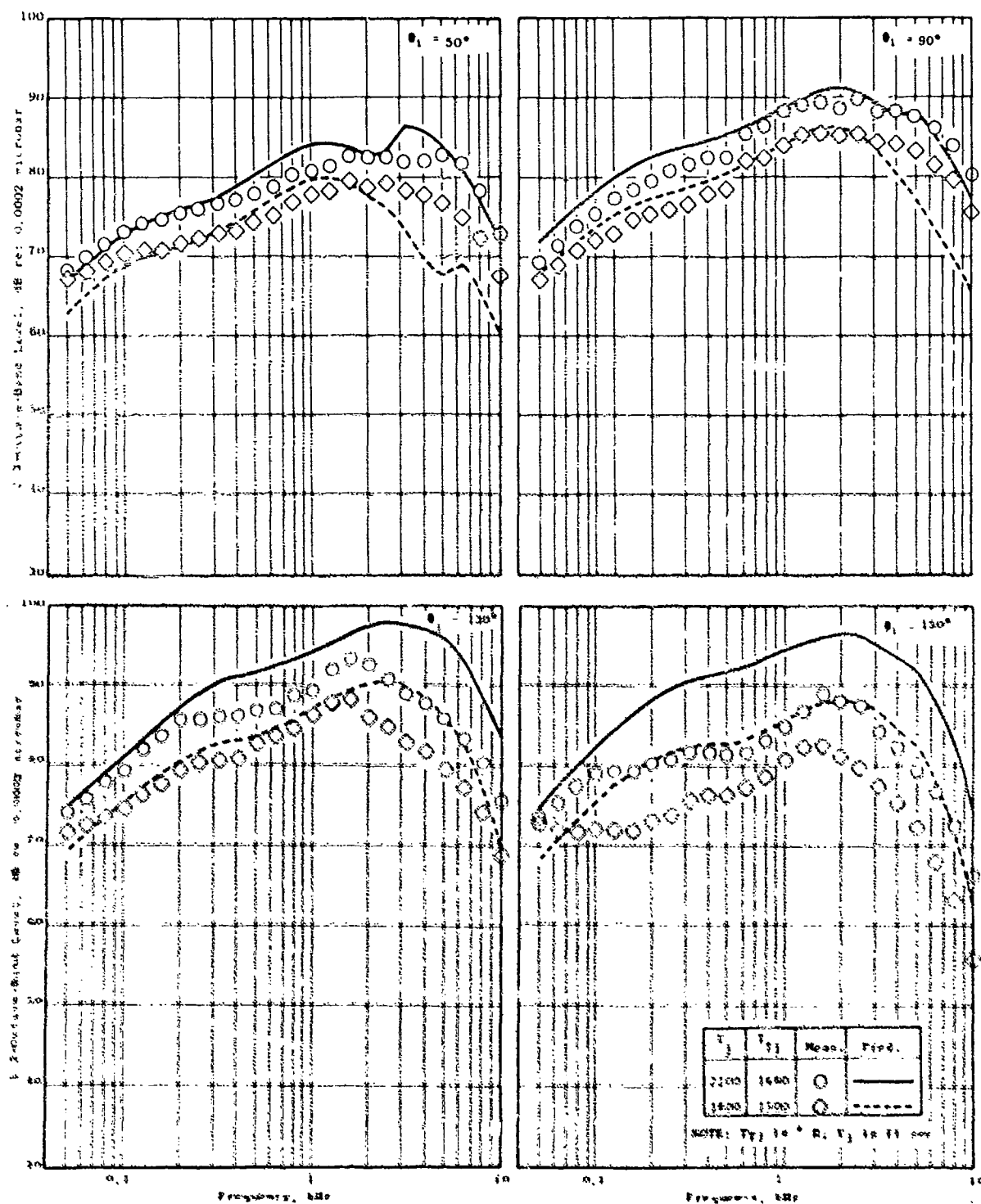


Figure 4-28. Predicted Vs. Measured SPL Spectra for an 8-Lobe Daisy Suppressor; $V_0 = 275$ ft/sec.

A comparison of predicted and measured PNL directivity patterns is shown in Figure 4-29. Although the peak PNL levels are in good agreement, the predicted directivity is somewhat flatter than the measured pattern. The noise level is therefore overpredicted near the inlet axis and the exhaust axis.

A comparison of predicted and measured SPL spectra is shown in Figure 4-30. At all angles, the predicted spectrum shape is much more peaky than the measured shape, and the characteristic double peak is much more pronounced than is evident in the data. The predicted effect of flight on the spectra are in qualitative agreement with the measured effect, as Figure 4-30 shows. A small increase in SPL levels is predicted at $\theta_i = 50^\circ$ due to flight. Little or no change occurs at $\theta_i = 90^\circ$, as is observed. At $\theta_i = 130^\circ$ and 150° , a drop in noise due to flight is predicted and observed, but the drop at low frequencies is substantially larger than the predicted drop.

Considering the complexity of the 104-tube nozzle jet plume aerodynamics and the cowl base-pressure levels discussed in Section 4.0 of Volume II, the predictions shown in Figure 4-29 and 4-30 are considered to be as good as can be expected without additional model development.

4.3.8 36-Chute, Dual-Flow Nozzle Data/Theory Comparison

The 36-chute, dual-flow, suppressor nozzle is the most complex and difficult to model of all the configurations listed in Table 4-1. It contains a multielement, segmented suppressor of high element number in combination with dual-flow, coannular streams with inverted velocity profiles. Additionally, the outer-stream exit plane is retracted relative to the core (inner stream) exit, and the outer and inner streams have inner flow-path boundaries. The outer stream follows a contoured cowl up to the core lip, and the core has a centerbody or plug.

It was discussed in the Task 2 final report that the Task 2 aeroacoustic model applicability is limited for noncoplanar-exit geometries and that certain centerbody/plug geometries were difficult to model. For the 36-chute, dual-flow nozzle it was not possible to account for the effects of both the fan cowl and core plug with the current version of the aeroacoustic model computer program. The plug and cowl were, therefore, omitted entirely by modeling the nozzle on an equivalent-area basis. The core (inner) nozzle was replaced by an equivalent-area, conical nozzle. The fan (outer) nozzle was replaced by an equivalent-area, annular-chute nozzle having the same inner diameter as the core nozzle. The axial stagger between the fan and core nozzles was maintained because the computer procedure can mechanically accommodate staggered nozzle elements, subject to the boundary-impingement limitations set forth in Reference 7.

The equivalent-area modeling of the actual nozzle geometry is illustrated qualitatively in Figure 4-31. The resulting fan suppressor has the same flow area and area ratio ($AR = 2.0$) as the actual geometry, but the chute aspect ratio becomes larger in the equivalent-area configuration.

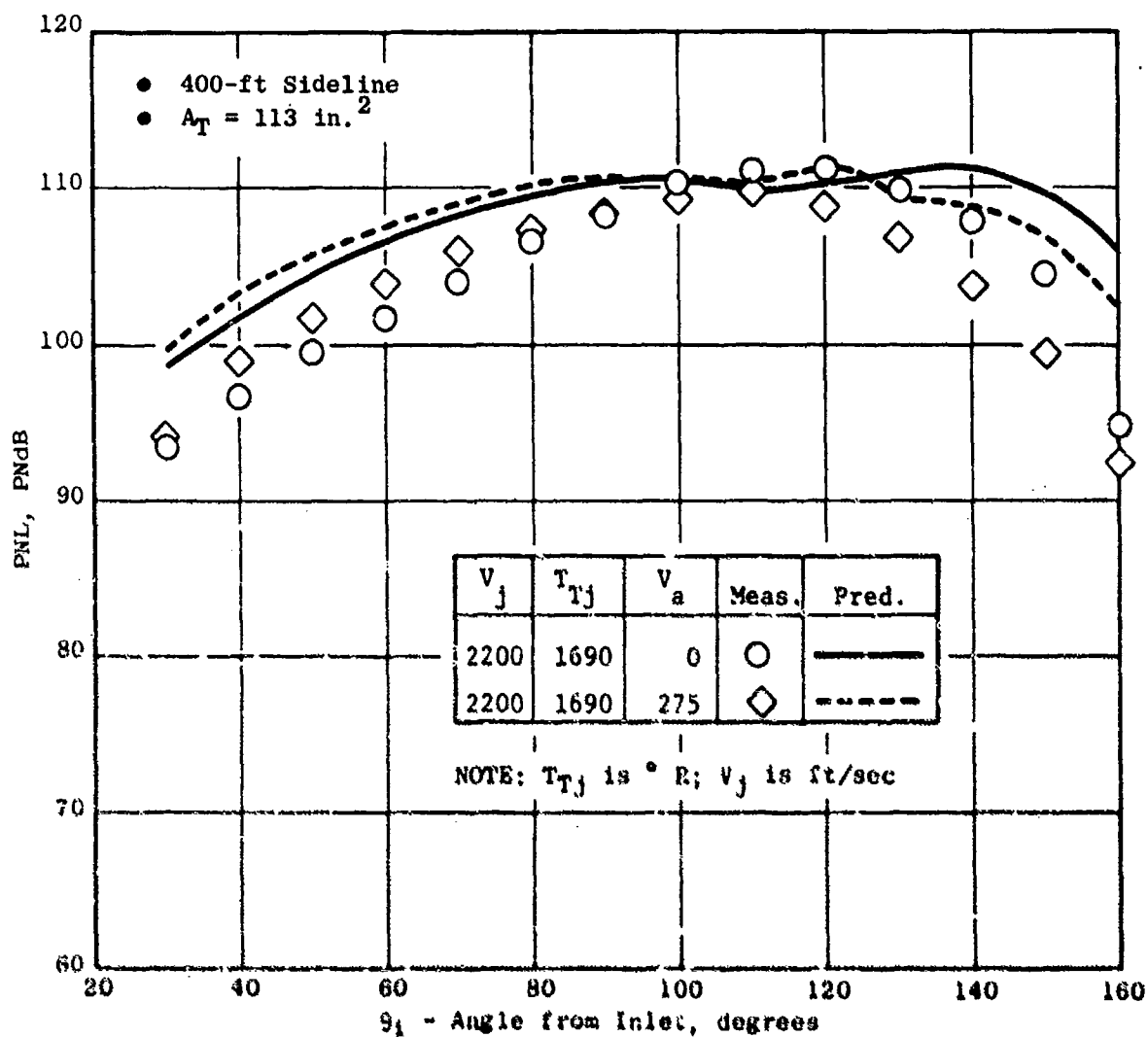


Figure 4-29. Predicted Vs. Measured PNL Directivity for a 104-Tube Suppressor Nozzle (Aerotrain).

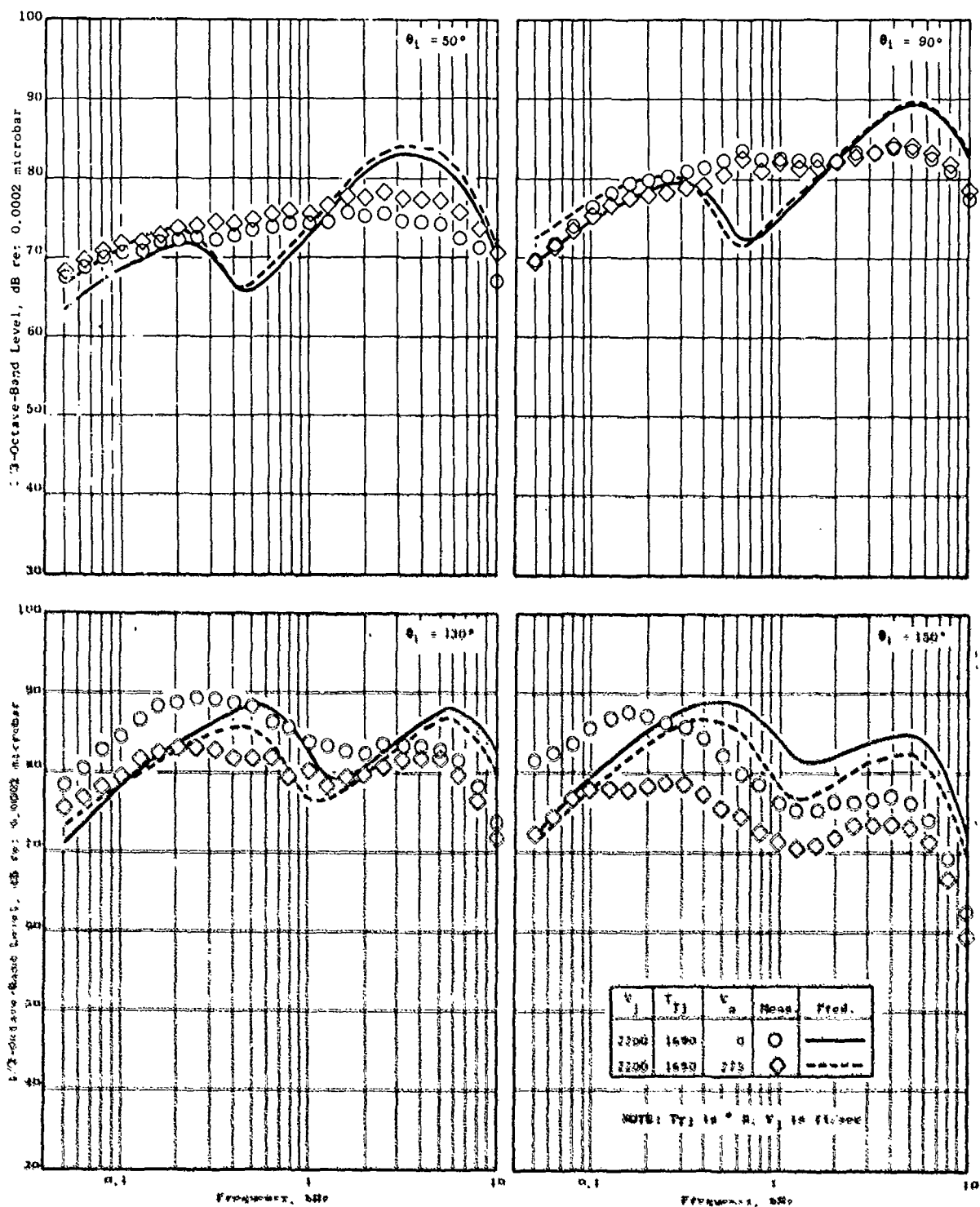


Figure 4-30. Predicted Vs. Measured SPL Spectra for a 104-Tube Suppressor Nozzle; $V_j = 2200$ ft/sec.

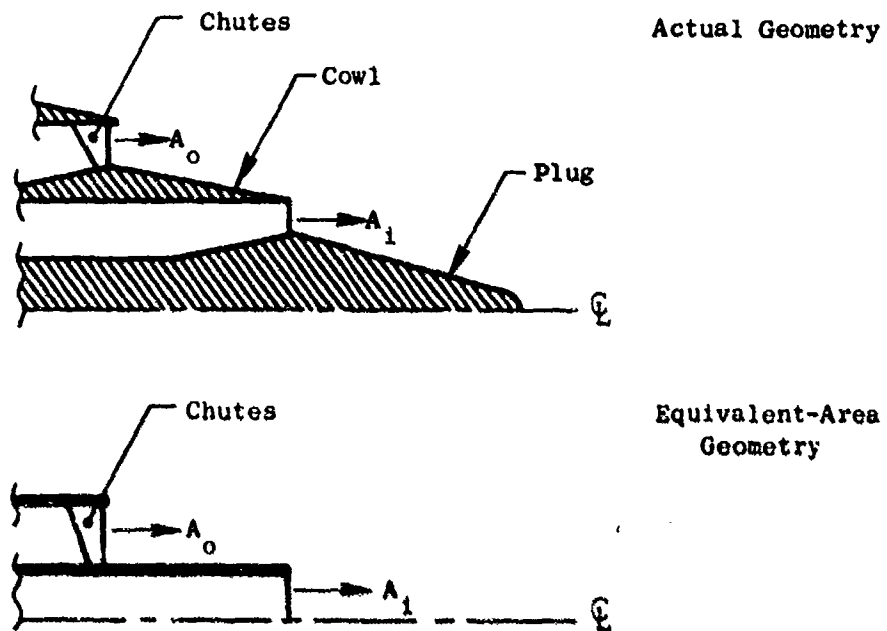


Figure 4-31. Equivalent-Area Modeling of Coannular Plug/Cowl Geometry for 36-Chute, $AR = 2.0$, Dual-Flow, Suppressor Nozzle; $A_0/A_1 = 1.92$.

The normalized PNL versus mass-averaged velocity trends, predicted using the equivalent-area modeling technique, gives excellent agreement with data as shown in Figure 4-14. A comparison of predicted and measured PNL directivity patterns is shown in Figure 4-32 for selected mass-averaged velocity points. The agreement between predicted and measured directivity patterns is good over the entire range of angles and velocities examined.

Examples of SPL spectra data/theory comparisons are shown in Figure 4-33. Again, the prediction model spectra agree well with the measured spectra. The high-velocity prediction ($V_{ma} = 2100$ ft/sec) shown in Figure 4-32 contains an erroneous spectrum at $\theta_i = 150^\circ$ due to a suspected anomaly in the numerical evaluation of the fluid-shielding effects, as discussed in Section 4.3.5. The dashed line drawn between 140° and 160° for this case in Figure 4-32 indicates the expected prediction in absence of this anomaly.

4.3.9 Discussion of Suppression Mechanisms

A thorough discussion of jet noise generation and emission mechanisms has been presented in the Task 2 final report. This discussion has been summarized briefly in Sections 4.1 and 4.2 of the present report. The objective of the present subsection is to identify the relative roles these mechanisms play in the suppression of jet noise.

The Task 2 M*G*B aeroacoustic model, as discussed in Section 4.2, is based on four noise-generation/emission mechanisms:

1. Turbulent-mixing noise generation
2. Convective amplification
3. Fluid shielding
4. Shock-cell broadband radiation.

The preceding subsections have demonstrated that the present mathematical model representation of these mechanisms (collectively) yields a fairly accurate prediction of the far-field acoustic characteristics of turbulent jets, for a wide variety of shapes and flow conditions. It is therefore of interest to evaluate how the individual mechanisms combine to yield the far-field result; more importantly, the changes which occur in these mechanisms due to the addition of a suppressor to a baseline nozzle are of interest.

A parametric computer study was performed to evaluate the relative contributions of the above four mechanisms to the far-field noise for both a baseline conical nozzle and a typical, high-suppression, multiclement nozzle. Configuration 4 (the 36-chute, $AR = 2.0$, turbojet suppressor) was chosen for this study as representative of a high-element number, high-suppression (10-12 PNdB), exhaust system. A typical static takeoff condition of $V_j = 2400$ ft/sec and $T_{Tj} = 1630^\circ R$ was selected for evaluation. Both the baseline

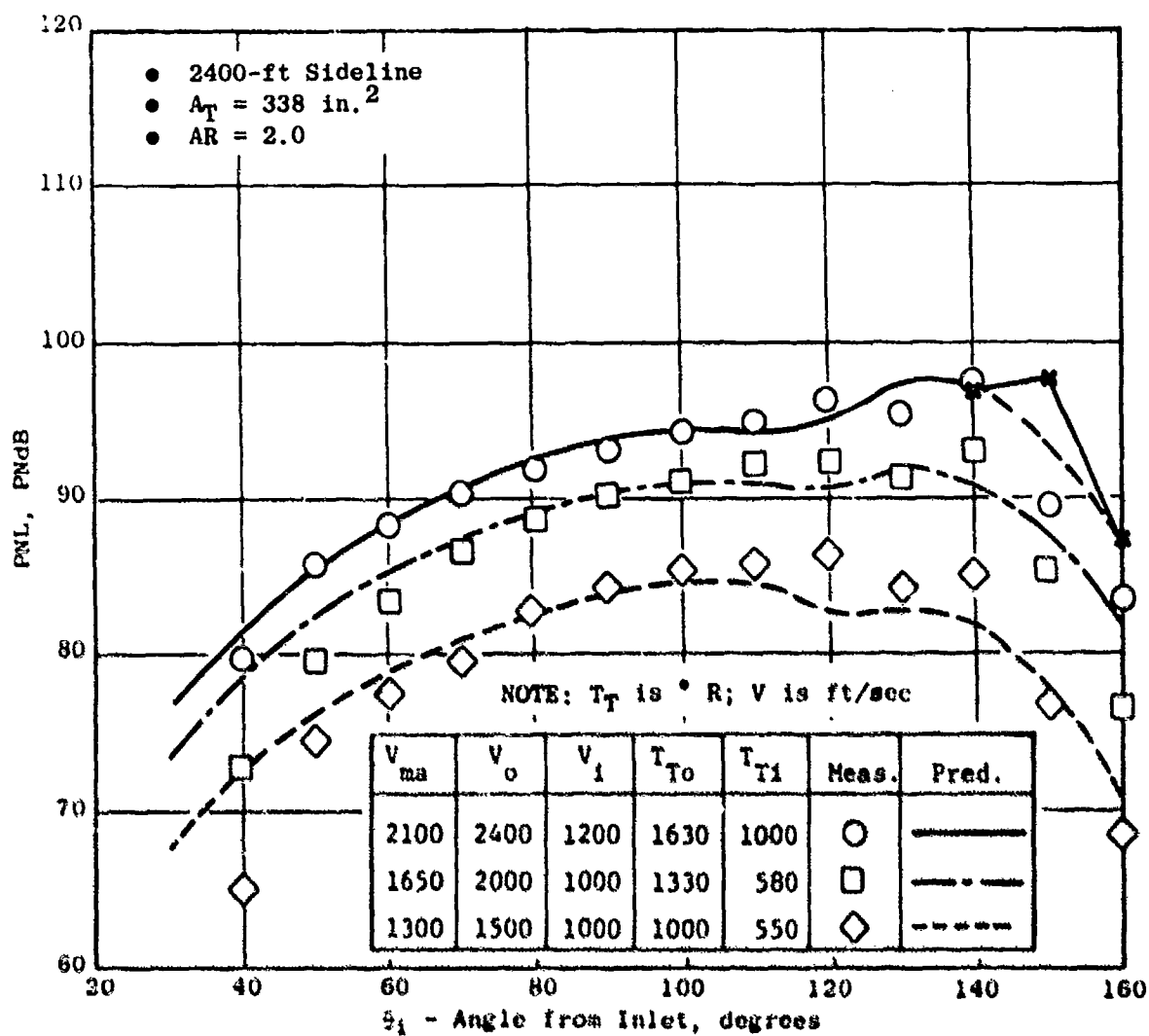
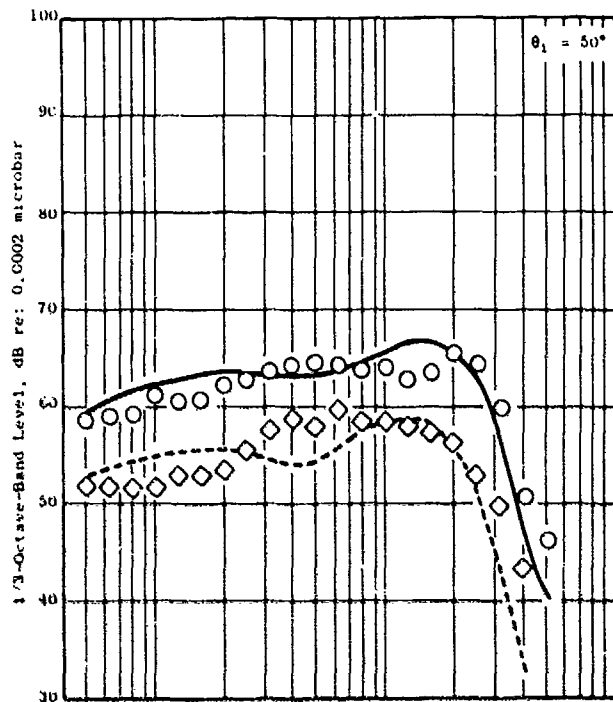


Figure 4-32. Predicted Vs. Measured PNL Directivity for a 36-Chute, Dual-Flow Suppressor.



- AR = 2.0
- $A_0/A_1 = 1.92$

V_{in}	V_o	V_i	T_{To}	T_{Ti}	Mass.	Pred.
2100	2400	1200	1630	1000	○	—
1300	1500	1000	1000	550	◇	- - -

NOTE: T_T is °R; V is ft/sec

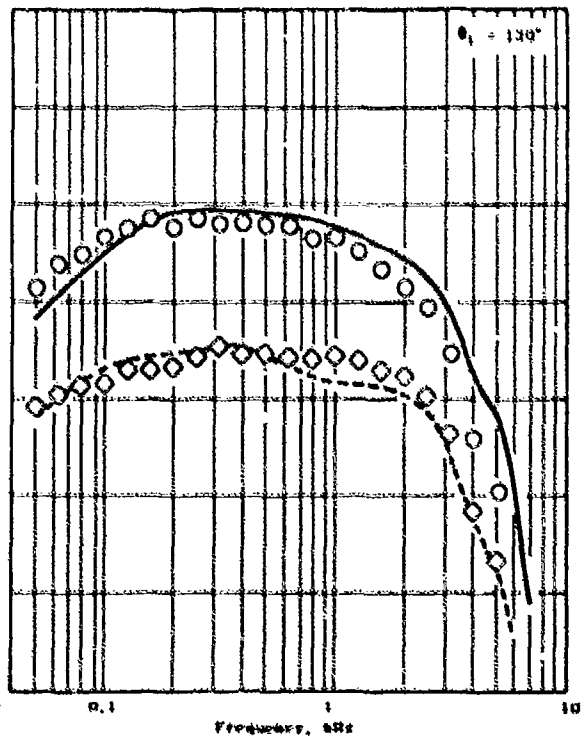
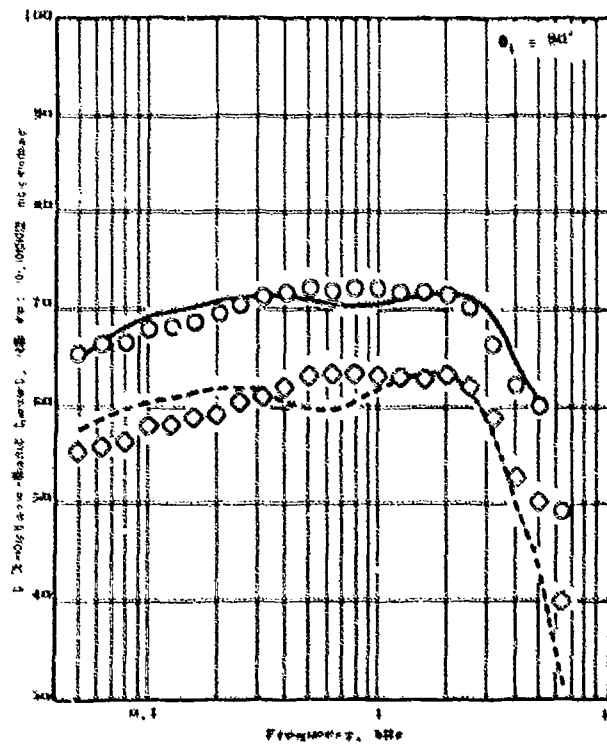


Figure 4-33. Predicted Vs. Measured SPL Spectra for a 36-Chute, Dual-Flow Suppressor.

conical nozzle and the 36-chute nozzle exit areas were 338 in.². Noise characteristics were evaluated on a 2400-ft sideline.

The computations were performed in four modes, as follows:

- (a) Complete acoustic calculation
- (b) As in (a), but shock-cell noise omitted
- (c) As in (b), but fluid shielding omitted
- (d) As in (c), but convective amplification omitted.

For the chute suppressor, mode (a) was omitted since the ability to model multichute nozzle shock-cell noise is not yet established. The difference in noise levels between modes (a) and (b) is a measure of the shock-cell noise contribution to the total jet noise signature. The difference in noise levels between modes (b) and (c) is a measure of the influence of fluid shielding on the jet noise. Finally, the difference in levels between modes (c) and (d) indicates the amount of convective amplification that is present in the jet.

The results of the above series of computations are summarized in Figures 4-34 through 4-37. Figure 4-34 shows the PNL directivity patterns for the different prediction modes. Also shown are the measured data, for reference, which should be compared with mode (a) predictions (mode b for the chute nozzle). Figures 4-35 through 4-37 display the corresponding spectra shapes (1/3-octave SPL) at $\theta_i = 50^\circ$, 90° , and 130° respectively. The measured spectra are also shown in Figures 4-35 through 4-37 for reference.

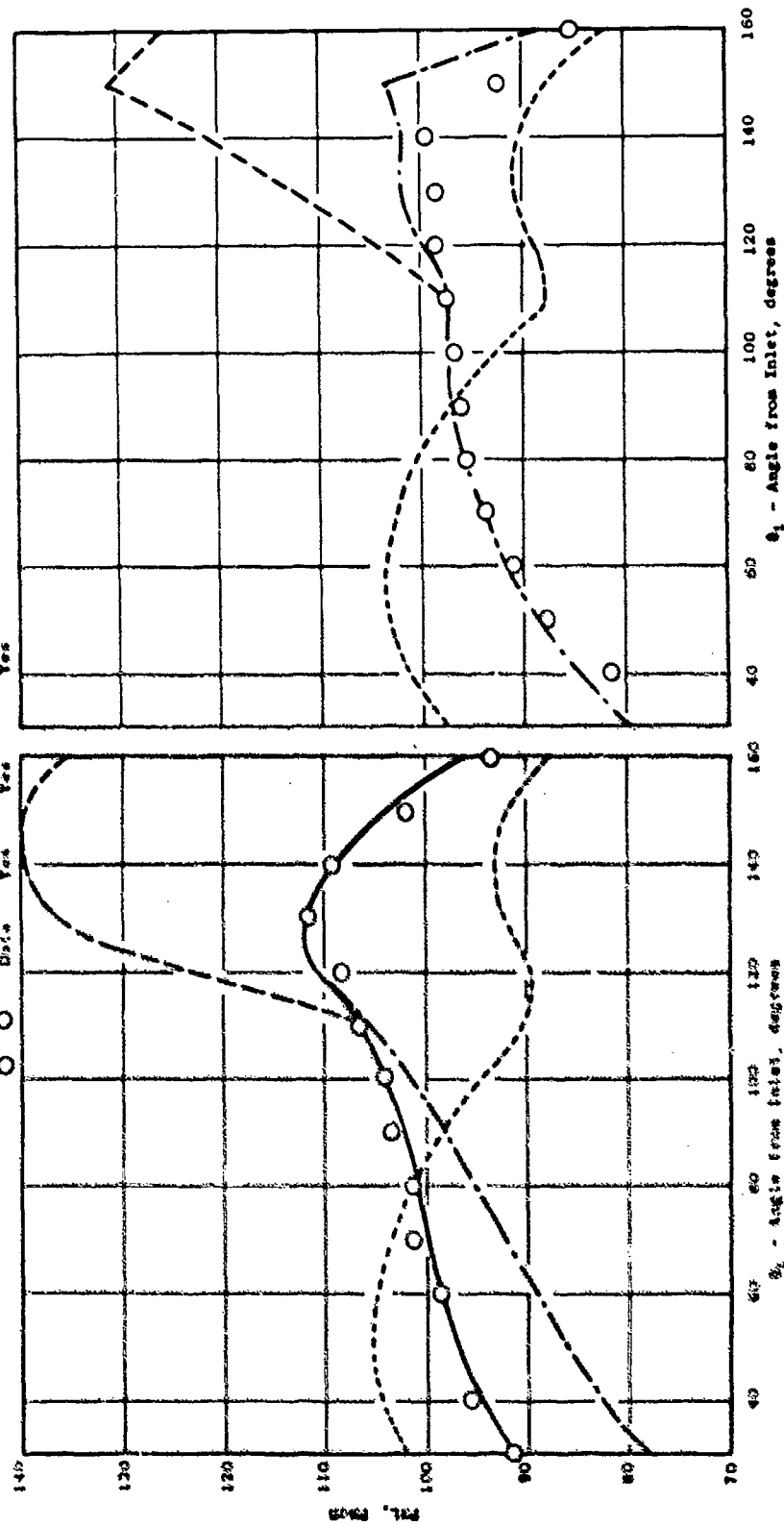
Considering the conical nozzle PNL directivity patterns, Figure 4-34a, it is observed that shock-cell noise contributes substantially to the total noise in the forward quadrant, $\theta_i < 90^\circ$. This can be seen by noting the difference between mode (a) and mode (b) predictions. There is no contribution of shock noise close to the jet axis ($\theta_i > 120^\circ$) because mode (a) and (b) predictions are identical in this region. There is no fluid shielding for observer angles less than about 110° based on comparing mode (b) and (c) predictions. For $\theta_i > 110^\circ$, however, shielding effects become quite substantial, on the order of 30 PNdB. Eddy-convection effects are also large; they increase the noise in the aft quadrant ($\theta_i > 90^\circ$) and reduce the noise in the forward quadrant ($\theta_i < 90^\circ$). This effect is apparent from comparing mode (c) and (d) predictions.

The mode (d) prediction shown in Figure 4-34a represents the basic turbulent-mixing noise in absence of convection and fluid-shielding effects. It possesses a basic nonconstant directivity pattern dictated by the weighted summation of various quadrupole types composing the turbulent eddies. This basic pattern is only symmetric about $\theta_i = 90^\circ$ when the local flow Mach number is zero because the quadrupole weighting factors are a function of local Mach number and bias the radiation toward the forward quadrant. For example, if the flow Mach number M is set equal to zero and $C/C_0 = C = 1.0$,

Model Shield Convect.

—	a	Yes	Yes	Yes
—	b	No	Yes	Yes
—	c	No	No	Yes
—	d	No	No	No
○	Data	Yes	Yes	Yes

- Static
- 2400-ft Sideline
- $V_j = 2400$ ft/sec
- $A_j = 338$ in.²



a. Conical Nozzle

b. 35-Center, AR = 2.0 Nozzle.

Figure 4-34. Relative Contributions of Noise Mechanisms to PNL Directivity.

	Mode	Shock	Shield.	Convec.	
————	a	Yes	Yes	Yes	• Static
- - - -	b	No	Yes	Yes	• 2400-ft Sideline
— · — ·	c	No	No	Yes	• $V_j = 2400$ ft/sec
- - - -	d	No	No	No	• $A_T = 338$ in. ²
○ ○	Data	Yes	Yes	Yes	

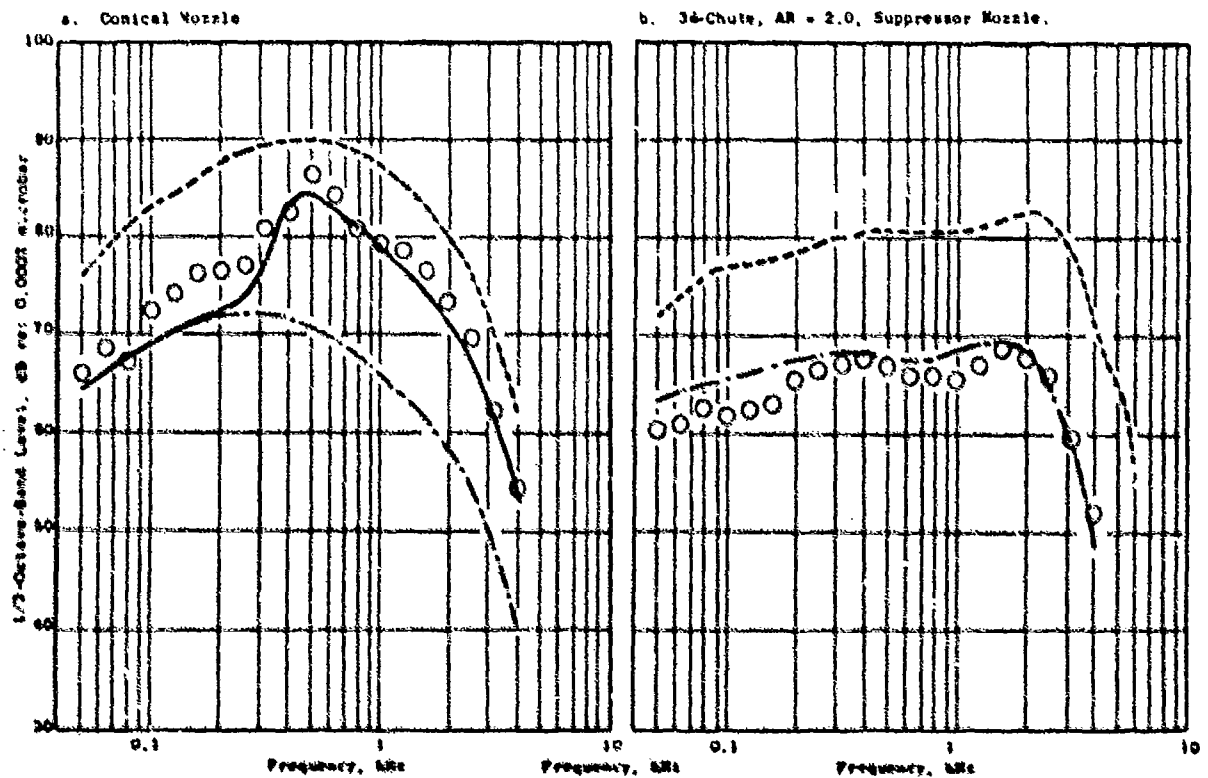


Figure 4-35. Relative Contributions of Noise Mechanisms to SPL Spectra at $\theta_1 = 50^\circ$.

	Mode	Shock	Shield.	Convec.
————	a	Yes	Yes	Yes
— · — · —	b	No	Yes	Yes
- - - - -	d	No	No	No
○ ○	Data	Yes	Yes	Yes

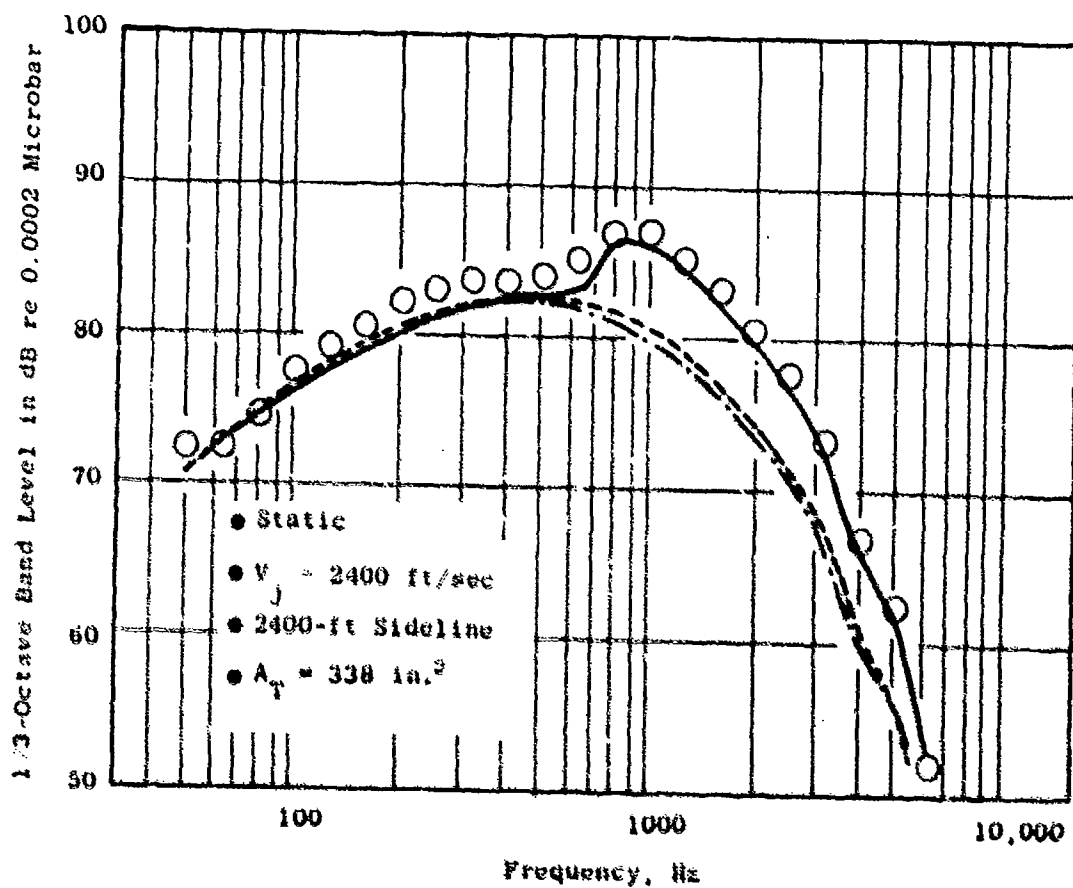


Figure 4-36. Relative Contributions of Noise Mechanisms to SPL Spectra at $\theta_1 = 90^\circ$, Conical Nozzle.

	Mode	Shock	Shield.	Convec.	
————	a	Yes	Yes	Yes	• Static
— · — ·	b	No	Yes	Yes	• 2400-ft Sideline
-----	c	No	No	Yes	• $V_j = 2400$ ft/sec
- - - -	d	No	No	No	• $A_j = 338$ in. ²
○ ○	Data	Yes	Yes	Yes	

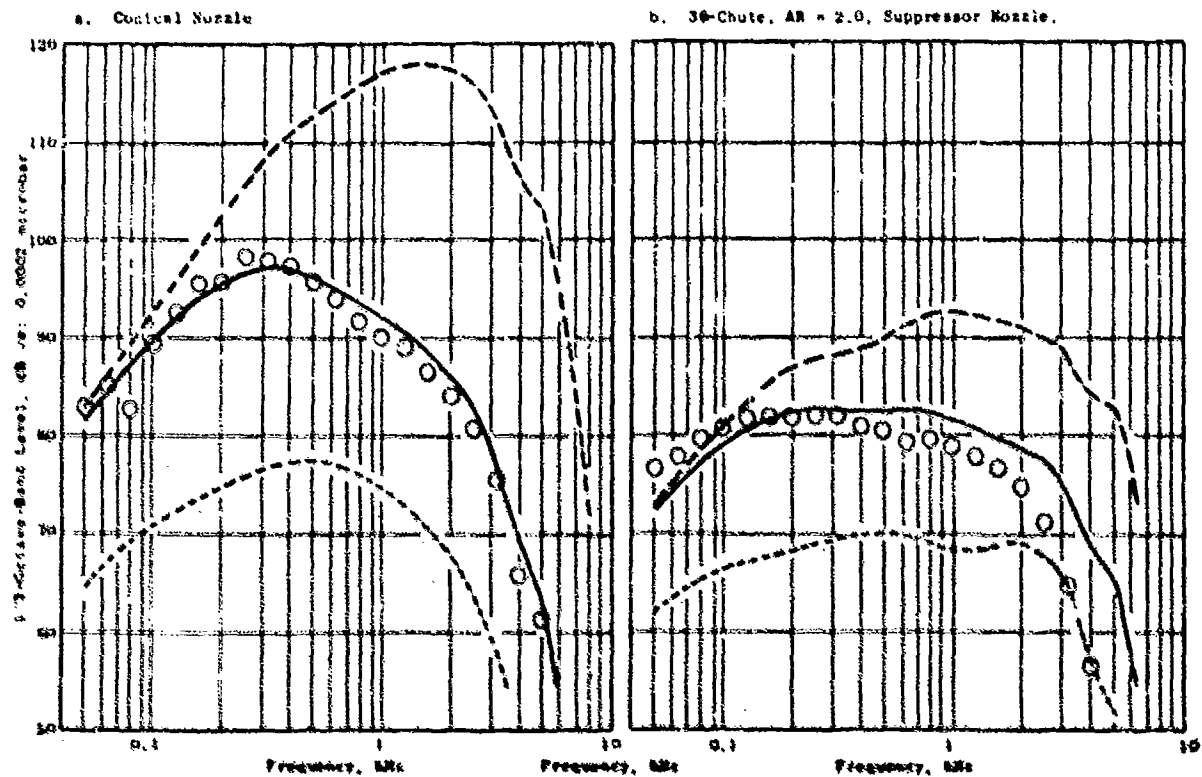


Figure 4-37. Relative Contributions of Noise Mechanisms to SPL Spectra at $\theta_j = 130^\circ$.

Equation (4-6) shows that the shielding function g^2 reduces to $\sin^2\theta$. Hence, the mean square sound pressure from Equation (4-9) will become independent of θ . The results shown in Figures 4-34 through 4-37 for mode d, therefore, do contain fluid-sound interaction effects. Only eddy convection effects (C) and the exponential shielding effects (δ^2) have been suppressed.

The corresponding PNL directivity patterns for the 36-chute suppressor are shown in Figure 4-34b. The trends discussed above the conical nozzle are qualitatively similar for the 36-chute nozzle, with the exception of the shock-cell noise contribution. The predictions were made neglecting shock-cell noise (mode b), and yet the predictions agree with the data, as Figure 3-34b shows. This suggests that shock-cell noise may not be a significant feature of multichute nozzles. It also appears, from the results shown in Figure 3-34b, that neither convection effects nor fluid-shielding effects are as strong as for the conical nozzle.

The breakdown of mechanisms for a typical, forward-quadrant angle of $\theta_i = 50^\circ$ is shown in Figure 4-35. No shielding occurs at this angle; therefore, the mode (c) results are omitted, as they are identical to the mode (b) results. The conical nozzle results, Figure 4-35a, shows an interesting counteraction among the mechanisms. The basic mixing-noise spectrum, mode (d), yields a high noise level, much higher than the measured level. The convection effect is to Doppler-shift and drop this spectrum to a level significantly lower than the data (except at very low frequencies), as indicated by the mode (b) prediction. Finally, the addition of the shock-cell noise spectrum raises the spectrum back up to the measured level at middle-to-high frequencies.

The corresponding 36-chute, 50° spectrum results are shown in Figure 4-35b. The good agreement between the mode (b) spectrum prediction and the measured spectrum substantiates the implication drawn from Figure 4-34b: Shock-cell noise is not a significant source for multichute suppressors. Again the effect of convection is to reduce the level and Doppler-shift the spectrum to lower frequencies.

The breakdown of mechanisms for the one-third-octave SPL spectrum at $\theta_i = 90^\circ$ is shown in Figure 4-36. Only the conical-nozzle results are shown for the following reasons. Fluid-shielding effects are absent at 90° , and convection effects are less than 0.5 dB throughout the frequency range. The shock-cell noise was not computed for the chute nozzle; thus, the only significant contribution at 90° for the chute nozzle is the basic, mixing-noise spectrum (see Figure 4-23). The results in Figure 4-36 illustrate the diminishing effect of shock-cell noise with increasing θ_i (compare to Figure 4-35a) and the almost negligible effect of convection.

Near the peak-noise angle, $\theta_i = 130^\circ$, convection effects again become significant. They produce a dramatic amplification of the mixing noise as the results in Figure 4-37 show. Another counteraction of mechanisms occurs at this angle, involving the competing effects of convection and fluid shielding. The basic, mixing-noise spectrum is much lower than the measured level, as shown in Figure 4-37a, mode (d). The effect of convection is to increase the levels by as much as 40-50 dB at high frequencies. The effect of shielding, however, is to reduce the noise levels by 20 to 30 dB at high frequencies, such that the net noise levels agree with the measured levels.

It is interesting to note that the convection effect Doppler-shifts the basic, mixing-noise spectrum to higher frequencies as would be expected from classical notions of moving-source acoustics. However, the fluid-shielding effects, which increase with increasing frequency, attenuate the high-frequency portion of the convected spectrum to such a large extent that the resulting spectrum peaks at a much lower frequency, lower than even the basic unconvected spectrum peak. This is the explanation for the observed "reverse Doppler shift" at angles close to the jet axis.

The competing influences of convection and fluid shielding are also evident in the 36-chute nozzle predictions shown in Figure 4-37b. The magnitudes of these effects are considerably smaller than those exhibited by the conical nozzle. For example, at 2000 Hz, the convective amplification is 22 dB for the chute nozzle, compared to 48 dB for the conical nozzle at the same frequency. Similarly, the fluid-shielding attenuation is only 12 dB at 2000 Hz for the chute nozzle, compared to 31 dB attenuation for the conical nozzle.

The various mechanisms can be isolated explicitly by examining the differences between the various prediction curves shown in Figures 4-34 through 4-37. First, the total PNL suppression as a function of θ_i is the difference between the conical and chute nozzle total noise PNL directivity patterns. This can be compared with measured PNL suppression and is shown in Figure 4-38. The chute nozzle prediction error at 150° (see Section 4.3.6) has been retained in these results. The predicted total PNL suppression is seen to compare well with the measured suppression.

From the results given in Figures 4-34 through 4-37, it can be concluded that the multichute nozzle almost completely suppresses the static shock-cell noise so as to permit the mixing noise to dominate the forward-quadrant spectra. The static shock-noise suppression is then approximated by the difference between mode (a) and (b) conical nozzle predictions. This estimated shock-cell noise suppression is also shown in Figure 4-38. The shock-cell noise suppression is seen to be higher than the total predicted suppression in the forward quadrant; hence some other mechanism is providing negative suppression, i.e., is increasing the PNL.

The suppression of convective amplification can be computed by first calculating the convective amplification for each nozzle [PNL(c) - PNL(d)], and then subtracting the chute-nozzle result from the conical-nozzle result. The convective-amplification suppression is shown in Figure 4-38. Note that it is negative in the forward quadrant; this explains why the shock-noise suppression is greater than the total, net suppression.

In a similar fashion, the difference between conical-nozzle fluid-shielding attenuation and 36-chute-suppressor fluid-shielding attenuation has been computed from the results shown in Figure 4-34, and this difference is shown in Figure 4-38. From this result, it is apparent that a multi-element suppressor exhibits reduced fluid-shielding effects relative to a conical nozzle; i.e., part of the beneficial effect of fluid shielding is lost by the addition of a suppressor.

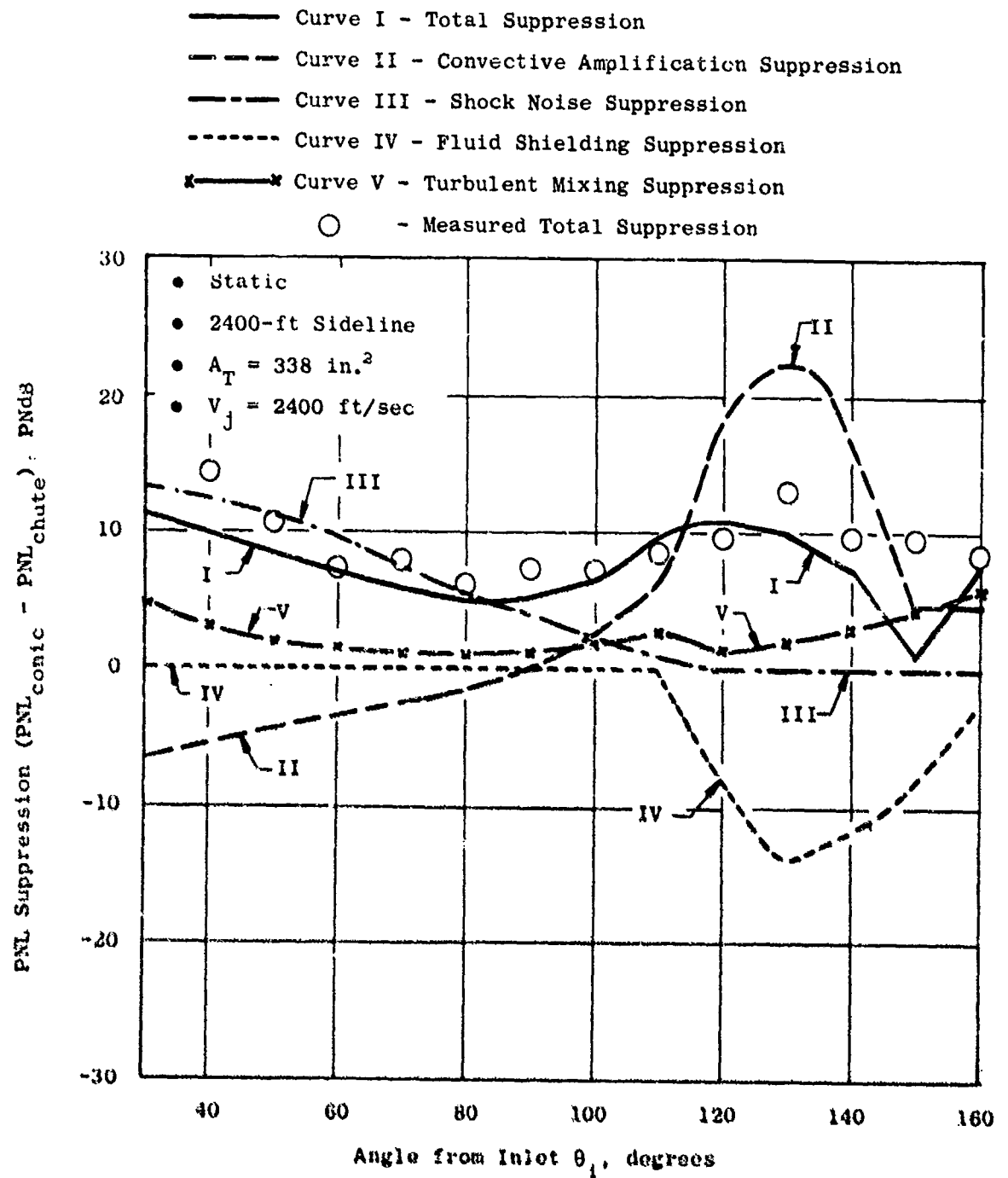


Figure 4-38. PNL Suppression Composition for a 36-Chute, AR = 2.0, Suppressor Nozzle.

Finally, the suppression of basic, turbulent-mixing noise generation has been evaluated by subtracting the mode (d) prediction for the chute nozzle from the conical nozzle, mode (d) prediction. This result is also shown in Figure 4-38. This basic mixing-noise suppression is seen to be quite small, from 1 to 5 dB over the range of angles shown, which is contrary to historical conceptions of how multielement suppressors suppress jet noise. The multichute suppressor in fact generates approximately the same total mixing noise as the equivalent conical nozzle but redistributes the noise to higher frequencies. This conclusion is dramatically illustrated in Figure 4-39, where the basic, mixing-noise spectra (mode d computations) for the two nozzles are compared. Also shown are these same spectra with the atmospheric (air) attenuation removed, i.e., the lossless spectra. The multichute lossless spectrum is seen to have about the same peak level as the conical-nozzle lossless spectrum but at a much higher frequency. The ratio of chute-nozzle peak-noise (lossless) frequency to conical-nozzle peak-noise (lossless) frequency is about 6:1. This is precisely the ratio of conical-nozzle diameter to chute-element equivalent-area diameter.

The major conclusions to be drawn from the above example are that: (1) the primary mechanism responsible for static noise suppression in the forward quadrant is shock-cell noise reduction; (2) the basic mixing-noise generation is not suppressed, only redistributed to higher frequencies where atmospheric attenuation can have a more pronounced effect on the spectrum shape, and (3) the observed suppression in the aft quadrant is primarily a result of reduced convective amplification, offset somewhat by a loss in fluid shielding. This delicate balance between convection and shielding effects in the aft quadrant is very difficult to predict accurately because these two effects are of large magnitude but opposite in sign. This is dramatically illustrated in Figure 4-40, where the convection and shielding effects for each of the two nozzles are compared.

The reduction in shock-cell noise produced by a multichute suppressor can be explained by the fact that breaking up a large, round jet into very small, discrete, rectangular jets will cause the shock-cell formation to be dissipated much more rapidly. The shock-cell spacings and cross-sectional dimensions will be much smaller, and the cells are likely to be fewer in number. The resulting broadband radiation is therefore likely to be much lower in level and higher in frequency than that for a conical nozzle.

The conclusion that the total generated mixing noise is not significantly different for a multichute suppressor is explained by the fact that the chute-nozzle mixing-layer perimeter close to the nozzle exit plane is considerably larger than an equivalent-area conical-nozzle perimeter. The high-frequency noise generated in the initial shear layers should therefore be higher by the ratio of perimeters, provided the premerged portion of the chute mixing layers have approximately the same turbulence characteristics. Once the chutes have merged, a large axisymmetric jet forms which has a substantially lower velocity than the exit value; therefore, the low-frequency noise levels should be lower than the corresponding conical-nozzle levels.

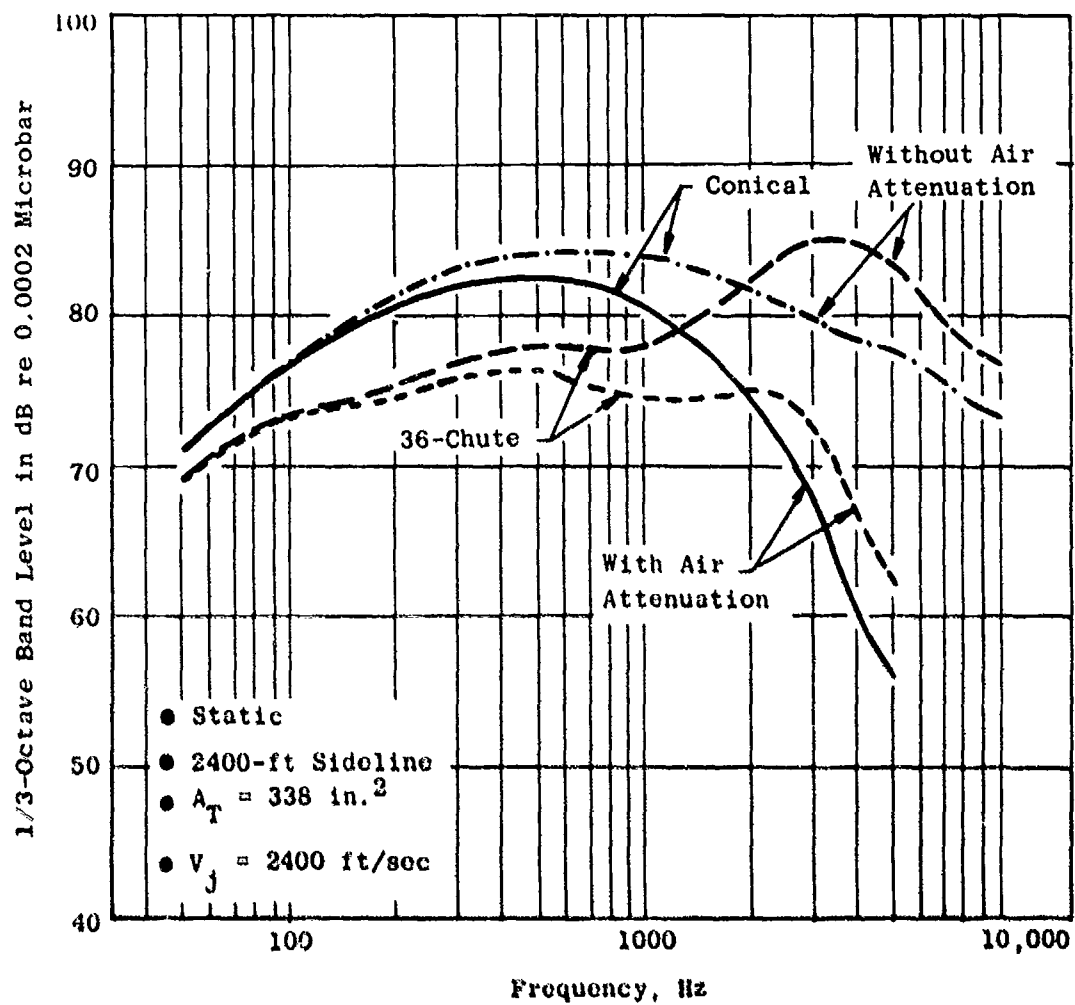


Figure 4-39. Comparison of Predicted, Basic, Turbulent-Mixing Noise Spectra at $\theta_1 = 90^\circ$ for a Conical and a 36-Chute Nozzle.

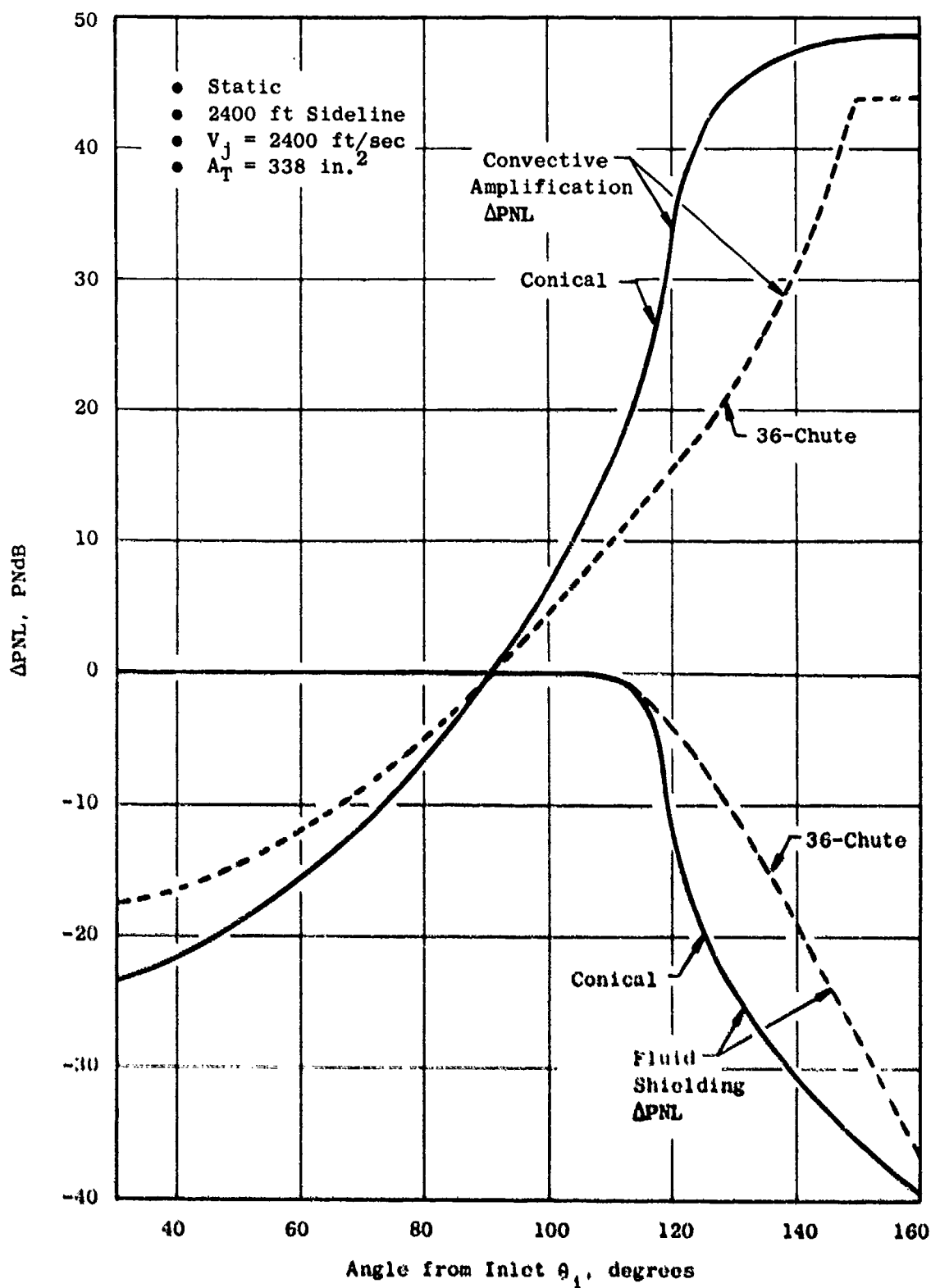


Figure 4-40. Modification of Basic Mixing-Noise PNL by Convective Amplification and Fluid Shielding.

The reduction in convection effects exhibited by a multichute nozzle is the result of lower eddy-convection velocities. The rapid plume mean-velocity decay exhibited by a multichute nozzle suggests that the majority of the noise-producing turbulent eddies in the plume are convecting downstream at a substantially lower velocity than in a conical nozzle.

The reduced fluid-shielding effects characteristic of a multichute nozzle can also be related to the rapid plume velocity (and temperature) decay. Fluid shielding, as discussed in Section 4.1, increases with increasing plume flow velocity and temperature; therefore, the lower velocity and temperature levels resulting from the rapid chute element mixing provide less fluid shielding than an equivalent-area conical nozzle.

From the above discussion, it can be concluded that the best suppression is achieved by producing the most rapid plume decay. This conclusion is supported by the area-ratio study results shown in Figure 4-24 and discussed in Section 4.3.5. The effect of chute area ratio (at high jet velocities) is to reduce the noise as area ratio is increased. The predicted peak axial mean-velocity decay for the three area ratios examined is shown in Figure 4-41. The effect of increasing area ratio is to produce more rapid plume decay, in concert with the observed (and predicted) improved noise suppression.

In the above studies, the effects of base pressure variations on nozzle plume aerodynamics and acoustic characteristics have been ignored. It is suspected that multielement nozzles (e.g., the 36-chute, $AR = 1.5$, turbojet nozzle) with area ratios less than two have significant base-pressure reduction (relative to ambient pressure). Large, base-pressure effects have also been measured on the 104-tube nozzle. The effects of base-pressure variations on the aeroacoustic characteristics of suppressors would be a useful future study.

4.3.10 Mean Velocity Decay Characteristics Data/Theory Comparisons

Having established a direct relationship between plume-velocity-decay characteristics and noise suppression, it is of interest to examine the ability of the aeroacoustic model to predict the observed changes in plume-decay rate as a function of nozzle geometry. A comparison of the predicted, peak, mean-velocity (maximum mean velocity at any given axial distance), axial distributions was made for the seven nozzles listed in Table 4-1. Laser Velocimeter (LV) measurements taken on these configurations were analyzed to evaluate the peak-velocity-decay rates. The results of these comparisons are shown in Figures 4-42 through 4-48 for Configurations 1-7, respectively.

The conical nozzle comparisons (Figures 4-42) show that the predicted decay is too rapid between $X/D_{eq} = 3$ and $X/D_{eq} = 10$. This is due in part to the external, supersonic expansion which takes place for an underexpanded jet and is not accounted for in the plume-mixing calculation. The Reichardt method also tends to predict more rapid diffusion in the potential core region than actually occurs, as discussed in the Task 2 final report.

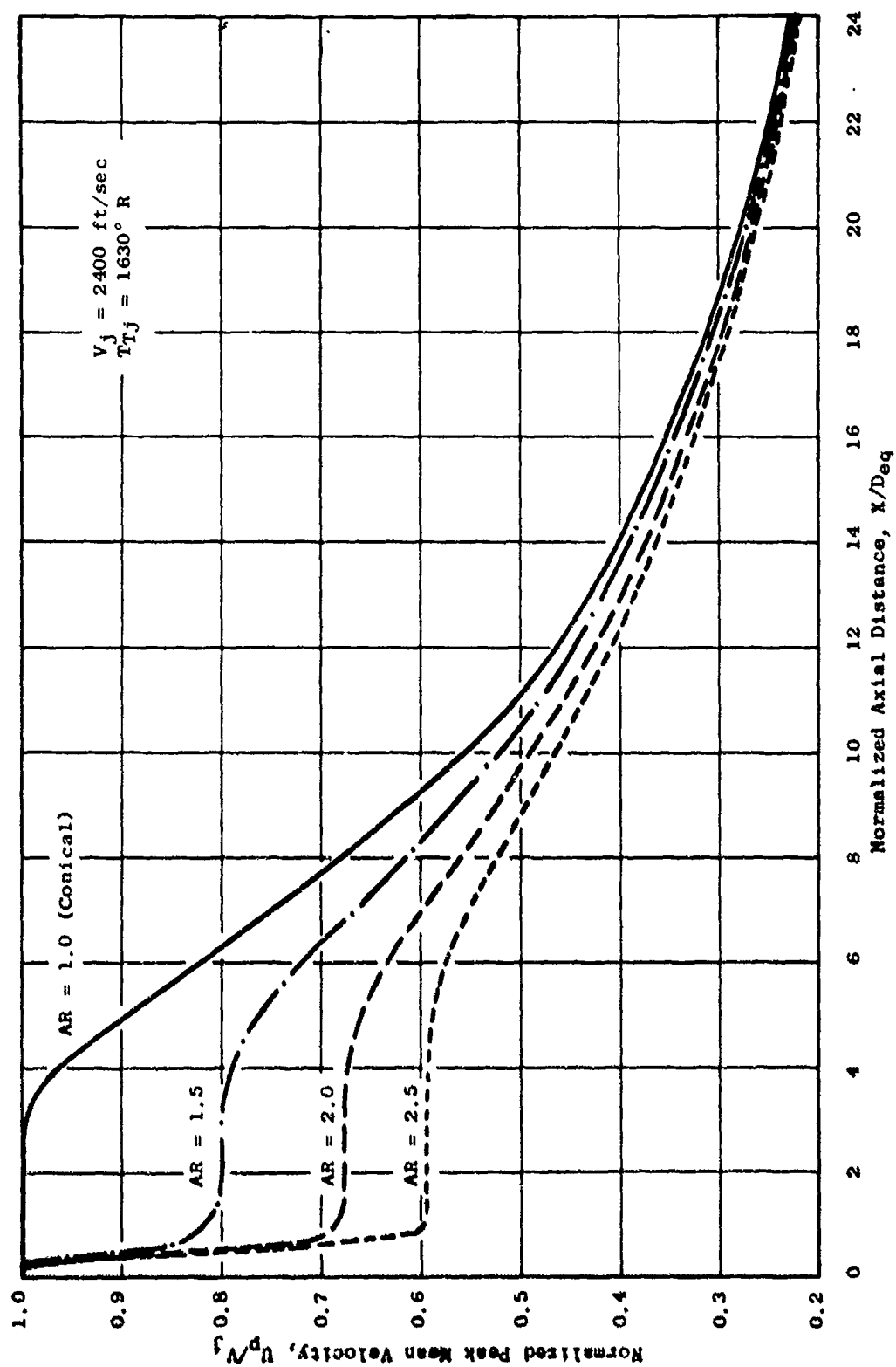


Figure 4-41. Comparison of Mean-Velocity Decay Rates for a 36-Chute Nozzle.

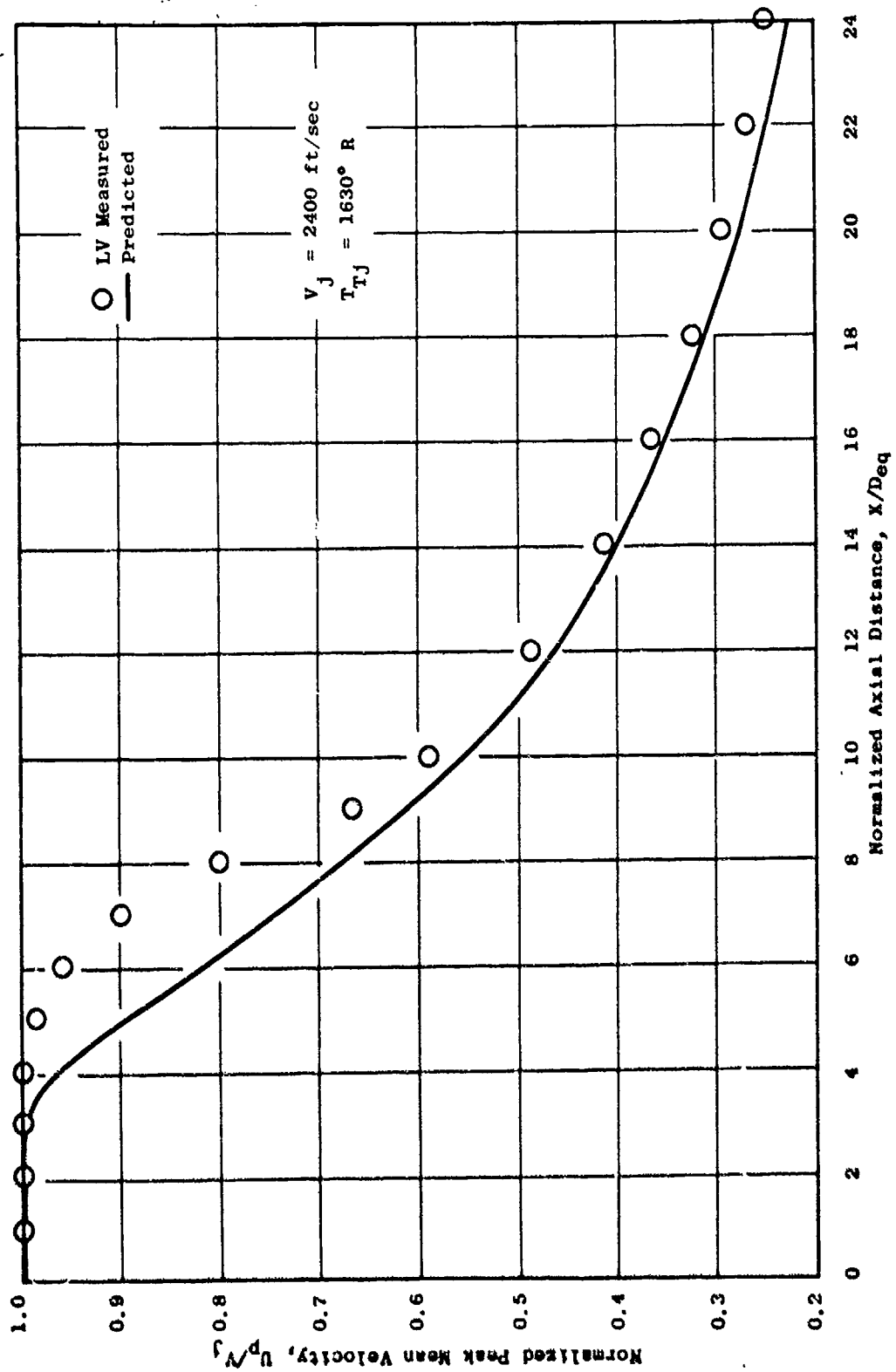


Figure 4-42. Predicted Vs. Measured Mean-Velocity Axial Decay; Conical Nozzle.

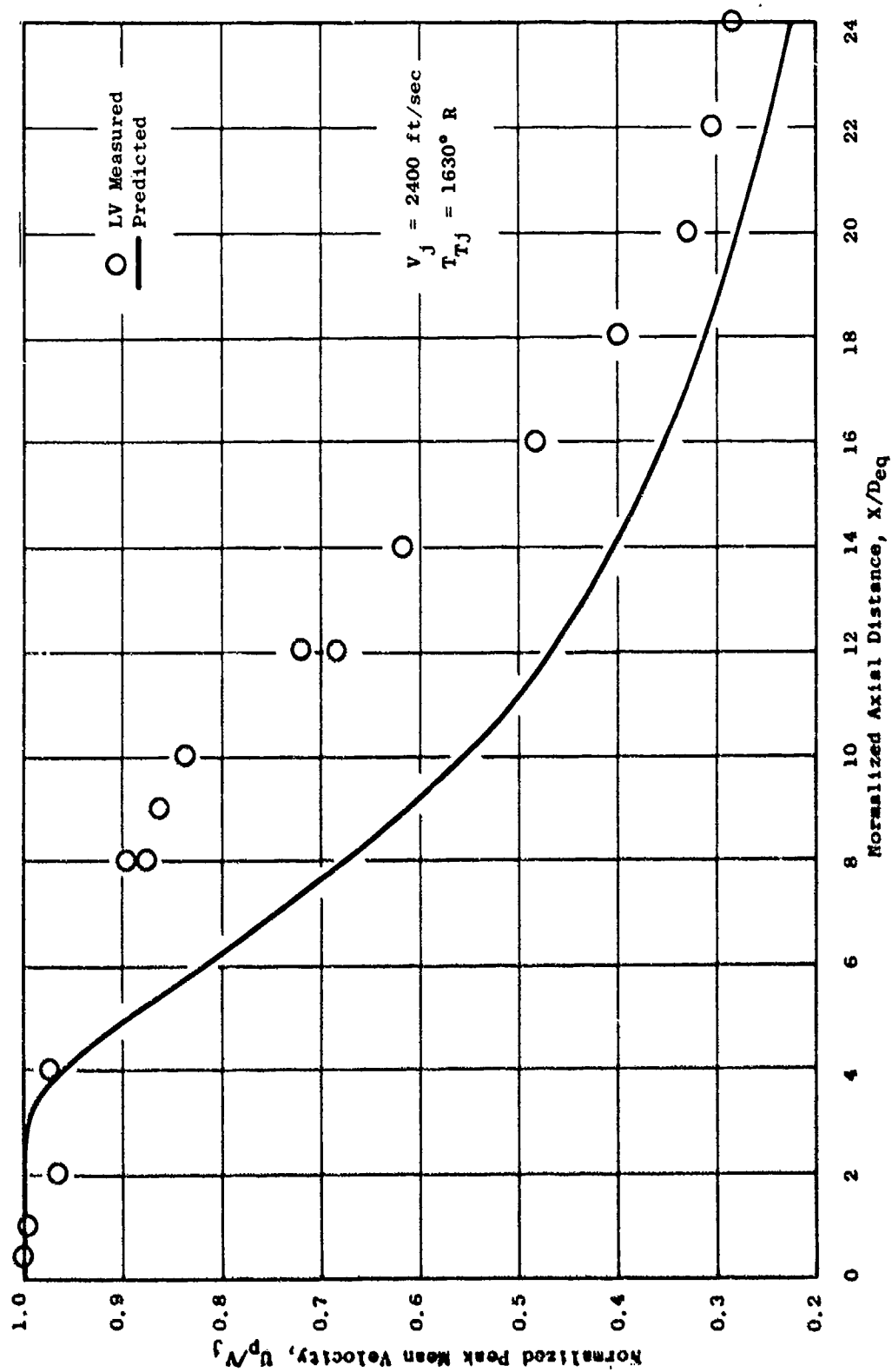


Figure 4-43. Predicted Vs. Measured Mean-Velocity Axial Decay; Convergent, Plug Nozzle.

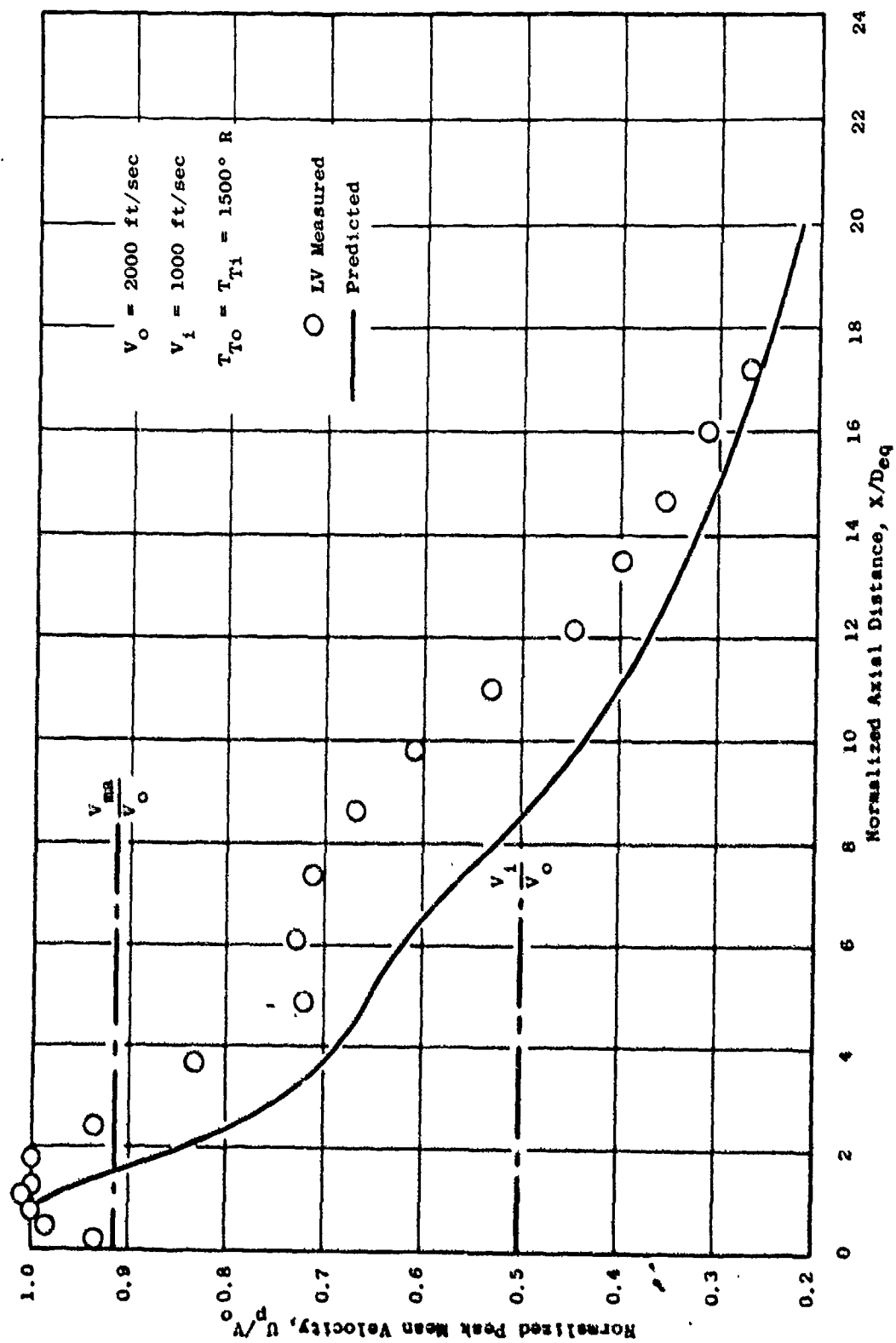


Figure 4-44. Predicted Vs. Measured Mean-Velocity Axial Decay; Coannular Nozzle.

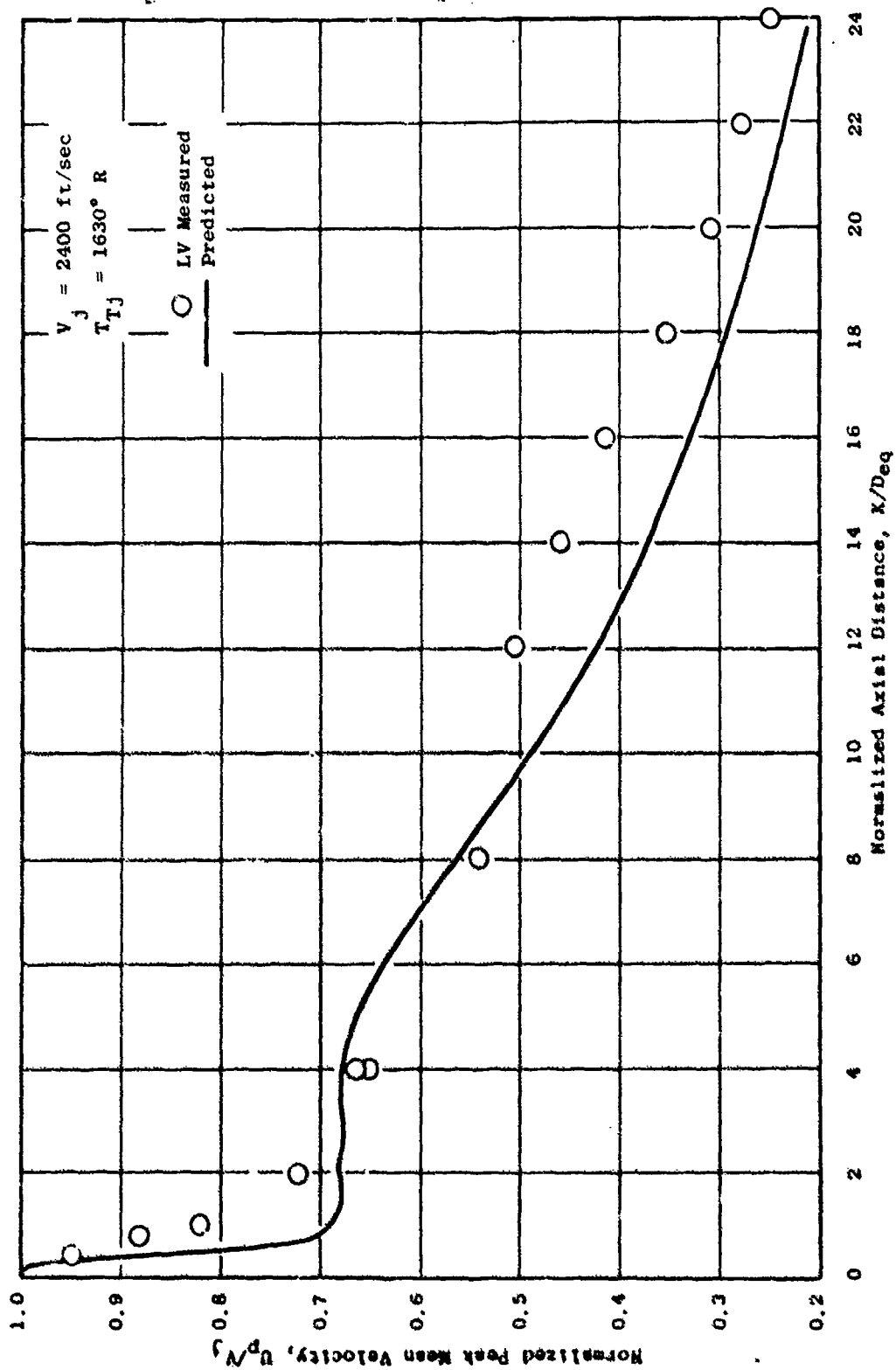


Figure 4-45. Predicted V_s . Measured Mean-Velocity Axial Decay; 36-Chute Nozzle.

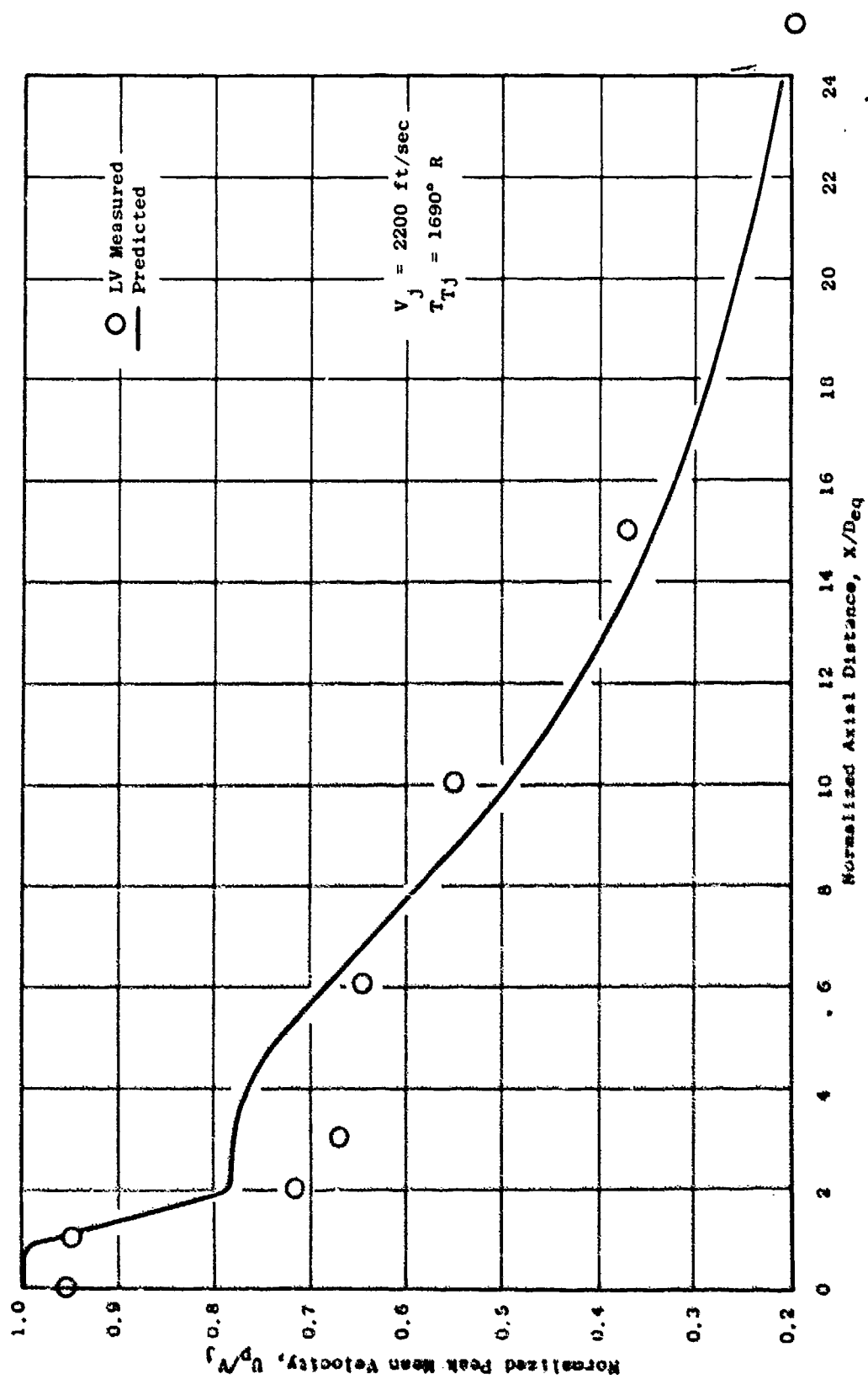


Figure 4-46. Predicted V_s . Measured Mean-Velocity Axial Decay; 8-Lobe Nozzle.

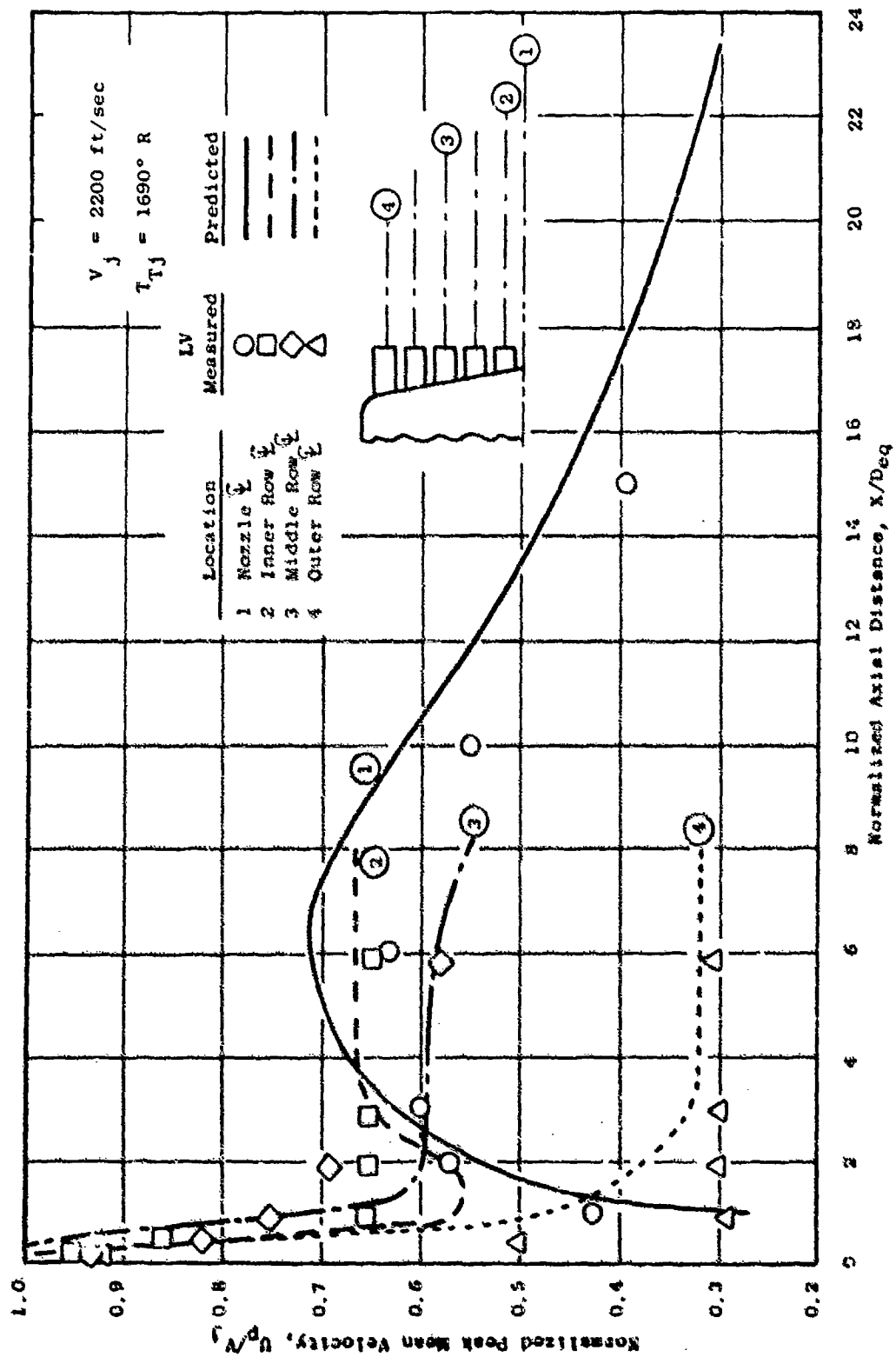


Figure 4-47. Predicted V_1 . Measured Mean-Velocity Axial Decay; 104-Tube Nozzle.

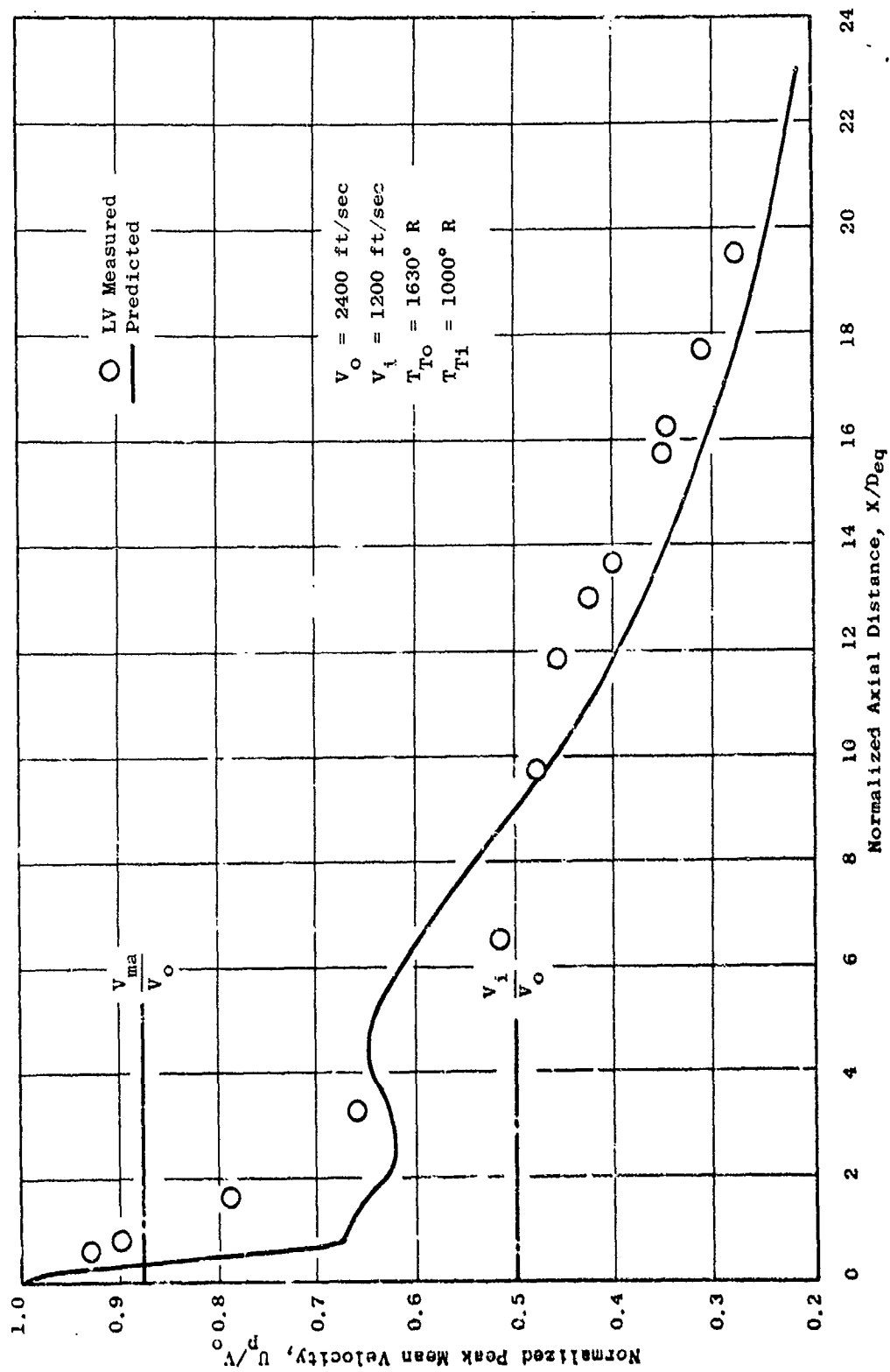


Figure 4-48. Predicted Vs. Measured Mean-Velocity Axial Decay; 36-Chute, Dual-Flow Nozzle.

The plug nozzle comparison (Figure 4-43) shows that the predicted decay is much more rapid than the measured decay. Again, the neglect of external, supersonic expansion is partially responsible for this discrepancy. Additional reasons for the poor agreement are: (1) the neglect of guided expansion along the plug surface, and (2) a possible inadequate modeling of the plug effects at high radius ratios. Predictions of plug nozzle flow-field characteristics for a low (0.67) radius-ratio, subsonic jet showed good agreement with LV measurements, as presented and discussed in the Task 2 final report.

The coplanar, coannular ($A_0/A_1 = 2.0$) nozzle, velocity-decay comparison (Figure 4-44) also show that the predicted decay is more rapid than the measured decay. Supersonic external expansion effects are, again, partially responsible for the discrepancies. The shape of the predicted decay curve is similar to the measured one, and a downstream shift of the predicted curve by approximately two diameters would give reasonable agreement with the data.

The 36-chute, $AR = 2.0$, turbojet-nozzle, velocity-decay comparisons (Figure 4-5) show reasonably good agreement between predictions and measurements for $X/D_{eq} < 8$. The downstream, measured-velocity levels ($X/D_{eq} > 8$) are somewhat higher than the predicted levels. No explanation of this discrepancy has been identified, but it is speculated that improper modeling of the plug effects at high radius ratio may be contributing to this problem since this nozzle has a large plug.

The 8-lobe, suppressor-nozzle, velocity-decay comparisons (Figure 4-46) show reasonably good agreement between prediction and measurements. The 104-tube-nozzle comparisons (Figure 4-47) also show good agreement between predictions and measurements. Axial-decay trends at several radial locations corresponding to the various tube-row centerlines are shown for comparison.

Finally, the 36-chute, $AR = 2.0$, dual-flow, suppressor-nozzle comparisons (Figure 4-48) show good agreement between predicted and measured, peak, mean-velocity, axial-decay trends.

In viewing all of the mean-velocity-decay comparisons as a whole, the prediction model appears to give the correct trends; i.e., the higher element-number and area-ratio nozzles give more rapid decay. Area ratio controls the merged velocity level plateau; higher area ratios yield lower merged-velocity levels. Element number controls how fast the merged-velocity level is reached; higher element numbers give more rapid decay to the merged-velocity level. The primary areas of improvement required in the prediction are in modeling the effect of a plug and the simulation of the external, supersonic expansion.

Comparisons of predicted and measured turbulence-intensity levels were not carried out because the turbulence intensity per se is not utilized in the prediction of the mixing noise. As discussed in the Task 2 final report, the mixing-noise source strengths and characteristic frequencies are computed from weighted combinations of the local values of radial, axial, and circumferential shear stresses. The weighted combination of shear stresses is

termed "equivalent turbulence intensity," but may not be equal to the axial component of root mean square turbulence velocity as measured by the LV system. It was therefore judged that comparisons of these parameters would not contribute to understanding of either jet noise suppression or model adequacy and could be misleading.

5.0 CONCLUSIONS

The major thrust of this study has been to develop and evaluate an empirical, jet-noise-prediction method, designated M*S, and to further evaluate the Task 2 theoretical prediction method, designated M*G*B, by comparison with far-field acoustic and mean-velocity data for seven exhaust nozzle configurations. The relative contributions of the four noise-generation/emission mechanisms (turbulent mixing, convective amplification, fluid shielding, and shock-cell broadband noise) have been quantitatively predicted using the M*G*B model for conical and suppressor nozzles.

The use of the M*S approach for predicting the noise of high velocity jet flows from suppressor nozzles has resulted in a computer program that enables the prediction of the maximum sideline PNL and EPNL (without flight effects) within 2.4 and 2.1 dB, respectively, with 80% confidence. Corresponding limits for 95% confidence are 3.7 and 3.3 dB, respectively. Better than average results are obtained when predicting conical nozzles, single-flow multichute nozzles, or dual-flow multitube or multichute nozzles. Below average results were obtained for single-flow, multitube nozzles primarily because of the limitations of the data base. Single- and dual-flow nozzles with hard-wall and treated shrouds were also successfully correlated. Best results were obtained on the dual-flow nozzles with the multichute suppressor on the outer stream.

The M*G*B model developed in Task 2 provides a reasonably accurate prediction of the acoustic characteristics of suppressor nozzles. It is capable of discerning the effects of suppressor area ratio and element number and shape on the subjective noise levels, PNL, for high velocity jets. The suppression characteristics of multielement nozzles can be explained by means of the four physical mechanisms upon which the prediction is based. It is concluded that multielement suppressors do not substantially reduce the turbulent-mixing-noise generation but, instead, redistribute this noise to higher frequencies where atmospheric (air) attenuation can mitigate the effects on the observer more easily. In the forward quadrant, the major effect of a multielement nozzle is to substantially reduce shock-cell, broadband, noise radiation. In the aft quadrant, substantial suppression is achieved by a reduction in convective-amplification effects. This reduction is offset somewhat by an accompanying loss in fluid-shielding suppression, but (for a "good" suppressor) the net effect is still a substantial noise reduction.

All of the above reasons explaining why multielement nozzles suppress jet noise are related to how fast the plume decays. High area-ratio suppressors decay the jet to a lower merged velocity level than do low area-ratio nozzles, and high element-number nozzles yield more rapid decay to the merged velocity level than do low element-number nozzles. Therefore, acoustic considerations dictate high element number and high area ratio for best suppression.

6.0 RECOMMENDATIONS

Based on the results obtained and the conclusions drawn from this study, several recommendations are made relative to modeling and understanding the characteristics of suppressor nozzles:

1. The empirical procedure evolved in Task 6 of this program to account for flight effects in the prediction of jet noise should be utilized in place of the procedure included herein upon publication of the Task 6 Design Guide.
2. The M*G*B aeroacoustic-prediction-model, aerodynamic-mixing calculation should be refined to give a more accurate prediction of plug/centerbody flow and to include the effects of external, supersonic expansion and base-pressure variations.
3. The acoustic-shielding portion of the M*G*B model should be further refined to eliminate the shallow-angle spectrum numerical-error problems.
4. The acoustic portion of the M*G*B model should be developed to improve the prediction at angles close to the jet axis, particularly for in-flight conditions.
5. The shock-cell noise portion of the aeroacoustic model (M*G*B) should be extended to multielement and dual-flow nozzle applications.

APPENDIX A

M*S - ENGINEERING CORRELATION MODEL - CDC VERSION

COMPUTER PROGRAM INPUT AND OUTPUT MANUAL

INTRODUCTION

This appendix documents the computer program for the prediction of jet noise by the engineering correlation method. The mathematical model appears in detail in Section 3.0 of this report. A description of the computer program is provided in this appendix, including examples of input preparation, output cases, and a listing of the Fortran computer code.

The computer program is written in Fortran Y language. It has been programmed for use on both the GE/Honeywell 6080 and the CDC 7600 computers.

The range of valid application of the program, the limiting assumptions, and documentation of the data base used for developing the correlation are provided in Section 3.0 of this report.

PROGRAM NOMENCLATURE

Table A-1 defines the Fortran symbols used in the program. The listing and descriptions of input variables are given in the "Input Description" section.

DESCRIPTION OF PROGRAM AND SUBROUTINES

Table A-2 gives a description of the overall flow of the computer program including all routines used in each step. Figure A-1 gives a detailed flow chart of the computer program logic. A description of the main program and each of the subroutines is given in the following paragraphs.

MS Routine - This routine reads the input curves needed for the various prediction routines. Depending on nozzle type it reads the nozzle input, initializes variables, and computes flow parameters and flow and physical geometries. The computation of gamma (ratio of specific heats) involves an iteration using input temperature and pressure ratio. Use of prediction subroutines and the output are controlled by this routine.

Following the preliminary calculations, control is routed through the multielement, conical, or dual-flow section of the program. In the multielement part, calculations are first made for the postmerged noise. The coefficients for the Potter and Crocker equation are set up, and, because it is a third-order equation (after simplification), a Newtonian convergence routine is used to determine the first root. Density and diameter are then calculated and a check is made for other possible roots. Static and total

Table A-1. Definition of Fortran Symbols.

<u>Fortran Symbol</u>	<u>Meaning</u>	<u>Related Subroutines</u>
A	Ejector treatment parameters	MS, EJECTS
AA8, A8	Inner nozzle flow area	MS, SHKSUB
AJ	Acoustic angle, degrees	MS, SUB3, SUB5 EXTP, SHKSUB, EJECTS
AJA	Jet plume spreading angle, radians	
AJR	Acoustic angle, radians	MS, EXTP, EJECTS
ALT	Input altitude or arc distance	MS, EXTP
AN	Noy Weighting	PNLPT
AN1	Number of elements	MS
ASK	Intermediate variable	PNTT8
AO	Ambient speed of sound	MS, SUB1 SHKSUB, PNTT8
A1	Intermediate variable	MS, EJECTS
A1	Ratio of merged to exit area	MS
A2	Ratio of merged to exit area	EJECTS
A3	Single-flow nozzle total exit area	MS
A3	Intermediate variable	EJECTS
A4	Intermediate variable	MS
A4	Ejector treatment PWL Insertion loss	EJECTS
A5	Area of multielement merged stream	MS
A5	Ejector treatment SPL insertion loss at given acoustic angle	EJECTS
A6	Ratio of ejector inlet area to nozzle total area	MS, EJECTS
A7	Multielement nozzle area ratio	MS
A9	Outer nozzle flow area	MS
B	Shock strength parameter, β	SHKSUB
B1	Intermediate variable	EXTP
B2	Intermediate variable	EXTP
B3	Intermediate variable	EXTP
B8	Tube or chute/spoke cant angle, radians	MS
B9	Tube or chute/spoke cant angle, degrees	MS
C	Normalized OASPL jet mixing noise curve-fit coefficients	MS, SUB1
CJ	Ten dB down value for EPNL	PNTT8
CMAX	Intermediate tone correction	TPNLC
C1	Jet mixing noise OASPL corrections	MS, SUB1
C1J	Intermediate variable	EXTP, SHKSUB
C2	Jet mixing noise relative velocity exponents	MS, SUB1
C3	Inner stream specific heat	MS
C4	Outer stream specific heat	MS
C9	Local speed of sound	MS, SHKSUB

Table A-1. Definition of Fortran Symbols (Continued).

<u>Fortran Symbol</u>	<u>Meaning</u>	<u>Related Subroutines</u>
D	Intermediate variable	MS, PNTT8
DE	Hard-wall ejector reference effect at θ_I	EJECTS
DEN	Density correction $(\rho_j/\rho_o)^\omega$	SUB1
DIS	Intermediate variable	EXTP
DJ	Characteristic element dimension	MS
DN	Nozzle outer diameter	MS
DT	Tube diameter	MS
DUM	Intermediate variable	SUB1
DO	Shock-noise normalization parameter	SHKSUB
D1	Reference far-field distance	MS, EXTP, SHKSUB
D2	Hard-wall ejector reference effect	EJECTS
D3	Ejector radius or diameter	EJECTS
D4	Equivalent area diameter	MS, EJECTS
D5	Merged flow diameter	MS
D7	Initial time for EPNL	PNTT8
D8	Nozzle characteristic dimension for shock noise	MS, SHKSUB
D9	Final time for EPNL	PNTT8
E	Jet mixing noise spectral distribution at θ	SUB1
E1	Ejector effect	EJECTS
E3	EPNL	PNTT8
E9	EGA indicator	MS, EXTP, PNTT8
F	Center frequency	MS, EXTP, SHKSUB PNTT8, EJECTS
F	Intermediate variable	TPNLC
FP	Peak frequency	EJECTS
F0	Critical frequency for effective number of elements	MS
F1	Intermediate variable	MS, SHKSUB
F2	Intermediate variable	MS, SHKSUB
F3	Intermediate variable	SHKSUB
G	Shock-cell noise prediction input curve	MS, SHKSUB
GJ	Critical refraction angle indicator	MS
G1	Intermediate variable	SHKSUB
G2	Outer stream ratio of specific heats, γ	MS
G3	EGA at output distance	EXTP
G8	Intermediate γ	MS
G9	Inner stream ratio of specific heats, γ	MS
H	Output sideline or arc distance	MS, EXTP, PNTT8
H1	Intermediate variable	SHKSUB
I	Index	MS, SUB1, SUB5, SUB4, SUB2, SUB6, EXTP, SHKSUB, TPNLC, PNTT8, EJECTS

Table A-1. Definition of Fortran Symbols (Continued).

<u>Fortran Symbol</u>	<u>Meaning</u>	<u>Related Subroutines</u>
IDCASE	Case Description	MS
IDENT	Run Description	MS
IM	Intermediate variable	MS
IP	Intermediate variable	EJECTS
II	Indicator	TPNLC
IIAS	Noise component identification	MS, PNTT8
IICASE	Case Description	MS, PNTT8
IIP	Intermediate variable	MS
ISPLF	Intermediate variable	TPNLC
J	Index	All Subroutines
JJ	Index	PNTT8, EJECTS
K	Index	SUB1, SUB3
KK	Jet mixing noise spectral distribution curve-fit coefficients	MS, SUB1
KSTART	Index	SHKSUB
KT	Intermediate variable	PNTT8
K0	Intermediate variable	MS
K1	Extrapolation indicator	MS, SUB3
K2	Intermediate variable	MS
K6	Intermediate variable	SUB1, EJECTS
K7	Shock-noise case indicator	MS
K8	Index	SHKSUB, EJECTS
K9	Print Indicator	MS
L	PNL calculation coefficients	MS, PNLPT
L1	Output acoustic range	EXTP
L2	Reflected axial source location	EJECTS
L3	Ejector length	EJECTS
L8	Ejector length effect	EJECTS
L9	Ejector length to suppressor nozzle equivalent diameter	
M	Mach number	MS, EJECTS
MP	Maximum PNL	PNTT8
MM	Intermediate variable	MS
N	Number of elements in nozzle	MS
N1	Angle indicator	MS, SUB1
O	OASPL	SUB1, SUB3, PNTT8
OJ	Critical refraction angle	MS, EJECTS
O9	OAPWL	SUB5, SUB6, PNTT8
P	PNL	SUB3, PNTT8
PA	Air attenuation	EXTP
PJ	Intermediate variable	MS
PTCOP	Tone correction	TPNLC
PO	Ambient static pressure	MS

Table A-1. Definition of Fortran Symbols (Continued).

<u>Fortran Symbol</u>	<u>Meaning</u>	<u>Related Subroutines</u>
P1	π (3.14159)	EXTP, SHKSUB
P3	Frequency	EXTP, EJECTS
P4	Inner nozzle total to ambient pressure ratio	MS
P5	Outer nozzle total to ambient pressure ratio	MS
P9	Nozzle total to ambient pressure ratio	MS
Q	Spherical spreading effect	EXTP
Q1	Intermediate variable	MS, PNNT8
Q2	Jet mixing noise normalization parameter	SUB1
R	Intermediate storage variable	SUB4, SUB6
RJ	Ambient density	MS, SUB1
RJ1	Intermediate variable	SUB1, PNNT8
RP	Centerbody plug radius	MS
RS, RR	Specific resistance	EJECTS
RVE	Storage	MS
RX	Specific reactance	EJECTS
R1	Tube equivalent radius	MS
R2	Nozzle outer diameter	MS
R3	Inner flow density	MS
R4	Chute/spoke outer flow width	MS
R5	Outer flow density	MS
R6	Chute/spoke inner flow width	MS
R7	Outer nozzle duct height	MS, SUB1
R8	Outer nozzle radius ratio	MS
R9	Centerbody plug radius	MS
S	Predicted SPL	MS, SUB1, SUB3, SUB5, SUB4, SUB2, SUB6, SHKSUB, PNNT8
SBAR	Intermediate variable	TPNLC
SC	Intermediate variable	TPNLC
SJ	Intermediate variable	MS, PNNT8
SL	Input sideline distance	MS, EXTP
SP	Intermediate variable	TPNLC
SPL	Intermediate variable	TPNLC
SPLP	Intermediate variable	TPNLC
SPLPP	Intermediate variable	TPNLC
SS	Outer chute/spoke width	MS
SX	Source location	MS
S1	Shock-cell noise prediction input curves	MS, SHKSUB
SLJ	Outer element spacing to characteristic diameter ratio	MS
S2J	Relative source strength	EJECTS

Table A-1. Definition of Fortran Symbols (Continued).

<u>Fortran Symbol</u>	<u>Meaning</u>	<u>Related Subroutines</u>
S6	Nozzle outer radius	MS, EJECTS
T	Temperature	SUB1
T	PNL	SUB3
T	Flyover time	PNTT8
TC	Cutoff effect	MS
TC2	Intermediate variable	TPNLC
TC3	Intermediate variable	TPNLC
TJ	Intermediate variable	PNLPT, PNTT3
TT	Intermediate variable	PNTT8
TT3, T3	Nozzle total temperature	MS
TT4, T4	Inner nozzle total temperature	MS
TT5, T5	Outer nozzle total temperature	MS, SUB1
TZ	Initial time for EPNL	PNTT8
T0	Ambient temperature	MS, SUB1, PNTT8
T1	Intermediate variable	PNTT8, EJECTS
T2	Intermediate variable	MS
T8	Total temperature	MS, SUB1
U	Arc or sideline indicator	MS, EXTP, PNTT8
U3	Nozzle fully expanded velocity	MS
U5	Outer nozzle fully expanded velocity	MS
V	Intermediate variable	SUB3, PNLPT
VJ	Suppressor merged velocity	MS
V0	Aircraft velocity	MS, SUB1, SHKSUB, PNTT8
V1	Ratio of merged velocity to exit velocity	MS
V6	Intermediate variable	MS
V7	Intermediate variable	MS
V8	Fully expanded jet velocity input to jet mixing noise routine	MS, SUB1
V9	Fully expanded jet velocity input to shock-cell noise routine	MS, SHKSUB
W	Density exponent curve-fit coefficients	MS, SUB1
WE	Density exponent	SUB1
WJ	Intermediate variable	SUB1, PNTT8
W4	Inner stream weight flow	MS
W5	Outer stream weight flow	MS
W8	Weight flow	MS, SUB1
X	Source location	MS, EJECTS
X	SPL	SUB3, EXTP, PNLPT
XJ	Intermediate variable	SUB1, EJECTS
XM	Point of merging	MS
X0	Potter and Crocker equation coefficient	MS
X1	Potter and Crocker equation coefficient	MS
X2	Potter and Crocker equation coefficient	MS

Table A-1. Definition of Fortran Symbols (Concluded).

<u>Fortran Symbol</u>	<u>Meaning</u>	<u>Related Subroutines</u>
X3	Potter and Crocker equation coefficient	MS
X4	Specific reactance	EJECTS
Y	PWL	SUB5, SUB4, SUB6, PNTT8
YJ	Intermediate variable	SUB5, EJECTS
Y1	Intermediate variable	MS, SUB4, SUB6
Y1J	Intermediate variable	MS
Y2	Intermediate variable	MS
Y9	Nozzle type indicator	MS, SUB1
Z1	Intermediate variable	SHKSUB
ZJ	Intermediate variable	EXTP, EJECTS
ZK	Intermediate variable	SHKSUB
ZZ	Effective number of elements effect	MS
Z1	Intermediate variable	SUB1, PNTT8
Z2	Intermediate variable	MS
Z3	Intermediate variable	MS, PNTT8
Z5	Number of rows of tubes	MS
Z8	Effective number of elements adder	MS
Z9	Total number of elements adder	MS
Z9	Constant	MS, SUB2

Table A-2. Overall Flow of Program.

1. Read Input Curves (MS).
2. Read Input and Calculate Flow Parameters for each Stream (MS).

The Following through 11 are used or Skipped as Necessary.

3. Determine Postmerged Noise (MS, SUB1, SUB5).
4. Determine Premerged Noise (MS, SUB1).
5. Determine Premerged Cutoff and Shielding Effects (MS).
6. Calculate Ejector Effects and Correct the Premerged Noise (MS, EJECTS, SUB5).
7. Sum the Premerged and Postmerged Noise (SUB6).
8. Calculate Shock Noise for Outer Stream and Apply Cutoff, Shielding, and Ejector Effects (MS, SHKSUB, EJECTS, SUB5).
9. Add to the Sum of Premerged and Postmerged (SUB6).
10. Calculate Shock Noise for Inner Stream (MS, SHKSUB, SUB5).
11. Add to the Sum of Premerged and Postmerged and Outer Stream Shock (SUB6).
12. Extrapolate and Calculate OASPL, PNL and PNLT (this may be done after each Component is Calculated for Print Purposes) (SUB3).
13. Print Output and Calculate EPNL (PNTT8).

MS ROUTINE

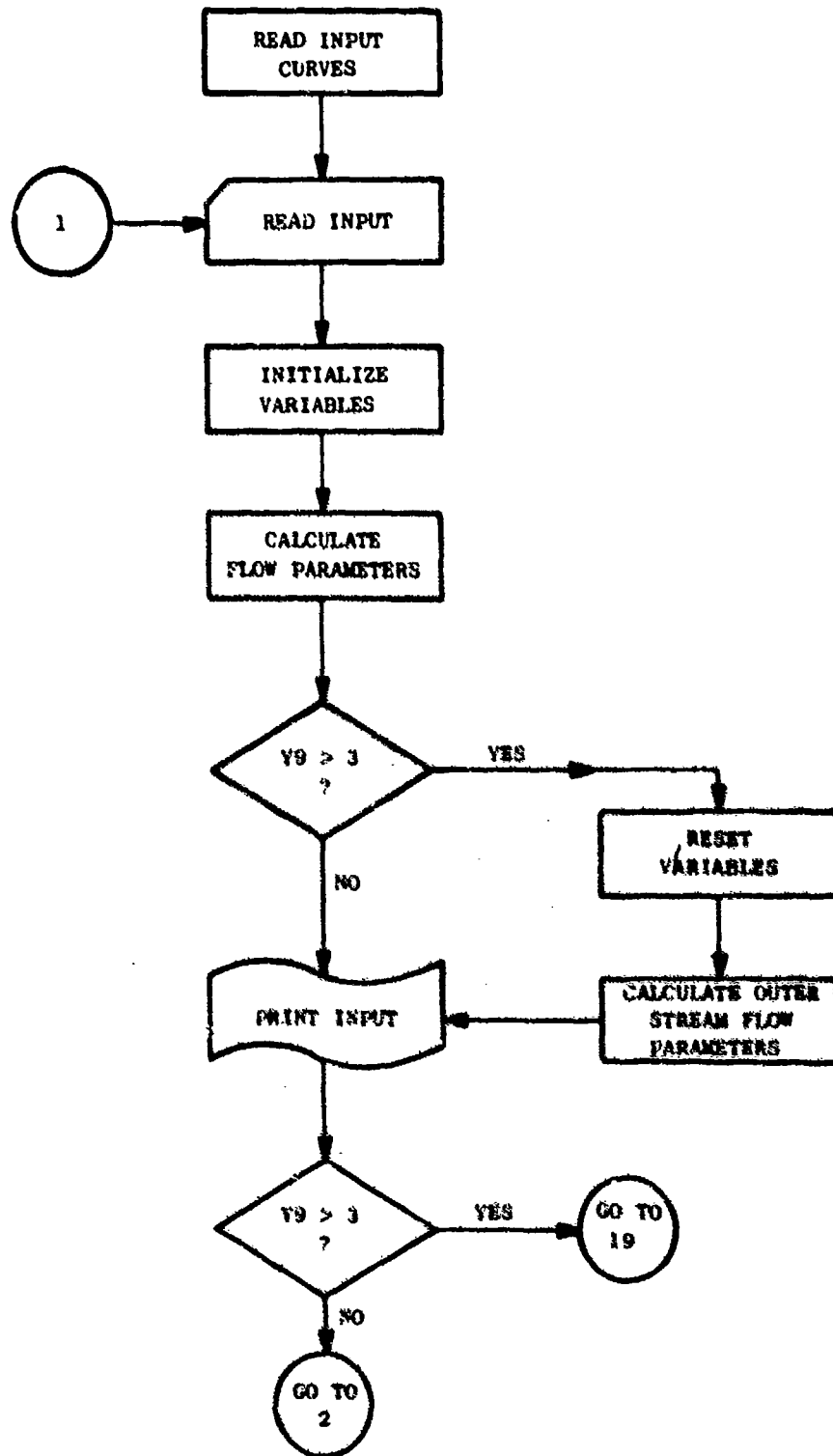


Figure A-1. Computer Program Flow Chart.

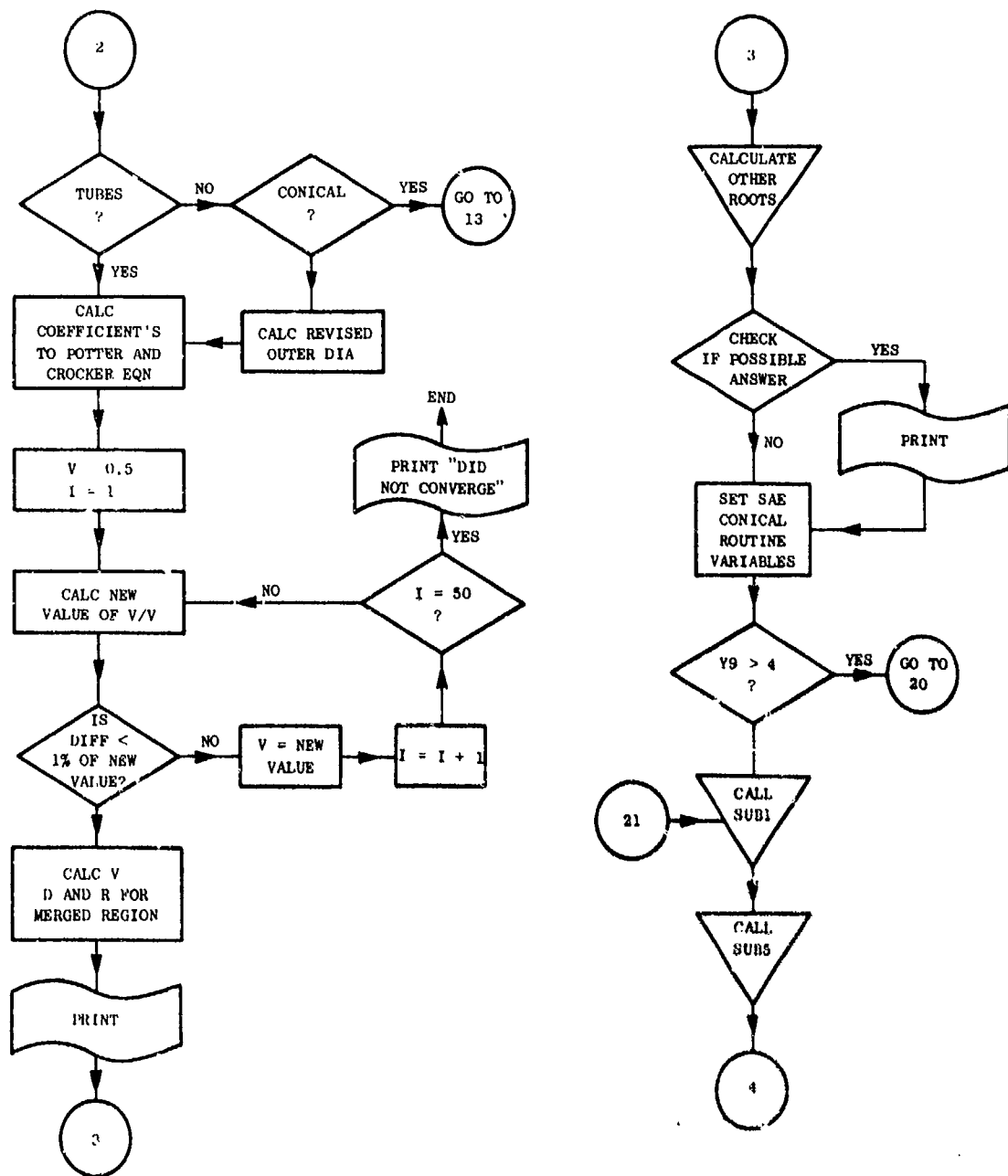


Figure A-1. Computer Program Flow Chart (Continued).

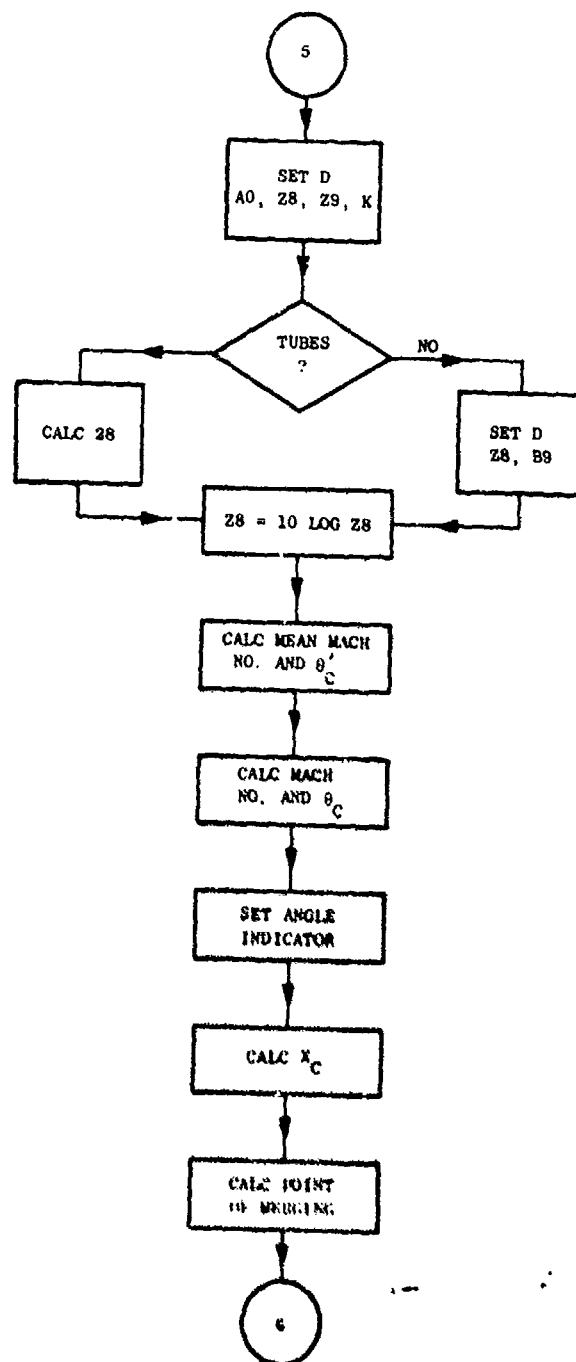
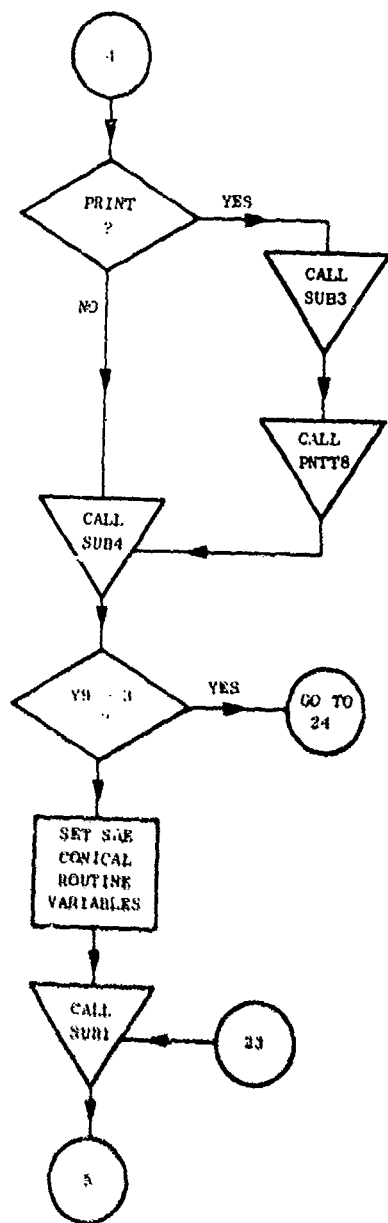


Figure A-1. Computer Program Flow Chart (Continued).

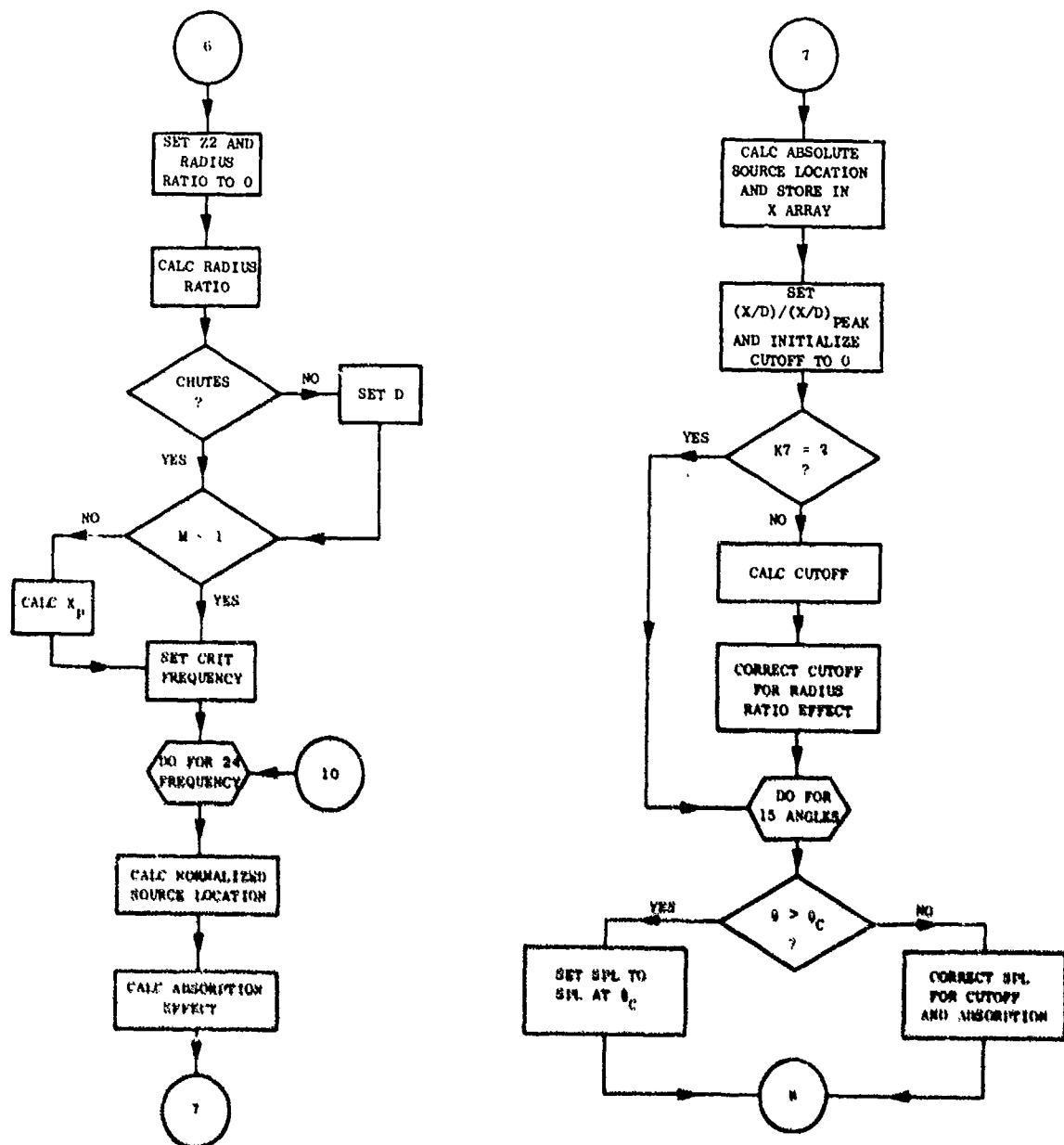


Figure A-1. Computer Program Flow Chart (Continued).

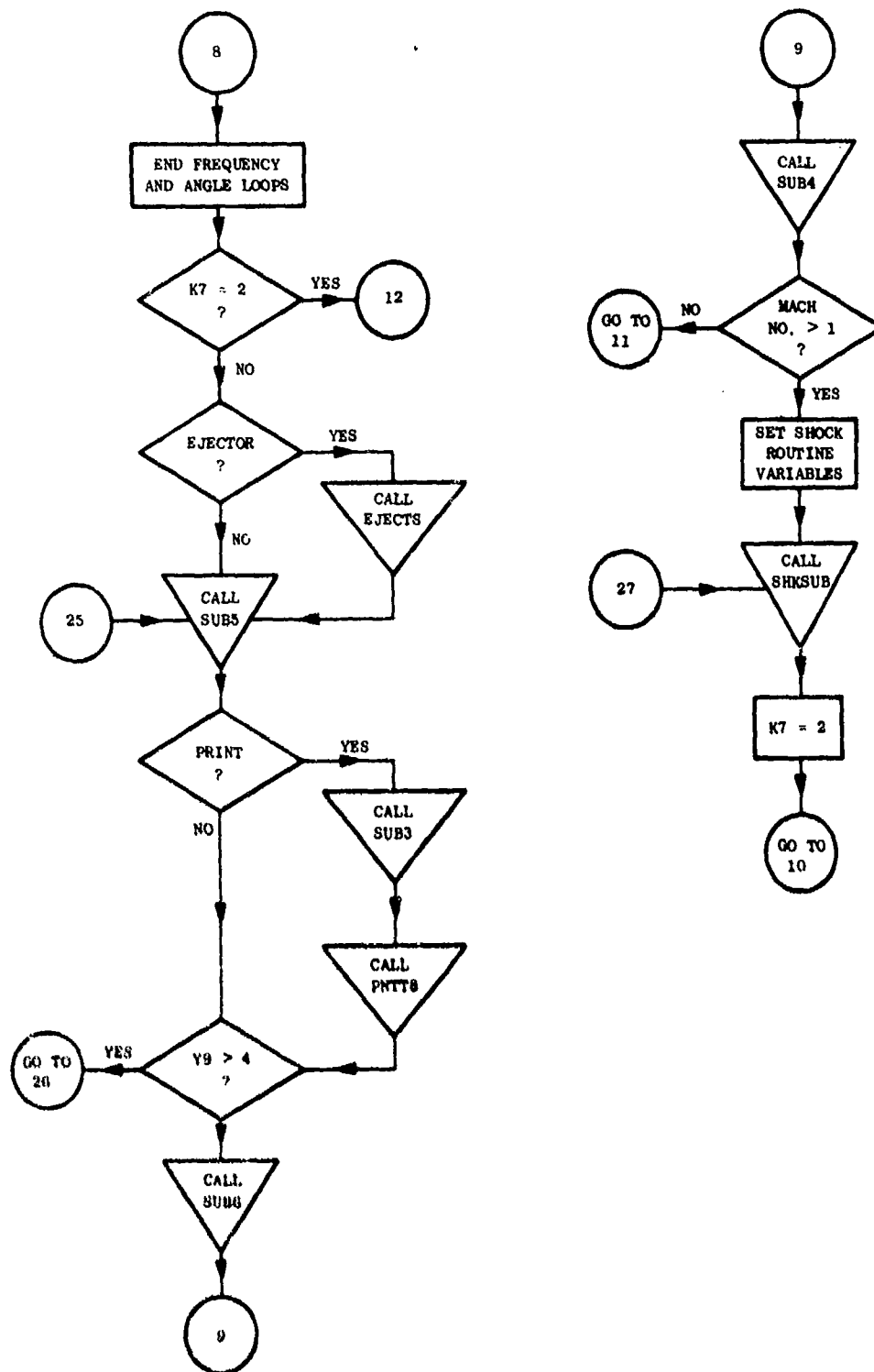


Figure A-1. Computer Program Flow Chart (Continued).

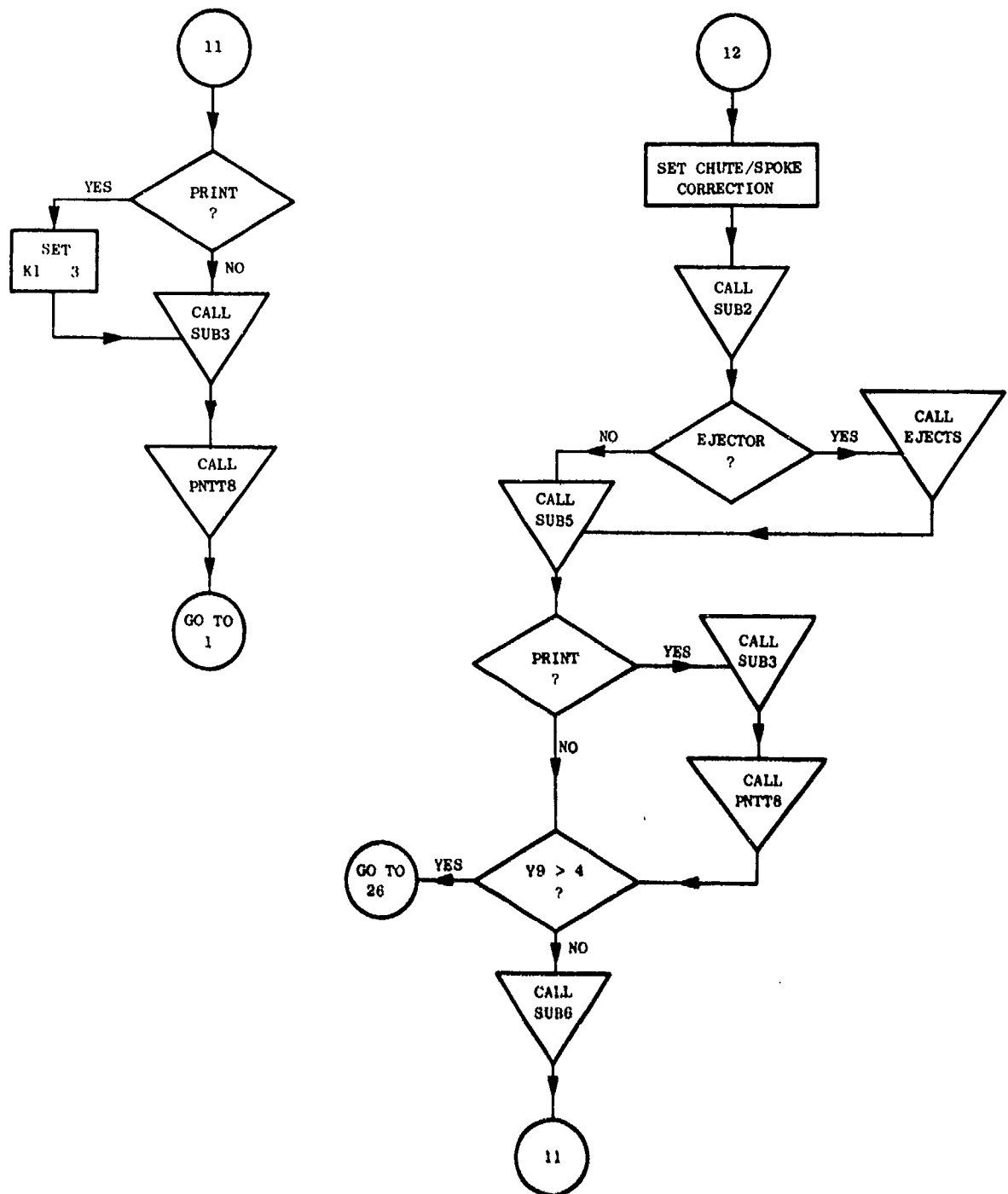


Figure A-1. Computer Program Flow Chart (Continued).

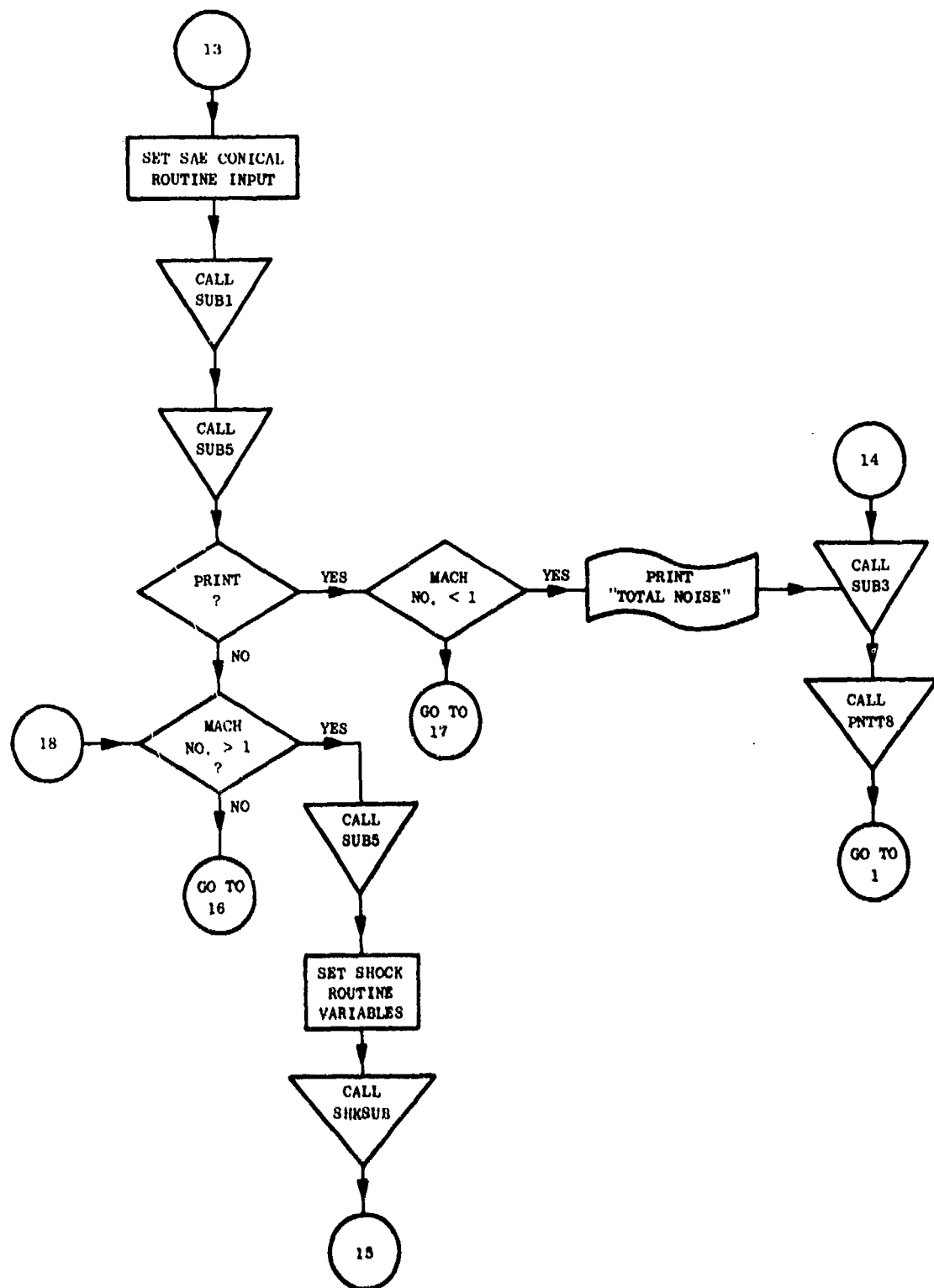


Figure A-1. Computer Program Flow Chart (Continued).

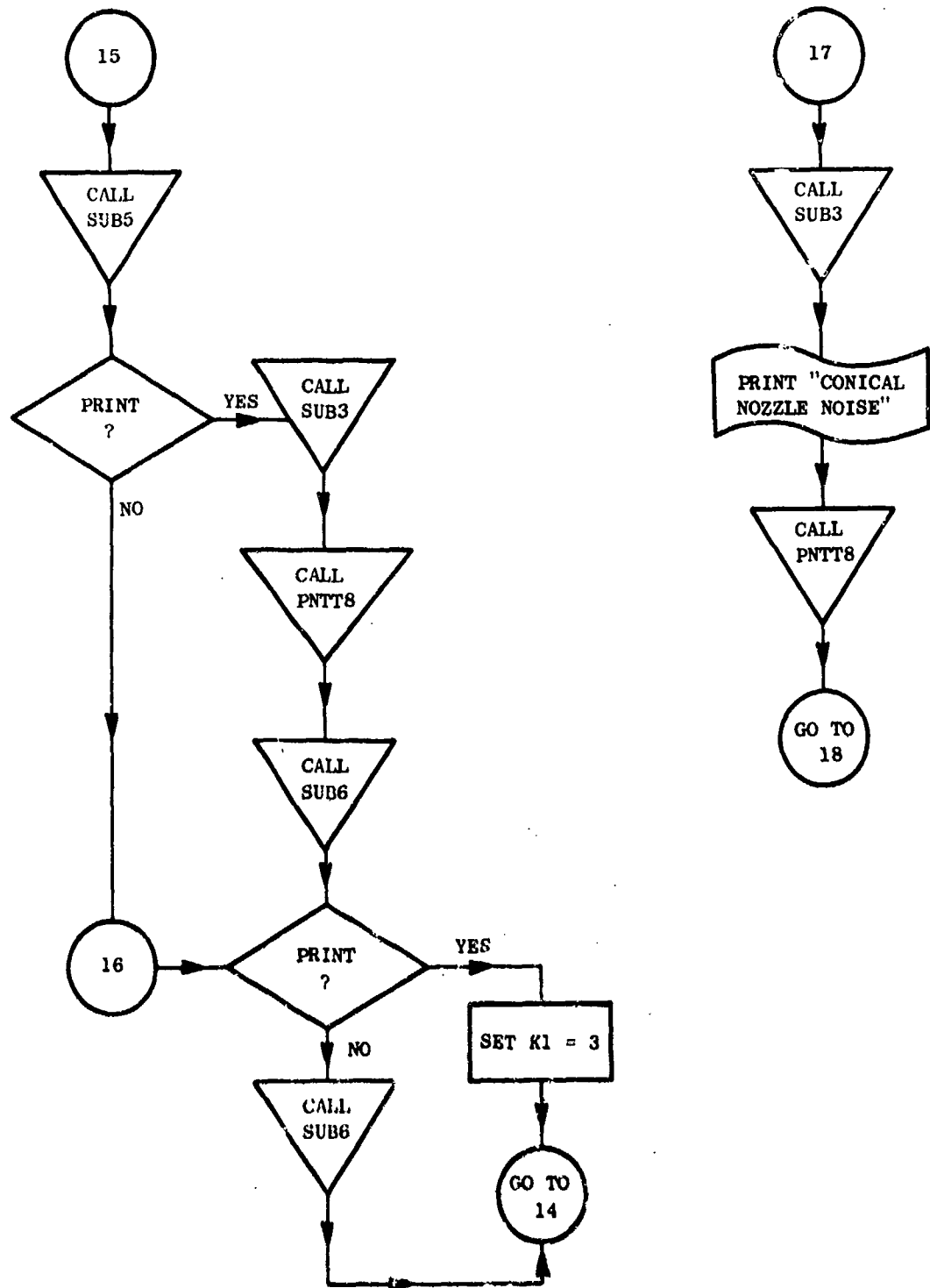


Figure A-1. Computer Program Flow Chart (Continued).

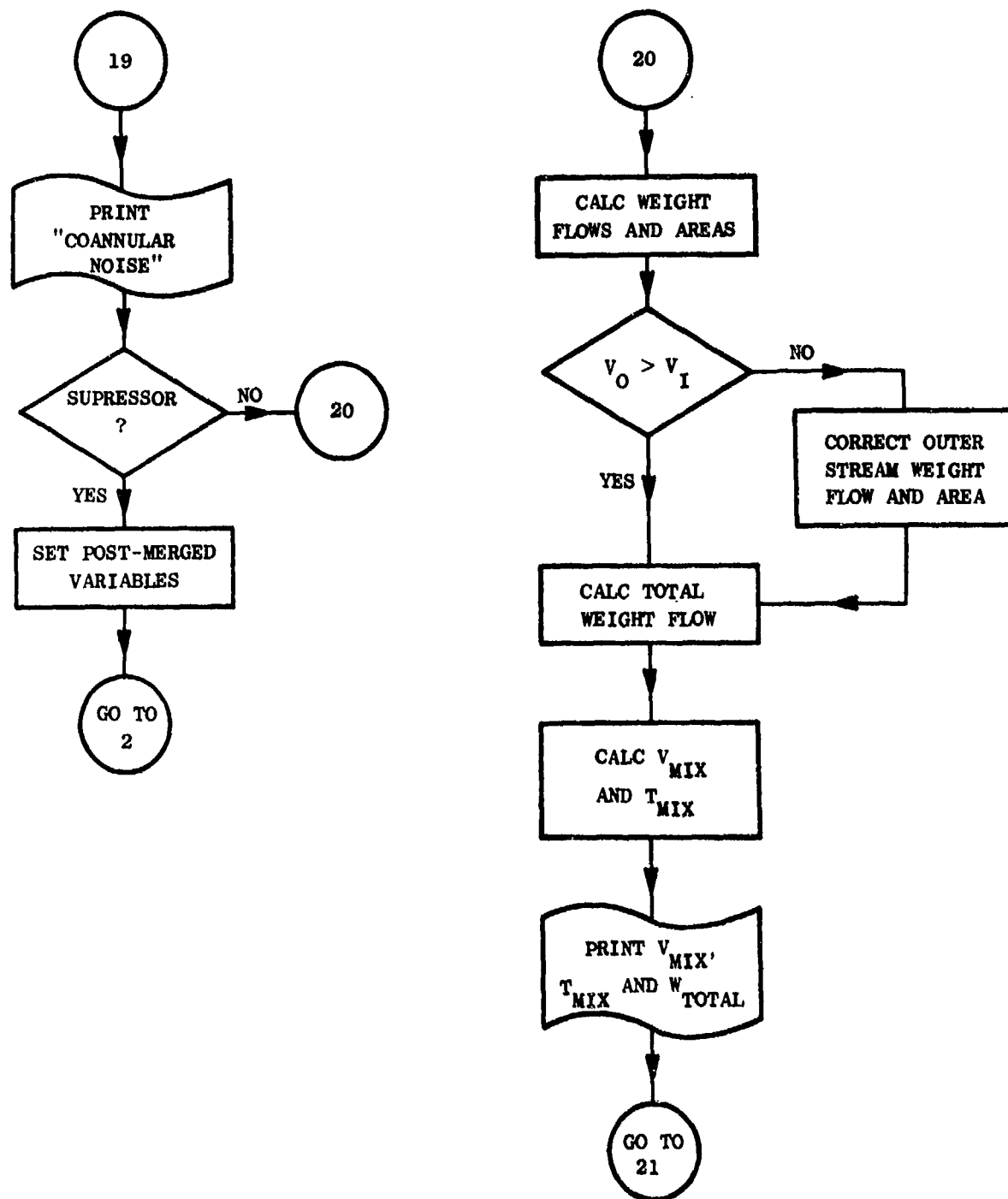


Figure A-1. Computer Program Flow Chart (Continued).

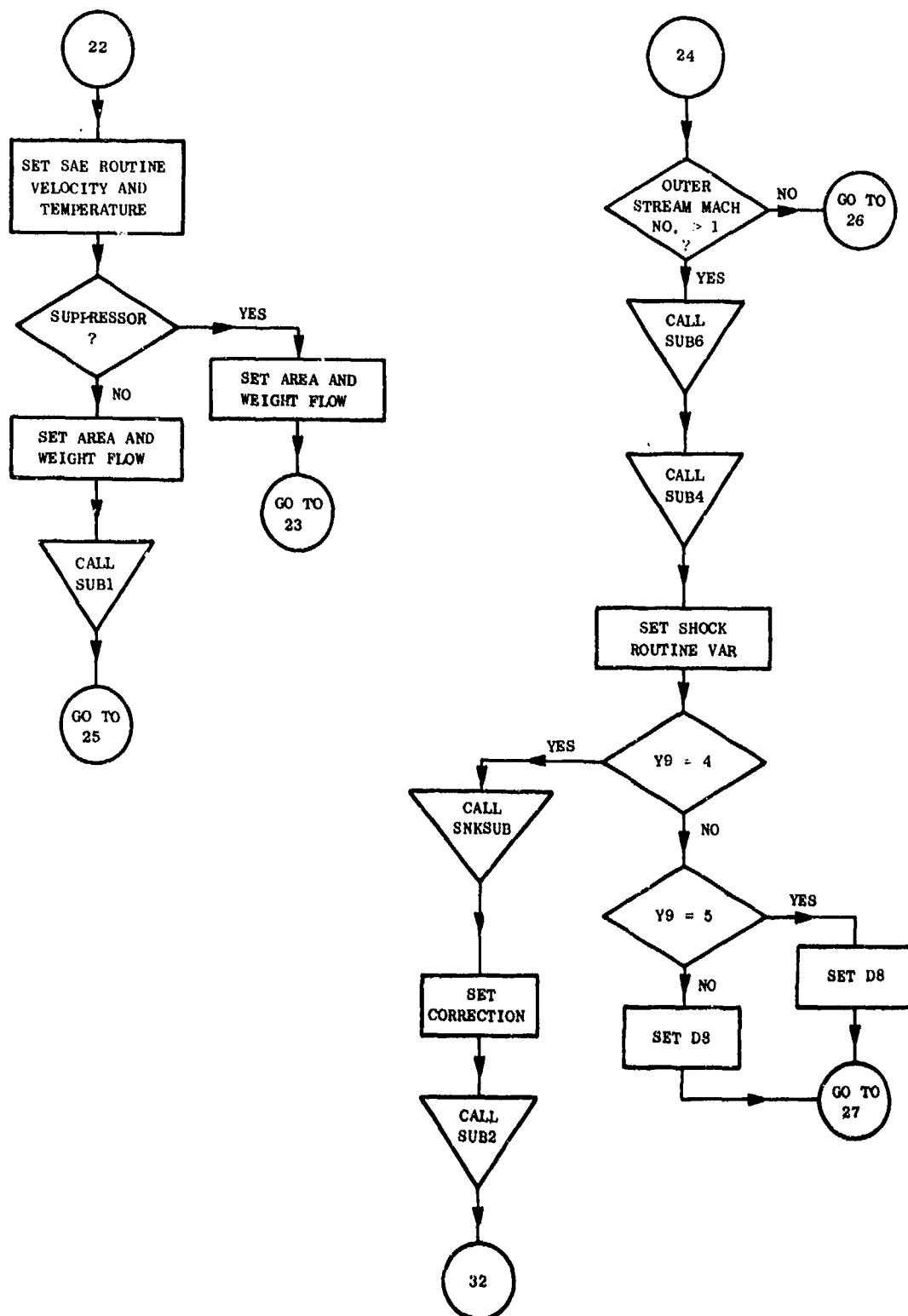


Figure A-1. Computer Program Flow Chart (Continued).

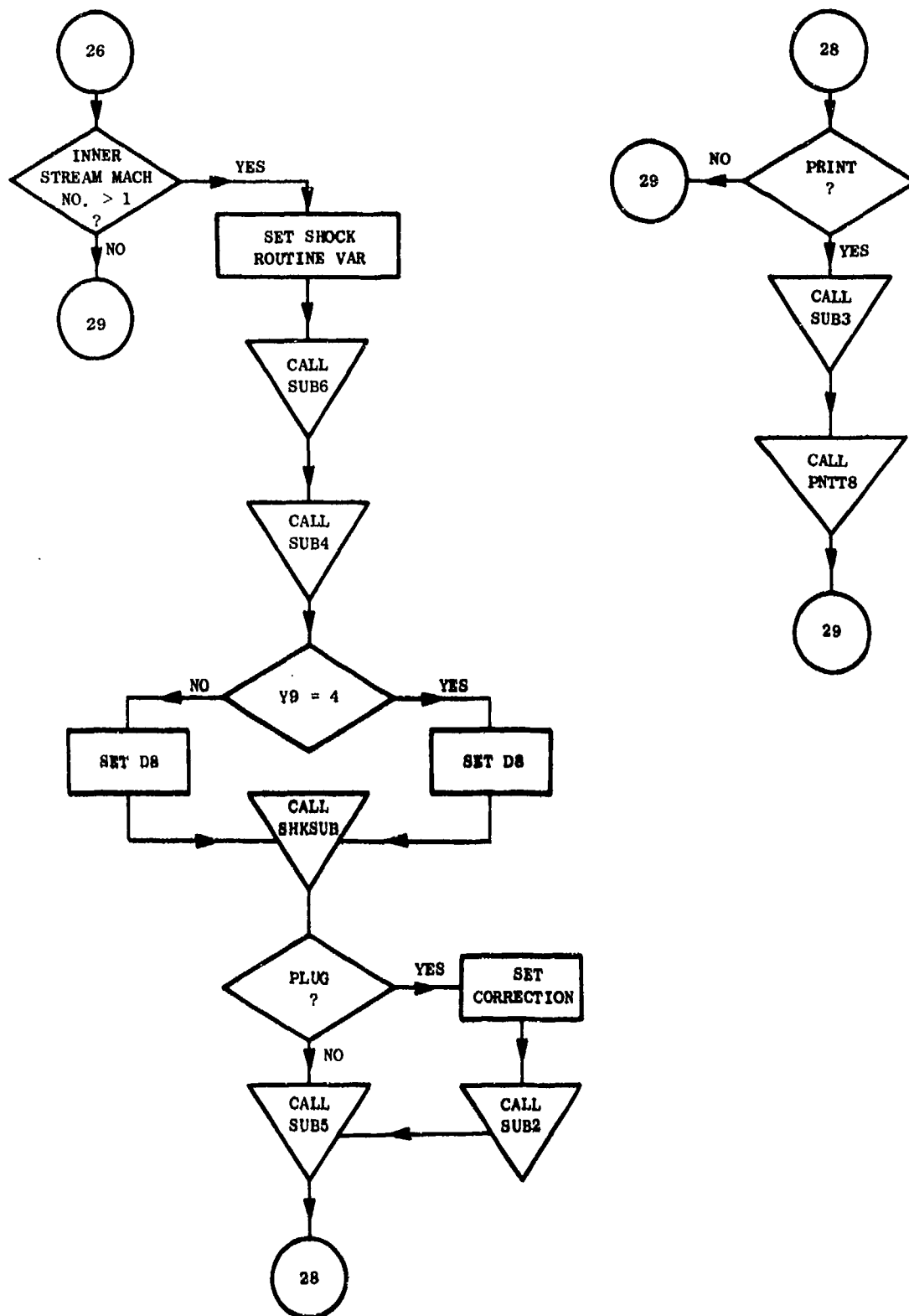


Figure A-1. Computer Program Flow Chart (Continued).

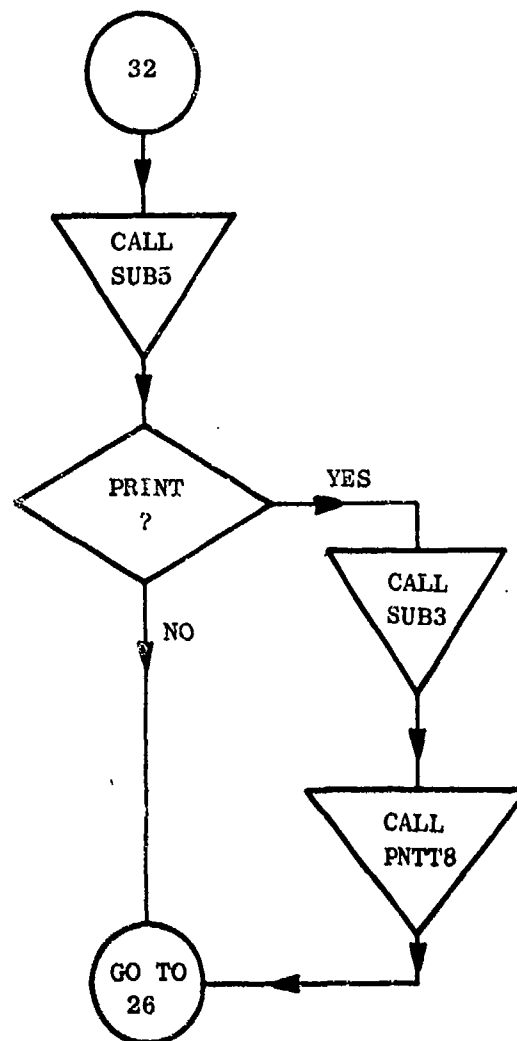
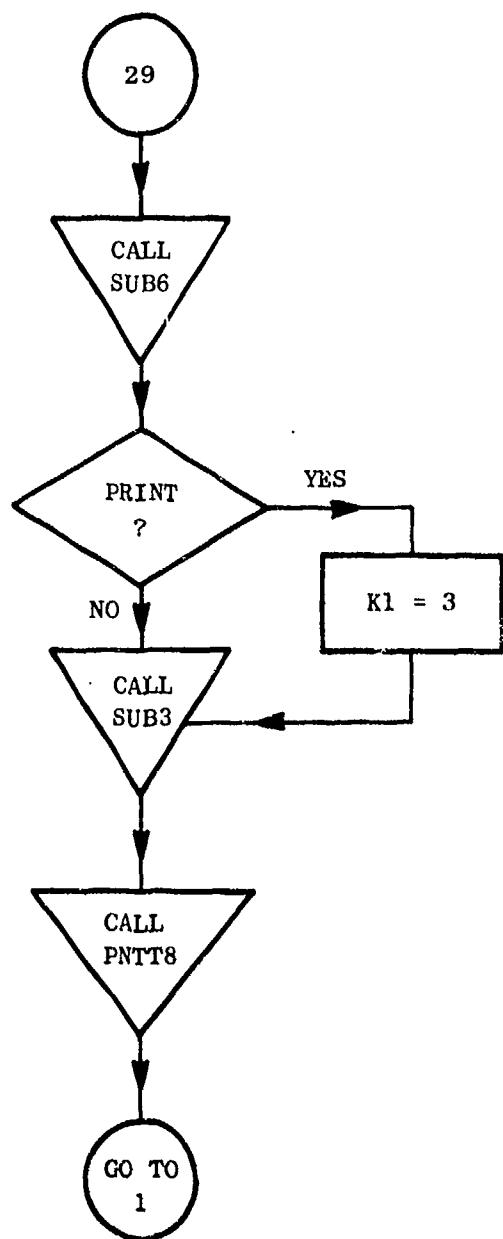


Figure A-1. Computer Program Flowchart (Continued).

a) SUBROUTINE SUB1

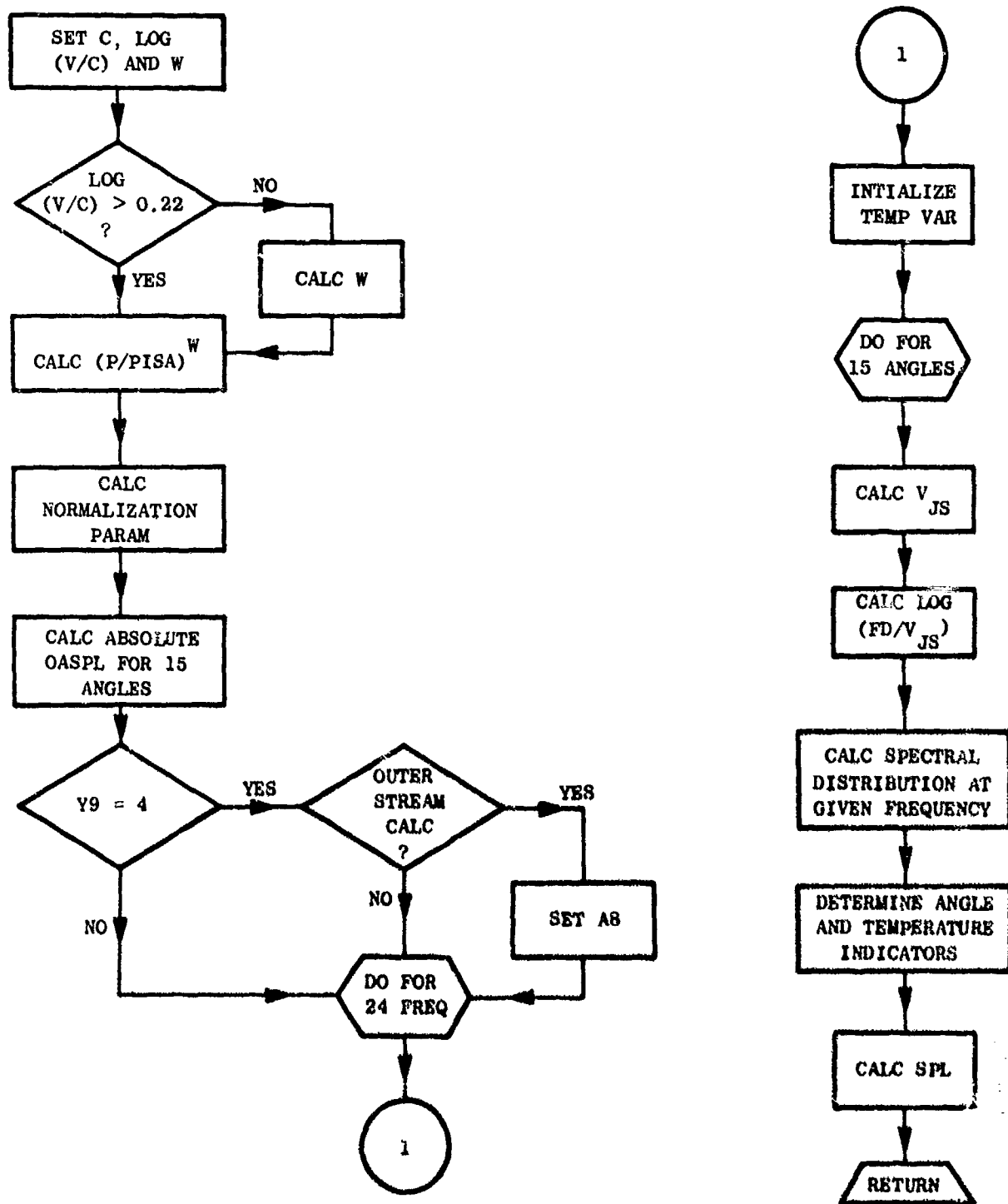


Figure A-1. Computer Program Flow Chart (Continued).

b) SUBROUTINE SUB3

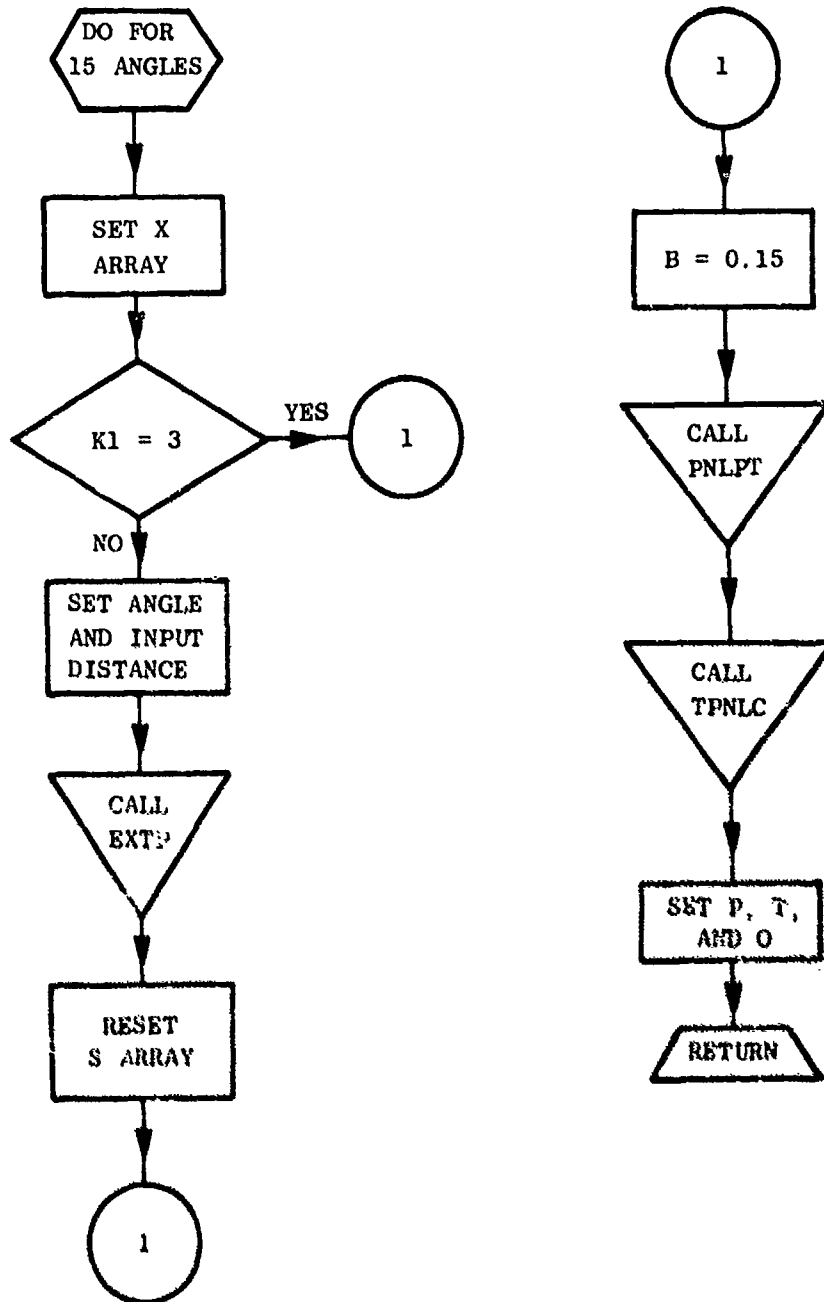


Figure A-1. Computer Program Flowchart (Continued).

c) SUBROUTINE SUB5

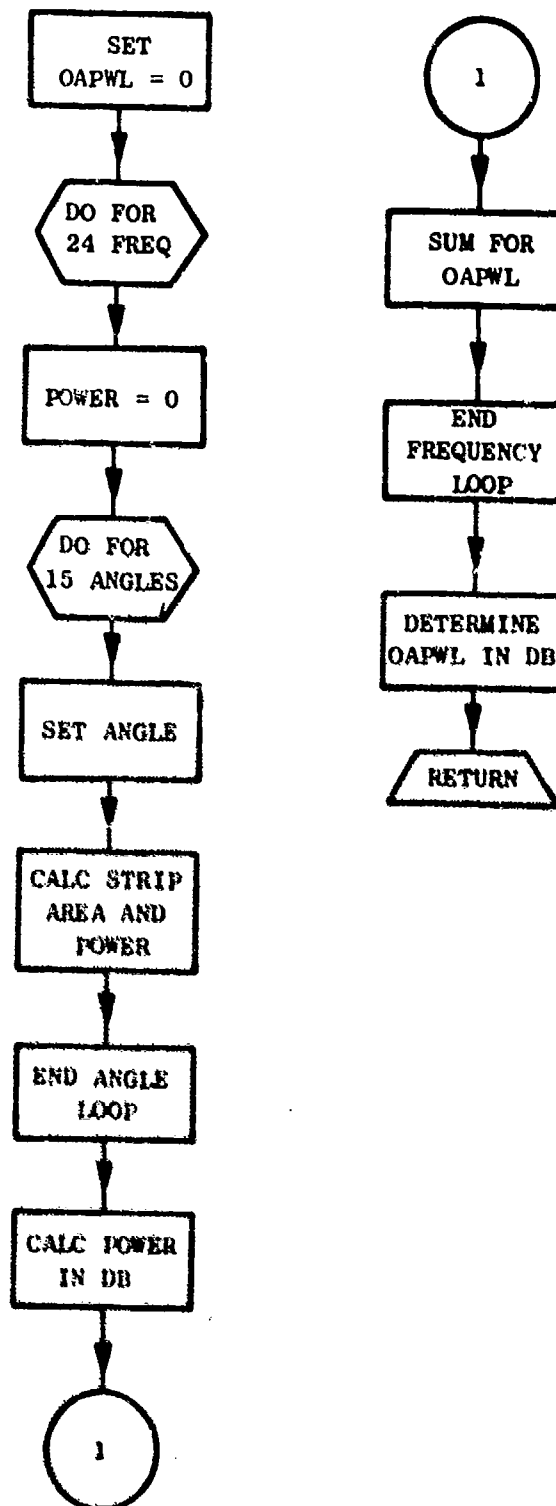
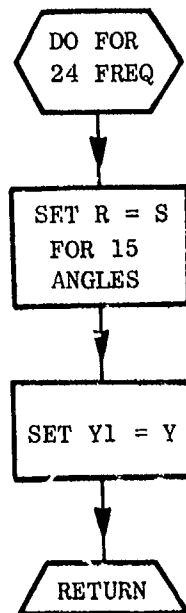


Figure A-1. Computer Program Flowpath (Continued).

d) SUBROUTINE SUB4



e) SUBROUTINE SUB2

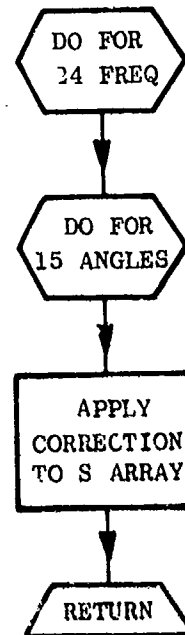


Figure A-1. Computer Program
Flowchart (Continued).

f) SUBROUTINE SUB6

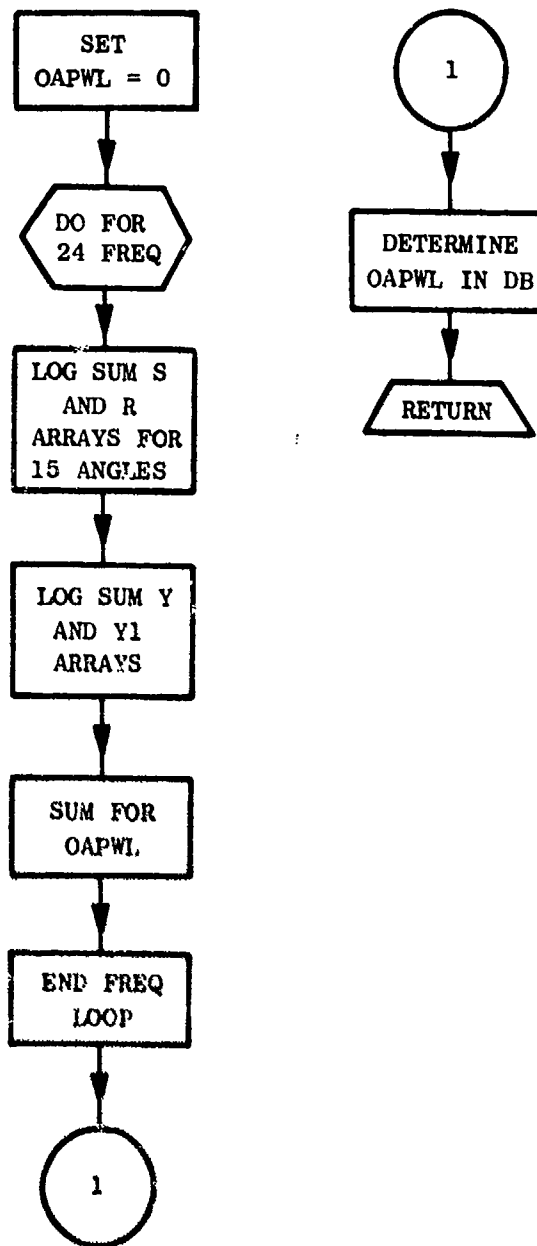


Figure A-1. Computer Program
Flowchart (Continued).

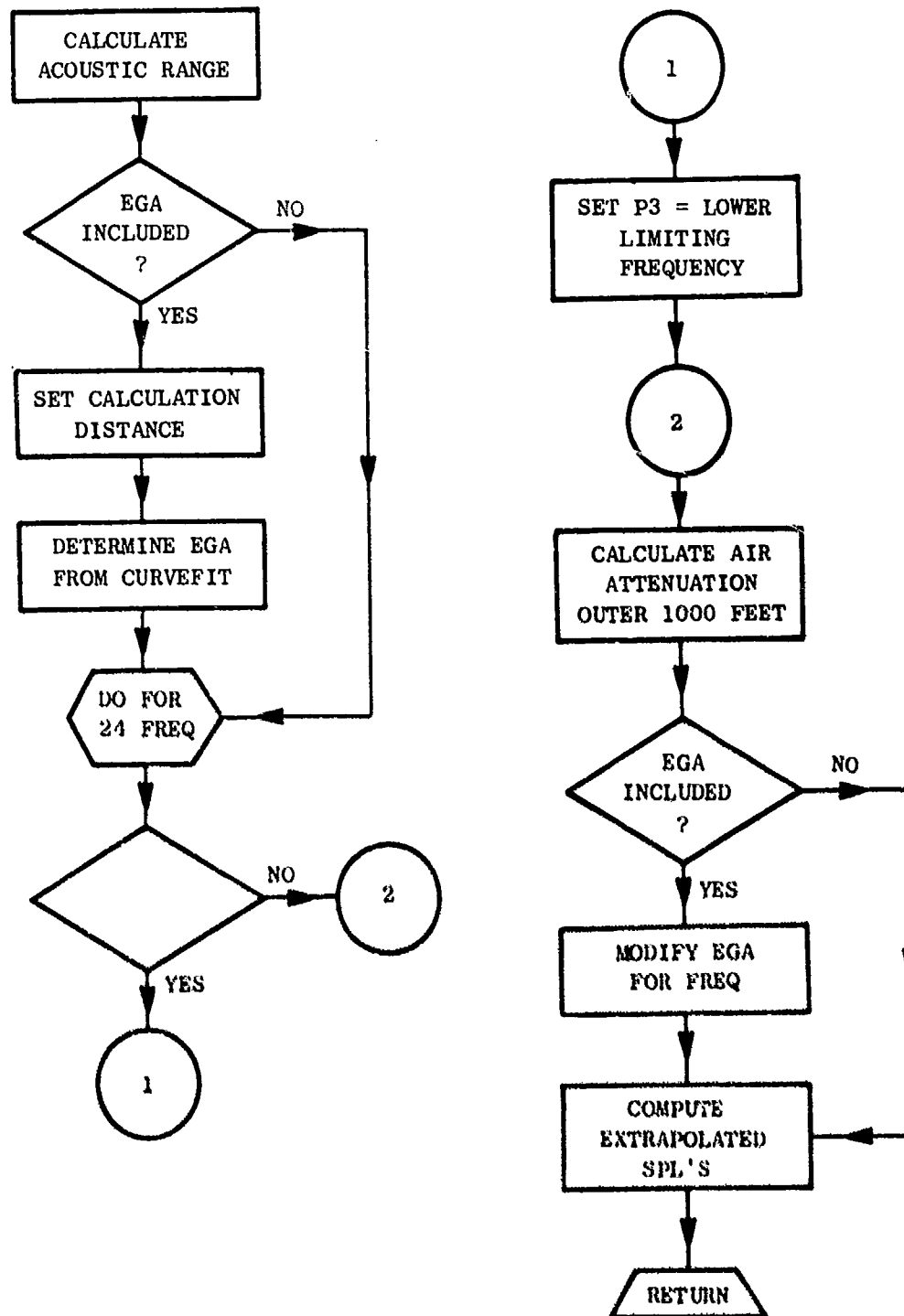


Figure A-1. Computer Program Flowchart (Continued).

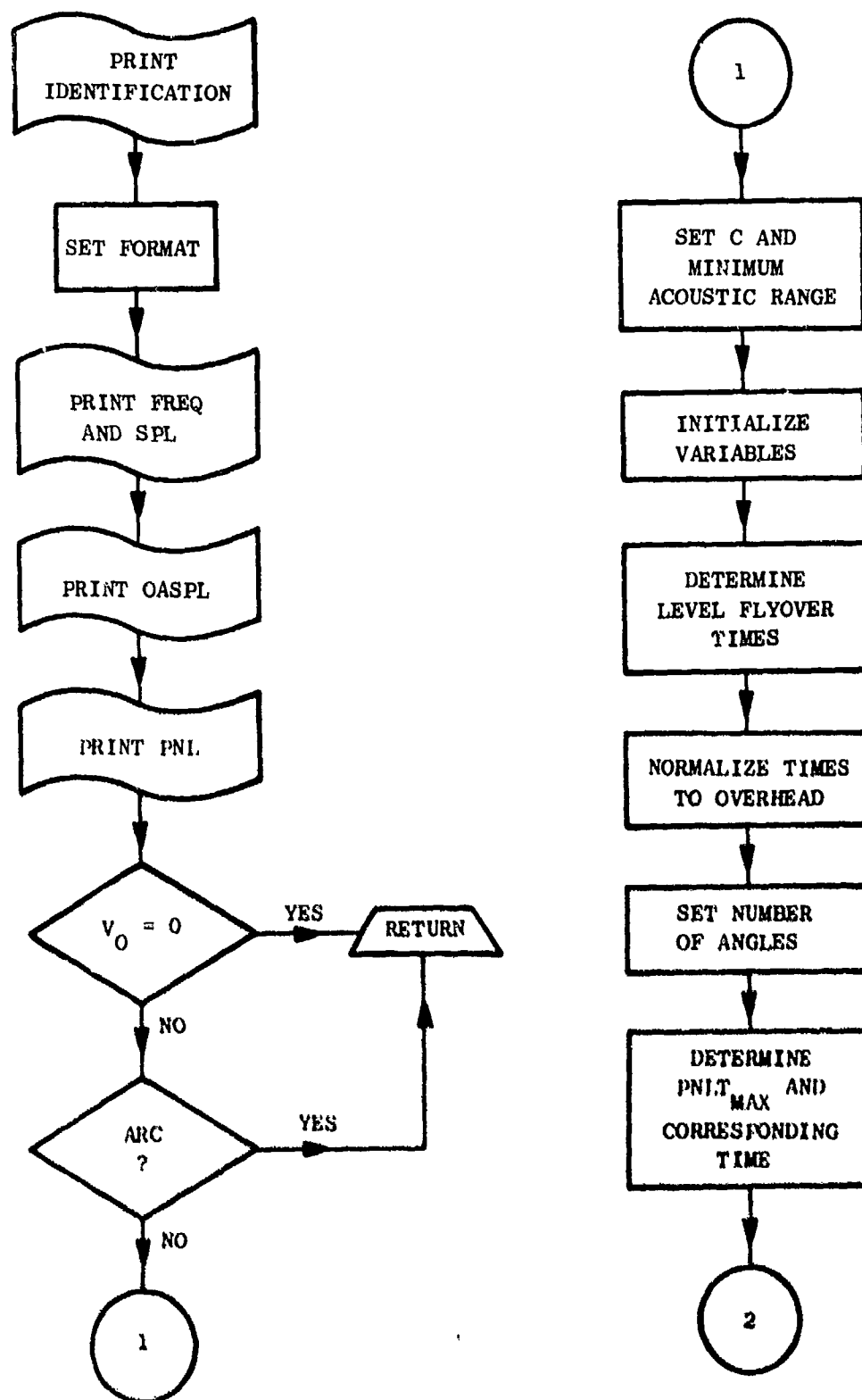


Figure A-1. Computer Program Flowchart (Continued).

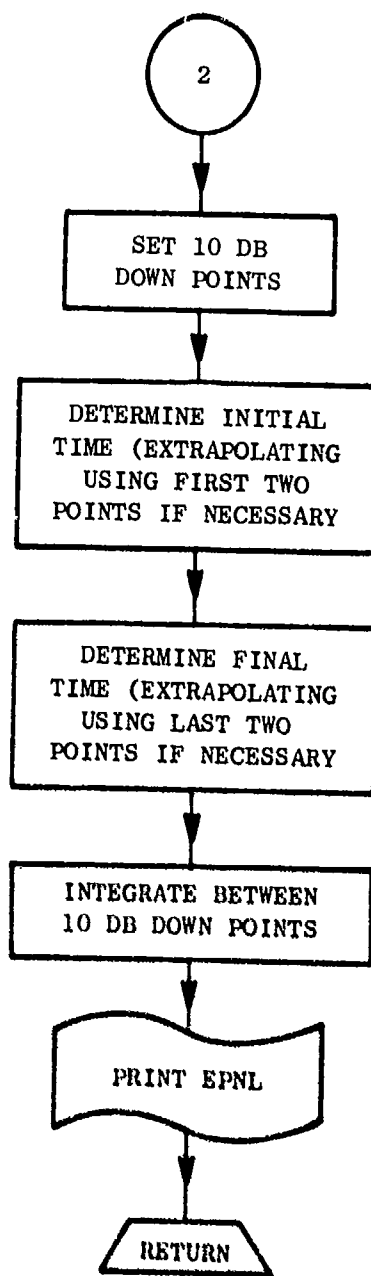


Figure A-1. Computer Program
Flowchart (Continued).

1) SUBROUTINE EJECTS

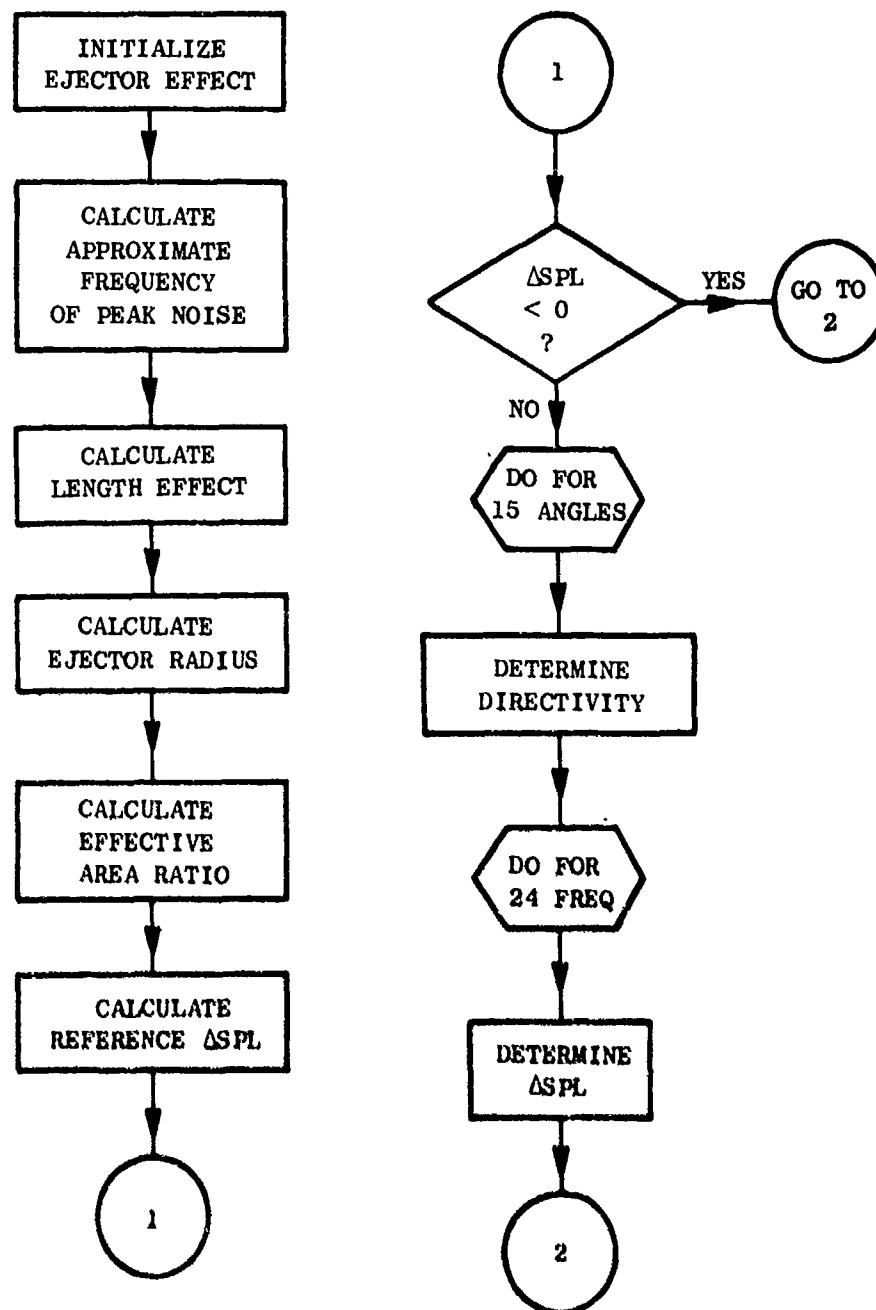


Figure A-1. Computer Program Flowchart (Continued).

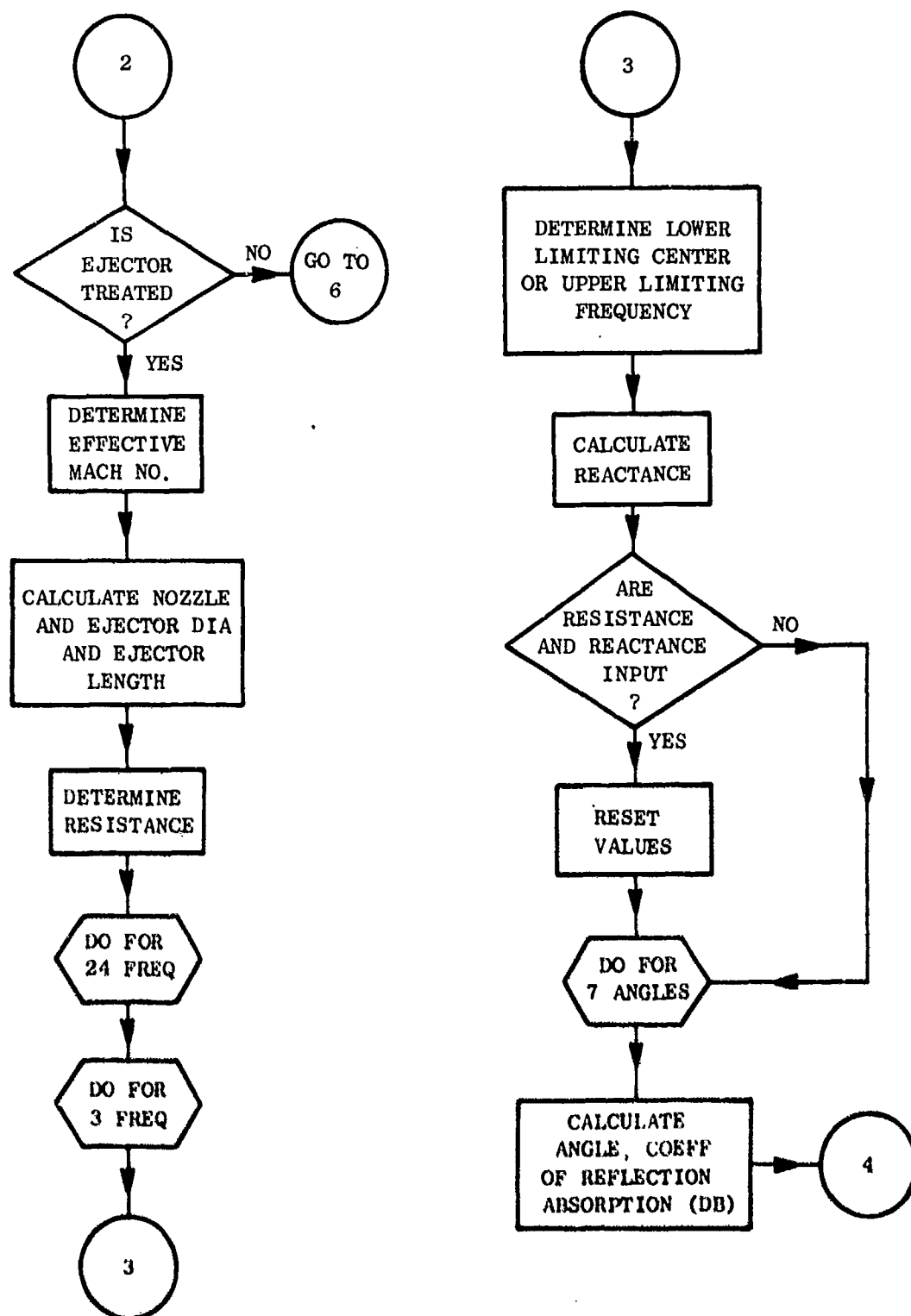
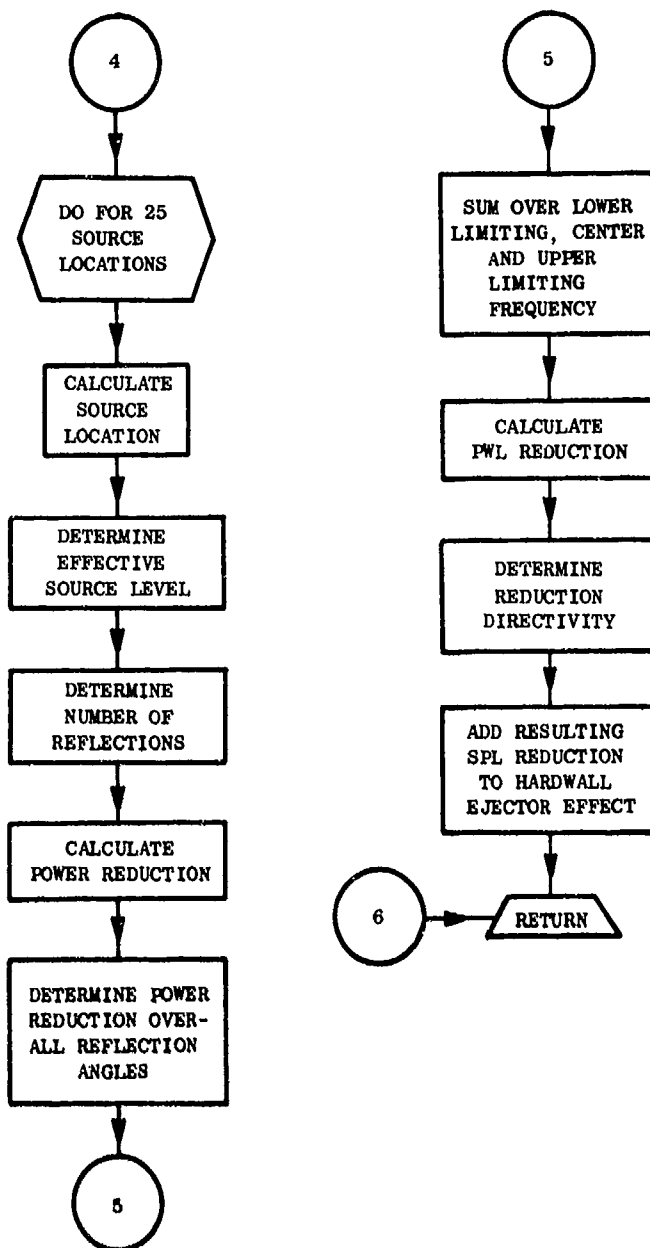


Figure A-1. Computer Program Flowchart (Continued).



NO FLOW CHART IS SUPPLIED FOR THE FOLLOWING ROUTINES BECAUSE OF THE COMPLETE NATURE OF THEIR DOCUMENTATION IN PUBLISHED LITERATURE

- SHKSUB
- PNLPT
- TPNLC

Figure A-1. Computer Program Flow Chart (Concluded).

temperature are determined, the input variables to the conical nozzle noise routine are set and the noise is calculated. This component is then extrapolated and printed if desired.

The premerged noise is then calculated. The effective number of tubes and the critical angle are determined. Then the length of the potential core, X_c , the point of merging (used for cutoff only), and the radius ratio are determined. The axial location of the beginning of peak noise generation, X_p , and the critical frequency for absorption are calculated before entering the frequency loop to calculate source locations, absorption effects, and cutoff effects. These are then applied to all angles forward of critical with angles aft of critical set equal to critical angle SPL. Ejector effects are determined and applied before extrapolation and printing (if desired). Shock-cell noise (if applicable) is determined after summing the premerged and postmerged components. It is then corrected for ejector effects and multielement corrections are applied, extrapolated, printed, and added to the other components. The total is then extrapolated (if required) and printed, and a return is made for the next case.

The conical part of the routine calculates the conical mixing noise and shock noise, extrapolates and prints them separately if desired, sums them, and prints the total; after which, a return is made for the next case.

The coannular part uses the premerged and postmerged routines of the multielement part if a suppressor is involved. Variables are set, and, if a suppressor is involved, the postmerged routine of the multielement part is entered to calculate merged flow conditions. Mixed conditions are then determined and the merged noise is calculated, extrapolated, and printed (if desired).

The premerged noise is now calculated depending on whether a suppressor is present or not. This component is extrapolated, printed if desired, and added to the postmerged. Outer-stream, shock-cell noise is determined, depending on whether a suppressor is present or not, extrapolated, printed (if desired), and added to the other components. Finally, the inner stream shock is computed, extrapolated, printed (if desired), and added to the other components. The total now is extrapolated as required, printed, and control is returned for the next case.

SUB1 Subroutine - This subroutine provides SAE ARP 876 (1975 revision) conical nozzle noise predictions. Use and limitations are as described in Appendix C. Output from this routine is on a one-foot arc. Basically, polynomial curve fits of the data in Appendix C were used. A correction was made to the predicted OASPL to increase the accuracy of the routine based on available data on suppressor nozzles. This correction amounts to +1 dB at all angles and frequencies.

SUB3 Subroutine - This routine resets the variables for input into the extrapolation and PNL calculation subroutines. It determines if extrapolation is required and calls EXTP. PNLPT is called to determine PNL and OASPL. TPNLC is called from PNLPT to determine PNLT. The variables are then reset maintaining the newly calculated values.

SUB5 Subroutine - This routine calculates sound power level from sound pressure level for each one-third-octave band and then antilogarithmically sums to obtain the overall levels.

SUB4 Subroutine - This routine places previously calculated sound pressure level and sound power level in other variable name storage for future use in the program.

SUB2 Subroutine - This routine adds a constant value to the one-third-octave band SPL at all angles and frequencies.

SUB6 Subroutine - This routine antilogarithmically sums different SPL and PWL spectra to obtain a total spectra and sums the total PWL spectrum to obtain OAPWL.

EXTP Subroutine - This routine extrapolates an input spectrum to a desired acoustic range using the inverse-square law (spherical spreading), air attenuation per SAE ARP 866 (Reference 34), and, if desired, extra ground attenuation (EGA) per the routine presented in SAE AIR 923 (Reference 35). A curve fit of the 59° F, 70% relative humidity, standard day air attenuation and curve fits for EGA are used. The routine automatically accounts for range changes from angle to angle on a sideline and includes the option of a 100-ft layer of EGA, full EGA, or no EGA as per SAE AIR 923.

SHKSUB Subroutine - This routine predicts shock-cell noise by the procedure defined in SAE ARP 876 (proposed, 1976, Appendix C). Output from this routine is on a one-foot arc. The definition of D8 was varied to allow calculations for nonround nozzles.

PNLPT Subroutine - This routine sums the SPL in a given spectrum antilogarithmically to obtain OASPL and uses the procedure defined in SAE ARP 865A (Reference 31) to calculate PNL.

TPNLC Subroutine - This routine calculated tone-corrected PNL via Section B36.3 of the FAA Noise Certification Document (Nov. 17, 1969) as a function of the uncorrected one-third-octave spectrum SPL.

PNTT8 Subroutine - This routine sets the format and prints the noise output from the main program. It prints the identification of the noise output and one-third-octave band SPL and PWL for 24 frequencies and 15 angles (20° to 160° to the inlet) as well as OASPL, PNL, and PNLT for each angle.

The second part of the routine calculates EPNL (if required) according to the procedure described in FAR Part 36. Times associated with given acoustic angles for a level flyover (assuming the engine centerline is

parallel to the ground) are determined first. Peak PNLT, the associated time, and the 10-dB down levels are determined. Initial and final times are then terminated by linear interpolation (extrapolation using the first or last two points is used when necessary). The PNLT history is then integrated between the 10-dB down points by summing half-second increments (determined by linear interpolation) to obtain the duration correction. This is added to the maximum PNLT to obtain EPNL; the EPNL is then printed.

EJECTS Subroutine - This routine first determines the effect of a hard-wall ejector of given geometry in terms of the reference SPL. Directivity and spectral effects are then determined. If no treatment is present in the ejector, control is returned to the main program. If treatment is present, an impedance prediction routine for SDOF treatment (single degree of freedom) is entered. The resistance and reactance of the treatment panel is determined; this yields a coefficient of absorption. The location of a given source and the strength relative to the peak are then calculated. The coefficient of absorption times the number of reflections for a given acoustic angle plus the relative source strength when summed over all sources yields an SPL reduction. This, when integrated over all angles, gives a sound power insertion loss. This reduction is log-averaged over the lower limiting, center, and upper limiting frequencies for the given one-third-octave band. The sound power insertion loss is then converted into a delta SPL for each acoustic angle and added to the hard-wall effect. Control is then returned to the main program.

INPUT DESCRIPTION

The input data is supplied through NAMELIST input format. Any number of successive cases can be run consecutively, limited only by the users execution time available. Each successive case requires only the INPUT NAMELIST. The data from preceding cases remains in storage; thus, only those variables which are to be changed from the preceding case input value need be included in the INPUT file of succeeding cases.

The input format is given in Table A-3. The definitions of each of the input variables given in Table A-3 are given in Table A-4. All variables are preset to zero before the first-case input is read. Only the input variables listed under a nozzle type in Table A-3 need be input for any case. Notes on the input follow the tables. Further descriptions of input variables are given in Figures A-2 and A-3.

OUTPUT DESCRIPTION

The output format is generally self-explanatory. The input is printed out using the nomenclature defined in Table A-5. Output flow conditions follow. Finally, SPL and PWL spectra, OASPL, OAPWL, PNL, PNLT, and EPNL are printed as required.

A warning flag is built into the iterations for gamma and merged velocity. The flag message is: DID NOT CONVERGE for either iteration, and the run terminates. Gross input errors have been the only cause of this message encountered in the development of the program.

Table A-3. Input Format.

At the beginning of each run, an unlimited number of cards can be input for the run identification. (A case identification card is available before each case also). The format for each card is:

60 - Character Title Card, Column's 1-60

To enter the case section of the input the following card is required:

CASES (Starting in Column 2)

The run or case identification cards may be omitted but the "CASES" card must be present. The case identification is saved and will be printed on succeeding cases unless another case identification card is read.

FOR CONICAL NOZZLES

Column

2



(60-Character Identification Card, Columns 1-60)

\$ INPUT Y9 = 1,

P9 = _____, TT3 = _____, A9 = _____,

R9 = _____, ALT = _____, SL = _____,

U = _____, E9 = _____, VO = _____,

\$

Table A-3. Input Format (Continued).

FOR SINGLE-FLOW, MULTITUBE NOZZLES

Column

2
↓

(60-Character Identification Card, Columns 1-60)

\$ INPUT Y9 = 2,

N = _____, RP = _____, B9 = _____,

DT = _____, A7 = _____, Z5 = _____,

SLJ = _____, TT3 = _____, P9 = _____,

K9 = _____, ALT = _____, SL = _____,

U = _____, E9 = _____, VO = _____,

A6 = _____, L9 = _____,

A = _____, _____, _____, _____,

Table A-3. Input Format (Continued).

Column

2
↓

RR = _____, _____, _____, _____, _____, _____, _____,
 _____, _____, _____, _____, _____, _____, _____,
 _____, _____, _____, _____, _____, _____, _____,
 _____, _____, _____, _____, _____, _____, _____,
 _____, _____, _____, _____, _____, _____, _____,
 _____, _____, _____, _____, _____, _____, _____,
 _____, _____, _____, _____, _____, _____, _____,

RX = _____, _____, _____, _____, _____, _____, _____,
 _____, _____, _____, _____, _____, _____, _____,
 _____, _____, _____, _____, _____, _____, _____,
 _____, _____, _____, _____, _____, _____, _____,
 _____, _____, _____, _____, _____, _____, _____,
 _____, _____, _____, _____, _____, _____, _____,
 _____, _____, _____, _____, _____, _____, _____,

\$

Table A-3. Input Format (Continued).

FOR SINGLE-FLOW, MULTICHUTE/SPOKE NOZZLES

Column

2



(60-Character Identification Card, Columns 1-60)

\$ INPUT Y9 = 3,

N = _____, RP = _____, B9 = _____,

R4 = _____, R6 = _____, SS = _____, A7 = _____,

TT3 = _____, P9 = _____,

K9 = _____, ALT = _____, SL = _____, U = _____,

E9 = _____, VO = _____, A6 = _____, L9 = _____,

A = _____, _____, _____, _____,

RR and RX as per the multitube nozzle case.

\$

Table A-3. Input Format (Continued).

FOR DUAL-FLOW NOZZLES WITH MULTITUBE
SUPPRESSORS ON THE OUTER STREAM

Column

2



(60-Character Identification Card, Columns 1-60)

\$ INPUT Y9 = 5,

RP = _____, DN = _____, AA8 = _____, A9 = _____,

TT4 = _____, P4 = _____, TT5 = _____, P5 = _____,

N = _____, DT = _____, A7 = _____, B9 = _____,

Z5 = _____, S1J = _____,

K9 = _____, ALT = _____, SL = _____, U = _____,

E9 = _____, VO = _____, A6 = _____, L9 = _____,

A = _____, _____, _____, _____,

RR and RX as per multitube case.

\$

Table A-3. Input Format (Concluded).

FOR DUAL-FLOW NOZZLES WITH MULTICHUTE/SPOKE
SUPPRESSOR ON THE OUTER STREAM

Column

2



(60-Character Identification Card, Columns 1-60)

\$ INPUT Y9 = 6,

RP = _____, DN = _____, AA8 = _____, A9 = _____,

TT4 = _____, P4 = _____, TT5 = _____, P5 = _____,

N = _____, B9 = _____,

R4 = _____, R6 = _____, SS = _____, A7 = _____,

K9 = _____, ALT = _____, SL = _____, U = _____,

E9 = _____, VO = _____, A6 = _____, L9 = _____,

A = _____, _____, _____, _____,

RR and RX as per multitube case.

\$

Table A-4. Input Variable Descriptions.

FOR CONICAL NOZZLES

Variable	Note	Description
P9		Nozzle Total to Ambient Pressure Ratio
TT3		Nozzle Exit Total Temperature, ° R
A9		Nozzle Exit Flow Area, ft ²
K9		Print Indicator: 0 = Total Nozzle Noise Only 1 = Nozzle Component and Total Noise
ALT	1	Altitude, Ground Sideline, or Arc Distance at which Prediction is to be made, ft
SL	1	Sideline Distance at Which Prediction is to be made, ft (Used for Flyover Cases Only)
U		Arc or Sideline Indicator 1 = Predictions to be made on an Arc 2 = Predictions to be made on a Sideline (or Flyover)
E9	2	EGA Indicator 0 = No EGA 1 = Full EGA 2 = 100-ft Layer of EGA
VO		Aircraft Flight Velocity

Table A-4. Input Variable Descriptions (Continued).

FOR SINGLE-FLOW, MULTITUBE NOZZLES

Variable	Note	Description
N		Number of Tubes
RP	3	Centerbody Plug Radius, ft
B9	4	Tube Centerline Cant Angle, degrees
DT	3	Tube Diameter, in.
A7		Nozzle Area Ratio
Z5		Number of Rows of Tubes Counting Center Tube (if Present) as zero
SLJ		Tube Centerline Spacing to Tube Diameter Ratio
TT3, P9, K9, ALT, SL, U, E9, VO		Same as Conical Nozzle
A6		Ratio of Ejector Inlet Area to Nozzle Total (or Annulus) Area (Input Zero for no Ejector)
L9		Ratio of Ejector Length to Suppressor Nozzle Equivalent Diameter
A(1)	3,5	Ejector Treatment Faceplate Thickness, in.
A(2)	3,5	Ejector Treatment Hole Diameter, in.
A(3)	3,5	Ejector Treatment Cavity Depth, in.
A(4)	3,5	Ejector Treatment Open Area Ratio
RR	6	Ejector Treatment Specific Resistance, Rayls (49 Values Required)
RX	6	Ejector Treatment Specific Reactance, Rayls (49 Values Required)

Table A-4. Input Variable Descriptions (Continued).

FOR SINGLE-FLOW, MULTICHUTE/SPOKE NOZZLES

Variable	Note	Description
N		Number of Elements
RP	3	Centerbody Plug Radius, ft
B9	4	Chute/Spoke Exit Cant Angle, degrees
R4		Outer Circumferential Flow Dimension, in.
R6		Inner Circumferential Flow Dimension, in.
SS		Outer Circumferential Element Dimension, in.
A7		Nozzle Area Ratio
TT3, P9, K9, ALT, SL, V, E9, VO,		Same as Conical Nozzle
A6, L9, A, RR, RX		Same as Multitube Nozzle

Table A-4. Input Variable Descriptions (Continued)

FOR DUAL-FLOW NOZZLES WITH A MULTITUBE
SUPPRESSOR ON THE OUTER STREAM

Variable	Note	Description
RP		Centerbody Plug Radius, ft
DN		Nozzle Outer Diameter, ft
AA8		Inner Nozzle Flow Area, ft ²
A9		Outer Nozzle Flow Area, ft ²
TT4		Inner Nozzle Exit Total Temperature, ° R
P4		Inner Nozzle Total to Ambient Pressure Ratio
TT5		Outer Nozzle Exit Total Temperature, ° R
P5		Outer Nozzle Total to Ambient Pressure Ratio
N, DT, A7, B9, Z5, S1J, A6, L9, A, RR, RX		Same as Multitube Nozzle
K9, ALT, SL, U, E9, VO		Same as Conical Nozzle

Table A-4. Input Variable Descriptions (Concluded).

FOR DUAL-FLOW NOZZLES WITH MULTICHUTE/SPOKE
SUPPRESSORS ON THE OUTER STREAM

Variable	Note	Description
RP, DN, AA8, A9, TT4, P4, TT5, P5		Same as Dual-Flow/Multitube
N, B9, R4, R6, SS, A7		Same as Multichute/Spoke
K9, ALT, SL, U, E9, VO		Same as Conical
A6, L9, A, RR, RX		Same as Multitube

NOTES ON INPUT:

1. The ALT variable is used as the main distance indicator; therefore, for ground static arc or sideline cases the distance of interest is input through this variable, and the SL variable is set to zero. In flyover cases, ALT is used as the altitude indicator, and SL is used as the sideline distance.
2. EGA is "Extra Ground Attenuation" as defined in SAE AIR 923 "Method for Calculating the Attenuation of Aircraft Ground to Ground Noise Propagation During Takeoff and Landing." The "100-ft layer" is defined in Figure 3 of the above-mentioned document.
3. Major nozzle dimensions are input in feet; element or ejector-treatment dimensions are input in inches. This alleviates inputting very small numbers (i.e., 0.1 inches versus 0.0083 feet).
4. Cant angles for multitube and multichute/spoke nozzles are defined in Figure A-4.
5. The "A" variables are input as 10 if treatment other than SDOF is used. In this case RR and RX must be input.
6. The specific resistances and reactances of the treatment used in the ejector are input through the RR and RX variables. Values at the lower limiting, upper limiting, and midpoint frequencies are used. For ease of input, the program assumes the value at the upper limiting frequency of one one-third-octave band to be equal to the value at the lower limiting frequency of the next highest band. Therefore, only 49 values must be input.

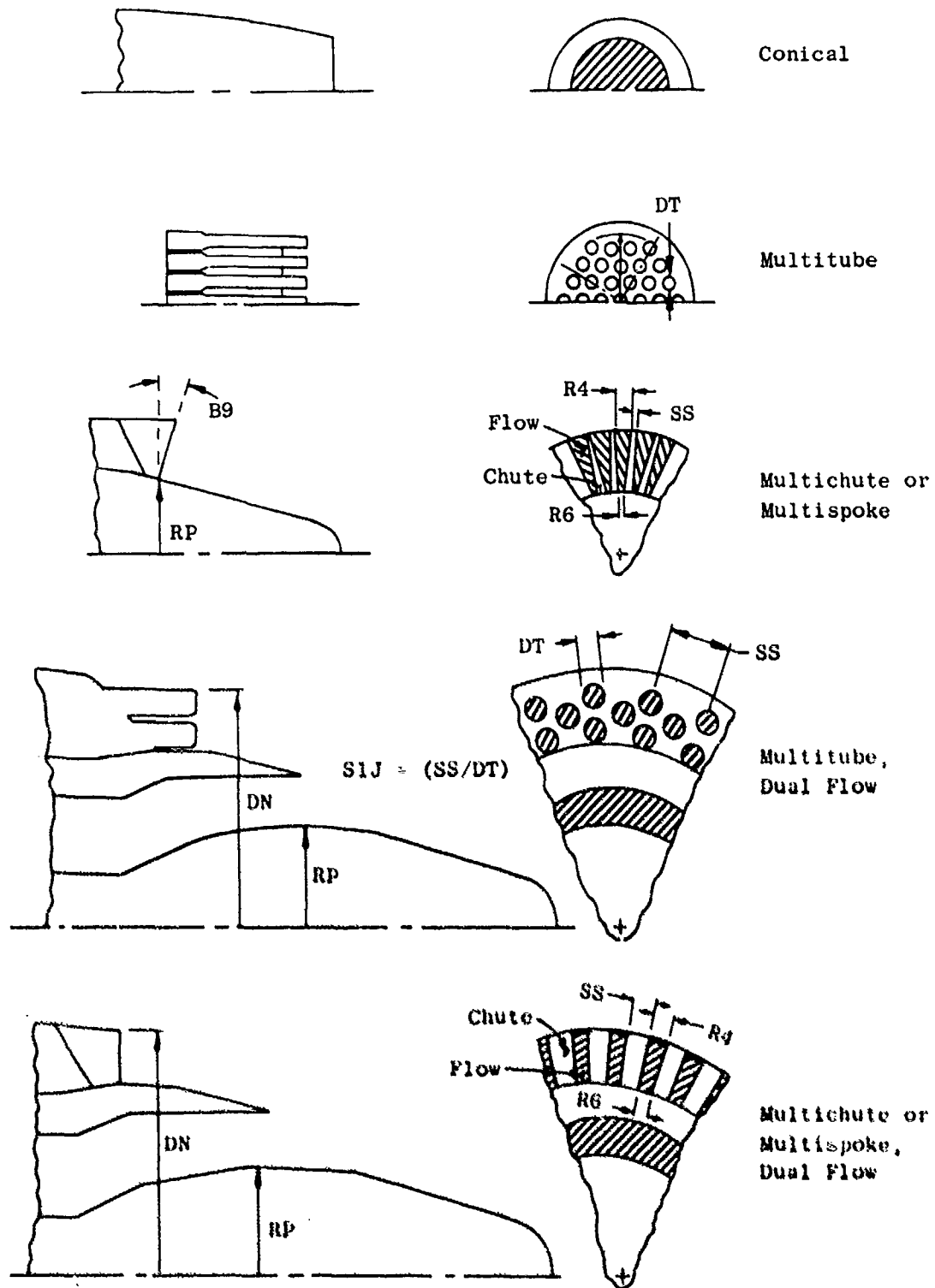


Figure A-2. Nozzle Types Included in the Correlation.

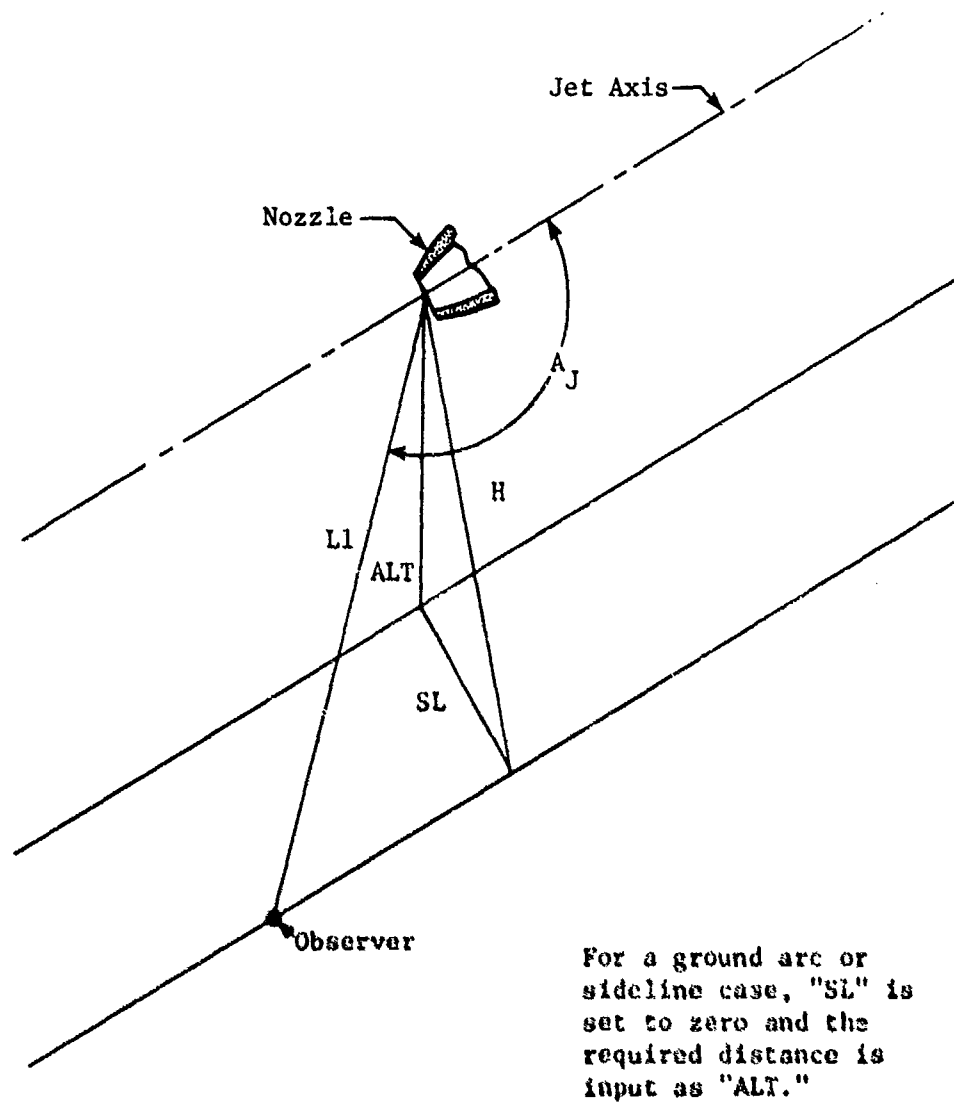
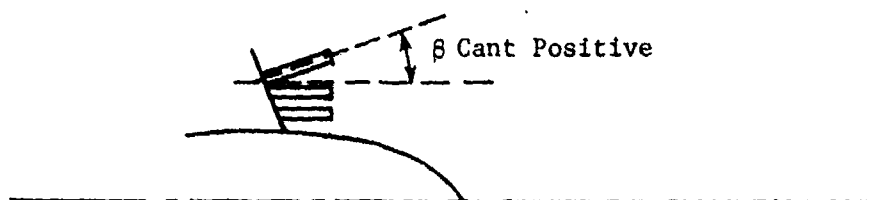


Figure A-3. Fortran Symbol Convention for Acoustic Arena Variables.

Multitube Nozzles



Multichute/Spoke Nozzles

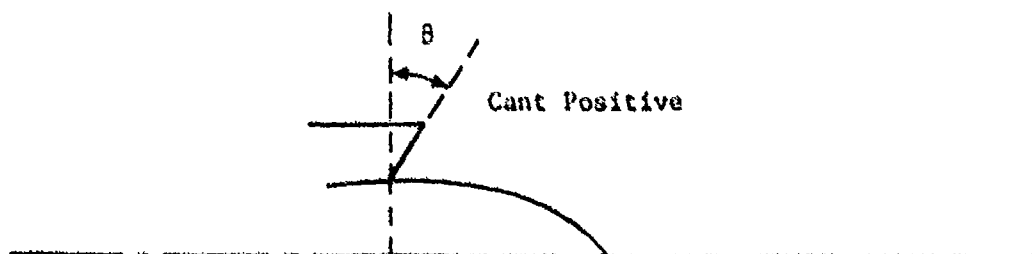


Figure A-4. Definition of Cant Angles for Multielement Nozzles.

Table A-5. Output Symbol Descriptions.

Symbol	Description
ARD	Suppressor Nozzle Area Ratio
AT	Area of an Individual Flow Element
A5	Merged Flow Area
A6	Mixed Flow Area
A8	Inner Nozzle Flow Area
A28	Outer Nozzle Flow Area
DUCT H	Outer Nozzle Duct Height
D5	Diameter of the Merged Flow Stream
P0	Ambient Pressure
PT8/P0	Inner Nozzle Pressure Ratio
PT28/P0	Outer Nozzle Pressure Ratio
RHO5	Density of the Merged Stream
RHO8	Density of the Inner Stream
RHO28	Density of the Outer Stream
T0	Ambient Temperature
TT5	Total Temperature of the Merged Stream
TT6	Total Temperature of the Mixed Stream
TT8	Total Temperature of the Inner Stream
TT28	Total Temperature of the Outer Stream
U5	Fully Expanded Merged Velocity
U6	Fully Expanded Mixed Velocity
U8	Fully Expanded Inner Stream Velocity
U28	Fully Expanded Outer Stream Velocity
W6	Mixed Stream Weight Flow
PWL	Sound Power Level, dB re: 10^{-13} watts
OASPL	Overall Sound Pressure Level re: 2 dynes/m ²
OAPWL	Overall PWL
PNL	Perceived Noise Level, PNdB
PNLT	Tone-Corrected PNL, PNdB
EPNL	Static Effective Perceived Noise Level, EPNdB

SAMPLE CASES

Example cases for a conical nozzle with and without EGA, a dual-flow nozzle with a multitube suppressor and a treated ejector, and a dual-flow nozzle with a multichute suppressor are given. The input data cards are listed in Table A-6 as per the format given in Table A-3.

Table A-6. Input Data Card Listing Sample Case.

```
AR SIECKMAN      TASK 3 HIGH VELOCITY JET NOISE PROGRAM
GENERAL ELECTRIC CO. BLDG 300 RIN 79 M.D. H77 Y22A1
MS -- ENGINEERING CORRELATION MODEL -- CDC VERSION

CASES
CONICAL NOZZLE CHECK CASE
$INPUT Y9#1,
P9#3.247, TT3#1380, A9#2.346, RP#0, K9#1,
ALT#2400, UN2, F9#0, V0#350, A6#0, L9#0, AN4#0,
$
$INPUT E9#2$
DUAL FLOW MULTI-TUBE CHECK CASE
$INPUT Y9#5,
RP#1.423, DN#6.887, AARN7.649, A9#5.083, TT4#1010,
P4#1.567, TT5#1632, P5#1.278, K9#1, NW#0,
DT#3.672, A7#2.75, B9#0, Z5#3,
SIJ#2.818, ALT#320, UN1, E0#0, V0#0,
A6#0, L9#0, AN4#0,
A6#1.303, L9#3.952, AN4#10,
RR#09#0.311,
RX#-87.135, -77.549, -69.239, -61.153, -54.949, -48.463,
-43.269, -38.767, -34.611, -31.008, -27.683, -24.219, -21.620,
-19.367, -17.287, -15.484, -13.819, -12.277, -10.954, -9.652, -8.608,
-7.702, -6.864, -6.088, -5.370, -4.762, -4.232, -3.771, -3.342,
-2.968, -2.619, -2.251, -1.970, -1.722, -1.487, -1.278, -1.077, -.882,
-.704, -.515, -.347, -.185, -.010, .185, .401, .703, 1.1, 1.794, 4.097,
$
DUAL FLOW MULTI-CHUTE CHECK CASE
$INPUT Y9#6,
RP#1.624, DN#2.671, AARN.811, A9#1.555, TT4#1470,
P4#1.490, TT5#1750, P5#1.97, K9#0, NW#0,
B9#0, H4#2.874, R4#2.060, SS#2.155,
A7#1.75, ALT#2400, UN2, E0#0, V0#350,
A6#0, L9#0, AN4#0,
$
```

NOTE: The symbol # indicates an equal sign (=).

```

XX      XX
XXX     XXX
XXXX    XXXX
XXXX    XXXX
XX XXXX XX
XX XX   XX
XX      XX
XX      XX
XX      XX
XX      XX
XX      XX
XX      XX
XX      XX
XX      XX

```

```

XXXXX X X XXXXX XXXXXX XXXXXX X X
X      X X X      X XX XX
XXX    XY XXX      X X XX X
      XXX X XXX    X XXX X
      X X XXXX    X X X
XXXXX X XXXXX X XXXXXX X X

```

HIGH VELOCITY JET NOISE PROGRAM(CONTRACT DOT-OS-30034)
 TASK3 -- ENGINEERING CORRELATION

AP SIFCKMAN TASK 3 HIGH VELOCITY JET NOISE PROGRAM
 GENERAL ELECTRIC CO. BLDG 300 Rm 79 M.D. H77 X2261
 WS -- ENGINEERING CORRELATION MODEL -- CDC VERSION

HIGH VELOCITY JET NOISE PROGRAM - ENGINEERING CORRELATION

CONICAL NOZZLE CHECK CASE

*** INPUT ***

T0 = 519. P0 = 14.700
 TTR = 1380. PTR/P0 = 3.247
 EJECTOR AREA RATIO PARAMETER = 0.000 V0 = 350.0
 PLUG DIA = 0.000 CANT = 0.000

*** OUTPUT ***

DIA OF OUTER ROW = 1.728 EQUIV AREA DIA = 1.728
 NOZZLE EXIT CONDITIONS
 U8 = 2184.0 RH08 = .0397 AT = 2.346 A8 = 2.346

HIGH VELOCITY JET NOISE PROGRAM - ENGINEERING CORRELATION

CONICAL NOZZLE CHECK CASE

- * CONICAL MIXING NOISE
- * 2400.0 FOOT ALTITUDE
- * 0.0 FOOT SIDELINE
- * NO EGA
- * 510 DEGREE STANDARD DAY

ACOUSTIC ANGLE FROM INLET

FREQ	20	30	40	50	60	70	80	90	100	110	120	130	140	150	160	PWL
50	56.2	59.2	61.3	62.9	64.5	65.6	67.2	69.0	70.6	72.9	75.7	82.0	85.7	87.4	84.0	162.3
63	57.9	61.1	63.2	64.8	66.5	67.6	69.2	71.0	72.7	74.9	78.3	84.8	88.5	90.0	86.2	164.9
80	59.5	62.8	65.1	66.7	68.4	69.5	71.2	72.9	74.6	77.2	82.7	89.1	92.5	93.1	88.1	168.3
100	60.9	64.3	66.6	68.3	70.0	71.2	72.9	74.6	76.5	79.1	84.4	90.6	93.6	93.6	88.0	169.2
125	62.0	65.6	68.0	69.8	71.5	72.7	74.4	76.2	78.3	81.0	86.1	92.0	94.4	93.7	87.2	169.8
160	63.0	66.8	69.3	71.2	73.0	74.2	75.9	77.7	79.8	82.5	87.3	92.8	94.7	93.2	86.0	170.1
200	63.6	67.6	70.3	72.2	74.1	75.3	77.1	78.9	81.0	83.7	88.3	93.4	94.6	92.3	84.2	170.1
250	64.0	68.2	71.0	73.0	75.0	76.1	77.9	79.9	82.1	84.8	89.0	93.6	94.2	91.0	82.0	169.9
315	64.0	68.5	71.5	73.7	75.7	77.0	78.9	80.6	82.9	85.5	89.4	93.5	93.3	89.1	79.2	169.6
400	63.7	68.6	71.7	74.0	76.1	77.5	79.4	81.2	83.4	86.0	89.4	93.0	92.1	87.1	76.1	169.2
500	63.0	68.2	71.6	74.1	76.3	77.7	79.6	81.4	83.6	86.1	89.1	92.2	90.5	84.5	72.5	168.7
630	61.8	67.5	71.2	73.8	76.1	77.7	79.6	81.4	83.4	85.8	88.4	91.0	88.4	81.4	68.3	168.0
800	59.9	65.7	70.3	73.2	75.6	77.2	79.2	81.1	83.4	85.1	87.3	89.4	86.0	78.1	63.8	167.3
1000	57.6	64.7	69.1	72.1	74.7	76.5	78.5	80.4	82.8	85.1	87.3	89.4	83.2	74.3	58.6	166.5
1250	54.4	62.5	67.3	70.7	73.5	75.3	77.4	79.3	81.8	84.0	85.8	87.4	79.4	69.3	51.8	165.5
1600	49.7	59.1	64.7	68.4	71.4	73.4	75.6	77.5	80.2	82.1	83.5	84.5	75.2	63.9	44.4	164.5
2000	43.9	55.0	61.4	65.6	68.9	71.1	73.4	75.3	78.0	79.7	80.7	81.2	75.2	63.9	44.4	164.5
2500	36.2	49.5	56.9	61.8	65.5	67.9	70.3	72.3	75.0	76.4	77.0	76.8	69.9	57.1	35.1	163.4
3150	24.9	41.5	50.6	56.3	60.6	63.4	66.0	68.0	70.6	71.7	71.8	70.9	62.7	48.0	22.5	162.2
4000	8.1	29.7	41.2	48.3	53.4	56.7	59.5	61.7	64.2	64.8	64.3	62.4	52.5	35.2	4.4	160.8
5000	-2.5	22.1	35.0	43.0	48.6	52.2	55.2	57.4	59.8	60.1	59.1	56.7	45.8	26.7	-7.2	159.4
6300	-31.8	1.7	18.9	29.3	36.4	40.8	44.3	46.6	48.9	48.5	46.6	42.6	29.2	5.7	-37.3	157.9
8000	-77.2	-29.8	-5.9	8.3	17.6	23.5	27.7	30.3	32.2	30.9	27.5	21.2	3.9	-26.4	-83.4	156.3
10000	-138.3	-72.0	-39.0	-19.7	-7.3	4.4	5.7	8.5	10.1	7.6	2.2	-7.1	-29.6	-69.1	-145.1	154.8
OASPL	73.4	78.1	81.3	83.7	85.9	87.4	89.3	91.2	93.0	95.4	98.8	103.0	103.8	102.2	96.0	180.8
PWL	76.7	82.7	86.7	89.7	92.6	94.4	96.6	98.5	100.6	102.7	105.1	108.5	107.7	104.0	95.6	
PNTL	76.7	84.1	87.8	89.7	92.6	94.4	96.6	98.5	100.6	102.7	105.1	108.5	108.8	105.4	95.6	

EPNL = 108.7

HIGH VELOCITY JET NOISE PROGRAM - ENGINEERING CORRELATION

CONICAL NOZZLE CHECK CASE

- * CONICAL SHOCK NOISE
- * 2400.0 FOOT ALTITUDE
- * 0.0 FOOT SIDEWALL
- * NO EGA
- * 519. DEGREE STANDARD DAY

ACOUSTIC ANGLE FROM INLET

FREQ.	25	30	40	50	60	70	80	90	100	110	120	130	140	150	160	PNL
50	48.1	51.7	54.2	56.9	57.3	58.1	59.0	59.3	59.3	59.0	58.3	57.3	55.7	53.4	49.9	137.3
63	50.6	54.4	57.0	58.9	60.4	61.5	62.3	62.8	62.9	62.6	62.0	60.9	59.4	57.0	53.5	140.7
80	52.7	56.6	59.4	61.6	63.3	64.6	65.6	66.2	66.5	66.3	65.7	64.7	63.1	60.8	57.2	144.2
100	53.9	58.1	61.1	63.5	65.5	67.1	68.3	69.2	69.7	69.7	69.2	68.2	66.6	64.2	60.5	147.3
125	54.6	58.9	62.1	64.7	67.0	69.0	70.7	72.0	72.7	73.0	72.6	71.7	70.1	67.6	63.8	150.3
160	55.3	59.6	62.8	65.5	68.1	70.5	72.7	74.5	75.8	76.5	76.4	75.5	73.9	71.4	67.4	153.6
200	57.9	61.6	64.1	66.3	68.5	71.0	73.6	76.0	78.0	79.1	79.4	78.7	77.1	74.4	70.2	156.4
250	64.6	67.6	69.7	71.1	72.7	74.3	75.9	77.4	79.1	81.0	81.7	81.3	79.7	76.8	72.3	158.7
315	71.7	75.3	76.7	78.5	79.1	80.3	81.3	82.3	83.4	84.5	84.8	84.8	83.2	79.8	74.3	163.7
400	71.9	76.8	80.5	83.2	84.8	86.4	87.9	89.3	90.7	92.0	92.2	92.2	90.8	84.7	79.3	164.5
500	71.4	76.8	80.5	83.2	84.8	86.4	87.9	89.3	90.7	92.0	92.2	92.2	90.8	84.7	79.3	164.5
630	69.8	74.8	77.7	80.1	82.6	84.7	86.1	87.6	89.1	90.6	92.1	93.6	95.1	96.6	98.1	164.1
800	67.5	73.3	76.8	78.9	80.9	82.9	84.9	86.9	88.9	90.9	92.9	94.9	96.9	98.9	100.9	163.2
1000	65.2	71.8	75.4	77.3	78.9	80.5	82.1	83.7	85.3	86.9	88.5	90.1	91.7	93.3	94.9	162.4
1250	61.3	68.6	72.7	75.7	77.6	79.2	80.9	82.6	84.2	85.9	87.5	89.2	90.8	92.5	94.2	161.5
1600	56.5	65.2	70.0	72.8	74.5	76.1	77.7	79.3	80.9	82.5	84.1	85.7	87.3	88.9	90.5	160.6
2000	50.7	60.8	66.3	69.7	72.0	73.2	74.4	75.6	76.8	78.0	79.2	80.4	81.6	82.8	84.0	159.7
2500	42.7	55.1	61.6	65.7	68.2	70.7	73.2	75.7	78.2	80.7	83.2	85.7	88.2	90.7	93.2	158.7
3150	31.1	46.7	54.8	59.6	62.7	65.4	68.0	70.6	73.2	75.8	78.4	81.0	83.6	86.2	88.8	157.2
4000	13.9	34.5	44.9	51.1	55.0	57.7	60.4	63.1	65.7	68.4	71.1	73.8	76.5	79.2	81.9	155.7
5000	3.2	26.7	38.6	45.6	49.9	52.6	55.1	57.6	60.1	62.6	65.1	67.6	70.1	72.6	75.1	154.4
6300	-26.0	6.3	22.5	31.9	37.7	41.2	43.1	43.8	43.1	41.2	37.7	31.9	22.4	6.3	-26.0	153.1
8000	-71.4	-25.2	-2.3	10.8	18.9	23.8	26.5	27.3	26.5	23.8	18.9	10.8	-2.3	-25.2	-71.4	151.7
10000	-132.5	-67.4	-35.5	-17.3	-6.1	4.3	5.5	4.3	4.3	4.3	4.3	4.3	4.3	4.3	4.3	150.3
PNL	83.6	89.2	92.7	95.0	96.6	97.3	97.7	97.4	96.8	97.1	97.5	97.6	95.8	91.4	85.1	
PNLT	83.6	90.6	93.8	95.0	96.6	97.3	97.7	97.4	96.8	97.1	97.5	97.6	96.9	92.8	85.1	

EPNL = 100.4

HIGH VELOCITY JET NOISE PROGRAM - ENGINEERING CORRELATION

CONICAL NOZZLE CHECK CASE

- CONICAL TOTAL NOISE
- 2450.0 FOOT ALTITUDE
- 9.0 FOOT SIDELINE
- 100 FOOT LAYER EGA
- 514.0 DEGREE STANDARD DAY

ACOUSTIC ANGLE FROM INLET

FREQ	20	30	40	50	60	70	80	90	100	110	120	130	140	150	160	PWL
50	56.2	59.4	61.6	63.2	64.7	65.8	67.3	68.9	68.1	70.4	75.2	81.5	85.1	86.9	83.5	162.3
63	58.0	61.3	63.0	65.3	66.5	68.0	69.5	71.0	70.6	72.7	77.8	84.2	87.9	89.4	85.5	164.9
80	59.6	63.1	65.5	67.0	68.9	70.1	71.6	73.2	73.0	75.1	80.2	86.6	90.2	91.3	86.8	166.9
100	60.8	64.5	67.0	68.9	70.7	72.0	73.6	75.1	75.2	77.3	82.2	88.4	91.8	92.3	87.2	168.3
125	61.7	65.6	68.2	70.2	72.2	73.6	75.3	76.9	77.3	79.4	84.0	90.0	92.9	92.9	87.0	169.3
160	62.6	66.6	69.4	71.5	73.5	75.0	76.9	78.7	79.6	81.6	85.8	91.3	93.7	92.8	86.2	169.9
200	63.5	67.6	70.3	72.4	74.4	75.9	78.0	80.0	81.2	83.4	87.2	92.2	94.0	92.3	84.9	170.2
250	66.0	69.9	72.1	74.7	76.3	77.7	79.6	80.7	82.4	84.8	88.3	92.6	93.9	91.4	83.2	170.4
315	71.0	75.0	76.9	77.4	77.5	77.8	79.2	81.2	83.2	85.8	89.2	93.1	93.4	90.1	81.2	170.5
400	72.8	77.8	80.8	82.2	82.4	81.3	83.6	85.5	83.5	86.3	89.7	93.1	92.6	88.4	78.9	170.6
500	70.4	76.2	80.0	82.7	84.4	84.7	83.4	82.3	83.4	86.2	89.6	92.6	91.5	86.5	76.3	170.5
630	68.7	74.2	77.4	80.0	82.5	84.5	85.2	84.1	83.6	85.8	88.9	91.7	89.9	84.0	73.0	170.0
800	66.3	72.7	76.5	78.9	80.3	81.6	83.7	84.8	84.3	85.2	87.9	90.4	87.8	80.9	68.9	169.2
1000	64.0	71.1	75.1	77.4	79.2	80.5	81.3	83.2	84.4	84.7	86.6	88.7	85.4	77.6	64.3	168.5
1250	60.1	68.4	72.5	75.7	77.9	78.9	80.2	82.9	83.1	84.0	85.0	86.6	82.6	73.8	59.3	167.7
1600	55.2	64.5	69.8	72.9	75.1	76.9	78.2	79.1	80.6	82.2	82.7	83.6	78.8	68.7	53.5	166.7
2000	49.3	63.2	66.1	69.9	72.6	74.2	75.6	76.8	78.3	79.5	80.0	80.2	74.5	63.3	48.4	165.8
2500	41.4	54.5	61.5	65.9	68.9	70.8	72.4	73.6	75.2	76.1	76.5	75.8	69.2	56.9	41.6	164.7
3150	29.8	46.2	54.8	60.0	63.6	65.9	67.7	69.1	70.7	71.3	71.2	69.9	62.1	48.5	30.0	163.4
4000	12.7	34.1	45.0	51.7	56.1	58.9	61.3	62.5	64.2	64.4	63.6	61.4	51.9	36.3	12.1	162.0
5000	2.0	26.3	38.8	46.2	51.2	54.3	56.6	58.1	59.8	59.7	58.5	55.7	45.1	28.2	1.3	160.6
6300	-27.2	6.0	22.7	32.5	38.9	42.9	45.7	47.4	48.8	48.1	45.9	41.7	28.6	7.4	-27.9	159.2
8000	-72.6	-25.5	-2.1	11.5	20.1	25.5	29.0	31.0	32.1	30.5	26.9	20.3	3.4	-24.4	-73.6	157.6
10000	-133.8	-67.8	-35.3	-16.6	-4.8	2.4	7.0	9.2	10.0	7.3	1.7	-8.0	-30.0	-66.8	-134.6	156.1
OASPL	78.5	83.7	86.9	89.0	90.5	91.4	92.1	92.8	93.8	95.6	98.7	102.4	103.1	101.5	95.2	181.4
PWL	83.3	89.3	93.0	95.4	97.4	98.4	99.4	100.0	101.2	102.8	105.0	107.9	107.0	103.3	95.0	
PNT	83.3	90.7	94.1	95.4	97.4	98.4	99.4	100.0	101.2	102.8	105.0	107.9	108.1	104.7	95.0	

EPNL = 109.4

HIGH VELOCITY JET NOISE PROGRAM - ENGINEERING CORRELATION

CONICAL NOZZLE CHECK CASE

*** INPUT ***

T0 = 519. P0 = 14.756
 TTR = 1380. PTR/P0 = 3.247
 EJECTOR AREA RATIO PARAMETER = 0.000 VC = 350.0
 PLUG DIA = 0.000 CANT = 0.000

*** OUTPUT ***

DIA OF OUTER ROW = 1.728 EQUIV AREA DIA = 1.728

NOZZLE EXIT CONDITIONS
 U8 = 2184.0 RHOR = .0397 AT = 2.346 AR = 2.346

HIGH VELOCITY JET NOISE PROGRAM - ENGINEERING CORRELATION

CONICAL NOZZLE CHECK CASE

- CONICAL MIXING NOISE
- 2400.0 FOOT ALTITUDE
- 3.0 FOOT SIDELINE
- 100 FOOT LAYER EGA
- 519.0 DEGREE STANDARD DAY

ACOUSTIC ANGLE FROM INLET

FREQ	20	30	40	50	60	70	80	90	100	110	120	130	140	150	160	PWL
50	55.3	58.7	60.8	62.4	64.0	65.6	67.2	68.7	69.4	70.1	75.2	81.5	85.1	86.9	83.5	162.3
63	57.3	60.5	62.7	64.3	65.9	67.0	68.7	70.4	72.4	72.4	77.7	84.2	87.9	89.4	85.5	164.9
80	58.8	62.2	64.4	66.1	67.8	68.9	70.6	72.3	72.3	72.4	80.0	86.6	90.2	91.3	86.8	166.9
100	60.0	63.6	65.9	67.7	69.4	70.5	72.3	74.0	74.0	74.0	82.0	88.4	91.8	92.3	87.2	168.3
125	61.0	64.8	67.3	69.1	70.8	72.0	73.0	75.5	75.5	75.5	83.7	89.9	92.9	92.8	87.0	169.2
160	61.0	65.0	68.5	70.4	72.2	73.5	75.2	77.0	77.6	80.3	85.4	91.2	93.6	92.8	86.1	169.8
200	62.4	66.6	69.4	71.4	73.3	74.6	76.4	78.1	79.1	81.7	86.5	92.0	93.9	92.3	84.8	170.1
250	62.7	67.2	70.1	72.2	74.2	75.5	77.3	79.1	80.3	82.8	87.5	92.5	93.7	91.3	82.9	170.1
315	62.6	67.4	70.5	72.8	74.8	76.2	78.0	79.8	81.3	83.9	88.1	92.7	93.2	89.9	80.6	169.9
400	62.2	67.4	70.7	73.1	75.2	76.7	78.5	80.3	82.1	84.7	88.5	92.5	92.2	88.0	77.7	169.6
500	61.4	67.0	70.6	73.1	75.3	76.8	78.7	80.6	82.5	85.1	88.5	92.0	91.0	85.8	74.5	169.2
630	60.0	66.2	70.1	72.8	75.1	76.7	78.7	80.5	82.6	85.1	88.1	91.2	89.3	83.2	70.8	168.7
800	58.1	65.0	69.2	72.1	74.6	76.3	78.3	80.1	82.4	84.8	87.4	89.9	87.2	80.1	66.5	168.0
1000	55.6	61.3	67.0	71.0	73.7	75.5	77.5	79.4	81.8	84.1	86.3	88.3	84.8	76.7	61.8	167.3
1250	52.4	61.0	66.1	69.5	72.4	74.3	76.4	78.3	80.8	82.9	84.7	86.2	81.9	72.8	56.6	166.5
1600	47.5	57.5	63.3	67.2	70.3	72.4	74.6	76.5	79.1	81.0	82.1	83.3	78.1	67.7	49.7	165.5
2000	41.7	53.4	60.0	64.3	67.8	70.0	72.3	74.2	76.9	78.5	79.6	79.0	73.8	62.2	42.1	164.5
2500	33.9	47.8	55.5	60.5	64.3	66.8	69.2	71.2	73.0	75.3	75.8	75.6	68.5	55.4	32.8	163.4
3150	27.7	39.9	49.2	55.1	59.4	62.3	64.9	66.9	69.5	70.6	70.6	69.7	61.3	46.4	20.2	162.2
4000	5.8	28.0	39.8	47.1	52.2	55.5	58.4	60.6	63.1	63.7	63.1	61.1	51.2	33.5	2.2	160.8
5000	-4.8	20.4	33.6	41.7	47.4	51.0	54.1	56.3	58.7	59.0	58.0	55.4	44.4	25.1	-9.4	159.4
6300	-34.0	0.0	17.5	28.0	35.2	39.7	43.2	45.6	47.8	47.4	45.4	41.3	27.8	4.0	-39.5	157.9
8000	-79.4	-31.5	-7.3	7.3	16.5	22.3	26.6	29.2	31.1	29.8	26.3	19.9	2.5	-28.1	-85.6	156.3
10000	-140.6	-73.7	-40.6	-21.0	-8.4	-7.7	4.6	7.4	9.0	6.5	1.1	-8.4	-31.0	-70.8	-147.3	154.8
OASPL	72.1	77.0	80.3	82.8	85.0	86.5	88.5	90.3	92.1	94.5	98.0	102.1	102.9	101.3	95.1	180.8
PWL	75.1	81.5	85.6	88.6	91.5	93.4	95.6	97.5	99.7	101.7	104.2	107.5	106.7	102.9	94.4	
PNLT	75.1	82.9	86.8	88.6	91.5	93.4	95.6	97.5	99.7	101.7	104.2	107.5	107.8	104.4	94.4	

EPNL = 107.7

HIGH VELOCITY JET NOISE PROGRAM - ENGINEERING CORRELATION

CONICAL NOZZLE CHECK CASE

- CONICAL SHOCK NOISE
- 2-000.0 FOOT ALTITUDE
- 0.0 FOOT SIDELINE
- 100 FOOT LAYER FOR
- 519.0 DEGREE STANDARD DAY

ACOUSTIC ANGLE FROM INLET

FREQ	20	30	40	50	60	70	80	90	100	110	120	130	140	150	160	PWL
50	47.5	51.2	53.7	55.5	56.8	57.8	58.4	58.8	58.4	58.5	57.8	56.7	55.2	54.9	49.4	137.3
63	50.0	53.8	56.4	58.2	59.9	61.0	61.7	62.2	62.3	62.0	61.4	60.4	58.8	56.5	52.8	140.7
80	51.9	55.0	57.6	59.0	60.9	62.7	64.0	65.0	65.6	65.7	65.1	64.1	62.5	60.1	56.4	144.2
100	53.1	57.3	60.4	62.8	64.4	66.4	67.7	68.6	69.0	69.0	68.6	67.6	65.9	63.5	59.6	147.3
125	53.6	58.1	61.3	64.0	66.4	68.4	70.0	71.3	72.1	72.3	71.9	71.0	69.3	66.8	62.8	150.3
160	54.2	58.7	62.0	64.8	67.3	69.8	72.0	73.4	75.1	75.7	75.6	74.8	73.1	70.5	66.3	153.6
200	54.8	59.7	63.2	66.0	68.6	71.2	73.4	75.3	77.2	78.4	78.6	77.9	76.3	73.5	69.0	156.4
250	55.4	60.6	64.1	67.0	69.7	72.4	74.8	76.5	78.3	80.2	80.9	80.5	78.8	75.8	71.0	158.7
315	56.3	61.6	65.2	68.2	71.0	73.8	76.3	78.1	80.0	81.9	82.7	82.5	80.8	77.6	72.4	161.3
400	57.4	62.8	66.6	69.6	72.4	75.2	77.6	79.3	81.2	83.0	83.6	83.4	82.2	78.6	72.8	163.7
500	58.8	64.2	68.0	71.0	73.8	76.6	79.0	80.7	82.6	84.4	84.9	84.7	83.4	79.1	71.7	164.5
630	60.1	65.5	69.3	72.4	75.2	77.9	80.1	81.6	83.4	85.1	85.6	85.4	84.1	79.6	71.3	164.1
800	61.6	67.0	70.8	73.9	76.6	79.2	81.3	83.0	84.7	86.4	86.8	86.6	85.3	80.8	73.6	163.2
1000	63.1	68.5	72.3	75.4	78.1	80.6	82.6	84.3	86.0	87.7	88.2	88.0	86.7	81.3	74.0	162.4
1250	64.6	69.9	73.7	76.8	79.4	81.8	83.7	85.3	87.0	88.7	89.1	88.9	87.6	82.0	74.8	161.5
1600	66.1	71.4	75.2	78.3	80.9	83.2	85.0	86.6	88.3	89.9	90.3	90.1	88.8	83.2	75.6	160.6
2000	67.6	72.9	76.7	79.8	82.4	84.6	86.3	87.9	89.5	91.1	91.5	91.3	90.0	84.4	76.4	159.7
2500	69.1	74.4	78.2	81.3	83.9	86.1	87.8	89.4	91.0	92.6	93.0	92.8	91.5	85.8	77.2	158.7
3150	70.6	75.9	79.7	82.8	85.4	87.6	89.3	90.9	92.5	94.1	94.5	94.3	93.0	87.2	78.0	157.2
4000	72.1	77.4	81.2	84.3	86.9	89.1	90.8	92.4	94.0	95.6	96.0	95.8	94.5	88.7	78.8	155.7
5000	73.6	78.9	82.7	85.8	88.4	90.6	92.3	93.9	95.5	97.1	97.5	97.3	96.0	89.9	79.6	154.4
6300	75.1	80.4	84.2	87.3	89.9	92.1	93.8	95.4	97.0	98.6	99.0	98.8	97.5	91.4	80.4	153.1
8000	76.6	81.9	85.7	88.8	91.4	93.6	95.3	96.9	98.5	100.1	100.5	100.3	99.0	92.9	81.2	151.7
10000	78.1	83.4	87.2	90.3	92.9	95.1	96.8	98.4	100.0	101.6	102.0	101.8	100.5	94.4	82.0	150.3
OASPL	77.4	82.6	86.4	89.5	92.1	94.3	96.0	97.6	99.2	100.8	101.2	101.0	99.7	93.6	84.8	150.3
PWL	82.0	88.0	91.6	94.9	97.6	99.8	101.5	103.2	104.9	106.6	107.0	106.8	105.5	99.4	90.2	83.5
PWL	82.0	89.4	92.7	95.9	98.6	100.8	102.5	104.2	105.9	107.6	108.0	107.8	106.5	100.4	91.6	83.5

EPWL = 99.3

HIGH VELOCITY JET NOISE PROGRAM - ENGINEERING CORRELATION

CONICAL NOZZLE CHECK CASE

- CONICAL TOTAL NOISE
- 2400.0 FOOT ALTITUDE
- 6.0 FOOT SIDELINE
- NO FGA
- 519.0 DEGREE STANDARD DAY

ACOUSTIC ANGLE FROM INLET

FREQ	20	30	40	50	60	75	90	100	110	120	130	140	150	160	PWL
50	56.8	60.0	62.1	63.7	65.2	66.3	67.4	68.7	70.9	75.8	82.0	85.7	87.4	84.0	162.3
63	58.7	61.9	64.2	65.8	67.4	68.5	69.9	71.6	73.3	78.4	84.8	88.5	90.0	86.2	164.9
80	60.4	63.8	66.1	67.9	69.6	70.7	72.3	73.8	75.7	80.8	87.2	90.8	91.9	87.5	166.9
100	61.7	65.2	67.7	69.6	71.3	72.4	74.2	75.9	77.9	82.9	89.1	92.5	93.1	88.1	168.3
125	62.7	66.4	69.3	71.3	72.9	74.1	76.0	77.6	80.0	84.7	90.7	93.7	93.7	88.0	169.3
160	63.7	67.5	70.2	72.2	74.2	75.7	77.6	79.4	82.3	86.5	92.1	94.5	93.7	87.2	169.9
200	64.7	68.6	71.2	73.2	75.1	76.7	78.7	80.7	84.1	88.0	93.0	94.8	93.3	86.1	170.2
250	67.3	70.9	73.8	75.5	77.1	77.5	79.4	81.5	85.6	89.1	93.6	94.8	92.4	84.5	170.4
315	72.4	76.1	77.8	78.3	78.4	78.7	80.1	82.0	86.7	90.1	94.0	94.4	91.2	82.6	170.5
400	74.3	78.0	81.8	83.2	83.3	82.1	81.4	82.4	87.2	90.6	94.0	93.7	89.6	80.4	170.6
500	72.0	77.4	81.0	81.7	85.3	85.4	84.3	83.2	87.1	90.5	93.6	92.6	87.7	77.9	170.5
630	78.4	75.5	78.6	81.0	83.5	85.4	86.2	85.0	86.7	84.9	92.8	91.0	85.3	74.7	170.0
800	68.2	74.1	77.7	79.9	81.3	82.6	84.7	85.7	86.2	84.9	91.4	89.0	82.3	70.7	169.2
1000	65.9	72.6	76.3	78.5	80.1	81.5	82.3	85.2	85.7	87.6	89.8	86.6	79.1	66.3	168.5
1250	62.1	69.5	73.8	76.0	78.4	80.0	81.2	81.9	85.0	86.1	87.7	83.9	75.3	61.3	167.7
1600	57.3	66.1	71.1	74.1	76.3	78.0	79.2	80.2	83.3	83.8	84.8	80.1	70.3	55.6	166.7
2000	51.5	61.8	67.5	71.1	73.8	75.3	76.7	77.9	80.6	81.2	81.4	75.9	65.0	50.6	165.8
2500	43.6	54.2	62.9	67.2	70.6	71.9	73.5	74.7	76.3	77.2	77.1	70.6	58.6	43.8	164.7
3150	32.0	47.4	54.2	61.3	64.8	67.1	68.8	70.1	71.8	72.4	72.4	71.1	50.2	32.2	163.4
4000	14.9	35.7	44.4	52.9	57.3	60.0	62.1	63.6	65.3	64.7	62.6	53.3	38.0	14.3	162.0
5000	4.2	28.0	40.2	47.5	52.3	54.4	57.7	59.2	60.8	59.6	57.0	46.5	29.9	3.5	160.6
6300	-25.0	7.6	24.1	33.8	40.1	44.0	46.8	48.4	49.9	49.2	47.1	42.9	9.0	-25.7	159.2
8000	-70.4	-23.9	-8	12.7	21.3	26.4	30.1	32.1	31.7	28.1	21.6	4.8	-22.7	-71.1	157.6
10000	-131.5	-66.7	-33.9	-15.3	-3.6	3.5	9.0	10.3	11.1	8.4	-6.7	-28.6	-65.2	-132.3	156.1
OASPL	80.0	84.9	87.9	90.9	91.5	92.3	93.0	93.7	94.7	96.5	99.6	104.0	102.3	96.2	181.4
PWL	84.9	90.5	94.1	96.5	98.4	99.3	100.3	100.9	102.2	103.8	105.9	108.9	106.3	96.3	
PMT	84.9	91.9	95.2	96.5	98.4	99.3	100.3	100.9	102.2	103.8	105.9	108.9	105.7	96.3	

EPWL = 109.4

HIGH VELOCITY JET NOISE PROGRAM - ENGINEERING CORRELATION

DUAL FLOW MULTI-TURE CHECK CASE

*** INPUT ***

NO OF TURES= 60
DIA OF TURES= .306 ARD= 2.750
NOZZLE OUTER DIA= 6.687
A8= 7.649 A2R= 5.083
TT28= 1632. P128/PO= 3.278
T0= 519. PO= 14.700
TT8= 1010. PTH/PO= 1.567
EJECTOR AREA RATIO PARAMETER= 1.303 V0= 0.0
PLUG DIA= 2.846 CANT= 0.000

*** OUTPUT ***

OUTER NOZZLE EXIT CONDITIONS
U28= 2389.2 RH02R= .0333 DUCT H= .749

INNER NOZZLE EXIT CONDITIONS
U8= 1209.8 RH0R= .0445

COANNULAR NOZZLE FLOW PARAMETERS

MERGED FLOW CONDITIONS
U5= 1024.5 RH05= .0558 O5= 6.178 A5= 29.978

MIXED FLOW CONDITIONS
U6= 1209.8 TT6= 1010. W6= 2027.780 A6= 37.627

HIGH VELOCITY JET NOISE PROGRAM - ENGINEERING CORRELATION

DUAL FLOW MULTI-TUBE CHECK CASE

MERGED NOISE

- 770.0 FOOT ARC
- ND FGA
- 519.0 DEGREE STANDARD DAY

ACOUSTIC ANGLE FROM INLET

FREQ	20	30	40	50	60	70	80	90	100	110	120	130	140	150	160	PWL
50	82.7	83.2	83.6	84.1	84.6	85.1	85.5	86.0	86.5	87.0	87.5	88.0	88.5	89.0	89.5	155.1
63	81.4	81.9	82.4	82.9	83.4	83.9	84.3	84.8	85.2	85.7	86.1	86.6	87.0	87.5	88.0	154.9
80	80.0	80.5	81.0	81.5	82.0	82.5	83.0	83.5	84.0	84.5	85.0	85.5	86.0	86.5	87.0	154.6
100	84.3	84.8	85.3	85.8	86.3	86.8	87.3	87.8	88.3	88.8	89.3	89.8	90.3	90.8	91.3	154.2
125	84.5	85.0	85.5	86.0	86.5	87.0	87.5	88.0	88.5	89.0	89.5	90.0	90.5	91.0	91.5	153.8
160	84.5	85.0	85.5	86.0	86.5	87.0	87.5	88.0	88.5	89.0	89.5	90.0	90.5	91.0	91.5	153.2
200	84.2	84.7	85.2	85.7	86.2	86.7	87.2	87.7	88.2	88.7	89.2	89.7	90.2	90.7	91.2	152.5
250	83.8	84.3	84.8	85.3	85.8	86.3	86.8	87.3	87.8	88.3	88.8	89.3	89.8	90.3	90.8	151.8
315	81.2	81.7	82.2	82.7	83.2	83.7	84.2	84.7	85.2	85.7	86.2	86.7	87.2	87.7	88.2	150.9
400	82.5	83.0	83.5	84.0	84.5	85.0	85.5	86.0	86.5	87.0	87.5	88.0	88.5	89.0	89.5	149.9
500	81.6	82.1	82.6	83.1	83.6	84.1	84.6	85.1	85.6	86.1	86.6	87.1	87.6	88.1	88.6	148.8
630	80.5	81.0	81.5	82.0	82.5	83.0	83.5	84.0	84.5	85.0	85.5	86.0	86.5	87.0	87.5	147.7
800	79.3	79.8	80.3	80.8	81.3	81.8	82.3	82.8	83.3	83.8	84.3	84.8	85.3	85.8	86.3	146.3
1000	78.0	78.5	79.0	79.5	80.0	80.5	81.0	81.5	82.0	82.5	83.0	83.5	84.0	84.5	85.0	145.0
1250	76.8	77.3	77.8	78.3	78.8	79.3	79.8	80.3	80.8	81.3	81.8	82.3	82.8	83.3	83.8	143.6
1600	75.0	75.5	76.0	76.5	77.0	77.5	78.0	78.5	79.0	79.5	80.0	80.5	81.0	81.5	82.0	142.0
2000	73.5	74.0	74.5	75.0	75.5	76.0	76.5	77.0	77.5	78.0	78.5	79.0	79.5	80.0	80.5	140.6
2500	71.9	72.4	72.9	73.4	73.9	74.4	74.9	75.4	75.9	76.4	76.9	77.4	77.9	78.4	78.9	139.2
3150	70.1	70.6	71.1	71.6	72.1	72.6	73.1	73.6	74.1	74.6	75.1	75.6	76.1	76.6	77.1	137.7
4000	68.1	68.6	69.1	69.6	70.1	70.6	71.1	71.6	72.1	72.6	73.1	73.6	74.1	74.6	75.1	136.3
5000	66.6	67.1	67.6	68.1	68.6	69.1	69.6	70.1	70.6	71.1	71.6	72.1	72.6	73.1	73.6	135.1
6300	64.6	65.1	65.6	66.1	66.6	67.1	67.6	68.1	68.6	69.1	69.6	70.1	70.6	71.1	71.6	133.9
8000	61.5	62.0	62.5	63.0	63.5	64.0	64.5	65.0	65.5	66.0	66.5	67.0	67.5	68.0	68.5	132.9
10000	59.1	59.6	60.1	60.6	61.1	61.6	62.1	62.6	63.1	63.6	64.1	64.6	65.1	65.6	66.1	132.2
OASPL	94.7	95.2	95.7	96.2	96.7	97.2	97.7	98.2	98.7	99.2	99.7	100.2	100.7	101.2	101.7	163.9
PWL	100.6	101.2	101.7	102.3	102.8	103.3	103.8	104.3	104.8	105.3	105.8	106.3	106.8	107.3	107.8	166.2
PWL	100.6	101.2	101.7	102.3	102.8	103.3	103.8	104.3	104.8	105.3	105.8	106.3	106.8	107.3	107.8	166.2

WIND VELOCITY JET NOISE PROGRAM - ENGINEERING CORRELATION

DUAL FLOW MULTI-TIME CHECK CASE

- UNWEIGHED NOISE
- 120.0 FOOT APC
- 40 FGS
- 519.0 DEGREE STANDARD DAY

ACOUSTIC ANGLE FROM INLET

FREQ.	20	30	40	50	60	70	80	90	100	110	120	130	140	150	160	PWL
50	66.1	65.2	64.7	64.5	65.1	65.4	64.0	70.1	73.0	77.4	75.6	73.6	72.8	72.2	71.7	132.6
63	68.6	67.8	67.3	67.0	67.5	67.9	66.5	72.6	75.2	79.4	77.6	75.6	74.7	73.3	72.7	133.9
80	71.2	70.4	70.0	69.7	70.2	70.6	69.2	75.2	77.8	81.9	80.1	78.1	77.3	76.7	76.2	135.7
100	73.6	72.8	72.3	72.0	72.5	72.9	71.5	77.6	80.2	84.3	82.5	80.5	79.6	78.2	77.7	137.6
125	75.9	75.1	74.7	74.4	74.9	75.3	73.9	79.9	82.5	86.6	84.8	82.8	81.9	80.5	79.9	139.6
160	78.4	77.6	77.2	76.9	77.4	77.8	76.4	82.4	85.0	89.1	87.3	85.3	84.4	83.0	82.4	142.0
200	80.5	79.7	79.3	79.0	79.5	79.9	78.5	84.5	87.1	91.2	89.4	87.4	86.5	85.1	84.5	144.2
250	82.5	81.7	81.3	81.0	81.5	81.9	80.5	86.5	89.1	93.2	91.4	89.4	88.5	87.1	86.5	146.3
315	84.4	83.6	83.2	82.9	83.4	83.8	82.4	88.4	91.0	95.1	93.3	91.3	90.4	89.0	88.4	148.6
400	86.2	85.4	85.0	84.7	85.2	85.6	84.2	90.2	92.8	96.9	95.1	93.1	92.2	90.8	90.2	150.8
500	87.7	86.9	86.5	86.2	86.7	87.1	85.7	91.9	94.5	98.6	96.8	94.8	93.9	92.5	91.9	152.7
630	89.1	88.3	87.9	87.6	88.1	88.5	87.1	93.9	96.5	100.6	98.8	96.8	95.9	94.5	93.9	154.6
800	90.2	89.4	89.0	88.7	89.2	89.6	88.2	95.9	98.5	102.6	100.8	98.8	97.9	96.5	95.9	156.3
1000	91.0	90.2	89.8	89.5	90.0	90.4	89.0	97.9	100.5	104.6	102.8	100.8	99.9	98.5	97.9	157.6
1250	91.5	90.7	90.3	90.0	90.5	90.9	89.5	99.9	102.5	106.6	104.8	102.8	101.9	100.5	99.9	158.6
1600	91.8	91.0	90.6	90.3	90.8	91.2	89.8	101.9	104.5	108.6	106.8	104.8	103.9	102.5	101.9	159.4
2000	92.5	91.7	91.3	91.0	91.5	91.9	90.5	103.9	106.5	110.6	108.8	106.8	105.9	104.5	103.9	160.7
2500	93.0	92.2	91.8	91.5	92.0	92.4	91.0	105.9	108.5	112.6	110.8	108.8	107.9	106.5	105.9	161.6
3150	93.7	92.9	92.5	92.2	92.7	93.1	91.7	107.9	110.5	114.6	112.8	110.8	109.9	108.5	107.9	162.7
4000	94.2	93.4	93.0	92.7	93.2	93.6	92.2	109.9	112.5	116.6	114.8	112.8	111.9	110.5	109.9	163.7
5000	94.7	93.9	93.5	93.2	93.7	94.1	92.7	111.9	114.5	118.6	116.8	114.8	113.9	112.5	111.9	164.7
6300	95.1	94.3	93.9	93.6	94.1	94.5	93.1	113.9	116.5	120.6	118.8	116.8	115.9	114.5	113.9	165.7
8000	95.6	94.8	94.4	94.1	94.6	95.0	93.6	115.9	118.5	122.6	120.8	118.8	117.9	116.5	115.9	166.7
10000	96.1	95.3	94.9	94.6	95.1	95.5	94.1	117.9	120.5	124.6	122.8	120.8	119.9	118.5	117.9	167.2
0ASPL	100.0	100.0	100.0	100.0	100.0	100.0	100.0	100.0	100.0	100.0	100.0	100.0	100.0	100.0	100.0	100.0
PWL	110.9	111.1	111.3	111.6	112.0	112.6	113.5	114.2	115.4	116.4	117.0	117.3	117.5	117.6	117.6	117.6
ONLY	110.9	111.1	111.3	111.6	112.0	112.6	113.5	114.2	115.4	116.4	117.0	117.3	117.5	117.6	117.6	117.6

QUAL FLOW MULTITIME CHECK CASE

- SMOKE (M-E) NOISE
- 320.0 FOOT ARL
- NO FGA
- 519.0 DEGREE STANDARD

ACCOMPLISH ANGLE FROM INLET

[illegible]

WIND VELOCITY JET NOISE PROGRAM - ENGINEERING CORRELATION

DUAL FLOW MULTI-TUBE CHECK CASE

* TOTAL NOISE

* 120.5 FOOT ARC

* 100 FGA

* 51.9 DEGREE STANDARD DAY

ACOUSTIC ANGLE FROM INLET

FOFO	70	75	80	85	90	95	100	110	120	130	140	150	160	PWL
50	82.4	83.2	83.7	84.1	84.4	84.6	84.8	85.0	85.2	85.4	85.6	85.8	86.0	155.1
100	83.4	84.2	84.7	85.1	85.4	85.7	86.0	86.3	86.6	86.9	87.2	87.5	87.8	155.0
150	84.7	85.5	85.9	86.3	86.6	86.9	87.2	87.5	87.8	88.1	88.4	88.7	89.0	154.3
200	85.6	86.4	86.8	87.2	87.5	87.8	88.1	88.4	88.7	89.0	89.3	89.6	89.9	153.9
250	86.4	87.2	87.6	88.0	88.3	88.6	88.9	89.2	89.5	89.8	90.1	90.4	90.7	153.5
300	87.2	88.0	88.4	88.7	89.0	89.3	89.6	89.9	90.2	90.5	90.8	91.1	91.4	153.1
350	87.9	88.7	89.1	89.4	89.7	90.0	90.3	90.6	90.9	91.2	91.5	91.8	92.1	152.9
400	88.7	89.5	89.9	90.2	90.5	90.8	91.1	91.4	91.7	92.0	92.3	92.6	92.9	152.9
450	89.4	90.2	90.6	90.9	91.2	91.5	91.8	92.1	92.4	92.7	93.0	93.3	93.6	153.5
500	90.2	91.0	91.4	91.7	92.0	92.3	92.6	92.9	93.2	93.5	93.8	94.1	94.4	154.3
550	90.9	91.7	92.1	92.4	92.7	93.0	93.3	93.6	93.9	94.2	94.5	94.8	95.1	155.6
600	91.6	92.4	92.8	93.1	93.4	93.7	94.0	94.3	94.6	94.9	95.2	95.5	95.8	157.0
650	92.4	93.2	93.6	93.9	94.2	94.5	94.8	95.1	95.4	95.7	96.0	96.3	96.6	158.2
700	93.0	93.8	94.2	94.5	94.8	95.1	95.4	95.7	96.0	96.3	96.6	96.9	97.2	159.2
750	93.6	94.4	94.8	95.1	95.4	95.7	96.0	96.3	96.6	96.9	97.2	97.5	97.8	160.0
800	94.2	95.0	95.4	95.7	96.0	96.3	96.6	96.9	97.2	97.5	97.8	98.1	98.4	159.7
850	94.8	95.6	96.0	96.3	96.6	96.9	97.2	97.5	97.8	98.1	98.4	98.7	99.0	157.7
900	95.4	96.2	96.6	96.9	97.2	97.5	97.8	98.1	98.4	98.7	99.0	99.3	99.6	155.2
950	96.1	96.9	97.3	97.6	97.9	98.2	98.5	98.8	99.1	99.4	99.7	100.0	100.3	152.5
1000	96.7	97.5	97.9	98.2	98.5	98.8	99.1	99.4	99.7	100.0	100.3	100.6	100.9	150.2
1050	97.3	98.1	98.5	98.8	99.1	99.4	99.7	100.0	100.3	100.6	100.9	101.2	101.5	148.3
1100	97.9	98.7	99.1	99.4	99.7	100.0	100.3	100.6	100.9	101.2	101.5	101.8	102.1	148.0
1150	98.5	99.3	99.7	100.0	100.3	100.6	100.9	101.2	101.5	101.8	102.1	102.4	102.7	148.0
1200	99.1	99.9	100.3	100.6	100.9	101.2	101.5	101.8	102.1	102.4	102.7	103.0	103.3	148.0
1250	99.7	100.5	100.9	101.2	101.5	101.8	102.1	102.4	102.7	103.0	103.3	103.6	103.9	148.0
1300	100.3	101.1	101.5	101.8	102.1	102.4	102.7	103.0	103.3	103.6	103.9	104.2	104.5	148.0
1350	100.9	101.7	102.1	102.4	102.7	103.0	103.3	103.6	103.9	104.2	104.5	104.8	105.1	148.0
1400	101.5	102.3	102.7	103.0	103.3	103.6	103.9	104.2	104.5	104.8	105.1	105.4	105.7	148.0
1450	102.1	102.9	103.3	103.6	103.9	104.2	104.5	104.8	105.1	105.4	105.7	106.0	106.3	148.0
1500	102.7	103.5	103.9	104.2	104.5	104.8	105.1	105.4	105.7	106.0	106.3	106.6	106.9	148.0
1550	103.3	104.1	104.5	104.8	105.1	105.4	105.7	106.0	106.3	106.6	106.9	107.2	107.5	148.0
1600	103.9	104.7	105.1	105.4	105.7	106.0	106.3	106.6	106.9	107.2	107.5	107.8	108.1	148.0
1650	104.5	105.3	105.7	106.0	106.3	106.6	106.9	107.2	107.5	107.8	108.1	108.4	108.7	148.0
1700	105.1	105.9	106.3	106.6	106.9	107.2	107.5	107.8	108.1	108.4	108.7	109.0	109.3	148.0
1750	105.7	106.5	106.9	107.2	107.5	107.8	108.1	108.4	108.7	109.0	109.3	109.6	109.9	148.0
1800	106.3	107.1	107.5	107.8	108.1	108.4	108.7	109.0	109.3	109.6	109.9	110.2	110.5	148.0
1850	106.9	107.7	108.1	108.4	108.7	109.0	109.3	109.6	109.9	110.2	110.5	110.8	111.1	148.0
1900	107.5	108.3	108.7	109.0	109.3	109.6	109.9	110.2	110.5	110.8	111.1	111.4	111.7	148.0
1950	108.1	108.9	109.3	109.6	109.9	110.2	110.5	110.8	111.1	111.4	111.7	112.0	112.3	148.0
2000	108.7	109.5	109.9	110.2	110.5	110.8	111.1	111.4	111.7	112.0	112.3	112.6	112.9	148.0
2050	109.3	110.1	110.5	110.8	111.1	111.4	111.7	112.0	112.3	112.6	112.9	113.2	113.5	148.0
2100	109.9	110.7	111.1	111.4	111.7	112.0	112.3	112.6	112.9	113.2	113.5	113.8	114.1	148.0
2150	110.5	111.3	111.7	112.0	112.3	112.6	112.9	113.2	113.5	113.8	114.1	114.4	114.7	148.0
2200	111.1	111.9	112.3	112.6	112.9	113.2	113.5	113.8	114.1	114.4	114.7	115.0	115.3	148.0
2250	111.7	112.5	112.9	113.2	113.5	113.8	114.1	114.4	114.7	115.0	115.3	115.6	115.9	148.0
2300	112.3	113.1	113.5	113.8	114.1	114.4	114.7	115.0	115.3	115.6	115.9	116.2	116.5	148.0
2350	112.9	113.7	114.1	114.4	114.7	115.0	115.3	115.6	115.9	116.2	116.5	116.8	117.1	148.0
2400	113.5	114.3	114.7	115.0	115.3	115.6	115.9	116.2	116.5	116.8	117.1	117.4	117.7	148.0
2450	114.1	114.9	115.3	115.6	115.9	116.2	116.5	116.8	117.1	117.4	117.7	118.0	118.3	148.0
2500	114.7	115.5	115.9	116.2	116.5	116.8	117.1	117.4	117.7	118.0	118.3	118.6	118.9	148.0
2550	115.3	116.1	116.5	116.8	117.1	117.4	117.7	118.0	118.3	118.6	118.9	119.2	119.5	148.0
2600	115.9	116.7	117.1	117.4	117.7	118.0	118.3	118.6	118.9	119.2	119.5	119.8	120.1	148.0
2650	116.5	117.3	117.7	118.0	118.3	118.6	118.9	119.2	119.5	119.8	120.1	120.4	120.7	148.0
2700	117.1	117.9	118.3	118.6	118.9	119.2	119.5	119.8	120.1	120.4	120.7	121.0	121.3	148.0
2750	117.7	118.5	118.9	119.2	119.5	119.8	120.1	120.4	120.7	121.0	121.3	121.6	121.9	148.0
2800	118.3	119.1	119.5	119.8	120.1	120.4	120.7	121.0	121.3	121.6	121.9	122.2	122.5	148.0
2850	118.9	119.7	120.1	120.4	120.7	121.0	121.3	121.6	121.9	122.2	122.5	122.8	123.1	148.0
2900	119.5	120.3	120.7	121.0	121.3	121.6	121.9	122.2	122.5	122.8	123.1	123.4	123.7	148.0
2950	120.1	120.9	121.3	121.6	121.9	122.2	122.5	122.8	123.1	123.4	123.7	124.0	124.3	148.0
3000	120.7	121.5	121.9	122.2	122.5	122.8	123.1	123.4	123.7	124.0	124.3	124.6	124.9	148.0
3050	121.3	122.1	122.5	122.8	123.1	123.4	123.7	124.0	124.3	124.6	124.9	125.2	125.5	148.0
3100	121.9	122.7	123.1	123.4	123.7	124.0	124.3	124.6	124.9	125.2	125.5	125.8	126.1	148.0
3150	122.5	123.3	123.7	124.0	124.3	124.6	124.9	125.2	125.5	125.8	126.1	126.4	126.7	148.0
3200	123.1	123.9	124.3	124.6	124.9	125.2	125.5	125.8	126.1	126.4	126.7	127.0	127.3	148.0
3250	123.7	124.5	124.9	125.2	125.5	125.8	126.1	126.4	126.7	127.0	127.3	127.6	127.9	148.0
3300	124.3	125.1	125.5	125.8	126.1	126.4	126.7	127.0	127.3	127.6	127.9	128.2	128.5	148.0
3350	124.9	125.7	126.1	126.4	126.7	127.0	127.3	127.6	127.9	128.2	128.5	128.8	129.1	148.0
3400	125.5	126.3	126.7	127.0	127.3	127.6	127.9	128.2	128.5	128.8	129.1	129.4	129.7	148.0
3450	126.1	126.9	127.3	127.6	127.9	128.2	128.5	128.8	129.1	129.4	129.7	130.0	130.3	148.0
3500	126.7	127.5	127.9	128.2	128.5	128.8	129.1	129.4	129.7	130.0	130.3	130.6	130.9	148.0
3550	127.3	128.1	128.5	128.8	129.1	129.4	129.7	130.0	130.3	130.6	130.9	131.2	131.5	148.0
3600	127.9	128.7	129.1	129.4	129.7	130.0	130.3	130.6	130.9	131.2	131.5	131.8	132.1	148.0
3650	128.5	129.3	129.7	130.0	130.3	130.6	130.9	131.2	131.5	131.8	132.1	132.4	132.7	148.0
3700	129.1	129.9	130.3	130.6	130.9	131.2	131.5	131.8	132.1	132.4	132.7	133.0	133.3	148.0
3750	129.7	130.5	130.9	131.2	131.5	131.8	132.1	132.4	132.7	133.0	133.3	133.6	133.9	148.0
3800	130.3	131.1	131.5	131.8	132.1	132.4	132.7	133.0	133.3	133.6	133.9	134.2	134.5	148.0
3850	130.9	131.7	132.1	132.4	132.7									

DUAL FLOW MULTI-CHUTE CHECK CASE

SECRET

NO OF CHUTES/SOOKES=	20	ARD=	1.750
DIA OF CHUTE EQUIV AREA TURE=			.315
NOZZLE OUTER DIA=	2.671		
AR=	.811	A2R=	1.555
TT28=	1750.	PT28/P4=	7.970
TC=	519.	P0=	14.700
TT8=	1470.	PT8/P0=	1.690
EJECTOR AREA RATIO PARAMETER=			5.000
PLUG DIA=	1.248	CANT=	5.000
		VD=	350.0

Identity

OUTER NOZZLE EXIT CONDITIONS		
UP8=	2615.4	P4029= .5326
		DUCT H= .379
INNER NOZZLE EXIT CONDITIONS		
UP8=	1382.8	P4029= .5299

COANNULAR NOZZLE FLOW PARAMETERS

MERGED FLOW CONDITIONS					
US=	1475.7	PHQS=	.0546	DS=	2.673
					AS=
					5.612
MIXED FLOW CONDITIONS					
U6=	1469.2	Y16=	949.	W5=	485.354
					A6=
					6.423

WIND VELOCITY AT NOISE PROGRAM - ENGINEERING CORRELATION

DUAL FLOW MULTI-CORRECTION CASE

- TOTAL NOISE
- 2400.0 FOOT ALTITUDE
- 0.0 FOOT SLOPE
- 10.0 DB
- 510.0 DEGREE STANDARD DAY

ACOUSTIC ANGLE FROM INLET

REF.	20	30	40	50	60	70	80	90	100	110	120	130	140	150	160	PWL
50	55.0	54.7	54.4	54.1	53.8	53.5	53.2	52.9	52.6	52.3	52.0	51.7	51.4	51.1	50.8	50.5
60	54.7	54.4	54.1	53.8	53.5	53.2	52.9	52.6	52.3	52.0	51.7	51.4	51.1	50.8	50.5	50.2
70	54.4	54.1	53.8	53.5	53.2	52.9	52.6	52.3	52.0	51.7	51.4	51.1	50.8	50.5	50.2	49.9
80	54.1	53.8	53.5	53.2	52.9	52.6	52.3	52.0	51.7	51.4	51.1	50.8	50.5	50.2	49.9	49.6
90	53.8	53.5	53.2	52.9	52.6	52.3	52.0	51.7	51.4	51.1	50.8	50.5	50.2	49.9	49.6	49.3
100	53.5	53.2	52.9	52.6	52.3	52.0	51.7	51.4	51.1	50.8	50.5	50.2	49.9	49.6	49.3	49.0
110	53.2	52.9	52.6	52.3	52.0	51.7	51.4	51.1	50.8	50.5	50.2	49.9	49.6	49.3	49.0	48.7
120	52.9	52.6	52.3	52.0	51.7	51.4	51.1	50.8	50.5	50.2	49.9	49.6	49.3	49.0	48.7	48.4
130	52.6	52.3	52.0	51.7	51.4	51.1	50.8	50.5	50.2	49.9	49.6	49.3	49.0	48.7	48.4	48.1
140	52.3	52.0	51.7	51.4	51.1	50.8	50.5	50.2	49.9	49.6	49.3	49.0	48.7	48.4	48.1	47.8
150	52.0	51.7	51.4	51.1	50.8	50.5	50.2	49.9	49.6	49.3	49.0	48.7	48.4	48.1	47.8	47.5
160	51.7	51.4	51.1	50.8	50.5	50.2	49.9	49.6	49.3	49.0	48.7	48.4	48.1	47.8	47.5	47.2
PWL	51.7	51.4	51.1	50.8	50.5	50.2	49.9	49.6	49.3	49.0	48.7	48.4	48.1	47.8	47.5	47.2

END=103.1

PROGRAM SOURCE CODE LISTING

This section contains the FORTRAN IV source code listing for the engineering correlation computer program, suitable for running on the CDC 7600 computer. The listing of subroutines is as follows:

- (1) Main Program (MS)
- (2) SUB1 (Contains SUB1 through SUB6)
- (3) EXTP
- (4) SHKSUB
- (5) PNLPT
- (6) TPNLC
- (7) PNTT8
- (8) A block data listing
- (9) EJECTS

```

1 PROGRAM MS (INPUT, OUTPUT, TAPES=INPUT, TAPES=OUTPUT)
C   MS -- ENGINEERING CORRELATION FOR TASK 3
COMMON /QM/ M,O,I
COMMON /CM1/ L(9,24),X(24),F(24),F(24),S(15,24),KK(24,5),C(15,5),
5 1 O(20),RR(49),RX(49),P(20),R(15,24),Y1(24),Y(24),C1(15),RVF(20),
1 S1(24),G(2,24),C2(15),T(20),D(20),W(5),A(4),V(3),E1(15,24)
COMMON /CM2/ V8,A0,W8,K1,Y9,T8,T5,R7,P1,Z9,DJ,AJ,H,U,E9
1 Y9,V9,C9,DH,D1,V4,U9,A8,O,L9,A6,A7,S6,P9,F9,ALT,SL,ANI
COMMON /CM3/ IIAS(2),IICASF(6),IDCASE(6),IDFNT(6)
1 REAL L, KK, K1
REAL M,K2,KO,L4
NAMLIST/INPUT/ Y9,P9,TT3,A9,PP,K9,N,H9,H4,H6,S1J,SS,A7,
1 N1,DT,Z5,DN,AAK,TT4,P4,TT5,ALT,SL,U,E9,V0,A6,L4,A,P5,PH,RX
C
15 DATA F/50.,63.,80.,100.,125.,160.,200.,250.,315.,400.,500.,630.,
DATA E/100.,125.,150.,160.,200.,250.,315.,400.,500.,630.,800.,
1 1000./
DATA C1/1501./
DATA IM/2L A/
DATA MM/2L C/
DATA S1/-,.699,-.602,-.542,-.398,-.301,-.201,-.097,0.,.097,.204,
1 .311,.304,.499,.602,.699,.799,.903,1.,1.097,1.204,1.301,1.398,
1 1.498,1.602/
25 DATA ((I(I,J),I=1,2),J=1,24)/171.H.,72,135.4.,72,139.2.,72,
1 142.4.,72,145.,7,147.5.,6H,148.6.,64,148.7.,6,148.,.55,
1 147.2.,5,146.5.,45,145.7.,70,144.8.,33,143.9.,27,142.5.,2,
1 141.,.15,139.5.,09,138.7.,14,137.,0.,135.5.,0.,134.1,0.,
1 132.6.,.131,3.0.,13.,6.2./
WRITE(A,101)
101 FORMAT(1H)//////////////////
1 5XX,XXX XX XXXXXXX/
1 5XX,XXXX XXX XXXXXXX/
1 5XX,XXXXX XXXV XX /
35 1 5XX,XXX XXXX AX XX /
1 5XX,XXX XX XX XXXXXXX/
1 5XX,XXX XX XXXXXXX/
1 5XX,XXX XX XXX/
1 5XX,XXX XX XXX/
40 1 5XX,XXX XX XXXXXX/
1 5XX,XXX XX XXXXXXX////////
X/40X.41H XXXXX X X XXXXX XXXXX XXXXXX P X
X/40X.41HX X X X X X XX XX
X/40X.41HXXV XX XXX X X X XX X
45 X/40X.41H XXX X XXX X XXXX X X
X/40X.41H X X X X X X X
X/40X.41HXXXXX X XXXXX X XXXXXX X X
WRITE(A,103)
103 FORMAT(///14X,4HHH)GM VELOCITY JET NOISE PROGRAM(CONTRACT DGT-NS,
16M30034)/44X,3THTASK) -- ENGINEERING CORRELATION //
12 READ(5,11)(IDFNT(I),I=1,6)
11 FORMAT(6A10)
IF(FOF(5)) GO TO 14
14 CONTINUE
55 IF((IDFNT(1).AND.7777000000000000000000).EQ.IM) GO TO 1A
IF((IDFNT(1).AND.7777000000000000000000).EQ.MM) GO TO 244
WRITE(A,111)(IDFNT(I),I=1,6)

```

```

13 FORMAT(28X,6A13)
GO TO 12
60 16 BACKSPACE 5
244 DO 23 I=1,6 & IICASE(I)=10H
23 CONTINUE
245 CONTINUE
READ(5,11)(IICASE(I),I=1,6)
65 IF(EOF(5)) 9999,15
15 CONTINUE
IF((IICASE(1).AND.77770000000000000000H).EQ.1H) GO TO 17
DO 22 I=1,6 & IICASE(I)=IICASE(I)
22 CONTINUE
70 GO TO 21
17 BACKSPACE 5
C
21 T0=519 & M0=14.7 & R1=(.76475 & P1=3.14159
K1=1
75 P7=0 & K2=0 & K7=0
A0=49.014050RT(T0)
171 READ(5,INPUT)
IF(EOF(5)) 9999,2500
2510 T3=T17 & M4=M0 & R1=INT & M2=M0 & AR=ARM
80 T4=T14 & T5=T15 & A11=N
PRINT 250
250 FORMAT(1H1///,0 HIGH VELOCITY JET NOISE PROGRAM - ENGINEERING*,
1 * CORRELATION*//)
WRITE(6,14)(IICASE(I),I=1,6)
85 19 FORMAT(2X,6A10//)
20 PRINT 260
2600 FORMAT(25X,17H000 INPUT 000/)
C
C
90 GO TO(295,370,320,415,425,425),Y9
C CONICAL NOISE ENTRY
295 Q1=SQRT(A0/P1) & A7=1 & M2=SQRT(A0/P1*.04002) & AN1=1 & R9=0
N=1
GO TO 306
95 C MULTI-CHUTE/SPOKE NOISE ENTRY
320 R2=N*(R4.55)/(2*P1)
Q1=SQRT(4*(R4.06)/2)*(R2-R9*12)/P1/24
R2=R2/12
S1.1=55/R4.1
100 PRINT 2002,N,2*R1,A7
2002 FORMAT(10 OF CHUTE/SPOKE S=,14/0 DIA OF CHUTE EQUIV AREA*,
1 * TUBE=,F10.1,5X,AND=,F10.1)
GO TO 306
C MULTI-TUBE NOISE ENTRY
105 370 P1=R1/24 & M2=SQRT(N*A7*R1*.02.04002)
PRINT 2004,N,2*R1,A7
390 PRINT 2004,T0,P0,T3,P0
395 PRINT 2016,A6,V0
2016 FORMAT(10 FACTOR AREA RATIO PARAMETER=,F10.1,5X,VO=,F10.1)
110 PRINT 2004,MQ*2,H9
2004 FORMAT(10 NO OF TUBES=,14,5X,
1/0 DIA OF TUBES=,F10.1,5X,AND=,F10.1)
2006 FORMAT(10 T0 =,F6.0,5X,00 =,F6.1/0 TTR=,F4.0,5X,PTR/P0=,
1F6.1)

```



```

115 200A FORMAT(* PLUG DIA=*.F10.3.5X.*CANT=*.F10.3//25X.
      I 13H***OUTPUT ***)
      GO TO 525
C      COANNULAR NOISE ENTRY
415      R1=SQRT(A9/P1)*A7=1
120 425 IF(Y9-5) 445,435,460
C      MULTI-TIME COANNULAR ENTRY
435      CONTINUE
      R1=R1/24
      PRINT 2010,M,2,R1,A7
125 2010 FORMAT(* NO OF TIMES=*.I4.5X.
      I /* DIA OF TUBES=*.F10.3.5X.*ARD=*.F10.3)
      GO TO 485
C      MULTI-CHUTE/SPOKE COANNULAR ENTRY
460      CONTINUE
      R1=SQRT(4*A9/(P1*M))/2
130      PRINT 2012,N,A7,2,R1
      2012 FORMAT(* NO OF CHUTES/SPOKES=*.I4.5X.*ARD=*.F10.3/
      I * DIA OF CHUTE EQUIV AREA TIME=*.F10.3)
      S1J=SS/R4+1
135 445      PRINT 2014,R2,AR,A9,T5,P5,T0,P0,T4,P4
      2014 FORMAT(* NOZZLE OUTLET DIA=*.F10.3/* AR=*.F10.3.5X.*A2H=*.
      I F10.3/* T12R=*.F10.3.5X.*PT2R/P0=*.F10.3/* T0=*.F10.3.5X.
      I *D=*.F10.3/* T1R=*.F10.3.5X.*PT1R/P0=*.F10.3)
      T1=T5*P0/P5
140      R7=(R2-SQRT(R2**2-4*A9*A7/P1))/2
      GO TO 105
      525      CONTINUE
      H=SQRT(1+2*SL**2)
      A7=H*A7
145 C      HADJIN RAYIN CALCULATION
      PR1=A7*A7/(P1*P2**2)*IF( PR.LT.0 ) GO TO 550*PB=SQRT(PR)
      GO TO 555
      550      PB=0
      555      TA=T1*GA=1.35
150 C      ITERATION FOR GAMMA
      DO 601 J=1,50
      T3=TA/(PQ**((GA-1)/GA))
      GA=1.4
      IF( T3.LT.748.302 ) GO TO 540
155      GO=2.2370P/T3**0.370271
      540      IF( ABS(GA-G0).LT..001 ) GO TO 615
      GA=GO
      600      CONTINUE
      GO TO 610
160 C      CALCULATION OF FLOW PARAMETERS
      615      C3=GO*.06455/(GO-1)
      H1=227.79*SQRT(TB*C3*(1-1/(PQ**((GO-1)/GO))))
      P3=2.7*P1/T1
      D4=2*SQRT(A3/P1)
165      IF( Y9.LT.4 ) GO TO 675
      IF( YR.F0.T4 ) GO TO 660
C      PRINT AND RESET VARIABLES
      PRINT 2017
      PRINT 2018,M3,P3,P7
170 2017 FORMAT(* OUTER NOZZLE EXIT CONDITIONS*
      2018 FORMAT(* U2R=*.F10.1.5X.*RMO2R=*.F10.4.5X.*DUCT H=*.F10.3)

```

```

T3=T4$D9=P4$U5=U3$R5=W3$G2=G4$C4=C3
GO TO 555
175 660 PRINT 2130
2130 FORMAT(/, 'INNER NOZZLE EXIT CONDITIONS')
PRINT 2124, U3, P3
2124 FORMAT(' U3=, F10.1, 5X, P3=, F10.4)
S6=R2/2
GO TO 1485
180 675 PRINT 2022, 2*P2, D4
PRINT 2023
PRINT 2124, U3, P3, A3/N, A3
2022 FORMAT(/, 'DIA OF CUTER ROW=, F10.3, 5X, EQUIV AREA DIA=, F10.3/)
2023 FORMAT(/, 'NOZZLE EXIT CONDITIONS')
185 2124 FORMAT(' U3=, F10.1, 5X, P3=, F10.4, 5X, A3=, F10.3, 5X,
1 * A3=, F10.3)
S6=R2+A9=A3
IF (Y4-2) 1425, 7105, 7105
C MULTI-ELEMENT POST-MERGED NOISE CALCULATIONS
190 7100 P2=R2-D2*SIN(P90*PI/180)/COS(H40*PI/180)
7105 IF (H4, LT, .6) GO TO 720
P2=R2*(1-1.447*ALOG10(H4/1.954))*(1-.2525*ALOG10(TA/1750))
P2=P2*SQRT(H4/.714)
195 720 A5=(H4*PI*(P2-P1)**2)/((SQRT(A1)-1)**2)
A1=A5/A3
PJ=(109-1)*P2*4633.561/(117**2*H3)+1
K0=((C)*T3)/(117**2/510*H2)-(T0*.24)/PJ
K2=P2/(117.77*P3*H2**2)
X1=K2*(C)-.241*28.966*A1
200 X2=(A1+K2*0.106,951*H4*(117**2/500R21))/X3
X1=(1-K1)/X3
X3=(1-10T1+.24)/X3
C ITERATE FOR U MEMG C/H4
VJ=.5
205 ON A5 1=1.50
P2=X1*X1*VJ*X2*VJ**2*VJ**3
F1=X1+2*X2*VJ*.3*VJ**2
V1=VJ-F2/F1
IF (ABS(V1-VJ), LT, .01*V1) GO TO 720
210 VJ=V1
705 CONTINUE
710 PRINT 2121
2121 FORMAT(' DID NOT CONVERGE')
GO TO 9999
215 720 VJ=V1*U3
D5=SQRT(1.271237*A5)
R5=R3*PJ/((VJ/U3)**2*A1)
PRINT 2120
2125 FORMAT(/, 'MERGED FLOW CONDITIONS')
720 PRINT 2024, VJ, H5, D5, A5
2124 FORMAT(' U5=, F10.1, 5X, P5=, F10.4, 5X, D5=, F10.3, 5X,
1 * A5=, F10.3)
C CHECK FOR OTHER POSSIBLE SOLUTIONS
225 X1=X1+V1*(X2+V1)
X2=X2+V1
Q1=X2**2-4*X1
IF (Q1, LT, 0) GO TO 910
V1J=(-X2-SQRT(Q1))/2

```

```

230      Y2=(-X2+SQRT(01))/2
      IF( Y1J.LT.0 ) GO TO R90
      IF( Y1J.GT.1 ) GO TO R90
      PRINT 232A,Y1J
232A      FORMAT( * ROOT 2=*,F14.4)
      R90      IF( Y2.LT.0 ) GO TO 910
235      IF( Y2.GT.1 ) GO TO 910
      PRINT 232A,Y2
232A      FORMAT( * ROOT 3=*,F14.4)
      C      SET INPUT VARIABLES TO CONICAL ROUTINE
      910      VR=VJ*AR=A5*WR=RS*A5*VR
240      TS=(P*2R.966*A1*V1**2)/(PJ*M3*14.73)
      GR=1.4
      IF( TS.LT.7R.302 ) GO TO 935
      GR=2.2714/TS**0.070271
245      935      M=VJ/SQRT(64*TS*1716.49)
      T9=TR
      TR=TS*(1+(GR-1)/2)*M**2
      IF( Y9.GT.4 ) GO TO 1515
      C      CALCULATE MERGED NOISE
      940      K1=1*CALL SUM1
250      IF( Y9.LT.4 ) GO TO 975*IF( H3.LT.VJ ) GO TO 975
      Z9=1+ALOG10(AS/A3)*5.R
      Z9=7904*(VJ/H3)-.51**2-79*CALL SUM2
      975      CALL SUM3*IF( K9.EQ.0 ) GO TO 995*CALL SUM3
      IAS(1)=1*MERGED NOI
255      IAS(2)=1*MSF
      CALL PRINT*
      990      CALL SUM4
      IF( Y9.GT.3 ) GO TO 1595
      C      MULTI-ELEMENT PRE-MERGED NOISE CALCULATIONS
      C      SET INPUT TO CONICAL ROUTINE
      VP=17*AR=A7/A1*G2=69*VR=M3*AR*VH*TR=T9
      1315      K1=2*CALL SUM1
      C      CUTOFF/SHIELDING CALCULATION
      K7=957R=0
265      DJ=2*PI * RH=4*PI/140.0
      Z9=1+ALOG10(AN)
      IF( Y9.LT.3 ) GO TO 1540
      IF( Y9.EQ.5 ) GO TO 1060
      ZR=1+AN/4*DJ=H4/12*RH=0
270      GO TO 1375
      1360      IP=75*1 * ON 1370 J=1.110
      ZR=74*(2*(ZK-J*1)*1*(1-1/S1J)**(J-1)
      1370      CONTINUE
      1375      ZR=5*ALOG10(ZR)
275      C      CALCULATION OF CRITICAL ANGLE
      M=.4*VR/SQRT(2368.76*(13+T9)/2150J=(AG/(VH*.6/M))/((1+M)
      M=VR/SQRT(62*13*1716.49)
      OJ=1R2-ATAN(SQRT(1-OJ**2)/OJ)*180/PI
      GJ=1F1*(OJ/10)-1
280      C      XC CALCULATION
      Z2=0.1*(4+.15*M+.85*H**2)
      A1W=ATAN(1/(2*Z2/OJ))
      C      POINT OF MERGING FOR CUTOFF
285      XM=(S1J-1)*OJ*SIN(1.57(R-AJR*RB)*(COS(AJR)/SIN(2*AJW-RR))
      Z2=0

```

```

1145 IF( Y9.EU.3 ) GO TO 11456 IF( Y9.F0.6 ) GO TO 11455 DJ=2*RI
      IF( M.LT.1 ) GO TO 1170
      DJ=2*RI
C      XP CALCULATION
290 Z2=DJ*6*(SQRT(M**2-1))**.77H151
C      CRITICAL FREQUENCY CALCULATION FOR ABSORPTION
1170 F0=AC/(2*D.J)
1175 DO 1295 J=1,24
      SX=.R/(IF(J)*DJ/V8)**.H2)
295 C      ABSORPTION EFFECT
      Z7=79
      IF( F(J).LT.F0 ) GO TO 1220
      Z7=78
      IF( F(J).GT.4*F0 ) GO TO 1220
300 Z7=((79-Z7)/(1-.60206))*.ALOG10(F(J)/F0)+79
C      SOURCE LOCATIONS
1220 Z3=Z7+DJ*SX
      SJ=XM/Z3
      TC=CSX(J)=05 IF( K7.EU.2 ) GO TO 1265 SX(J)=Z3
305 C      CUTOFF EFFECT
      IF( RA.GT..65 ) GO TO 1265 IF( SJ.GF.4 ) GO TO 1265
      TC=22.652929-46.888294*SJ+.43.858243*SJ**2-25.284491*SJ**3
      TC=TC+.4645899*SJ**4-1.4693944*SJ**5+.1039457*SJ**6
310 IF( RA.LT..6 ) GO TO 1245
      TC=TC-TC*(RA-.6)/.05
1265 DO 1295 I=1,15
      IF( K7.F0.2 ) GO TO 1290
      IF( (1+I*IC).LT.OJ ) GO TO 1290
      S(I,J)=S(GJ,J)
315 GO TO 1295
      S(I,J)=S(I,J)-TC+77
1290 CONTINUE
1295 C      EJECTION EFFECTS DETERMINED
      IF( A5.F0.0 ) GO TO 1310 IF( K7.F0.2 ) GO TO 1305 CALL FJECTS
320 1305 DO 1309 J=1,24 DO 1309 I=1,15
      S(I,J)=S(I,J)+F(I,I,J)
1309 CONTINUE
1310 IF( K7.F0.2 ) GO TO 1355 CALL SUMS
      IF( K9.F0.0 ) GO TO 1335
325 CALL SUR3
      IAS(1)=1300EMERGED
      IAS(2)=100NOISE
      CALL PNTR
1335 IF( Y9.GT.1 ) GO TO 1330 CALL SUR4CALL SUM4
330 C      CHECK FWD SHIFR CILL NOISE
      IF( P9.LT.1.9 ) GO TO 1395 SV9=(U3BC9+.1.43)*SMT(G9*Y3)S08=2*RI
      IF( Y9.LT.3 ) GO TO 1355 SH=(R4+RA)/12
1355 CALL SHKSURK7=2400 TO 1175
C      CRUTE OR SPOKE CORRECTION
335 1365 Z9=-2*P9
1370 CALL SUR2
      CALL SUR5
      IF( K9.F0.0 ) GO TO 1390
340 IAS(1)=100SHOCK (M-E
      IAS(2)=100 NOISE
      CALL SUM7CALL PNTR
1390 IF( Y9.GT.4 ) GO TO 1355 CALL SUR6

```



```

400      1615      AR=.075*AR*WR=.075*W5$CALL SUH1
           GO TO 1710
C      CHECK FOR OUTER STREAM SHOCK
      1630      IF (P4.LT.1.0) GO TO 1A85$CALL SUH4$CALL SUH4
           PQ=05
405      VQ=(155CQ=41.43*SQRT(62*2.7*PQ/R51$D8=2.5*07
           IF (VQ-5) 1660,1655,1650
      1650      D8=(P4+R6)/12$GO TO 1355
      1655      D8=2*R1$GO TO 1355
      1660      CALL SHK$SUR579=10*ALOG10(SQRT(4*AR/P11/D8)$CALL SUH2
410      CALL SUR5
           IF (K9.EQ.0) GO TO 1A85
           CALL SUR7
           IIAS(1)=10*OUTER SHOC
           IIAS(2)=10*NOISE
415      CALL PNTT
C      CHECK FOR INNER STREAM SHOCK
      1A85      IF (P4.LT.1.0) GO TO 1725$CQ=41.43*SQRT(69*2.7*PQ/R31$VQ=U3
           CALL SUR4$CALL SUR4
           D8=SQRT(4*AR/P11)$IF (VQ.EQ.4) GO TO 1700
           D8=SQRT(D8**2+(2*PQ)**2)-(2*R9)
420      1700      CALL SHK$SUR
           IF (PQ.EQ.0) GO TO 1710$Z9=-3$CALL SUR2
      1710      CALL SUR5
           IF (K9.EQ.0) GO TO 1725$CALL SUR3
425      IIAS(1)=10*INNER SHOC
           IIAS(2)=10*NOISE
           CALL PNTT
      1725      CALL SUR6$IF (K9.EQ.0) GO TO 1730$K1=3
      1730      CALL SUR7
430      IIAS(1)=10*TOTAL NOIS
           IIAS(2)=10*NO
           CALL PNTT
           GO TO 265
      9999      STOP
435      END

```

```

1  CSUM1
      SUBROUTINE SUM1
      COMMON/CH1/L(9,24),X(24),F(24),E(24),S(15,24),KK(24,5),C(15,5),
5      O(20),RR(49),RX(49),P(20),R(15,24),Y1(24),Y(24),C1(15),RVF(20),
      S1(24),G(2,24),C2(15),T(20),D(20),W(5),A(4),V(3),F1(15,24)
      COMMON /CM2/ VH,A0,WR,K1,Y9,TR,T5,R7,P1,Z9,DJ,AJ,H1,F9
1      ,T9,V9,C9,DH,D1,V0,O9,AR,Q,L9,A6,A7,S6,P9,R9,ALT,SL,AN1
      COMMON /CM3/ TIAS(2),IICASE(6),IDCASE(6),IDENT(6)
      REAL L,KK,K1
10     C      SAE AMP A76 (1475 KEV) CONICAL NOZZLE NOISE
      XJ=ALOG10(VR/A0)
      WF=2
      IF (XJ.GT.0.22) GO TO 3010
      WF=W(1)+W(2)*XJ+W(3)*XJ**2+W(4)*XJ**3+W(5)*XJ**4
15     3010     DEN=(VR/(AR*V-1))/0.764751**WF
      Q2=1+ALOG10(DEN*(AR/(1+Q2)))
      DO 3024 I=1,15
      O(I)=Q2*C(1,I)+C(1,21)*XJ+C(1,31)*XJ**2+C(1,41)*XJ**3+C(1,51)*XJ**4
1      C(I,I)
20     3024     CONTINUE
      IF (V0.NE.0) GO TO 3025
      DO 3028 I=1,24
      T(I)=5400*(21+I)*AR*(1+I)/A25
      DO 3066 I=1,15
25     3028     Z1=5*(H(I)+1)*P1/101
      XJ=ALOG10(F(I,I)+2*SUMT(AR/P1)/(VH*Z1+A0*(1-Z1)))
      DO 3062 K=1,24
      F(K)=KK(K,1)+KK(K,21)*XJ+KK(K,31)*XJ**2+KK(K,41)*XJ**3+KK(K,51)*XJ**4
30     3062     CONTINUE
      K6=1-7
      IF (KA.GT.0) GO TO 3050
      KA=1
3050     IF (TR.GT.1000) GO TO 3058
      N1=3*KA-2
35     DJ1=1
      GO TO 3062
3068     N1=1*KA-1
      DJ1=2
3062     S(I,I)=O(I)+((F(N1+1)-F(N1))*(18-T(DJ1))/(T(DJ1+1)-T(DJ1)))*E(N1)
40     3066     CONTINUE&RETURN
      CSUM1
      ENTRY SUM1
      C      EXTRAPOLATION AND OASPL AND PNL CALCULATION
      DO 3110 K=1,15
45     DO 310 DJ1=244*(1+5*(P,I))
10     CONTINUE
      IF (K1.EQ.1) GO TO 3108
      AJ=(K+1)*10
      DJ=1
50     CALL FXP
      DO 3062 I=2445(K,I)+Z1,I
20     CONTINUE
3108     CALL PNLPTST(K)=V(210(K)=V(11)*P(K)=V(3)
3110     CONTINUE&RETURN
55     CSUM1
      ENTRY SUM1
      C      PNL CALCULATION

```

```

09=0500 3207 I=1.241A2=0500 3204 J=1.155AJ=(J+1)*10
YJ=1.5*PI*(COS((AJ-5)*PI/180)-COS((AJ+5)*PI/180))
60 3206 A2=A2*(2.227525E-6*4E-8*YJ*10**((S(J,1)/10))
      CONTINUE
      Y(1)=10**ALOG10(A2)+130+1.24939
      09=09+10**((Y(1)/10)
65 3207 CONTINUE
      09=10**ALOG10(09)
      RETURN
CSUR6
      ENTRY SUM4
      C      RESET VARIABLES
70 DO 3402 J=1.248DO 3401 I=1.158R(I,J)=S(I,J)
      3401 CONTINUEY1(J)=Y(J)
      3402 CONTINUERETURN
CSUR7
      ENTRY SUM2
75 C      DELTA SPL CORRECTION
      DO 3406 J=1.248DO 3404 I=1.158S(I,J)=S(I,J)+79
      3404 CONTINUERETURN
CSUR8
      ENTRY SUM6
80 C      SPL AND PWL ADDITION
      09=0
      DO 3504 J=1.248DO 3503 I=1.15
      S(I,1)=10**ALOG10(10**((S(I,J)/10)+10**((P(I,J)/10))
85 3503 CONTINUE
      Y(J)=10**ALOG10(10**((Y1(J)/10)+10**((Y(J)/10))
      09=09+10**((Y(J)/10)
      3504 CONTINUE
      09=10**ALOG10(09)
      RETURNEND

```



```

1      SUBROUTINE EXTP
      C      EXTP -- SPL EXTRAPOLATION SUBROUTINE
      COMMON/CM1/L(9,24),X(24),F(24),E(24),S(15,24),KK(24,5),C(15,5),
5      1 O(20),RR(49),RX(49),P(20),R(15,24),Y1(24),Y(24),C1(15),RVF(20),
      1 S1(24),G(2,24),C2(15),T(24),D(20),W(5),A(4),V(3),E1(15,24)
      COMMON /CM2/ VR,A0,WB,K1,Y9,TR,T5,R7,P1,Z9,OJ,AJ,H,U,E9
      1 ,T0,V9,C9,DR,D1,V0,O9,AR,Q,L9,A6,A7,S6,P9,R9,ALT,SL,ANI
      COMMON /CM3/ IIAS(2),IICASE(6),IDCASE(6),IDENT(6)
      REAL L,KK,K1
10     REAL L1
      G3=0
      LI=H
      IF (U.EQ.2.) LI=H/SIN(AJ*PI/183)
      Q=20*(ALOG10(L1/D1))
15     IF (E9.EQ.0.) GO TO 470
      DIS=L1
      IF (E9.LT.2.0) GO TO 400
      IF (ALT/DIS.LT..035) GO TO 400
      IF (ALT.LT.100.0) GO TO 400
20     DIS=L1*100.0/ALT
      C      EGA CURVE FIT
      400     CIJ=(.20411435E-20*DIS)-.66703095E-16
      CIJ=(CIJ*DIS)+.72854603E-12
      CIJ=(CIJ*DIS)-.32650913E-08
25     CIJ=(CIJ*DIS)+.49614255E-05
      CIJ=(CIJ*DIS)+.4466377E-02
      G1=(CIJ*DIS)+.59387702
      CIJ=(.16573369E-24*DIS)-.46152934E-20
      CIJ=(CIJ*DIS)+.32361609E-16
30     CIJ=(CIJ*DIS)+.39118972E-13
      CIJ=(CIJ*DIS)-.10464995E-08
      CIJ=(CIJ*DIS)+.29126338E-05
      CIJ=(CIJ*DIS)-.54370996E-03
      G2=(CIJ*DIS)+.59506112
35     IF (DIS.LE.4000.) GO TO 470
      G2=5.010264
      G1=15.44041+.0001*(DIS-4000)
      DO 670 J=1,24
470     IF (F(J).GT.0.000.) GO TO 510
      P3=F(J)
40     GO TO 520
      P3=.89*F(J)
      C      AIR ATTENUATION CURVE FIT
      520     R1=(-.19973807E-14*P3)+.36618630E-10
45     R2=(R1*P3)+.32351924E-07
      R3=(R2*P3)+.13498887E-02
      PA=(R3*P3)+.17604677E-01
      IF (E9.EQ.0.) GO TO 660
      IF (P3.EQ.63) GO TO 610
50     IF (P3.GE.2000.) GO TO 630
      ZIP=P3/62.5
      ZJ=.2*ALOG(ZIP)/ALOG(2.0)
      GO TO 640
610     ZJ=0
55     GO TO 640
630     ZJ=1.0
640     G3=(ZJ*(G1-G2))+G2
660     X(J)=X(J)-G3-PA*((L1-D1)/1000)
670     CONTINUE
60     RETURN
      END

```

```

1      SUBROUTINE SHKSUR
      C      SHKSUR -- SAE SHOCK CELL NOISE PREDICTION SUBROUTINE
      COMMON/CM1/L(9,24),X(24),F(24),E(24),S(15,24),KK(24,5),C(15,5),
1      O(20),RW(49),RX(49),P(20),R(15,24),Y1(24),Y(24),C1(15),RVF(20),
5      S1(24),G(2,24),C2(15),T(26),D(20),W(5),A(4),V(3),F1(15,24)
      COMMON /CM2/ V8,A0,W8,K1,Y9,TR,T5,R7,P1,Z9,DJ,AJ,H,U,F9
1      T,V9,C9,DR,D1,V0,O9,AR,O,L9,A6,A7,S6,P9,R9,ALT,SL,ANI
      COMMON /CM3/ IIAS(2),IICASE(6),IDCASE(6),IDENT(6)
      REAL L,KK,K1
10     A0=49.014*SQR(T0)
      D1=15R=SQR((V9/C9)**2-1)
      DC=10*ALOG10(((R**2)*DR/D1)**2)
      DO 390 K=1,15
      AJR=(KR+1)*PI*10/180
15     DO 380 J=1,24
      SJ=ALOG10(F(J)*1.1*DR*H/A0)
      DO 250 K=2,24
      IF(SJ,GT,S1(K)) GO TO 210
210     CIJ=G(2,K-1)+(SJ-S1(K-1))*(G(2,K)-G(2,K-1))/(S1(K)-S1(K-1))
20     G1=G(1,K-1)+(SJ-S1(K-1))*(G(1,K)-G(1,K-1))/(S1(K)-S1(K-1))
      GO TO 260
240     IF(K,EO,24) GO TO 210
250     CONTINUE
260     W1=0
25     F1=(2*P)*F(1)*.31*W*DR/(.7*V9)*(1+(.7*V9/A0)*COS(AJR))
      DO 360 I=1
      F2=0
      KEND=4-(I+1)
      KSTART=0800 330 K=KSTART,KEND
30     Z1=I * 7K=K
      F3=F1*(Z1*(1.0-.04*((Z1+1.0)/2.0+ZK)))
      F2=F2+(COS(F3)*SIN(.115*F3)/(1.15*F3))
330     CONTINUE
      IF(C1J,LT,.01) GO TO 360
35     H1=W1+((CIJ**((I**2))*F2)
360     CONTINUE
      S(KR,1)=DO,G1*10*ALOG10(1+.25*H1)
380     CONTINUE
390     CONTINUE
40     RETURN
      END

```

```

1      SUBROUTINE PNLPT
      C      PNLPT -- CALCULATES PNL, OASPL, AND PNL
      COMMON/CM1/L(9,24),Y(24),F(24),E(24),S(15,24),KK(24,5),C(15,5),
5      O(20),RP(49),RX(49),P(20),R(15,24),Y1(24),Y(24),C1(15),RVF(20),
      S1(24),G(2,24),C2(15),T(20),D(20),W(5),A(4),V(3),F1(15,24)
      COMMON /CM2/ V8,A0,WR,K1,Y9,TR,T5,R7,P1,Z9,D1,AJ,H,U,E9
1      TC,V9,C9,D8,D1,VC,U9,AB,Q,L9,A6,A7,S6,P9,R9,ALT,SL,ANI
      COMMON /CM3/ IIAS(2),IICASE(6),IDCASE(6),IDENT(6)
      REAL L,KK,K1
10     TJ=0
      V(1)=0
      V(2)=0
      DO 370 J=1,24
15     IF(X(J).GT.0.) GO TO 200
      X(1)=1
      200    IF(X(J).GE.L(7,J)) GO TO 320
      IF(X(J).GE.L(5,J)) GO TO 300
      IF(X(J).GE.L(3,J)) GO TO 280
      IF(X(J).GE.L(1,J)) GO TO 260
20     AN=0
      GO TO 330
      260    AN=0.1*(10**((L(2,J)*(X(J)-L(1,J))))
      GO TO 330
      280    AN=10**((L(4,J)*(X(J)-L(5,J))))
25     GO TO 330
      300    AN=10**((L(6,J)*(X(J)-L(5,J))))
      GO TO 330
      320    AN=10**((L(8,J)*(X(J)-L(9,J))))
30     V(1)=V(1)+10**((X(J)/10)
      V(2)=V(2)+AN
      IF(TJ.GT.AN) GO TO 370
      TJ=AN
      370    CONTINUE
      V(2)=37.22*LOG10(V(2)*.15*TJ*.85)+40
35     V(1)=10*ALOG10(V(1))
      CALL TPNLC(X,P2)
      940    V(3)=V(2)*P2
      RETURN
      END

```

```

1      *TPNLC      THIS SECTION CALCULATES TONE CORRECTED PNL
C      SPECTRAL IRREGULARITY CORRECTION
C
C      THIS PROCEDURE DETERMINES A SPECTRAL IRREGULARITY
5      C      (E.G., PURE TONE) CORRECTION FACTOR ECE VIA SECTION 836.3
C      OF THE FAA NOISE CERTIFICATION DOCUMENT (NOV 17, 1969) AS
C      A FUNCTION OF THE UNCORRECTED 1/3 OCTAVE SPECTRUM, SPL.
C
C      SUBROUTINE TPNLC(SPL,PTCOR)
10     DIMENSION SPL(24),ISPLF(24),SC(24),SPLP(24),SPLPP(24),SP(25),
C      1      SRAR(24),F(24)
C
C      *INITIALIZE SPL FLAG*
C      DO 1 I=1,24
15     1      ISPLF(I) = 0
C
C      *STEP 1*
C      DO 5 I=4,24
C      5      SC(I)=SPL(I) - SPL(I-1)
20     C
C      *STEP 2 AND 3*
C      DO 10 I=5,24
C      10      IF(ABS(SC(I)-SC(I-1)).LE.5.0) GO TO 10
C      IF(SC(I).GT.0.0.AND.SC(I-1).GT.0.0) ISPLF(I)=1
25     IF(SC(I).LE.0.0.AND.SC(I-1).GT.0.0) ISPLF(I-1)=1
C      10      CONTINUE
C
C      *STEP 4*
C      DO 25 I=1,24
30     IF (ISPLF(I).EQ.0) GO TO 20
C      IF(I.EQ.24) GO TO 15
C      STEP 4A MODIFIED SUCH THAT PRECEDING AND FOLLOWING
C      NON-FLAGGED SOUND PRESSURE LEVELS EMPLOYED IN AVERAGE.
C      II = I
35     DO 11 J=1,20
C      11      II = II-1
C      IF (ISPLF(II).EQ.0) GO TO 12
C      12      SPLL = SPL(II)
C      12      IPL = I+1
40     DO 13 J=I+1,24
C      13      IF (ISPLF(J).EQ.0) GO TO 14
C      13      CONTINUE
C      J = 24
45     14      SPLU = SPL(J)
C      SPLP(I) = (SPLL+SPLU)/2.
C      GO TO 25
C      15      SPLP(24) = SPL(23)+SC(23)
C      GO TO 25
50     20      SPLP(I) = SPL(I)
C      25      CONTINUE
C
C      *STEP 5*
C      DO 30 I=4,24
55     30      SP(I) = SPLP(I)-SPLP(I-1)
C      SP(3) = SP(4)
C      SP(25) = SP(24)

```

```
C
C   *STEP 6*
60      DO 35 I=3,23
      35      SRAR(I) = (SP(I)+SP(I+1)+SP(I+2))/3.
C
C   *STEP 7*
65      SPLPP(1) = SPL(1)
      SPLPP(2) = SPL(2)
      SPLPP(3) = SPL(3)
      DO 40 I=4,24
      40      SPLPP(I) = SPLPP(I-1)+SRAR(I-1)
C
C   *STEP 8*
70      DO 45 I=1,24
      45      F(I) = SPL(1)-SPLPP(I)
C
C   *STEP 9 AND 10*
75      CMAX = 0.0
      DO 65 I=1,24
      IF(I.GE.11.AND.I.LE.21) GO TO 50
C   *FREQ 500HZ OR FREQ=5000HZ*
      TC2 = F(I)/6.
80      TC3 = 3.333
      GO TO 55
C   *500 =FREQ =5000HZ*
      50      TC2 = F(I)/3.
      TC3 = 6.666
85      55      IF(F(I).LT.3.0) GO TO 65
      IF(F(I).GE.20.0) GO TO 60
      CMAX = AMAX1(CMAX,TC2)
      GO TO 65
      60      CMAX = AMAX1(CMAX,TC3)
90      65      CONTINUE
      PTCOP=CMAX
      500      RETURN
      END
```

```

1      SURROUTINE PNTTR
C PNTTR -- PRINT AND EPNL CALC SUBROUTINE
C
COMMON/CM1/L(9,24),X(24),F(24),E(24),S(15,24),KK(24,5),C(15,5),
5      O(20),RR(49),RX(49),P(20),R(15,24),Y1(24),Y(24),CI(15),RVE(20),
      S1(24),G(2,24),C2(15),T(20),D(20),W(5),A(4),V(3),F1(15,24)
COMMON /CM2/ V8,A0,WH,K1,Y9,T8,T5,R7,P1,Z9,DJ,AJ,H,U,E9
1      ,T0,V9,C9,DR,D1,V0,U9,A8,Q,L9,A6,A7,S6,P9,R9,ALT,SL,ANI
COMMON /CM3/ IIAS(2),IICASE(6),IDCASE(6),IDENT(6)
10     REAL L,KK,K1
      REAL MP,KT
C
1000  FORMAT(/////50X,3H* ,2A10)
1001      FORMAT(50X,1H*,F7.1,* FOOT ALTITUDE*)
15     1002      FORMAT(50X,1H*,F7.1,* FOOT SIDELINE*)
1004      FORMAT(50X,1H*,F7.1,* FOOT ARC*)
1006      FORMAT(50X,9H* NO EGA )
1008      FORMAT(50X,11H* FULL EGA )
1009      FORMAT(50X,21H* 100 FOOT LAYER EGA )
20     1010  FORMAT(50X,1H*,F6.0,*DEGREE STANDARD DAY*//50X,*ACOUSTIC ANGLE*,
      1 * FROM INLET*//) FREQ      20      30      40      50      60      70*,
      1 *      80      90      100      110      120      130      140      150*,
      1 *      160      PNL*)
1012      FORMAT(F7.0,16F7.1)
25     1014      FORMAT(1X,A6,16F7.1)
1016      FORMAT(* EPNL=*,F6.1)
1017  FORMAT(1H1///,33X,*HIGH VELOCITY JET NOISE PROGRAM - *
      1 *ENGINEERING CORRELATION*//)
1019  FORMAT(31X,6A10)
30     C
      PRINT 1017
      WRITE(6,1014)(IICASE(I),I=1,6)
      999  PRINT 1000,(IIAS(I),I=1,2)
      IF(I,EO,1.) GO TO 160
35     IF (SL,NE,0.0) GO TO 159 & IF (V0,NE,0.0) GO TO 159
      PRINT 1002,H & GO TO 170
159     PRINT 1001,ALT
      PRINT 1002,SL
      GO TO 170
40     160     PRINT 1004,H
170     IF(F9=1) 171,172,173
171     PRINT 1006 & GO TO 200
172     PRINT 1008 & GO TO 200
173     PRINT 1009
45     200     PRINT 1010,T0
      DO 320 J=1,24
      PRINT 1012,F(J),(S(I,J),I=1,15),Y(J)
320     CONTINUE
      IIAS(1)=5H0ASPL
50     PRINT 1014,IIAS(1),(O(I),I=1,15),O9
      IIAS(1)=3HPNL
      PRINT 1014,IIAS(1),(T(I),I=1,15)
      IIAS(1)=4HPNL
      PRINT 1014,IIAS(1),(P(I),I=1,15)
55     PRINT 325
325  FORMAT(1H0)
      IF(V0,EO,0.) GO TO 1040

```

```

        IF(U.EQ.1.) GO TO 1040
    C      FPNL CALCULATION
60      T1=0.
        MP=0.0
        Z1=0.
        Z3=0.
        SJ=0.

65      C      FLYOVER TIME CALCULATION
        DO 530 J1=1,15
        AJ=(J1+1)*10
        T(J1)=(H/SIN(AJ*PI/180.))/A0
7670      WJ=H/(SIN(AJ*PI/180.)/COS(AJ*PI/180.))
70      ASK=(AJ-10)*PI/180.
        KT=(H/(SIN(ASK)/COS(ASK))-WJ)/V0
7685      IF(J1.EQ.1) GO TO 490
        D(J1)=T(J1)+D(J1-1)+KT-T(J1-1)
        GO TO 500
75      490      D(J1)=T(J1)+KT
        500      CONTINUE
        KT=D(8)
        DO 540 J=1,15
        T(J)=D(J)-KT
80      540      CONTINUE
    C      PNL MAX SEARCH
        DO 610 J=1,15
        IF(P(J).GT.MP) GO TO 590
        GO TO 610
85      590      MP=P(J)
        TJ=T(J)
        610      CONTINUE
        CJ=MP-10.
    C      INITIAL AND FINAL TIME DETERMINATION
90      DO 680 JJ=1,15
        IF(P(J).LT.CJ) GO TO 680
        IF((J-1).LT.1) GO TO 750
        D7=T(J)-((J-1)-T(J-1))*(P(J)-CJ)/(P(J)-P(J-1))
        GO TO 690
95      680      CONTINUE
        690      DO 740 JJ=1,15
        J=16-JJ
        IF(P(J).LT.CJ) GO TO 740
        IF((J+1).GT.15) GO TO 780
100      D9=T(J)+((J+1)-T(J))*(P(J)-CJ)/(P(J)-P(J+1))
        GO TO 740
        740      CONTINUE
        Z1=P(2)-P(1)
        750      D7=T(1)-((P(1)-CJ)/Z1)*(T(2)-T(1))
        GO TO 690
105      780      Z3=P(14)-P(15)
        D9=T(15)+((P(15)-CJ)/Z3)*(T(15)-T(14))
        T(16)=D9
        P(16)=CJ
110      C      INTEGRATION START
        820      IF(Z1.EQ.0.) GO TO 880
        T1=IFIX(2.*TJ-D7)
        I=0
        GO TO 900

```

```
115      880      T1=IFIX(2.*(TJ-T(I)))  
          I=1  
          900      TJ=TJ-T1/2  
          910      IF(TJ.GT.T(I+1)) GO TO 1020  
          TT=T(I)  
120      IF(I.EQ.0) TT=07  
          IF(TT.EQ.T(I+1)) GO TO 950  
          Q1=(TJ-TT)/(T(I+1)-TT)  
          GO TO 960  
          950      Q1=(TJ-T(I+1))/(T(I+2)-T(I+1))  
125      960      RJ=P(I)+Q1*(P(I+1)-P(I))  
          IF(RJ.LT.CJ) GO TO 990  
          SJ=SJ+10.*(RJ/10.)  
          990      TJ=TJ+.5  
          GO TO 910  
130      1020      I=I+1  
          IF(Z3.EQ.0.) GO TO 1050  
          IF(I.GT.15) GO TO 1060  
          GO TO 910  
          1050      IF(I.LE.(16)) GO TO 910  
135      1060      F3=(10.*ALOG10(SJ))-13.  
          PRINT 1016, .1*IFIX(10.*E3+.5)  
          1080      RETURN  
          END
```


1 BLOCK DATA
COMMON/CM1/L(9,24),X(24),F(24),E(24),S(15,24),KK(24,5),C(15,5),
1 O(20),RP(49),RX(49),P(20),R(15,24),Y1(24),Y(24),C1(15),RVF(20),
5 S1(24),G(2,24),C2(15),T(20),D(20),W(5),A(4),V(3),E1(15,24)
COMMON /CM2/ V8,A0,W8,K1,Y9,T8,T5,R7,P1,Z9,DJ,AJ,H,II,E9
1 T6,V9,C9,D8,D1,V0,09,AR,Q,L9,A6,A7,S6,P9,R9,ALT,SL,ANI
COMMON /CM3/ IIAS(2),IICASE(6),IUCASE(6),IDENT(6)
REAL L,KK,K1
C SAF JET MIXING NOISE CURVE FIT COEFFICIENTS
10 DATA W/
1 .79847856,6.0060324,2.6130686,-17.028296,-31.584975/
DATA ((C(I,N),N=1,5),I=1,15)/
1 134.2671,78.13129,13.57216,-35.85844,-86.82891,
1 134.5827,77.92338,14.75807,-33.24901,-101.6692,
15 1 135.0606,77.93685,16.55295,-33.08064,-109.8477,
1 135.5862,77.94105,18.44398,-31.98636,-124.1251,
1 136.3070,78.56058,20.13687,-32.57560,-131.9922,
1 137.0408,78.27523,22.26973,-35.10086,-143.0645,
1 137.9991,79.13467,22.17358,-29.12441,-136.9456,
20 1 139.2326,80.80132,23.77031,-31.64966,-146.2695,
1 141.7755,83.32237,21.13044,-34.51163,-119.4629,
1 142.7436,86.50671,22.49117,-33.24900,-111.0132,
1 144.8893,92.72220,28.02726,-47.22204,-120.3369,
1 147.1450,101.6591,50.97311,-80.30287,-254.0784,
25 1 149.5492,105.6868,40.77499,-108.0806,-262.8197,
1 151.9042,107.0227,32.56691,-150.7574,-323.1343,
1 151.189,98.95452,-15.66443,-131.8180,-88.57726/
DATA ((KK(I,N),N=1,5),I=1,12)/
30 1 -10.54902,1.771008,-8.731992,1.01391,0.636305,
1 -10.47272,-2.038364,-9.375026,1.117183,0.9349618,
1 -10.92039,-2.967566,-8.844933,1.269824,0.7043903,
1 -10.61639,4.452847,-8.556268,-.4737891,0.7829865,
1 -10.04622,-1.11499,-10.29365,1.407477,0.9611449,
1 -10.27116,-1.654881,-10.75808,1.045175,1.144233,
35 1 -10.57207,3.833069,-8.472411,0.446222,0.7277405,
1 -10.23615,-1.286685,-11.13199,1.076169,1.066819,
1 -10.64444,-3.383546,-11.9354,1.695872,1.544894,
1 -10.52771,2.105704,-8.993265,0.4974295,0.7882992,
1 -11.03052,-3.665336,-10.5132,1.784495,0.7993335,
40 1 -11.68293,-6.134871,-10.17043,1.993965,0.5740519/
DATA ((KK(I,N),N=1,5),I=13,24)/
1 -11.20320,-1.423282,-8.568622,1.369792,0.5003525,
1 -12.46326,-7.189952,-9.684162,2.504981,0.4032442,
1 -13.19018,-9.252206,-7.828105,3.004999,-.2370745,
45 1 -11.88213,-5.22407,-8.782326,1.981059,0.7470906,
1 -14.57744,-11.73308,-8.161804,3.560226,-.2413976,
1 -16.53499,-15.38885,-5.695258,4.655082,-.9454673,
1 -12.96843,-10.26358,-8.530573,3.485636,1.95912,
1 -17.11334,-17.86003,-6.628826,4.850326,-.8765574,
50 1 -20.08749,-21.11827,-3.229256,5.637981,-1.727925,
1 -14.20673,-14.80845,-7.367175,4.301735,-.494157,
1 -19.20943,-22.94389,-5.903727,6.094622,-1.100433,
1 -22.78446,-26.49346,-1.355867,6.749632,-2.499507/
C PNL CALCULATION COEFFICIENTS
55 DATA ((L(J,I),J=1,9),I=1,12)/
1 49.0,079520,55.0,058098,64.0,043478,91.01,030103,52.0,
1 44.0,068160,51.0,058094,64.0,040570,85.88,030103,51.0,

60 1 39...068160.46...052288.56...036831.87.32...030103.49..
1 34...059640.42...047534.51...036831.79.85...030103.47..
1 30...053013.39...043573.51...035336.79.76...030103.46..
1 27...053013.36...043573.48...033333.75.96...030103.45..
1 24...053013.33...040221.46...033333.73.96...030103.43..
1 21...053013.30...037349.44...032051.74.91...030103.42..
1 18...053013.27...034859.42...030675.94.63...030103.41..
65 1 16...053013.25...034859.40...030103.100.0...030103.40..
1 16...053013.25...034859.40...030103.100.0...030103.40..
1 16...053013.25...034859.40...030103.100.0...030103.40./
DATA ((I(J,I),J=1,9),I=13,24)/
70 1 16...053013.25...034859.40...030103.100.0...030103.40..
1 16...053013.25...034859.40...030103.100.0...030103.40..
1 15...059640.23...034859.38...030103.100.0...030103.38..
1 12...053013.21...040221.34...029960.100.0...029960.34..
1 09...053013.18...037349.32...029960.100.0...029960.32..
1 05...047712.15...034859.38...029960.100.0...029960.30..
75 1 04...047712.14...034859.29...029960.100.0...029960.29..
1 05...053013.14...034859.29...029960.100.0...029960.29..
1 06...053013.15...034859.30...029960.100.0...029960.30..
1 10...068160.17...037349.31...029960.100.0...029960.31..
1 17...079520.23...037349.37...042285.44.29...029960.34..
80 1 21...059640.29...043573.41...042285.51.72...029960.37./
END

```

1      SUBROUTINE EJECTS
      C      EJECTS -- EJECTOR EFFECT SUBROUTINE
      COMMON /NM/ M, OJ
      COMMON /CM1/ L(9,24), X(24), F(24), E(24), S(15,24), KK(24,5), C(15,5),
5      1 O(20), RR(49), RX(49), P(20), R(15,24), Y(24), Y(24), C1(15), RVE(20),
      1 S1(24), G(2,24), C2(15), T(2), D(20), W(5), A(4), V(3), F1(15,24)
      COMMON /CM2/ V8, A0, W8, K1, Y9, T8, T5, R7, P1, Z9, DJ, AJ, H, U, E9
      1 T0, V9, C9, D8, D1, V0, O9, A8, O, L9, A6, A7, S6, P9, P9, ALT, SL, ANI
      COMMON /CM3/ IIAS(2), IICASE(6), IDCASE(6), IDFNT(6)
10     REAL L, KK, K1
      REAL LR, L9, L2, K6, L3, M
      C      HARDWALL EJECTOR EFFECTS
      DO 110 I=1,15
15     DO 110 J=1,24
      F1(I,J)=0.0
      FP=.3*V8/SORT(4*AR/P1)
      LR=5*ALOG10(L9/2)
      D3=SORP(AA*A7*AR*ANI/P1+S6**2-A7*AR*ANI/P1)
      A5=A6 & IF(Y9,GT,3) GO TO 133 & IF(R9,EQ,0) GO TO 140
20     133 A5=A6/(10**((12.7H*(D3/S6-1)**2+.046)))
      140 D2=LX-23.59*A5-(110*(ALOG10(P9/1.91)**2)+.005*(T8-T0)+30
      IF(D2,LT,0) GO TO 280
      C      DIRECTIVITY EFFECTS
      DO 270 I=1,15 & AJ=(I+1)*10
25     IF(AJ,GT,0J-60) GO TO 165 & DE=.64*D2 & GO TO 220
      165 IF(AJ,LT,0J-30) GO TO 180
      IF(AJ,GT,0J) GO TO 200 & DE=.2*D2 & GO TO 220
      180 DE=D2*(-4.888E-4*(AJ-0J+60)**2+.64)
      IF(D2,GT,0) GO TO 220 & DE=0 & GO TO 270
30     210 IF(AJ,GT,0J+20) GO TO 210 & DE=D2*SORP((AJ-0J)/20) & GO TO 220
      210 DE=D2*(1.00925*(AJ-0J-21)+1)
      C      SPECTRAL EFFECTS
      DO 260 J=1,24 & IF(FP,GT,1.12*F(J)) GO TO 250
35     IF(F(J)/FP,GT,H) GO TO 240
      F1(I,J)=.2*(F(J)/FP-1)**2-DE & GO TO 260
      240 F1(I,J)=9.5-DE & GO TO 260
      250 F1(I,J)=-DE
      260 CONTINUE
      270 CONTINUE
40     280 IF(A(1),EQ,0) GO TO A20
      C      EJECTOR TREATMENT EFFECTS
      XJ=M/5.0 & IF(M,LT,1.13) GO TO 330 & XJ=.22A
      310 D4=SORP(4*AR*ANI/P1) & L3=L9*D4
      D3=D3*D2.0
45     C      SORE RESISTANCE AND REACTANCE
      YJ=.8216-2.5094*XJ
      IF(XJ,LT,.08929) GO TO 460
      YJ=.66594-1.48606*(XJ-.08929)
50     IF(XJ,LT,.22721) GO TO 460
      YJ=.17819-2.00751*(XJ-.22721)
      IF(XJ,LT,.26786) GO TO 460
      YJ=.14855-.90634*(XJ-.26786)
      IF(XJ,LT,.32143) GO TO 460
      YJ=0
95     460 T1=(A(1)+.85*A(3)*YJ)/12
      RS=(1.7*XJ)/A(2)
      500 DO 515 J=1,24 & A6=0

```

```

C      FREQUENCY DETERMINATION
60      DO 755 KA=1.3 & IF (KH-2) 520,530,540
          520      P3=F(J)*6.28318*.89 & GO TO 550
          530      P3=F(J)*6.28318 & GO TO 550
          540      P3=F(J)*6.28318*1.12
          550      X4=(P3*T1)/(A0*A(2))-1/TAN((P3*A(4)/12)/A0)
          IF (A(1).NE.10) GO TO 590
65      IP=KH+2-J-2
          RS=RR(IP)
          X4=RX(IP)
          590      A3=0 & DO 730 I=9.15 & K6=0 & AJR=((I+1)*10-90)*P1/180
          A1=4*RS*COS(AJR)/((1+RS*COS(AJR))**2+(X4*COS(AJR))**2)
70      C      ABSORPTION PER REFLECTION
          A2=1-C*ALOG10(1-A1)
          DO 690 K=1.25 & XJ=((2.5*X(J))/25)*K
          C      SOURCE LOCATIONS
          ZJ=XJ/X(J)
75      S2J=-11.19136+32.76997*ZJ-37.633732*ZJ**2+23.970385*ZJ**3
          S2J=S2J-10.115712*ZJ**4+2.4045214*ZJ**5-.23576954*ZJ**6
          S2J=S2J-11.6
          C      EFFECT FOR ALL REFLECTIONS
          DO 675 J1=1.115 IF (J1.GT.1) GO TO 660 S12=((13/2-S6)*TAN(AJR)+XJ
          GO TO 675
          660      L2=L2+D3*TAN(AJR)
          670      IF (L2.GT.L3) GO TO 660
          675      CONTINUE
          680      K6=K6+100*((L3-J1)*A2+S2J)/100
          85      680      CONTINUE
          C      POWER LEVEL REDUCTION
          AJ=(1+1)*10 & KA=10*ALOG10(K6)
          Y1=1.5*P1*(COS((AJ-5)*P1/180)-COS((AJ+5)*P1/180))
          A3=A1*(2.227525E-6*4E-H*Y1)*100*(K6/101)
90      730      CONTINUE
          A3=1-C*ALOG10(A3+13)-6.45175
          A4=A4+100*(L3/10)
          755      CONTINUE & A4=10*ALOG10(A4/3)
          C      DIRECTIVITY EFFECTS
95      DO 815 I=1.15 & AJ=(1+1)*10 & A5=A4
          IF (AJ.LT.0J-50) GO TO 800 & IF (AJ.LT.0J) GO TO 810
          810      A5=A4/2
          815      F1(I,J)=F1(I,J)*(A5+1.2)
          815      CONTINUE
100     820      RETURN & END

```

APPENDIX B

DATA BASE FOR THE ENGINEERING CORRELATION FROM PUBLISHED LITERATURE

The published literature which supplied the data base for the engineering correlation is identified in Tables B-1 through B-13. The tables are organized according to type of nozzle and type of suppressor; a table is provided for each combination. Following the tables, a bibliography is provided to identify each source listed in the tables; this bibliography is separate and independent of the Reference List at the end of this report.

Phosphorus-31 NMR spectra of the phospholipids in the lipid bilayers of the membranes of the *Escherichia coli* cells.

294

Table B-1. Unsuppressed Conical Nozzle (Continued).

Data Source	Engine or Model	Experimental Results					Bibliography Location	Comments
		Static Jet Noise	Flight Vel. Infl.	Source Distrib.	Flow Field	Physical Shielding		
Paper presented to 6th International Congress on Instrumentation	Model	Farfield	Wind Tunnel	---	---	---	14	Sept. 1975
Paper presented to 2nd International Symposium on Air Breathing Engines	Model	Farfield	Rotating ARM	---	---	---	15	
NASA TNX-68122	Model	Farfield	---	---	---	---	16	
NASA TNX-68259	Model	Farfield	Free Jet	---	Yes	---	17	
ALAA 73-869	Model	Farfield	Free Jet	---	---	---	18	Flight Effect Data Correlation
ALAA 73-461	Full Size	Farfield	Yes	---	---	---	19	Flight Effect Data Correlation
ALAA 73-506	Full Size	Farfield	Yes	---	---	---	20	
FAA-SS-72-42	Model	Farfield	---	---	Yes	---	21	
ASD-YER-63-226	Model	Farfield	---	---	---	(Limited)	22	
TRCSD 764	Model	Farfield	---	---	Yes	Shroud	23	
ALAA 73-1041	Model	---	---	Hole in Wall	Yes	---	24	
NASA CR - 1493	Model	Farfield	---	Yes	Yes	---	25	

Table B-1. Unsuppressed Conical Nozzle (Continued).

Data Source	Engine or Model	Static Test Nozzle	Experimental Results				Bibliography Location	Comments
			Flight Vel. Inft.	Source Distrib.	Flow Field	Physical Smoothing		
NASA TWC-118-9	---	---	---	---	---	---	26	Flight Effects Data Correlation
DA-1501	Model	Partfield	---	Yes	Yes	---	27	
NASA TN-333	Engine	Partfield	---	---	Yes	Ejector	28	
NUTE R-331	Model	Partfield	---	---	---	---	29	
FAA-55-73-29	Model	Partfield	---	---	LV	---	30	
NASA TWC-118-3	Model	Partfield	---	---	---	OTW	31	
ALAA 75-97	Model	Partfield	---	---	Yes	OTW	32	
NASA TWC-68346	Model	Partfield	---	---	---	OTW	33	
NASA TWC-71797	Model	Partfield	Free Jet	---	---	OTW	34	
BAEPD 224	Model	Partfield	---	---	Yes	---	35	
AFAPL-TN-72-53	Model	Partfield	---	---	---	---	36	
ALAA 77-792	Model	---	Wind Tunnel No Noise	---	Yes	---	37	
J Sound 19:3	Model	Partfield	---	---	---	---	38	
30. 7								
ALAA 78-368	Model	Partfield	---	---	---	OTW	39	Data Correlation Included

Table B-1. Unsuppressed Conical Nozzle (Continued).

Data Source	Engine or Model	Experimental Results					Bibliography Location	Comments
		Static Jet Noise	Flight Vel. Infl.	Source Distrib.	Flow Field	Physical Shielding		
AFDL-TR-66-127	157	Wearfield	---	---	---	---	40	Data Correlation Included
NASA TND-1801	Model	---	---	---	Yes	---	41	
R/R Report AF5531	Model	---	---	---	Yes	---	42	
Contract No. F33615-71-C-3032	Model	Farfield 6	---	---	Yes	---	43	(Limited)
ALCA Report 1292	Model	Wearfield	---	---	Yes	---	44	
AFAPL-TR-72-52	Model	Farfield	---	---	Yes	---	45	
AFAPL-TR-74-25	Model	Farfield	---	---	Yes	---	46	
FAA-ED-76-79	Model	Farfield	---	---	Yes	Yes	47	
ASTIA AD-702294	Model	---	---	---	Yes	---	48	
NADC-ED-5401	Model	---	---	---	Yes	---	49	
Warren, W.R. PhD Dissertation Princeton University	Model	---	---	---	Yes	---	50	
Potter, R.C. Jones, J.H. Wyle Lab. Report	Model	---	---	Yes	Yes	---	51	
Contract No. NAS-1784	Model	Farfield	---	---	Yes	---	52	

Table B-1. Unsuppressed Conical Nozzle (Concluded).

Data Source	Engine or Model	Experimental Results					Bibliography Location	Comments
		Static Jet Noise	Flight Vel. Infl.	Source Distrib.	Flow Field	Physical Shielding		
NR 66-46	Model	---	---	---	Yes	---	53	
NSU Research Report No. 39	Model	---	---	---	Yes	---	54	
Contract SOas 59-6160-C	Model	Farfield PWL	---	Yes	---	Shroud	91	
ASD-IDR -62-578	Model	Farfield Nearfield	---	Yes	Yes	---	92	
ALAA 75-480	Model	Farfield	---	---	---	---	94	

3/1

Table B-2. Daisy Suppressors.

Data Source	Engine or Model	Experimental Results					Bibliography Location	Comments
		Static Jet Noise	Flight Vel. Infl.	Source Distrib.	Flow Field	Physical Shielding		
NASA TRD-874	B57	Farfield	Yes	---	---	Ejector	5	Yes (Limited)
NAPTC AED-1897	Model	Farfield	---	---	---	---	6	(Limited)
NACA TN-4261	10,000-lbf Engine	Farfield	---	---	---	---	55	Yes
AIAA 75-506	Engine	Farfield	Yes	---	---	---	20	---
AIAA 73-1041	Model	---	---	Hole in Wall	---	---	24	---
AIAA 75-97	Model	Farfield	---	---	Yes	OTW	32	---

Table B-3. Multitube Suppressors.

Data Source	Engine or Model	Experimental Results					Bibliography Location	Comments
		Static Jet Noise	Flight Vel. Infl.	Source Distrib.	Flow Field	Physical Shielding		
FAA-SS-72-40	Model & Some J75	Farfield	---	---	---	---	2	Some with Greatrex tube ends
NASA TMX-71578	J85	Farfield	Yes	---	---	Ejector	56	
NASA TMX-3049	J85	Farfield	Yes	---	---	Ejector W & W/O Scoops	57	
NASA CR-2382	Model and J85	Farfield Nearfield	---	---	Yes	Ejector	8	Lined and unlined
AFOSR-TR-73-0591	Model	---	---	---	---	---	58	Very low velocity theory for mixing noise
NACA TN 4261	10,000-lbf Engine	Farfield	---	---	---	---	55	
NASA CR-114741	J85	Farfield Nearfield	Wind Tunnel	---	---	Ejector	9	
R71AEG 156	Model	---	---	---	---	---	59	Draws on published data. Correlation data for farfield peak noise.
NASA TMX-71450	Model	---	---	---	---	---	60	Fluid Shielding using published data
NASA TMX-68259	Model	Farfield	Free Jet	---	Yes	Ejector (Variable)	17	
FAA-SS-72-42	Model	Farfield	---	---	Yes	Ejector	21	
AIAA 72-131	Model	Farfield	---	---	Some	Shroud	61	

Table B-3. Multitube Suppressors (Concluded).

Data Source	Engine or Model	Experimental Results						Bibliography Location	Comments
		Static Jet Noise	Flight Vel. Infl.	Source Distrib.	Flow Field	Physical Shielding	Aero Data		
72CRD 264	Model	Farfield	—	—	Yes	Shroud	—	23	
AIJA 73-1041	Model	—	—	Hole in Wall	—	—	—	24	
D6-15071	Model	Farfield	—	Yes	Yes	—	Yes	27	
R64FPD 224	Model	Farfield	—	—	Yes	—	—	35	
70-C-142	Model	Farfield	—	—	—	—	—	62	
FMA-SS 73-11	Model	Farfield	Wind Tunnel	Hole in Wall	Yes	Ejector	Yes	63	
Contract M0as 59-6160-C	Model	Farfield PWL	—	—	—	—	—	91	
AIJA 71-153	Model	Farfield	—	—	Some	Shroud	Yes	93	

Table B-4. Chute or Spoke Suppressors.

Data Source	Engine or Model	Experimental Results					Bibliography Location	Comments
		Static Jet Noise	Flight Vel. Infl.	Source Distrib.	Flow Field	Physical Shielding	Aero Data	
FAA-SS-72-40	Model & Some J75 & J93	Farfield	---	---	---	With & W/O Ejector on Some	Yes	2
R65FPD 196	Model	Farfield PWL only	---	---	---	---	---	64
FAA-SS-72-42	Model	Farfield	---	---	Yes	---	Yes	21
D6-15071	Model	Farfield	---	Yes	Yes	---	Yes	27
Contract NOas 59-6160-C	Model	Farfield PWL only	---	---	---	---	---	91

Table B-5. Unconventional Nozzles.

Data Source	Engine or Model	Experimental Results						Bibliography Location	Comments
		Static Jet Noise	Flight Vel. Infl.	Source Distrib.	Flow Field	Physical Shielding	Aero Data		
MASA TNX-71470	Model	Farfield	---	---	---	Wing	---	65	Slot Nozzle
MASA TBD-60	Engine	Farfield	---	---	---	---	---	66	Slot Nozzle Theory
MASA TNX-2758	Model	Farfield	---	---	Yes	---	---	67	Slot Nozzle
MASA TNX-68032	Model	Farfield	---	---	---	Wing	---	68	Slot Nozzle Theory
FAA-RD-76-79	Model	Farfield	---	---	LV	---	---	47	
FAA-SS-72-42	Model	Farfield	---	---	---	Ejector	Yes	21	
MACA TN 3974	Engine	Farfield	---	---	---	---	---	88	
69-C-169	Model	Farfield	---	---	Yes	Shroud	---	90	

Table B-6. Unsuppressed Annular Nozzle.

Data Source	Engine or Model	Experimental Results						Bibliography Location	Comments
		Static Jet Noise	Flight Vel. Infl.	Source Distrib.	Flow Field	Physical Shielding	Aero Data		
NASA CR-120961	J85	Farfield	Yes	---	---	---	Yes	4	Data Questionable
NATC-AED-1897	Model	Farfield	---	---	---	---	(Limited)	6	
NASA-TMX-3049	J85	Farfield	Yes	---	---	---	Yes	57	See TMX-2854
NASA-TMX-2856	J85	Farfield	Yes	---	---	---	Yes	69	See NASA CR-120961 and TMX 2854
NASA-TMX-2854	J85	Farfield	Yes	---	---	---	Yes	7	See NASA CR-120961 Cooled and Uncooled Plug
NASA TMX-2841	J65	Farfield	---	(Limited)	---	Various Ejectors	Yes	70	
NASA CR-2382	J75	Farfield Nearfield	---	---	Yes	Ejector	Yes	8	Lines and Unlined
NACA TR-4261	10,000-lbf Engine	Farfield	---	---	---	With and Without Ejector	Yes	55	
NASA TMX-2573	Model	---	---	---	---	Shroud	Yes	71	
NASA TMX-68182	Model	Farfield	---	---	---	---	---	16	
FAA-SS-72-42	Model	Farfield	---	---	Yes	---	Yes	21	
Cont. No. X69-62-0887-D PR-10	Model	Farfield PWL Only	---	(Limited)	---	Shroud	---	72	Theory for Flow Field

Table B-6. Unsuppressed Annular Nozzle (Concluded).

Data Source	Engine or Model	Experimental Results					Bibliography Location	Comments
		Static Jet Noise	Flight Vel. Infl.	Source Distrib.	Flow Field	Physical Shielding		
R6SFD196	Model	Farfield	—	—	—	—	64	Cont. No., Now 62-0887-d
FAA-ADS-56	Model Small Turbjet	Farfield	—	—	—	—	73	Extended Plugs
ASD-TDR-63-326	Model	Farfield	—	—	—	—	22	
FAA-SS-73-29	Model J79	Farfield	—	—	LV	—	30	
R64TDP224	Model	Farfield	—	—	Yes	—	35	
FAA-ED-73-131	Model JT3D-38	PWL only Farfield	—	—	—	—	74	JT3D Dual Flow Data Correlation for Farfield SPL
FAA-SS-72-40	Model	Farfield	—	—	—	—	2	HW-AP-12
Contract No. MAS3-18008	Model	Farfield	—	—	LV	—	75	(Leaky Core)
AIAA 4th Aero-acoustics Conf. Paper	Model	Farfield	—	—	—	—	76	To be Published - 10/77
Contract WDas 59-6160-C	Model	Farfield PWL only	—	—	—	—	91	

Table B-7. Daisy Suppressor with Plug.

Data Source	Engine or Model	Experimental Results					Bibliography Location	Comments
		Static Jet Noise	Flight Vel. Infl.	Source Distrib.	Flow Field	Physical Shielding		
NACA TN-6261	10,000-lbf Engine	Farfield	---	---	---	---	55	
MSAF0224	Model	Farfield PSL only	---	---	Yes	---	35	
JASA Vol. 36 No. 3	JTEC	Farfield	---	---	---	Ejector	96	
NAPTC-AED-1597	Model	Farfield SPL	---	---	---	---	6	
Contract N00019-6160-C	Model	Farfield PSL only	---	---	---	---	91	

Table B-8. Simple Plug with Multitube Suppressor.

Data Source	Engine or Model	Experimental Results					Bibliography Location	Comments
		Static Jet Noise	Flight Vel. Infl.	Source Distrib.	Flow Field	Physical Shielding		
NASA TMX-1919	J85	Farfield	Yes	---	---	Ejector	77	Some Data with Scoops, See TMX-2854
FAA-S5-72-42	Model	Farfield	---	---	---	---	21	
FAA-S5-73-29	Model	Farfield	---	---	LV	---	30	
NASA TMX-71453	Model	Farfield	---	---	---	Ejector OTV	31	
ADAA 73-93	Model	Farfield	---	---	Yes	OTV	32	Models BH-AP-35-59-B (Leaky Core)
NASA TMX-71792	Model	Farfield	Free Jet	---	---	OTV	34	
ADAA 72-792	Model	---	Wind Tunnel No Noise	---	Yes	---	37	
FAA-S5-72-40	Model	Farfield	---	---	---	---	2	
Contract No. NAS-14008	Model	Farfield	---	---	LV	---	75	(Limited)
FAA-S5-73-11	Model	Farfield	---	---	---	---	63	

Table B-9. Simple Plug with Chute or Spoke Suppressor.

Data Source	Engine or Model	Experimental Results					Physical Shielding	Aero Data	Bibliography Location	Comments
		Engine or Model	Test Method	Velocity, ft/sec	Ref. Radi.	Source	Field			
MAE-4A, MAE-53-16, 114-AD-36	Model 1	Model 1	Passive	---	---	---	---	Yes	2	MAE-4A, MAE-53-16, 114-AD-36
MAE-4A, MAE-53-16, 114-AD-36	Model 1	Model 1	Passive	Yes	---	---	---	Yes	4	MAE-4A, MAE-53-16, 114-AD-36
MAE-4A, MAE-53-16, 114-AD-36	Model 1	Model 1	Passive	Yes	---	---	---	Yes	69	MAE-4A, MAE-53-16, 114-AD-36
MAE-4A, MAE-53-16, 114-AD-36	Model 1	Model 1	Passive	Yes	---	---	---	Yes	9	MAE-4A, MAE-53-16, 114-AD-36
MAE-4A, MAE-53-16, 114-AD-36	Model 1	Model 1	Passive	---	---	---	---	Yes	21	MAE-4A, MAE-53-16, 114-AD-36
MAE-4A, MAE-53-16, 114-AD-36	Model 1	Model 1	Passive	---	---	---	---	Yes	21	MAE-4A, MAE-53-16, 114-AD-36
MAE-4A, MAE-53-16, 114-AD-36	Model 1	Model 1	Passive	---	---	---	---	Yes	22	MAE-4A, MAE-53-16, 114-AD-36
MAE-4A, MAE-53-16, 114-AD-36	Model 1	Model 1	Passive	Yes	---	---	---	Yes	24	MAE-4A, MAE-53-16, 114-AD-36
MAE-4A, MAE-53-16, 114-AD-36	Model 1	Model 1	Passive	---	---	---	---	Yes	30	MAE-4A, MAE-53-16, 114-AD-36
MAE-4A, MAE-53-16, 114-AD-36	Model 1	Model 1	Passive	---	---	---	---	---	35	MAE-4A, MAE-53-16, 114-AD-36
MAE-4A, MAE-53-16, 114-AD-36	Model 1	Model 1	Passive	---	---	---	---	Yes	75	MAE-4A, MAE-53-16, 114-AD-36

Table B-10. Unsuppressed Coannular Nozzle.

Data Source	Engine or Model	Experimental Results						Bibliography Location	Comments
		Static Jet Noise	Flight Vel. Infl.	Source Distrib.	Flow Field	Physical Shielding	Aero Data		
Sytacuse Reports	Model	Farfield	—	—	—	—	Limited	79	No plug, shadow graphs. Some three-stream data
SNECMA TN YMA560	Model	Farfield	—	—	—	—	—	80	
Journal Sound-ing & Vib. (1971) 17(2)	—	—	—	—	—	—	—	81	Data survey
J. Mech. Eng. Sci. Vol. 11, No. 2	Model	—	—	—	Limited	—	—	82	Data correlation for spectral density
ASME 74-SA/Aero-4	Model	Farfield	Free Jet	—	—	—	—	83	Data correlation for refraction
NASA TRX-71503	Model	Farfield	—	—	—	—	—	84	Coplanar noncoplanar with and without plug
SASA TRX-68259	Model	Farfield	Free Jet	—	Yes	—	—	17	
AIJA 75-461	Engine	Farfield	Yes	—	—	—	—	19	Data correlation for flight effects
FAA-ED-74-225	Model	Farfield	—	—	Limited	—	—	85	Coplanar without plug, noncoplanar with plug; data correlation for SPL
Cont. No. XAS3-18008	Model	Farfield	—	—	LV	—	Yes	75	Coplanar without plug noncoplanar with plug
NASA TRX-2378	Model	Farfield	—	—	—	—	—	86	Various configurations
NASA TRX-71553	Model	Farfield	—	—	—	OTW	—	31	
AIJA 74-568	Model	Farfield	—	—	—	OTW	—	39	Data correlation
FAA-ED-73-131	PT 30-15	Farfield	—	—	—	—	Limited	74	Plug core

Table B-10. Unsuppressed Coannular Nozzle (Concluded).

Data Source	Engine or Model	Experimental Results						Bibliography Location	Comments
		Static Jet Nozzle	Flight Test Infl.	Source Distrib.	Flow Field	Physical Shielding	Aero Data		
WATER 3.1.1.1	Model	Partfield	---	---	---	---	---	87	Data correlation
WALL 10th. Reattachment Cond. Paper	Model	Partfield	---	---	---	---	Limited	76	10/77
ALAA 10-104	CFD-6 ITED	Partfield	Aircraft Flyover	---	---	---	Limited	97	
ALAA 10-116	TF10	Partfield	Wind Tunnel	---	---	---	Limited	98	
ASME 11-CT-43	TF10	Partfield	Flyover	---	Velocity Profile	---	Limited	99	
ALAA 12-114410	Model	Partfield	---	---	---	---	---	89	
Cheng 10-114410-C	Model	Partfield 50%	---	---	---	---	---	91	
ALAA 10-114	Model	Partfield 50%	---	---	---	---	---	95	

Table B-11. Coannular Nozzle with Daisy Suppressor.

Data Source	Engine or Model	Experimental Results						Bibliography Location	Comments
		Static Jet Noise	Flight Vel. Infl.	Source Distrib.	Flow Field	Physical Shielding	Aero Data		
NASA TOS-2806	Model	---	---	---	---	---	Yes	10	Mix r Nozzle
F34-42-74-125	Model	Farfield	---	---	---	---	---	85	Core plug, suppressor data correlation
NASA TOS-3412	TF34	Farfield	---	---	Wake Survey	---	Yes	100	Velocity - Decayer

Table B-12. Coannular Nozzle with Multitube Suppressor.

Data Source	Engine or Model	Experimental Results						Bibliography Location	Comments
		Static Jet Noise	Flight Vel. Infl.	Source Distrib.	Flow Field	Physical Shielding	Aero Data		
F14-74-123	Model	Farfield	---	---	---	---	---	85	Core plug suppressor data correlation
Cont. No. XAS-16008	Model	Farfield	---	---	LV	Ejector	Yes	75	Outer suppressor, noncoplanar with plug
NASA CR-134910	Model	Farfield	---	---	---	Shroud	Yes	89	

Table B-13. Coannular Nozzle with Chute or Spoke Suppressor.

Data Source	Engine or Model	Experimental Results						Bibliography Location	Comments
		Static Jet Noise	Flight Vel. Infl.	Source Distrib.	Flow Field	Physical Shielding	Aero Data		
FAA-ED-74-125	Model	Farfield	---	---	---	---	---	85	Core plug, suppressor Data correlation
Cont. No. NAS3-18008	Model	Farfield	---	---	LV	Ejector	Yes	75	Outer suppressor, noncoplanar with plug
NASA CR-134910	Model	Farfield	---	---	---	Shroud	Yes	89	

BIBLIOGRAPHY

1. Knott, P.R., et al. "Supersonic Jet Exhaust Noise Investigation," Technical Report AFAPL-TR-76-68, July 1976.
2. Lu, H.Y., Morden, D.B., Benefiel, R.L, and Simcox, C.D., "SST Technology Follow-On Program - Phase I, Performance Evaluation of an SST Noise Suppressor Nozzle System," FAA-SS-72-40, February 1972.
3. Wright, C.P., Morden, D.B., and Simcox, C.D., "SST Technology Follow-On Program - Phase I, A Summary of the SST Jet Noise Suppression Test Program," FAA-SS-72-41, February 1972.
4. Brausch, J.F., "Flight Velocity Influence on Jet Noise of Conical Ejector, Annular Plug and Segmented Suppressor Nozzles," NASA CR-120961, August 1972.
5. Coles, W.D., Mihalow, J.A., and Swann, W.H., "Ground and In-Flight Acoustic Performance Characteristics of Jet-Aircraft Exhaust Noise Suppressors," NASA TND-874, August 1961.
6. Benham, R.B., "Investigation of New Concepts for the Suppression of Jet Noise," NAPTC-AED-1897, February 1969.
7. Burley, R.A., Karabinus, R.J., and Friedman, R.J., "Flight Investigation of Acoustic and Thrust Characteristics of Several Exhaust Nozzles Installed on Underwing Nacelles on a F-106 Airplane," NASA TMX-2854, August 1973.
8. Atvars, J., et al. "Development of Acoustically Lined Ejector Technology for Multitube Jet Noise Suppressor Nozzles by Model and Engine Tests Over a Wide Range of Jet Pressure Ratios and Temperatures," NASA CR-2382, April 1974.
9. Beulke, M.R. et al., "A Forward Speed Effects Study on Jet Noise from Several Suppressor Nozzles in the NASA/Ames 40- BY 80-Foot Wind Tunnel," NASA CR-114741.
10. Maiden, D.L., "Performance Comparison of a Lobed-Daisy Mixer Nozzle With a Convergent Nozzle at Subsonic Speeds," NASA TMX-2806, September 1973.
11. Hoch, R. and Hawkins, R., "Recent Studies Into Concorde Noise Reduction," AGARD-CP-131.
12. Hoch, R.G., DuPonchel, J.P., Cocking, B.J., and Bryce, W.D., "Studies of the Influence of Density on Jet Noise," A paper presented at the First International Symposium on Air Breathing Engines, June 1972.

13. Maestrello, L., and McDaid, E., "Acoustic Characteristics of a High-Subsonic Jet," AIAA Journal Vol. 9, No. 6, pp 1058-1066, June 1971.
14. de Belleval, J.F., Chen, C.Y., and Perulli, M., "Investigation of In-Flight Noise Based on Measurements in an Anechoic Wind Tunnel," Paper presented to Sixth International Congress on Instrumentation in the Installation of Aerospace Simulation, September 1975.
15. Smith, W., "The Use of a Rotating Arm Facility to Study Flight Effects on Jet Noise," Paper Presented at the 2nd International Symposium on Air Breathing Engines, March 1974.
16. Olsen, W.A., Gutierrez, O.A., and Dorsch, R.G., "The Effect of Nozzle Inlet Shape, Lip Thickness, and Exit Shape and Size on Subsonic Jet Noise," NASA TMX-68182, January 1973.
17. von Glahn, V., Groesbeck, D., and Goodykoontz, J., "Velocity Decay and Acoustic Characteristics of Various Nozzle Geometries with Forward Velocity," NASA TMX-68259, July 1973.
18. Packman, A.B., Ng, K.W., and Patterson, R.W., "Effect of Simulated Foreward Flight On Subsonic Jet Exhaust Noise," AIAA 75-869, June 1975.
19. Bushell, K.W., "Measurement and Prediction of Jet Noise in Flight," AIAA 75-461, March 1975.
20. Brooks, J.R., and Woodrow, R.J., "The Effects of Forward Speed on a Number of Turbojet Exhaust Silencers," AIAA 75-506, March 1975.
21. Brausch, J.F. and Doyle, V.L., "Supersonic Transport Noise Reduction Technology Summary - Phase I," FAA-SS-72-42, December 1972.
22. "Fundamental Study of Jet Noise Generation and Suppression," ASD-TDR-63-326, March 1963.
23. Nagamatsu, H.T., Sheer, R.E., Jr., and Bigelow, E.C., "Subsonic and Supersonic Jet Flow and Acoustic Characteristics and Supersonic Suppressors," General Electric Co., 72CRD264, September 1972.
24. MacGregor, G.R., and Simcox, C.D., "The Location of Acoustic Sources in Jet Flows By Means of the 'Wall Isolation' Technique," AIAA 73-1041, October 1973.
25. Nagamatsu, H.T., Sheer, R.E., Jr., and Gill, M.S., "Flow and Acoustic Characteristics of Subsonic and Supersonic Jets from Convergent Nozzle," NASA CR-1693, December 1970.
26. Stone, J.R., "On the Effects of Flight on Jet Engine Exhaust Noise," NASA TMX-71819, 1975.

27. Ranner, J.A., "Velocity and Shear Profiles in the Subsonic Jet Efflux From Model Scale Sound Suppressors," The Boeing Co., Report No. D6-15071, March 1966.
28. North, W.J. and Coles, W.D., "Effect of Exhaust-Nozzle Ejectors on Turbo-jet Noise Generation," NACA TN 3573, October 1955.
29. Cocking, B.J., "The Effect of Temperature on Subsonic Jet Noise," N.G.T.E. Report No. R-331, May 1974.
30. Blozy, J.T., et al., "Supersonic Transport Noise Reduction Technology Program," FAA-SS-73-29, September 1975.
31. von Glahn, U., Goodykoontz, J., and Wagner, J., "Nozzle Geometry and Forward Velocity Effects on Noise for CTOL Engine - Over-The-Wing Concept," NASA TMX-71453, October 1973.
32. von Glahn, U. and Groesbeck, D., "Influence of Mixer Nozzle Velocity Decay Characteristics on CTOL-OTW Jet Noise Shielding," AIAA 75-97, January 1975.
33. Reshotko, M., Goodykoontz, J.H., and Dorsch, R.G., "Engine - Over-The-Wing Noise Research," NASA TMX -68246, July 1973.
34. von Glahn, U. and Goodykoontz, J., "Installation and Airspeed Effects on Jet Shock-Associated Noise," NASA TMX-71792, November 1975.
35. Semrau, W, "Research on Jet Noise Generation and Suppression," General Electric Co., R63FPD224, August 1964.
36. Plumblee, H.E., et al. "The Generation and Radiation of Supersonic Jet Noise," AFAPL-TR-72-53, July 1972.
37. von Glahn, U., Sekas, N., and Huff, R., "Forward Flight Effects on Mixer Nozzle Design and Noise Considerations for STOL Externally Blown Flap Systems," AIAA 72-792, August 1972.
38. Ahuja, K.K., and Bushell, K.W., "An Experimental Study of Subsonic Jet Noise and Comparison With Theory," Journal of Sound and Vibration (1973) 30(3), pp 317-341, May 1973.
39. von Glahn, U., Groesbeck, D., and Reshotko, M., "Geometry Considerations For Jet Noise Shielding With CTOL Engine - Over-The-Wing Concept," AIAA 74-568, June 1974.
40. Hermes, P.H., and Smith, D.L., "Measurement and Analysis of the J57-P21 Noise Field," AFFDL-TR-66-147, November 1966.
41. Eggers, J.M., "Velocity Profiles and Eddy Viscosity Distribution Downstream of a Mach 2.22 Nozzle Exhausting Into Quiescent Air," NASA TND-3601, 1966.

42. Trevett, E.G., "Velocity Measurement in a Jet From a Convergent Nozzle," Rolls Royce Report AP5531, 1968.
43. Plumblee, H.E., et al., "The Generation and Radiation of Supersonic Jet Noise," Final Report, Contract No. F33615-73-C-2032, December 1975.
44. Laurence, J.C., "Intensity Scale and Spectra of Turbulence in Mixing Region of Free Subsonic Jet," NACA Report 1292, 1956.
45. Benzakein, M.J. and Knott, P.R., "Supersonic Jet Exhaust Noise," Technical Report AFAPL-TR-72-52; August 1972.
46. Knott, P.R., "Supersonic Jet Exhaust Noise Investigation," Technical Report AFAPL-TR-74-25, June 1974.
47. Mani, R., et al., "Theoretical Developments and Basic Experiments," FAA-RD-76-79, II, May 1978
48. Pitkin, E.T. and Glassman, "Experimental Mixing Profiles of a Mach 2.6 Free Jet," ASTIA AD-202294, August 1958.
49. Anderson, A. and Johns, F., "Non-Dimensional Characteristics of Free and Deflected Supersonic Jets Exhausting Into Quiescent Air," NADC - ED-5401, March 1954.
50. Warren, W.R., "An Analytical and Experimental Study of Compressible Free Jets," Doctoral Dissertation, Princeton University, 1957.
51. Potter, R.C. and Jones, J.H., "An Experiment to Locate the Acoustic Sources in a High Speed Jet Exhaust Stream," Wyle Lab Report, 1967.
52. Nagamatsu, H.T., Sheer, R.E. Jr., and Gill, M.S., "Flow and Acoustic Characteristics of Subsonic and Supersonic Jets From Convergent Nozzle," Final Report Contract No. NASW-1784, July 1969.
53. Ollerhead, J.B., "Some Shadowgraph Experiments With a Cold Supersonic Jet," Wyle Research Report WR 66-44, October 1966.
54. Faris, G.N., "Some Entrainment Properties of a Turbulent Axi-Symmetric Jet," Miss State University Aerophysics Department Research Report No. 39, January 1963.
55. Ciepluch, C.C., et al., "Acoustic, Thrust, and Drag Characteristics of Several Full-Scale Noise Suppressors for Turbojet Engines," NACA TN-426, April 1958.
56. Burley, R.R., "Suppressor Nozzle and Airframe Noise Measurements During Flyover of a Modified F106B Aircraft With Underwing Nacelles," NASA TM-71578, November 1974.

57. Burley, R.R., "Flight Velocity Effects on the Jet Noise of Several Variations of a 104-Tube Suppressor Nozzle," NASA TMX-3049, July 1974.
58. Fabris, G. and Fejer, A.A., "Confined Mixing of Multiple Jets," AFOSR-TR-73-0591, November 1972.
59. Motsinger, R.E. and Sieckman, A.R., "Prediction of Supersonic Jet Noise Reduction Using Multitube Nozzle Suppressors," General Electric Co., R73AEG156, March 1973.
60. Gray, V.H., Gutierrez, O.A., and Walker, D.Q., "Assessment of Jets as Acoustic Shields by Comparison of Single and Multitube Suppressor Nozzle Data," NASA TMX-71450, October 1973.
61. Lawrence, R.L., O'Keefe, J.R., and Tate, R.B., "Multielement Suppressor Nozzles for Thrust Augmentation Systems," AIAA 72-131, January 1972.
62. Nagamatsu, H.T., and Sheer, R.E., Jr., "Flow, Thrust, and Acoustic Characteristics of 50 Tubes With 50 Shrouds Supersonic Jet Noise Suppressor," 70-C-142, February 1972.
63. Atvars, J., et al., "SST Technology Follow-on Program - Phase II," FAA-SS-73-11, March 1975.
64. Sowers, H.D., "Research on Jet Noise Suppressor Designs," General Electric Co., R65FPD196, August 1965.
65. Stone, J.R. and Gutierrez, O.A., "Noise Tests of a High Aspect Ratio Slot Nozzle With Various V-Gutter Target Thrust Reverser," NASA TMX-71470, November 1973.
66. Coles, W.D., "Jet-Engine Exhaust Noise From Slot Nozzles," NASA TND-60, September 1959.
67. Stone, J.R. and Gutierrez, O.A., "Small-Scale Noise Tests of a Slot Nozzle with V-Gutter Target Thrust Reverser," NASA TMX-2758, April 1973.
68. Reshotko, M., "Preliminary Noise Tests of the Engine OTW Concept," NASA TMX-68032, March 1972.
69. Chamberlin, R., "Flyover and Static Tests to Study Flight Velocity Effects on Jet Noise of Suppressed and Unsuppressed Plug Nozzle Configurations," NASA TMX-2856, August 1973.
70. Clark, B.J., "Full-Scale Experiments With an Ejector to Reduce Jet Engine Exhaust Noise," NASA TMX-2841, August 1973.
71. Bresnahan, D.L., "Internal Performance of a 10° Conical Plug Nozzle With a Multispoke Primary and Translating External Shroud," NASA TMX-2573, June 1972.

72. Lee, R. and Semrau, W., "Jet Noise Suppression Research Program," Final Report Contract No. Now-62-0887-D, April 1973.
73. Moore, H.B. and Clinch, J.M., "Application of Extended Plug Nozzle Noise Suppression Theory to a Small Turbojet Engine," FAA-ADS-56, August 1965.
74. Mayer, J.E., et al., "FAA JT3D Quiet Nacelle Retrofit Feasibility Program," FAA-RD-73-131, June 1973.
75. Knott, P.R., et al., "Acoustic Tests of Duct-Burning Turbofan Jet Noise Simulation," NASA Contract Report 2966, July 1978.
76. Cargill, A.M. and Duponchel, J.P., "The Noise Characteristics of Inverted Velocity Profile Coannular Jets," Paper proposed for Publication at the AIAA 4th Aeroacoustic Conference, October 1977.
77. Burley, R.R. and Head, V.L., "Flight Velocity Effects of Jet Noise of Several Variations of a 48 Tube Suppressor Installed on a Plug Nozzle," NASA TMX-2919, February 1974.
78. Burley, R.R., and Johns, A.L., "Flight Velocity Effects of Jet Noise of Several Variations of a Twelve-Chute Suppressor Installed On A Plug Nozzle," NASA TMX-2918, February 1974.
79. Dosanjh, et al., "Noise Reduction From Supersonic Jet Flows," Grant NGR-33-022-082, DOT-08-20054, Syracuse University, Quarterly Reports.
80. Anon., "Experimental Results From Noise Tests on Coplanar, Coaxial, Subsonic Jets," Snecma TN #YKA560, July 1972.
81. Bushell, K.W., "A Survey of Low Velocity and Coaxial Jet Noise With Application to Prediction," J. Sound Vib (1971) 17(2), pp 271-282.
82. Williams, T.J., Ali, M.R.M.V., and Anderson, J.S., "Noise and Flow Characteristics of Coaxial Jets," Journal Mech. Eng. Sci, Vol. II No. 2, 1969.
83. Reed, D.H., "Effect of Forward Velocity on the Noise Characteristics of Dual-Flow Jet Nozzles," ASME 74-WA/AERO-4, August 1974.
84. Olsen, W. and Freedman, R., "Jet Noise From Coaxial Nozzles Over a Wide Range of Geometric and Flow Parameters," NASA TMX-71503, 1974.
85. Bilwakesh, K.R., et al., "Core Engine Noise Control Program," FAA-RD-74-125, August 1974.
86. Kantarges, G.E. and Cowthorn, J.M., "Effects of Temperature on Noise of Bypass Tests as Measured in the Langley Noise Research Facility," NASA D-2378, August 1964.

87. Cocking, B.J., "An Experimental Study of Coaxial Jet Noise," N.G.T.E. Report No. R-333; April 1976.
88. Coles, W.D. and Callaghan, E.E., "Full Scale Investigation of Several Jet Engine Noise Reduction Nozzles," NACA TN 3974, April 1957.
89. Kozlowski, H., et al., "Aero-Acoustic Tests of Duct-Burning Turbofan Exhaust Nozzles," NASA CR-134910, December 1975.
90. Nagamatsu, H.T., Sheer, R.E., Jr., and Gill, M.S., "Effects of Rods, Shrouds, Transversely Impinging Jets, and Reverse Slotted Cone on Supersonic Jet Exhaust Noise," General Electric, 69-C-169, April 1969.
91. Lee, R., et al., "Research Investigation of the Generation and Suppression of Jet Noise," Contract NOas 59-6160-C, Navy, Bureau of Weapons, January 1961.
92. Eldred, K.M., et al., "Suppression of Jet Noise with Emphasis on the Near Field," ASD-TDR-62-578, February 1963.
93. Nagamatsu, H.T., Sheer, R.E. Jr., and Gill, M.S., "Flow and Acoustic Characteristics of 191 Tubes and 191 Shrouds Supersonic Jet Noise Suppressor," AIAA 71-153, November 1969.
94. Tanna, H.K., and Dean, P.D., "An Experimental Study of Shock-Free Supersonic Jet Noise," AIAA 75-480, March 1975.
95. Kozlowski, H., Packman, A., and Gutierrez, O., "Jet Noise Characteristics of Unsuppressed Duct Burning Turbofan Exhaust System," AIAA 76-149, January 1976.
96. Tirumalesa, Duvvuri, "Effect of Ejector Spacing on Ejector-jet Noise Characteristics," NASA Vol. 56 No. 3, February 1973.
97. Merriman, J.E., et al., "Forward Motion Installation Effects on Engine Noise," AIAA 76-584, July, 1976.
98. Strout, F.G., and Atencio, A. Jr., "Flight Effects on JT8D Engine Jet Noise as Measured in the NASA Ames 40- by 80-Foot Wind Tunnel," AIAA 76-556, July 1976.
99. Burchom, F.W. Jr., Lasagna, P.L., and Kurtenbach, F.J., "Static and Flyover Noise Measurements of an Inverted Profile Exhaust Jet," ASME 77-GT-81, December 1976.
100. Samanich, N.E. and Heidelberg, L.J., "Acoustic, Performance, and Wake Survey Measurements of a Lobed Velocity-Decayer Nozzle Installed on a Quieted TF-34 Turbofan Engine," NASA TMX-3413, August 1976.

APPENDIX C

PROPOSED ARP 876 GAS TURBINE JET
EXHAUST NOISE PREDICTION

The following is the text of the letter (dated 14 July 1975) transmitting the ballot version of proposed SAE ARP 876 to the A-21 Committee members.

Dear Member,

The A21 Committee will shortly be balloted on the revision to AIR 876.

As those of you who managed to get to London in April will realize the subcommittee meeting agreed certain editorial changes and minor modifications to the technical content of the draft, and set a deadline of the end of May for afterthought. To those of you who did not attend the meeting I am sending relevant additional paperwork.

We received some comment from Boeing in the afterthought period, and have spent some time analyzing this comment against the document.

Clearly, had it not been for the considerable delay in being able to correspond and the unlikely event that all concerned could obtain funds to attend a special session, another review would have been desirable before balloting. However, I feel that perhaps the only way of bringing the first phase of our work to a satisfactory conclusion is to get final comment via the ballot.

On other matters dealt with at the subcommittee meeting I am sure that the initiative now lies largely with members of the group. Our proposals for shockcell noise and in-flight effects need appraisal and comment as soon as you are able. On the question of coaxial flow noise we will shortly be sending a revised proposal.

Naturally I hope that there will be sufficient response for a useful discussion at the next A21 meeting, but if no substantive material has been received by then we may opt to leave these matters for a further six months.

Yours sincerely,

M.J.T. Smith

Introduction - AIR 876, issued on October 7, 1965, presented a summary correlation of jet engine exhaust noise data available at that time. It dealt both with static and with flight modes; because the data was from full-scale engines, no attempt was made to subdivide the information into the

relevant component sources. Work in recent years on good-quality, noise facilities has established that most engine exhaust systems are influenced in the noise characteristics by far more than the noise due to the external mixing process along, and this work has provided the opportunity to develop a clearer picture of the influence of other effects.

AIR 876 was also limited to velocities above 1,000 ft/sec, i.e., the range of exhaust velocities associated with early jet engines. The introduction of more advanced engine designs demands a prediction technique for exhaust sources over a far wider range of velocity conditions.

Therefore it is intended that ARP 876 be developed on a long-term basis as a document definitive in most aspects of the prediction of exhaust noise, consistent with the state of the art, and specific recommended procedures will be issued as Appendices.

The document will offer a method of estimating the exhaust noise from single, unsilenced engines. To be useful in estimating the noise from aircraft installations, a number of additional effects must be considered, and it is intended that these also will be covered as substantive evidence becomes available.

Areas that will not be addressed, due to source variability with detailed engine design parameters, are aerodynamic blade noise sources; that is, the noise generated by interaction effects between rotating and stationary components of the fan, compressor, and turbine systems.

Each Appendix will be dated, and will represent an approach to a particular topic as agreed by members of the SAE-A21 Subcommittee with experience or data on that subject. Lists of members and affiliated bodies contributing experimental data or other information as used in compiling any one Appendix will be included. Correspondence should be addressed to the Secretary to the A21 Committee for appropriate distribution.

Sources of Exhaust Noise - The exhaust system noise of an aircraft gas turbine engine can be considered to comprise the following main sources:

- (a) Pure jet mixing noise resulting from a hot core exhaust stream mixing with the surrounding environment (which may be influenced by a bypass flow).
- (b) Pure jet mixing noise resulting from a cold bypass stream mixing with both the surrounding environment and the core flow.
- (c) Shock-associated noise, where either or both hot and cold exhaust systems comprise a choked final nozzle.
- (d) Noise from the core engine resulting from aerodynamic disturbances upstream of the final nozzle, including combustion noise.
- (e) Aerodynamic noise, tonal and broadband, resulting from blade interaction effects in fan, compressor, or turbine systems.

All the above sources combine in varying degrees to produce the overall exhaust-noise characteristics. The relevance of each source is a function of both engine operating conditions and aircraft speed. Because of the dependence of aerodynamic blading noise on the intimate design configuration of any given engine, this aspect is specifically excluded from subsequent consideration, and every attempt has been made to remove such phenomena from any engine data used.

Notes on Use of Prediction Procedures - Prediction methods contained in this Appendix are self-contained.

To develop an estimate of the total exhaust-noise signature from an engine, it is necessary to integrate the individual source components. This is effected by estimating each component spectrum and summing the levels in each one-third octave logarithmically. This is most conveniently carried out prior to any extrapolation to the relevant distance or corrections for atmospheric conditions and ground reflection effects. It is also necessary to incorporate any estimated turbomachinery content (not covered herein) at the initial stage, in order to obtain a complete engine picture. Furthermore, it is advisable that any assumed modification to the noise by virtue of silencing or installation effects is made in the component calculation stage.

Methods contained in this Appendix are expressed in terms of noise levels that would be measured under free-field conditions. Reflective augmentations and cancellations from real surfaces, primarily the ground surface over which measurements are made, produce peaks and troughs in the observed test spectra; these have been corrected out of the experimental data used where it has not been obtained under laboratory conditions.

Spectra and directivity plots in this Appendix must, therefore, be converted to nonfree-field conditions to make them representative of typical "in the field" measurements. SAE AIR 1327 provides guidance on such a conversion for an acoustically hard surface (i.e. concrete, tarmac) and advice on how to deal with other typical surfaces (e.g. grassland).

The prediction methods provide spectral information derived from measurements taken in the acoustic far field, but corrected back to a reference distance of less than one nozzle diameter.

Since distances involved in aircraft noise calculations are large, apart from the normal inverse square law correction, allowance must be made for atmospheric absorption. SAE-ARP 866 provides a standard method of allowing for atmospheric absorption under a range of ambient temperature and humidity conditions.

If a subjective assessment is required, perceived noise levels (PNL) may be calculated using the methods in SAE-ARP 865A.

Symbols

a_o	Ambient speed of sound
A_j	Cross-sectional area of jet exhaust nozzle
C_v	Velocity coefficient for relevant discharge nozzle
dB	Sound Pressure Level (re: 0.00002 N/m^2)
D_j	Nozzle diameter
f	One-third-octave, center band frequency
g	Gravitational constant
NPR	Nozzle pressure ratio
OASPL	Overall Sound Pressure Level (dB re: 0.00002 N/m^2)
r	Radial distance from source to observer
R	Gas constant
S	Free-field overall sound pressure level
SPL	Sound Pressure Level (dB re: 0.00002 N/m^2)
T_j	Jet total temperature (kelvins)
V_a	Forward speed of engine/airplane
V_j	Fully expanded jet velocity
γ	Ratio of specific heats for propulsive medium
θ_i	Angle to engine inlet axis (degrees)
θ_j	Angle to jet axis (degrees)
ρ_{ISA}	Atmospheric density under ISA conditions
ρ_j	Fully expanded jet density
ω	Variable density index used in computing jet mixing noise OASPL

NOTE: Variables for which units are not designated above are used only in dimensionless ratios.

Appendix I to Proposed ARP 876: Single-Stream Jet Mixing-Noise Prediction

Static Conditions - Definitive, model-scale, experimental work of recent years has provided a firm data base for the study of mixing noise over a wide range of jet velocity and temperature conditions. This work has shown that jet mixing noise level and spectral character are a function of the following principal parameters:

- (a) The velocity differential between the jet and the environment.
- (b) The jet density relative to the environment.
- (c) The jet dimensions.

It has been concluded that one of the most convenient ways to express jet noise characteristics is to consider firstly the normalized overall sound pressure level (OASPL) as a function of jet velocity (V_j) and angle of measurement (θ_i or θ_j) and to then relate the spectral character (on one-third-octave basis) to the overall level at any point in the field. This procedure may be adopted by using Figures C-1 through C-10 et seq.

The method of calculation is as follows:

Step 1 - Calculate the fully expanded mean jet velocity (V_j) from a knowledge of jet temperature and pressure, where:

$$V_j = C_v \left[\left(\frac{2\gamma R}{\gamma-1} \right) T_j \left(1 - \text{NPR}^{1/\gamma} \right) \right]^{1/2} \quad (\text{C-1})$$

or, where a definition of temperature and pressure is not readily available (for example, from engine test stand measurements) an alternative method of calculating V_j is from thrust and mass flow, where:

$$V_j = g \left[\frac{\text{Static Gross Thrust}}{\text{Mass Flow}} \right] \quad (\text{C-2})$$

Step 2 - Using V_j obtained from Step 1 and the ambient speed of sound (a_0) obtain the variable density index (ω) from Figure C-1.

Step 3 - Using Figure C-2 obtain the normalized, free-field, overall sound pressure level (S) where:

$$S = \text{OASPL} - 10 \log \left[\left(\frac{\rho_j}{\rho_{\text{ISA}}} \right)^{\omega} \frac{A_j}{r^2} \right] \quad (\text{C-3})$$

for the value of V_j at any desired angle.

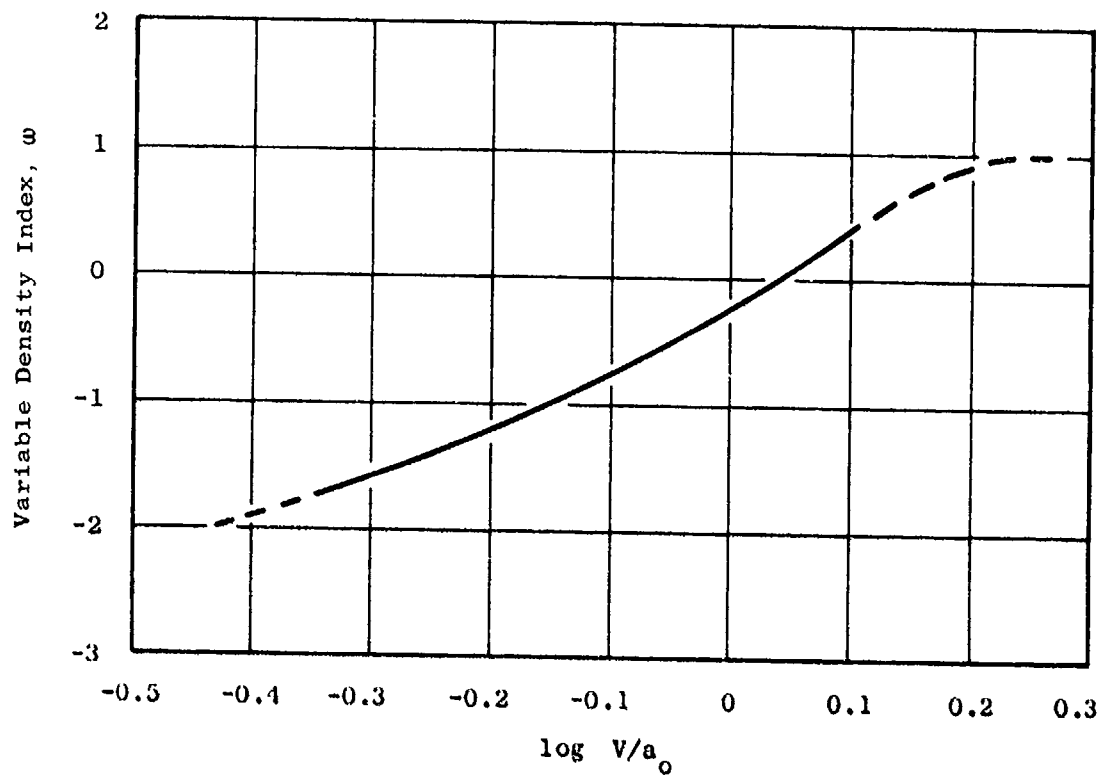


Figure C-1. Variable Density Index, ω .

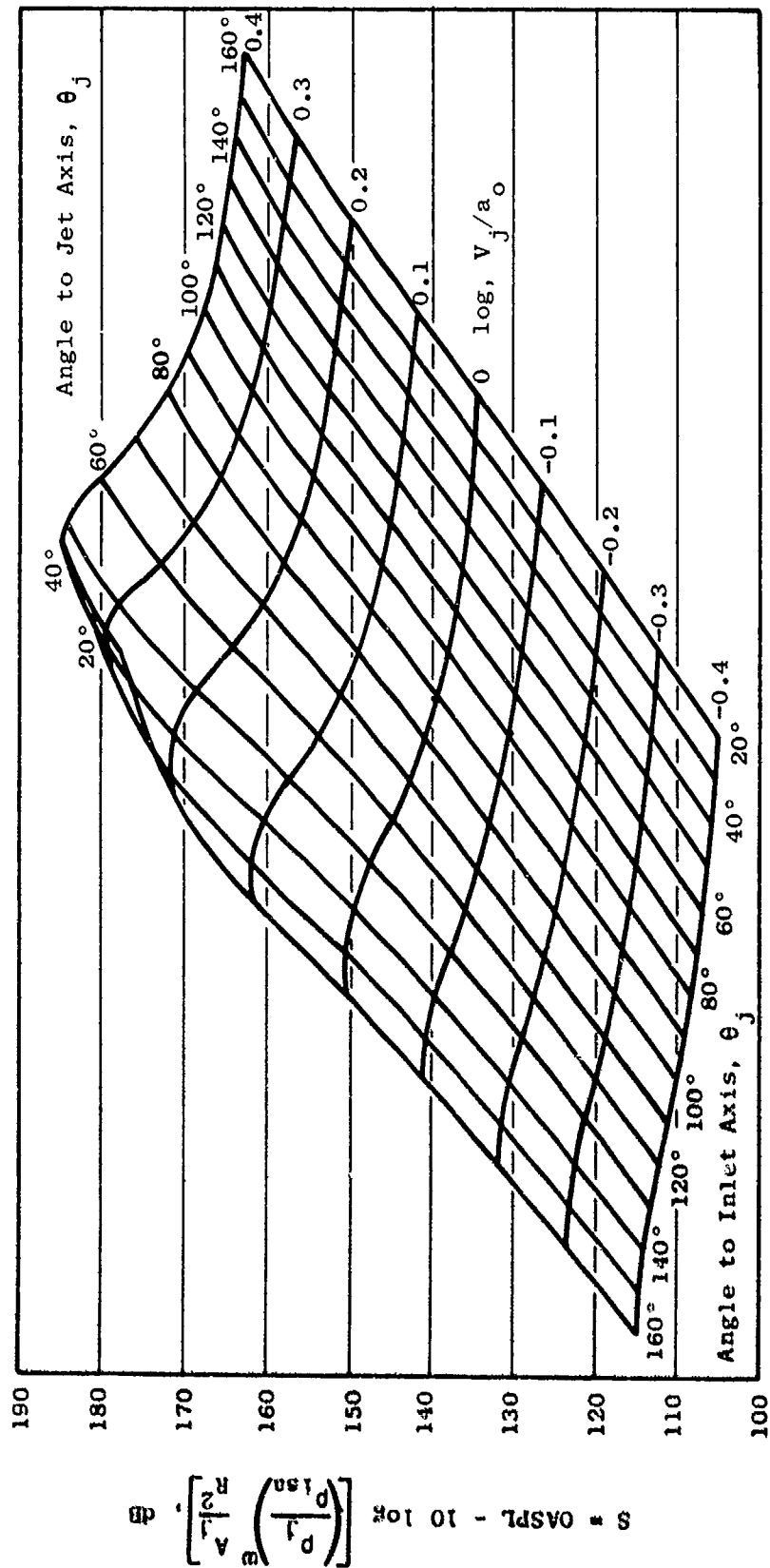


Figure C-2. Pure Jet Mixing Noise Nondimensional Polar Prediction Carpet.

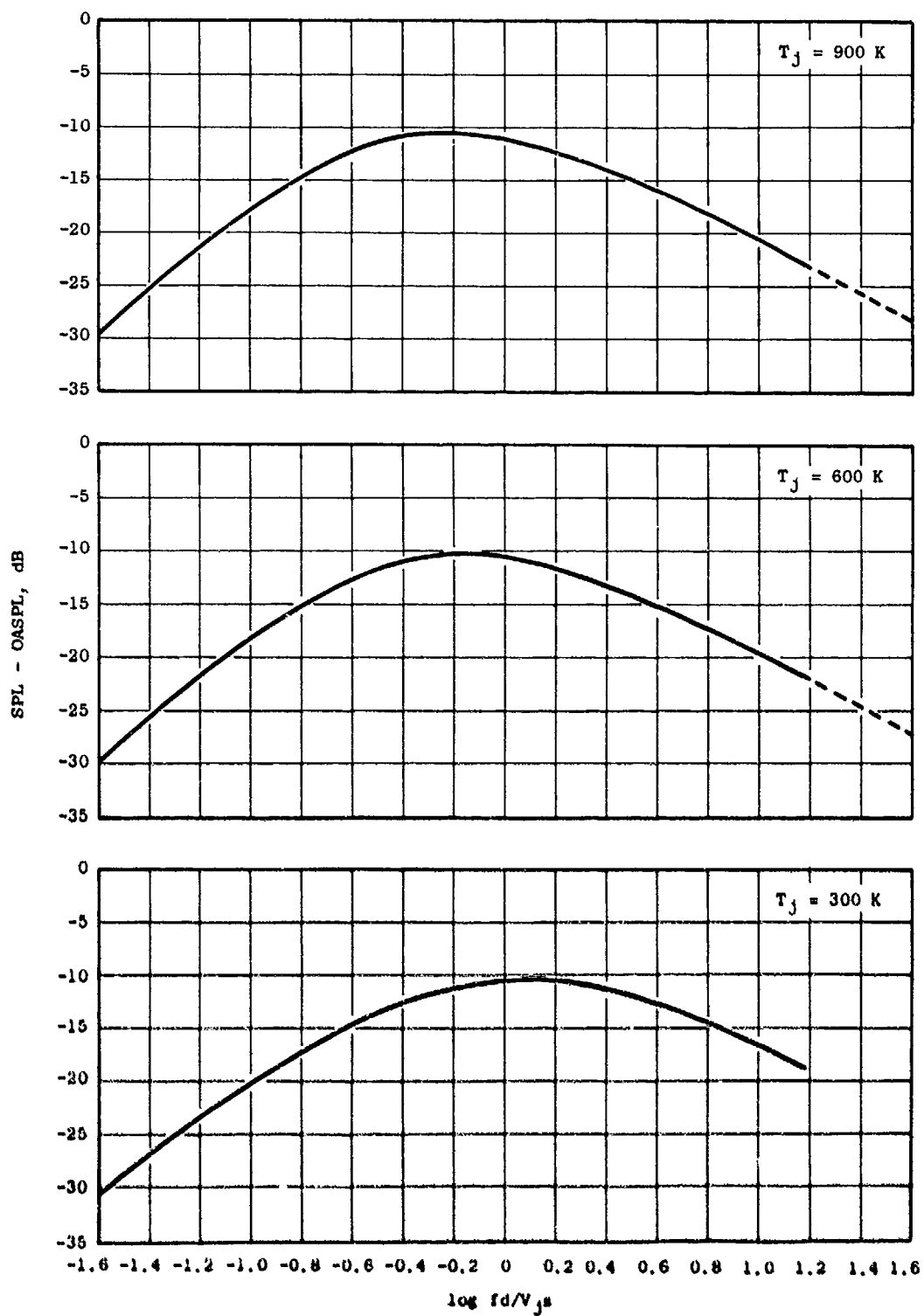


Figure C-3. Jet Noise Characteristics, 90° to 20° Angle to Intake Axis, 90° to 160° Angle to Jet Axis.

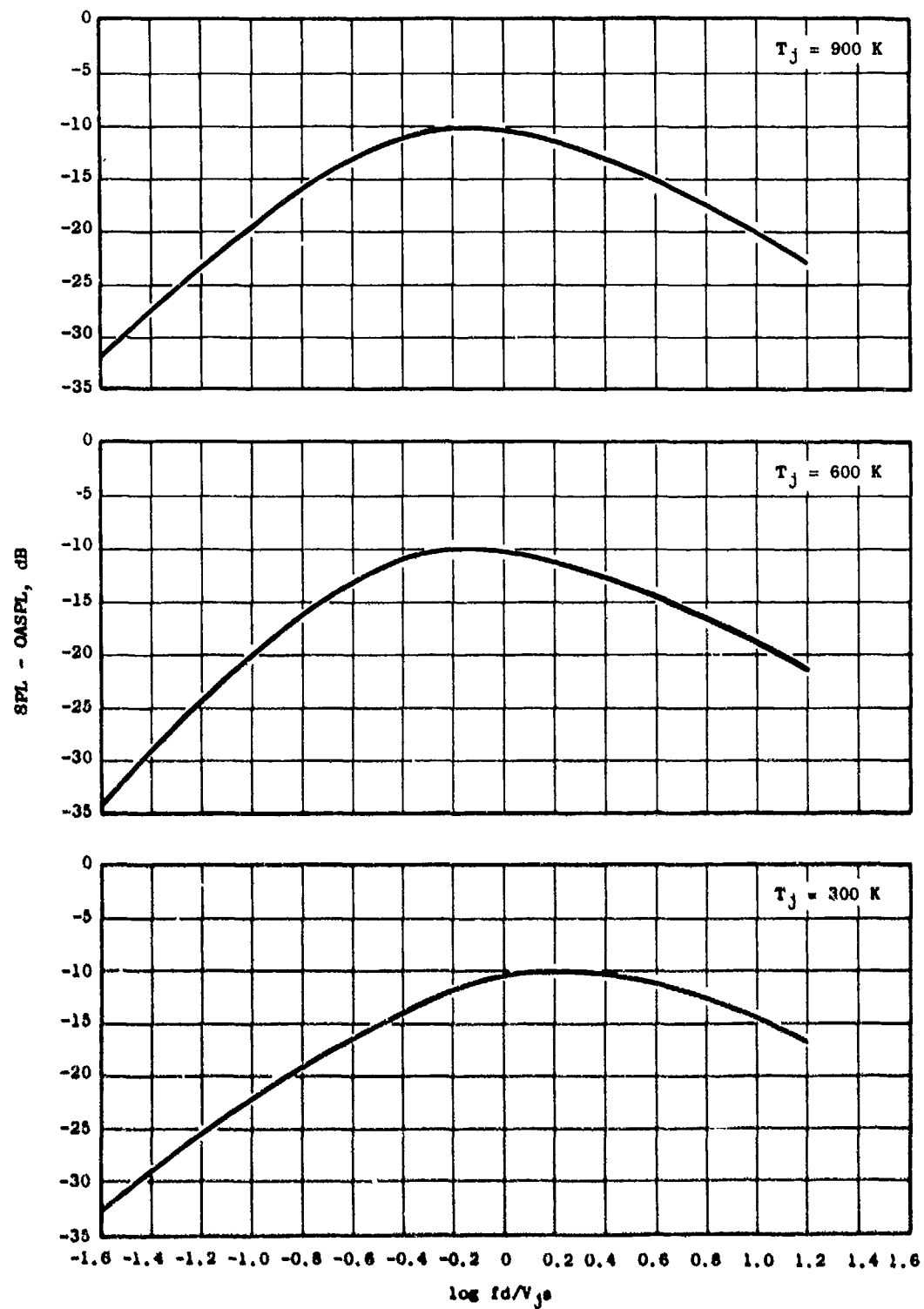


Figure C-4. Jet Noise Characteristics, 100° Angle to Intake Axis, 80° Angle to Jet Axis.

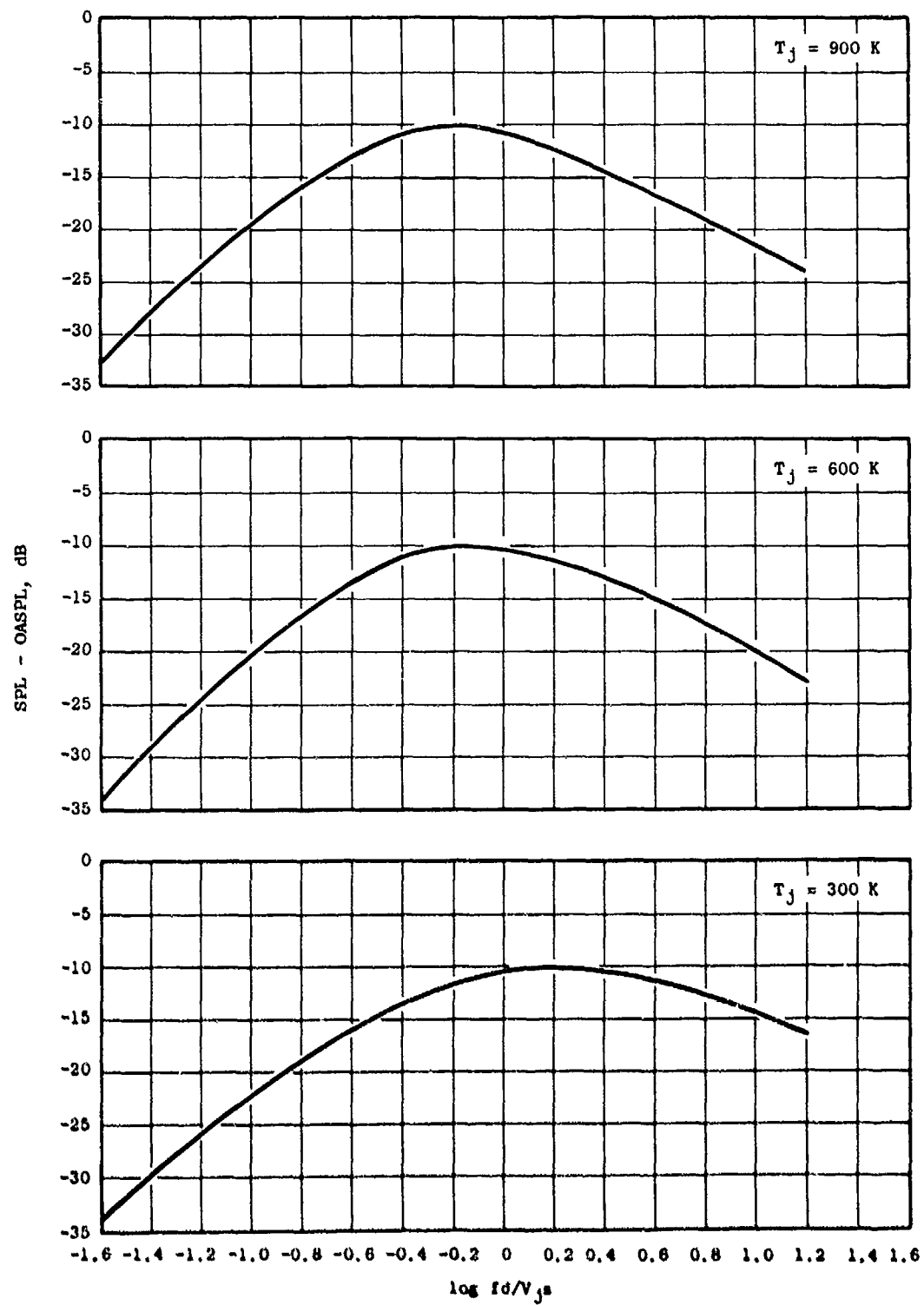


Figure C-5. Jet Noise Characteristics, 110° Angle to Intake Axis, 70° Angle to Jet Axis.

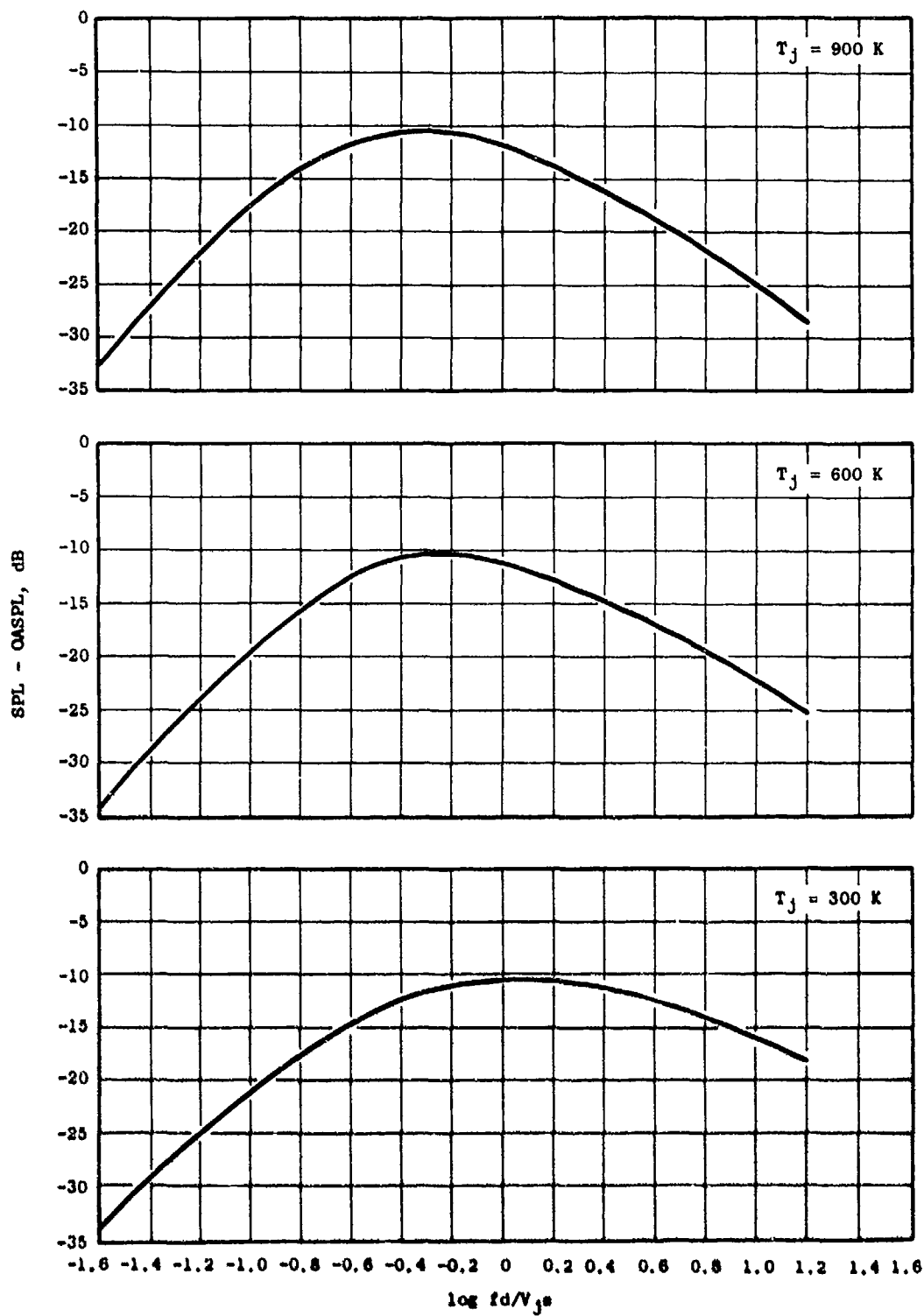


Figure C-6. Jet Noise Characteristics, 120° Angle to Intake Axis, 60° Angle to Jet Axis.

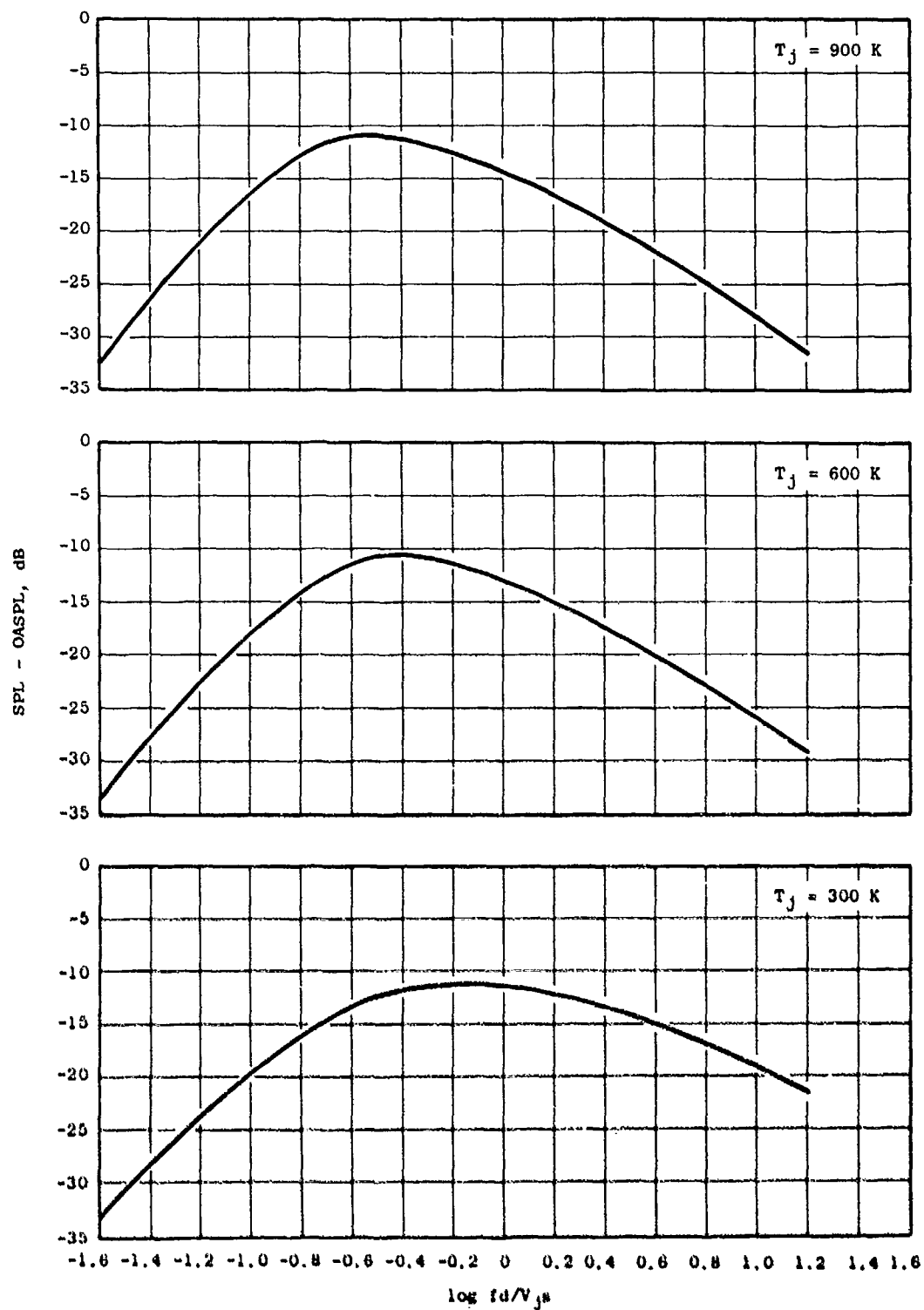


Figure C-7. Jet Noise Characteristics, 130° Angle to Intake Axis, 50° Angle to Jet Axis.

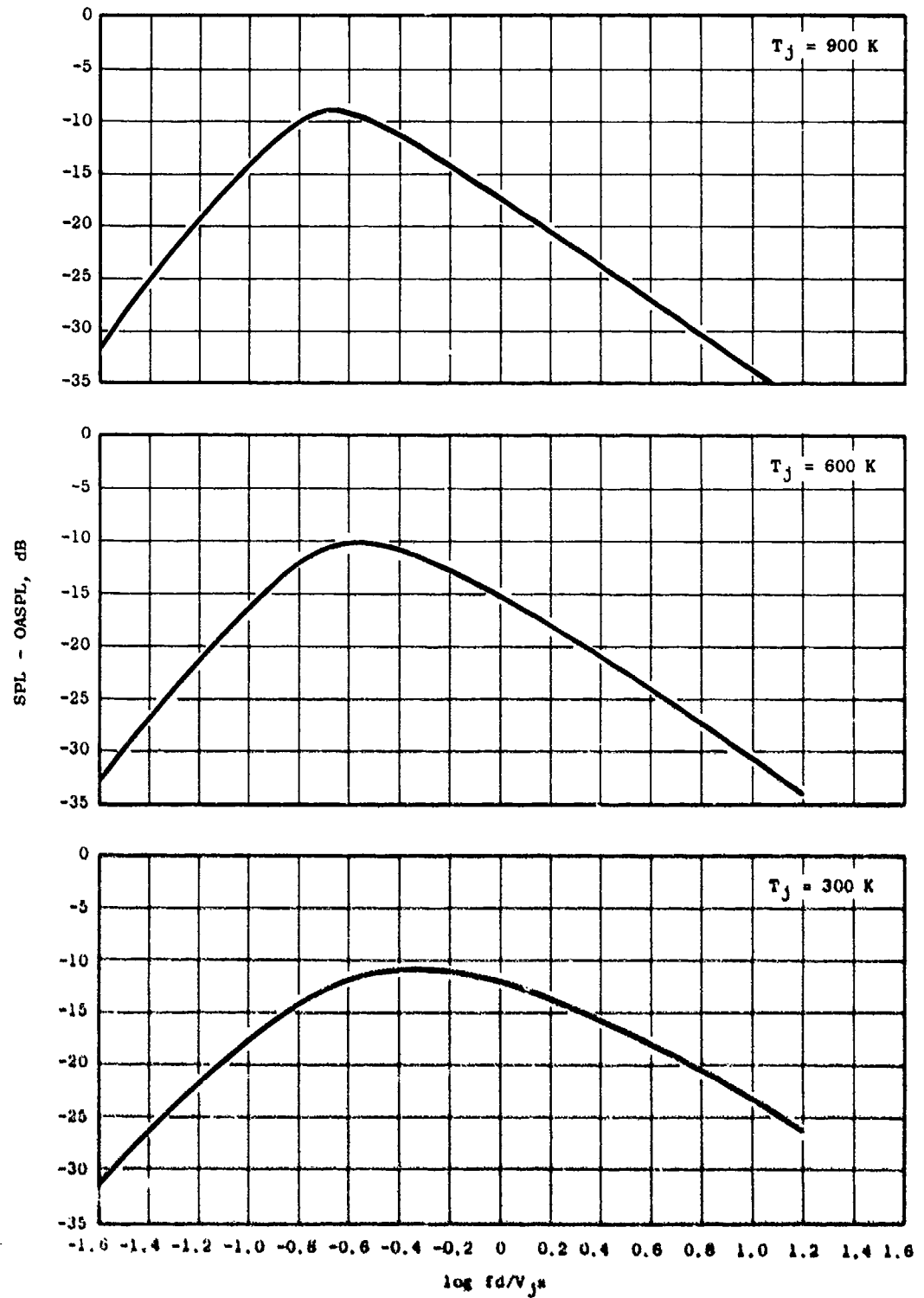


Figure C-8. Jet Noise Characteristics, 140° Angle to Intake Axis, 40° Angle to Jet Axis.

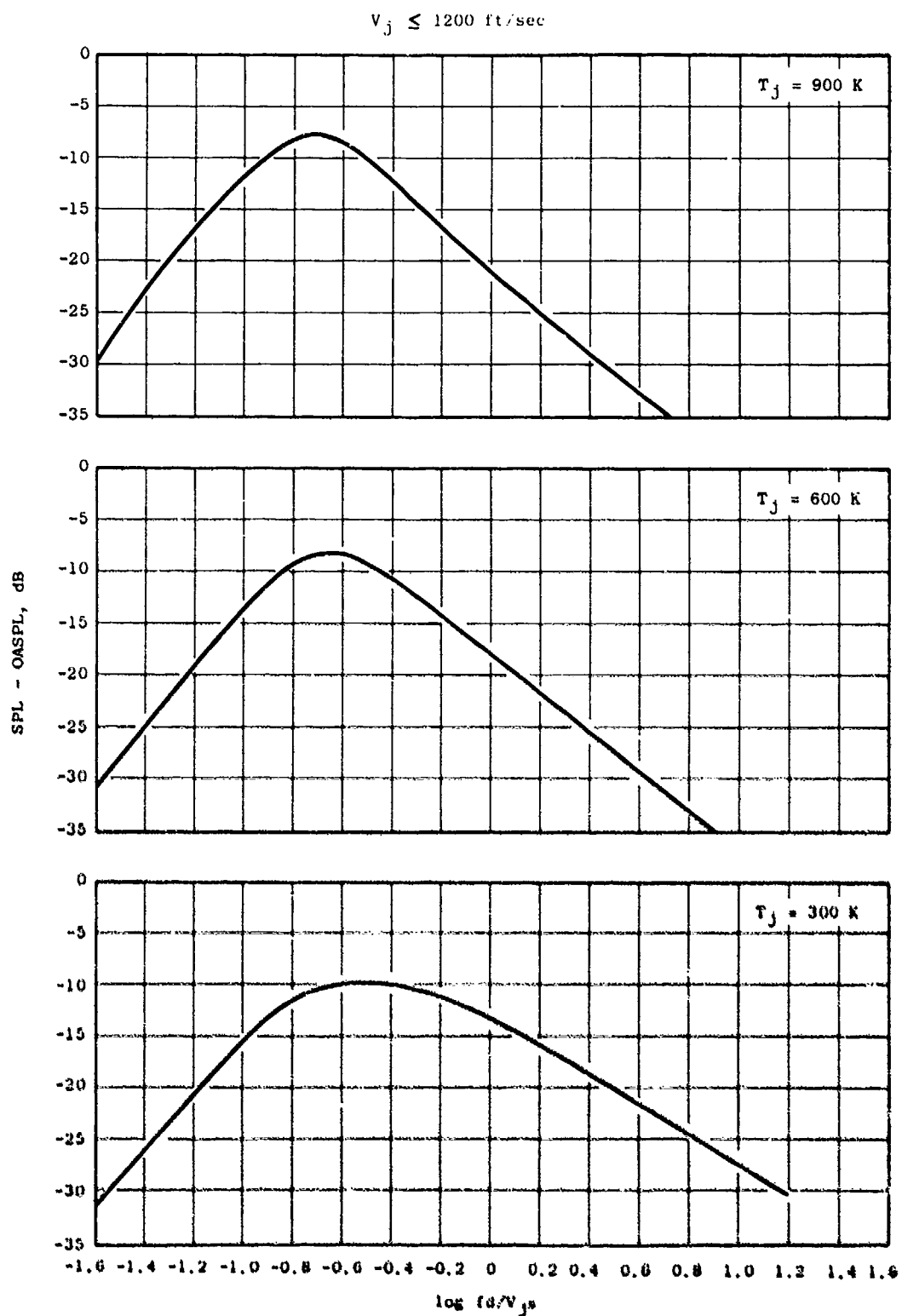


Figure C-9. Jet Noise Characteristics, 150° Angle to Intake Axis, 30° Angle to Jet Axis.

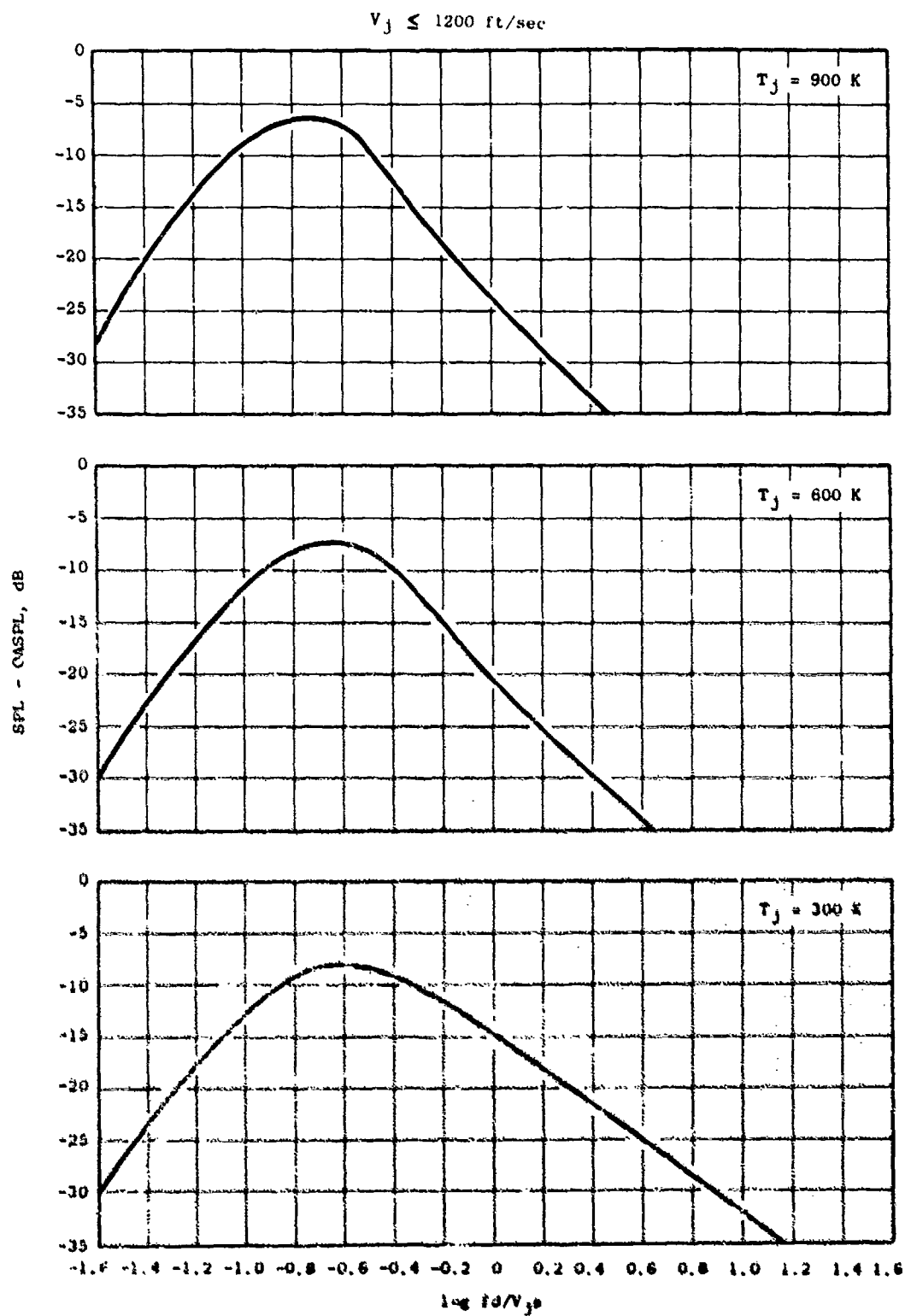


Figure C-10. Jet Noise Characteristics, 160° Angle to Intake Axis, 20° Angle to Jet Axis.

Step 4 - Calculate the overall sound pressure level (OASPL)
where:

$$\text{OASPL} = S + \omega \times 10 \log \left(\frac{\rho_j}{\rho_{15A}} \right) + 10 \log \left(\frac{A_j}{2} \right) \quad (\text{C-4})$$

Step 5 - Obtain one-third-octave band spectrum levels from Figures C-3 to C-10 using a knowledge of the jet velocity (V_j), the jet temperature (T_j), and the final nozzle diameter (D_j) to determine:

$$\log \frac{fd}{V_j s} \quad (\text{C-5})$$

where

$$V_j s = V_j \sin(\theta_j) + a_o (1 - \sin(\theta_j)) \quad (\text{C-6})$$

For angles and temperatures other than the values specified in Figures C-3 through C-10 linear interpolation is recommended.

Origins of Experimental Data For Appendix I - Experimental model rig data used in this appendix has been obtained from the following sources:

- General Electric, 1 Jimson Road, Cincinnati, Ohio, USA.
SAE Communication (W.G. Cornell to SAE-A21) 11th October 1972.
SAE Communication (W.G. Cornell to M.J.T. Smith)
14th May 1974.
SAE Communication (W.S. Fisk to M.J.T. Smith) 31st December 1974.
- Lockheed Georgia Company, Marietta, Georgia, U.S.A.
"Effect of Temperature on Supersonic Jet Noise" -
Tanner & Dean paper AIAA 73-991
October 1973.
"An Experimental Study of Shock-Free Supersonic Jet Noise"
-Tanner & Dean paper AIAA 75-480
March 1975.
- National Gas Turbine Establishment, Pyestock,
Farnborough, Hampshire, England.
Paper "Studies of the Influence of Density on Jet Noise" - Marseilles First International Symposium on Air Breathing Engines, June 1973.

Communication (B. Cocking to K. Bushell)
12th October 1973.

- Rolls-Royce (1971) Limited, Derby and Bristol, Engine.

Report INM 00067 8th September 1971.

Report GN 14181 4th October 1971.

Report INR 20142 22nd April 1972.

K.K. Ahuja and K.W. Bushell - An Experimental Study of Subsonic Jet Noise and Comparison With Theory. Journal of Sound and Vibration pp 317-341, 1973.
- Societe National d'Etude et de Construction de Moteurs d'Aviation, 77 Moissy-Cramayel, France.

Report 545ZA62 17th April 1970

Paper "Studies of the Influence of Density on Jet Noise" - Marseilles First International Symposium on Air Breathing Engines, June 1973.

Report YKA No. 4851/73 JPD/GM 14th September 1973.

Report YKA No. 5009/74 JPD/MTL 29th March 1974.

Report YKA No. 5317/75 RH/MTL 31st January 1975.
- The Boeing Company, Settle, Washington, USA.

Document No. D6-40604 2nd October 1972

Co-ordination Sheet No. ANS-RES-442
1st April 1973.

Co-ordination Sheet No. ANS-RES-512
18th March 1974.

N.B.: Engine data has been supplied by the above and other contributors listed below but has not been used in compiling the definitive curves and spectra, due to the probable presence of other sources. Nevertheless, comparisons have been made between the method and such engine data showing good agreement at frequencies where other sources are thought to have little influence.

Parties Contributing to Compilation of Appendix I

Douglas Aircraft Company, USA.

General Electric, USA.

Hamilton Standard, USA.

Lockheed California Company, USA.

National Aero & Space Administration, Langley, USA.

National Gas Turbine Establishment, United Kingdom.

Pratt & Whitney Aircraft Company, USA.

Rolls-Royce (1971) Limited, UK.

SNECMA, France.

The Boeing Company, USA.

Department of Transportation, USA.

APPENDIX D

PREDICTION OF SINGLE STREAM SHOCK-CELL NOISE - REVISED PROCEDURE

A prediction method for broadband, shock-cell noise was issued to the SAE on September 25, 1974. The method was based on a simplified version of the work of Harper-Bourne and Fisher.

The simplification was the assumption that the shock pattern was equally spaced along the jet axis. This assumption gave results which were unacceptable. In order to match the data, an empirical modification to the results was made.

A revised version of the method was issued to members on April 1, 1975. This method now includes a variable, shock-cell spacing. This method also included minor editorial changes. The prediction method which resulted is of a slightly different form from that given by Harper-Bourne and Fisher, and for this reason an appendix was issued which fully detailed the derivation of the method.

Prediction of Single-Stream, Shock-Cell Noise - In an incorrectly expanded, supersonic jet flow, shock waves will be formed which have a semiregular structure. The interaction of flow turbulence with this shock structure produces a noise source in addition to that associated with turbulent mixing.

This source has two components, one consists of harmonically related, discrete tones, often termed screech. This component is rarely, if ever, present in engine measurements because the acoustic feedback to the nozzle is interrupted due to nozzle-flow irregularities.

The other, more broadband yet strongly peaked source is usually termed shock-cell or shock-associated noise. This source is often significant in high speed jet flows, and it is for this source that the prediction method has been derived.

Method - The method given is based on the work of Harper-Bourne and Fisher.

The method of calculation is as follows:

$$SPL(f) = 10 \log_{10} \left[\frac{\beta^2 D_j}{r} \right]^2 H(f)$$

where $\beta = \sqrt{M_j^2 - 1}$

M_j = fully expanded jet Mach no. $\frac{V_j}{a_j}$

D_j = Nozzle diameter (ft)

r = Radial distance from source to observer (ft)

$$H(f) = G_{(sn)} \left(1 + \frac{2}{N} \sum_{i=1}^{N-1} C_{(sn)}^{(i)2} \sum_{s=0}^{N-(i+1)} \frac{\cos(F) \sin(F 0.115)}{F 0.115} \right) \quad (D-1)$$

$$F = \frac{2\pi f 1.31 \beta D_j}{0.7 V_j} \left\{ 1 + \frac{0.7 V_j}{a_o} \cos \theta_i \right\} \left\{ i \left[1 - 0.06 \left(\frac{i+1}{2} + s \right) \right] \right\} \quad (D-2)$$

V_j = Fully expanded jet velocity (ft/sec)

a_o = Ambient speed of sound (ft/sec)

θ_i = Angle to engine inlet axis (degrees)

f = One-third-octave, center-band frequency (Hz)

$$sn = \frac{f 1.1 \beta D_j}{a_o}$$

and values of $G_{(sn)}$ and $C_{(sn)}$ are shown in Figure D-1.

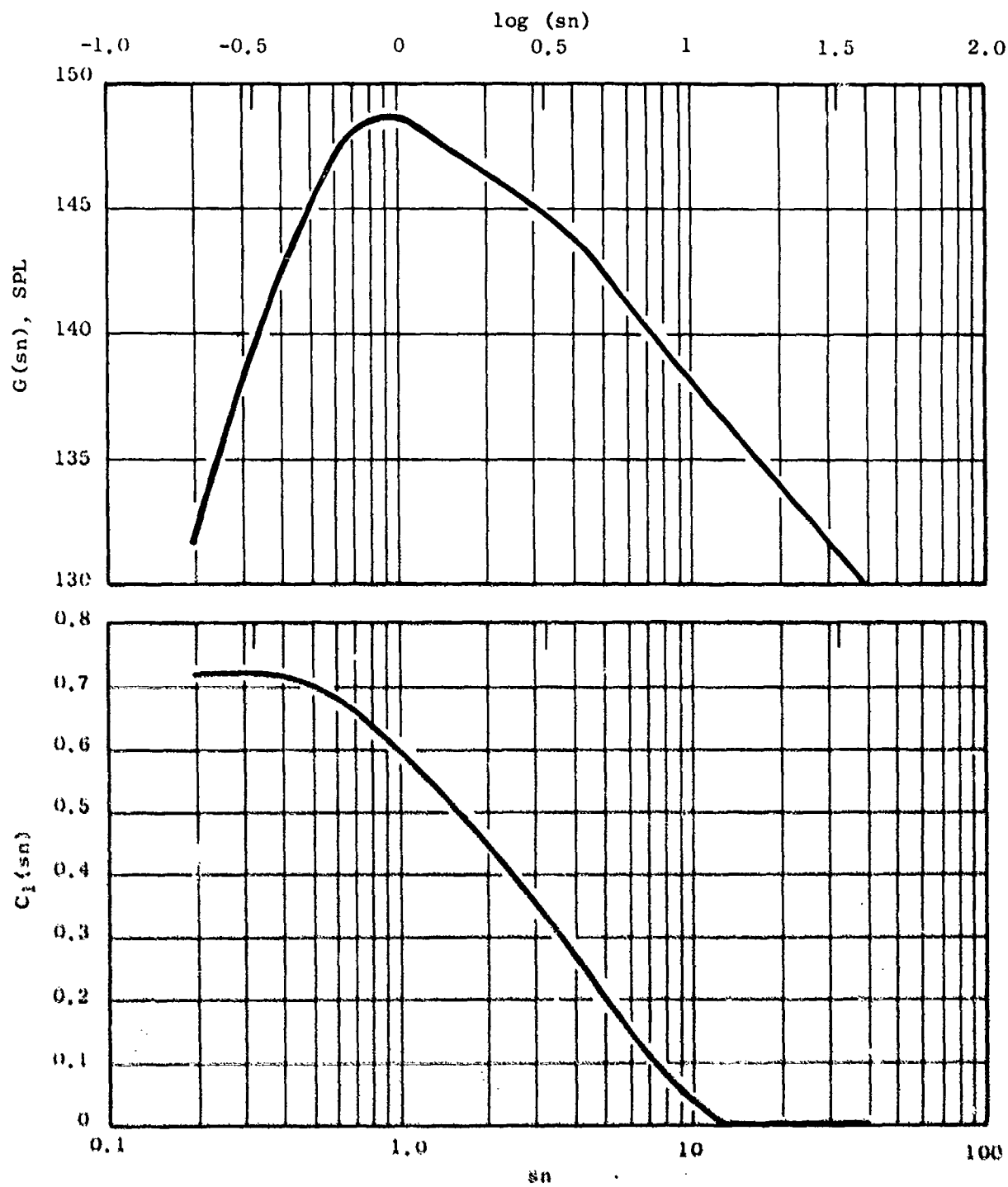


Figure D-1. Group Source Spectrum, $G(\text{sn})$, and Average Correlation Coefficient, $C_1(\text{sn})$.

LIST OF SYMBOLS

Symbol

A	Nozzle exhaust area, ft^2
a_0	Ambient speed of sound, ft/sec
AR	Suppressor area ratio; determined by the total nozzle area, excluding any plug, to the flow area of the nozzle
AR_{ej}	Ejector area ratio; determined by the ratio of the minimum flow area of the inlet to the ejector to the flow area of the nozzle
C, c	Speed of sound, ft/sec ; also constant pressure specific heat
D, d	Diameter, ft
f	One-third-octave band frequency, Hz
F_s	Ideal gross thrust, lb_f
K	Number of rows of tubes; also, variation in coannular jet noise with nozzle area ratio
L	Ejector length, ft
M	Jet Mach number
N	Number of elements
P	Pressure, $\text{lb}_f/\text{in.}^2$
PNL	Perceived noise level, PNdB
PNLT	Tone-corrected perceived noise level, PNdB
EPNL	Effective perceived noise level, EPNdB
PWL	Sound power level, $\text{dB re: } 10^{-13} \text{ watts}$
OAPWL	Overall sound power level
SPL	Sound pressure level, $\text{dB re: dynes/in.}^2$
OASPL	Overall sound pressure level
R	Acoustic treatment resistance rays; also, noise measurement radius, ft

LIST OF SYMBOLS (Continued)

Symbols

R_r	Suppressor radius ratio, determined by the ratio of the inner radius to the outer radius for the particular flow passage
R_g	Centerbody plug radius, ft
S	Distance, ft
T	Temperature, ° R
U, V	Jet velocity, isentropic, fully expanded, ft/sec
W	Weight flow rate, lbm/sec
X	Axial distance, ft; also, acoustic treatment specific reactance, rayls
α_a	Effective absorption coefficient
β	Cant angle, degrees; also, $\sqrt{M^2-1}$
γ	Ratio of specific heats
δ	Mixing zone radius, ft
Δ	Difference in noise from a conical nozzle due to a bypass stream, dB
θ	Angle, degrees
θ_i	Angle of incidence, degrees
θ_c	Critical refraction angle, degrees
λ	Wavelength, ft
ρ	Density, lbm/ft ³
ω	Density ratio exponent

Superscript

i	Inner stream
o	Outer stream

LIST OF SYMBOLS (Concluded)

Symbol

Subscript

a, ISA, 0	Ambient or aircraft conditions
c	Potential core
eff	Effective
ej	Ejector conditions
eq	Equivalent dimension based on flow area = $\sqrt{4A/\pi}$
H	Hard wall
i	Inner stream
I, i	Inlet conditions
J, j	Jet (exhaust) conditions
M, S	Merged or mean conditions
mix, ma	Mixed or mass average conditions
n	Nozzle condition
o	Outer row/outer stream
p	Initial noise generation; also, peak
p, peak	Peak
S	Static
s	Suppressor
T, t	Total condition, tube, or treated
1	Individual tube
2	Nozzle outer diameter
3, 8	Conditions at core Nozzle exit (fully expanded)

REFERENCES

1. Lee, R., Kendall, R.M., et al., "Research Investigation of the Generation and Suppression of Jet Noise," General Electric Company, NOas 59-6160-C, January 1961.
2. Simcox, C.D., et al., "SST Technology Follow-On Program - Phase I - A Summary of the SST Jet Noise Suppression Test Program, Boeing Company, FAA-SS-72-41, February 1972.
3. Brausch, J.F. and Doyle, V.L., "Summary of GE4/SST Acoustic Suppression Research, Supersonic Transport Noise Reduction Technology Program, Phase I," General Electric Company, FAA-SS-72-42, December 1972.
4. Stringas, E.J. and Kazin, S.B., "Supersonic Transport Noise Reduction Technology Program - Phase II," General Electric Company, FAA-SS-73-29-1, September 1975.
5. Atvars, J., et al.; "SST Technology Follow-On Program - Phase II," Boeing Company, FAA-SS-73-11, March 1975.
6. Hawkins, R. and Hoch, R., "Studies Into Concorde's Engine Noise Reduction," NATO, AGARD-CPP-131.
7. Mani, R., and Stringas, E.J., "High Velocity Jet Noise Source Location and Reduction - Task 2 - Theoretical Developments and Basic Experiments," General Electric Company, FAA-RD-76-79, II, May 1978.
8. Howes, W.L., Callaghan, E.E., Coles, W.D., and Null, H.R., "Near Noise Field of a Jet Engine Exhaust," NACA Report 1338, 1957.
9. Potter, R.C. and Jones, J.H., "An Experiment to Locate the Acoustic Sources in a High Speed Jet Exhaust Stream (Preliminary Results)," Wyle Lab Report, November 1967.
10. "DOT/SST Technology Program Low Noise Nozzle System Development," The Boeing Co., Progress Report Presented to FAA, November 16, 1972.
11. Chen, C.Y., "Calculation of Supersonic Jet Flow with Different Turbulence Levels at the Jet Exit," GE Internal Memo, February 1970.
12. Eggers, J.M., "Velocity Profiles and Eddy Viscosity Distribution Downstream of a Mach 2.22 Nozzle Exhausting Into Quiescent Air," NASA TND-3601, 1966.
13. Trevett, E.G., "Velocity Measurement in a Jet from a Convergent Nozzle," Rolls Royce Report AP5531, 1968.
14. Plumblee, H.E., et al., "The Generation and Radiation of Supersonic Jet Noise," Final Report, Contract No. F33615-73-C-2032, December 1975.

15. Laurence, J.C., "Intensity, Scale and Spectra of Turbulence in Mixing Region of Free Subsonic Jet," NACA Report 1292, 1956.
16. Benzakein, M.J. and Knott, P.R., "Supersonic Jet Exhaust Noise," General Electric Company, AFAPL-TR-72-52, August 1972.
17. Knott, P.R., "Supersonic Jet Exhaust Noise Investigation," General Electric Company, AFAPL-TR-74-25, June 1974.
18. Pitkin, E.T. and Glassman, "Experimental Mixing Profiles of a Mach 2.6 Free Jet, ASTIA AD-202294, August 1958.
19. Anderson, A. and Johns, E., "Non-Dimensional Characteristics of Free and Deflected Supersonic Jets Exhausting Into Quiescent Air," NADC-ED-5401, March 1954.
20. Warren, W.R. "An Analytical and Experiments Study of Compressible Free Jets," Doctoral Dissertation, Princeton University, 1957.
21. MacGregor, G.R., and Simcox, C.D.; "The Location of Acoustic Sources in Jet Flows by Means of the Wall Isolation Technique," AIAA Paper 73-1041, October 1973.
22. Nagamatsen, H.J., Sheer, R.E. Jr., and Gill, M.S., "Flow and Acoustic Characteristics of Subsonic and Supersonic Jets From Convergent Nozzle," Final Report Contract No. NASW-1784, July 1969.
23. Ollerhead, J.B., "Some Shadowgraph Experiments with a Cold Supersonic Jet," Wyle Research Report WR 66-44, October 1966.
24. Faris, G.N. "Some Entrainment Properties of a Turbulent Axi-Symmetric Jet," Mississippi State University Aerophysics Dept., Research Report No. 39, January 1963.
25. Clapper, W.S., et al., "Development/Evaluation of Techniques for 'Inflight' Investigation," General Electric Company, FAA-RD-74-79, IV, February 1977.
26. Eldred, K.M., et al., "Suppression of Jet Noise with Emphasis on the Near Field," ASD-TDR-62-578, February 1963.
27. Middleton, D. and Clark P.J.F, "Assessment and Development of Methods of Acoustic Performance Prediction for Jet Noise Suppressors," UTIAS TN No. 134, AFUSR 69-0780 TR, April 1969.
28. Gray, V.H., Gutierrez, O.A., and Walker, D.Q., "Assessment of Jets as Acoustic Shields by Comparison of Single and Multitube Suppressor Nozzle Data," NASA TMX-71450, October 1973.

29. Potter, R.C., and Crocker, M.J., "Acoustic Prediction Methods for Rocket Engines, Including the Effects of Clustered Engines and Deflected Exhaust Flow," NASA CR-566, October 1966.
30. Sokolnikoff, I.S. and Redshaffer, R.M., Mathematics of Physics and Modern Engineering, McGraw-Hill Book Co. Inc., 1958.
31. "Definitions and Procedures for Computing the Perceived Noise Level of Aircraft Noise," SAE, ARP 865, October 1964.
32. "Gas Turbine Jet Exhaust Noise Prediction," SAE, ARP 876 (Proposed), July 1975.
33. "Prediction of Single Stream Shockcell Noise," SAE, ARP 876 (Proposed), April 1975.
34. "Standard Values of Atmospheric Absorption as a Function of Temperature and Humidity for Use in Evaluating Aircraft Flyover Noise," SAE, ARP 866, August 1964.
35. "Method of Calculating the Attenuation of Aircraft Ground-to-Ground Noise Propagation During Takeoff and Landing," SAE, AIR 923, August 1965.
36. Zorumski, W.E., Brown, C.G., Andre, M.L., and Kapper, C.P., "An Evaluation of Circular Jet Noise Prediction Methods with Respect to the Lockheed Turbulent Jet Mixing Noise Experiments," September 1976.
37. Bilwakesh, K.R., et al., "Core Engine Noise Control Program," General Electric Company, FAA-RD-74-125, August 1974.
38. Knott, P.R., et al., "Acoustic Tests of Duct Burning Turbofan Jet Noise Simulation," General Electric Company, NASA Contract Report 2966, July 1978.
39. Kozlowski, H. and Packman, A.B., "Aero-Acoustic Tests of Duct-Burning Turbofan Exhaust Nozzles," NASA CR-134910, July 1976.
40. Atvars, J., et al., "Development of Acoustically Lined Ejector Technology for Multitube Jet Noise Suppressor Nozzles by Model and Engine Tests Over a Wide Range of Jet Pressure Ratios and Temperatures," Boeing Company, NASA CR-2382, April 1974.
41. Lighthill, M.J., "On Sound Generated Aerodynamically, 1. General Theory," *Proceedings of the Royal Society London*, Vol. A211, 1952, pp. 564-587.
42. Ribner, H.S., "Aerodynamic Sound From Fluid Dilations - A Theory of the Sound from Jets and Other Flows," UTIA Report No. 86, July 1962.
43. Ffowcs-Williams, J.E., "The Noise from Turbulence Convected at High Speed," *Phil. Trans. Roy. Soc. Lond.*, Vol. A255, 1963, pp. 469-503.

44. Ahuja, K.K. and Bushell, K.W., "An Experimental Study of Subsonic Jet Noise and Comparison with Theory," *Journal of Sound and Vibration*, Vol. 30, No. 3, 1973, pp. 317-341.
45. Lush, P.A., "Measurements of Subsonic Jet Noise and Comparison with Theory," *Journal of Fluid Mechanics* Vol. 46, Part 3, 1971, pp. 477-500.
46. Hoch, R.G., Duponchel, J.P., Cocking, B.J., and Bryce, W.D., "Studies of the Influence of Density on Jet Noise," *Journal of Sound and Vibration*, Vol. 28, No. 4, 1973, pp. 649-668.
47. Phillips, O.M., "On the Generation of Sound by Supersonic Turbulent Shear Layers," *Journal of Fluid Mechanics*, Vol. 9, 1960, pp. 1-28.
48. Lilley, G.M., Morris, P.J., and Tester, B.J., "On the Theory of Jet Noise and Its Applications," AIAA paper No. 73-987, October 1973.
49. Goldstein, M.E. and Howes, W.L., "New Aspects of Subsonic Aerodynamic Noise Theory," NASA TN D-7158, 1973.
50. Rao, S.P., "Analytical Properties of Noise Generating Mechanisms in a Supersonic Jet Exhaust Flow," NASA CR-1848, May 1971.
51. Tester, B.J. and Burrin, "On Sound Radiation from Sources in Parallel Sheared Jet Flows," AIAA paper No. 74-57, January 1974.
52. Berman, C.H., "Noise From Nonuniform Turbulent Flows," AIAA paper No. 74-2, January 1974.
53. Schubert, L.K., "Numerical Solution of Sound Refraction by Jet Flow, Parts I and II," *Journal of the Acoustical Society of America*, Vol. 51, No. 2, 1972, pp. 439-463.
54. Powell, A., "Concerning the Noise of Turbulent Jets," *Journal of the Acoustical Society of America*, Vol. 32, No. 12, 1960, pp. 1609-1612.
55. Csandy, G.T., "The Effects of Mean Velocity Variations on Jet Noise," *Journal of Fluid Mechanics*, Vol. 26, Pt. 1, 1966, pp. 183-197.
56. Mani, R., "A Moving Source Problem Relevant to Jet Noise," *Journal of Sound and Vibration*, Vol. 25, No. 2, 1972, pp. 337-347.
57. Mani, R., "Further Studies on Moving Source Solutions Relevant to Jet Noise," *Journal of Sound and Vibration*, Vol. 35, No. 1, 1974, pp. 101-117.
58. Mani, R., "The Jet Density Exponent Issue for the Noise of Heated Subsonic Jets," *Journal of Fluid Mechanics*, Vol. 64, Part 3, 1974, pp. 611-622.

59. Mani, R., "The Influence of Jet Flow on Jet Noise, Part 1. The Noise of Unheated Jets," Journal of Fluid Mechanics, Vol. 73, Part 4, 1976, pp. 753-778.
60. Mani, R., "The Influence of Jet Flow on Jet Noise. Part 2. The Noise of Heated Jets," Journal of Fluid Mechanics, Vol. 73, Part 4, 1976, pp. 779-793.
61. Harper-Bourne, M. and Fisher, M.J., "The Noise From Shock Waves in Supersonic Jets," NATO, AGARD Conference Paper No. CPP-131, 1973.
62. Drevit, P., Duponchel, J.P., and Jacques, J.R., "Effect of Flight on the Noise From a Convergent Nozzle as Observed on the Bertin Aerotrain," AIAA paper No. 76-557, July 1976.
63. Siddon, T.E., "Investigations of Nozzle Lip Noise," interim progress report, University of British Columbia, Dep't of Mech. Eng'rg, UBC-GE/DOT OS-30034, June 1975.
64. Browand, F.K., Chu, W.T., and Laufer, J., "Exploratory Experiments on the Engrance Effects in Subsonic Jet Flows," University of Southern California Dep't. of Aerospace Eng'rg. report No. USCAE 130, April 1975.
65. Reichardt, H., "New Theory of Free Turbulence," Royal Aeronautical Society Journal, Vol. 47, 1943, pp. 167-196.
66. Alexander, L.G., Baron, T., and Comings, W., "Transport of Momentum, Mass and Heat in Turbulent Jets," University of Illinois Engineering Bulletin No. 413, May 1953.
67. Lee, R., Kendall, R., et al., "Research Investigation of the Generation and Suppression of Jet Noise," General Electric, WDas-59-6160-C, ASTIA No. AD-251887, 1961.
68. Grose, R.D. and Kendall, R.M., "Theoretical Predictions of the Sound Produced by Jets Having an Arbitrary Cross-Section," A.S.N.E. Symposium on Fully Separated Flows, May 1964.
69. Gliche, P.R. and Balsa, T.F., "The Aerodynamics and Acoustics of Coaxial Jet Noise," AIAA paper No. 76-492, July 1976.
70. Balsa, T.F., "Fluid Shielding of Low Frequency Convected Sources by Arbitrary Jets," Journal of Fluid Mechanics, Vol. 70, Part 1, 1975, pp. 17-36.
71. Balsa, T.F., "The shielding of a Convected Source by an Annular Jet with an Application to the Performance of Multitube Suppressors," Journal of Sound and Vibration, Vol. 44, No. 2, 1976, pp. 179-189.

72. Balsa, T.F., "The Far Field of High Frequency Convected Singularities in Sheared Flows, With Application to Jet-Noise Prediction," Journal of Fluid Mechanics, Vol. 74, Part 2, 1976, pp. 193-208.
73. Davis, P.O.A.L., Fisher, M.J., and Barratt, M.J., "The Characteristics of the Turbulence in the Mixing Region of a Round Jet," Journal of Fluid Mechanics, Vol. 15, 1963, pp. 337-367.
74. Ribner, H.S., "Quadrupole Correlations Governing the Pattern of Jet Noise," Journal of Fluid Mechanics, Vol. 38, Part 1, 1969, pp. 1-24.
75. Ribner, H.S., "Shock-Turbulence Interaction and the Generation of Noise," NACA report No. 1233, 1955.